University of Strathclyde

Department of Pure and Applied Chemistry

Assessment of Novel Measurement Technologies for Process Monitoring and Use of Chemometric Advances to Facilitate Their Application

Catriona McFarlan

A thesis submitted to the Department of Pure and Applied Chemistry, University of Strathclyde, Glasgow, in part fulfilment of the regulations for the degree of Doctor of Philosophy.

March 2020

Copyright

Abstract

Mid-infrared (MIR) spectroscopy and nuclear magnetic resonance (NMR) spectroscopy are common laboratory techniques, but are not so widely used in process analysis. The high attenuation of MIR light inhibits the ability to locate delicate instruments away from harsh processes using long lengths of optical fibre, and the large size and cost of high-field NMR spectrometers prevent them from being easily installed in process plants. Recent advances in technology have led to the availability of miniaturised, robust MIR spectrometers and benchtop NMR spectrometers operating at low field.

The performance of a novel, robust MIR spectrometer, designed for use in process environments, was assessed for the quantitative *in situ* analysis of liquids and was found to be comparable to a laboratory MIR spectrometer. A reaction was then monitored using the novel spectrometer and accurate predictions of concentration could be obtained by multivariate curve resolution. This demonstrates the suitability of the spectrometer for *in situ* process monitoring. Calibration transfer between the two MIR spectrometers was also performed, demonstrating the ability to build a model in the laboratory for subsequent application to a process.

The instrumental stability of a low-field NMR spectrometer was evaluated, and when multiple samples were analysed, shifting of peaks and deterioration of lineshape occurred over time. To eliminate peak shift, a range of alignment methods were assessed. Alignment was successful for small peak shifts, but less effective when large peak shifts were present. However accurate predictions of concentration could still be obtained by PLS. Calibration transfer and reference deconvolution were compared as a solution to lineshape deterioration, and the transfer of PLS models between low-field NMR spectra collected under different conditions was demonstrated. Calibration transfer was found to be more effective overall, and produced accurate predictions of concentration. These results demonstrate the suitability of low-field NMR spectroscopy for quantitative analysis.

Acknowledgements

I would firstly like to thank my supervisor Dr Alison Nordon for her expertise, guidance and support over the past four years. I would also like to thank Dr Andrew Parrott for all of his help throughout, particularly with the NMR spectroscopy work.

Thank you to Dr Jaclyn Dunn for her assistance with the mid-infrared spectroscopy work and for helping me to get started. I would also like to acknowledge Molly Hogg, a final year project student involved with the mid-infrared spectroscopy calibration transfer work.

In addition, I would like to thank Keit spectrometers for the use of their instrument, and Professor Paul Gemperline of East Carolina University for kindly providing me with a copy of GUIPRO software.

I would like to acknowledge CPACT and EPSRC for providing the funding which made this research possible.

Lastly I would like to thank the Analytical Chemistry group and the Postgraduate Society for making this an enjoyable four years.

Contents

1 Introduction

Process analysis provides information which can be used to monitor and control chemical processes in industry. The ability to monitor processes in real time is important as it allows quality control, optimisation of the process and the ability to quickly detect and solve any problems which arise. This can save time and resources, as well as ensuring safety. Analysis can be performed off-line, at-line or on-line. In off-line analysis, samples from the process are transferred to a central laboratory located elsewhere. Although this allows the use of more sophisticated instruments, it results in a time delay so the measurements cannot be used for process control. At-line analysis is an alternative, in which samples are transported to an analyser located near the process to save time. However manual sampling is necessary, so the analysis cannot be automated.[1-3]

On-line analysis involves the location of an analyser within the manufacturing environment, and allows measurements to be made in real time. Samples can be extracted from the process (e.g. using a flow system) or measurements can be carried out *in situ*, either non-invasively or by inserting a probe into the mixture (in-line analysis).[1-3] The requirements of on-line process analysers differ to those of laboratory based instruments. Process environments are often harsh, therefore instruments need to be able to withstand vibrations and elevated temperature/pressure. Smaller instruments are more suitable as they are easier to install in process environments, and less flexibility is required as analysers normally have a dedicated application.[4]

Optical spectroscopy techniques provide a number of advantages in process analysis. They are fast, non-destructive, do not require sample preparation or extractive sampling and can be used *in situ*.[2, 5-7] This allows them to provide continuous information in real time. Near infrared (NIR) spectroscopy is one of the most widely used techniques in process analysis and is employed in a variety of industries, including the pharmaceutical industry,[2, 8] the food industry,[9] the chemical and petrochemical industry,[10, 11] and the biotechnology industry.[12] The low absorptivity of NIR light allows long pathlengths (in the order of mm), and NIR light can easily be transmitted through optical fibres made of silica or quartz to allow remote analyses to be carried out.[5, 13, 14] This avoids exposure of the analyser to harsh conditions and

allows the use of a single analyser to carry out measurements from multiple sampling points. However NIR spectra arise from overtones and combinations of the fundamental molecular vibrations, thus peaks are broad and extensively overlapped. The interpretation of NIR spectra can therefore be challenging.[5, 13, 15]

More detailed spectra can be obtained using Raman spectroscopy, which produces strong bands of high chemical specificity.[2, 15, 16] Raman spectroscopy is therefore well suited to qualitative analysis and can be used to provide detailed information on the structures of molecules, e.g. in the pharmaceutical industry,[16, 17] polymer analysis[17, 18] and biomedical analysis.[17, 18] The weak scattering of water means that Raman spectroscopy can be easily applied to aqueous systems, making it particularly useful in bioprocess monitoring.[15, 19] Fibre optics can also be used to allow remote analysis.[16, 20] The main disadvantage of Raman spectroscopy is that fluorescence can produce noise in the spectra or even obscure the Raman signal.[19, 21] Quantitative analysis can also be difficult as the intensity of the peaks is dependent on a number of factors in addition to concentration, such as the intensity of the incident light, the optical configuration of the instrument and the particle size of solid samples.[16]

Gas chromatography, particularly when coupled to a mass spectrometer (GC-MS), has also been utilised extensively for on-line analysis, e.g. in the petrochemical industry and the food industry.[2, 22] GC-MS is able to provide detailed information on the chemical composition of a variety of analytes, and can simplify the analysis of mixtures by separation of the components.[2, 21] However extractive sampling is required, the technique is destructive and it is time consuming compared to optical spectroscopy.[1, 19] This inhibits the ability to perform real-time monitoring of reactions.

Mid-infrared (MIR) spectroscopy is a particularly sensitive form of optical spectroscopy and produces defined spectra with highly distinct peaks.[5, 23, 24] This provides a major advantage over NIR spectroscopy. Quantitative information can be obtained more easily than with Raman spectroscopy (as the absorbance of an analyte is proportional to its concentration), and fluorescence is not an issue.[21, 25] In addition, MIR spectroscopy provides complementary information to Raman spectroscopy, as functional groups which exhibit weak Raman scattering often produce strong infrared bands.[21]

A disadvantage of optical spectroscopy is that only functional groups can be detected, so it may not always be possible to deduce the full structure of molecules. Nuclear magnetic resonance (NMR) spectroscopy can be used to deduce molecular structure based on the chemical shifts and splitting patterns of peaks, which provides a major advantage over optical spectroscopy.[26-28] NMR spectroscopy is also inherently quantitative.[27, 28] In addition, it is non-destructive, highly reproducible and sample preparation is simple.[29] However compared to other techniques such as optical spectroscopy, the sensitivity of NMR spectroscopy is relatively low.[28-30]

Although MIR spectroscopy and NMR spectroscopy are common laboratory techniques, they have not been so widely used in process analysis. This is due to difficulties in locating the spectrometers in process environments. Traditional laboratory based MIR spectrometers are expensive, delicate and generally large, so are unsuitable for use in harsh environments.[12, 31, 32] The fibre optic materials used for the transmission of NIR light are unsuitable for the transmission of MIR light, as attenuation is too high. This inhibits the ability to locate delicate instruments away from the process.[5, 33] Chalcogenide glasses (based on As_2S_3) and polycrystalline silver halides ($AgCl_{1-x}Br_x$) are alternative materials which can transmit in the MIR region.[5, 12, 25, 33] Chalcogenide glasses cover the range 1700 – 6700 cm^{-1} and polycrystalline silver halides cover the range 600 – 3300 cm^{-1}.[12, 34] However the usable length of fibre is limited to less than 5 m, as attenuation is high due to absorption and scattering, and increases with distance. Silver halide fibres also have short lifetimes, becoming opaque with time.[5, 33]

The superconducting magnets used in high-field NMR spectrometers are extremely large and expensive, and require cryogenic cooling. Therefore these instruments are unsuitable for installation in process environments.[30] Recent advances in technology have facilitated the availability of robust, miniaturised MIR spectrometers suitable for process analysis and benchtop NMR spectrometers capable of achieving sub-ppm resolution at low field. These advances are the focus of this research, and will be discussed in more detail in the following sections.

1.1 Mid-Infrared Spectroscopy

1.1.1 Applications in Process Analysis

The sensitivity and molecular specificity of MIR spectroscopy provide a major advantage in process analysis, and the use of MIR spectroscopy to monitor a variety of different reactions has been demonstrated. Examples include on-line[35] and *in situ*[36] monitoring of esterification reactions, *in situ* monitoring of polymerisation reactions,[37, 38] on-line[39-41] and *in situ*[42] monitoring of bioprocesses, and on-line monitoring of the kinetics of a consecutive organic reaction.[43] A NIR/MIR dual region spectrometer has also been developed for the on-line analysis of ethanol fermentation.[13] It has a transmission probe for NIR spectroscopy and an ATR probe for MIR spectroscopy, and the different probes can be used by switching the light path.

The ability to perform quantitative analysis is also an advantage of MIR spectroscopy. To resolve the spectra of mixtures into their pure component contributions, calibration models such as partial least squares (PLS) are most commonly used. However calibration-free methods such as multivariate curve resolution (MCR) have also been demonstrated[44-46] to avoid the need to build calibration models. These methods of data analysis will be described in more detail in Chapter 2.

Some commercially available fibre-coupled MIR spectrometers have been designed to provide real-time *in situ* reaction monitoring, e.g. the Mettler-Toledo ReactIR[47] and the Bruker MATRIX-MF.[48] These instruments utilise diamond or silicon ATR crystals, silver halide fibre-coupled probes, mercury-cadmium-telluride (MCT) or deuterated triglycine sulfate (DTGS) detector technology and moving part interferometers. The use of the ReactIR spectrometer to monitor a range of different reactions *in situ* has been demonstrated, e.g. polymerisation,[49-51] fermentation,[52] active pharmaceutical ingredient manufacturing,[53] and silicon network formation reactions.[54] The disadvantages of such spectrometers are that the presence of moving parts may result in sensitivity to vibrations, and the length of optical fibre which can be used is limited.

In order for spectrometers to be robust enough to operate under particularly harsh process conditions (for example large amounts of vibration), an absence of moving parts is desirable. The majority of the above examples utilise FTIR spectrometers

containing moving part interferometers, therefore these instruments may not be able to withstand such environments. In addition, the miniaturisation of spectrometers would facilitate their installation in process environments. Over the past couple of decades, novel technologies such as quantum cascade lasers (QCLs), filters based on micro electro mechanical systems (MEMS) and uncooled detector arrays have become available. This has resulted in a drive towards the miniaturisation of spectrometers, to allow their use outwith laboratory environments and reduce their cost.[55-57] The recent advances in each MIR spectrometer component will be discussed in turn.

1.1.2 Advances in Instrumentation

1.1.2.1 Light Sources

Thermal blackbody light sources such as silicon carbide globars are conventionally used in MIR spectroscopy. They emit broadband light over the whole MIR region, but limited energy density is possible for a given wavelength.[7, 25] Synchotron radiation is an alternative broadband MIR source, produced by ring accelerators or free-electron lasers. It allows generation of extremely bright radiation, but is not widely used due to the complexity of the setup.[25] A disadvantage of broadband light sources is that the use of an interferometer or filter is required, which may make it more difficult to reduce the size of the spectrometer.[25, 56]

QCLs have a number of advantages over broadband sources of MIR radiation. They are a type of semiconductor laser, first demonstrated in 1994 by Faist et al.[58] Semiconductor diode lasers, e.g. lead salt diode lasers, have been used in the past but required cryogenic cooling and were only able to operate at very low power levels.[59, 60] The operation of semiconductor diode lasers involves recombination of electrons from the conduction band and holes from the valence band to produce photons, with a wavelength dependent on the size of the band gap and thus the semiconductor material. QCLs, however, consist of a series of coupled quantum wells (heterostructured layers) of varying thickness, e.g. an InGaAs/AlInAs/InP system. The potential of the coupled quantum wells depends on the thicknesses of the layers present, so a “potential staircase” of energy subbands is formed. As electrons travel down the “potential staircase”, photons are emitted with each intersubband transition, as shown in Figure 1.1. The emission wavelength is dependent on the thickness of the active layer rather

than the material used, thus can be easily altered without having to use different materials. QCLs are referred to as “unipolar lasers”, since the photons are generated by electrons alone.[58, 60, 61]

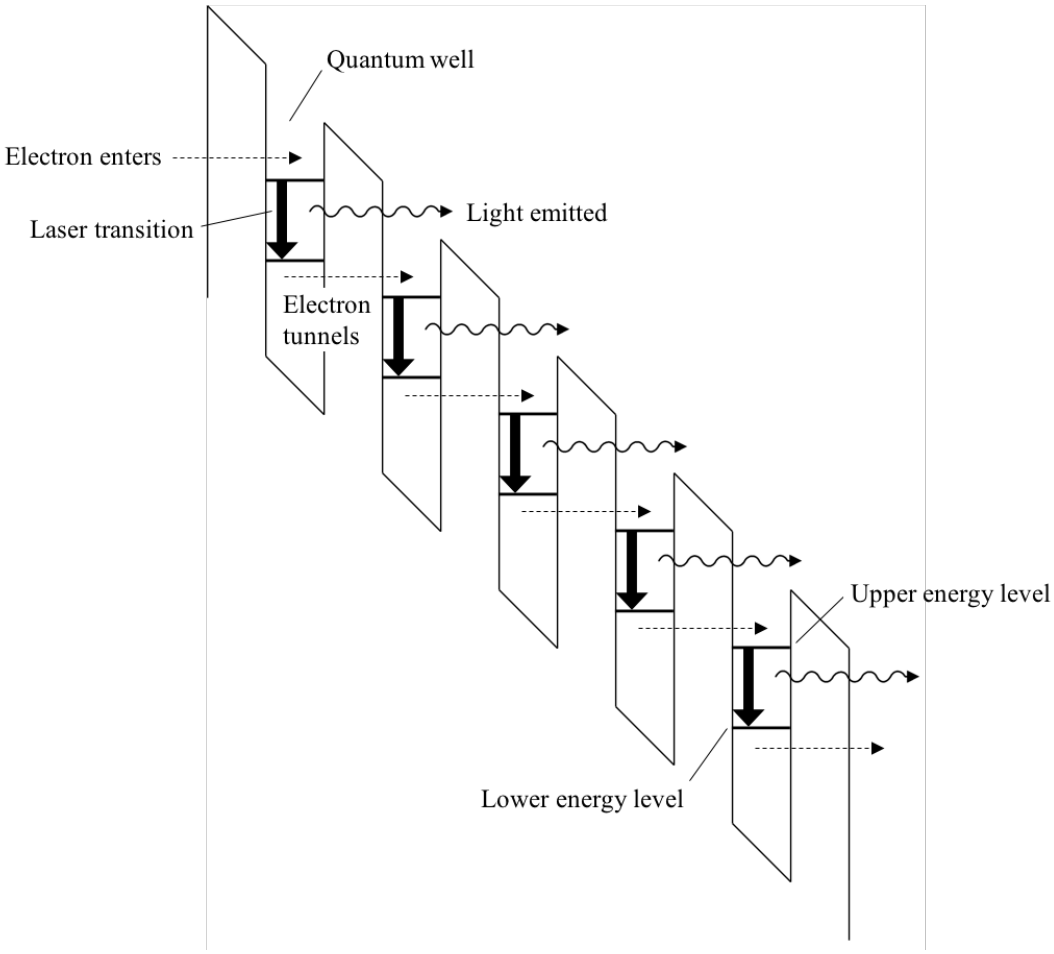

Figure 1.1 - Operation of quantum cascade laser, reproduced from reference 62.

Continuous-wave emission of QCLs was initially only possible at cryogenic temperatures, but significant advances have been made since they were first demonstrated and in 2001 the operation of QCLs at room temperature was first reported.[63] The inclusion of a diffraction grating in the laser cavity to control the emitted wavelength gives an external cavity quantum cascade laser (EC-QCL). EC-QCLs can be tuned to emit different wavelengths, and the linewidth of the emitted light is narrow, thus EC-QCLs are suitable for use as light sources in spectrometers.[64] High power continuous-wave EC-QCLs able to operate at room temperature are now commercially available across the MIR region up to approximately 3000 cm^{-1}, and can be tuned through more than 100 cm^{-1} by rotation of the diffraction grating.[59, 64-66] They

are ideal radiation sources for use in miniaturised spectrometers as they are compact, robust and sensitive.[61, 67] A range of QCLs are commercially available, for example Daylight Solutions offers a range of fixed wavelength and tunable QCLs operating across the region 800 – 3000 cm^{-1} and tunable up to 1000 cm^{-1}.[68] Block Engineering offers QCL sources with the widest gap-free tuning range on the market, covering the region 780 – 1850 cm^{-1}.[69]

Widely tunable QCLs operating in the range 1100 – 1600 cm^{-1} without external cavities have recently been demonstrated.[70] A broadband QCL wafer is monolithically integrated with an array of eight sampled grating distributed feedback (SGDFB) lasers and a beam combiner on a single chip, creating a compact laser system. The QCL wafer is heterogeneous with five cores, and functions as the laser gain medium. The use of SGDFB lasers broadens the QCL tunability by an order of magnitude. The system contains no moving parts and allows broadband spectroscopy to be carried out rapidly. Spectral measurement of methane was demonstrated using the laser system and the results were found to be comparable to those obtained using an FTIR spectrometer.[70]

QCL based sensors were primarily used for analysis of gases initially, but the wider tuning range available with EC-QCLs has led to their use in analysis of liquids,[71] e.g. human blood[72, 73] and the determination of glucose and lactate in aqueous solution.[61] The use of EC-QCL spectroscopy for secondary structure analysis of proteins and polypeptides at low concentrations has recently been demonstrated,[71, 74, 75] and the results were found to be comparable to those obtained using conventional FTIR spectroscopy. However, QCL based spectrometers cover limited spectral ranges and are generally designed for specific applications.

Interband cascade lasers (ICLs) are also commercially available, covering the region between 1800 and 3400 cm^{-1}. They operate in the same manner as QCLs, but involve interband transitions of electrons and holes, as for semiconductor diode lasers. Like QCLs, ICLs are able to provide continuous wave emission at room temperature and can be tuned across a wide range when an external cavity is incorporated into the design.[76-81] Quantum dot lasers have also been demonstrated as light sources, e.g. by using quantum dots in place of quantum wells in QCLs[82] or as single-photon sources.[83]

However cryogenic cooling is required and the majority of devices have not yet achieved emission wavelengths longer than the NIR range.[25]

Laser frequency combs emit radiation as a series of equally spaced frequencies produced by laser pumping. Originally they were only able to emit NIR and visible radiation, but emission of MIR radiation has now become possible. Use of the technique is limited, however, due to the complexity of the instrumentation involved.[25, 84, 85] Supercontinuum lasers generate bright radiation over the range 750 – 7100 cm^{-1} by passing ultrashort laser pulses from praseodymium-doped fibre lasers into waveguides, but at present the technique is unsuitable for use in process environments.[25, 86-89] Light emitting diodes (LEDs) are another suitable source of mid-infrared radiation. Their advantages include small size, high brightness, low power and long lifetime. The wavelength and intensity of the output are susceptible to variation with temperature, however, and the output becomes gradually poorer during operation.[90-92]

QCLs and ICLs therefore appear to be the most promising light source technology for the development of robust, miniature MIR spectrometers. However at present their high cost and limited spectral ranges are a major drawback, and have prevented them from becoming widely used as spectrometer light sources.

1.1.2.2 Detectors

Thermal or photon based detectors can be used for detecting radiation in the mid-infrared range.[7] The wavelength measured is dependent on the detector material and can be altered by changing its composition.[93] Pyroelectric thermal detectors, e.g. DTGS or lithium tantalite, are the most commonly used detectors in the MIR region, operating at room temperature. However semiconductor photodetectors, e.g. MCT detectors, provide more sensitive, faster measurements.[7, 25] Cryogenic cooling of MCT detectors is required to achieve the greatest sensitivity, but uncooled devices are now emerging.[25, 94-96]

The use of detector arrays can increase the achievable performance.[93, 97] For example, a pyroelectric array detector has been used in a miniature mid-infrared spectrometer, with a zippered configuration to avoid thermal crosstalk by increasing the spacing between elements without increasing the size of the detector.[24] Quantum cascade or

quantum well photodetectors can also be used, based on heterostructures of group III – V materials, e.g. HgTe or GaAs/AlGaAs. Subband or intersubband transitions are used to detect MIR photons, as for QCLs/ICLs. This can aid in the integration of spectrometer components for miniature systems, as the same material can be used for the detector and light source. In addition, quantum dots can be used as MIR detectors, either alone or in combination with quantum wells. Although not widely used at present, such detectors provide great potential for the miniaturisation of MIR spectrometers in the future.[25, 56, 97-99]

1.1.2.3 Filters

The Michelson interferometer (Figure 1.2) is the most commonly used type of interferometer in FTIR spectrometers.[12, 23, 32] In this design, the light from the source (1) is passed to a beam splitter (2), which directs two orthogonal beams to a stationary mirror (3) and a moving mirror (4). The beams are then directed back to the beamsplitter, where they interfere, and the interference pattern is measured as a function of time by the detector (5). The resolution of the spectrometer increases with the variation in the optical pathlength difference.[32, 100]

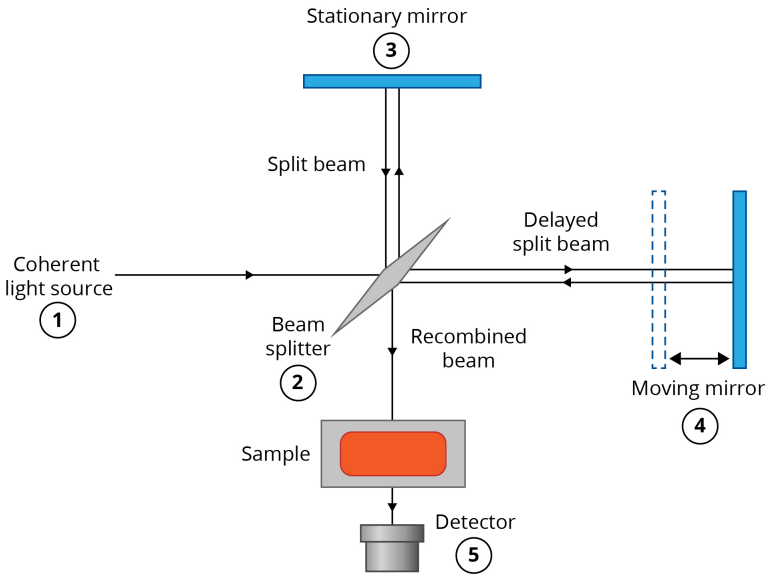

Figure 1.2 - The Michelson interferometer, taken from reference 100.

The combination of multi-channel MIR sensor systems with ATR technology has been demonstrated as an alternative to FTIR. Protype analysers have been designed for the

simultaneous in-line detection of ethanol and carbohydrates[12] and the on-line monitoring of an esterification reaction.[5] Such analysers are compact, robust, low cost and easy to install in process environments. However these advantages were achieved at the expense of spectral resolution and wavelength range. As operation is only possible within a narrow wavelength range, the analysers are limited to specific applications.

The desire for smaller instruments has led to the development of MEMS spectrometers. MEMS are integrated systems in the millimetre to sub-micrometre size range, involving electrical and mechanical components.[101] Both FTIR and grating based MEMS spectrometers have been demonstrated. The size of actuator travel initially limited the range and resolution achievable by FTIR devices, however rapid scanning MEMS FTIR spectrometers operating in the range 700 – 4000 cm^{-1} with resolution of 10 cm^{-1} have been demonstrated.[102]

The mirrors in these instruments are prone to tilting during scanning, so a mirrorless MEMS Fourier transform spectrometer has been demonstrated for analysis in the NIR region. The spectrometer utilises electro-optic modulation by a Mach-Zehnder interferometer with $LiNbO_3$ waveguides and push-pull electrodes.[31] Splitting of the beam can also be carried out using a birefringent material such as a Wollaston prism, eliminating the need for beamsplitters or mirrors. A compact prototype Fourier transform spectrometer with no moving parts, operating in the near infrared region, has been demonstrated using Wollaston prisms.[32]

The Czerny-Turner configuration is a compact, grating based MEMS configuration, suitable for use in miniature spectrometers. It consists of two concave mirrors and a flat diffraction grating. The first mirror directs emitted light to the diffraction grating, and the second directs the light from the diffraction grating to the detector. The spectral range and resolution achievable are dependent on the focal length of the mirrors.[93]

Fabry-Pérot filters are also suitable for use in MEMS spectrometers, and consist of two mirrors with a cavity between, as shown in Figure 1.3. The wavelengths which interfere constructively within the cavity are passed through, and the cavity can be tuned by altering the distance between the mirrors.[90, 101] The resolution has been improved by etching a grating on top of the Fabry-Pérot filter.[103] MEMS based Fabry-

Pérot filters are available in two of the most useful MIR regions, 830 – 1250 cm^{-1} and 2000 – 3300 cm^{-1}.[104-108]

Figure 1.3 - MEMS Fabry-Pérot interferometer, taken from reference 109.

A thin-film dielectric Fabry-Pérot bandpass filter, known as a linear variable filter (LVF), is used as the dispersive element in a commercially available miniature NIR spectrometer, the MicroNIR™ Spectrometer.[57, 110-112] The thickness of the thin-film coating, which varies along the length of the LVF, determines the centre wavelength of the filter. Therefore the wavelength that is transmitted varies with time across the length of the LVF rather than with position. The LVF is positioned at the surface of a 128 element linear diode-array detector, enabling a different wavelength to be detected at each element and eliminating the need for moving parts.[57, 110-112] A miniature ATR spectrometer with no moving parts has also been demonstrated using the LVF, operating in the MIR range 900 – 1800 cm^{-1}. However the resolution achievable was lower than that of a laboratory ATR spectrometer.[24]

Another alternative to the standard Michelson interferometer is the Sagnac interferometer. The Sagnac interferometer design contains no moving parts, and is illustrated in Figure 1.4. Light from the sample is split into two beams (1), however instead of varying the pathlength with moving mirrors, the beams are directed around a loop interferometer in opposite directions (2). The whole interferogram is formed simultaneously on the detector array (3) and any noise present from vibration is eliminated, as it will have the same effect on both beams. This makes the Sagnac

interferometer extremely robust, and it can even be utilised in space applications.[113-116] FTIR technology based on the Sagnac interferometer was originally developed to be attached to a satellite, but owing to advances in detector technology such as uncooled detector arrays, it is now possible to use this type of interferometer within a MIR spectrometer.[100] This provides a promising alternative to the use of moving part interferometers.

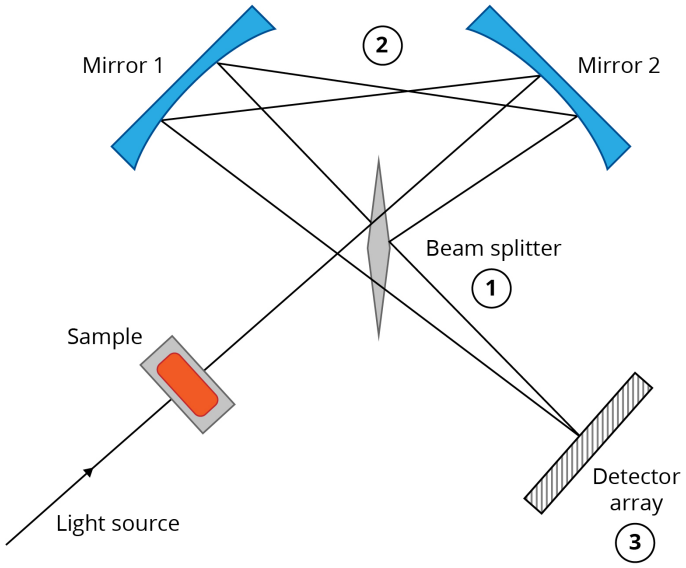

Figure 1.4 - The Sagnac interferometer, taken from reference 100.

1.1.2.4 Waveguides

An alternative waveguide material to chalcogenide glasses and polycrystalline silver halides are hollow core waveguides (HGWs). They consist of a silica outer layer and a metallic inner layer coated with a dielectric film. A core of air is present in the centre, through which the light propagates. The presence of the dielectric film significantly decreases losses at MIR wavelengths. The use of HGWs reduces insertion loss, non-linearity and end reflection, and provides high power threshold. However, bending can cause high losses to occur.[117-119]

Photonic crystal fibres (PCFs) have also become available in recent years. Light is corralled within a microscopic array of air holes, producing subtle differences in refractive index and allowing the light to travel along the fibre. They provide many advantages over conventional optical fibres including tailorable optical properties, higher power and a wide range of possible materials. In addition, they allow MIR light

to be transmitted over longer distances without the attenuation that occurs in silica fibres.[7, 120]

Silicon exhibits low losses above 1250 cm^{-1}, and is a promising material for MIR waveguides.[90, 121-123] However, the silicon-on-insulator platform used in the transmission of NIR radiation (silicon with a SiO_2 cladding) is unsuitable for use in the MIR range, as SiO_2 strongly absorbs light below 2500 cm^{-1}.[121-123] Silicon-on-sapphire platforms are an alternative which exhibit low losses in the MIR region, but they are expensive. The oxide layer can also be etched away to form a suspended platform, and MIR ring resonators have been demonstrated in the range 1900 – 2900 cm^{-1} using this technique.[123] A method of integrating silicon and any heterogeneous substance has also been demonstrated.[122]

The integration of all spectrometer components on a single chip, whilst maintaining performance, is desirable for the development of compact systems. The use of single-mode waveguides allows the characteristics of the radiation emitted from QCLs and ICLs to be preserved in such single chip systems.[25, 124-126] Planar single-mode waveguides have been demonstrated using a variety of materials such as mercury-cadmium-telluride (MCT),[127] chalcogenide,[128] silver nitrate,[129] polymers (e.g. polyethylene and polypropylene)[130], germanium on a silicon substrate[124] and diamond (which is resistant to harsh conditions).[25] The integration of a surface plasmon polariton (SPP) waveguide, in which radiation is directed along the interface between a metal and a dielectric material, with a QCL light source and detector has also been demonstrated.[125, 126]

Another alternative is to attach the probe directly to the instrument to avoid the need for long lengths of waveguide to be used. This allows on-line and in-line MIR analysis to be carried out more easily. A miniaturised spectrometer with an ATR probe directly attached has been demonstrated for the in-line monitoring of esterification reactions[33, 131] and the on-line batch process monitoring of a polymerisation reaction.[132] Chalcogenide fibres were used within the probe to direct the radiation to the spectrometer unit, and the radiation was dispersed onto the detector using a diffraction grating. As the length of fibre required was significantly reduced by attaching the probe directly to the instrument, less light was lost through attenuation.

Miniaturisation was achieved by covering only a limited spectral region (1000 – 2000 cm^{-1}), and the spectral range used can be adapted to suit a specific process. Although the instrument was able to provide accurate and reproducible measurements, it lacked the robustness required for process monitoring.

The Keit spectrometer is a recently developed compact, robust spectrometer with a probe directly attached. It utilises FTIR technology and operates in the MIR range. The robustness of the instrument is due to the use of the Sagnac interferometer (Figure 1.4), which contains no moving parts. The spectrometer contains no fibre optics, and light within the instrument is instead guided using only mirrors and solid light pipes. The light source of the instrument is an etched silicon wafer MEMS device and the ATR crystal of the probe is made of AMTIR-1 (with AMTIR an acronym for amorphous material transmitting infrared radiation), a type of chalcogenide glass. An amorphous silicon based microbolometer detector array, designed for use in thermal imaging cameras, is also utilised within the instrument. The Keit spectrometer is therefore well suited to harsh environments, and would provide a solution to the issues associated with the use of MIR spectroscopy in process monitoring. A disadvantage of the instrument is that the diameter of the probe is large, so it is not suited for use with standard laboratory glassware. This restricts its use to process environments, inhibiting the ability to use the spectrometer in a laboratory environment for process development.

1.1.3 Conclusions

The desire for miniaturisation of MIR spectrometers has led to significant advances in technology. QCLs and ICLs are available over the majority of the MIR region, providing widely tunable light sources of high power and compact size. The use of planar single-mode waveguides allows the characteristics of these light sources to be preserved, and QCL/ICL materials can be used as detectors to aid in the integration of the spectrometer components. The availability of MEMS filters facilitates the miniaturisation of spectrometers, and several compact spectrometers based on MEMS technology have been demonstrated. Detector arrays operating at room temperature are also available, and can increase the performance of miniature spectrometers.

However at present, the majority of miniature MIR spectrometers have limited resolution or lack robustness due to the presence of moving parts.

Although MIR spectroscopy is not widely used in process analysis compared to other techniques, a range of applications have been demonstrated. The development of novel technologies such as QCLs and MEMS filters overcomes many of the limitations which have prevented the widespread use of traditional MIR spectrometers in process environments. These advances in technology will allow MIR spectroscopy to become more widely utilised in process analysis in the future, by reducing the size and cost of instruments and increasing their sensitivity.

A compact mid-infrared spectrometer, utilising a MEMS light source and uncooled detector array, has recently been developed for process monitoring. The spectrometer contains no moving parts so is not sensitive to vibrations, and has a probe directly attached to avoid the need for fibre optics. The instrument is therefore suitable for use in particularly harsh environments, and provides a promising solution to the issues which have limited the use of MIR spectroscopy in process monitoring. The performance of the spectrometer for quantitative *in situ* analysis will be evaluated in this work.

1.2 NMR Spectroscopy

1.2.1 Modes of Measurement

The ability of NMR spectroscopy to provide details of molecular structure in addition to quantitative information provides a major advantage in process analysis. Various different modes of measurement can be used to monitor reactions by NMR spectroscopy. The reaction can be carried out within the NMR tube rather than a reaction vessel, known as static monitoring.[133, 134] This method has been demonstrated for a variety of applications including common processes such as esterification and metalation,[135] the hydrolysis of acetic anhydride,[136] active pharmaceutical ingredient (API) development[137] and biological reaction monitoring.[138] However only very small scale reactions can be monitored using this approach, and mixing is difficult. Off-line or at-line monitoring can be performed by extracting samples from the reaction vessel

for analysis by an NMR spectrometer located elsewhere,[133, 139, 140] but this results in a time delay so real-time analysis cannot be carried out.

On-line reaction monitoring can be performed using flow NMR spectroscopy, in which a stream of the reaction mixture is allowed to flow from the vessel to the instrument (travelling through the bore of the magnet for analysis), at a controlled speed. After analysis, the sample can be transferred back to the vessel or discarded. Flow NMR spectroscopy has been used for on-line reaction monitoring in a range of different applications, for example pharmaceutical process development,[141] the kinetic study of urea,[142] the study of equilibria and kinetics of complex mixtures,[143] and the study of esterification reaction kinetics.[143, 144] A disadvantage of flow NMR spectroscopy is that specialised NMR probes or customised tubes are necessary, and that the reaction conditions (e.g. temperature) within the sample may alter during the time it is outside the reaction vessel.[133, 145] Insulation of the flow tube with a thermostating fluid can prevent this issue.[144] In addition the flow NMR spectroscopy method is not suitable for monitoring fast reactions, as there is a delay between mixing the reagents and beginning the measurement.[146, 147]

Stopped-flow NMR spectroscopy can be used to monitor fast reactions (occurring 2.5 – 100 ms after the reagents have been mixed). The reagents are passed to the spectrometer at a very high flow rate, via a mixing chamber. The flow is stopped in order for the NMR measurement to be made and the extent of the reaction can be determined. Different delay values can be used in the pulse sequence in order to measure different time points of the reaction. Again, specialised probes are required.[133, 148] This technique has allowed the study of reaction kinetics,[146, 147] the study of protein folding mechanisms[149] and the study of short-lived intermediates.[150] The disadvantage of stopped-flow compared to continuous flow is that it is more difficult to control conditions such as temperature, pressure and viscosity, but an advantage is that it is not necessary to consider the effect of flow on the NMR signal.

An alternative method for the monitoring of fast reactions (within the range 40 ms – 1 s) is rapid injection NMR spectroscopy. A sample tube is placed in the NMR spectrometer, and the reagents are rapidly injected into the tube using an injection capillary. A disadvantage of this technique compared to flow NMR spectroscopy is

that cleaning is required before additional measurements can be carried out.[133, 151] Rapid injection NMR spectroscopy has also been demonstrated for the observation of short-lived intermediates,[151, 152] the observation of protein unfolding,[153] and the study of kinetics of fast organic reactions.[154-156]

Although a number of different methods have been demonstrated for monitoring reactions by high-field NMR spectroscopy, the installation of high-field NMR spectrometers in process environments is inhibited by the large size and cost of superconducting magnets. This has prevented the widespread application of NMR spectroscopy in process monitoring.[157] A more suitable alternative is low-field NMR spectroscopy, which will be discussed in the following section.

1.2.2 Low-Field NMR Spectroscopy

Conventional high-field NMR spectrometers utilise superconducting magnets of high magnetic field strength. These magnets produce strong homogeneous fields of up to 23.5 T, providing frequencies of up to 1.1 GHz for ^{1}H NMR spectroscopy and giving measurements of relatively high sensitivity and resolution.[30, 158] However, they require cryogenic cooling and are very large and expensive, therefore high-field NMR spectrometers are normally situated in dedicated laboratories and cannot easily be installed in process environments.[158, 159]

The sensitivity of NMR measurements can be enhanced by increasing the field strength, as shown in Equation 1.1 (where the left hand side represents the relative difference between the nuclear spin populations in the upper (n_+) and lower (n_-) energy states, h is Planck's constant, γ is the gyromagnetic ratio, B is the magnetic field, k_B is the Boltzmann constant and T is the temperature).[30] In the past, the desire for increased sensitivity led to an increase in the size of the magnets used in NMR spectrometers, as larger magnets have larger field strengths. From the 1970s, electromagnet and permanent magnet based NMR spectrometers began to be replaced with those based on stronger cryogenically-cooled superconducting magnets.[27, 160] Benchtop instruments based on permanent magnets were only available for measurement of relaxation times and diffusion coefficients in the time domain, as these instruments lacked the homogeneity required to achieve sufficient resolution in the frequency domain.[27, 158]

$$(n_- - n_+)/(n_- + n_+) \approx h\,\gamma\,B/(4\,\pi\,k_B\,T) \qquad \textbf{Equation 1.1}$$

Advances in magnet design, involving high precision correction of the stray field, has now led to the development of compact permanent magnets capable of achieving high homogeneity.[27, 157, 158] This has facilitated the design of low-field NMR spectrometers operating in the frequency domain, which are significantly smaller than high-field instruments and can be situated on a benchtop or in a fume hood. Permanent magnet arrays made of materials such as NdFeB or SmCo are used in the spectrometers, providing field strengths of 1 – 2 T and frequencies of 40 – 80 MHz for ^{1}H NMR spectroscopy.[27, 157, 158] These instruments have become commercially available over the past few years.[30] They are cheaper than high-field instruments and do not require cryogenic cooling so are easier to maintain.[28] The reduced size, lower cost and lack of need for cryogenic cooling mean that low-field NMR spectrometers are far more suited to process environments than high-field instruments.

The main drawback of low-field NMR spectroscopy compared to high-field is that the sensitivity is poorer. For a given chemical shift difference, the frequency difference will be lower at low field than at high field (e.g. at an operating frequency of 400 MHz, a difference of 1 ppm corresponds to a difference of 400 MHz, but at an operating frequency of 40 MHz, a difference of 1 ppm corresponds to a difference of 40 MHz). Therefore the chemical shift dispersion (i.e. the spread of the chemical shifts of the nuclei in frequency) is smaller and the separation of peaks is poorer, as illustrated in Figure 1.5.[161] However, low-field NMR spectrometers are still capable of achieving measurements of sub-ppm resolution.[28, 158] In addition, the magnetic field of alloys such as SmCo and NdFe varies with temperature[162] and the isolation of the magnet from the sample is generally poor in low-field instruments. This means that the performance of low-field NMR spectrometers is sensitive to temperature.[157, 158] Therefore thermal management is important in order to maintain the homogeneity of the magnetic field and prevent deterioration of the spectra.[28, 163]

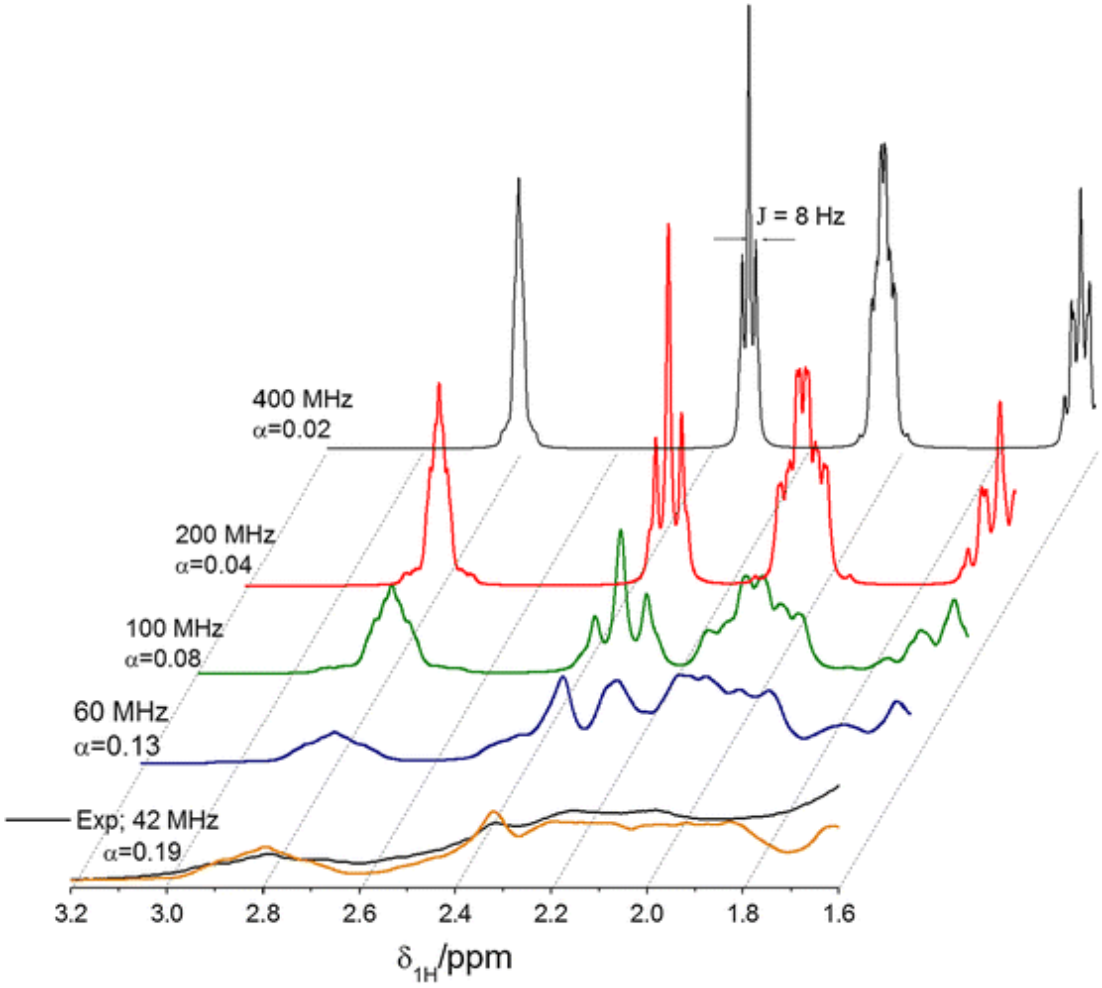

Figure 1.5 - Example NMR spectra of a complex biodiesel mixture acquired at different magnetic field strengths, taken from reference 161.

1.2.2.1 Applications in Process Analysis

Low-field NMR spectroscopy has been demonstrated for a variety of applications. A range of different organic reactions have been monitored by flow NMR spectroscopy using low-field instruments, such as esterification,[134, 146, 164] polymerisation,[165] hydrogenation[158, 166] and acetalisation.[167] An esterification reaction, a Suzuki coupling and an oxime formation have also been monitored by injection into a low-field NMR spectrometer.[134] The ability to locate the NMR spectrometer within a fume hood allows the on-line monitoring of hazardous reactions, for example the trimerisation of propionaldehyde.[159] It is possible to monitor different nuclei simultaneously by low-field NMR spectroscopy, and the monitoring of an esterification reaction by ^{19}F and ^{1}H NMR spectroscopy simultaneously has been demonstrated.[144, 168] Homonuclear and

heteronuclear 2D NMR spectroscopy experiments have also been carried out at low field to determine the structure of complex small molecules.[157] In addition, hyphenation of low-field NMR spectroscopy with other techniques such as near infrared spectroscopy, rheometry and size exclusion chromatographic separation has been performed.[169, 170] The insertion of an electrochemical cell into a low-field NMR spectrometer for *in situ* monitoring of electrochemical reactions has also been demonstrated.[171]

It was possible to effectively follow the progress of these reactions by low-field NMR spectroscopy, however the sensitivity is lower than that of high-field NMR spectroscopy, and overlapping or complex structures are difficult to monitor.[134, 158] In addition, if the spectrometer is located close to the reactor then the presence of a magnetic stirrer can interfere with the magnetic field of the instrument.[158] Another drawback is that reactions usually have to be performed at a similar temperature to the magnet, as the performance of the magnet is sensitive to temperature.[134] However a microreactor "probe head", which allows reactions to be monitored at a broad range of temperatures has been demonstrated.[146] The "probe head" contained a micromixer, reactor and NMR flow cell and was mounted inside the bore of an NMR spectrometer.

High-field NMR spectroscopy can be used for the study of large biomolecules or complex mixtures of small biomolecules. Low-field NMR spectroscopy can also be used for the analysis of biomolecules, however only relatively simple solutions of small molecules can be studied due to the lower sensitivity and resolution of low-field NMR spectroscopy.[27] Structural information has been determined using low-field NMR spectroscopy for biomolecules such as complex alkaloids[172] and secondary metabolites.[173] The monitoring of biotechnological processes such as fermentation has also been demonstrated.[174] In addition, low-field NMR spectroscopy has been used in the petroleum industry for the real-time monitoring of biodiesel production,[175, 176] analysis of crude oils[177] and determination of the liquid-liquid equilibrium in oxygenated fuel components,[178] amongst other applications. Again, low-field NMR spectroscopy was found to be effective and the lack of sample preparation required was an advantage.

Low-field NMR spectroscopy has also been successfully applied in product and quality control, e.g. for detecting adulteration in the food industry[179, 180] and validating the quality of rubber.[181] Automated real-time quality control of pharmaceutical production using a low-field NMR sensor has recently been demonstrated.[182] The sensor was able to monitor a metal-organic reaction, in addition to providing concentration data to iteratively optimise the plant performance and reference values to calibrate a NIR spectrometer. A configurable platform for in-line monitoring and control of organic reactions by flowing a small scale reaction mixture through a low-field NMR spectrometer has also been presented.[183] This platform was fully automated and able to monitor and control a range of reactions in real time, as well as performing self-optimisation.

These applications demonstrate the potential of low-field NMR spectroscopy as a suitable alternative to high-field NMR spectroscopy in process analysis. However the temperature sensitivity of the magnet can lead to deterioration of the performance of the instrument,[158, 184] and this is likely to be a major issue. Inhomogeneities in the magnetic field can produce problems such as variations in linewidth and shifting of peaks.[27, 29] Peak shifts in NMR spectra can also occur due to a variety of other factors, such as interaction of components and changes in pH or temperature,[185] and the smaller chemical shift dispersion at low field compared to high field will worsen the effect of such shifts.

1.2.3 Conclusions

Although NMR spectroscopy provides detailed structural information and is inherently quantitative, it has not been widely used in process monitoring due to the size and expense of high-field instruments and the necessity for cryogenic cooling. The recent availability of low-field benchtop NMR spectrometers capable of achieving sub-ppm resolution in the frequency domain provides a solution. These spectrometers can easily be located in process environments to facilitate on-line reaction monitoring, and are small enough to be situated in fume hoods for the analysis of hazardous materials. A variety of applications of low-field NMR spectroscopy have been demonstrated, including monitoring a range of different reactions, the study of biomolecules, and product and quality control. Low-field NMR spectroscopy therefore

provides a promising solution to the issues associated with high-field NMR spectroscopy, and will allow NMR spectroscopy to become more widely used in process analysis.

A drawback of low-field NMR spectroscopy is that the sensitivity of permanent magnets to temperature is a major issue and can cause deterioration of the spectra. Investigation into the instrumental stability of low-field NMR spectrometers, particularly with respect to the insertion/removal of samples from the instrument, is therefore an important consideration for reaction monitoring. The issue has not been explored, so in this research the instrumental stability of a low-field NMR spectrometer will be investigated and the effectiveness of chemometric procedures for solving the problem of spectral deterioration will be evaluated.

1.3 Aims

The first aim of this work is to assess the performance of the Keit spectrometer (a novel MIR spectrometer designed for use in process environments) and a benchtop NMR spectrometer. The suitability of the Keit spectrometer for the quantitative *in situ* analysis of liquids will be evaluated and the ability of the instrument to monitor a reaction will then be assessed. The instrumental stability of the low-field NMR spectrometer will also be investigated and its suitability for quantitative analysis evaluated.

The second aim is to utilise chemometric procedures for quantitative analysis of the data and the solution of problems. Calibration models will be used to compare the predictive ability of the Keit spectrometer to that of a laboratory based MIR spectrometer. As the Keit spectrometer is not designed for laboratory use, the transfer of calibration models between the two spectrometers will then be demonstrated. MCR will also be utilised as a calibration-free method of decomposing MIR reaction mixture spectra, and different MCR software programmes will be compared. To solve the problem of peak shift in low-field NMR spectra, a variety of alignment methods will be evaluated. The effectiveness of calibration transfer and reference deconvolution for solving the problem of lineshape deterioration will be compared, and these methods will be applied to low-field NMR spectra collected under different conditions in an attempt to eliminate the differences between the spectra. The effectiveness of reference

deconvolution for removing the variation between spectra acquired under the same conditions will also be investigated.

1.4 References

1. F. Dalitz, M. Cudaj, M. Maiwald and G. Guthausen, *Prog. Nucl. Magn. Reson. Spectrosc.*, 2012, **60**, 52–70.
2. J. Workman, B. Lavine, R. Chrisman and M. Koch, *Anal. Chem.*, 2011, **83**, 4557–4578.
3. S. Kueppers and M. Haider, *Anal. Bioanal. Chem.*, 2003, **376**, 313–315.
4. H. H. Willard, L. L. Merritt Jr., J. A. Dean and F. A. Settle Jr., *Instrumental Methods of Analysis*, Wadsworth, Inc., Belmont, California, U.S.A., 7th edn., 1988.
5. D. Geörg, R. Schalk, F. J. Methner and T. Beuermann, *Meas. Sci. Technol.*, 2015, **26**, 065501.
6. R. Ulber, J. G. Frerichs and S. Beutel, *Anal. Bioanal. Chem.*, 2003, **376**, 342–348.
7. N. D. Lourenço, J. A. Lopes, C. F. Almeida, M. C. Sarraguça and H. M. Pinheiro, *Anal. Bioanal. Chem.*, 2012, **404**, 1211–1237.
8. M. Jamrógiewicz, *J. Pharm. Biomed. Anal.*, 2012, **66**, 1–10.
9. K. A. Lee, in *Near-Infrared Spectroscopy in Food Science and Technology*, eds. Y. Ozaki, W. F. McClure and A. A. Christy, John Wiley and Sons, Inc., Hoboken, NJ, USA, 2007, ch. 9, pp. 361–378.
10. M. Watari, H. Higashiyama, N. Mitsui, M. Tomo and Y. Ozaki, *Appl. Spectrosc.*, 2004, **58**, 248–255.
11. Y. Ozaki, *Anal. Sci.*, 2012, **28**, 545–563.
12. A. Bogomolov, M. Heßling, U. Wenzel, S. Princz, T. Hellmuth, M. J. B. Bernal, T. Sakharova, I. Usenov, V. Artyushenko and H. Meyer, *Sens. Actuators, B*, 2015, **221**, 1601–1610.
13. T. Genkawa, M. Watari, T. Nishii and Y. Ozaki, *Appl. Spectrosc.*, 2012, **66**, 773–781.
14. S. P. Gurden, J. A. Westerhuis and A. K. Smilde, *AIChE J.*, 2002, **48**, 2283–2297.

15. N. R. Abu-Absi, B. M. Kenty, M. E. Cuellar, M. C. Borys, S. Sakhamuri, D. J. Strachan, M. C. Hausladen and Z. J. Li, *Biotechnol. Bioeng.*, 2011, **108**, 1215–1221.
16. Z. P. Chen, L. M. Li, J. W. Jin, A. Nordon, D. Littlejohn, J. Yang, J. Zhang and R. Q. Yu, *Anal. Chem.*, 2012, **84**, 4088–4094.
17. K. A. Esmonde-White, M. Cuellar, C. Uerpmann, B. Lenain and I. R. Lewis, *Anal. Bioanal. Chem.*, 2017, **409**, 637–649.
18. R. S. Das and Y. K. Agrawal, *Vib. Spectrosc.*, 2011, **57**, 163–176.
19. J. A. Iversen, R. W. Berg and B. K. Ahring, *Anal. Bioanal. Chem.*, 2014, **406**, 4911–4919.
20. F. Adar, R. Geiger and J. Noonan, *Appl. Spectrosc. Rev.*, 1997, **32**, 45–101.
21. G. Socrates, *Infrared and Raman Characteristic Group Frequencies*, John Wiley & Sons Ltd., Chichester, UK, 3rd edn., 2001.
22. J. Workman Jr., D. J. Veltkamp, S. Doherty, B. B. Anderson, K. E. Creasy, M. Koch, J. F. Tatera, A. L. Robinson, L. J. Bond, L. W. Burgess, G. N. Bokerman, A. H. Ullman, G. P. Darsey, F. Mozayeni, J. A. Bamberger and M. S. Greenwood, *Anal. Chem.*, 1999, **71**, 121–180.
23. D. Landgrebe, C. Haake, T. Höpfner, S. Beutel, B. Hitzmann, T. Scheper, M. Rhiel and K. Reardon, *Appl. Microbiol. Biotechnol.*, 2010, **88**, 11–22.
24. D. S. Kim, T. R. Lee and G. Yoon, *Opt. Eng.*, 2014, **53**, 074108.
25. J. Haas and B. Mizaikoff, *Annual Rev. Anal. Chem.*, 2016, **9**, 17.11–17.24.
26. H. Günther, *NMR Spectroscopy: Basic Principles, Concepts and Applications in Chemistry*, John Wiley & Sons, Weinheim, Germany, 3rd edn., 2013.
27. B. Blumich and K. Singh, *Angew. Chem.-Int. Ed.*, 2018, **57**, 6996–7010.
28. K. Meyer, S. Kern, N. Zientek, G. Guthausen and M. Maiwald, *Trends Anal. Chem.*, 2016, **83**, 39–52.
29. L. R. Euceda, G. F. Giskeodegard and T. F. Bathen, *Scand. J. Clin. Lab. Invest.*, 2015, **75**, 193–203.
30. B. Blumich, *Trends Anal. Chem.*, 2016, **83**, 2–11.
31. J. Li, D. F. Lu and Z. M. Qi, *Appl. Spectrosc.*, 2015, **69**, 1112–1117.
32. S. Prunet, C. Durieu and B. Journet, *Opt. Eng.*, 2003, **42**, 985–993.

33. C. A. McGill, R. H. Ferguson, K. Donoghue, A. Nordon and D. Littlejohn, *Analyst*, 2003, **128**, 1467–1470.
34. V. Artyushenko, A. Bocharnikov, G. Colquhoun, C. Leach, V. Lobachev, T. Sakharova and D. Savitsky, *Vib. Spectrosc.*, 2008, **48**, 168–171.
35. M. G. Trevisan, C. M. Garcia, U. Schuchardt and R. J. Poppi, *Talanta*, 2008, **74**, 971–976.
36. P. MacLaurin, N. C. Crabb, I. Wells, P. J. Worsfold and D. Coombs, *Anal. Chem.*, 1996, **68**, 1116–1123.
37. S. J. Moravek, J. M. Messman and R. F. Storey, *J. Polym. Sci., Part A: Polym. Chem.*, 2009, **47**, 797–803.
38. S. Quinebeche, C. Navarro, Y. Gnanou and M. Fontanille, *Polymer*, 2009, **50**, 1351–1357.
39. M. Dabros, M. Amrhein, D. Bonvin, I. W. Marison and U. von Stockar, *Biotechnol. Prog.*, 2009, **25**, 578–588.
40. P. Fayolle, D. Picque and G. Corrieu, *Food Control*, 2000, **11**, 291–296.
41. E. L. Veale, J. Irudayaraj and A. Demirci, *Biotechnol. Prog.*, 2007, **23**, 494–500.
42. H. Kornmann, S. Valentinotti, P. Duboc, I. Marison and U. von Stockar, *J. Biotechnol.*, 2004, **113**, 231–245.
43. M. Tjahjono, H. H. Chong, E. Widjaja, K. Sa-ei and M. Garland, *Talanta*, 2009, **79**, 856–862.
44. J. Diewok, M. J. Ayora-Canada and B. Lendl, *Anal. Chem.*, 2002, **74**, 4944–4954.
45. S. Richards, M. Ropic, D. Blackmond and A. Walmsley, *Anal. Chim. Acta*, 2004, **519**, 1–9.
46. A. Dominguez-Vidal, M. P. Saenz-Navajas, M. J. Ayora-Canada and B. Lendl, *Anal. Chem.*, 2006, **78**, 3257–3264.
47. Mettler Toledo, http://www.mt.com, (accessed 8th December, 2016).
48. Bruker, https://www.bruker.com/products/infrared-near-infrared-and-raman-spectroscopy/ftirnir-for-process/matrix-mf/overview.html, (accessed 9th November, 2018).

49. X. Y. Chen, R. Pell, S. Sarsani, B. Cramm, C. Villa and R. Dixit, *Appl. Spectrosc.*, 2013, **67**, 940–948.
50. H. J. Deng, Z. Q. Shen, L. F. Li, H. Yin and J. Z. Chen, *J. Appl. Polym. Sci.*, 2014, **131**, 40503.
51. A. J. Pasquale, R. D. Allen and T. E. Long, *Macromolecules*, 2001, **34**, 8064–8071.
52. D. L. Doak and J. A. Phillips, *Biotechnol. Prog.*, 1999, **15**, 529–539.
53. I. M. Clegg, A. M. Daly, C. Donnelly, R. Hardy, D. Harris, H. Jackman, R. Jones, A. Luan, D. McAndrew, P. McGauley, J. Pearce, G. Scotney and M. L. Yeow, *Appl. Spectrosc.*, 2012, **66**, 574–579.
54. J. Scherble, B. Ivan and R. Mulhaupt, *Macromol. Chem. Phys.*, 2002, **203**, 1866–1871.
55. J. M. Eichenholz, J. McCaffrey and J. Lane, in *Optical Biopsy VII*, ed. R. R. Alfano, SPIE-Int. Soc. Optical Engineering, Bellingham, WA, USA, 2010, vol. 7561.
56. S. S. Kim, C. Young and B. Mizaikoff, *Anal. Bioanal. Chem.*, 2008, **390**, 231–237.
57. N. A. O'Brien, C. A. Hulse, D. M. Friedrich, F. J. Van Milligen, M. K. von Gunten, F. Pfeifer and H. W. Siesler, in *Next-Generation Spectroscopic Technologies V*, eds. M. A. Druy and R. A. Crocombe, SPIE-Int. Soc. Optical Engineering, Bellingham, WA, USA, 2012, vol. 8374.
58. J. Faist, F. Capasso, D. L. Sivco, C. Sirtori, A. L. Hutchinson and A. Y. Cho, *Science*, 1994, **264**, 553–556.
59. T. Day, M. Weida, D. Arnone, M. Pushkarsky, R. Pritchett and D. Caffey, in *Novel In-Plane Semiconductor Lasers VIII*, eds. A. A. Belyanin and P. M. Smowton, SPIE-Int. Soc. Optical Engineering, Bellingham, WA, USA, 2009, vol. 7230.
60. A. Hugi, R. Maulini and J. Faist, *Semicond. Sci. Technol.*, 2010, **25**, 083001.
61. M. Brandstetter, A. Genner, K. Anic and B. Lendl, *Analyst*, 2010, **135**, 3260–3265.
62. J. Hecht, *Understanding Lasers: An Entry-Level Guide*, John Wiley & Sons, Inc., Hoboken, New Jersey, USA, 3rd edn., 2008.

63. M. Beck, D. Hofstetter, T. Aellen, J. Faist, U. Oesterle, M. Ilegems, E. Gini and H. Melchior, *Science*, 2002, **295**, 301–305.
64. M. Pushkarsky, M. Weida, T. Day, D. Arnone, R. Pritchett and D. Caffey, *Rev. Laser Eng.*, 2008, **36**, 80–83.
65. J. H. van Helden, N. Lang, U. Macherius, H. Zimmermann and J. Röpcke, *Appl. Phys. Lett.*, 2013, **103**, 131114.
66. D. Lopatik, S. Niemietz, M. Fröhlich, J. Röpcke and H. Kersten, *Contrib. Plasma Phys.*, 2012, **52**, 864–871.
67. M. Sieger, F. Balluff, X. Wang, S. S. Kim, L. Leidner, G. Gauglitz and B. Mizaikoff, *Anal. Chem.*, 2013, **85**, 3050–3052.
68. Daylight Solutions, http://www.daylightsolutions.com, (accessed 27th November, 2018).
69. Block Engineering: Quantum Cascade Lasers and FTIR Spectrometers, https://www.blockeng.com/products/index.html, (accessed 27th November, 2018).
70. W. J. Zhou, N. Bandyopadhyay, D. H. Wu, R. McClintock and M. Razeghi, *Sci. Rep.*, 2016, **6**, 25213–25213.
71. A. Schwaighofer, M. R. Alcaráz, C. Araman, H. Goicoechea and B. Lendl, *Sci. Rep.*, 2016, **6**, 33556.
72. M. Brandstetter, T. Sumalowitsch, A. Genner, A. E. Posch, C. Herwig, A. Drolz, V. Fuhrmann, T. Perkmann and B. Lendl, *Analyst*, 2013, **138**, 4022–4028.
73. M. Brandstetter, L. Volgger, A. Genner, C. Jungbauer and B. Lendl, *Appl. Phys. B*, 2013, **110**, 233–239.
74. M. R. Alcaráz, A. Schwaighofer, C. Kristament, G. Ramer, M. Brandstetter, H. Goicoechea and B. Lendl, *Anal. Chem.*, 2015, **87**, 6980–6987.
75. M. R. Alcaráz, A. Schwaighofer, H. Goicoechea and B. Lendl, *Anal. Bioanal. Chem.*, 2016, **408**, 3933–3941.
76. D. Caffey, T. Day, C. S. Kim, M. Kim, I. Vurgaftman, W. W. Bewley, J. R. Lindle, C. L. Canedy, J. Abell and J. R. Meyer, *Opt. Express*, 2010, **18**, 15691–15696.

77. J. Röpcke, P. B. Davies, N. Lang, A. Rousseau and S. Welzel, *J. Phys. D: Appl. Phys.*, 2012, **45**, 423001.
78. D. Lopatik, N. Lang, U. Macherius, H. Zimmermann and J. Röpcke, *Meas. Sci. Technol.*, 2012, **23**, 115501.
79. S. Hofling, R. Weih, M. Dallner and M. Kamp, in *Novel In-Plane Semiconductor Lasers XIII*, eds. A. A. Belyanin and P. M. Smowton, SPIE - Int. Soc. Optical Engineering, Bellingham, WA, USA, 2014, vol. 9002.
80. W. W. Bewley, C. L. Canedy, C. S. Kim, M. Kim, C. D. Merritt, J. Abell, I. Vurgaftman and J. R. Meyer, *Opt. Express*, 2012, **20**, 3235–3240.
81. I. Vurgaftman, W. W. Bewley, C. L. Canedy, C. S. Kim, M. Kim, C. D. Merritt, J. Abell and J. R. Meyer, *IEEE J. Sel. Top. Quantum Electron.*, 2013, **19**, 2100210.
82. N. Zhuo, F. Q. Liu, J. C. Zhang, L. J. Wang, J. Q. Liu, S. Q. Zhai and Z. G. Wang, *Nanoscale Res. Lett.*, 2014, **9**, 7.
83. Y. M. He, Y. He, Y. J. Wei, D. Wu, M. Atature, C. Schneider, S. Hofling, M. Kamp, C. Y. Lu and J. W. Pan, *Nat. Nanotechnol.*, 2013, **8**, 213–217.
84. A. Schliesser, N. Picque and T. W. Hansch, *Nat. Photonics*, 2012, **6**, 440–449.
85. F. Adler, P. Maslowski, A. Foltynowicz, K. C. Cossel, T. C. Briles, I. Hartl and J. Ye, *Opt. Express*, 2010, **18**, 21861–21872.
86. I. Kubat, C. S. Agger, U. Moller, A. B. Seddon, Z. Q. Tang, S. Sujecki, T. M. Benson, D. Furniss, S. Lamrini, K. Scholle, P. Fuhrberg, B. Napier, M. Farries, J. Ward, P. M. Moselund and O. Bang, *Opt. Express*, 2014, **22**, 14.
87. C. R. Petersen, U. Moller, I. Kubat, B. B. Zhou, S. Dupont, J. Ramsay, T. Benson, S. Sujecki, N. Abdel-Moneim, Z. Q. Tang, D. Furniss, A. Seddon and O. Bang, *Nat. Photonics*, 2014, **8**, 830–834.
88. A. Al-Kadry, M. El Amraoui, Y. Messaddeq and M. Rochette, *Opt. Express*, 2014, **22**, 31131–31137.
89. U. Moller, Y. Yu, I. Kubat, C. R. Petersen, X. Gai, L. Brilland, D. Mechin, C. Caillaud, J. Troles, B. Luther-Davies and O. Bang, *Opt. Express*, 2015, **23**, 3282–3291.
90. J. Malinen, A. Rissanen, H. Saari, P. Karioja, M. Karppinen, T. Aalto and K. Tukkiniemi, in *Next-Generation Spectroscopic Technologies VII*, eds. M. A.

Druy and R. A. Crocombe, SPIE-Int. Soc. Optical Engineering, Bellingham, WA, USA, 2014, vol. 9101.

91. J. Malinen, M. Känsäkoski, R. Rikola and C. G. Eddison, *Sens. Actuators, B*, 1998, **51**, 220–226.
92. B. A. Matveev, G. A. Gavrilov, V. V. Evstropov, N. V. Zotova, S. A. Karandashov, G. Y. Sotnikova, N. M. Stus, G. N. Talalakin and J. Malinen, *Sens. Actuators, B*, 1997, **39**, 339–343.
93. R. V. Chimenti and R. J. Thomas, *Laser Focus World*, 2013, **49**, 34–44.
94. M. Vuillermet, L. Rubaldo, F. Chabuel, C. Pautet, J. C. Terme, L. Mollard, J. Rothman and N. Baier, in *Infrared Technology and Applications XXXVII*, eds. B. F. Andresen, G. F. Fulop and P. R. Norton, SPIE-Int. Soc. Optical Engineering, Bellingham, WA, USA, 2011, vol. 8012.
95. P. Martyniuk and A. Rogalski, *Opt. Quant. Electron*, 2014, **46**, 581–591.
96. A. Piotrowski, in *Mid-Infrared Exchanges and Exploitation*, Vigo System S. A., Zurich, Switz., 2014.
97. C. Downs and T. E. Vandervelde, *Sensors*, 2013, **13**, 5054–5098.
98. M. Zavvari and V. Ahmadi, *IEEE Electron Device Lett.*, 2013, **34**, 783–785.
99. M. Sieger and B. Mizaikoff, *Anal. Chem.*, 2016, **88**, 5562–5573.
100. Keit Spectrometers, http://keit.co.uk/ftir-spectrometer-technology/, (accessed 25th May, 2016).
101. L. P. Schuler, J. S. Milne, J. M. Dell and L. Faraone, *J. Phys. D: Appl. Phys.*, 2009, **42**, 133001.
102. A. Kenda, S. Luettjohann, T. Sandner, M. Kraft, A. Tortschanoff and A. Simon, in *Next-Generation Spectroscopic Technologies IV*, eds. M. A. Druy and R. A. Crocombe, SPIE-Int. Soc. Optical Engineering, Bellingham, WA, USA, 2011, vol. 8032.
103. Z. D. Shi, L. Fang and C. X. Zhou, *Appl. Opt.*, 2014, **53**, 76–81.
104. H. F. Mao, K. Silva, M. Martyniuk, J. Antoszewski, J. Bumgarner, B. D. Nener, J. M. Dell and L. Faraone, *J. Microelectromech. Syst.*, 2016, **25**, 227–235.
105. Spectral Engines, http://www.spectralengines.com, (accessed 20th July, 2016).
106. N. Neumann, M. Ebermann, E. Gittler, M. Meinig, S. Kurth and K. Hiller, in *IEEE Sensors*, IEEE, New York, NY, USA, 2010, pp. 2383–2387.

107. M. Meinig, M. Ebermann, N. Neumann, S. Kurth, K. Hiller and T. Gessner, in *16th International Solid-State Sensors, Actuators and Microsystems Conference*, IEEE, Beijing, China, 2011, pp. 2538–2541.
108. N. Neumann, M. Ebermann and S. Kurth, *J. Micro/Nanolithogr., MEMS, MOEMS*, 2008, **7**, 021004.
109. J. Antila, A. Miranto, J. Makynen, M. Laamanen, A. Rissanen, M. Blomberg, H. Saari and J. Malinen, in *Next-Generation Spectroscopic Technologies III*, eds. M. A. Druy, C. D. Brown and R. A. Crocombe, SPIE-Int. Soc. Optical Engineering, Orlando, FL, USA, 2010, vol. 7680.
110. M. Alcala, M. Blanco, D. Moyano, N. W. Broad, N. O'Brien, D. Friedrich, F. Pfeifer and H. W. Siesler, *J. Near Infrared Spectrosc.*, 2013, **21**, 445–457.
111. C. G. Pederson, D. M. Friedrich, C. Hsiung, M. von Gunten, N. A. O'Brien, H. J. Ramaker, E. van Sprang and M. Dreischor, in *Next-Generation Spectroscopic Technologies VII*, eds. M. A. Druy and R. A. Crocombe, SPIE-Int. Soc. Optical Engineering, Bellingham, WA, USA, 2014, vol. 9101.
112. J. J. R. Rohwedder, C. Pasquini, P. R. Fortes, I. M. Raimundo, A. Wilk and B. Mizaikoff, *Analyst*, 2014, **139**, 3572–3576.
113. G. Pascoli, *C. R. Phys.*, 2017, **18**, 563–569.
114. B. Barrett, R. Geiger, I. Dutta, M. Meunier, B. Canuel, A. Gauguet, P. Bouyer and A. Landragin, *C. R. Phys.*, 2014, **15**, 875–883.
115. *WO Pat.,* 086 357, 2011.
116. C. Jentsch, T. Muller, E. M. Rasel and W. Ertmer, *Gen. Relativ. Gravitation*, 2004, **36**, 2197–2221.
117. P. Patimisco, V. Spagnolo, M. S. Vitiello, G. Scamarcio, C. M. Bledt and J. A. Harrington, *Sensors*, 2013, **13**, 1329–1340.
118. J. A. Harrington, *Fiber Integr. Opt.*, 2000, **19**, 211–227.
119. J. A. Harrington, C. Rabii and D. Gibson, *IEEE J. Sel. Top. Quantum Electron.*, 1999, **5**, 948–953.
120. S. A. Cerqueira, *Rep. Prog. Phys.*, 2010, **73**, 21.
121. R. Shankar, I. Bulu and M. Lončar, *Appl. Phys. Lett.*, 2013, **102**, 051108.
122. Y. Chen, H. Lin, J. Hu and M. Li, *ACS Nano*, 2014, **8**, 6955–6961.

123. Y. Xia, C. Qiu, X. Zhang, W. Gao, J. Shu and Q. Xu, *Opt. Lett.*, 2013, **38**, 1122–1124.

124. Y. C. Chang, P. Waegli, V. Paeder, A. Homsy, L. Hvozdara, P. van der Wal, J. Di Francesco, N. F. de Rooij and H. P. Herzig, *Lab Chip*, 2012, **12**, 3020–3023.

125. B. Schwarz, P. Reininger, D. Ristanic, H. Detz, A. M. Andrews, W. Schrenk and G. Strasser, *Nat. Commun.*, 2014, **5**, 4085.

126. D. Ristanic, B. Schwarz, P. Reininger, H. Detz, T. Zederbauer, A. M. Andrews, W. Schrenk and G. Strasser, *Appl. Phys. Lett.*, 2015, **106**, 041101.

127. X. F. Wang, J. Antoszewski, G. Putrino, W. Lei, L. Faraone and B. Mizaikoff, *Anal. Chem.*, 2013, **85**, 10648–10652.

128. A. B. Seddon, N. S. Abdel-Moneim, L. Zhang, W. J. Pan, D. Furniss, C. J. Mellor, T. Kohoutek, J. Orava, T. Wagner and T. M. Benson, *Opt. Eng.*, 2014, **53**, 071824.

129. G. Ramer, J. Kasberger, M. Brandstetter, A. Saeed, B. Jakoby and B. Lendl, *Appl. Phys. B*, 2014, **116**, 325–332.

130. S. Wu and A. Deev, in *Quantum Sensing and Nanophotonic Devices IX*, eds. M. Razeghi, E. Tournie and G. J. Brown, SPIE-Int. Soc. Optical Engineering, Bellingham, WA, USA, 2012, vol. 8268.

131. A. W. Owen, E. A. J. McAulay, A. Nordon, D. Littlejohn, T. P. Lynch, J. S. Lancaster and R. G. Wright, *Anal. Chim. Acta*, 2014, **849**, 12–18.

132. E. N. M. van Sprang, H. J. Ramaker, H. F. M. Boelens, J. A. Westerhuis, D. Whiteman, D. Baines and I. Weaver, *Analyst*, 2003, **128**, 98–102.

133. D. A. Foley, A. L. Dunn and M. T. Zell, *Magn. Reson. Chem.*, 2016, **54**, 451–456.

134. M. V. S. Elipe and R. R. Milburn, *Magn. Reson. Chem.*, 2016, **54**, 437–443.

135. T. R. Hoye, B. M. Eklov, T. D. Ryba, M. Voloshin and L. J. Yao, *Org. Lett.*, 2004, **6**, 953–956.

136. F. Susanne, D. S. Smith and A. Codina, *Org. Process Res. Dev.*, 2012, **16**, 61–64.

137. I. M. Clegg, C. M. Gordon, D. S. Smith, R. Alzaga and A. Codina, *Anal. Methods*, 2012, **4**, 1498–1506.

138. Y. Yokoyama, M. Nakakoshi, H. Okuno, Y. Sakamoto and S. Sakurai, *Magn. Reson. Chem.*, 2010, **48**, 811–817.
139. T. Bartik, B. Bartik, B. E. Hanson, T. Glass and W. Bebout, *Inorg. Chem.*, 1992, **31**, 2667–2670.
140. M. M. Achmatowicz, O. R. Thiel, J. T. Colyer, J. Hu, M. V. S. Elipe, J. Tomaskevitch, J. S. Tedrow and R. D. Larsen, *Org. Process Res. Dev.*, 2010, **14**, 1498–1508.
141. D. A. Foley, J. Wang, B. Maranzano, M. T. Zell, B. L. Marquez, Y. Q. Xiang and G. L. Reid, *Anal. Chem.*, 2013, **85**, 8928–8932.
142. E. J. Kibrik, O. Steinhof, G. Scherr, W. R. Thiel and H. Hasse, *Ind. Eng. Chem. Res.*, 2014, **53**, 12602–12613.
143. M. Maiwald, H. H. Fischer, Y. K. Kim, K. Albert and H. Hasse, *J. Magn. Reson.*, 2004, **166**, 135–146.
144. N. Zientek, C. Laurain, K. Meyer, M. Kraume, G. Guthausen and M. Maiwald, *J. Magn. Reson.*, 2014, **249**, 53–62.
145. D. A. Foley, E. Bez, A. Codina, K. L. Colson, M. Fey, R. Krull, D. Piroli, M. T. Zell and B. L. Marquez, *Anal. Chem.*, 2014, **86**, 12008–12013.
146. E. von Harbou, R. Behrens, J. Berje, A. Bracher and H. Hasse, *Chem. Ing. Tech.*, 2017, **89**, 369–378.
147. M. D. Christianson, E. H. P. Tan and C. R. Landis, *J. Am. Chem. Soc.*, 2010, **132**, 11461–11463.
148. A. Gomez-Hens and D. Perezbendito, *Anal. Chim. Acta*, 1991, **242**, 147–177.
149. C. Frieden, S. D. Hoeltzli and I. J. Ropson, *Protein Sci.*, 1993, **2**, 2007–2014.
150. C. A. Fyfe, M. Cocivera and S. W. H. Damji, *Acc. Chem. Res.*, 1978, **11**, 277–282.
151. J. F. McGarrity, J. Prodolliet and T. Smyth, *Org. Magn. Reson.*, 1981, **17**, 59–65.
152. J. F. McGarrity and J. Prodolliet, *J. Org. Chem.*, 1984, **49**, 4465–4470.
153. G. E. Wagner, P. Sakhaii, W. Bermel and K. Zangger, *Chem. Commun.*, 2013, **49**, 3155–3157.
154. A. C. Jones, A. W. Sanders, M. J. Bevan and H. J. Reich, *J. Am. Chem. Soc.*, 2007, **129**, 3492–3493.

155. S. E. Denmark, B. J. Williams, B. M. Eklov, S. M. Pham and G. L. Beutner, *J. Org. Chem.*, 2010, **75**, 5558–5572.
156. J. Kind and C. M. Thiele, *J. Magn. Reson.*, 2015, **260**, 109–115.
157. K. Singh and B. Blumich, *Trends Anal. Chem.*, 2016, **83**, 12–26.
158. E. Danieli, J. Perlo, A. L. L. Duchateau, G. K. M. Verzijl, V. M. Litvinov, B. Blumich and F. Casanova, *ChemPhysChem*, 2014, **15**, 3060–3066.
159. S. K. Kuster, E. Danieli, B. Blumich and F. Casanova, *Phys. Chem. Chem. Phys.*, 2011, **13**, 13172–13176.
160. E. Moser, E. Laistler, F. Schmitt and G. Kontaxis, *Front. Phys.*, 2017, **5**, 33.
161. Y. G. Linck, M. H. M. Killner, E. Danieli and B. Blumich, *Appl. Magn. Reson.*, 2013, **44**, 41–53.
162. L. A. Colnago, F. D. Andrade, A. A. Souza, R. B. V. Azeredo, A. A. Lima, L. M. Cerioni, T. M. Osan and D. J. Pusiol, *Chem. Eng. Technol.*, 2014, **37**, 191–203.
163. S. S. Zalesskiy, E. Danieli, B. Bluemich and V. P. Ananikov, *Chem. Rev.*, 2014, **114**, 5641–5694.
164. F. Dalitz, L. Kreckel, M. Maiwald and G. Guthausen, *Appl. Magn. Reson.*, 2014, **45**, 411–425.
165. M. A. Vargas, M. Cudaj, K. Hailu, K. Sachsenheimer and G. Guthausen, *Macromolecules*, 2010, **43**, 5561–5568.
166. G. Guthausen, A. von Garnier and R. Reimert, *Appl. Spectrosc.*, 2009, **63**, 1121–1127.
167. K. Singh, E. Danieli and B. Blumich, *Anal. Bioanal. Chem.*, 2017, **409**, 7223–7234.
168. N. Zientek, C. Laurain, K. Meyer, A. Paul, D. Engel, G. Guthausen, M. Kraume and M. Maiwald, *Magn. Reson. Chem.*, 2016, **54**, 513–520.
169. V. Rantzsch, M. Wilhelm and G. Guthausen, *Magn. Reson. Chem.*, 2016, **54**, 494–501.
170. M. Cudaj, G. Guthausen, T. Hofe and M. Wilhelm, *Macromol. Chem. Phys.*, 2012, **213**, 1933–1943.
171. B. F. Gomes, C. M. S. Lobo and L. A. Colnago, *Appl. Sci.*, 2019, **9**, 498.
172. K. Singh and B. Blumich, *Analyst*, 2017, **142**, 1459–1470.

173. D. P. Killeen, O. C. Watkins, C. E. Sansom, D. H. Andersen, K. C. Gordon and N. B. Perry, *Phytochem. Anal.*, 2017, **28**, 50–57.
174. D. Kreyenschulte, E. Paciok, L. Regestein, B. Blumich and J. Buchs, *Biotechnol. Bioeng.*, 2015, **112**, 1810–1821.
175. M. H. M. Killner, Y. G. Linck, E. Danieli, J. J. R. Rohwedder and B. Blumich, *Fuel*, 2015, **139**, 240–247.
176. K. Singh, S. P. Kumar and B. Blumich, *Fuel*, 2019, **243**, 192–201.
177. Y. X. Feng, X. L. Chu, Y. P. Xu and S. B. Tian, *China Pet. Process. Petrochem. Technol.*, 2014, **16**, 34–39.
178. N. Schmitz, A. Friebel, E. von Harbou, J. Burger and H. Hasse, *Fluid Phase Equilib.*, 2016, **425**, 127–135.
179. W. Jakes, A. Gerdova, M. Defernez, A. D. Watson, C. McCallum, E. Limer, I. J. Colquhoun, D. C. Williamson and E. K. Kemsley, *Food Chem.*, 2015, **175**, 1–9.
180. T. Parker, E. Limer, A. D. Watson, M. Defernez, D. Williamson and E. K. Kemsley, *Trends Anal. Chem.*, 2014, **57**, 147–158.
181. K. Singh and B. Blumich, *Macromol. Symp.*, 2016, **365**, 191–193.
182. S. Kern, L. Wander, K. Meyer, S. Guhl, A. R. G. Mukkula, M. Holtkamp, M. Salge, C. Fleischer, N. Weber, R. King, S. Enge, A. Paul, M. P. Remelhe and M. Maiwald, *Anal. Bioanal. Chem.*, 2019, **411**, 3037–3046.
183. V. Sans, L. Porwol, V. Dragone and L. Cronin, *Chem. Sci.*, 2015, **6**, 1258–1264.
184. Magritek, The Lock and the importance of field stability, http://www.magritek.com/2014/08/12/the-lock-and-the-importance-of-field-stability/, (accessed 29th April, 2019).
185. T. N. Vu and K. Laukens, *Metabolites*, 2013, **3**, 259–276.

2 Theory

2.1 Mid-Infrared Spectroscopy

Infrared spectroscopy involves the irradiation of a sample with infrared light. Certain wavenumbers of light are absorbed by the sample, and a spectrum of absorbance or transmittance versus wavenumber is produced. The wavenumbers of light absorbed correspond to vibrations of bonds in the molecule. Absorbance of light in the MIR region, 400 – 4000 cm^{-1}, arises from fundamental vibrations. Different functional groups give rise to different vibrations, so the position of peaks can be used to qualitatively analyse the spectra.[1, 2]

The concentration of an analyte can be calculated from the spectra to allow quantitative analysis to be carried out. Absorbance is related to concentration by the Beer Lambert law (Equation 2.1),[3] where A is the spectral absorbance, c is the concentration of the component, D is the absorption pathlength and ε is the molar absorption coefficient. The absorbance can be defined in terms of transmittance (T) or intensity (I), where I_0 is the intensity of the incident light and I is the intensity of the transmitted light.

$$A = \log\left[\frac{I_0}{I}\right] = \log\left[\frac{1}{T}\right] = D\ c\ \varepsilon \qquad \textbf{Equation 2.1}$$

The components of a MIR spectrometer typically include a light source, waveguides through which the light travels, a probe, a detector and a filter to control the wavenumber of light which is passed through the waveguides or into the detector.[1, 3] MIR spectrometers are traditionally either grating based or interference based (e.g. Fourier transform infrared (FTIR) instruments). In grating based instruments, the incident light is dispersed using a grating or prism. However they are now scarcely used, as FTIR instruments have significantly greater performance.[1, 4] In FTIR spectroscopy, a difference in optical pathlength is introduced to the radiation and the interference of the signals is converted to a spectrum as a function of wavenumber. The difference in optical pathlength is usually introduced using a two-beam interferometer involving moving optical parts, e.g. mirrors.[1, 5, 6]

Probes are used as the interface between the sample and the spectrometer, and are usually connected to the instrument by waveguides such as optical fibres. Optical

fibres consist of a high refractive index core with a low refractive index cladding. Light travels through the core by total internal reflection.[1, 3] Attenuated total reflectance (ATR) probes are the most common type of probe in MIR spectroscopy. In ATR spectroscopy, radiation is directed into a crystal of high refractive index by a set of mirrors, and travels through the crystal by total internal reflection. The crystal is placed in contact with a sample and the evanescent wave penetrates a short distance into the sample, as shown in Figure 2.1. The radiation interacts with the sample and is guided to the detector by another set of mirrors.[1, 7] The crystal is made of a material with significantly greater refractive index than the sample, for example ZnSe, Ge, ZrO_2, Si or diamond. Diamond is the most suitable material, as it is extremely stable and lasts a long time, but it is very expensive.[2, 8]

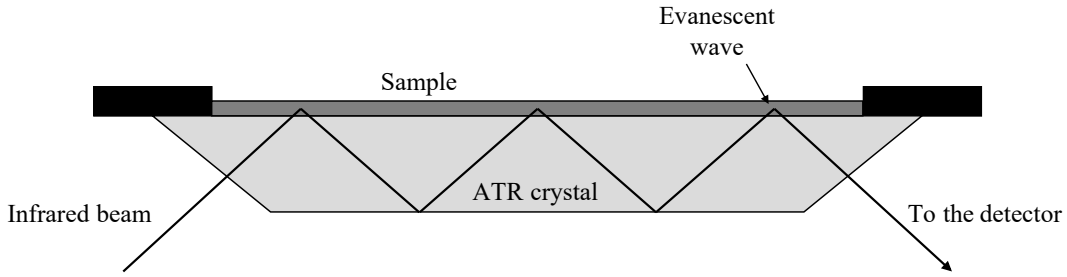

Figure 2.1 - Principle of ATR spectroscopy, reproduced from reference 2.

In NIR spectroscopy, pathlengths are of the order of mm and transmittance probes are used to pass light straight through the sample.[1, 9] But in MIR spectroscopy, molar absorptivity is much higher, thus pathlengths of the order of μm are necessary so that the relationship between absorbance and concentration is linear and corresponds to the Beer Lambert Law (Equation 2.1).[9] The pathlength in ATR spectroscopy is dependent on the penetration depth of the evanescent wave times the number of internal reflections. The penetration depth is determined by the refractive indices of the crystal and sample, and the angle at which the light enters the crystal. It is usually around 0.5 – 2 μm. The number of internal reflections depends on the crystal material and its geometry. ATR probes provide short pathlengths, around 0.5 – 5 μm, thus are suitable for mid-infrared spectroscopy.[2, 7, 8]

2.2 NMR Spectroscopy

NMR spectroscopy is based on the magnetic properties of nuclei. Nuclei possessing a non-zero spin quantum number, *I*, (e.g. ^{1}H, ^{13}C, ^{19}F, ^{14}N and ^{15}N) have non-zero magnetic moments and are NMR active.[10, 11] When a magnetic field, B_0, is applied to such nuclei, the nuclear magnetic moments interact with the field. The lowest energy arrangement of the magnetic moments is in alignment with B_0, so a net magnetisation is produced in this direction. The process of reaching this equilibrium is called relaxation.[10-12]

If a short radio frequency (RF) pulse is applied (normally lasting a few microseconds), an oscillating magnetic field is produced transverse to B_0. This alters the net magnetisation from the equilibrium, causing it to rotate around the new effective magnetic field at a constant angle (known as precession), before relaxing to the equilibrium state. The precession is detected as an oscillating current in a coil and gives rise to a free induction decay (FID) signal, measured in the time domain.[10, 11, 13]

The measured FID is converted from the time domain to the frequency domain by Fourier transform to produce a spectrum of intensity versus frequency, or more conventionally, chemical shift.[11-13] The chemical shift scale is independent of operating frequency and is based on a reference signal, e.g. tetramethylsilane (TMS). It conveys the measured frequency as a deviation from the reference in parts per million (ppm), as shown in Equation 2.2 (where υ is the operating frequency of the instrument, υ_{ref} is the frequency of the reference signal and δ is the chemical shift).[10]

$$\delta\ (\text{ppm}) = 10^6 \times \frac{\upsilon - \upsilon_{ref}}{\upsilon} \qquad \textbf{Equation 2.2}$$

Changing the electronic environment of the nuclei changes the way in which they interact with the magnetic field, therefore differences in chemical shift within the spectrum arise due to differences in the chemical environments of the nuclei.[11] Splitting of peaks can occur as a result of coupling of the spins of nearby nuclei, producing multiplets.[10] The chemical shifts and splitting patterns can be used to deduce the structure of molecules.[11, 14, 15] The area of each peak is proportional to the number of nuclei giving rise to the peak, so quantitative information on the composition of mixtures can also be obtained.[14, 15] The use of 2D NMR spectroscopy is possible to

obtain more detailed structural information,[10] however it has limited use for process monitoring so this work will focus on 1D NMR spectroscopy.

The magnetic field is produced by a cryogenically cooled superconducting magnet in high-field instruments, or a permanent magnet in low-field instruments.[14, 16, 17] RF pulses are produced by an RF transmitter coil, and the signals are detected by a receiver coil.[10] In high-field spectrometers, these coils are contained in a probe, along with a number of other components. The probe is contained in the bore of the magnet and the sample is inserted into the probe. Alteration of the probe is possible, e.g. for different applications.[10] In low-field spectrometers, the transmitter and receiver coils are built into the instrument and there is no removable probe.

Inhomogeneities in the magnetic field can occur, and shimming is performed in order to correct for these variations. The process of shimming involves passing an electric current through a set of shim coils to adjust the magnetic field.[10, 16, 17] Shimming must be performed regularly (usually either on every sample or daily), and if the magnetic field varies between shimming then the saved settings of shim will no longer correct the inhomogeneities present.[16, 17]

To prevent slow drifts in the magnetic field over time, a field-frequency lock is employed. The lock is a feedback system, and in high-field instruments it is based on the signal of a deuterium reference sample. If the resonance of the deuterium signal changes, the magnetic field is adjusted.[10] Low-field NMR spectrometers do not require the use of deuterated solvents to correct for drifts in magnetic field strength, as this can be achieved using a hardware lock which provides a magnetic field to automatically correct the frequency.[18, 19]

2.3 Chemometrics

Spectra are often complex and are usually a combination of several different components, so the use of chemometrics is necessary in order to perform quantitative analysis. Chemometrics allows the reduction of data matrices in order to simplify them. The reduced data contains the most useful information, reflecting the variation in the dataset, and redundant information is present in the residual.[2, 7] Predictions (e.g. of concentration) can be carried out using methods such as classical least squares

(CLS), principal component regression (PCR) and partial least squares (PLS). Calibration using samples of known concentration is first carried out, and the calibration data is then used to build models for prediction of unknown concentrations.[7] To transfer calibration models between spectra acquired using different instruments/sets of conditions without having to re-measure every calibration sample, calibration transfer can be performed. For NMR spectra, reference deconvolution can be applied to remove variations in lineshape. In addition, it is possible to perform calibration-free predictions of concentration using multivariate curve resolution (MCR). These methods will be described in the following subsections.

2.3.1 Preprocessing

Before building chemometric models, preprocessing of the data is usually performed so that only the most relevant information is used in the model. Mean-centring and derivatisation are examples of common preprocessing methods. Mean-centring involves subtracting the mean of each variable from every value of the variable, so that the intensity becomes relative and the variation in response is enhanced. Derivatisation allows removal of any baseline offset present in the spectra and the correction of sloping baselines.[1, 2, 20] While these preprocessing techniques are normally sufficient for MIR spectroscopy, NMR spectra are prone to phase shifts, frequency shifts and distortions, and so usually require further treatment.[21]

The first stage of processing NMR data is to perform a Fourier transform to convert the free induction decay (FID) from the time domain into a spectrum in the frequency domain.[22] Zero filling of the spectrum can be carried out to improve the resolution, and involves adding zeros to the end of the FID signal. The number of points in the FID must equal a power of two in order for fast Fourier transform to be performed.[22, 23] Phase shifts can arise due to small time delays between switching off the pulse and beginning to record the signal. This can be corrected by phasing the spectra, which involves calculating a linear combination of the real and imaginary portions of the FID to find an angle which will correct the spectrum. Phasing can either be carried out manually, or automatically using an algorithm.[23, 24] Distortion of the baseline may be present due to a variety of reasons related to the sample or the instrument, for example

large differences in relaxation time between different components of a sample or corruption in the first few data points of the FID. The baseline can be corrected in either the time or the frequency domain, using a range of methods e.g. iterative polynomial fitting or asymmetric least squares smoothing.[12, 22, 23] Shifts of the spectra in the x direction (i.e. in chemical shift) can be corrected using various warping or alignment methods. These methods will be discussed in more detail in Chapter 5.

2.3.2 Prediction Using Calibration Models

2.3.2.1 Partial Least Squares

PLS was used for the prediction of concentration in this work. PLS involves reduction of the data matrix to a lower dimension by creating latent variables (LVs). Latent variables are best fit lines which aim to simultaneously describe the variance present in the spectral response matrix **X** and the correlation between **X** and the concentration data matrix **Y**, i.e. the covariance. The first LV is in the direction of maximum covariance, and subsequent LVs are orthogonal, each capturing less covariance in the data than the previous LV, as shown in Figure 2.2.[1, 20, 25]

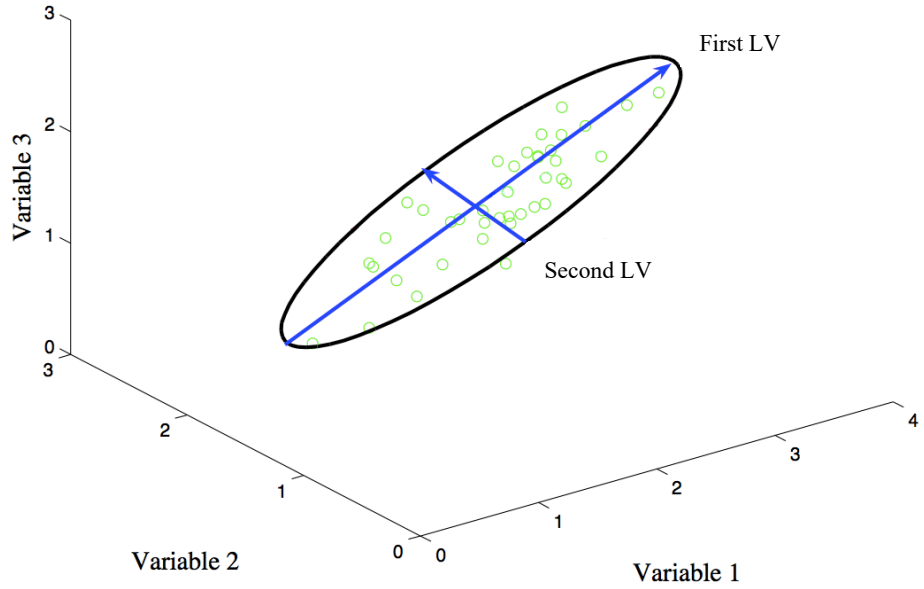

Figure 2.2 - Example illustration of latent variables, taken from reference 25.

LVs consist of scores (**t**) and loadings (**p**), as shown in Figure 2.3. Data points are projected onto the LV as shown in Figure 2.3 (a), and scores are the distances along

the LV at which the projected points lie. They provide information on the relations between samples. Loadings are cosines of the angle at which a unit vector in the direction of the LV lies against the axes of the plot, as shown in Figure 2.3 (b). They describe how the variables relate to each other.[20, 26]

$$\mathbf{X} = \mathbf{t}_1 \mathbf{p}_1^T + \mathbf{t}_2 \mathbf{p}_2^T + \ldots + \mathbf{t}_A \mathbf{p}_A^T + \mathbf{E} \qquad \textbf{Equation 2.3}$$

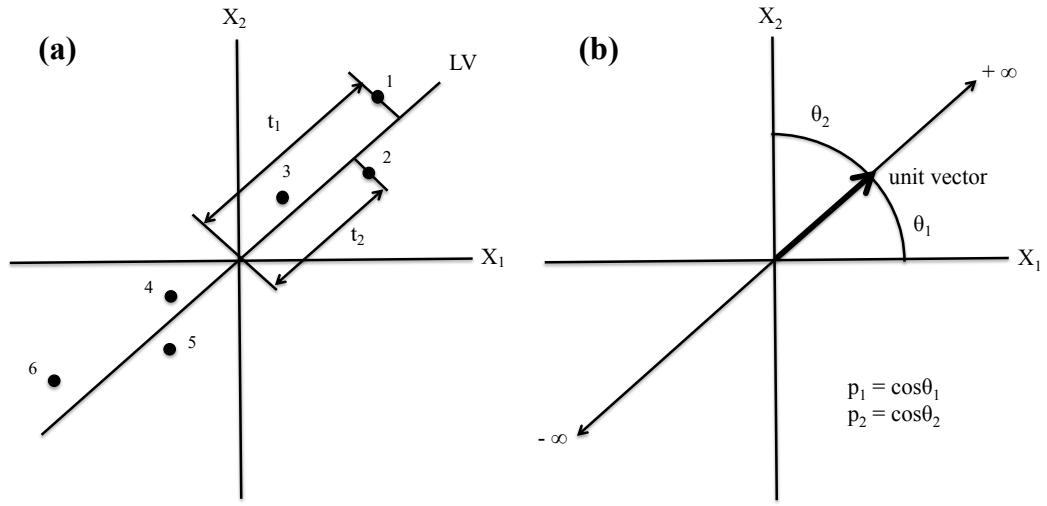

Figure 2.3 - Example illustration of (a) scores and (b) loadings, reproduced from reference 20.

PLS describes the response and concentration data matrices with separate scores and loadings, as shown in Equation 2.4 and Equation 2.5 (where **T** and **P** are the scores and loadings for the spectral response matrix **X**, **U** and **Q** are the scores and loadings for the concentration matrix **Y**, and **E** and **F** are the errors present in each matrix).[20, 25, 26] It aims to determine the maximum variance in the response, whilst at the same time achieving maximum correlation between the two sets of scores using Equation 2.6 (where **B** represents the regression coefficients and **H** represents the error present in the model).[20, 25, 26] The regression coefficients can be calculated using the pseudoinverse of **T** along with the known concentrations of a set of calibration samples (from which **U** can be determined using Equation 2.5). Equation 2.4 can then be used to calculate **T** for unknown samples given their spectral responses; **T** and the calculated regression coefficients can be used to calculate **U** based on Equation 2.6; and **U** can be used to calculate the concentrations of the samples based on Equation

2.5. There are two types of PLS model, PLS1 and PLS2. For PLS1 a separate model is built for each analyte, and for PLS2 a single model is built using all of the analytes.[26]

$$\mathbf{X} = \mathbf{T}\,\mathbf{P}^{T} + \mathbf{E} \qquad \textbf{Equation 2.4}$$

$$\mathbf{Y} = \mathbf{U}\,\mathbf{Q}^{T} + \mathbf{F} \qquad \textbf{Equation 2.5}$$

$$\mathbf{U} = \mathbf{T}\,\mathbf{B} + \mathbf{H} \qquad \textbf{Equation 2.6}$$

The number of LVs to retain in the model is usually chosen by cross validation, which involves predicting the residual error of several different sample subsets. The sample subsets are used to predict the analyte concentrations present in the samples which were left out, and the root mean square error of cross validation (RMSECV) is calculated as shown in Equation 2.7 (where $\hat{y}_i$ and y_i^{ref} are the predicted and reference concentrations of the component of interest in calibration sample i, and n is the number of calibration samples used to build the model).[27] A graph of the RMSECV value versus the number of LVs used to build the model is plotted, and the optimum number of LVs to use is signified by the point at which the graph reaches a minimum or levels out.[27, 28]

$$\text{RMSECV} = \sqrt{\frac{\sum_{i=1}^{n}(\hat{y}_i - y_i^{ref})^2}{n}} \qquad \textbf{Equation 2.7}$$

An advantage of PLS is that latent variables are chosen based on the variation in response which is relevant for predicting the concentration, rather than the variation in response alone. This is the main difference between PLS and PCR.[20, 25, 29] It is assumed that the error arises from both the spectral responses and the concentrations, and this is an advantage over CLS (which assumes that the spectral responses are equal to the concentrations of the analytes present multiplied by their pure component spectra).[25, 30] In addition, the pure spectra of all components do not need to be known, and PLS can be used when the data is collinear.[25, 26, 29] The effect of the error can be reduced by choosing an appropriate number of LVs, however it is possible for too few or too many LVs to be chosen, resulting in underfitting or overfitting of the model.[20, 25] The main

disadvantage of PLS is that it is more complex than methods such as PCR and CLS, and PLS1 in particular is more time-consuming to carry out.

2.3.2.2 Root Mean Square Error of Prediction

In order to assess the effectiveness of a calibration model, the root mean square error of prediction (RMSEP) can be calculated. The RMSEP is a measure of the accuracy of prediction of a model. It is calculated using Equation 2.8, where $\hat{y}_i$ and y_i are the predicted and measured concentrations of the component of interest in test sample i, and n is the number of test samples.[31] Comparison of RMSEP values can allow the effectiveness of different calibration models (or the effectiveness of including different numbers of LVs) to be compared, with lower RMSEP values indicating greater accuracy.

$$\text{RMSEP} = \sqrt{\frac{\sum_{i=1}^{n} (\hat{y}_i - y_i)^2}{n}} \qquad \textbf{Equation 2.8}$$

2.3.2.3 Variance and Bias Indicators

The use of cross validation to select the optimum number of LVs has some limitations. The RMSECV is an indicator of the bias present in a model, i.e. the level of accuracy to which predictions can be made. It does not take into account the variance of the model, i.e. the precision of predictions, thus is prone to overfitting.[32] In addition, interpretation of RMSECV plots can be subjective. Green and Kalivas[32] proposed that examination of variance indicators in conjunction with bias indicators is a more suitable method of selecting the optimum number of LVs than examination of bias indicators (e.g. RMSECV) alone.

One example of a variance indicator is the Euclidean norm of the regression vector. The regression vector is estimated by Equation 2.9, where **p** is the vector of the regression coefficients, **R** is the matrix of spectral responses for the calibration samples, and **c** is the concentration (or other quantitative information to be predicted) of the analyte of interest in the calibration samples.[32]

$$\hat{\mathbf{p}} = \mathbf{R}^{+}\,\mathbf{c} \qquad \textbf{Equation 2.9}$$

An alternative bias indicator to the RMSECV is the root mean square error of calibration (RMSEC). The RMSEC is calculated using Equation 2.10, where c_i and $\hat{c}_i$ are the actual and predicted concentrations of the component of interest in calibration sample i using the model, and m is the number of calibration samples used to build the model.[32] The advantage of using the RMSEC over the RMSECV is that it eliminates the need for cross validation to be carried out.[32]

$$\text{RMSEC} = \sqrt{\frac{\sum_{i=1}^{m}(c_i - \hat{c}_i)^2}{m}} \qquad \textbf{Equation 2.10}$$

The Euclidean norm of the regression vector can be plotted against the RMSEC for each number of LVs to produce an L-shaped plot. The corner of the L-shape (the point at which the decrease in bias is small relative to a large increase in variance) represents the optimum number of LVs. These plots were found to be similar to those of the Euclidean norm of the regression coefficients against the RMSECV.[32]

Determination of corners in the plots of Euclidean norm versus RMSEC can be subjective, so a variation of the method has been demonstrated in an attempt to remove ambiguity. The norm and RMSEC values are scaled and added together, as shown in Equation 2.11, to give a value (C1) ranging from 0 to 1. The C1 value is then plotted against Euclidean norm for each number of LVs, to produce a U-shaped curve. The minimum point of the U-curve represents the optimum number of LVs, with far less ambiguity than is present in the L-shaped plots.[33-35] An example of each type of plot is displayed in Figure 2.4.

$$\text{C1}_i = \left(\frac{\|\hat{\mathbf{p}}_i\| - \|\hat{\mathbf{p}}\|_{\min}}{\|\hat{\mathbf{p}}\|_{\max} - \|\hat{\mathbf{p}}\|_{\min}}\right) + \left(\frac{\text{RMSEC}_i - \text{RMSEC}_{\min}}{\text{RMSEC}_{\max} - \text{RMSEC}_{\min}}\right) \qquad \textbf{Equation 2.11}$$

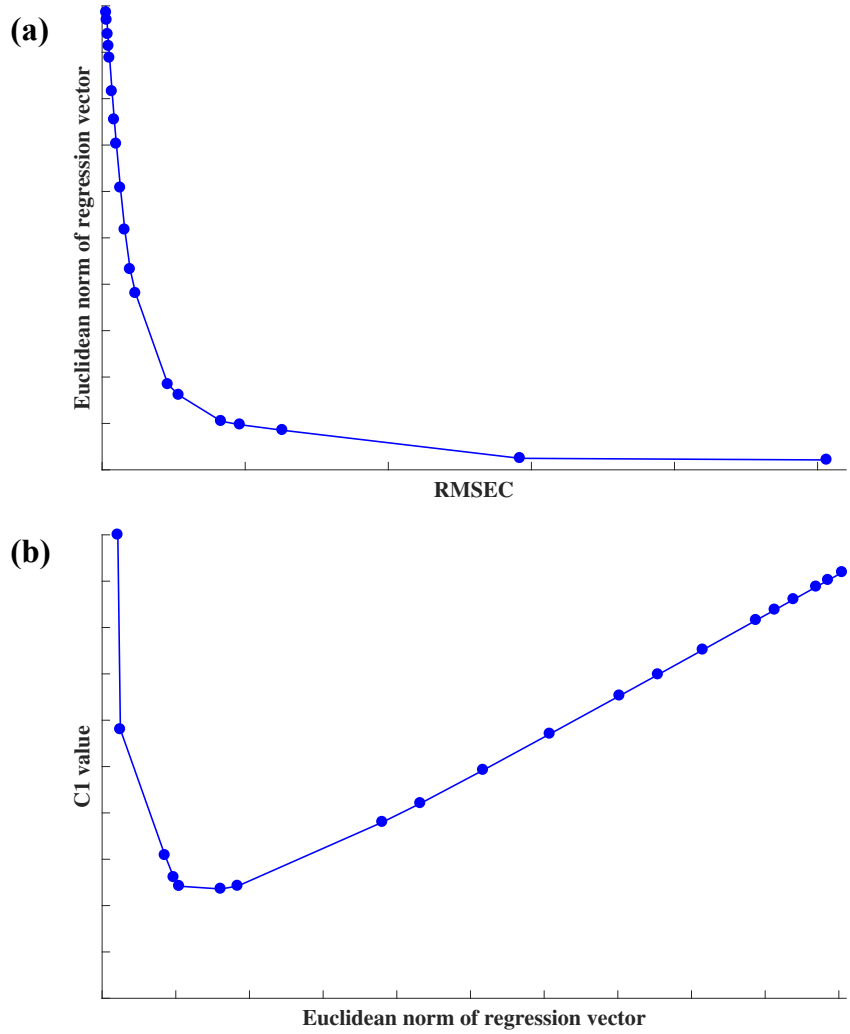

Figure 2.4 - Example of (a) L-shaped and (b) U-shaped plots for determination of the optimum number of LVs.

2.3.3 Calibration Transfer

Calibration transfer allows the transfer of a calibration model between different instruments or sets of measurement conditions. It aims to remove any differences in the spectra which can be attributed to the changes in instrument/measurement conditions. This can save resources by allowing calibration models to be developed at laboratory scale and transferred to a process environment, where different instruments are likely to be used. In addition, it can account for instrumental differences without having to re-measure every calibration sample, which can be advantageous when the number of samples used in the model is large. A subset of calibration samples (known as the transfer samples) can be measured on both instruments/under both sets of

conditions, and a transfer function can be calculated using the two sets of transfer samples. The transfer function is then applied to test spectra collected using the new instrument/conditions, so that they resemble the spectra collected using the original instrument/conditions, and the original calibration model can be used.[36-38] Calibration transfer can be performed using a variety of different methods, and some common methods which have been used in this work will be discussed.

Direct standardisation (DS) and piecewise direct standardisation (PDS) are two of the most widely used methods of calibration transfer.[39] In DS, the spectra acquired using one instrument/under one set of conditions ($\mathbf{S}_1$) are directly related to those collected using the other instrument/set of conditions ($\mathbf{S}_2$) by a linear relationship, as shown in Equation 2.12. **F** can be estimated using PCR or PLS. This assumes that all variation between the two sets of transfer spectra can be attributed to the changes in instrument/conditions, which may not be valid if variation in the chemical compositions of the samples is present.[38, 40]

$$\mathbf{S}_1 = \mathbf{S}_2\,\mathbf{F} \qquad \textbf{Equation 2.12}$$

Unlike DS, where all wavelengths are treated simultaneously, PDS calculates correlations within small windows of the spectra. Regression vectors calculated for each window are combined to create the transfer function **F**. The window size can be defined by the user. The use of spectral windows allows the model to handle relative shifts between the two sets of transfer spectra along the wavelength axis, as well as differences in the intensity and widths of peaks.[38, 40]

Spectral space transformation (SST) is a method of calibration transfer in which a subset of spectra is measured on each instrument (or under both sets of conditions), and the differences between the spectra are removed by transformation between the spectral spaces spanned by the two sets of spectra. The transformed spectra, $\mathbf{x}_{trans}$, can be described by Equation 2.13, where $\mathbf{x}_{test}$ represents the measured test spectra before transformation and $\mathbf{P}_1$ and $\mathbf{P}_2$ are derived from the singular value decomposition of $\mathbf{X}_{comb}$ (Equation 2.14), where $\mathbf{X}_{comb}$ is the combined matrix of the transfer spectra collected using each instrument/set of conditions. In Equation 2.14, $\mathbf{T}_s = \mathbf{U}_s \sum_s$; $\mathbf{P}_s = \mathbf{V}_s$; $\mathbf{E} = \mathbf{U}_n \sum_n \mathbf{V}_n^T$; $\mathbf{P}_s^T = [\mathbf{P}_1^T, \mathbf{P}_2^T]$ and the subscripts s and n denote spectral information

and noise. Equation 2.13 is derived using Equation 2.14 and the Beer Lambert law, as described by Du et al.[39]

$$\mathbf{x}_{trans} = \mathbf{x}_{test} \left(\mathbf{P}_2^{\mathrm{T}}\right)^{+} \mathbf{P}_1^{\mathrm{T}} + \mathbf{x}_{test} \left(\mathbf{P}_2^{\mathrm{T}}\right)^{+} \mathbf{P}_2^{\mathrm{T}} \qquad \textbf{Equation 2.13}$$

$$\mathbf{X}_{comb} = [\mathbf{U}_s, \mathbf{U}_n] \begin{bmatrix} \sum_s & 0 \\ 0 & \sum_n \end{bmatrix} [\mathbf{V}_s, \mathbf{V}_n]^{\mathrm{T}} = \mathbf{T}_s \mathbf{P}_s^{\mathrm{T}} + \mathbf{E} = \mathbf{T}_s \left[\mathbf{P}_1^{\mathrm{T}}, \mathbf{P}_2^{\mathrm{T}}\right] + \mathbf{E} \qquad \textbf{Equation 2.14}$$

SST was shown by Du et al.[39] to perform better than common methods of calibration transfer such as piecewise direct standardisation, univariate slope and bias correction and global partial least squares. The main advantage over PDS is that it is simpler to perform, as selection of an appropriate number of singular values is more straightforward than selection of an appropriate window size.[39]

2.3.4 Reference Deconvolution

In NMR spectroscopy, distortions from ideal lineshape can occur due to instrumental imperfections e.g. magnetic field inhomogeneity, radiofrequency pulse phase error and variation in receiver gain.[41] Reference deconvolution is a method of correcting for these distortions in order to improve the lineshapes of NMR peaks. The concept of reference deconvolution is similar to that of calibration transfer. However unlike calibration transfer, the transformation is based on the differences between a reference peak in the spectrum and its ideal lineshape.[42]

The reference signal used to perform reference deconvolution is normally a well-resolved singlet peak. Fourier transformation (FT) and phase correction of the FID is first carried out to obtain an experimental NMR spectrum. The whole spectrum apart from the reference signal is then set to zero and an inverse Fourier transformation (IFT) is carried out to produce a spectrum of the reference signal in the time domain. This reference signal is divided by an ideal reference signal (based on e.g. a Lorentzian lineshape) to obtain a correction factor. The time-domain experimental spectrum is then divided by the correction factor to obtain a corrected FID, which can be transformed into a corrected frequency domain experimental spectrum.[43-45] A diagram of this process is displayed in Figure 2.5. Although a singlet reference peak is desirable, reference deconvolution using multiplet reference peaks has also been

demonstrated.[46] The main limitation of reference deconvolution is the requirement of a well resolved reference signal to be present in every sample. When no well resolved peaks are present it is necessary to add an internal standard, which can be impractical in reaction monitoring (e.g. when flow NMR spectroscopy is used).

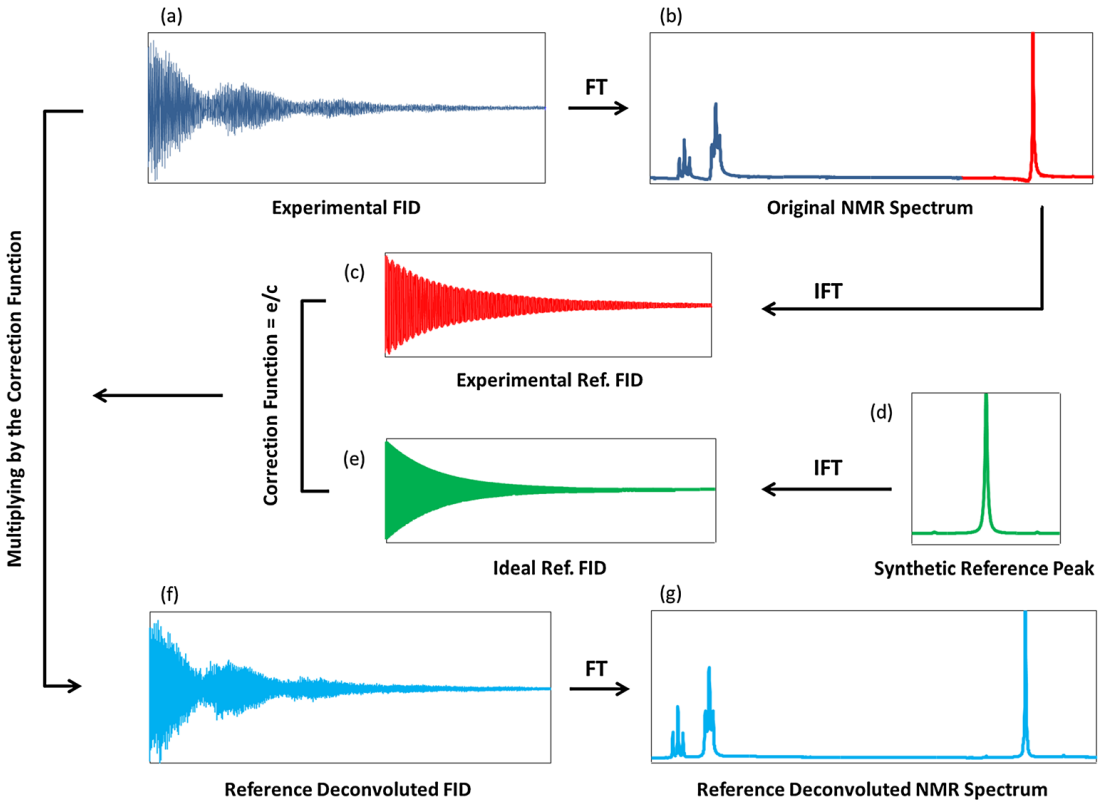

Figure 2.5 - The process of reference deconvolution, taken from reference 41.

2.3.5 Calibration-Free Prediction

In addition to the prediction of concentration using calibration models, it is also possible to utilise calibration-free methods such as multivariate curve resolution (MCR). MCR allows the decomposition of a matrix into its pure component contributions. It is based on Equation 2.15, where **D** is the measured experimental data matrix, **C** describes the variation in the rows of **D** (normally representing the contribution of each component to the total absorbance of the mixture, i.e. the relative concentration), **S** describes the variation in the columns of **D** (normally representing the pure spectra of each component), and **E** describes the error in the model. Decomposition of **D** into **C** and **S** is commonly carried out by iterative optimisation, using an algorithm such as alternating least squares (ALS). ALS involves two steps;

determination of the value of **C** which minimises || **D** – **CS**^{T} || given an initial estimate of **S** and a set of constraints, and determination of the value of **S** which minimises || **D** – **CS**^{T} || given an initial estimate of **C** and a set of constraints. These steps are repeated in an alternating manner until the standard deviations of the residuals between the calculated and experimental values reach a chosen convergence criterion.[47-49]

$$\mathbf{D} = \mathbf{C}\,\mathbf{S}^T + \mathbf{E} \qquad \textbf{Equation 2.15}$$

Initial estimates of **C** and **S** can be calculated using a variety of methods e.g. evolving factor analysis, pure variable detection and needle search.[49, 50] Evolving factor analysis[51] utilises factor analysis along with the order of the spectra in the data matrix to produce plots of eigenvalues as a function of elution time. The elution of a new component can be observed as the evolution of a new significant eigenvalue. This is repeated in the reverse direction and the profiles are connected to produce an estimate of **C** for each component. Pure variable detection is based on the SIMPLISMA (simple-to-use interactive self-modelling mixture analysis) method.[52, 53] SIMPLISMA is a reference-free method of curve resolution which relies on the calculation of a purity function based on the ratio of the standard deviation to the mean in order to resolve the spectra into their pure component contributions.[54] In the needle search method,[55, 56] a narrow peak function is fitted to each time point in the data matrix using a least-squares fit. The residual sum of squares for each time point is displayed, and local minima are present at the points at which the maximum relative concentration of a component occurs. The detected local minima are displayed, and the user selects a local minimum for each component of the mixture (i.e. the time point at which the maximum relative concentration of each component is present). Alternatively the pure spectra and/or estimated relative concentration profiles can be used as initial estimates, if known.

The number of components can be inputted manually or calculated using a method such as singular value decomposition.[50, 57] Constraints can include non-negativity, unimodality (i.e. one maximum), closure (i.e. the sum of the component contributions is equal to a constant) and equality.[48, 49] Gemperline and Cash[49] developed a variation of the ALS method in which a least squares penalty function is applied to produce "soft" rather than "hard" constraints. The application of soft constraints allows

deviations in the estimates, providing greater flexibility. This will be discussed in more detail in Chapter 4.

A major advantage of MCR is that it eliminates the need to build a calibration model, which can save time and resources. In addition, the identities of the pure components do not need to be known (although knowledge of the pure spectra will improve the predictions). However it is not possible to perform MCR when peak shift is present (as often occurs in low-field NMR spectra), and the method is unable to distinguish between different components which form at the same rate. The main limitation of MCR is that there may be a number of feasible solutions to the optimisation, therefore it is possible for the ALS algorithm to select an incorrect solution as the optimum. The application of appropriate constraints allows the number of possible solutions to be reduced, and can solve this issue.[58]

2.4 References

1. N. D. Lourenço, J. A. Lopes, C. F. Almeida, M. C. Sarraguça and H. M. Pinheiro, *Anal. Bioanal. Chem.*, 2012, **404**, 1211–1237.
2. D. Landgrebe, C. Haake, T. Höpfner, S. Beutel, B. Hitzmann, T. Scheper, M. Rhiel and K. Reardon, *Appl. Microbiol. Biotechnol.*, 2010, **88**, 11–22.
3. J. Haas and B. Mizaikoff, *Annual Rev. Anal. Chem.*, 2016, **9**, 17.11–17.24.
4. L. P. Schuler, J. S. Milne, J. M. Dell and L. Faraone, *J. Phys. D: Appl. Phys.*, 2009, **42**, 133001.
5. S. Prunet, C. Durieu and B. Journet, *Opt. Eng.*, 2003, **42**, 985–993.
6. K. Murayama, T. Genkawa, D. Ishikawa, M. Komiyama and Y. Ozaki, *Rev. Sci. Instrum.*, 2013, **84**, 023104.
7. D. S. Kim, T. R. Lee and G. Yoon, *Opt. Eng.*, 2014, **53**, 074108.
8. A. Bogomolov, M. Heßling, U. Wenzel, S. Princz, T. Hellmuth, M. J. B. Bernal, T. Sakharova, I. Usenov, V. Artyushenko and H. Meyer, *Sens. Actuators, B*, 2015, **221**, 1601–1610.
9. D. Geörg, R. Schalk, F. J. Methner and T. Beuermann, *Meas. Sci. Technol.*, 2015, **26**, 065501.
10. J. Keeler, *Understanding NMR Spectroscopy*, John Wiley & Sons Ltd, Chichester, UK, 2nd edn., 2010.

11. H. Günther, *NMR Spectroscopy: Basic Principles, Concepts and Applications in Chemistry*, John Wiley & Sons, Weinheim, Germany, 3rd edn., 2013.
12. L. R. Euceda, G. F. Giskeodegard and T. F. Bathen, *Scand. J. Clin. Lab. Invest.*, 2015, **75**, 193–203.
13. A. Nordon, C. A. McGill and D. Littlejohn, *Analyst*, 2001, **126**, 260–272.
14. B. Blumich and K. Singh, *Angew. Chem.-Int. Ed.*, 2018, **57**, 6996–7010.
15. K. Meyer, S. Kern, N. Zientek, G. Guthausen and M. Maiwald, *Trends Anal. Chem.*, 2016, **83**, 39–52.
16. K. Singh and B. Blumich, *Trends Anal. Chem.*, 2016, **83**, 12–26.
17. E. Danieli, J. Perlo, A. L. L. Duchateau, G. K. M. Verzijl, V. M. Litvinov, B. Blumich and F. Casanova, *ChemPhysChem*, 2014, **15**, 3060–3066.
18. Magritek, The Lock and the importance of field stability, http://www.magritek.com/2014/08/12/the-lock-and-the-importance-of-field-stability/, (accessed 29th April, 2019).
19. P. Giraudeau and F. X. Felpin, *React. Chem. Eng.*, 2018, **3**, 399–413.
20. P. Geladi and B. R. Kowalski, *Anal. Chim. Acta*, 1986, **185**, 1–17.
21. H. Witjes, W. J. Melssen, H. Zandt, M. van der Graaf, A. Heerschap and L. M. C. Buydens, *J. Magn. Reson.*, 2000, **144**, 35–44.
22. F. Jiru, *Eur. J. Radiol.*, 2008, **67**, 202–217.
23. M. Staniszewski, A. Skorupa, L. Boguszewicz, M. Sokol and A. Polanski, in *Information Technologies in Medicine*, eds. E. Pietka, P. Badura, J. Kawa and W. Wieklawek, ITIB, Kamien Slaski, Poland, 2016, vol. 1, pp. 341–352.
24. B. Worley and R. Powers, *Chemom. Intell. Lab. Syst.*, 2014, **131**, 1–6.
25. B. M. Wise, N. B. Gallagher, R. Bro, J. M. Shaver, W. Windig and R. S. Koch, *Chemometrics Tutorial for PLS_Toolbox and Solo*, Eigenvector Research Incorporated, Wenatchee, WA, USA, 2006.
26. A. Ferrer, D. Aguado, S. Vidal-Puig, J. M. Prats and M. Zarzo, *Appl. Stochastic Models Bus. Ind.*, 2008, **24**, 551–567.
27. A. Bogomolov, T. Grasser and M. Hessling, *J. Chemom.*, 2011, **25**, 389–399.
28. P. Geladi, B. Sethson, J. Nyström, T. Lillhonga, T. Lestander and J. Burger, *Spectrochim. Acta, Part B*, 2004, **59**, 1347–1357.

29. Y. Roggo, P. Chalus, L. Maurer, C. Lema-Martinez, A. Edmond and N. Jent, *J. Pharm. Biomed. Anal.*, 2007, **44**, 683–700.
30. C. L. Erickson, M. J. Lysaght and J. B. Callis, *Anal. Chem.*, 1992, **64**, 1155–1163.
31. Y. F. Ge, C. L. S. Morgan and J. P. Ackerson, *Geoderma*, 2014, **221**, 61–69.
32. R. L. Green and J. H. Kalivas, *Chemom. Intell. Lab. Syst.*, 2002, **60**, 173–188.
33. J. H. Kalivas, K. Heberger and E. Andries, *Anal. Chim. Acta*, 2015, **869**, 21–33.
34. J. H. Kalivas and J. Palmer, *J. Chemom.*, 2014, **28**, 347–357.
35. A. A. Gowen, G. Downey, C. Esquerre and C. P. O'Donnell, *J. Chemom.*, 2011, **25**, 375–381.
36. J. J. Workman, Jr., *Appl Spectrosc*, 2018, **72**, 340–365.
37. T. Fearn, *J. Near Infrared Spectrosc.*, 2001, **9**, 229–244.
38. R. N. Feudale, N. A. Woody, H. W. Tan, A. J. Myles, S. D. Brown and J. Ferre, *Chemom. Intell. Lab. Syst.*, 2002, **64**, 181–192.
39. W. Du, Z. P. Chen, L. J. Zhong, S. X. Wang, R. Q. Yu, A. Nordon, D. Littlejohn and M. Holden, *Anal. Chim. Acta*, 2011, **690**, 64–70.
40. Y. D. Wang, D. J. Veltkamp and B. R. Kowalski, *Anal. Chem.*, 1991, **63**, 2750–2756.
41. P. Ebrahimi, M. Nilsson, G. A. Morris, H. M. Jensen and S. B. Engelsen, *J. Chemom.*, 2014, **28**, 656–662.
42. T. M. Alam and M. K. Alam, *J. Chemom.*, 2010, **24**, 261–272.
43. G. A. Morris, H. Barjat and T. J. Horne, *J. Prog. Nucl. Magn. Reson. Spectrosc.*, 1997, **31**, 197–257.
44. K. R. Metz, M. M. Lam and A. G. Webb, *Concepts Magn. Reson.*, 2000, **12**, 21–42.
45. T. J. Horne and G. A. Morris, *J. Magn. Reson., Ser. A*, 1996, **123**, 246–252.
46. H. Barjat, G. A. Morris, A. G. Swanson, S. Smart and S. C. R. Williams, *J. Magn. Reson., Ser. A*, 1995, **116**, 206–214.
47. J. Jaumot, R. Gargallo, A. de Juan and R. Tauler, *Chemom. Intell. Lab. Syst.*, 2005, **76**, 101–110.
48. A. de Juan, J. Jaumot and R. A. Tauler, *Anal. Methods*, 2014, **6**, 4964–4976.

49. P. J. Gemperline and E. Cash, *Anal. Chem.*, 2003, **75**, 4236–4243.
50. J. Jaumot, A. de Juan and R. Tauler, *Chemom. Intell. Lab. Syst.*, 2015, **140**, 1–12.
51. M. Maeder and A. D. Zuberbuehler, *Anal. Chim. Acta*, 1986, **181**, 287–291.
52. W. Windig and J. Guilment, *Anal. Chem.*, 1991, **63**, 1425–1432.
53. W. Windig and D. A. Stephenson, *Anal. Chem.*, 1992, **64**, 2735–2742.
54. A. Bogomolov, M. Hachey and A. Williams, *Prog. Chemom. Res.*, 2005, 119–135.
55. P. J. Gemperline, *J. Chem. Inf. Comput. Sci.*, 1984, **24**, 206–212.
56. P. J. Gemperline, *Anal. Chem.*, 1986, **58**, 2656–2663.
57. G. H. Golub and C. Reinsch, *Numer. Math.*, 1970, **14**, 403–420.
58. M. Garrido, F. X. Rius and M. S. Larrechi, *Anal. Bioanal. Chem.*, 2008, **390**, 2059–2066.

3 Performance Assessment of a Novel Mid-Infrared Spectrometer and Calibration Transfer Between Laboratory and Process Instruments

3.1 Introduction

As discussed in Chapter 1, the recent availability of novel technologies such as MEMS devices and uncooled detector arrays has facilitated the design of MIR spectrometers which are suited for use in process environments. The Keit spectrometer is one such instrument, and is particularly robust due to an optical design based on the Sagnac interferometer. In addition, it has a probe directly attached to avoid the need for fibre optics. There have not yet been any studies published on the performance of the Keit spectrometer, so this will now be assessed. The performance of the Keit spectrometer for the quantitative *in situ* analysis of liquids was compared to that of a laboratory based FTIR spectrometer with a fibre coupled probe (the MB3000). Laboratory based spectrometers provide greater sensitivity and flexibility than the Keit spectrometer, however they are larger and less robust due to the presence of delicate moving parts, so are not as suitable for process analysis.

The diameter of the Keit spectrometer probe is large (25 mm), therefore the spectrometer is not suited for use with standard laboratory glassware. This makes it difficult to build calibration models in the laboratory using the Keit spectrometer and inhibits its use for process development. The ability to perform calibration transfer between laboratory and process instruments would therefore be advantageous, as it would allow calibration models built in the laboratory to be applied to spectra collected in a process environment. In addition, the development of a model in the laboratory as opposed to a process environment would save resources.

Calibration transfer was described in section 2.3.3, and is extensively applied in optical spectroscopy.[1, 2] The majority of examples utilise NIR spectroscopy, but calibration transfer has also been demonstrated between different MIR spectrometers, using methods such as DS, PDS and SST.[3-6] However the transfer of calibration models between laboratory and process MIR spectrometers has not been demonstrated. The aims of this chapter are to assess the basic performance of the Keit spectrometer

against the MB3000, and to evaluate the effectiveness of calibration transfer between the MB3000 and Keit spectrometers.

3.2 Experimental

3.2.1 Instrumental Details

In this work, the Echo+ model of the Keit spectrometer (Keit Ltd., Didcot, UK) and the MB3000 spectrometer (ABB, Zurich, Switzerland) were used. The Keit spectrometer is compact, as shown in Figure 3.1, with the unit measuring 204 mm x 97 mm x 32 mm. The attached probe measures 257 mm in length, with a diameter of 25 mm. The components of the spectrometer were detailed in section 1.1.2.4. It covers the spectral range 800 – 2000 cm^{-1}, with a resolution of 16 cm^{-1}, and the data are interpolated to give a data point every 8.28 cm^{-1}.

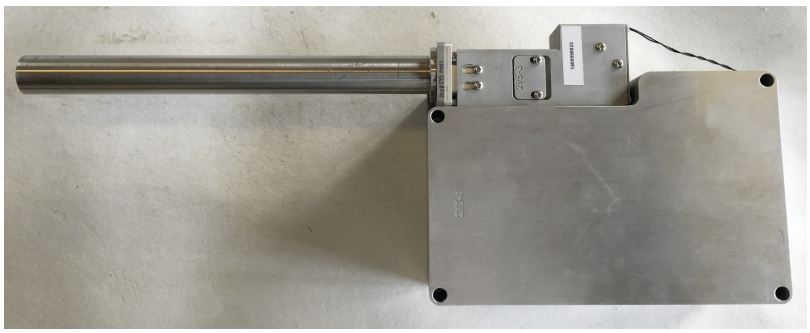

Figure 3.1 - The Keit spectrometer

The MB3000 spectrometer is a benchtop FTIR spectrometer with a fibre-coupled ATR probe from Art Photonics, as displayed in Figure 3.2. The spectrometer unit measures 370 mm x 435 mm x 280 mm. The probe is 10 mm in diameter with a diamond cone, and is coupled to the instrument using polycrystalline silver halide fibres. A Michelson interferometer, DTGS detector and ceramic globar light source are used in the instrument. The MB3000 spectrometer covers the range 485 – 8500 cm^{-1}, and the range 600 – 1900 cm^{-1} is available with the current probe. The resolution of the MB3000 spectrometer can be altered from 1 – 64 cm^{-1}, and a resolution of 16 cm^{-1} was used in this work to match the resolution of the Keit spectrometer. The resolution of the MB3000 instrument is reduced by taking measurements at fewer wavenumbers, i.e. every 1 cm^{-1} at the highest available resolution and every 64 cm^{-1} at the lowest

resolution. At each resolution, the data are interpolated to give approximately 2 data points per measurement (e.g. every 7.71 cm^{-1} at 16 cm^{-1} resolution and every 1.93 cm^{-1} at 4 cm^{-1} resolution).

Figure 3.2 - The MB3000 spectrometer

3.2.2 Basic Performance Assessment

In order to compare the basic performance of the Keit and MB3000 spectrometers, a single spectrum of acetone (≥ 99.8 %, VWR, Fontenay-sous-Bois, France) was first measured using each instrument. With both instruments, one scan was acquired at a resolution of 16 cm^{-1}. The time for acquisition of a spectrum was 1.5 s and 0.8 s for the Keit and MB3000 spectrometers, respectively. The same spectral range, 800 – 1800 cm^{-1}, was used to compare the instruments. The region below 800 cm^{-1} was not included as it is outside the range covered by the Keit spectrometer, and the region above 1800 cm^{-1} was not included due to the presence of noise in the MB3000 spectrum. This will be discussed in more detail in the Results and Discussion section. Over the range 800 – 1800 cm^{-1}, 121 data points were present in the Keit spectrum and 130 data points were present in the MB3000 spectrum. The signal to noise ratio was calculated for each spectrum by dividing the height of the peak at approximately 1360 cm^{-1} by the standard deviation of the noise over the region 960 – 1040 cm^{-1}.

3.2.3 Analysis of Solvent Mixtures

In order to compare the predictive ability of each instrument, quantitative *in situ* analysis of ternary solvent mixtures was carried out using the Keit and MB3000 spectrometers. Sixteen calibration samples and six test samples were prepared, containing varying concentrations of acetone (≥ 99.8 %, VWR, Fontenay-sous-Bois, France), ethanol (≥ 99.8 %, VWR, Fontenay-sous-Bois, France) and ethyl acetate (≥ 99.5 %, Sigma Aldrich, Steinheim, Germany) in units of % w/w, as shown in Table 3.1. The samples were prepared by mass, to a precision of 0.0001 g. The compositions of the mixtures were chosen to span the range of the ternary diagram displayed in Figure 3.3. Each of the samples was analysed using the Keit spectrometer and the MB3000 spectrometer at 16 cm^{-1} resolution. Three repeat measurements were collected per sample, in a random order, and each measurement was an average of 19 scans (based on the number of scans acquired by the Keit spectrometer over a 30 second period).

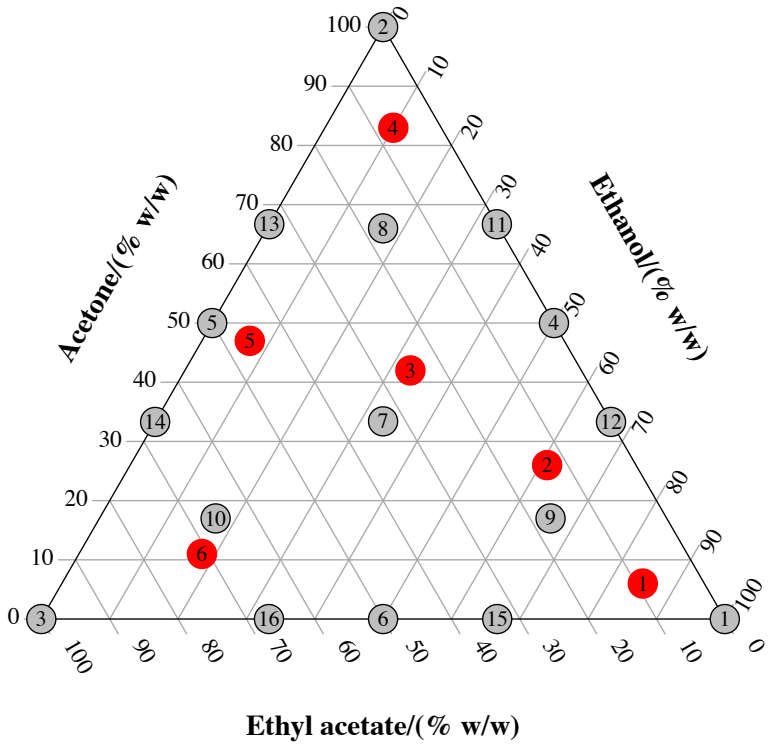

Figure 3.3 - Concentrations (in units of % w/w) of solvents in ternary mixtures, calibration samples shown in grey and test samples shown in red.

Table 3.1 - Concentrations of solvents in calibration and test samples.

Sample	Concentration/(% w/w)		
	Acetone	Ethanol	Ethyl acetate
Calibration sample 1	0.0	100.0	0.0
Calibration sample 2	100.0	0.0	0.0
Calibration sample 3	0.0	0.0	100.0
Calibration sample 4	50.1	49.9	0.0
Calibration sample 5	50.0	0.0	50.0
Calibration sample 6	0.0	50.0	50.0
Calibration sample 7	33.2	33.3	33.4
Calibration sample 8	66.1	16.9	17.0
Calibration sample 9	17.1	65.8	17.1
Calibration sample 10	17.0	17.0	65.9
Calibration sample 11	66.6	33.4	0.0
Calibration sample 12	34.4	65.6	0.0
Calibration sample 13	66.7	0.0	33.3
Calibration sample 14	33.3	0.0	66.7
Calibration sample 15	0.0	66.6	33.4
Calibration sample 16	0.0	33.3	66.7
Test sample 1	6.4	84.6	9.0
Test sample 2	26.0	60.9	13.1
Test sample 3	42.0	32.9	25.1
Test sample 4	82.6	10.3	7.1
Test sample 5	46.9	7.3	45.8
Test sample 6	11.0	18.0	70.9

3.2.4 PLS1 Models

To compare the predictive ability of each spectrometer, PLS1 models were built using PLS Toolbox version 8.2.1 (Eigenvector, Washington, USA) in MATLAB 2016b (MathWorks, Massachusetts, USA). The spectra of the calibration samples were used to build the models, and the models were used to predict the concentration (in % w/w)

of each solvent present in the test samples. Mean centring of the data was carried out prior to modelling. A custom method of cross-validation was used based on contiguous blocks, where each block contained the three repeat measurements of each sample. Calibration samples 1 – 3 (the pure solvents) were included in every calculation, to give a total of thirteen splits.

The number of latent variables to include in each model was chosen by examination of bias/variance plots of C1 against RMSEC (as described by Kalivas and Palmer[7] and detailed in section 2.3.2.3) along with plots of RMSECV and RMSEP against the number of latent variables. These plots are displayed in Appendix 3. It was found that the total number of latent variables included in the plots of C1 against RMSEC could affect the point at which the minimum of the U-curve occurred, so the maximum possible number of latent variables (48, based on the number of calibration measurements) were included in these plots. Four latent variables were chosen as the optimum for each model, as this appeared to be the optimum number for the MB3000 data. The optimum numbers for the Keit data were less clear (either three or five latent variables could have been chosen in most cases), so four latent variables were chosen so that the models would be comparable to those built using the MB3000 data.

RMSEP values were calculated using PLS Toolbox, to compare the predicted and measured solvent concentrations. For each model, the predicted versus actual concentrations were plotted and the best fit lines and R^2 values of the plots were calculated using the "fitlm" function in MATLAB. The ordinary, unadjusted R^2 values were used. Residual error versus concentration was also plotted for each model. The average absolute relative error in the predictions was calculated by taking the absolute difference between each actual and predicted concentration, converting the value to a percentage and calculating the average for each solvent.

3.2.5 Calibration Transfer

3.2.5.1 Initial Method Comparison

Calibration transfer between the MB3000 and Keit spectrometers was performed in order to make the spectra collected on the Keit spectrometer resemble those collected on the MB3000 spectrometer. Initially, the measurements of calibration samples 1, 2, 3, 8, 9 and 10 acquired using the Keit and MB3000 spectrometers were used to

calculate a transfer function between the two spectrometers. The transfer samples were chosen to include each of the pure components and three additional samples which contained all of the components. Three different methods of calibration transfer were compared; DS, PDS and SST. A description of each method can be found in section 2.3.3.

DS and PDS were performed using PLS Toolbox version 8.6.2 (Eigenvector, Washington, USA) in MATLAB 2016b (MathWorks, Massachusetts, USA). SST was performed in MATLAB, using the algorithm described by Du et al.[3] A SST algorithm incorporating a scaling step has also been demonstrated by McIntyre[8] to improve the results of SST when large differences in absorbance are present between the two sets of spectra. The algorithm involves the application of a scaling factor to the data from the second dataset, and the scaling factor is calculated as shown in Equation 3.1 (where ydata1 represents the transfer samples from the first dataset, ydata2 represents the transfer samples from the second dataset, *i* represents each data point, and *n* is the total number of data points across all the transfer samples in one of the datasets).

$$\text{Scaling factor} = \frac{\sqrt{\sum_{i=1}^{n} \text{ydata1}_i^{\,2}}}{\sqrt{\sum_{i=1}^{n} \text{ydata2}_i^{\,2}}} \qquad \textbf{Equation 3.1}$$

The SST algorithms with and without scaling were both used, and the results compared. The spectra acquired using the Keit spectrometer were interpolated in MATLAB prior to calculating the transfer function so that the wavenumbers of the measurements would match those of the spectra acquired on the MB3000 spectrometer. Interpolation was carried out using the MATLAB “interp1” function with the “spline” method.

The PLS1 models built using the MB3000 calibration data (described in section 3.2.4) were used to predict the compositions of the test spectra acquired using the Keit spectrometer, first after interpolation only and then after interpolation followed by calibration transfer (using DS, PDS, SST without scaling and SST with scaling). The RMSEP values obtained for each model were compared in order to assess the effect of

calibration transfer on the PLS predictions and to compare the different methods of calibration transfer. Example transferred spectra for each method were also compared to the corresponding MB3000 spectra.

In order to determine the optimum window size for PDS, PDS was carried out using each possible window size between 1 and 51 data points (every odd number) and the window size was plotted against RMSEP. The lowest RMSEP value was obtained for a window size of 41, so this value was used to build all PDS models. SST was performed using one to ten singular values, and the RMSEP values obtained for each were compared. Inclusion of five singular values was found to produce the minimum RMSEP value, so this number was used to compare SST to DS and PDS. The plots of RMSEP versus PDS window size and number of singular values can be found in Appendix 3.

3.2.5.2 Transfer Sample Comparison

3.2.5.2.1 Choice of Transfer Samples

An investigation into the effect of changing the transfer sample set was also carried out for each method of calibration transfer. In order for calibration transfer to be effective, the transfer samples need to be representative of the whole dataset,[9] therefore the transfer sample sets used in this work were chosen to symmetrically span the compositions covered by the ternary diagram (Figure 3.3). Retaining symmetry within the ternary diagram ensures that each component is equally represented. In order to compare the effects of including/excluding pure, binary and ternary samples, four different sets of six transfer samples were compared: calibration samples 1 – 3 and 8 – 10 (pure and ternary); calibration samples 4 – 6 and 8 – 10 (binary and ternary); calibration samples 1 – 3, 12, 13 and 16 (pure and binary); and calibration samples 11 – 16 (binary only).

According to the PLS Toolbox "stdsslct" function, the six calibration samples with the highest leverage for the MB3000 spectrometer were samples 1 – 3 (pure components) and samples 4, 5 and 16 (binary mixtures). For the Keit spectrometer, samples 1 – 3 (pure components) and samples 11, 14 and 16 (binary mixtures) had the highest leverage. Therefore for the transfer sample set consisting of pure and binary samples, calibration samples 1 – 3 and 16 were included, as these were shown to have the

highest leverage using both instruments. Calibration samples 12 and 13 were also included in order to retain the symmetry of the ternary diagram. For SST, the RMSEP values obtained for each possible number of singular values from one to ten were compared for each set of transfer samples. The overall optimum was again found to be five, so five singular values were used for all SST models in this work. The optimum PDS window size was not recalculated for the additional sets of transfer samples, as the number of possible window sizes was too large and the previous optimum of 41 was found to be effective.

The subset of samples used to calculate the transfer function may not always be included in the calibration model, as it is possible to select the transfer samples from the test dataset (the samples acquired using the second instrument) rather than the calibration dataset (the samples acquired using the first instrument).[9] The RMSEP values obtained when the transfer samples were excluded from the PLS1 model (i.e. only ten calibration samples were used) were compared to the results obtained when the transfer samples were included (i.e. all sixteen calibration samples were used).

3.2.5.2.2 Number of Transfer Samples

The effect of changing the number of samples in the transfer set was then investigated. Du et al.[3] state that the number of samples used to calculate the transfer function should be equal to at least the number of significant spectral variation sources. At least two sources of variation were present in this case, as the compositions of the samples were based on a ternary design with a total concentration of 100 % w/w. Therefore three transfer samples were chosen as the minimum number to examine, in order to retain the symmetry in the ternary diagram and to account for any non-linearity present in the measurements. Three transfer samples (calibration samples 8 – 10 or calibration samples 1 – 3), four transfer samples (calibration samples 7 – 10 or calibration samples 1 – 3 and 7) and seven transfer samples (calibration samples 1 – 3 and 7 – 10) were compared to the results obtained using six transfer samples (calibration samples 1 – 3 and 8 – 10). Each of these transfer sample sets were chosen to be as similar as possible to the initial set of six transfer samples, while retaining the symmetry within the ternary diagram. It was not possible to select five calibration samples which symmetrically spanned the range of the diagram, therefore no set of five transfer samples was

included. As a benchmark, calibration transfer was also carried out using all sixteen calibration samples as the transfer set.

3.3 Results and Discussion

3.3.1 Basic Performance Assessment

Spectra of acetone acquired using the MB3000 spectrometer (red) and the Keit spectrometer (blue) are displayed in Figure 3.4, in order to compare the basic performance of the instruments. An assignment of the main peaks present in the spectra is displayed in Table 3.2. In the spectrum acquired using the Keit spectrometer, the absorbance of the three largest peaks (at approximately 1220 cm^{-1}, 1360 cm^{-1} and 1710 cm^{-1}) is lower than for the MB3000 spectrometer, particularly the peak at 1710 cm^{-1} which is around 0.5 smaller in height. The smaller peaks have similar absorbance in each spectrum. As the same resolution was used to acquire both spectra, this is could be due to the pathlength of the light differing for each instrument, as the ATR crystals are made of different materials and may have different geometry. The calculated signal to noise ratios were 180.0 for the MB3000 spectrometer and 106.9 for the Keit spectrometer. The signal to noise ratio is poorer in the spectrum acquired using the Keit spectrometer, but is still relatively high. This basic assessment suggests that the performance of the Keit spectrometer is comparable to that of the MB3000 spectrometer.

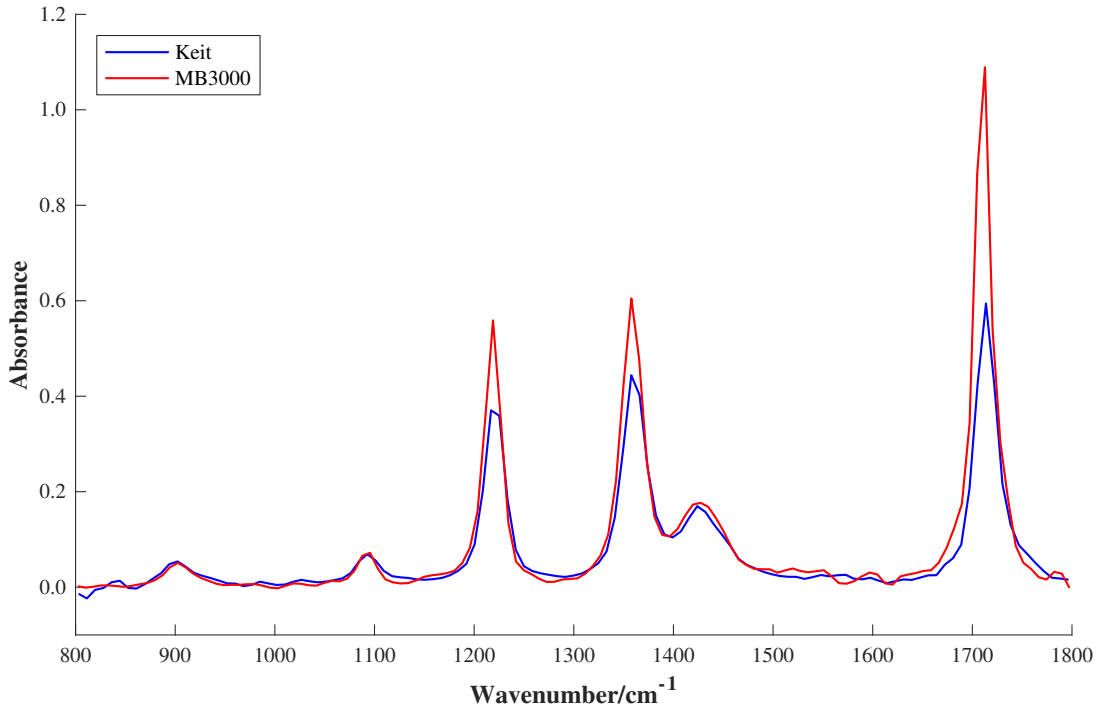

Figure 3.4 - Single scan of acetone at 16 cm^{-1} resolution obtained using the MB3000 spectrometer (red) and the Keit spectrometer (blue).

Table 3.2 - Assignment of the main peaks in IR spectra of acetone acquired using the MB3000 and Keit spectrometers.[10]

Peak position/cm^{-1}	Peak assignment
1710	C=O stretch
1430	CH_3 deformation
1360	CH_3 deformation
1220	C–C stretch

A large amount of noise was present below 600 cm^{-1} and above 1800 cm^{-1} in the spectra acquired using the MB3000 spectrometer, with absorbance exceeding the detection limit of the instrument. (The full spectrum of acetone including the noise can be found in Appendix 3). Figure 3.5 displays the intensity of the MIR light measured by the detector of the MB3000 spectrometer through air (which was used as the background reference spectrum) and through acetone. There is no optical throughput in the regions where the noise was observed due to the limits of the fibre-coupled probe, which explains why absorbance could not be measured in these regions.

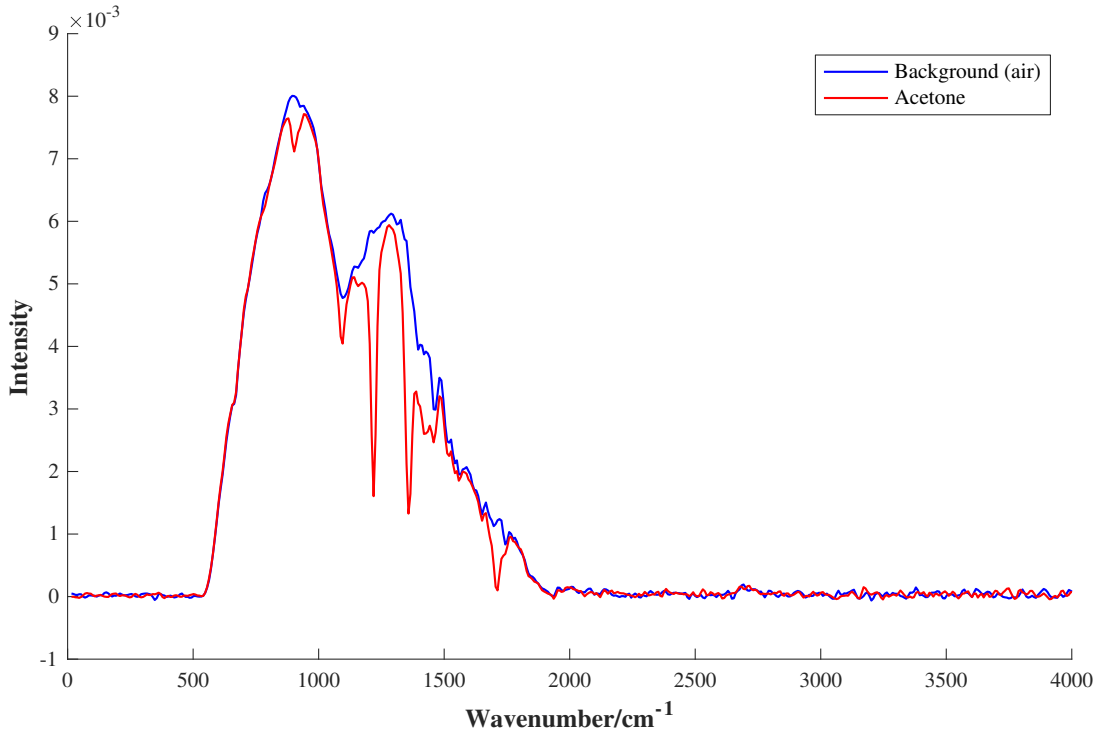

Figure 3.5 - Transmitted light intensity measured by the MB3000 spectrometer through air (blue) and acetone (red).

Variations in the height of the peak at 1710 cm^{-1} were observed when repeat measurements were carried out using the MB3000 spectrometer. Experiments at 4 cm^{-1} resolution showed that absorbance in this region exceeds the limit of the fibre-coupled probe, as shown in Figure 3.6. The low throughput of light in this region can also be observed in Figure 3.5. This effect was not observed in the spectra acquired at 16 cm^{-1} resolution, because at 16 cm^{-1} resolution, absorbance was only measured at every fourth wavenumber in the 4 cm^{-1} resolution spectra and the wavenumbers selected did not include the point at which the peak maximum occurred. For this reason, the spectral range 800 – 1600 cm^{-1} will be used to perform data analysis for both of the spectrometers.

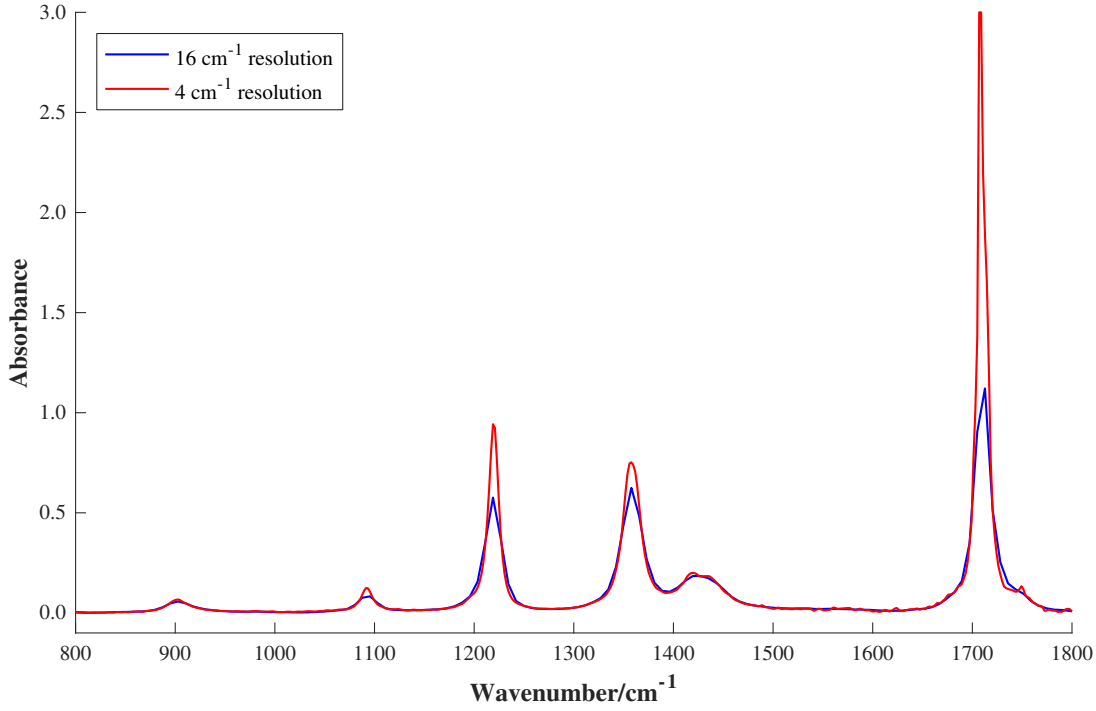

Figure 3.6 - Spectrum of acetone (16 scans) obtained using the MB3000 spectrometer at 16 cm^{-1} (blue) and 4 cm^{-1} (red) resolutions.

3.3.2 Analysis of Solvent Mixtures

The spectra of ethanol, acetone and ethyl acetate acquired using (a) the Keit spectrometer and (b) the MB3000 spectrometer are shown in Figure 3.7. The spectra of the other calibration and test samples can be found in Appendix 3. For both spectrometers, the spectra of each sample were as expected (when compared to the AIST Spectral Database for Organic Compounds, SDBS).[11] An assignment of the main peaks in the ethanol and ethyl acetate spectra is displayed in Table 3.3 (and an assignment of the peaks in the acetone spectra can be found in Table 3.2). The peaks in the spectra acquired using the Keit spectrometer have slightly lower absorbance (up to 0.2 less) than those acquired using the MB3000 spectrometer, but otherwise the spectra are similar. There is significant overlap of the peaks for the different constituent components, particularly ethyl acetate which overlaps with ethanol at 1050 cm^{-1} and acetone in the regions 1200 – 1300 cm^{-1} and 1350 – 1400 cm^{-1}. Therefore, multivariate analysis is required to evaluate the changes in absorbance with concentration.

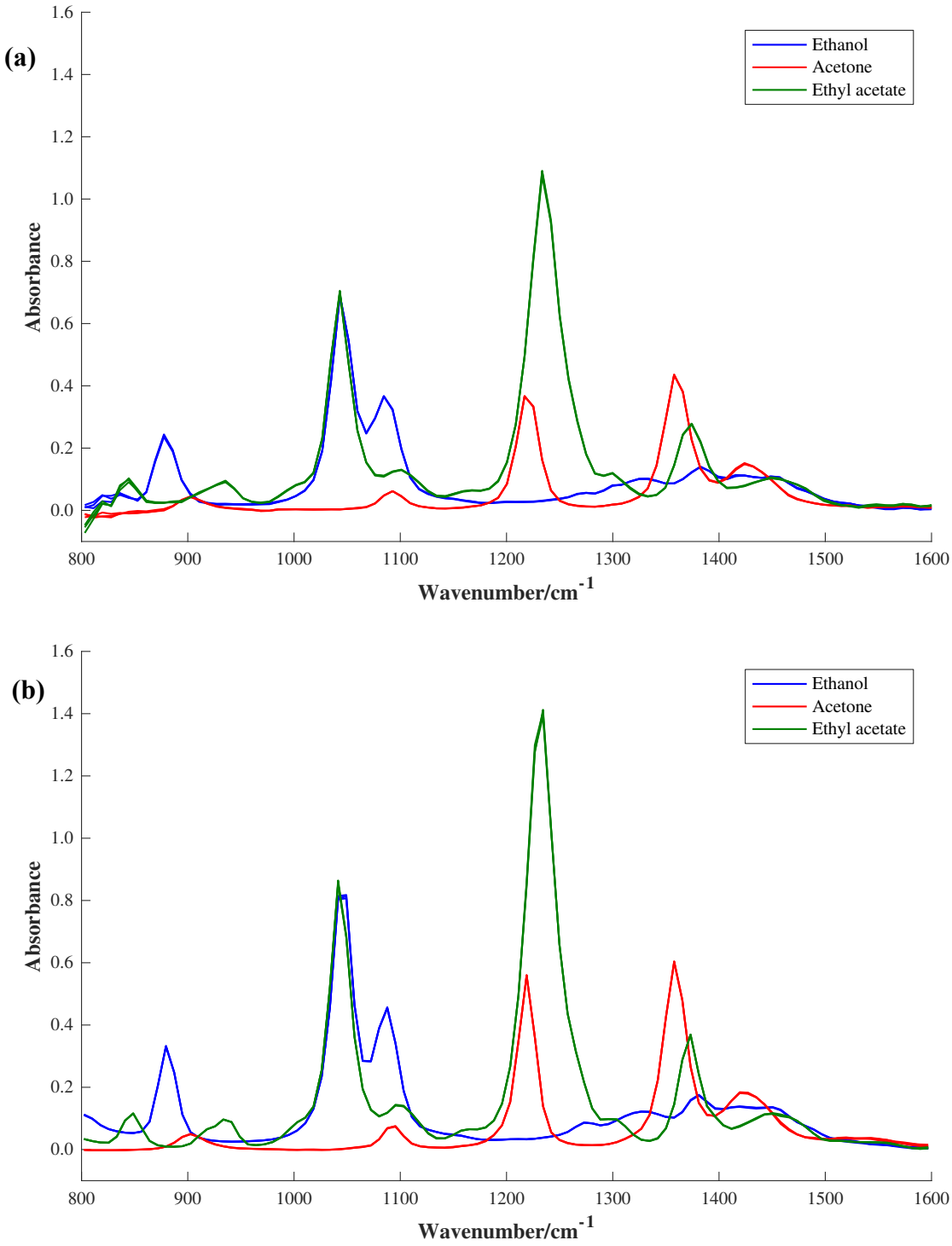

Figure 3.7 - Spectra of ethanol (blue), acetone (red) and ethyl acetate (green) obtained using (a) the Keit spectrometer and (b) the MB3000 spectrometer at 16 cm^{-1} resolution. Each spectrum is an average of 19 scans.

Table 3.3 - Assignment of the main peaks in IR spectra of ethanol and ethyl acetate acquired using the MB3000 and Keit spectrometers.[12, 13]

Solvent	Peak position/cm^{-1}	Peak assignment
Ethanol	1250 – 1500	C–H bend
	1090	C–O stretch
	1040	C–O stretch
	880	C–C stretch
Ethyl acetate	1370	C–H bend
	1230	C–O stretch
	1040	C–O stretch

As the sample compositions were based on a ternary mixture design with a total concentration of 100 % w/w, only two sources of variation should be present. Therefore it would be expected that two latent variables should be sufficient to describe the variation in the data. Mark et al.[14, 15] have demonstrated that in electromagnetic spectroscopy, the absorbance of a component within a mixture is dependent on its volume fraction rather than its weight fraction, according to the Beer Lambert law. The weight fraction of each component in a mixture does not have a linear relationship with its volume fraction (as the weight fraction cannot be converted to the volume fraction using a single scaling factor). Therefore when concentration is measured by weight, a greater number of latent variables may be required to compensate for the non-linearity of the response. This provides a possible explanation as to why four latent variables are necessary to describe the variation in the data. Additional non-linearity could also have arisen as a result of the interaction between the solvents. Du et al.[3] have built PLS models using a similar ternary system, and included four latent variables in order to account for possible background interference.

The plots of predicted versus actual concentration for each solvent are displayed in Figure 3.8, Figure 3.9 and Figure 3.10. The equations of the best fit lines and R^2 values are displayed in Table 3.4, along with the RMSEP values and average absolute relative errors in prediction for each model. For all three solvents, the predictions were accurate with all points in the plots of predicted versus actual concentration lying on or very

close to the y = x line. The equations of the best fit lines were very close to y = x in each case, with all R^2 values greater than 0.998. Slightly more accurate predictions were obtained for the MB3000 models than the Keit models, but the differences were not large. In the plot of predicted versus actual concentration of ethyl acetate, the replicate measurements of test sample 6 (the test sample containing the highest concentration of ethyl acetate) acquired using the Keit spectrometer displayed poorer repeatability than the replicate measurements of the other test samples. This could be due to the high absorbance of ethyl acetate in the region 1200 – 1300 cm^{-1}, as the absorbance of the pure sample exceeded 1 in this region. When this occurs, the relationship between absorbance and concentration described by the Beer Lambert law may begin to deviate from linearity.[16] Each set of repeat measurements otherwise produced precise predictions.

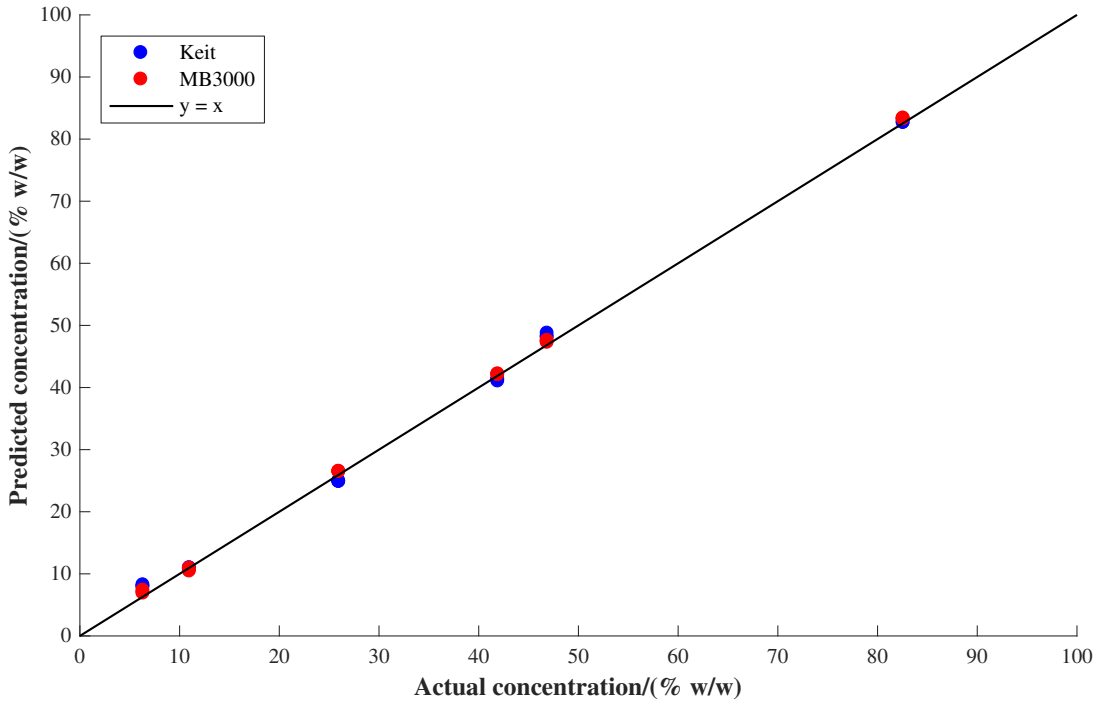

Figure 3.8 - Predicted versus actual acetone concentration for the PLS1 models built using spectra obtained by the Keit and MB3000 spectrometers.

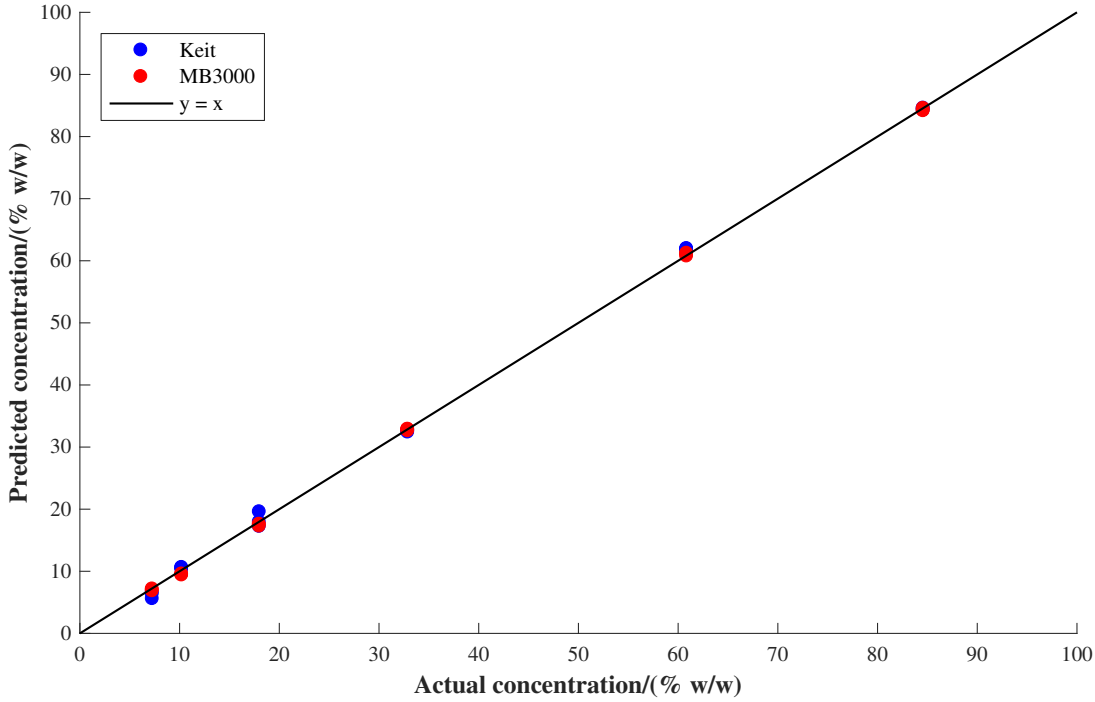

Figure 3.9 - Predicted versus actual ethanol concentration for the PLS1 models built using spectra obtained by the Keit and MB3000 spectrometers.

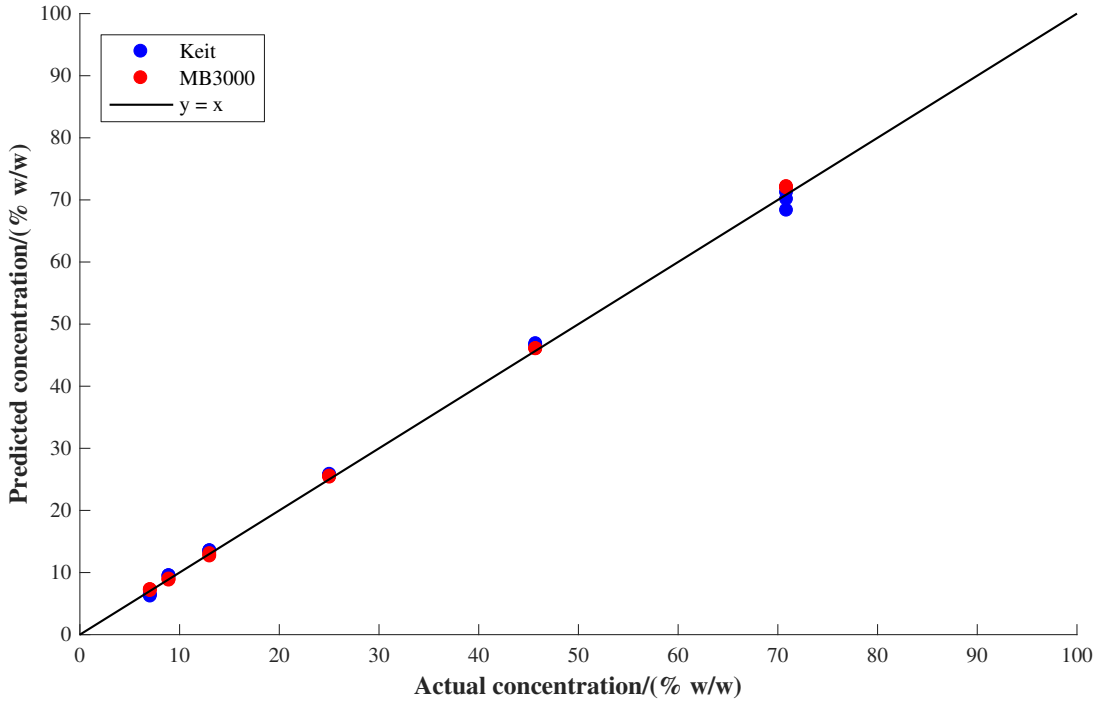

Figure 3.10 - Predicted versus actual ethyl acetate concentration for the PLS1 models built using spectra obtained by the Keit and MB3000 spectrometers.

Table 3.4 - Equations of best fit lines and R^2 values for predicted vs actual concentrations, RMSEP values and average absolute relative errors in prediction for the PLS1 models built using solvent mixture spectra acquired with the Keit and MB3000 spectrometers.

Model		Equation of best fit line for predicted vs actual concentration/(% w/w)	R^2 value	RMSEP value/ (% w/w)	Average absolute relative error/%
Keit	**Acetone**	y = 0.9969 x + 0.2511	0.9983	1.06	6.18
	Ethanol	y = 1.0080 x – 0.4054	0.9993	0.79	4.32
	Ethyl acetate	y = 0.9912 x + 0.2627	0.9986	0.88	4.03
MB3000	**Acetone**	y = 1.0059 x + 0.0820	0.9998	0.50	2.94
	Ethanol	y = 1.0056 x – 0.6155	0.9999	0.53	3.14
	Ethyl acetate	y = 1.0174 x – 0.3442	0.9999	0.48	1.46

The RMSEP values for both instruments were low (less than 1.1 % w/w), demonstrating that each of the models produced accurate predictions. The average absolute relative error values were also low (less than 5 % for all models other than the Keit acetone model). The RMSEP values and average absolute relative errors of prediction for the MB3000 data were lower than those of the Keit data, however the results are comparable. For the Keit data, the average absolute relative error was higher for acetone than the other solvents. This is likely to be a result of increased relative error at low concentration, as small differences between predicted and actual concentration have a significantly greater effect on the relative error at low concentrations than at high concentrations (and lower concentrations of acetone were present in the test samples compared to the other solvents). This effect can be observed in the plots of absolute and percentage residual error versus concentration, which are displayed in Appendix 3. The similarity of the predictions obtained using the Keit and MB3000 spectrometers and the overall accuracy of the predictions demonstrate that the Keit spectrometer is suitable for the quantitative *in situ* analysis of liquids.

3.3.3 Calibration Transfer

3.3.3.1 Initial Method Comparison

It has been demonstrated that both the Keit and MB3000 spectrometers are capable of achieving accurate predictions of concentration. However the probe of the Keit spectrometer is too large to be used with standard laboratory glassware, so the ability to build a calibration model using the MB3000 spectrometer for application to spectra collected by the Keit spectrometer will now be explored. In this section, the effectiveness of DS, PDS and SST will be compared.

The replicate measurements of test sample 2 acquired using the MB3000 spectrometer and the Keit spectrometer (with interpolation but without DS, PDS or SST) are shown in Figure 3.11. There was a noticeable difference in absorbance between the two sets of spectra, and deviations were also present below 860 cm^{-1} due to noise in the baseline of the Keit spectra in this region. Table 3.5 displays the RMSEP values of the PLS1 predictions obtained using the MB3000 calibration spectra and the following sets of test spectra; those acquired on the MB3000 spectrometer, those acquired on the Keit spectrometer with interpolation applied, and those acquired on the Keit spectrometer with each method of calibration transfer applied. Before the application of DS, PDS or SST, the RMSEP values for the Keit test spectra were more than an order of magnitude greater than those of the MB3000 test spectra. As expected, this demonstrates that the application of a transfer function is necessary in order to obtain accurate predictions of concentration from spectra acquired on the Keit spectrometer using a model built with the MB3000 spectrometer. The RMSEP value for acetone was the highest, followed by ethyl acetate, indicating the greatest variation in spectra between the two instruments.

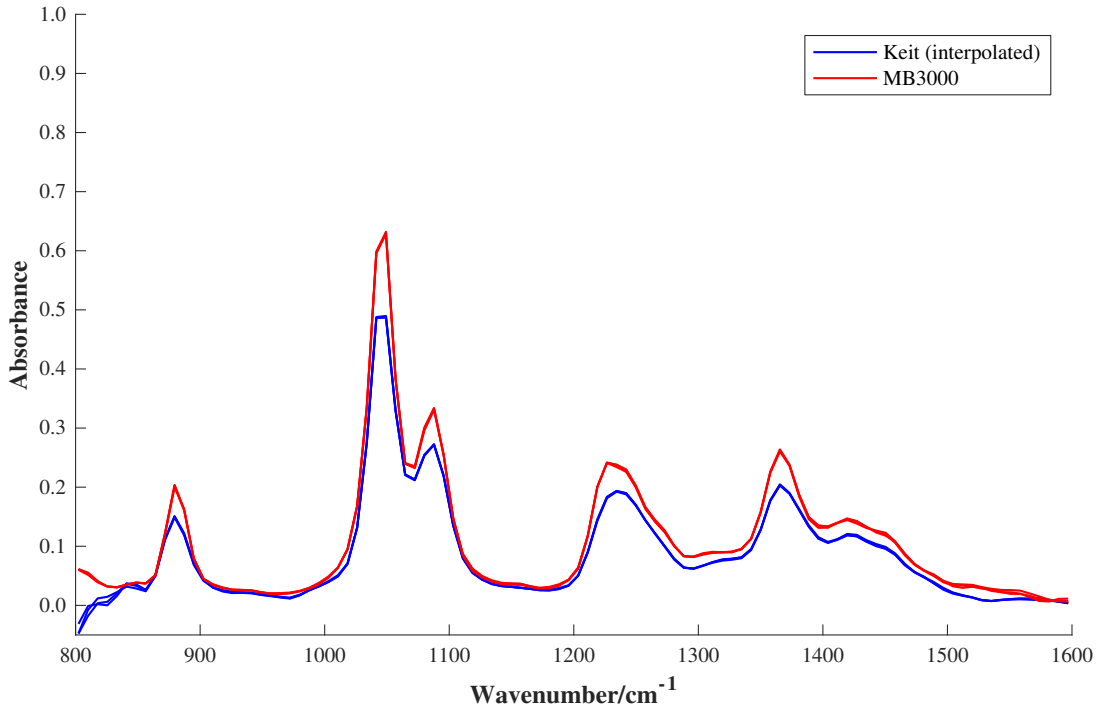

Figure 3.11 - Spectra of test sample 2 (3 repeats) acquired using the Keit spectrometer with interpolation (blue) and the MB3000 spectrometer (red) at 16 cm^{-1} resolution. Each spectrum is an average of 19 scans.

Table 3.5 - RMSEP values for the PLS1 models built using the calibration solvent mixture spectra measured using the MB3000 spectrometer, applied to the test spectra measured using the MB3000 spectrometer, the Keit spectrometer with interpolation and the Keit spectrometer with calibration transfer by DS, PDS and SST.

Model	Acetone RMSEP/ (% w/w)	Ethanol RMSEP/ (% w/w)	Ethyl acetate RMSEP/ (% w/w)	Mean RMSEP/ (% w/w)
MB3000	0.50	0.53	0.48	0.50
Keit after interpolation only	9.24	5.75	7.77	7.59
Keit after DS	1.09	2.16	1.12	1.46
Keit after PDS	0.68	1.38	0.92	0.99
Keit after SST (unscaled)	0.69	1.14	0.96	0.93
Keit after SST (scaled)	0.62	1.03	0.89	0.85

After the application of DS (using the initial subset of six pure/ternary transfer samples), the spectra of test sample 2 acquired on the Keit spectrometer much more

closely resembled those acquired on the MB3000 spectrometer (Figure 3.12). A slight difference in the shape of the peak between 1200 cm^{-1} and 1300 cm^{-1} was present, but the two sets of spectra were otherwise similar. The application of PDS (Figure 3.13) produced similar results, with a slight improvement to the peak shape in the region 1200 – 1300 cm^{-1}, indicating that PDS may be a little more effective than DS. The transferred spectra of the other test samples can be found in Appendix 3.

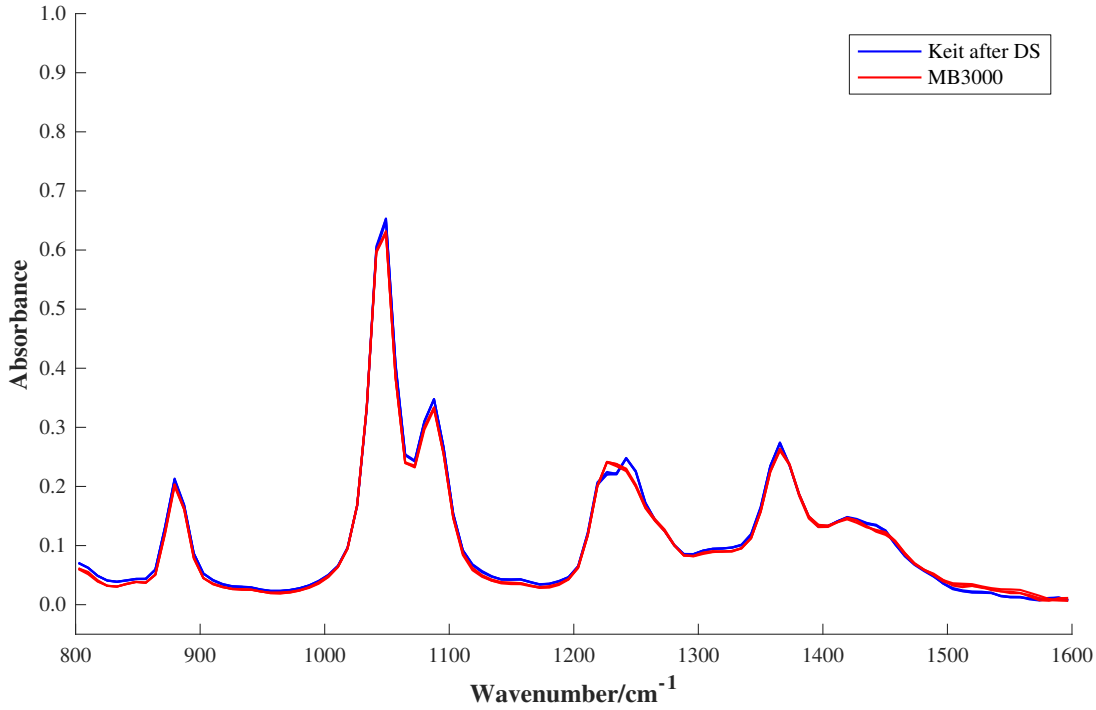

Figure 3.12 - Spectra of test sample 2 (3 repeats) acquired using the Keit spectrometer with calibration transfer by DS (blue) and the MB3000 spectrometer (red) at 16 cm^{-1} resolution. Each spectrum is an average of 19 scans.

The RMSEP values of the PLS predictions obtained with DS were significantly lower than without DS (1.46 % w/w on average compared to 7.59 % w/w on average), demonstrating the effectiveness of calibration transfer. However, the values were still higher than for the MB3000 test spectra (0.50 % w/w on average). The RMSEP values obtained with PDS (0.99 % w/w on average) were lower than for DS, confirming that PDS was the more effective method. For both methods, the lowest RMSEP value was obtained for acetone and the highest for ethanol. This indicates that DS and PDS were less effective for the ethanol peaks than the other solvent peaks, possibly due to the

presence of the broad regions between 1250 cm^{-1} and 1500 cm^{-1} and below 860 cm^{-1} in the ethanol spectra.

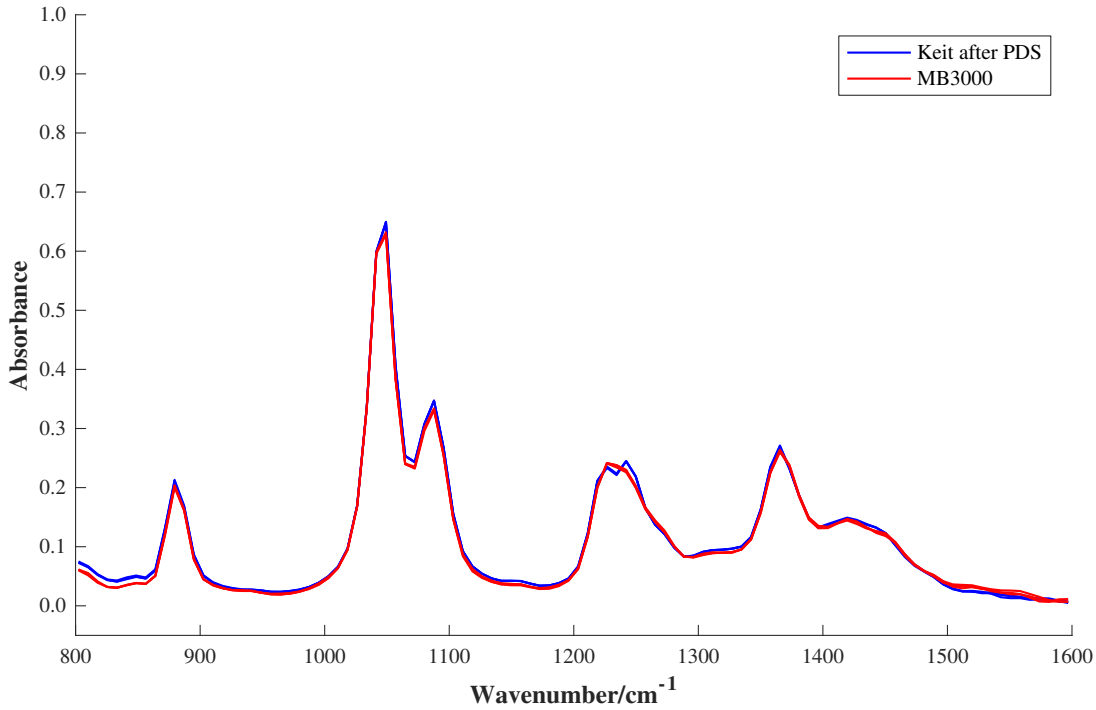

Figure 3.13 - Spectra of test sample 2 (3 repeats) acquired using the Keit spectrometer with calibration transfer by PDS (blue) and the MB3000 spectrometer (red) at 16 cm^{-1} resolution. Each spectrum is an average of 19 scans.

The spectra of test sample 2 with calibration transfer by SST are displayed in Figure 3.14. The transformed spectra again resembled the MB3000 spectra, and the peak between 1200 cm^{-1} and 1300 cm^{-1} was more similar than for DS or PDS. Small deviations were present in the Keit spectra below 860 cm^{-1} due to noise in this region, however there was very little difference in the spectra overall. The RMSEP values obtained using SST were similar to those obtained for PDS, with a slight improvement in the ethanol prediction (1.14 % w/w compared to 1.38 % w/w). Between the solvents, the trend was similar to that observed for DS and PDS. The application of the scaling step during SST produced slightly improved RMSEP values compared to when the scaling step was absent (0.85 % w/w on average compared to 0.93 % w/w on average), however the difference was not significant. This was as expected, since the difference in absorbance between the Keit and MB3000 spectra was not particularly large (no more than around 0.2 in difference within the spectral region used) and thus scaling

was not necessary. In situations where a larger difference in absorbance is present between the two sets of spectra, the scaling step would be more advantageous.

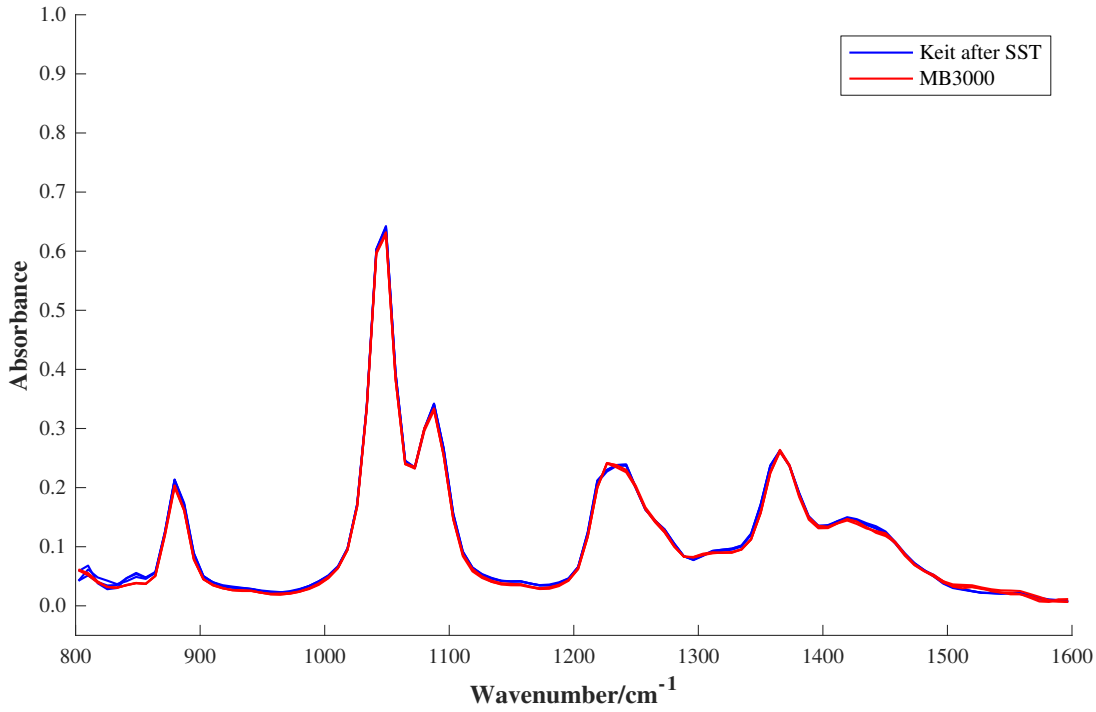

Figure 3.14 - Spectra of test sample 2 (three repeats) acquired using the Keit spectrometer with calibration transfer by SST (blue) and the MB3000 spectrometer (red) at 16 cm^{-1} resolution. Each spectrum is an average of 19 scans.

The improvements in RMSEP observed and the similarity of the spectra clearly demonstrate the effectiveness of calibration transfer. Based on this initial comparison, PDS and SST appear to be the most effective methods of calibration transfer as they produced similar predictions, of greater accuracy than DS. However, the advantage of DS is that input of parameters such as window size or number of singular values are not necessary, which increases the ease of use of the method and removes subjectivity. The main advantage of SST over PDS is that selection of an appropriate number of singular values is easier and less time consuming than selection of an appropriate window size (since the number of possible window sizes greatly exceeds the possible numbers of singular values which would be sensible to use). In addition, Du et al.[3] have stated that when the number of transfer samples used is small then the number of singular values to include in the calculation of the transfer function can be taken as equal to the number of transfer samples.

3.3.3.2 Transfer Sample Comparison

3.3.3.2.1 Choice of Transfer Samples

To determine the most suitable subset of samples to use for calculation of the transfer function, the results obtained using different sets of transfer samples were compared. The RMSEP values obtained when DS, PDS and SST (without scaling) were performed using different sets of six transfer samples are shown in Table 3.6. All PLS1 models were built using the full set of calibration spectra acquired on the MB3000 spectrometer, and used to predict the concentration of each solvent present in the transformed test spectra acquired on the Keit spectrometer. It would be expected that a transfer sample set of pure and ternary samples would be the most effective, as ternary mixtures are the most representative of the test samples and the inclusion of the pure components ensures that the transfer sample set spans the full range of the ternary diagram. A transfer sample set containing only binary samples would be expected to be the least effective.

For DS, the poorest RMSEP values were obtained using the pure/ternary (calibration samples 1 – 3 and 8 – 10) and binary only (calibration samples 11 – 16) sample subsets for calculation of the transfer function. The best predictions were obtained using the binary/ternary (calibration samples 4 – 6 and 8 – 10) and pure/binary (calibration samples 1 – 3, 12, 13 and 16) transfer sample sets. No clear trend was observed between the solvents upon changing the transfer sample set used for DS. The majority of the RMSEP values were low (with the mean RMSEP value below 1.5 % w/w for all transfer sample sets), however, suggesting that relatively accurate predictions can be obtained by DS regardless of which six transfer samples are chosen.

When PDS was applied, the RMSEP values were generally lower than those obtained using DS, by up to 0.5 % w/w. However the RMSEP values obtained when the pure/binary transfer sample set was used to calculate the PDS transfer function were significantly higher (2.24 % w/w on average compared to 0.96 % w/w on average for DS). This indicates that examination of leverage is not always the best method of choosing the transfer samples. The mean RMSEP values obtained using the other transfer sample sets were all below 1 % w/w, demonstrating the effectiveness of PDS. These results suggest that although DS is less effective than PDS overall, it may be

more effective at modelling the differences between the spectra when the transfer sample set is not representative of the test samples. However when the transfer sample set consisting of binary samples only (which is not representative of the test samples either) was used for PDS, accurate predictions were obtained (with a mean RMSEP value of 0.89 % w/w). For SST, similar RMSEP values to PDS were obtained and the trend observed upon changing the transfer sample set was also very similar to PDS. The only significant difference was that the poorest transfer sample set (calibration samples 1 – 3, 12, 13 and 16) was more effective for ethanol and less effective for acetone and ethyl acetate than when PDS was used.

Table 3.6 - RMSEP values for the PLS1 models built using the calibration solvent mixture spectra (transfer samples included) measured with the MB3000 spectrometer, applied to the test spectra measured using the Keit spectrometer after DS, PDS and SST with different transfer sample subsets.

Method	Calibration samples used for transfer	Acetone RMSEP/ (% w/w)	Ethanol RMSEP/ (% w/w)	Ethyl acetate RMSEP/ (% w/w)	Mean RMSEP/ (% w/w)
DS	**1–3 and 8–10**	1.09	2.16	1.12	1.46
	4–6 and 8–10	1.12	0.77	1.03	0.97
	1–3, 12, 13 and 16	1.11	0.94	0.83	0.96
	11–16	1.36	1.36	1.53	1.42
PDS	**1–3 and 8–10**	0.68	1.38	0.92	0.99
	4–6 and 8–10	0.61	0.68	0.76	0.68
	1–3, 12, 13 and 16	1.58	3.37	1.78	2.24
	11–16	0.52	1.10	1.04	0.89
SST	**1–3 and 8–10**	0.69	1.14	0.96	0.93
	4–6 and 8–10	0.79	0.71	0.90	0.80
	1–3, 12, 13 and 16	2.09	1.14	2.72	1.99
	11–16	0.63	0.91	1.23	0.92

For PDS and SST, the most accurate predictions were obtained when the binary/ternary transfer sample set was used (with a mean RMSEP of 0.68 % w/w for PDS and 0.80 % w/w for SST). This is presumably because these samples are most

similar to the test samples. The increase in RMSEP upon including pure rather than binary samples (as observed when samples 1 – 3 and 8 – 10 were compared to samples 4 – 6 and 8 – 10, and when samples 1 – 3, 12, 13 and 16 were compared to samples 11 – 16), suggests that inclusion of the pure components may slightly worsen the model. This is likely to be because the pure component samples differed the most to the test samples. Therefore it appears that the similarity of the transfer samples to the test samples has a greater effect on the results than the leverage of the transfer samples. However the differences observed are only small (with the mean RMSEP value varying by no more than 0.3 % w/w for all transfer sample sets other than the poorest).

The overall similarity of the RMSEP values for each transfer sample set indicates that the choice of sample subset to use for calibration transfer does not significantly affect the predictions obtained. Inclusion of the pure components in the transfer sample set in addition to mixtures reduces the amount of sample preparation required and also ensures that the transfer sample set spans the range of the ternary diagram, so may be advantageous, despite the small increase in RMSEP observed. Again, the performance of PDS and SST appeared to be similar and better than the performance of DS.

A plot of the number of singular values versus the average RMSEP value obtained using each set of transfer samples is shown in Figure 3.15. The plots containing the individual RMSEP values for each solvent can be found in Appendix 3. Seven singular values appears to be the optimum for the pure/binary transfer sample set, but even with seven singular values the RMSEP did not improve beyond the other transfer sample sets. The optimum number of singular values was found to be five for the pure/ternary and binary only sample sets (however for the binary only sample set, five singular values provided only a very small improvement over four), and four for the binary/ternary sample set. This provides further indication that the pure/binary transfer sample set was less effective than the others.

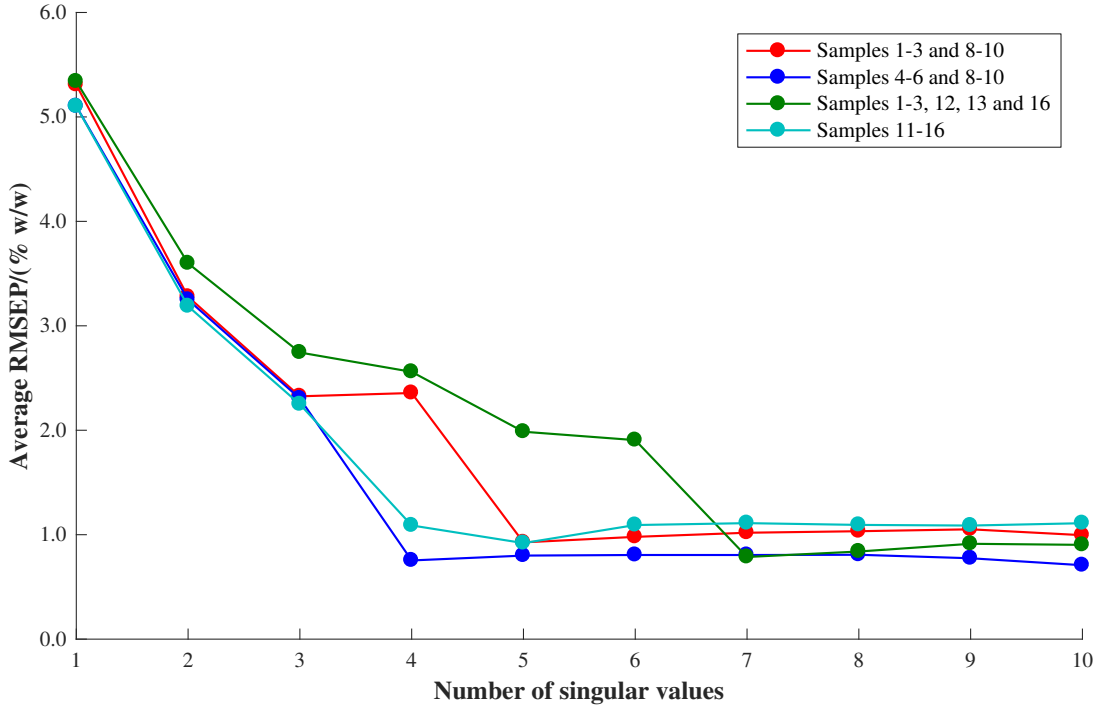

Figure 3.15 - Average RMSEP value (for acetone, ethanol and ethyl acetate) versus number of singular values for PLS1 models built using MB3000 calibration data and applied to Keit test data with SST, when different sets of six calibration samples were used as transfer samples.

Table 3.7 displays the RMSEP values acquired when the transfer samples were excluded from the calibration models. For DS, this appears to have made little difference to the results obtained. For PDS and SST, the RMSEP values were slightly poorer (0.05 – 0.15 % w/w higher) when the sample sets containing ternary samples were used for transfer and excluded from the calibration model compared to when they were included in the calibration model. However for the two sample sets which did not contain ternary samples, a slight improvement in RSMEP (of 0.08 – 0.14 % w/w) was observed upon exclusion of the transfer samples from the calibration model. This was unexpected, as it would be thought that the inclusion of fewer samples in the calibration model would worsen the RMSEP values obtained in every case. However the differences in RMSEP were only small, so may not be significant.

These results suggest that accurate predictions can still be obtained when the transfer samples are not included in the calibration model (e.g. when the transfer samples were taken from the test set rather than the calibration set), although slightly poorer results

were obtained when the calibration samples became less representative of the test samples (i.e. when fewer ternary mixtures were included). In practice, there would be no reason to exclude the transfer samples from the calibration model as their spectra will already have been obtained on the primary instrument in order to perform calibration transfer and inclusion of more calibration samples should, in theory, improve the model.

Table 3.7 - RMSEP values for the PLS1 models built using the calibration solvent mixture spectra (transfer samples excluded) acquired with the MB3000 spectrometer, applied to the test spectra acquired using the Keit spectrometer after DS, PDS and SST with different transfer sample subsets.

Method	Calibration samples used for transfer	Acetone RMSEP/ (% w/w)	Ethanol RMSEP/ (% w/w)	Ethyl acetate RMSEP/ (% w/w)	Mean RMSEP/ (% w/w)
DS	**1–3 and 8–10**	1.25	1.82	1.13	1.40
	4–6 and 8–10	1.19	0.75	1.01	0.98
	1–3, 12, 13 and 16	1.15	1.00	0.72	0.96
	11–16	1.45	1.22	1.54	1.40
PDS	**1–3 and 8–10**	0.96	1.14	1.02	1.04
	4–6 and 8–10	0.70	0.73	0.80	0.74
	1–3, 12, 13 and 16	2.09	2.99	1.22	2.10
	11–16	0.42	0.99	1.01	0.81
SST	**1–3 and 8–10**	0.86	1.17	1.21	1.08
	4–6 and 8–10	0.77	0.77	1.25	0.93
	1–3, 12, 13 and 16	1.13	1.87	2.64	1.88
	11–16	0.80	0.69	0.91	0.80

3.3.3.2.2 Number of Transfer Samples

The effect of changing the number of transfer samples was then compared. This knowledge is important, as too few transfer samples will not be effective, and the inclusion of an unnecessary number of transfer samples will make the process of calibration transfer more time consuming. The RMSEP values obtained when the number of samples included in the transfer set was varied are shown in Table 3.8. As

before, the PLS models were built using the full set of calibration spectra acquired on the MB3000 spectrometer and used to predict the concentration of each solvent present in the transformed test spectra acquired on the Keit spectrometer. As expected, the inclusion of more transfer samples generally improved the RMSEP values. The worst results were obtained when only the pure components (calibration samples 1 – 3) or the pure components and calibration sample 7 were used to calculate the transfer function, particularly when DS and PDS were used. This is because the pure component samples were least representative of the test samples, which were all ternary mixtures. The predictions obtained when all sixteen calibration samples were used to calculate the transfer function are the best, as would be expected. Although the full calibration set would not be used to calculate the transfer function in practice as it negates the effect of calibration transfer, it demonstrates the theoretical optimum result, which can be used as a benchmark.

For DS, the other combinations of transfer samples all produced similar results (with mean RMSEP values ranging from 1.63 % w/w for three transfer samples to 1.23 % w/w for seven transfer samples). With PDS and SST, there was a more noticeable improvement in RMSEP as the number of transfer samples was increased (with mean RMSEP values decreasing from 1.47 % w/w to 0.94 % w/w and from 1.97 % w/w to 0.90 % w/w for PDS and SST respectively upon switching from three to seven transfer samples). However all RMSEP values were relatively low (less than 2 % w/w) other than when calibration samples 1 – 3 (the pure components) or calibration samples 1 – 3 and 7 were used, suggesting that calibration transfer can still be relatively effective when as few as three transfer samples are used. However, it may be that different results are observed with more complex sample sets and this would be a suggestion for future work.

For SST, the RMSEP values obtained using seven transfer samples were similar to those obtained when all sixteen calibration samples were used in the transfer function, and for PDS they were only slightly higher. The RMSEP values obtained for SST and PDS using six and seven transfer samples were similar, therefore six would be suggested as the optimum. When larger numbers of transfer samples were used (e.g. above four), the most accurate predictions were generally obtained for acetone and the poorest for ethanol, but when smaller numbers of transfer samples were used, the best

predictions were generally obtained for ethanol. This suggests that altering the number of transfer samples had a lesser effect on the predictions of ethanol than of the other solvents, as it appears that ethanol can be modelled relatively well with only a few components.

Table 3.8 - RMSEP values for the PLS1 models built using the calibration solvent mixture spectra measured with the MB3000 spectrometer, applied to the test spectra measured using the Keit spectrometer after DS, PDS and SST with different numbers of transfer samples.

Method	Number of transfer samples	Calibration samples used for transfer	Acetone RMSEP/ (% w/w)	Ethanol RMSEP/ (% w/w)	Ethyl acetate RMSEP/ (% w/w)	Mean RMSEP/ (% w/w)
DS	**3**	**8–10**	1.61	1.79	1.49	1.63
	3	**1–3**	7.65	3.77	5.14	5.52
	4	**7–10**	1.61	1.46	1.25	1.44
	4	**1–3 and 7**	5.81	2.02	4.85	4.23
	6	**1–3 and 8–10**	1.09	2.16	1.12	1.46
	7	**1–3 and 7–10**	1.12	1.79	0.77	1.23
	16	**All**	0.54	0.83	0.78	0.72
PDS	**3**	**8–10**	1.72	1.24	1.44	1.47
	3	**1–3**	7.56	2.91	5.07	5.18
	4	**7–10**	1.58	1.27	1.48	1.44
	4	**1–3 and 7**	5.30	1.49	5.24	4.01
	6	**1–3 and 8–10**	0.68	1.38	0.92	0.99
	7	**1–3 and 7–10**	0.71	1.29	0.83	0.94
	16	**All**	0.46	0.78	0.62	0.62
SST	**3**	**8–10**	2.76	1.14	2.00	1.97
	3	**1–3**	4.19	1.67	3.11	2.99
	4	**7–10**	1.03	1.10	1.00	1.04
	4	**1–3 and 7**	3.86	1.49	3.09	2.81
	6	**1–3 and 8–10**	0.69	1.14	0.96	0.93
	7	**1–3 and 7–10**	0.63	1.15	0.93	0.90
	16	**All**	0.50	0.98	0.99	0.83

Du et al.[3] have compared PDS and SST for the transfer of PLS models built using MIR spectra of similar ternary mixtures acquired with two different probes. Three samples were used to calculate the transfer function (one pure, one binary and one ternary mixture). Larger RMSEP values were obtained for PDS (0.80 – 1.55 % w/w) than SST (0.69 – 1.35 % w/w), and the values were in the same range as those obtained using four or more transfer samples in this work. The ability to obtain lower RMSEP values using only three transfer samples may be because the spectra were more similar to begin with. Less of a difference was observed between the performance of PDS and SST in this work. Du et al. observed that once the number of transfer samples reaches a certain threshold then the inclusion of more transfer samples has little effect on the predictions obtained. Although this was observed to some extent in this work, as the decrease in RMSEP upon including six or more transfer samples was not large, there was still a noticeable decrease in RMSEP when sixteen calibration samples were included compared to six or seven.

3.4 Conclusions

The performance of a novel, robust spectrometer for the quantitative *in situ* analysis of liquids has been demonstrated. The use of the Sagnac interferometer within the instrument eliminates sensitivity to vibrations, making the spectrometer ideal for use in harsh environments. The absence of optical fibres overcomes the issues associated with transmission of MIR light over long lengths of fibre optics, and the robustness and compact size of the spectrometer allow it to be used within process environments. The accuracy of the predictions of solvent mixture composition and the similarity of the predictions to those obtained using the MB3000 spectrometer demonstrate the potential of the novel spectrometer for the quantitative *in situ* analysis of liquid processes. This will allow MIR spectroscopy to be more easily applied in process monitoring.

The overall accuracy of the predictions which can be obtained by calibration transfer clearly demonstrate its effectiveness, and show that it is possible to build calibration models in the laboratory for subsequent application to a process. This would avoid the need to build calibration models within the process environment, saving time and resources. SST and PDS were the most effective methods, as overall they produced

similar predictions, of greater accuracy than DS. SST would be recommended for future use, as selection of an appropriate number of singular values is easier than selection of an appropriate window size. The choice of transfer samples appears to have a greater effect than the number of transfer samples, and the most accurate predictions were obtained when the transfer samples were representative of the test samples (i.e. contained ternary mixtures). However, the RMSEP values generally improved with the inclusion of more transfer samples and six appeared to be the optimum.

3.5 References

1. J. J. Workman, Jr., *Appl Spectrosc*, 2018, **72**, 340–365.
2. Y. B. Monakhova and B. W. K. Diehl, *Magn. Reson. Chem.*, 2016, **54**, 712–717.
3. W. Du, Z. P. Chen, L. J. Zhong, S. X. Wang, R. Q. Yu, A. Nordon, D. Littlejohn and M. Holden, *Anal. Chim. Acta*, 2011, **690**, 64–70.
4. R. R. T. Rodrigues, J. T. C. Rocha, L. Oliveira, J. C. M. Dias, E. I. Muller, E. V. R. Castro and P. R. Filgueiras, *Chemom. Intell. Lab. Syst.*, 2017, **166**, 7–13.
5. C. Grelet, J. A. F. Pierna, P. Dardenne, H. Soyeurt, A. Vanlierde, F. Colinet, C. Bastin, N. Gengler, V. Baeten and F. Dehareng, *J. Dairy Sci.*, 2017, **100**, 7910–7921.
6. Y. T. Cao, H. F. Yuan and Z. Zhao, *Spectrosc. Spectral Anal.*, 2018, **38**, 973–981.
7. J. H. Kalivas and J. Palmer, *J. Chemom.*, 2014, **28**, 347–357.
8. A. C. McIntyre, PhD thesis, University of Strathclyde, 2011.
9. E. Bouveresse and D. L. Massart, *Chemom. Intell. Lab. Syst.*, 1996, **32**, 201–213.
10. R. L. Hudson, P. A. Gerakines and R. F. Ferrante, *Spectrochim. Acta, Part A*, 2018, **193**, 33–39.
11. AIST, Spectral Database for Organic Compounds, SDBS, https://sdbs.db.aist.go.jp/sdbs/cgi-bin/direct_frame_top.cgi, (accessed 14th November, 2018).

12. S. Corsetti, F. M. Zehentbauer, D. McGloin and J. Kiefer, *Fuel*, 2015, **141**, 136–142.
13. B. Nolin and R. N. Jones, *Can. J. Chem.*, 1956, **34**, 1392–1404.
14. H. Mark, R. Rubinovitz, D. Heaps, P. Gemperline, D. Dahm and K. Dahm, *Appl. Spectrosc.*, 2010, **64**, 995–1006.
15. H. Mark and J. Workman, *Spectroscopy*, 2014, **29**, 24–37.
16. W. Mantele and E. Deniz, *Spectrochim. Acta, Part A*, 2017, **173**, 965–968.

4 Application of Novel Mid-Infrared Spectrometer to Reaction Monitoring

4.1 Introduction

In Chapter 3, the basic performance of the Keit spectrometer for the *in situ* analysis of liquids was assessed. In order to further assess the performance of the Keit spectrometer, its suitability for *in situ* reaction monitoring will now be evaluated. The instrument was used to monitor the esterification reaction between acetic anhydride and butan-1-ol, with a pyridine catalyst, forming butyl acetate and acetic acid. This reaction was selected as it is simple and has been well-studied.[1-7] A mechanism for the reaction has been proposed by Richards et al.,[2] and is shown in Figure 4.1. Nucleophilic attack of the acetic anhydride by the pyridine first takes place, to form an activated tetrahedral intermediate. Butan-1-ol then attacks the intermediate, releasing pyridine and forming acetic acid and 1-butyl acetate.

The reaction has been monitored by NIR spectroscopy,[2-4] and has been used to demonstrate the performance of a thermal vaporiser for process mass spectrometry[1] and reaction calorimeters.[7, 8] Monitoring of the reaction by MIR spectroscopy has also been demonstrated using a reaction calorimeter with an integrated ATR probe, coupled via mirrors to a MIR spectrometer (the Bruker Equinox 55 FTIR spectrometer).[8] The reaction has been used to assess the performance of the SpectraProbe Linx 5-10,[1] a MIR spectrometer which has a probe directly attached and utilises short lengths of optical fibre within the spectrometer unit. However the instrument lacked the robustness required for process monitoring. The Keit spectrometer is extremely robust and contains no fibre optics or moving parts, as discussed in Chapter 1, which provides an advantage over the MIR spectrometers previously used.

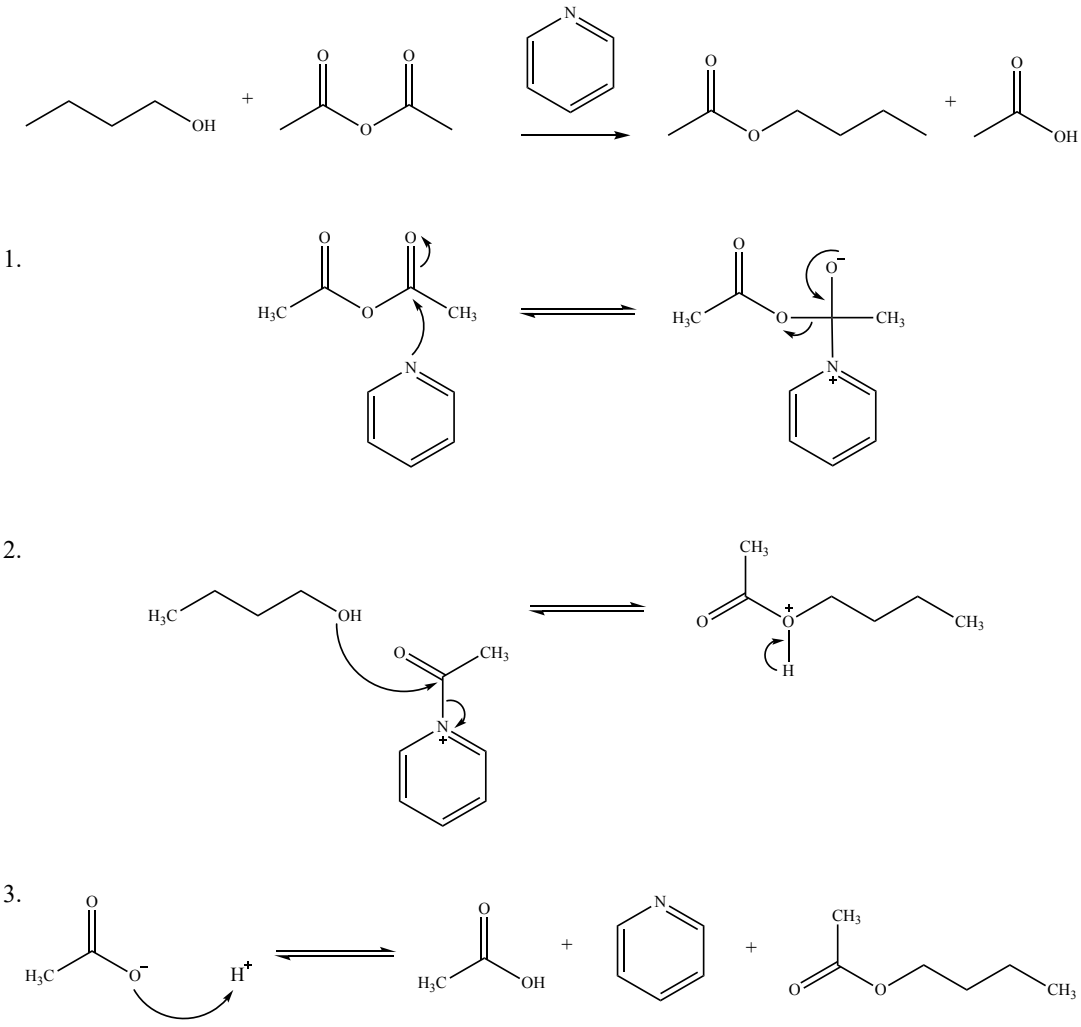

Figure 4.1 - Proposed mechanism for esterification reaction between acetic anhydride and butan-1-ol, reproduced from reference 2.

Multivariate curve resolution (MCR) can be used to resolve the spectra of reaction mixtures into their pure component contributions. This produces spectral and concentration profiles for each component (where the "concentration" is a measure of the relative contribution of each component to the total absorbance of the mixture), and a description of the method is given in section 2.3.5. A major advantage of MCR over PLS is that it avoids the need to build a calibration model, which can save time and resources. The use of MCR to resolve reaction mixture spectra acquired using a variety of different techniques has been demonstrated, including MIR,[9-11] NIR,[12-14] Raman,[15, 16] NMR,[17, 18] ultraviolet-visible[19-21] and fluorescence[22, 23] spectroscopies. However there have been few applications involving real-time reaction monitoring, as

optimisation of a large number of constraints and parameters is necessary, therefore guidance in this area would be valuable.

The most commonly used software for MCR is the MCR-ALS toolbox,[24, 25] as it is freely available online. However the use of GUIPRO software has also been demonstrated for a number of applications.[2, 26, 27] GUIPRO is an MCR toolbox developed by Gemperline and Cash,[26] which utilises least squares penalty functions. This involves the application of a penalty function weighting factor (i.e. a sensitivity value) between 0.01 (soft) and 20 (hard) to the spectral and concentration constraints in order to alter the hardness/softness with which they are applied. Hard constraints do not allow any deviation from the defined conditions, whereas soft constraints allow small deviations. The application of soft constraints can reduce distortion and the lack of fit of the model, improving results. The performance of GUIPRO has been compared to that of MCR-ALS for analysis of the esterification reaction between acetic anhydride and butanol by NIR spectroscopy,[2] and the use of GUIPRO with soft constraints was found to produce the most accurate results. An MCR function is also available in PLS Toolbox and it allows the application of weightings to the constraints, based on the same algorithm as GUIPRO.

The available constraints and parameters differ between MCR-ALS, GUIPRO and the MCR function in PLS Toolbox, so in this chapter the three toolboxes will be compared and the parameters optimised. The most effective toolbox will then be used to decompose the esterification reaction mixture spectra acquired by the Keit spectrometer into their pure component contributions. The aims of this chapter are to evaluate the performance of the Keit spectrometer for reaction monitoring, and to compare the effectiveness of different MCR toolboxes for the analysis of MIR spectra.

4.2 Experimental

4.2.1 Esterification Reaction

The esterification reaction discussed in section 4.1 was monitored using the Keit spectrometer. 125 mL of acetic anhydride (99+ %, Acros Organics, Geel, Belgium) was added to a 250 mL reaction vessel (Reactor-Ready, Radleys, Essex, UK), stirring at a speed of 150 rpm using a stirrer (Eurostar digital, IKA, Oxford UK). The probe of

the Keit spectrometer was inserted into the reaction vessel and spectra were recorded every 1.6 seconds until the end of the reaction. Each spectrum consisted of a single scan, with an acquisition time of 1.5 seconds. The vessel was heated to 40 °C using a water jacket connected to a heater/cooler unit (Brookfield TC-502, AMETEK Brookfield, Essex, UK) and allowed to equilibrate at this temperature for 5 minutes. 10 mL of pyridine (≥ 99 %, Sigma Aldrich, Steinheim, Germany) was added, and the mixture was allowed to equilibrate for another 5 minutes. 121 mL of butan-1-ol (99 %, Acros Organics, Geel, Belgium) was then added and the reaction was allowed to progress for an hour. This reaction was repeated a further twice at 40 °C, once at 50 °C and once at 20 °C. Spectra of pure acetic anhydride, butan-1-ol, acetic acid (99 – 100 %, Sigma Aldrich, Steinheim, Germany) and butyl acetate (≥ 99.5 %, Sigma Aldrich, Steinheim, Germany) were collected at 40 °C for reference.

The products formed at the same rate during the reaction, so in order for the MCR model to distinguish between the two products, the correlation must be broken. Dosing of one component can be used to eliminate linear dependency,[3] therefore addition of one of the products to the reaction mixture at the end of the reaction will break the correlation. The esterification reaction was repeated at 40 °C, with extra acetic acid dosed into the vessel after one hour. The temperature profile of this reaction was recorded using a thermocouple (YC-747UD 4 Channel Data Logger Thermometer, YCT), which was inserted into the reaction mixture. The consumption of the reactants was anti-correlated to the formation of the products, and was overcome by beginning the spectral acquisitions before butanol was added to the reaction vessel.

4.2.2 Data Analysis

4.2.2.1 Multivariate Curve Resolution Software Comparison

In order to determine the most effective MCR toolbox for analysis of the esterification reaction data, three different MCR toolboxes were compared; GUIPRO (version GP 2016b),[26] MCR-ALS GUI 2.0[24, 25] and the MCR function in PLS Toolbox version 8.6.2 (Eigenvector, Washington, USA). GUIPRO and PLS Toolbox were used in MATLAB 2016b (MathWorks, Massachusetts, USA) and MCR-ALS was used in MATLAB 2014b (MathWorks, Massachusetts, USA). Each toolbox was used to perform MCR on the spectra collected during the esterification reaction at 40 °C with extra acetic

acid dosed in at the end. The differences between each toolbox will be discussed in section 4.3.1.

The first 1000 seconds of the reaction, in which the acetic anhydride was being heated, were not included. The spectral region between 1070 cm^{-1} and 1170 cm^{-1} was also removed since the absorbance of acetic anhydride was very high in this region. Pyridine was not included when building the model due to its low concentration. The reference spectra collected at 40 °C were used as spectral equality constraints. The concentration equality constraints for butanol, acetic acid and butyl acetate were set to zero in the region of time when only acetic anhydride and pyridine were present. Non-negativity constraints were applied to the spectra and concentration profiles. The effect of changing each of the other possible constraints/parameters was investigated for each toolbox, and the optimum settings determined.

The results obtained from each toolbox were then compared in order to determine which toolbox was the most effective at resolving the esterification reaction spectra into their pure component contributions. Concentration profiles published in the literature were used to assess the results, as the reaction has been well studied and the expected profiles are known. The difference between the estimated and reference pure component spectra was quantified by calculating the root mean square spectral residual, in order to determine the extent of deviation of the estimated spectra from the references. This involved calculating the square root of the sum of squares of the residual (i.e. the difference between the estimated and reference spectrum) for each component.

4.2.2.2 Evaluation of Esterification Reaction Data

To resolve the spectra acquired during the rest of the esterification reactions into their pure component contributions, GUIPRO software[26] was used. A spectral constraint sensitivity of 0.1 (soft) and a concentration constraint sensitivity of 20 (hard) were used. The maximum number of iterations was set to 500 and the convergence tolerance (i.e. the difference between iterations required in order for the algorithm to converge to a solution) was set to 1×10^{-4}. These parameters were chosen based on the results of the MCR software comparison (section 4.3.2). The root mean square spectral residual was again calculated for each of the spectral estimates.

The average rate of formation of butyl acetate was measured over the first five minutes of the reactions performed at 20 °C, 40 °C (using the reaction in which acetic acid was dosed in) and 50 °C. For each reaction, the relative concentration of butyl acetate estimated by GUIPRO (i.e. its contribution to the total absorbance of the mixture) five minutes after the addition of butanol was divided by time, to obtain a measure of average reaction rate in a.u./min. Five consecutive estimates of relative butyl acetate concentration were used in each case and an average was taken, due to the presence of noise in the concentration profiles.

4.2.3 Product Ratio Analysis

4.2.3.1 Mid-Infrared Spectroscopy

Butyl acetate and acetic acid are expected to form in a 1:1 molar ratio during the reaction,[1] however the results of the MCR analysis indicated that the concentration of butyl acetate present at the end of the reaction was approximately double the concentration of acetic acid. It was hypothesised that the difference observed was due to absorbance in electromagnetic spectroscopy being dependent on the volume fraction rather than the molar fraction of the components.[28, 29] This will be discussed in more detail in section 4.3.4.1. To determine whether the results acquired using the Keit spectrometer were in agreement with the literature, two reference mixtures were prepared; a 1:1 molar mixture of acetic acid and butyl acetate, and a 1:1 mixture of acetic acid and butyl acetate by volume. The spectrum of each mixture was measured five times using the Keit spectrometer.

To resolve the spectra of the reference mixtures, MCR was performed using GUIPRO. The reference spectra of each product were used as the spectral equality constraints, and the same parameters and constraints were used as for the reaction mixtures. The estimates of relative concentration obtained for the reference mixtures were then compared to the estimates of relative concentration obtained at the end of the esterification reaction.

4.2.3.2 Low-Field NMR Spectroscopy

4.2.3.2.1 Esterification Reaction

To provide further confirmation that the composition of the reaction mixtures measured by the Keit spectrometer was accurate, low-field NMR spectroscopy was used as a complementary technique. An additional esterification reaction was carried out at 40 °C, and 1 mL aliquots of the reaction mixture were removed from the reaction vessel at 5 minutes, 30 minutes and 1 hour after the addition of butanol. 0.2 mL of each aliquot was added to 4.8 mL of chloroform to inhibit the progress of the reaction, and 0.6 mL of each resulting mixture was transferred to an NMR tube for analysis by low-field ^{1}H NMR spectroscopy.

A Magritek Spinsolve Carbon NMR spectrometer operating at 43 MHz was used, operated via Spinsolve Expert software. The receiver gain was set to 31 dB, the dwell time was set to 200 μs and the number of scans was set to 4, with a repetition time of 70 s. An acquisition delay of 20 μs, an acquisition time of 3.2768 s, a bandwidth of 5 kHz and a 90° pulse duration of 11.1 μs were used. Each NMR spectrum consisted of 32,768 points, which was zero filled to 131,072 points in order to increase the digital resolution of the spectra. Automatic phase correction was performed by the software, consisting of an unoptimised first order correction which is automatically applied to all spectra and a zero order correction optimised for each spectrum.

4.2.3.2.2 Reference Mixtures

For comparison to the sample extracted at the end of the esterification reaction, two reference mixtures were prepared. The first reference mixture contained 45 % acetic acid, 45 % butyl acetate, 5 % acetic anhydride and 5 % butanol by molarity (the expected mixture at the end of the esterification reaction if the products formed in a 1:1 ratio), and the second contained 60 % butyl acetate, 30 % acetic acid, 5 % acetic anhydride and 5 % butanol by molarity (the expected mixture at the end of the reaction if the products formed in a 2:1 ratio). For each reference mixture, 0.1 mL was added to 4.9 mL of chloroform and 0.6 mL of this mixture was then transferred to an NMR tube. Low-field ^{1}H NMR spectroscopy was performed using the settings described in section 4.2.3.2.1.

4.3 Results and Discussion

4.3.1 Description of MCR Toolboxes

In order to determine the most effective MCR toolbox for evaluation of the esterification reaction data, GUIPRO, MCR-ALS and the MCR function in PLS Toolbox were compared. All three methods of MCR are based on an ALS algorithm, as described in section 2.3.5. A summary of the key features of each MCR toolbox are shown in Table 4.1, and these features will be discussed in more detail in the following sections. The settings and constraints available within each toolbox differ, and these will be compared for analysis of the esterification reaction data.

4.3.1.1 GUIPRO

In GUIPRO software, the number of components present in the spectra can be chosen manually or determined by an F-test. Initial estimates of concentration are determined either by a needle search or by evolving factor analysis. A matrix of initial estimates (e.g. reference spectra) cannot be supplied, which is a disadvantage of GUIPRO. Within GUIPRO, curve resolution can be applied using two different methods of factor analysis (automated window factor analysis[30] and iterative target transformation factor analysis[31]), non-negative ALS or constrained ALS. Constrained ALS allows the user to define the constraints which are applied to the spectral and concentration estimates, while the other methods do not, therefore constrained ALS is the method which was used in this work.

Non-negativity, closure and unimodality constraints can be applied to the concentration data, but only non-negativity can be applied to the spectral data. However it is possible to load matrices as equality constraints for the concentration and/or spectral data. In addition, it is possible to apply separate spectral/concentration constraints to each of the components in the mixture, which is an advantage of GUIPRO. For each component, the spectral/concentration equality constraint is entered as a vector the same length as the data matrix in the spectral/time dimension respectively.

Table 4.1 - Summary of features of MCR toolboxes.

Feature	PLS Toolbox	MCR-ALS	GUIPRO
Determination of number of components	Manual	Manual Singular value decomposition	Manual F-test
Initial estimates	Manual Euclidean distance Normalisation	Manual Pure variable detection Evolving factor analysis	Needle search Evolving factor analysis
Concentration constraints	Non-negativity Closure Equality	Non-negativity Unimodality Closure Equality	Non-negativity Unimodality Closure Equality
Spectral constraints	Non-negativity Equality	Non-negativity Unimodality Closure Equality	Non-negativity Equality
Ability to treat each component separately	Yes	No	Yes
Penalty functions	Yes	No	Yes
Kinetic fitting	No	Yes	Yes
Ability to modify input data	No	No	Yes
Ability to save parameters	Yes (as variable in MATLAB workspace)	No	Yes
Graphical user interface	Reduced functionality compared to command line	Yes	Yes

If equality constraints are only desired in certain regions of the data matrix (e.g. it might be desirable to apply a concentration equality constraint of zero when a component is known to be absent but no equality constraint when it is known to be present) then "NaN" can be entered in the equality constraint matrix. If the intervals between the reference concentration/spectral data inputted as the equality constraints do not match those of the data matrix, nearest neighbours or interpolation can be used by selecting "discrete" or "continuous" respectively. In addition, kinetic fitting is possible. The maximum number of iterations and the convergence tolerance (the relative change in residual sum of squares between iterations) can be specified.

An advantage of GUIPRO is the ability to modify the data matrix within the graphical user interface, for example altering the wavelength and time ranges, removing outliers, adjusting the baseline, normalising and scaling the data. Wavelength and time axes can also be loaded, and are applied to the graphical output. Another advantage of GUIPRO is that the graphical user interface containing the inputted data and parameters can be saved and reloaded for future use. The output plots of concentration and spectral estimates can be saved as an image or MATLAB figure, and the estimates can be exported to the MATLAB workspace as matrices.

The greatest advantage of GUIPRO is the ability to apply penalty functions to the constraints. Sensitivity values between 0.01 (soft, i.e. small deviations from the constraints) and 20 (hard, i.e. no deviations from the constraints) can be chosen for the spectral and concentration constraints. The ability to apply soft constraints allows deviations of the estimates from the constraints, providing greater flexibility in the model. For example, the pure component spectra can be applied as spectral equality constraints, allowing deviation to account for interactions between components during the reaction. NWAY penalty-ALS[2] can also be applied in GUIPRO, to allow the application of penalty-ALS to multi-batch data.

4.3.1.2 MCR-ALS

In the MCR-ALS toolbox, the number of components can either be determined by singular value decomposition or inputted manually. Initial estimates of either concentration or spectra can be inputted manually or calculated using pure variable detection or evolving factor analysis. The ability to manually input a matrix of initial

estimates is an advantage over GUIPRO. An uncertainties estimation can be added by providing a matrix containing a standard deviation estimate of the uncertainty for each value in the data matrix. It is also possible to upload an augmented dataset and split the data into multiple matrices within the graphical user interface.

Spectral and concentration constraints of non-negativity (forced to zero, non-negative least squares or fast non-negative least squares), unimodality (vertical, horizontal or average) and closure (with the condition "equal than", "least squares closure" or "lower or equal than") are possible. Unimodality can be applied to individual components but the other constraints cannot, unlike in GUIPRO.

An advantage of MCR-ALS over GUIPRO is that the user can input a matrix as an equality constraint and specify whether the results should be "equal than" or "lower or equal than". If a component is known to be absent in a certain time region (e.g. before it has been added to the reaction vessel), an equality constraint of less than or equal to zero can be applied to its concentration profile, while equality constraints of less than or equal to e.g. one (i.e. the highest possible relative concentration) can be applied to the concentration profiles of the components known to be present. However the ability to apply equality constraints with varying sensitivity values is absent, which is the main disadvantage of the MCR-ALS toolbox. The spectral/concentration equality constraints must be inputted as a matrix matching the spectral/time dimension (respectively) of the data matrix by the number of components. "NaN" can be entered for the points at which equality constraints are not desired, as for GUIPRO. Advanced constraints of correlation and kinetic hard modelling can also be applied to the concentration data.

At the final stage, normalisation of the pure component spectra can be performed. The available normalisation options are "spectra equal height", "spectra divided by total sum norm" and "spectra divided by Euclidean norm". The maximum number of iterations and the convergence criterion (the minimum percentage difference in the standard deviations of the residuals between two iterative cycles required for the algorithm to achieve convergence[32]) of the ALS algorithm can also be specified.

Unlike in GUIPRO, the data matrix cannot be modified within the graphical user interface and wavelength/time axes cannot be inputted for application to the graphical

output. It is not possible to save the output plots as an image, however the concentration and spectral estimates can be exported to the MATLAB workspace as in GUIPRO. Another disadvantage over GUIPRO is that it is not possible to save the inputted data/parameters to reload for future use, so they must all be manually entered again.

4.3.1.3 PLS Toolbox

An MCR function is also available within PLS Toolbox. It is necessary to input either an initial estimate of concentration/spectra (in the form of a matrix) or the number of components present in the data matrix. Evolving factor analysis or evolving window factor analysis (which is similar to EFA but utilises a moving window of defined width) can be performed within PLS Toolbox prior to MCR to calculate the initial estimates, but they are separate to the MCR function. If the number of components is inputted then an initial guess of concentration or spectral data is generated automatically by selecting samples outside the dataspace either based on Euclidean distance or after normalising the samples. An initial guess of the minimum norm value can also be defined.

Normalisation of the data is required (to unit area, unit length or unit maximum), unless equality constraints are applied. Equality constraints can be inputted as a matrix the same size as the data matrix, with "NaN" entered in the cells where they are not applied. It is possible to apply weights to the concentration and spectral equality constraints (based on the penalty ALS algorithm used in GUIPRO), as either a scalar value between zero and infinity (with infinity corresponding to hard constraints and a value of one corresponding to the weight which has the same influence as the average single variable in the data) or a vector of values. Non-negativity constraints can be applied to the spectral and concentration data using fast non-negative least squares, forcing negative values to zero after least squares (called "reset"), or "reset" with polynomial baseline fitting. Closure can be applied to the concentration data and weights can be applied to the closure constraints, as for the equality constraints. A contrast constraint can also be applied to the spectra of images. Unimodality constraints are not available.

The tolerance on non-negativity and convergence can be altered, and a maximum number of iterations or maximum time for iterations can be specified. The ability to specify a maximum time is an advantage, as this may be more useful than specifying a maximum number of iterations. Norm conditioning (i.e. conditioning each spectrum/contribution to its norm) can be applied to the spectral and concentration data before each regression step to stabilise the regression when large differences in magnitude are present between the components. The way rank deficiencies are handled can also be specified (for example dropping the deficient components from the model, resetting them to the initial guess, replacing them with a random vector or stopping the analysis).

Although there is an MCR graphical user interface in PLS Toolbox, it is designed for use with calibration and validation X and Y block data, thus it is not clear how to use it for decomposition of a data matrix by MCR. Therefore the PLS Toolbox MCR function was accessed via the command line. The lack of usable graphical user interface is a disadvantage for inexperienced users, as performing MCR via the command line is less intuitive than using MCR-ALS or GUIPRO. The necessity for normalisation if no equality constraints are applied is another disadvantage, as normalisation may not be desired. A disadvantage of the PLS Toolbox MCR function over GUIPRO is the inability to alter the inputted data matrix, as (unlike in GUIPRO) pre-processing functions such as the ability to crop the data matrix, the ability to adjust the baseline and the ability to remove outliers are not available. The ability to apply weightings to the constraints is an advantage over the MCR-ALS toolbox, and the ability to input a matrix (e.g. reference spectra) as an initial estimate is an advantage over GUIPRO.

4.3.2 Comparison of MCR Toolboxes

To compare the performance of the three MCR toolboxes, analysis of the esterification reaction mixture spectra acquired by the Keit spectrometer (from the reaction at 40 °C in which extra acetic acid was added) was performed using each toolbox. The reaction mixture spectra are displayed in Figure 4.2 (with black representing the start of the reaction and red representing the end), and an assignment of the main peaks present in each compound is displayed in Table 4.2. The absorbance of the acetic anhydride

peaks significantly decreased during the course of the reaction (from up to 2.1 to less than 0.3 in absorbance), and the product peaks at 1200 – 1300 cm^{-1} and 1700 – 1800 cm^{-1} (each of which arise due to both products overlapping) increased in absorbance. The spectrum of butanol was of relatively low absorbance and the peaks were obscured by the other components. Due to the large extent of peak overlap present, multivariate curve resolution is necessary to decompose the spectra into their pure component contributions.

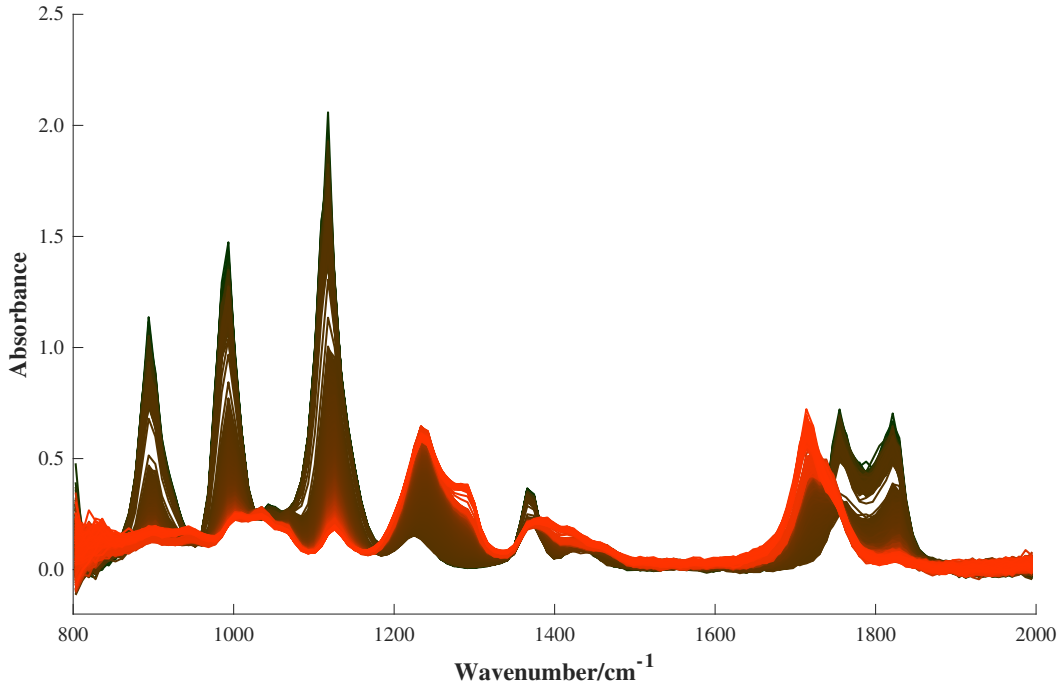

Figure 4.2 - Spectra collected during esterification reaction at 40 °C with acetic acid dosed in approximately one hour after the addition of butanol (last 240 spectra), acquired using the Keit spectrometer (single spectrum measured every 1.6 seconds). Black represents the start of the reaction and red represents the end of the reaction.

The concentration and spectral estimates obtained using each toolbox were compared by visual inspection of the plots and comparison to those published in the literature, as poor estimates produced obvious deviations from the expected results. Concentration profiles obtained by CLS of the same esterification reaction, monitored by direct liquid sampling mass spectrometry, have been published by Owen et al.[1] and are displayed in Figure 4.3. The reactants were present in a 1:1 molar ratio and their concentrations are expected to decrease at the same rate, as the products form. The concentrations of the products are expected to increase at the same rate, as they form in a 1:1 molar ratio.

Table 4.2 - Assignment of the main peaks in the IR spectra collected during the esterification reaction using the Keit spectrometer.[33, 34]

Component	Peak position/cm^{-1}	Peak assignment
Acetic anhydride	890	C–O stretch
	990	C–O stretch
	1120	C–O stretch
	1760	C=O stretch
	1830	C=O stretch
Butanol	1000 – 1100	C–O stretch
Acetic acid	1290	C–O stretch
	1410	C–O stretch and O–H deformation
	1710	C=O stretch
Butyl acetate	1030	C–O stretch
	1230	C–O stretch
	1740	C=O stretch

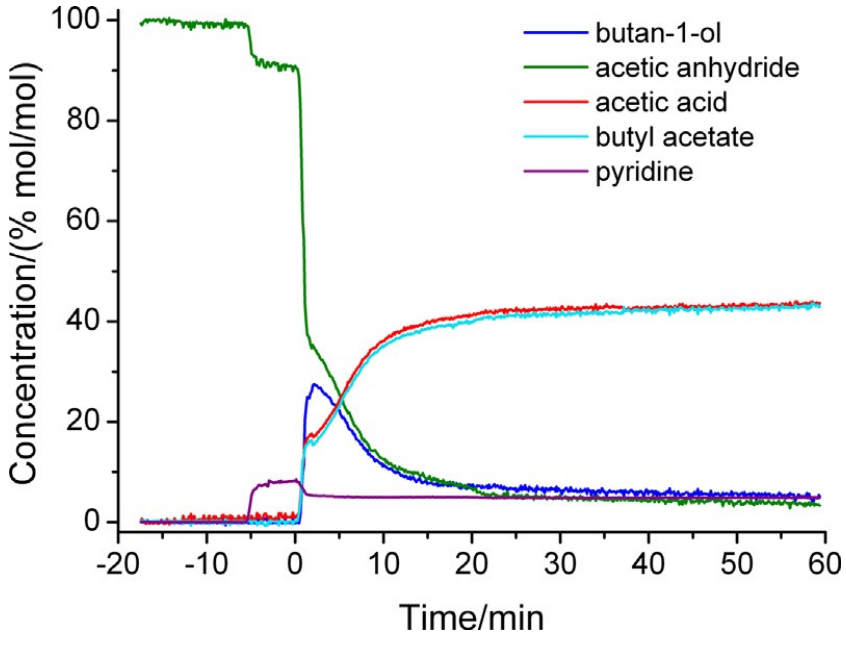

Figure 4.3 - Estimated concentration profiles by Owen et al. of components present during esterification reaction monitored by direct liquid sampling mass spectrometry, taken from reference 1.

Richards et al.[2] utilised GUIPRO with soft constraints to obtain concentration profiles of the reaction, monitored by NIR spectroscopy. They obtained similar profiles to Owen et al., however they treated the two products together as one pseudo-product. The reference spectrum of each component is displayed in Figure 4.4 (with the region between 1070 cm^{-1} and 1170 cm^{-1} removed due to the high absorbance of acetic anhydride in this region). The estimated spectra are expected to be similar to the references, with small differences present due to interaction of the components.

It is not possible to compare the three toolboxes using the same settings, as the parameters within each toolbox differ. PLS Toolbox automatically normalises the spectra unless equality constraints are applied. The available normalisation options differ for each toolbox so the normalised data cannot be directly compared. Equality constraints can be applied to the concentration profiles using all three toolboxes, but the MCR-ALS "lower or equal than" function is not available in GUIPRO or PLS Toolbox, so the constraints would have to be hard (as soft constraints are not available in the MCR-ALS toolbox). It is undesirable to apply hard constraints to the concentration profiles of every component, as in the case of the esterification reaction (and the majority of reactions which would be monitored) the concentrations present in every step of the reaction are not known precisely, and the purpose of MCR is usually to obtain these concentration profiles.

The initial estimates of spectra/concentration in GUIPRO cannot be supplied manually and have to be determined by a needle search or evolving factor analysis. It would be possible to perform evolving factor analysis to obtain the initial estimates for each toolbox (using the evolving factor analysis function external to the MCR function in PLS Toolbox to obtain the estimates), but it would then not be possible to supply the pure component spectra to the MCR-ALS model (except for as a hard spectral constraint), which would reduce its effectiveness. In addition, MCR-ALS utilises a convergence criterion of a different order of magnitude to the convergence tolerance values used by GUIPRO and PLS Toolbox.

Therefore in order to compare the toolboxes, a variety of constraints were applied to determine the optimum settings for each toolbox, and the results obtained using the best settings for each method were then compared. For all methods, the estimated

concentrations were relative values between 0 and 1, dependent on their contributions to the absorbance.

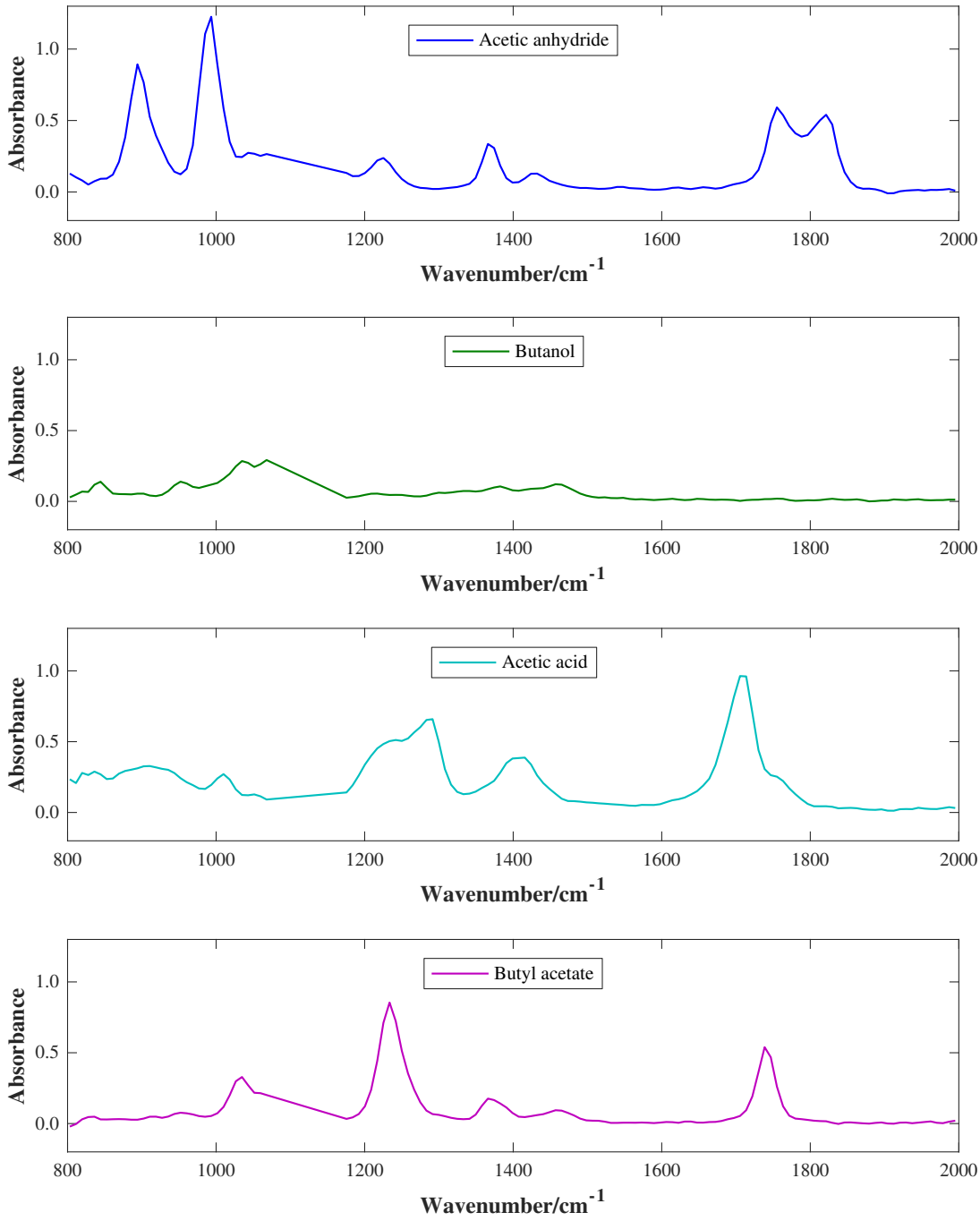

Figure 4.4 - Reference spectra of components present in esterification reaction mixture, acquired using the Keit spectrometer (with the region between 1070 cm^{-1} and 1170 cm^{-1} excluded).

4.3.2.1 GUIPRO

When GUIPRO was applied to the esterification reaction spectra, the reference spectra were used as spectral equality constraints and non-negativity was applied to both the spectral and concentration profiles (as it would be inaccurate for either to fall below zero). Concentration constraints of zero were applied to butanol, acetic acid and butyl acetate in the time region before butanol was added. A matrix of equality constraints was applied, using zero in the regions where each component was known to be absent and "NaN" (i.e. no constraint) when it known to be present in the reaction mixture. This eliminated the noise present in the butanol, acetic acid and butyl acetate profiles in the region where only acetic anhydride and pyridine were present, but otherwise did not affect the results.

A sensitivity value of 20 was applied to the concentration constraints, as non-negativity was the only constraint used and deviation in this constraint would be undesirable. For the spectral constraints, a range of sensitivity values were applied; 0.01, 0.1, 0.2, 0.5, 1 and 20. Poor estimates were obtained using the sensitivity value of 0.01, as shown in Figure 4.5. The concentrations of the reactants are expected to decrease at the same rate,[1, 2] but the concentration estimate of acetic anhydride immediately dropped to less than 0.2 a.u. upon the addition of butanol, while the concentration of butanol was as high as 0.8 a.u. A large difference was present between the concentration estimates of the products (which are expected to form in a 1:1 ratio[1]), and when extra acetic acid was dosed into the reaction (at approximately 88 minutes), the concentration estimate of acetic acid dropped and the concentration estimate of butyl acetate increased. A large amount of noise was also present in the profiles. Therefore, the sensitivity value of 0.01 appeared to allow too much deviation from the constraints. The other sensitivity values used produced sensible results, so the sensitivity value of 0.1 was chosen in order to allow the greatest possible deviation from the reference spectra while still producing accurate estimates of concentration.

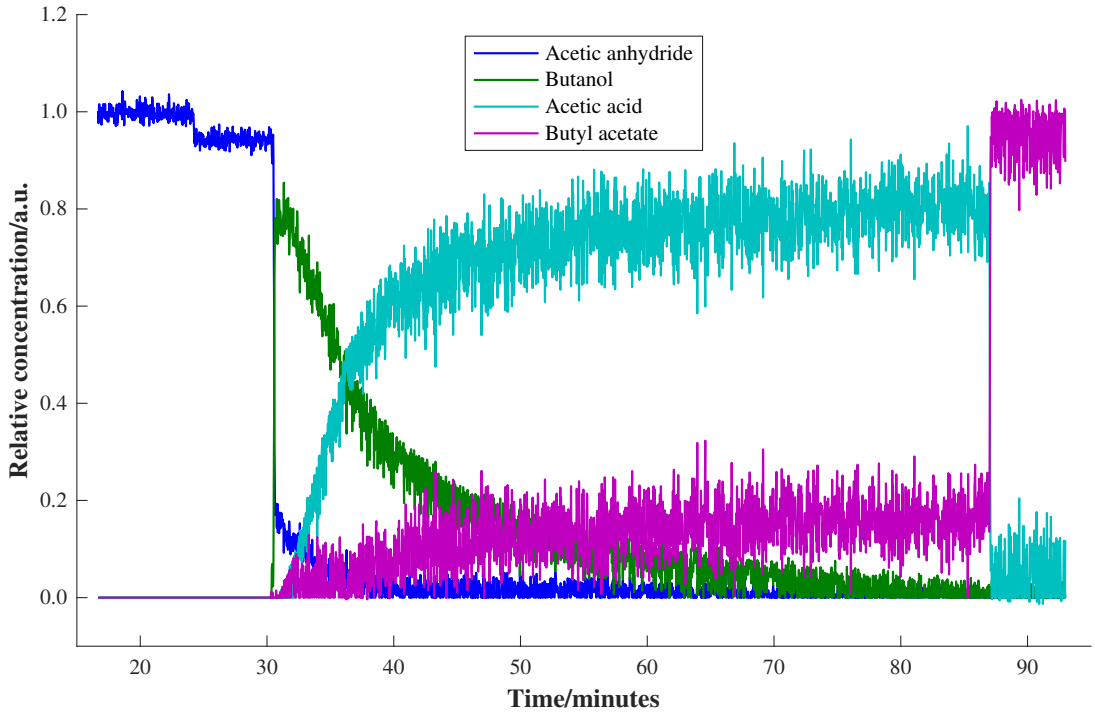

Figure 4.5 - Estimated concentration profiles (by GUIPRO) of components present in the reaction mixture spectra collected during esterification reaction at 40 °C with acetic acid dosed in approximately one hour after the addition of butanol (acquired using the Keit spectrometer), with a sensitivity of 0.01 applied to the spectral constraints.

When unimodality was applied to the concentration profiles, the estimates significantly worsened, even when very soft sensitivity values were used. This is presumably due to the presence of noise in the spectra, which results in multiple maxima. An example is shown in Figure 4.6, in which the concentration estimate of butanol increased to almost double the initial relative concentration of acetic anhydride (i.e. the total relative concentration possible) and the concentration of butyl acetate was estimated as zero throughout the course of the reaction.

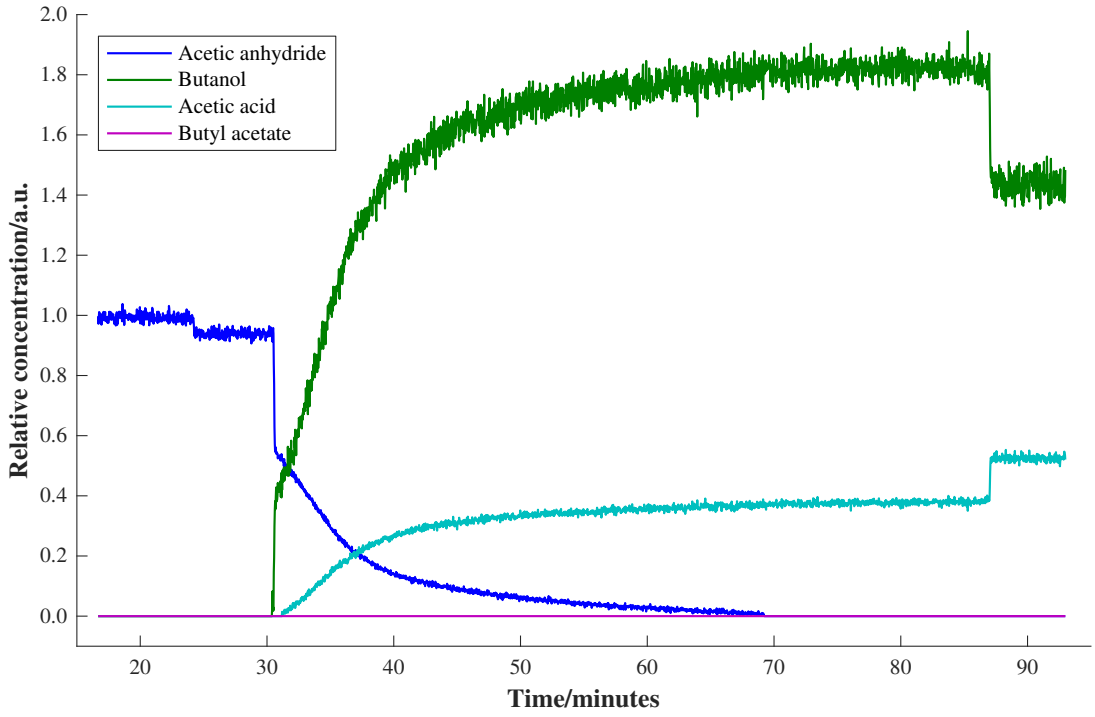

Figure 4.6 - Estimated concentration profiles (by GUIPRO) of components present in the reaction mixture spectra collected during esterification reaction at 40 °C with acetic acid dosed in approximately one hour after the addition of butanol (acquired using the Keit spectrometer), with unimodality applied to the concentration estimates.

Convergence tolerance values of 1 x 10^{-3} or lower produced similar results, so 1 x 10^{-4} was chosen as it is the default value. Values of 0.1 and 0.01 produced less accurate results. The needle search method was used to obtain the initial estimates rather than EFA because for a large dataset such as this, the EFA window takes a significantly long time to load (approximately 10 minutes using a MacBook Air with OS version 10.13.6, a 1.7 GHz Intel Core i7 processor and 8 GB memory, compared to a couple of seconds for the needle search method). The choice of peak locations to use as initial estimates by needle search was not found to affect the final estimate. In addition, it is difficult to select the same points every time, as they could only be selected manually from a large number of overlapping points. Therefore the points chosen as initial estimates were an approximation of the points at which the maximum concentration of each component occurred.

The concentration and spectral estimates for the esterification reaction carried out at 40 °C with acetic acid dosed in at the end, using the chosen optimum GUIPRO settings,

are shown in Figure 4.7 and Figure 4.8 respectively. The profiles are as expected,[1, 2] other than the apparent difference in concentration of the products, which will be investigated in section 4.3.3. These concentration profiles will also be discussed in more detail in section 4.3.3.

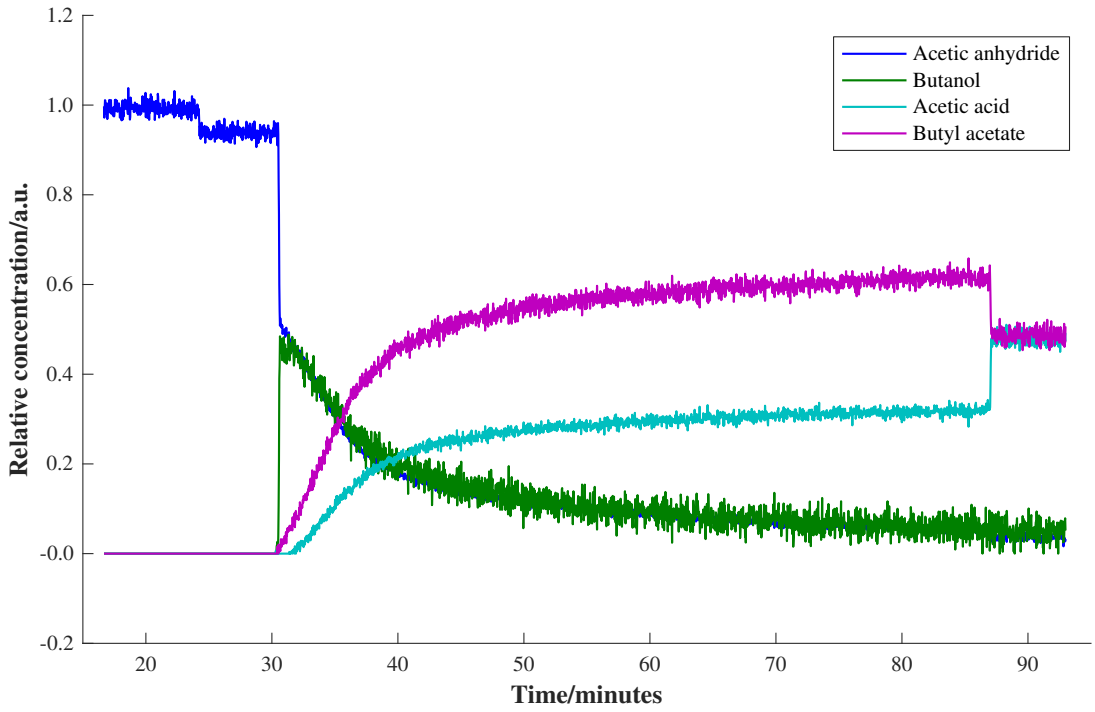

Figure 4.7 - Estimated concentration profiles (by GUIPRO) of components present in the reaction mixture spectra collected during esterification reaction at 40 °C with acetic acid dosed in approximately one hour after the addition of butanol (acquired using the Keit spectrometer), using the chosen optimum parameters.

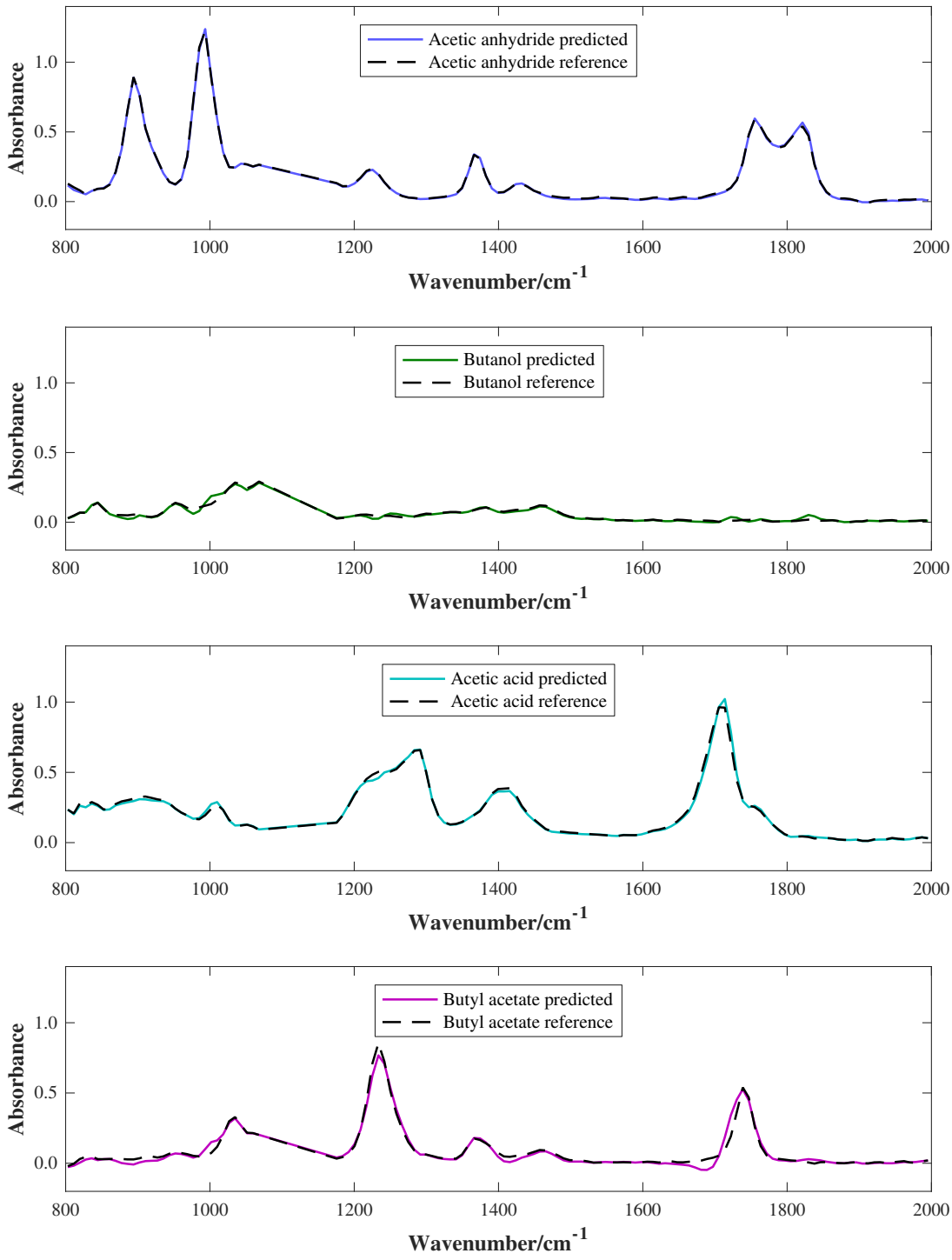

Figure 4.8 - Estimated pure spectra (by GUIPRO, using the chosen optimum parameters) of components present in the reaction mixture spectra collected during esterification reaction at 40 °C with acetic acid dosed in approximately one hour after the addition of butanol (solid lines) and reference pure component spectra (dashed lines), all acquired using the Keit spectrometer.

4.3.2.2 MCR-ALS

With the MCR-ALS toolbox, the reference spectra were used as initial estimates. A matrix of concentration equality constraints was applied using the "lower or equal than" option, with a value of 1 set when a component was known to be present and 0 when it was known to be absent. Non-negativity using the fast non-negative least squares option was selected for the concentration and spectral data. The default convergence criterion value of 0.1 was used, as smaller values either failed to converge or produced inaccurate estimates such as Figure 4.9, in which the butanol concentration sharply dropped to zero at 50 minutes.

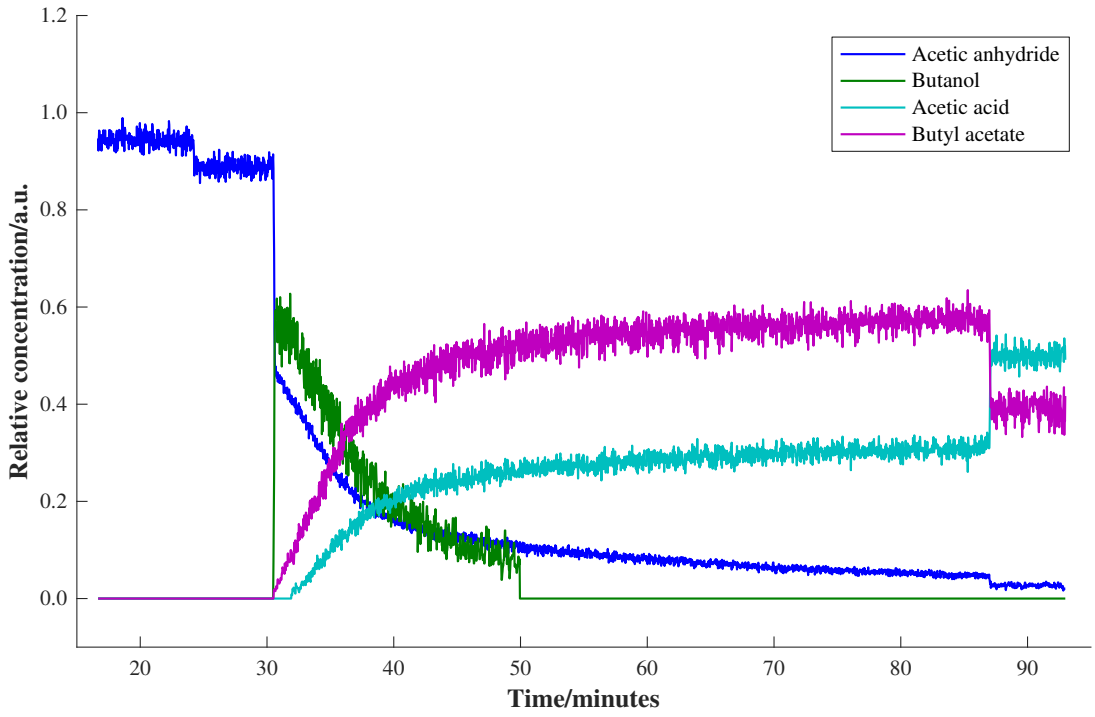

Figure 4.9 - Estimated concentration profiles (by MCR-ALS) of components present in the reaction mixture spectra collected during esterification reaction at 40 °C with acetic acid dosed in approximately one hour after the addition of butanol (acquired using the Keit spectrometer), with a convergence criterion of 0.01 applied.

The MCR-ALS toolbox was significantly slower than GUIPRO and PLS Toolbox, taking 45 seconds to perform 50 iterations, compared to less than 3 seconds for GUIPRO and less than 1 second for PLS Toolbox (using a MacBook Air with OS version 10.13.6, a 1.7 GHz Intel Core i7 processor and 8 GB memory). However less than 5 iterations were generally required to produce accurate results (presumably

because little variation from the reference spectra was required and these were provided as the initial estimate). When the algorithm failed to converge within the first few iterations (< 10) then the estimates typically deviated further from the expected results, and if the fit did not improve for 20 consecutive iterations then the algorithm automatically stopped.

When no unimodality constraint was applied to the concentration profiles, the algorithm did not converge for 69 iterations, producing the estimates shown in Figure 4.10. A large amount of noise was present in the profiles and the concentration profile of butanol was inaccurate, starting at nearly double the relative concentration of acetic anhydride and sharply increasing at the point at which acetic acid was dosed into the reaction vessel. Unimodality was more effective than in GUIPRO, since a tolerance value could be applied. The tolerance is entered as a number greater than 1, with 1.1 representing 10 % and 1.2 representing 20 %, etc. A range of different tolerance values were applied (within reason) and there did not appear to be an upper limit. The "average" implementation was selected and unimodality was applied to all components. The most accurate results were obtained using tolerance values of 1.3, 1.4, 1.7 and 2.0 (all converging after three iterations). The tolerance value of 1.3 was chosen as the overall best, as the magnitude of the noise present in the butanol profile was slightly less in this case. When equality constraints were not applied to the concentration profiles, convergence was not achieved until iteration 138, producing inaccurate results. Normalisation also reduced the accuracy of the results, and when the "spectra divided by Euclidean norm" normalisation option was chosen then an error occurred.

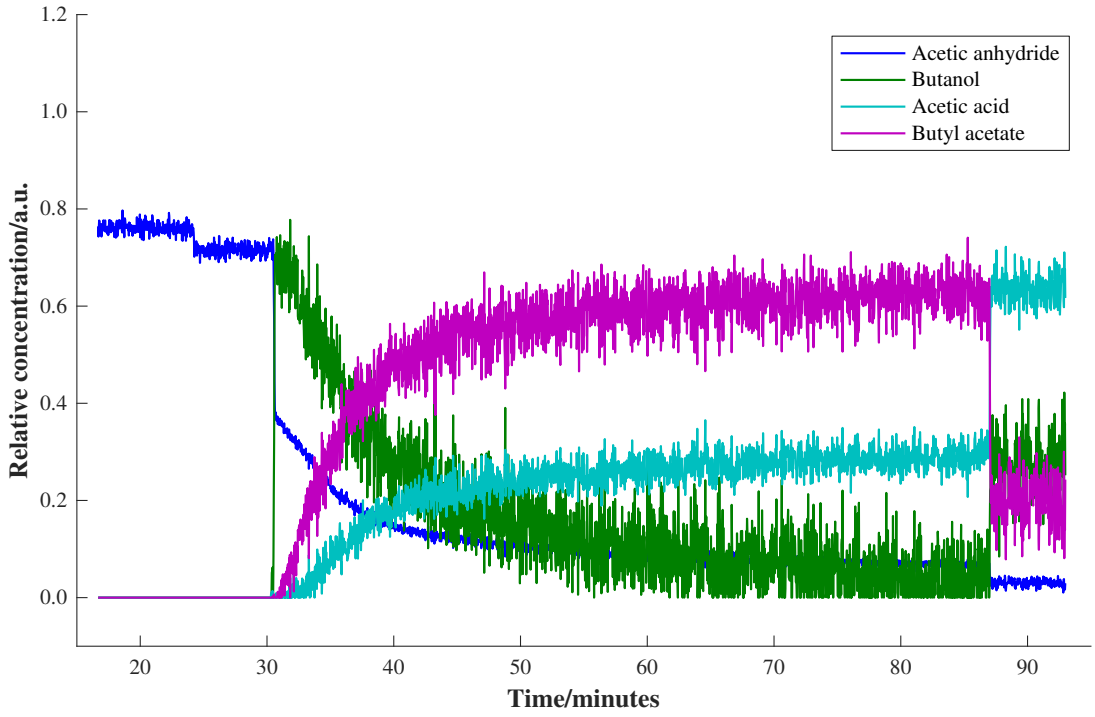

Figure 4.10 - Estimated concentration profiles (by MCR-ALS) of components present in the reaction mixture spectra collected during esterification reaction at 40 °C with acetic acid dosed in approximately one hour after the addition of butanol (acquired using the Keit spectrometer), with no unimodality applied.

The chosen optimum results were therefore obtained by applying the reference spectra as initial estimates, manually inputting the number of components, and applying non-negativity to the spectral and concentration profiles, unimodality with a tolerance value of 1.3 to the concentration profiles and concentration equality constraints using the "lower or equal than" function. The convergence criterion was set to 0.1, the maximum number of iterations was set to 500 (although the algorithm did not reach as many iterations as that for any of the settings applied) and no normalisation was applied.

The concentration profiles obtained using these parameters are shown in Figure 4.11. The profiles were relatively similar to those obtained using GUIPRO, however at 40 minutes (10 minutes after the reaction began) the concentration of butanol appeared to decrease faster than the concentration of acetic anhydride, before sharply dropping to zero at 55 minutes. This is not what is expected,[1, 2] and is likely to be due to difficulty in resolving butanol from the other components due to its low absorbance. Changing

the parameters as described above did not result in a better estimate, therefore GUIPRO was more effective at resolving the reaction mixture spectra than MCR-ALS.

The spectral profiles obtained using MCR-ALS are shown in Figure 4.12. The estimated spectra are similar to the references, however they differ to the references slightly more than the GUIPRO estimates did. The root mean square spectral residuals are displayed in Table 4.3, and the mean value for the MCR-ALS estimates was approximately double that of the GUIPRO estimates (0.347 compared to 0.180). The butanol estimate (with a root mean square spectral residual of 0.470) differed the most to the corresponding reference spectrum and was relatively poor. Peaks from the other components, particularly acetic anhydride, appear to have interfered with the butanol profile and caused extra peaks to appear (e.g. at 1000 cm^{-1}, 1250 cm^{-1} and just above 1800 cm^{-1}). This again suggests that MCR-ALS was less effective at resolving the components than GUIPRO, and that better estimates can be obtained by applying the reference spectra as soft equality constraints than as initial estimates.

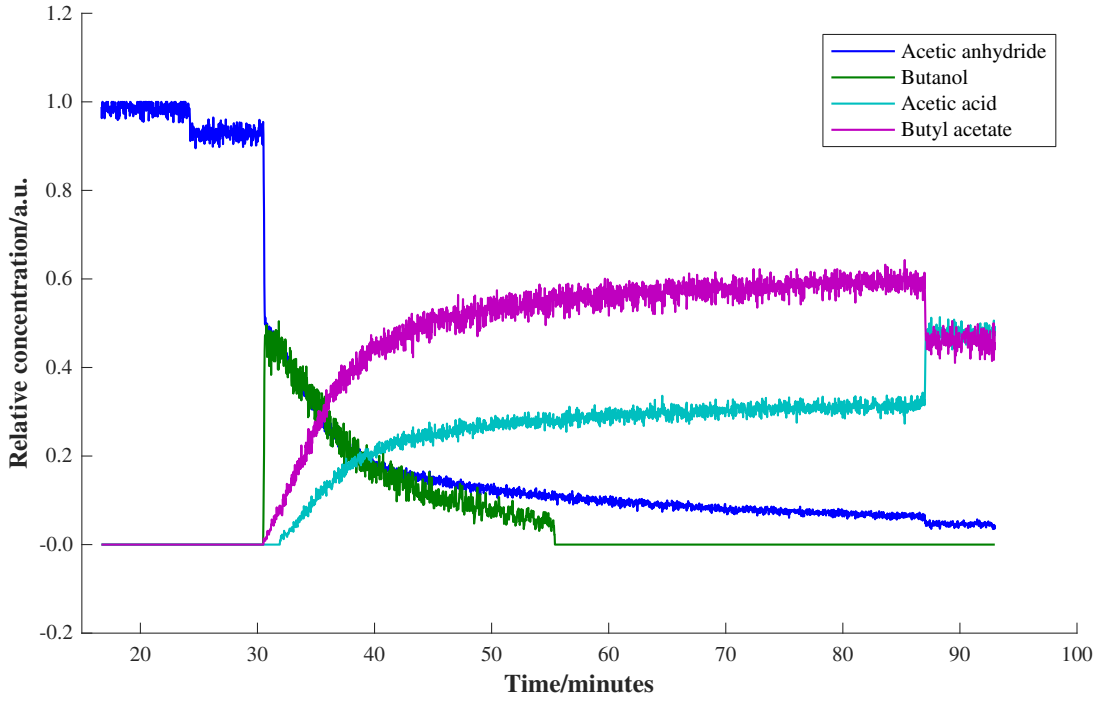

Figure 4.11 - Estimated concentration profiles (by MCR-ALS) of components present in the reaction mixture spectra collected during esterification reaction at 40 °C with acetic acid dosed in approximately one hour after the addition of butanol (acquired using the Keit spectrometer), using the chosen optimum parameters.

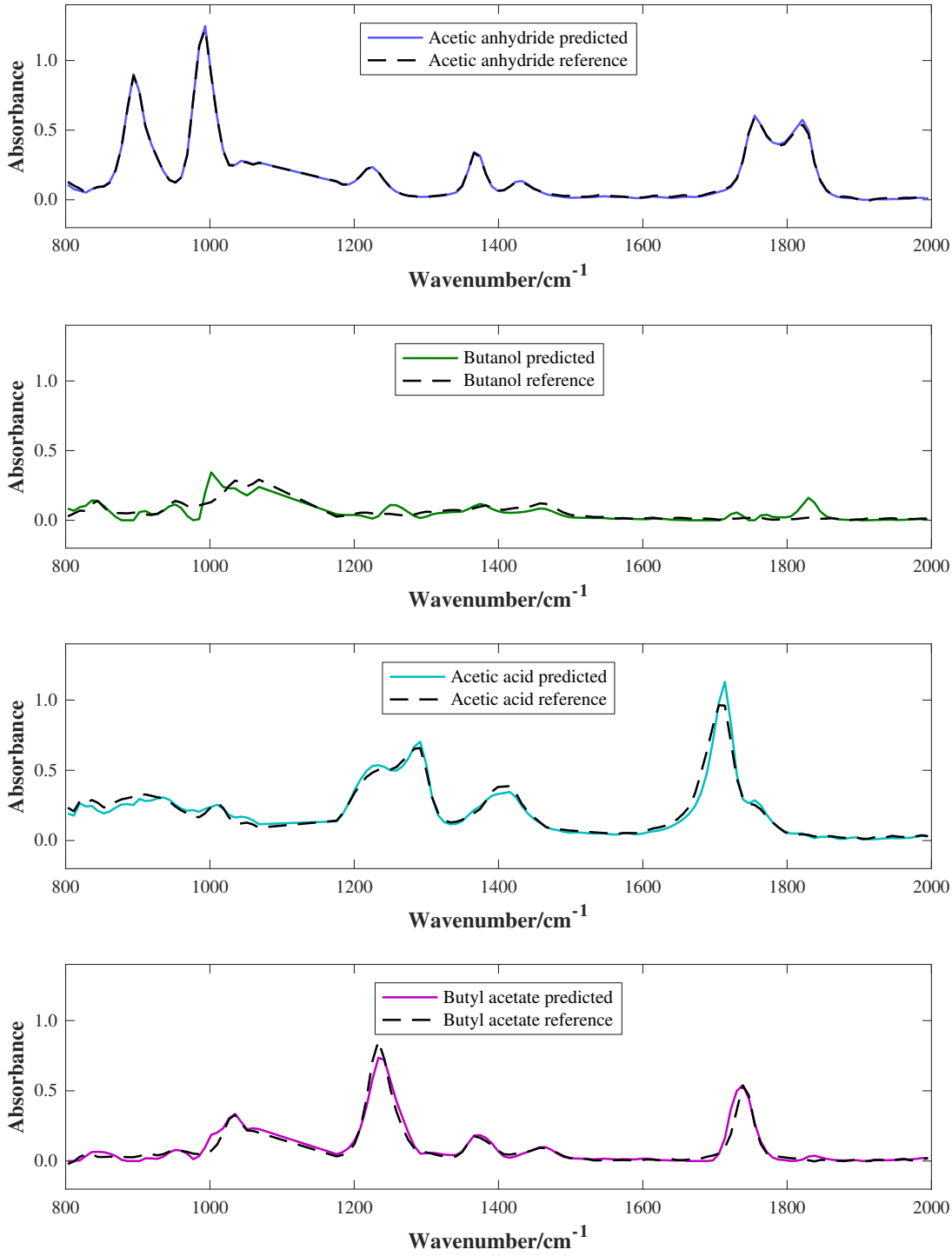

Figure 4.12 - Estimated pure spectra (by MCR-ALS, using the chosen optimum parameters) of components present in the reaction mixture spectra collected during esterification reaction at 40 °C with acetic acid dosed in approximately one hour after the addition of butanol (solid lines) and reference pure component spectra (dashed lines), all acquired using the Keit spectrometer.

Table 4.3 - Root mean square spectral residual values of estimated pure spectra (by GUIPRO and MCR-ALS, using the chosen optimum parameters) of components present in esterification reaction mixture spectra (from the reaction at 40 °C with acetic acid dosed in approximately one hour after the addition of butanol) acquired using the Keit spectrometer.

Component	Root mean square spectral residual	
	GUIPRO	MCR-ALS
Acetic anhydride	0.077	0.091
Butanol	0.135	0.470
Acetic acid	0.180	0.430
Butyl acetate	0.326	0.396
Mean value	0.180	0.347

4.3.2.3 PLS Toolbox

In PLS Toolbox, the reference spectra can be supplied as an initial estimate, equality constraints (with or without weightings) or both. If they are not supplied as an initial estimate then the number of components can be entered as the initial input instead. When the reference spectra were applied as initial estimates but not as equality constraints, the algorithm did not achieve convergence. When the reference spectra were applied as equality constraints, using the number of components as the initial input and using the reference spectra as the initial estimate produced the same results. However convergence was achieved with fewer iterations when the reference spectra were supplied as the initial estimate, as the initial estimate more closely resembled the optimum result.

Non-negativity was applied to the spectral and concentration estimates using fast non-negative least squares and the non-negativity tolerance values were left as the default of 1×10^{-5}. The default convergence tolerance of 1×10^{-8} was used, and the maximum number of iterations was set to 1000. A variety of different weightings were applied to the spectral constraints. When weightings less than or equal to 1 were applied (values of 0, 0.1 and 1 were used) then the algorithm failed to converge before it reached the maximum number of iterations. For weightings above 1 (values of 10, 20, 100, 1000, 10,000, 100,000 and 1,000,000 were used), convergence was achieved but

the results were poor. An example is shown in Figure 4.13, in which a weighting of 20 was used and the relative concentration of acetic anhydride was significantly higher than expected in comparison to butanol (approximately 1 a.u. greater). When a weighting of infinity (hard) was applied, relatively accurate results were obtained. However no deviation from the reference spectra can occur when hard spectral equality constraints are applied, so the model is not able to account for any deviation due to the interaction of components.

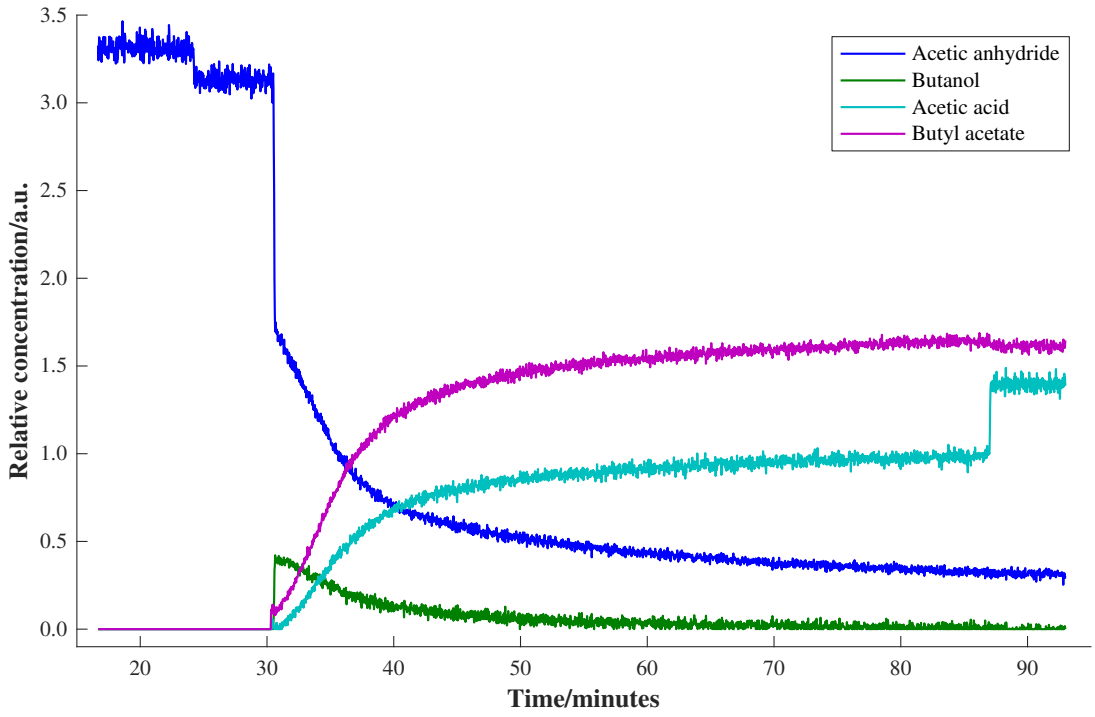

Figure 4.13 - Estimated concentration profiles (by PLS Toolbox) of components present in the reaction mixture spectra collected during esterification reaction at 40 °C with acetic acid dosed in approximately one hour after the addition of butanol (acquired using the Keit spectrometer), with a weighting of 20 applied to the spectral constraints.

As for GUIPRO, a matrix of equality constraints was applied to the concentration data, using zero in the regions where each component was known to be absent and "NaN" (i.e. no constraint) when it was known to be present in the reaction mixture. Again, this eliminated the noise present in the butanol, acetic acid and butyl acetate profiles in the region where only acetic anhydride and pyridine were present, but otherwise did not affect the results.

Normalisation is not applied by the toolbox when equality constraints are present and is always applied when equality constraints are absent. When the reference spectra were used as initial estimates and not as equality constraints, the algorithm failed to achieve convergence regardless of which method of normalisation was used. Norm conditioning also did not improve the results when soft spectral equality constraints were applied. Changing the convergence tolerance to 1 x 10^{-4} (the value used in GUIPRO) did not improve the results either. Therefore the optimum results were obtained when the reference spectra were applied as hard spectral equality constraints and zero was applied as a hard concentration equality constraint whenever a component was known to be absent from the reaction mixture.

The concentration and spectral profiles obtained using the chosen optimum parameters are displayed in Figure 4.14 and Figure 4.15 respectively. The spectral estimates were the same as the reference spectra, since hard constraints were applied (therefore the root mean square spectral residual values were all equal to 0). The concentration profiles appeared relatively accurate compared to those expected.[1, 2] However the relative concentration of butanol was slightly lower than that of acetic anhydride throughout the whole reaction (particularly at the start when it was approximately 0.04 a.u. less). Although the concentration profiles were more accurate than those obtained using MCR-ALS, no deviation from the reference spectra was allowed using these parameters. The inability to achieve accurate results using soft spectral equality constraints was a major disadvantage of using the PLS Toolbox MCR function to decompose this dataset. Therefore the use of GUIPRO software produced the most accurate results of the three toolboxes, and was most suitable for analysis of this data.

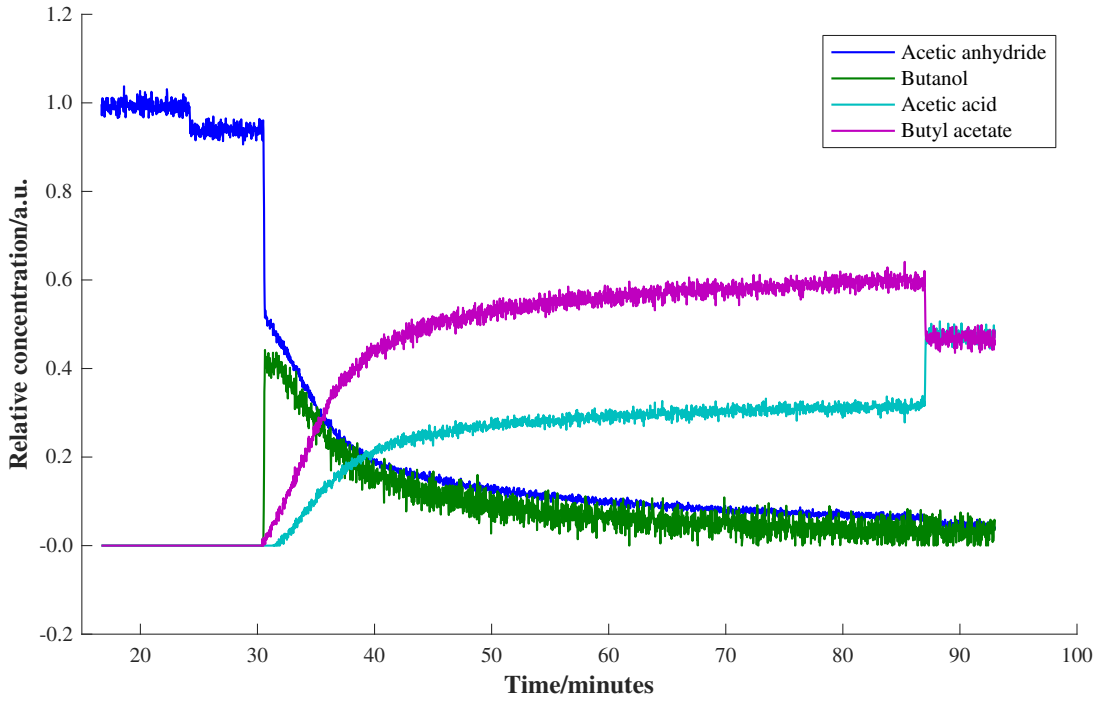

Figure 4.14 - Estimated concentration profiles (by PLS Toolbox) of components present in the reaction mixture spectra collected during esterification reaction at 40 °C with acetic acid dosed in approximately one hour after the addition of butanol (acquired using the Keit spectrometer), using the chosen optimum parameters.

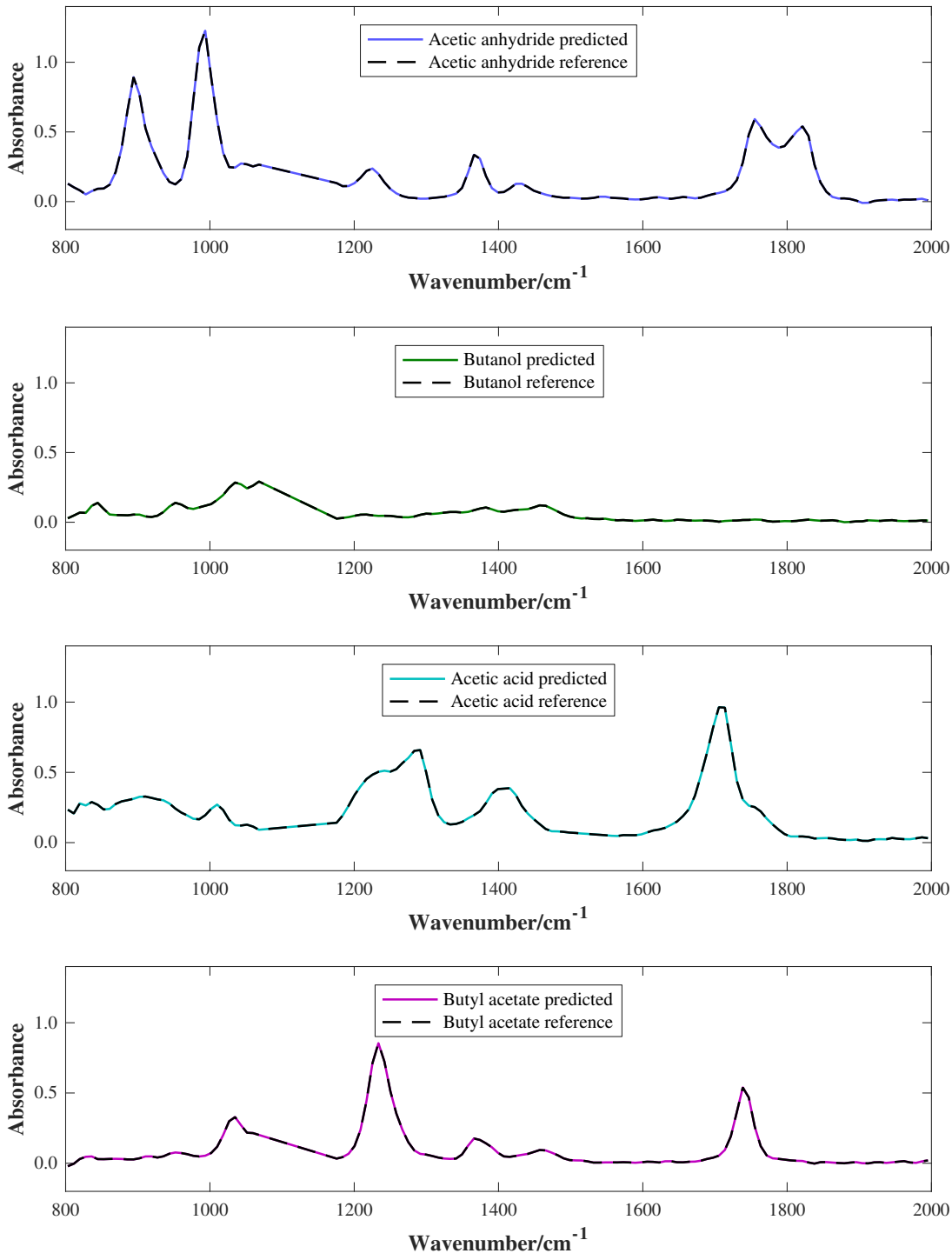

Figure 4.15 - Estimated pure spectra (by PLS Toolbox, using the chosen optimum parameters) of components present in the reaction mixture spectra collected during esterification reaction at 40 °C with acetic acid dosed in approximately one hour after the addition of butanol (solid lines) and reference pure component spectra (dashed lines), all acquired using the Keit spectrometer.

4.3.2.4 Conclusions

Of the three toolboxes evaluated, GUIPRO was the most effective for decomposition of the esterification reaction mixture spectra. This was due to the ability to apply the reference spectra as soft equality constraints to allow small deviations. Although the application of weightings to the constraints was also possible in PLS Toolbox, it worsened the results. In the MCR-ALS toolbox, it was not possible to apply soft constraints so the reference spectra had to be inputted as initial estimates rather than equality constraints. The choice of sensitivity value/weighting was an important consideration in GUIPRO and PLS Toolbox, as it affected the accuracy of the results obtained and the ability to achieve convergence. The choice of convergence tolerance/criterion value was also important, as was the application of non-negativity in all three toolboxes and the application of unimodality in MCR-ALS.

4.3.3 Esterification Reactions at 40 °C

In the previous section, GUIPRO was found to be the most effective of the three MCR toolboxes. This toolbox will now be used to evaluate data from the esterification reactions conducted under different conditions. The spectra collected during the course of one of the esterification reactions at 40 °C using the Keit spectrometer were shown in Figure 4.2 and discussed in section 4.3.2, and the spectra collected during the course of the other repeat reactions at 40 °C were similar and can be found in Appendix 4. The estimated concentration profiles and spectra of the first esterification reaction at 40 °C are displayed in Figure 4.16 and Figure 4.17 respectively. These profiles were calculated by GUIPRO, using the optimised parameters described in section 4.3.2. The estimated concentration profiles and spectra of the other reactions carried out at 40 °C can be found in Appendix 4.

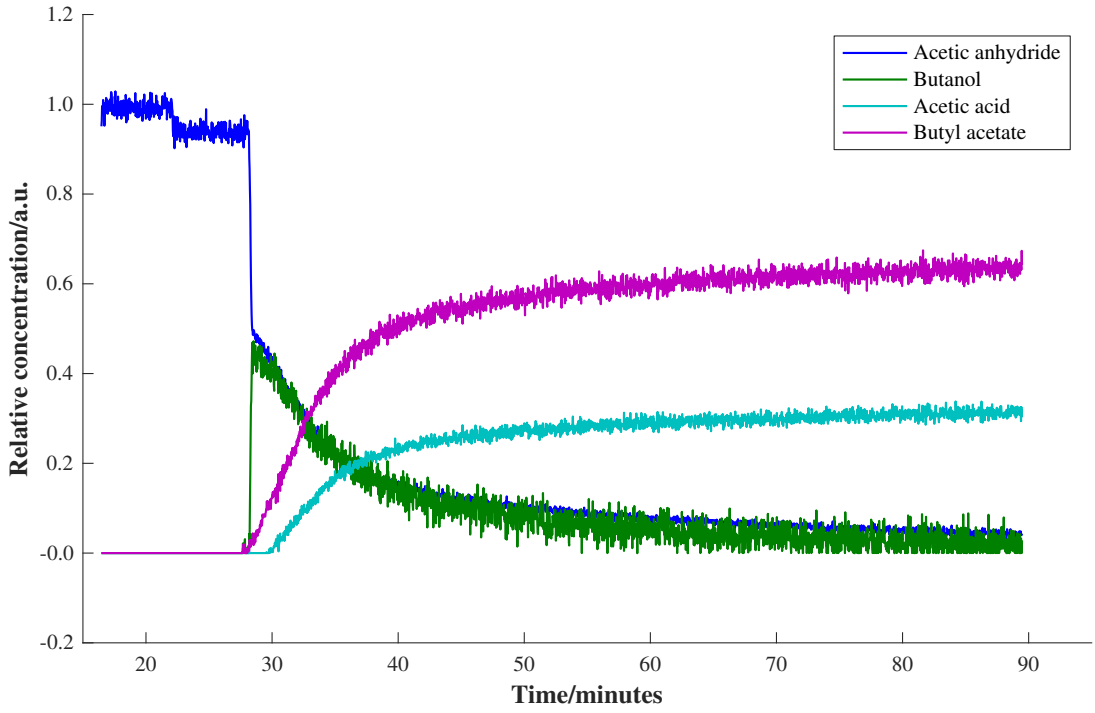

Figure 4.16 - Estimated concentration profiles (by GUIPRO) of components present in the reaction mixture spectra collected during esterification reaction at 40 °C (first repeat) using the Keit spectrometer.

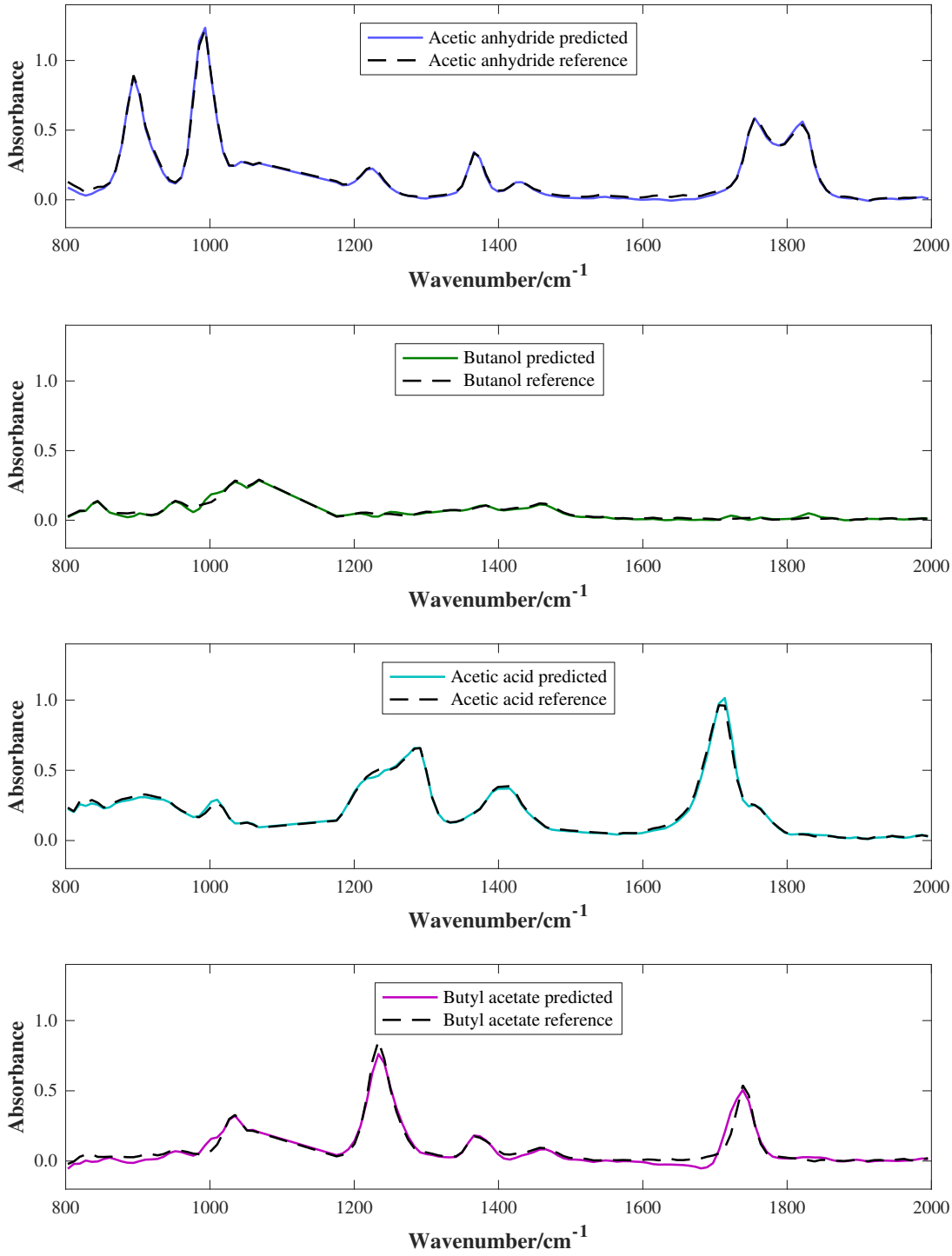

Figure 4.17 - Estimated pure spectra (by GUIPRO) of components present in the reaction mixture spectra collected during esterification reaction at 40 °C (first repeat) using the Keit spectrometer (solid lines), and reference pure component spectra collected using the Keit spectrometer (dashed lines).

At the start of the reaction, only acetic anhydride (blue) was present. A slight decrease in concentration was observed at just after 20 minutes, due to the addition of pyridine. When butanol (green) was added, the relative concentration of acetic anhydride halved and became equal to that of butanol. The concentrations of the two reactants then decreased at the same rate (rapidly in the first fifteen minutes after the addition of butanol), as the concentrations of the products increased. Noise was present in the profiles due to variation of the spectra between scans, as the data consisted of unaveraged single scans. The noise can be reduced by averaging the spectra or by increasing the number of scans at the expense of temporal resolution, if desired. The noise was absent when hard concentration equality constraints of zero were applied (i.e. in the concentration profiles of butanol, butyl acetate and acetic acid before butanol was added to the reaction vessel), and was greatest in the butanol profile due to the low relative absorbance of butanol compared to the other components.

The concentration profiles obtained during the reaction were similar to those described by Owen et al.[1] and Richards et al.[2], however the relative concentration of butyl acetate (purple) formed during the reaction was estimated as double the relative concentration of acetic acid (turquoise) rather than the same. It was hypothesised that the observed difference could be due to absorbance in electromagnetic spectroscopy being dependent on the volume fraction rather than the molar fraction of the components.[28, 29] Owen et al.[1] used mass spectrometry to monitor the reaction, and Richards et al.[2] used NIR spectroscopy but treated the two products together as one pseudo-product. This hypothesis will be investigated in section 4.3.4. The estimated final concentration of each reactant was similar, as expected. Acetic anhydride and butanol have similar volume and molar ratios (as 125 mL of acetic anhydride and 121 mL of butanol are equimolar), so this observation is consistent with the hypothesis.

The spectral estimates of each component (Figure 4.17) were similar to the references, however slight variations were observed. This was due to interaction of the components within the reaction mixture (which will not be observed in the reference spectra). The ability to apply the reference spectra as soft equality constraints during MCR allows for this deviation, and is an advantage of GUIPRO. The root mean square spectral residual values for the three repeat reactions at 40 °C are displayed in Table 4.4 and were similar overall for each repeat, with the mean value differing by no more

than 0.035. The value obtained for acetic anhydride in the first reaction was higher than for the second and third reactions, however the difference was less than 0.1 and no other significant differences in root mean square spectral residual were observed between the repeats. This further illustrates that the predictions obtained by GUIPRO were reproducible.

Table 4.4 - Root mean square spectral residual values of estimated pure spectra (by GUIPRO) of components present in esterification reaction mixture spectra acquired at 40 °C (three repeats) using the Keit spectrometer.

Component	Root mean square spectral residual		
	1st repeat	2nd repeat	3rd repeat
Acetic anhydride	0.160	0.068	0.073
Butanol	0.133	0.137	0.130
Acetic acid	0.172	0.173	0.165
Butyl acetate	0.372	0.327	0.329
Mean value	0.209	0.176	0.174

4.3.3.1 Addition of Acetic Acid

As the products formed at the same rate, an additional reaction was performed at 40 °C, in which extra acetic acid was dosed into the vessel at the end of the reaction. This was to break the rank deficiency of the spectra, to ensure that it had not caused inaccuracies in the concentration estimates of the products. The estimated concentration profile of this reaction is shown in Figure 4.18, overlaid with the temperature profile of the reaction. The spectra collected during the course of the reaction were displayed in Figure 4.2. The concentration estimates obtained were similar to those observed in Figure 4.16. The point at which acetic acid was added can be observed by a sharp decrease in the butyl acetate concentration accompanied by a sharp increase in the acetic acid concentration, just before 90 minutes.

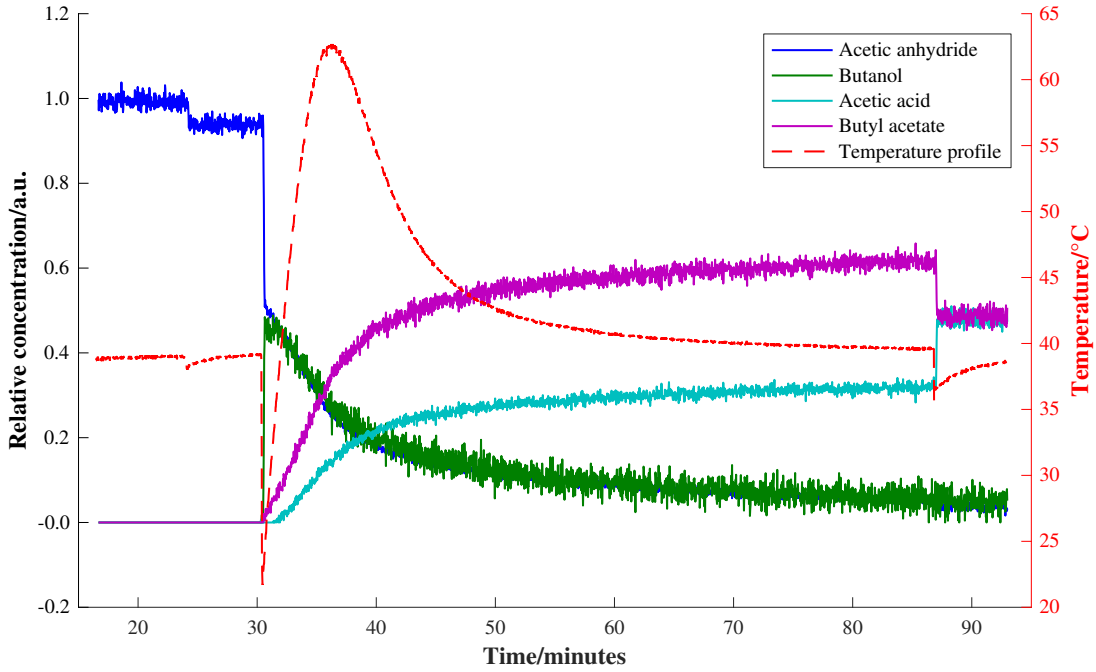

Figure 4.18 - Estimated concentration profiles (by GUIPRO) of components present in the reaction mixture spectra collected during esterification reaction at 40 °C with acetic acid dosed in approximately one hour after the addition of butanol (acquired using the Keit spectrometer), and temperature profile recorded using a thermocouple.

The relative concentration of butyl acetate at the end of the reaction was still approximately double that of acetic acid, until the point where extra acetic acid was dosed into the reaction (after which the relative concentrations of the two products were similar). The estimated spectra of the components (Figure 4.8) were also similar to those observed when acetic acid was not dosed into the reaction vessel. This indicates that the dosing of extra acetic acid into the reaction mixture had little effect on the estimates, and that GUIPRO was able to resolve the two products effectively based on their reference spectra alone.

Changes in temperature during the course of the reaction may affect the spectra, therefore the temperature profile of the reaction mixture was measured and overlaid with the concentration estimates (Figure 4.18). Initially the temperature was stable at 40 °C, with a marginal decrease observed when pyridine was added, before the temperature returned to 40 °C again. When butanol was added (at approximately 30 minutes), the temperature significantly decreased to around 20 °C. However the reaction was exothermic and the temperature rapidly increased, reaching almost 65 °C

before the water jacket was able to cool the reaction mixture. Although the cooling was initially rapid, it slowed once the reaction mixture reached 45 °C and the mixture did not reach 40 °C again until approximately 30 minutes after the butanol was added. A small decrease in temperature (approximately 5 °C) was also observed when acetic acid was dosed into the vessel at the end of the reaction, and the temperature was again slow to recover.

Reference spectra of each product were measured at 70 °C to investigate whether the increase in temperature affected the GUIPRO estimates. The concentration profiles obtained when the reference spectra collected at 70 °C were used instead of those collected at 40 °C are shown in Figure 4.19 and the corresponding spectral estimates can be found in Appendix 4. Similar estimates were obtained as to when the reference spectra were collected at 40 °C, with a slightly larger difference in estimated concentration between the two products (around 0.09 a.u. greater). This confirms that the increase in temperature was not the cause of the differences observed between the estimated acetic acid and butyl acetate concentration profiles.

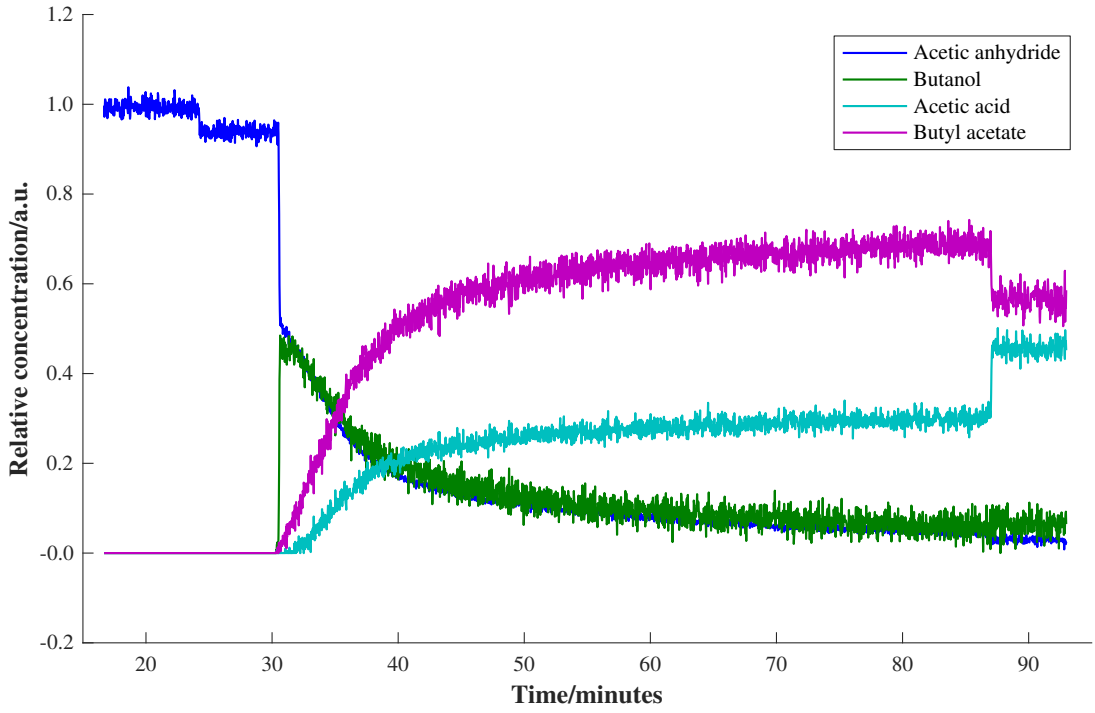

Figure 4.19 - Estimated concentration profiles (by GUIPRO) of components present in the reaction mixture spectra collected during esterification reaction at 40 °C with acetic acid dosed in approximately one hour after the addition of butanol (acquired using the Keit spectrometer). Product reference spectra collected at 70 °C.

4.3.4 Product Ratio Analysis

4.3.4.1 Mid-Infrared Spectroscopy

Mark et al.[28, 29] have demonstrated that in electromagnetic spectroscopy, the absorbance of a component within a mixture is dependent on its volume fraction rather than its weight or molar fraction, according to the Beer Lambert law. If acetic acid and butyl acetate were formed in a 1:1 molar ratio during the reaction, the volume ratio of the products would be 1:2.3 (assuming that no change in the volume ratio occurred upon mixing). This may be the explanation for the difference observed in the estimates of relative concentration, as the concentration profiles were calculated based on the contribution of each component to the absorbance. The volume ratio of butanol to acetic anhydride in a 1:1 molar mixture would be 1:1.03, which explains why little difference was observed between the concentration profiles of the reactants.

The estimated concentration profiles of the 1:1 reference mixtures of the products by volume (first five data points) and by molarity (last five data points), calculated using

GUIPRO, are shown in Figure 4.20. The measured spectra of the reference mixtures can be found in Appendix 4. There was a small amount of variation between each set of five repeat measurements (< 0.05 a.u.), but overall the concentration estimates of each repeat were similar.

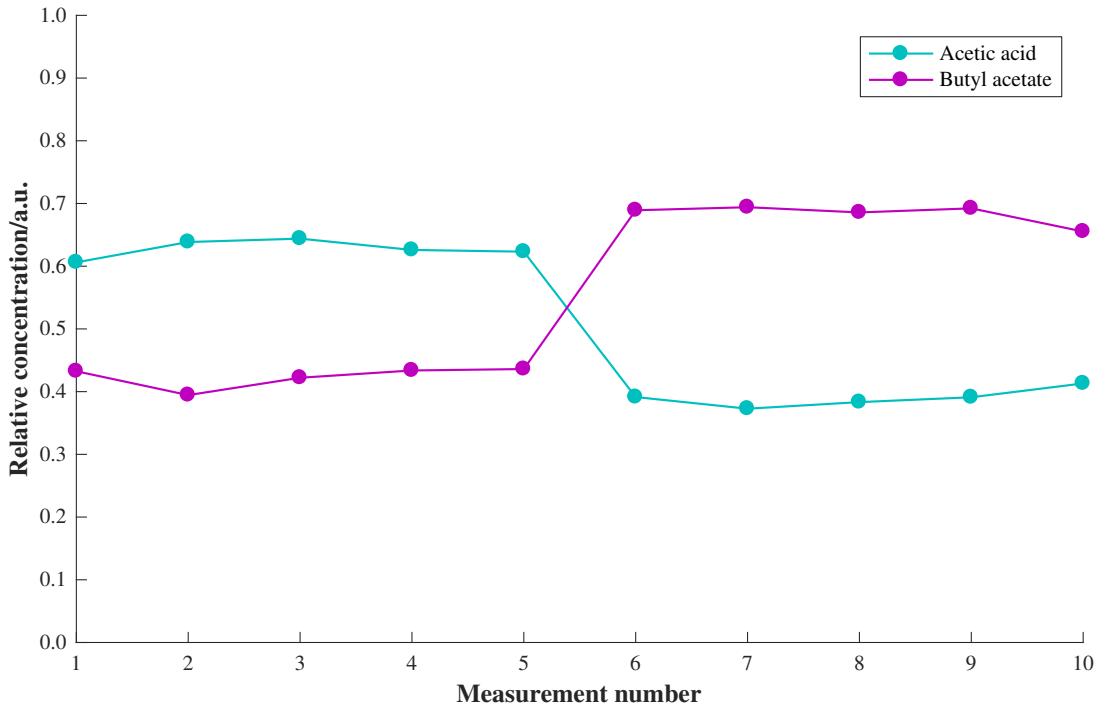

Figure 4.20 - Estimated concentration profiles (by GUIPRO) of 1:1 mixture by volume of acetic acid and butyl acetate (first five data points) and 1:1 molar mixture of acetic acid and butyl acetate (last five data points) measured using the Keit spectrometer.

The average estimated relative concentrations of acetic acid and butyl acetate in the 1:1 mixtures by molarity and volume are compared to those measured at the end of the reaction (taken from the last five data points) in Table 4.5. The 1:1 molar mixture far more closely resembled the estimated concentrations of the products at the end of the esterification reaction, with the relative concentration of butyl acetate significantly higher than that of acetic acid (0.68 ± 0.03 a.u. and 0.39 ± 0.02 a.u. respectively, compared to 0.62 ± 0.02 a.u. and 0.33 ± 0.01 respectively at the end of the reaction). This suggests that at the end of the reaction the products were present in a 1:1 molar ratio, as expected. The small difference observed (approximately 0.06 a.u.) could be due to the presence of the reactants and catalyst in the reaction mixture, as interaction of the products with these components may produce small alterations to the spectra.

Table 4.5 - Estimated relative concentrations by GUIPRO of acetic acid and butyl acetate present in spectra of 1:1 mixture by molarity, 1:1 mixture by volume and the last five spectra acquired during the esterification reaction at 40 °C before the addition of extra acetic acid, all acquired using the Keit spectrometer.

Mixture	Relative concentration of acetic acid/a.u., n = 5	Relative concentration of butyl acetate/a.u., n = 5
1:1 by molarity (1:2.3 by volume)	0.39 ± 0.02	0.68 ± 0.03
1:1 by volume (1:0.43 by molarity)	0.63 ± 0.02	0.42 ± 0.03
End of reaction	0.33 ± 0.01	0.62 ± 0.02

For the 1:1 mixture of the products by volume, the estimated relative concentration of butyl acetate was lower than that of acetic acid (0.42 ± 0.03 a.u. and 0.63 ± 0.02 a.u. respectively). If absorbance in MIR spectroscopy is dependent on volume fraction, the ratio of the estimated concentrations should be 1:1. The difference observed could be due to change in the volume fraction upon mixing the components. Alternatively it could have been caused by experimental error or by inability to fully resolve the components by GUIPRO. The corresponding estimated spectra are shown in Figure 4.21 and were similar to the estimates of the product spectra at the end of the esterification reaction (Figure 4.8 and Figure 4.17), although a slight difference (< 0.1 in absorbance) was observed between the estimated and reference acetic acid peaks at approximately 1300 cm^{-1} and 1700 cm^{-1}. The root mean square spectral residuals of the estimates were 0.287 and 0.305 for acetic acid and butyl acetate respectively, confirming that the difference between the estimated and reference spectra was relatively small.

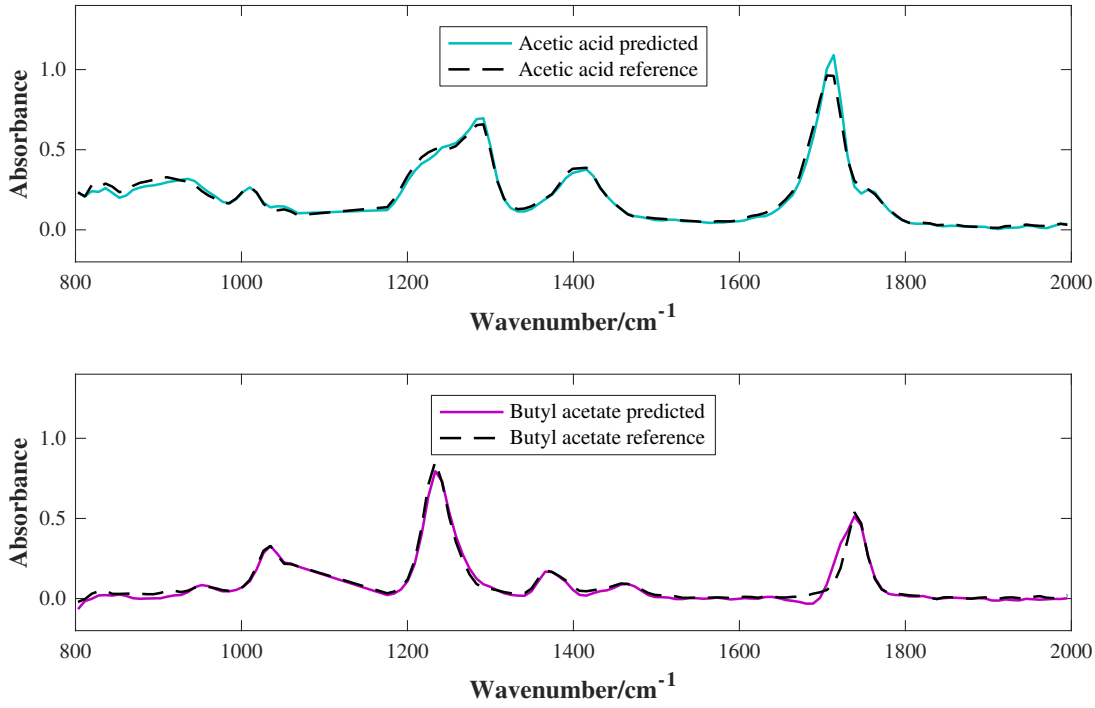

Figure 4.21 - Estimated pure spectra (by GUIPRO) of acetic acid and butyl acetate present in 1:1 mixtures by volume and molarity measured using the Keit spectrometer (solid lines), and reference pure component spectra measured using the Keit spectrometer (dashed lines).

4.3.4.2 Low-Field NMR Spectroscopy

To further assess the accuracy of prediction of the product concentrations by the Keit spectrometer, low-field NMR spectroscopy was used. The low-field ^{1}H NMR spectra of the samples extracted from the reaction vessel at 5 minutes, 30 minutes and 1 hour after the addition of butanol to the reaction mixture are shown in Figure 4.22. The MIR spectra collected during the course of the reaction and the concentration profiles and pure component spectra estimated by GUIPRO can be found in Appendix 4.

An assignment of the peaks present in the NMR spectra is displayed in Table 4.6. The singlet peaks arising from the acetyl groups of acetic acid and butyl acetate increased in intensity during the course of the reaction, and the singlet peak arising from the acetyl group of acetic anhydride decreased in intensity. The peak at just below 6 ppm after 5 minutes, just above 8 ppm after 30 minutes and just below 9 ppm after one hour arises from the OH group of acetic acid, and shifted due to the decrease in pH of the mixture as the reaction progressed.

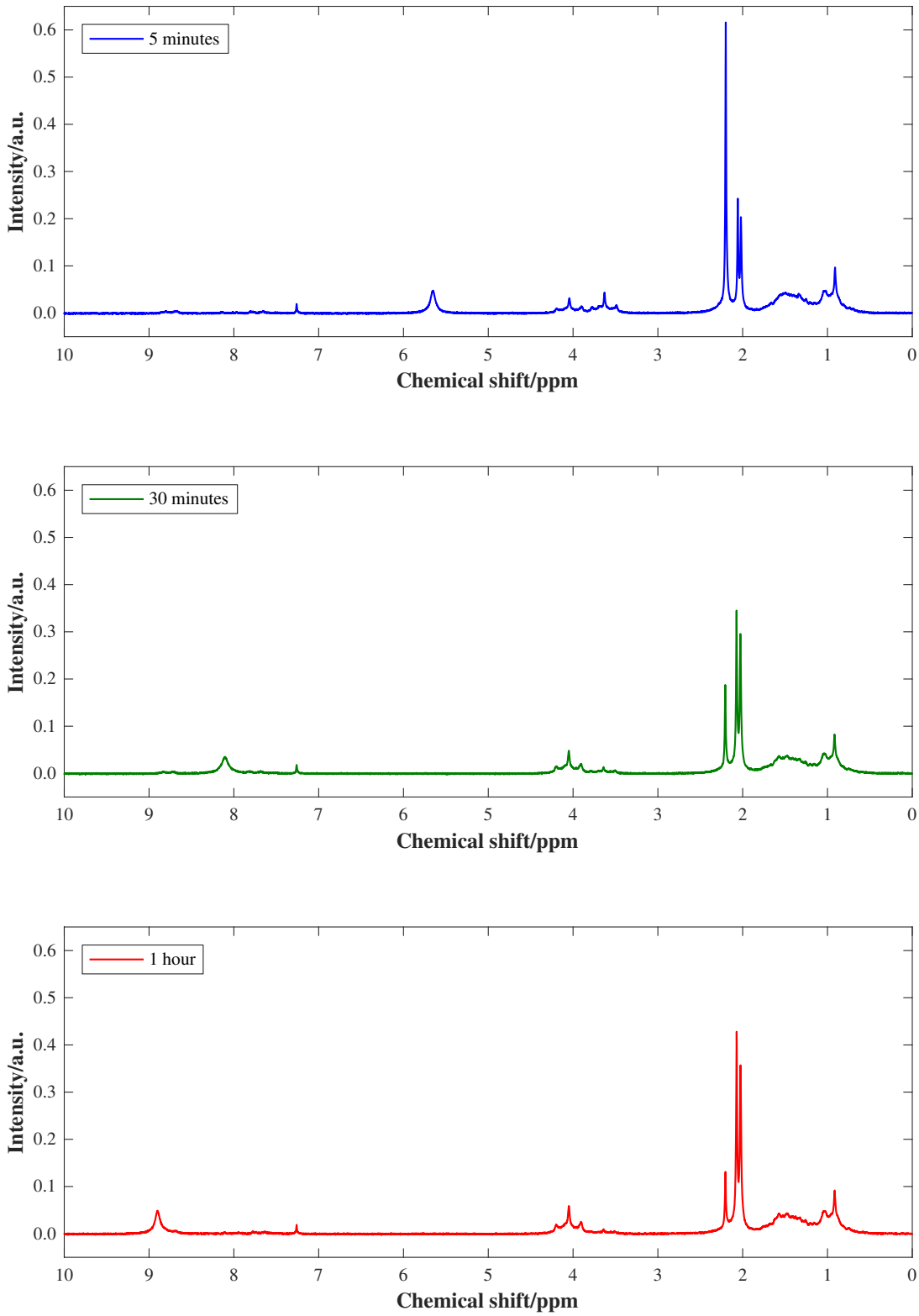

Figure 4.22 - Low-field ^{1}H NMR spectra of esterification reaction mixture samples in chloroform, extracted at 5 minutes, 30 minutes and 1 hour after the addition of butanol.

Table 4.6 - Assignment of the main peaks in low-field ^{1}H NMR spectra of samples extracted from esterification reaction mixture.

Peak position/ppm	Multiplicity	Peak assignment
0.5 – 2.0	Overlapping multiplets	Butyl groups of butanol and butyl acetate
2.03	Singlet	Acetyl group of butyl acetate
2.07	Singlet	Acetyl group of acetic acid
2.20	Singlet	Acetyl group of acetic anhydride
3.5 – 4.3	Overlapping multiplets	Butyl groups of butanol and butyl acetate
5.65, 8.10 or 8.90	Singlet	OH group of acetic acid
7.26	Singlet	Chloroform

The low-field ^{1}H NMR spectrum of the mixture expected at the end of the reaction (containing 45 % by molarity of each product and 5 % of each reactant) is shown in Figure 4.23. This spectrum approximately resembled the spectrum of the reaction mixture collected at one hour, confirming that the products formed in a 1:1 ratio during the reaction. The only difference between the two spectra was that the OH peak appeared at lower chemical shift in the expected mixture (just below 8 ppm compared to just below 9 ppm), and this can be attributed to a difference in pH between the two mixtures due to the absence of pyridine in the reference mixture.

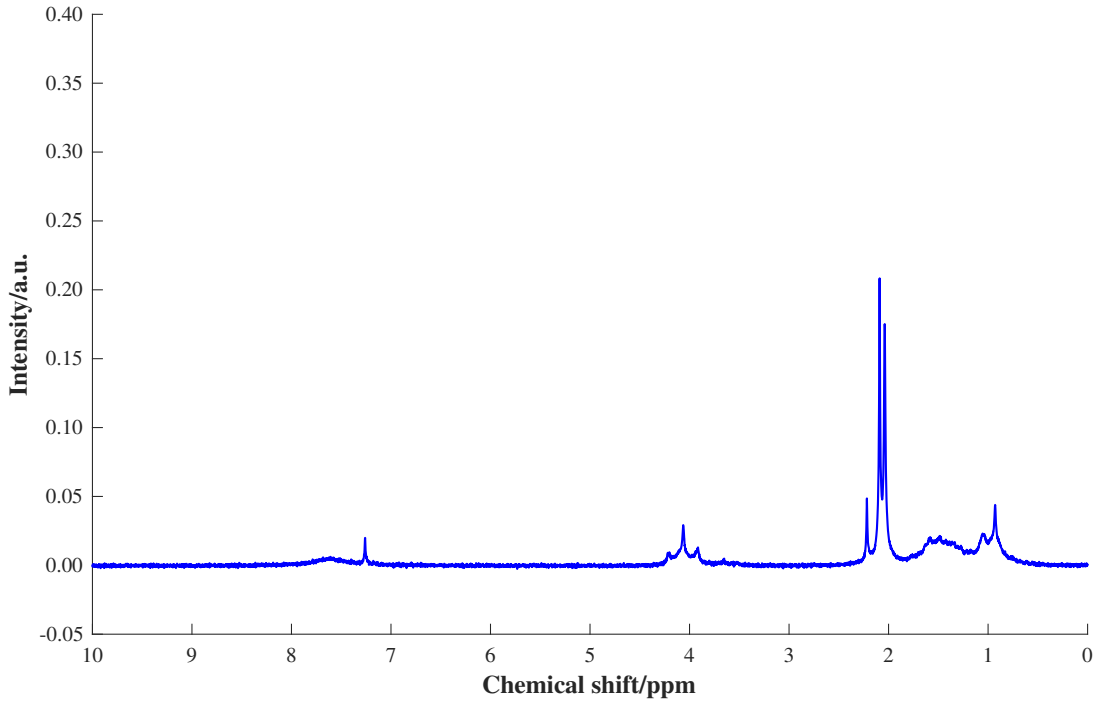

Figure 4.23 - Low-field ^{1}H NMR spectra of expected mixture at end of esterification reaction (45 % acetic acid, 45 % butyl acetate, 5 % acetic anhydride and 5 % butan-1-ol by molarity, in chloroform).

The low-field ^{1}H NMR spectrum of the mixture containing 60 % butyl acetate, 30 % acetic acid and 5 % of each reactant (by molarity) is shown in Figure 4.24. This is the approximate composition which would be expected if the estimates of relative concentration obtained using the Keit spectrometer represented the molar ratios of the components present at the end of the esterification reaction. The acetyl singlet peak at lowest chemical shift (butyl acetate) now has a higher intensity than the adjacent acetyl singlet (acetic acid). In the spectrum of the mixture at the end of the esterification reaction, the acetic acid singlet peak had a higher intensity than the butyl acetate singlet. In addition, the chemical shift of the OH peak in Figure 4.24 was significantly lower than at the end of the reaction (just below 7 ppm compared to just below 9 ppm). These results confirm that butyl acetate and acetic acid formed in a 1:1 molar ratio rather than a 2:1 molar ratio, and that the difference in concentration observed in the GUIPRO estimates can be attributed to absorbance being dependent on the volume ratio of the components present in the MIR spectra. Therefore the Keit spectrometer was able to provide accurate predictions of concentration during the esterification reaction.

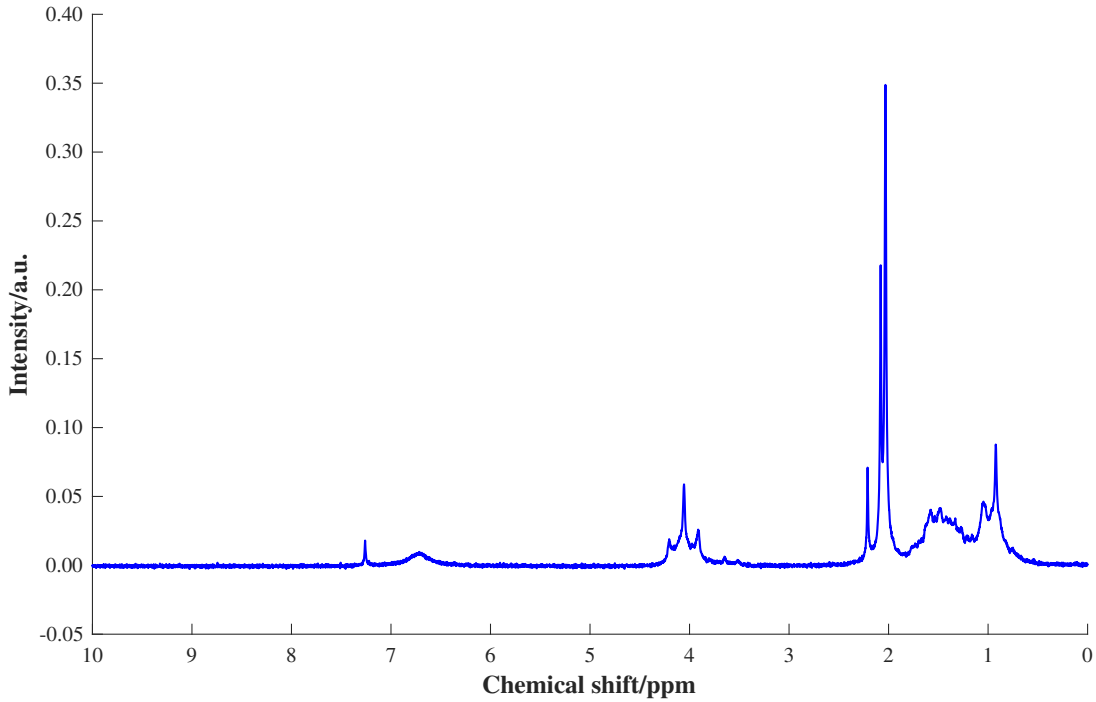

Figure 4.24 - Low-field ^{1}H NMR spectra of 60 % butyl acetate, 30 % acetic acid, 5 % acetic anhydride and 5 % butan-1-ol (by molarity) in chloroform.

4.3.5 Esterification Reactions at 50 °C and 20 °C

To assess the effectiveness of the Keit spectrometer at detecting differences in reaction rate, the esterification reaction was repeated at 50 °C and 20 °C. The estimated concentration profiles of the reactions carried out at 50 °C and 20 °C are shown in Figure 4.25 and Figure 4.26 respectively. The spectra collected during the reactions can be found in Appendix 4. When the reaction was carried out at 50 °C, an increase in the rate of disappearance of the reactants and the rate of formation of the products was observed (with the majority of the reaction complete within approximately 10 minutes, rather than approximately 15 minutes when the temperature was 40 °C). At 20 °C, a significant decrease in the rate of reaction was observed and the rate of formation of the products/disappearance of the reactants was much less rapid. The final concentration estimates of the reactants were also higher, particularly butanol (the estimated relative concentration of which was around 0.1 a.u. higher than at 40 °C), indicating that the reaction had not fully progressed to completion after an hour.

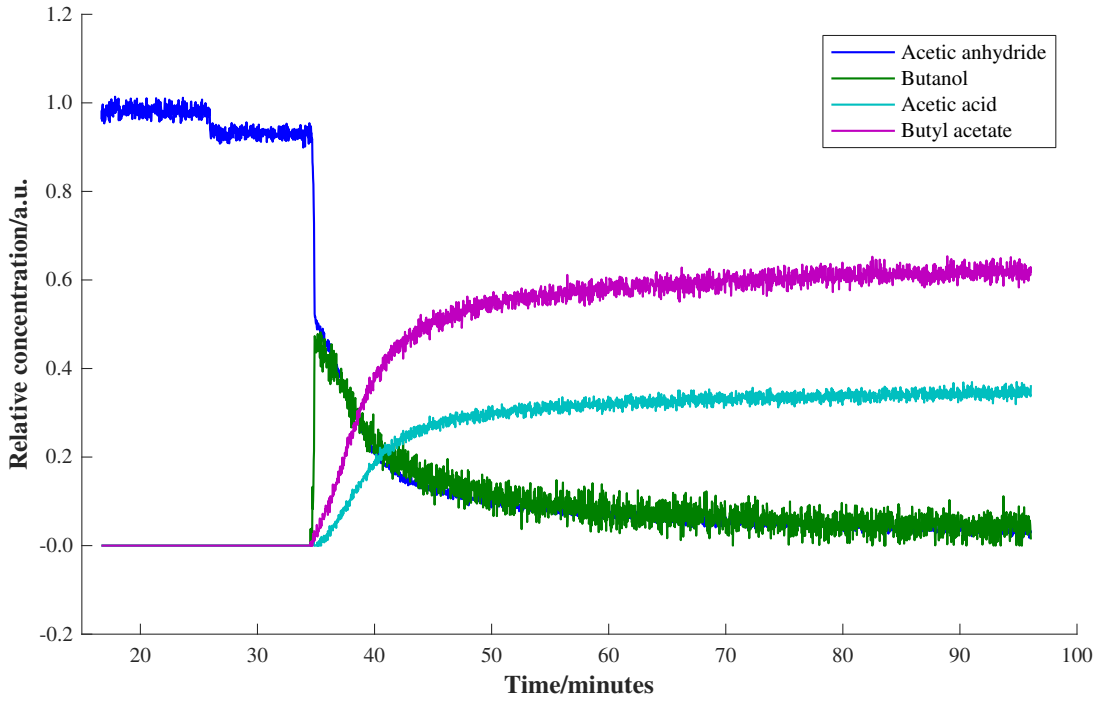

Figure 4.25 - Estimated concentration profiles (by GUIPRO) of components present in the reaction mixture spectra collected during esterification reaction at 50 °C using the Keit spectrometer.

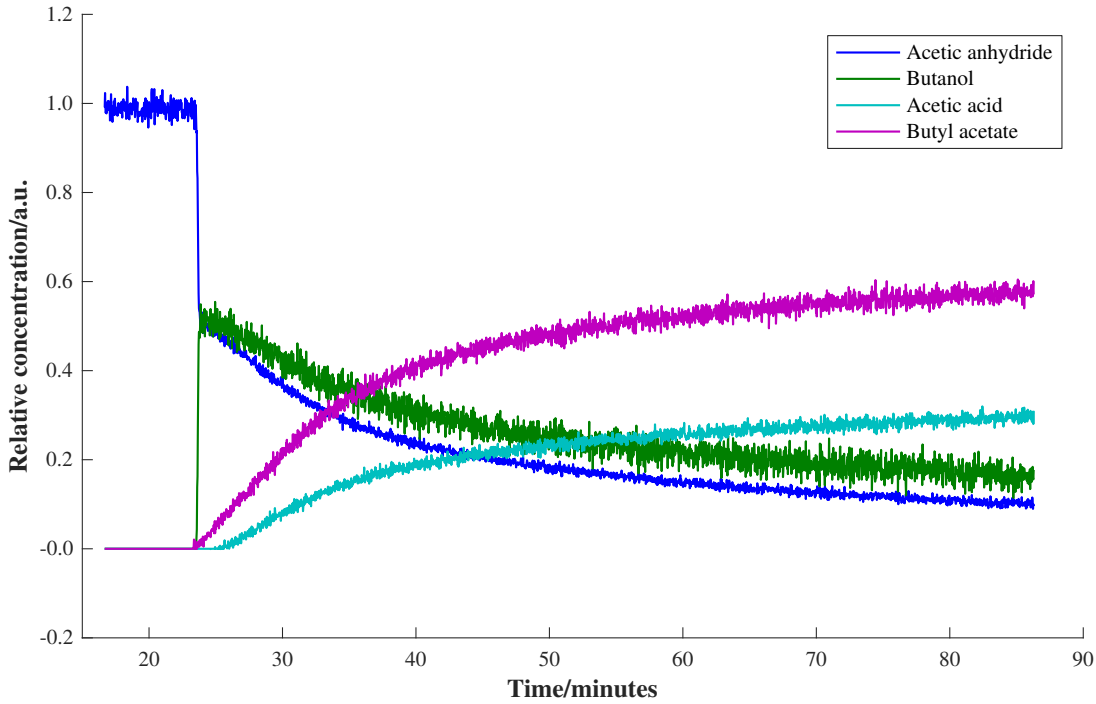

Figure 4.26 - Estimated concentration profiles (by GUIPRO) of components present in the reaction mixture spectra collected during esterification reaction at 20 °C using the Keit spectrometer.

The root mean square spectral residuals are displayed in Table 4.7, with the values obtained for the reaction at 40 °C in which extra acetic acid was added shown for comparison. The estimated spectra can be found in Appendix 4. Similar values were obtained for the reactions performed at 40 °C and 50 °C, but the values were slightly larger for the reaction performed at 20 °C (0.234 on average, compared to 0.180 and 0.160). This indicates that small changes in the spectra occurred due to the difference in temperature (as the reference spectra were acquired at 40 °C), and that GUIPRO was able to estimate these changes.

Table 4.7 - Root mean square spectral residual values of estimated pure spectra (by GUIPRO) of components present in esterification reaction mixture spectra acquired at 20 °C, 40 °C and 50 °C (with reference spectra acquired at 40 °C) using the Keit spectrometer.

Component	Root mean square spectral residual		
	20 °C	**40 °C**	**50 °C**
Acetic anhydride	0.136	0.077	0.066
Butanol	0.251	0.135	0.100
Acetic acid	0.177	0.180	0.167
Butyl acetate	0.371	0.326	0.305
Mean value	0.234	0.180	0.160

The average rates of formation of butyl acetate over the first five minutes of the reactions performed at 20 °C, 40 °C and 50 °C are shown in Table 4.8. At 40 °C, the average rate of formation of butyl acetate was 0.062 a.u./min, and at 50 °C the average rate increased by 0.013 a.u./min. The average rate of formation of butyl acetate was significantly lower at 20 °C (0.034 a.u.); nearly half the average rate calculated at 40 °C and less than half the average rate calculated at 50 °C. This corresponds to the differences observed in the concentration profiles of the reactions performed at different temperatures and is as expected, since increasing the temperature of the vessel should increase the rate of the reaction. These results demonstrate the effectiveness of the Keit spectrometer at measuring concentration changes throughout the course of a reaction and detecting differences in reaction rate. The Keit spectrometer is therefore suitable for *in situ* reaction monitoring of liquid processes.

Table 4.8 - Average rate of butyl acetate formation over first five minutes of the esterification reactions performed at 20 °C, 40 °C and 50 °C, based on the relative concentration of butyl acetate estimated by GUIPRO after 5 minutes (average of 5 consecutive data points).

Reaction temperature/°C	Relative butyl acetate concentration after 5 min/a.u.	Average reaction rate/(a.u./min)
20	0.173 ± 0.019	0.034
40	0.309 ± 0.017	0.062
50	0.375 ± 0.025	0.075

4.4 Conclusions

The suitability of the Keit spectrometer for *in situ* reaction monitoring has been demonstrated. The concentration changes occurring during the course of the esterification reaction could be measured accurately, and were in agreement with those obtained using low-field NMR spectroscopy. It was also possible to detect differences in reaction rate due to changes in the temperature of the reaction vessel. These results confirm the ability of the Keit spectrometer to effectively monitor liquid processes *in situ*, providing new opportunities for process monitoring in the mid-infrared region.

Multivariate curve resolution has been shown to be suitable for decomposition of the spectra collected during the course of the esterification reaction into their pure component contributions. Of the three MCR toolboxes used, GUIPRO was found to be the most effective due to the ability to apply penalty functions to the constraints. Although it was also possible to apply penalty functions using PLS Toolbox, this produced poorer results than when the reference spectra were applied as hard equality constraints. GUIPRO would therefore be recommended for the decomposition of MIR reaction mixture spectra in future. The choice of sensitivity value and convergence tolerance also affected the results obtained, so these parameters are important to consider.

4.5 References

1. A. W. Owen, E. A. J. McAulay, A. Nordon, D. Littlejohn, T. P. Lynch, J. S. Lancaster and R. G. Wright, *Anal. Chim. Acta*, 2014, **849**, 12–18.

2. S. Richards, R. Miller and P. Gemperline, *Appl. Spectrosc.*, 2008, **62**, 197–206.
3. G. Puxty, Y. M. Neuhold, M. Jecklin, M. Ehly, P. Gemperline, A. Nordon, D. Littlejohn, J. K. Basford, M. De Cecco and K. Hungerbuhler, *Chem. Eng. Sci.*, 2008, **63**, 4800–4809.
4. M. Maeder, Y. M. Neuhold, G. Puxty and P. Gemperline, *Chemom. Intell. Lab. Syst.*, 2006, **82**, 75–82.
5. W. Stevens and A. van Es, *Recl. Trav. Chim. Pays-Bas*, 1964, **83**, 1287.
6. M. Salavati-Niasari, T. Khosousi and S. Hydarzadeh, *J. Mol. Catal. A: Chem.*, 2005, **235**, 150–153.
7. G. Richner, Y. M. Neuhold and K. Hungerbuhler, *Org. Process Res. Dev.*, 2010, **14**, 524–536.
8. G. Puxty, U. Fischer, M. Jecklin and K. Hungerbuhler, *Chimia*, 2006, **60**, 605–610.
9. J. Diewok, M. J. Ayora-Canada and B. Lendl, *Anal. Chem.*, 2002, **74**, 4944–4954.
10. S. Richards, M. Ropic, D. Blackmond and A. Walmsley, *Anal. Chim. Acta*, 2004, **519**, 1–9.
11. A. Dominguez-Vidal, M. P. Saenz-Navajas, M. J. Ayora-Canada and B. Lendl, *Anal. Chem.*, 2006, **78**, 3257–3264.
12. M. Blanco, M. Castillo, R. Beneyto and M. Porcel, *Spectrosc. Lett.*, 2005, **38**, 825–837.
13. M. Garrido, M. S. Larrechi and F. X. Rius, *Anal. Chim. Acta*, 2007, **585**, 277–285.
14. M. Blanco, A. C. Peinado and J. Mas, *Anal. Chim. Acta*, 2006, **556**, 364–373.
15. M. Lopez-Pastor, A. Dominguez-Vidal, M. J. Ayora-Canada, M. Valcarcel and B. Lendl, *J. Mol. Struct.*, 2006, **799**, 146–152.
16. B. Muik, B. Lendl, A. Molina-Diaz, M. Valcarcel and M. J. Ayora-Canada, *Anal. Chim. Acta*, 2007, **593**, 54–67.
17. E. Bezemer and S. Rutan, *Anal. Chim. Acta*, 2002, **459**, 277–289.
18. J. Jaumot, V. Marchan, R. Gargallo, A. Grandas and R. Tauler, *Anal. Chem.*, 2004, **76**, 7094–7101.

19. J. M. Amigo, A. de Juan, J. Coello and S. Maspoch, *Anal. Chim. Acta*, 2006, **567**, 245–254.
20. E. Bezemer and S. C. Rutan, *Chemom. Intell. Lab. Syst.*, 2006, **81**, 82–93.
21. W. Kessler and R. W. Kessler, *Anal. Bioanal. Chem.*, 2006, **384**, 1087–1095.
22. M. Bosco, M. P. Callao and M. S. Larrechi, *Talanta*, 2007, **72**, 800–807.
23. S. Navea, A. de Juan and R. Tauler, *Anal. Chem.*, 2002, **74**, 6031–6039.
24. Multivariate Curve Resolution Homepage, https://mcrals.wordpress.com, (accessed 15th September, 2017).
25. J. Jaumot, A. de Juan and R. Tauler, *Chemom. Intell. Lab. Syst.*, 2015, **140**, 1–12.
26. P. J. Gemperline and E. Cash, *Anal. Chem.*, 2003, **75**, 4236–4243.
27. J. Jaumot, P. J. Gemperline and A. Stang, *J. Chemom.*, 2005, **19**, 97–106.
28. H. Mark, R. Rubinovitz, D. Heaps, P. Gemperline, D. Dahm and K. Dahm, *Appl. Spectrosc.*, 2010, **64**, 995–1006.
29. H. Mark and J. Workman, *Spectroscopy*, 2014, **29**, 24–37.
30. E. R. Malinowski, *J. Chemom.*, 1996, **10**, 273–279.
31. P. J. Gemperline, *J. Chem. Inf. Comput. Sci.*, 1984, **24**, 206–212.
32. J. Jaumot, R. Gargallo, A. de Juan and R. Tauler, *Chemom. Intell. Lab. Syst.*, 2005, **76**, 101–110.
33. G. Socrates, *Infrared and Raman Characteristic Group Frequencies*, John Wiley & Sons Ltd., Chichester, UK, 3rd edn., 2001.
34. D. L. Pavia, G. M. Lampman and G. S. Kriz, *Introduction to Spectroscopy*, Thomson Learning, Bellingham, Washington, USA, 3rd edn., 2001.

5 Alignment of Low-Field NMR Spectra

5.1 Introduction

The commercial availability of benchtop NMR spectrometers operating in the frequency domain at low field provides a promising solution to some of the limitations that have prevented the widespread use of NMR spectroscopy in process monitoring, e.g. the size and cost of high-field instruments (as discussed in Chapter 1). However one issue with NMR spectroscopy is that the shifting of peaks occurs to a much greater extent than in optical spectroscopy. Peak shifts can arise due to a variety of factors, such as interaction of components and changes in pH or temperature.[1] Deviations from the optimum operating conditions of the instrument can also cause peaks to shift.[2] The effect of peak shifts on the spectra is likely to be more detrimental at low field than at high field due to the smaller chemical shift dispersion.

The shifting of peaks of the same analyte between spectra can produce problems when chemometrics is performed.[1, 3] It can reduce the effectiveness of calibration models, e.g. PLS, as the algorithm may not recognise shifted peaks as the same analyte. This will also prevent multivariate curve resolution from working. In calibration transfer, peak movement can cause difficulties in calculating the transfer function, and application of the transfer function to the test spectra may not be successful if peaks have shifted.

Bucketing (or binning) is a common solution to the problem of peak shift. It involves reduction of the spectra by dividing them into regions called buckets, within which the data points are combined. The bucketed spectra therefore consist of fewer data points than the original spectra, and the variation between the spectra is reduced. This also has the advantage of decreasing the size of the dataset, making it easier to handle computationally.[4, 5] In conventional bucketing, each bucket is the same size, therefore some peaks may be split across different buckets.[4] An optimised bucketing algorithm has been demonstrated by Sousa et al.[4] as a solution to this issue. This algorithm allows variation in the boundaries of buckets by the inclusion of a slackness parameter. The slackness defines the amount of movement allowed by the bucket boundary, as a percentage of the bucket width. Local minima are selected as the boundaries between buckets, using user-defined bucket size and slackness values, and the resulting buckets

vary in size. However if one of the local minima occurs within a multiplet peak, it may still be possible for peaks to be split across different buckets. A drawback of bucketing is that the fine structure of the peaks is lost due to the inclusion of fewer data points. In addition, it can only eliminate peak shifts which are small enough to occur within the spectral range of a bucket, so when large peak shifts are present then large bucket sizes are necessary and more of the peak structure will be lost.

An alternative solution to the issue of peak shift is to perform alignment of the peaks in the spectra. A variety of methods have been demonstrated for alignment of peaks in high-field NMR spectra, but there is no information in the literature on their effectiveness at low field. In this chapter, a selection of alignment methods used at high field have been evaluated for the alignment of peaks in low-field NMR spectra. Two different sets of spectra were used, one exhibiting little peak movement or overlap and the other exhibiting a large amount of peak movement and overlap. The performance of the alignment methods was assessed in each case. The alignment methods evaluated are described in the following subsections, and were chosen because the algorithms are publicly available and they have been shown to be effective at high field. Bucketing was also performed on each set of spectra, as a comparison.

5.1.1 Description of Alignment Methods

5.1.1.1 Correlation Optimised Warping

Correlation optimised warping (COW)[6] was originally developed for the alignment of chromatographic peaks. It separates spectra into segments of equal length, and uses piecewise linear stretching and compression (warping) of the segments to align peaks to those of a target spectrum. The peaks are warped by linear interpolation in the x direction only and the algorithm aims to match peak shape. The sections are prevented from overlapping and their order is retained. The optimum solution is determined through the use of dynamic programming, a programming method which calculates the global optimum by examination of all possible solutions one by one. Correlation coefficients between the warped and target spectra are calculated for each segment, and the combination of warpings which produces the largest total correlation coefficient is selected as the optimum. The segment length, slack (the maximum amount of warping allowed) and target spectrum can be chosen manually by the user.

Although COW was designed for the alignment of chromatographic peaks, it has also been demonstrated for the alignment of peaks in high-field NMR spectra.[7-9] In some cases it was necessary to split the spectra into regions before COW was performed in order for it to work effectively.

5.1.1.2 Peak Alignment by FFT and Recursive Alignment by FFT

Peak alignment by FFT (PAFFT) and recursive alignment by FFT (RAFFT)[10] both use fast Fourier transform (FFT) cross-correlation to optimise the alignment of spectral segments to those of a reference spectrum. They were developed for the alignment of chromatographic and spectral data (demonstrated on gas chromatography and mass spectrometry datasets). In PAFFT, the spectra are split into segments of equal size, which are then aligned. In RAFFT the whole spectrum is first aligned, then it is divided into two segments which are aligned again. This process is repeated until a minimum segment size is reached. The minimum segment size is determined automatically in RAFFT, which reduces the number of input parameters required, and the initial global alignment of the spectra reduces the extent of local alignment necessary. In both methods, the spectra are aligned by shifting rather than warping and the segments are treated independently. The absence of warping eliminates peak distortion, however insertion/deletion of data points at the segment boundaries is necessary and can produce artefacts in the spectra.

The maximum shift allowed for each segment can be defined in both algorithms, and for PAFFT, the minimum size of each segment must also be defined. In RAFFT a "lookahead" parameter can be applied, which allows the algorithm to "look ahead" a certain number of iterations and check for local misalignments after the global optimum has been determined. The use of PAFFT and RAFFT has been demonstrated for the alignment of high-field NMR spectra. These methods were shown to be faster than COW (as FFT is faster than dynamic programming) and produced comparable results, with RAFFT performing best.[11]

5.1.1.3 Recursive Segment-Wise Peak Alignment

Recursive segment-wise peak alignment (RSPA)[12] utilises a recursive algorithm to align segments by FFT, first globally then locally, like RAFFT. It differs to RAFFT

through the use of a segmentation method designed to keep multiplets within the same segment and align them together instead of as separate peaks. The sample with peaks most closely matching the other spectra can be chosen as the reference by the algorithm, through the calculation of a "closeness index" based on the correlation coefficients of the spectra. The segments are again treated independently. The parameters which can be altered are the peak height and J-coupling constant thresholds during the segmentation step, the minimal segment size and validation of segment alignment (measured as the correlation between scaled reference and test segments) during the recursive alignment step, and the maximal shift size and alignment acceptance criterion (to prevent local misalignment).

RSPA has been demonstrated for the alignment of high-field NMR spectra of metabolites.[12-14] The performance of RSPA was compared to that of COW and PAFFT, but not RAFFT. RSPA was found to align smaller peaks more effectively than PAFFT due to the local recursion step. The advantages of RSPA over COW were that the shapes of peaks were preserved (due to the use of shifting instead of warping) and that the RSPA algorithm was computationally faster.

5.1.1.4 Interval Correlation Shifting

Interval correlation shifting (*i*coshift) was designed for the alignment of 1D NMR spectra.[3] The spectra are split into segments, which are independently shifted in order to maximise the cross-correlation to a target spectrum using FFT, similar to PAFFT and RAFFT. However the advantage of *i*coshift is that it is possible to customise the intervals of the segments so that they do not necessarily have to be the same length. This can help to avoid the occurrence of artefacts. Like most methods, it is not possible to change the order of the peaks. The method is rapid, as all spectra are aligned simultaneously. The target spectrum, number/length of intervals and maximum shift correction can be specified. It is also possible to calculate the target spectrum from the inputted spectra in a number of ways (e.g. averaging the spectra or selection of the corresponding spectrum having the maximum features for each segment), apply the algorithm to the whole spectrum with no intervals, shift the spectra according to reference signals, choose between using the previous point or "NaN" to fill the gaps

in the spectra, and carry out a co-shift preprocessing step (similar to *i*coshift but the whole spectrum is aligned globally rather than splitting into intervals).

There are a number of examples of *i*coshift being used to align peaks in high-field NMR spectra,[15-19] and a couple of examples of it being applied to low-field NMR spectra.[20, 21] However the success of its performance at low field has not been discussed. At high field, *i*coshift has been found to be comparable to PAFFT and RAFFT,[11] and more effective than COW for the alignment of metabolomic spectra.[3] It has also been compared to RSPA for the alignment of metabolomic spectra[3, 14] and was more effective in some cases, but less effective in other cases. In addition, the *i*coshift algorithm was computationally faster than COW and RSPA.[3]

5.1.1.5 Progressive Consensus Alignment of NMR Spectra

In progressive consensus alignment of NMR spectra (PCANS),[22] peak profiles (consisting of the heights, widths and chemical shifts of peaks) are created for each spectrum. Similar pairs of peak profiles are first identified by calculation of the correlation, and naive alignment of the peaks in these profiles is then performed. The naive alignment step involves the alignment of corresponding peaks in each pair of profiles (those in which all peak attributes exhibit ≥ 90 % similarity). Crossover of peaks is not allowed and the maximum movement of peaks is limited to a user defined chemical shift value. The unaligned regions of the resulting spectra are then aligned using dynamic programming recursion, which involves the assignment of similarity scores for each alignment based on the height, width and chemical shift position for each peak, with penalties inflicted for unaligned peaks. This produces a consensus spectrum, and pairs of consensus spectra are aligned as before until a final consensus spectrum is obtained. A number of different parameters can be altered, including maximum expected chemical shift, minimum separation, number of points in peaks, number of neighbouring points, percentage of neighbours kept, gap penalty, boundary penalty, minimum similarity for match, minimum similarity for naive alignment and zero fill value. The final consensus spectrum is used to align the original spectra, and eliminates the need for a reference. PCANS has been demonstrated for the alignment of small peak shifts in high-field NMR spectra of metabolites.[22]

5.2 Experimental

5.2.1 Solvent Mixture Analysis

5.2.1.1 Toluene, Octene and Dibutyl Ether Mixtures

To produce a set of spectra on which to perform a comparison of the alignment methods, sixteen calibration samples and six test samples were prepared. The samples contained varying concentrations of toluene (≥ 99.3 %, Sigma Aldrich, Steinheim, Germany), octene (≥ 98 %, Sigma Aldrich, Steinheim, Germany) and dibutyl ether (≥ 99.0 %, Merck KGaA, Darmstadt, Germany) in units of % w/w, as detailed in Table 5.1. A ternary diagram of the solvent concentrations is displayed in Figure 5.1 and is the same as for the solvent mixture analysis performed by MIR spectroscopy (section 3.2.3), with toluene in place of acetone, octene in place of ethanol, and dibutyl ether in place of ethyl acetate. These mixtures were chosen as each component has at least one clearly resolvable peak, and a small amount of peak shift was present between the samples (< 0.2 ppm).

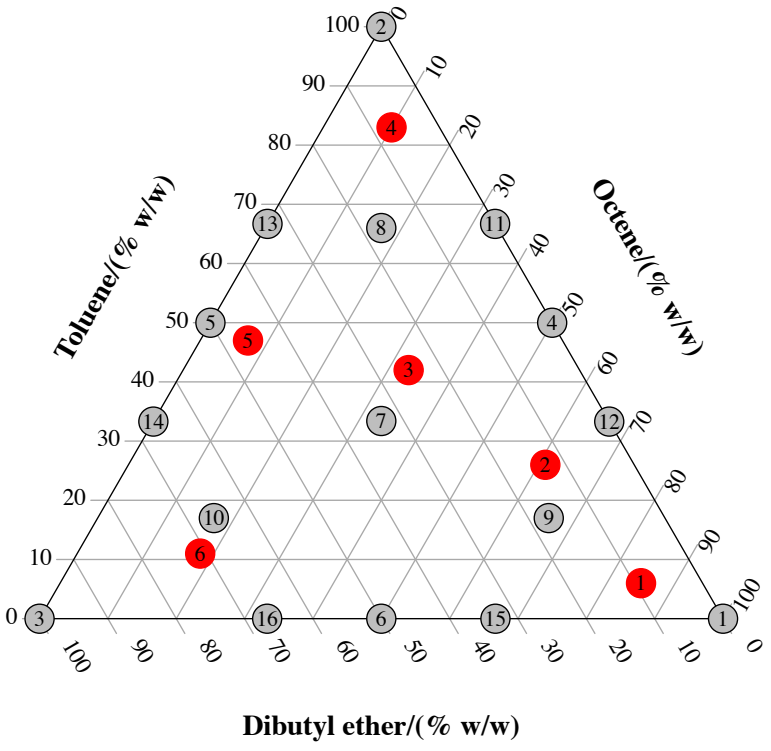

Figure 5.1 - Concentrations (in units of % w/w) of solvents in ternary mixtures, calibration samples shown in grey and test samples shown in red.

Table 5.1 - Concentrations of toluene, octene and dibutyl ether present in mixtures.

Sample	Concentration/(% w/w)		
	Toluene	Octene	Dibutyl ether
Calibration sample 1	0.0	100.0	0.0
Calibration sample 2	100.0	0.0	0.0
Calibration sample 3	0.0	0.0	100.0
Calibration sample 4	50.2	49.8	0.0
Calibration sample 5	50.1	0.0	49.9
Calibration sample 6	0.0	50.1	49.9
Calibration sample 7	33.0	33.4	33.6
Calibration sample 8	65.7	17.0	17.3
Calibration sample 9	17.7	64.5	17.8
Calibration sample 10	18.3	17.4	64.3
Calibration sample 11	66.7	33.3	0.0
Calibration sample 12	33.4	66.6	0.0
Calibration sample 13	66.8	0.0	33.2
Calibration sample 14	34.0	0.0	66.0
Calibration sample 15	0.0	66.7	33.3
Calibration sample 16	0.0	34.2	65.8
Test sample 1	6.0	83.6	10.4
Test sample 2	26.9	60.0	13.1
Test sample 3	40.4	34.1	25.5
Test sample 4	81.6	11.0	7.5
Test sample 5	46.3	7.2	46.6
Test sample 6	11.2	18.7	70.1

Each mixture was prepared to a total mass of 5 g, and 150 µl of TMS (≥ 99.5 %, Sigma Aldrich, Steinheim, Germany) was then added as an internal reference. The internal reference was added in order to provide a peak of known chemical shift to which the spectra could be globally aligned and a singlet reference peak for reference deconvolution (which will be discussed in Chapter 6). After the addition of TMS,

0.6 mL of each sample was added to an NMR tube for analysis by low-field ^{1}H NMR spectroscopy.

A Magritek Spinsolve Carbon NMR spectrometer with a proton channel operating at 43 MHz was used throughout this work, operated via Spinsolve Expert software. The receiver gain was set to 31 dB and the dwell time was set to 200 µs. An acquisition delay of 20 µs, an acquisition time of 3.2768 s, a bandwidth of 5 kHz and a 90° pulse duration of 11.1 µs were used. Each measurement was a single scan consisting of 16,384 data points, and was zero filled to 65,536 data points in order to improve the digital resolution of the spectra. Automatic phase correction was performed by the software, consisting of an unoptimised first order correction which is automatically applied to all spectra and a zero order correction optimised for each spectrum. Shimming was performed using a standard containing 90 % D_2O and 10 % H_2O, supplied by Magritek. The frequency of the transmitter and receiver were set to the frequency of the peak in the spectrum of the D_2O/H_2O sample used for shimming.

In order to minimise the effect of sample temperature on the instrument, each tube was heated in a water bath at approximately 30 °C for two minutes before insertion into the NMR spectrometer. This should allow the sample to reach approximately the temperature of the magnet (28.5 °C) by the time the tube was removed from the water bath, dried and taken to the instrument for analysis (as measured using a thermocouple inserted into an NMR tube containing an example mixture). Between analyses, the tubes were stored in a freezer at approximately –20 °C to prevent evaporation of the solvents. Before analysis, each sample was left in the instrument for five minutes to ensure that it had reached the temperature of the magnet and to allow time for polarisation to occur. This will be discussed in more detail in Chapter 6. Each sample was analysed three times and the measurements were made in a random order to avoid the effect of systematic instrumental changes over time.

5.2.1.2 Toluene, Ethanol and Ethyl Acetate Mixtures

An additional set of ternary mixtures, exhibiting greater peak shift than the toluene, octene and dibutyl ether mixtures (up to 1.5 ppm) were then analysed in order to further evaluate the effectiveness of the alignment methods. These mixtures contained varying concentrations of toluene (≥ 99.3 %, Sigma Aldrich, Steinheim, Germany), ethanol

(99.9 %, VWR, Fontenay-sous-Bois, France) and ethyl acetate (≥ 99.5 %, Sigma Aldrich, Steinheim, Germany), as detailed in Table 5.2.

Table 5.2 - Concentrations of toluene, ethanol and ethyl acetate present in solvent mixtures.

Sample	Concentration/(% w/w)		
	Toluene	Ethanol	Ethyl acetate
Calibration sample 1	0.0	100.0	0.0
Calibration sample 2	100.0	0.0	0.0
Calibration sample 3	0.0	0.0	100.0
Calibration sample 4	50.2	49.8	0.0
Calibration sample 5	50.0	0.0	50.0
Calibration sample 6	0.0	50.0	50.0
Calibration sample 7	33.3	33.1	33.7
Calibration sample 8	64.4	17.8	17.9
Calibration sample 9	17.3	65.7	17.0
Calibration sample 10	17.3	16.9	65.7
Calibration sample 11	66.7	33.3	0.0
Calibration sample 12	33.7	66.3	0.0
Calibration sample 13	66.6	0.0	33.4
Calibration sample 14	33.4	0.0	66.6
Calibration sample 15	0.0	66.3	33.7
Calibration sample 16	0.0	33.7	66.3
Test sample 1	6.6	84.5	9.0
Test sample 2	26.1	60.6	13.4
Test sample 3	41.9	33.2	24.9
Test sample 4	82.3	10.4	7.4
Test sample 5	47.0	7.2	45.8
Test sample 6	11.2	18.2	70.6

The compositions of the mixtures can be described by the ternary diagram in Figure 5.1, with ethanol in place of octene and ethyl acetate in place of dibutyl ether. Each sample was prepared to a mass of 10 g in total, and 300 µl of TMS (≥ 99.5 %, Sigma

Aldrich, Steinheim, Germany) was added. Analysis was performed as for the toluene, octene and dibutyl ether mixtures (section 5.2.1.1).

5.2.1.3 Alteration of Shim Settings

Spectra with different lineshapes were generated in order to simulate the effect of changing instrument/conditions (which will be discussed in more detail in Chapter 6). In this chapter, the effectiveness of optimising the alignment parameters under one set of conditions and applying these optimised parameters to spectra of the same samples acquired under different conditions was assessed. This will be described in section 5.2.2. In Chapter 6, these datasets will be used to compare the effectiveness of calibration transfer and reference deconvolution. In order to generate spectra with different lineshapes, previously saved shims which are not optimal can be loaded. With this instrument, similar spectra are produced when the shim is optimised prior to analysis on different days, therefore changes in lineshape were produced by loading previously saved shims. Such changes in lineshape may occur if an instrument is changed or repaired, or if a long process is monitored (and shimming during the process is not practical).

Analysis of each mixture set was first performed using a shim optimised before analysis, and was repeated on a different day using sub-optimal shim settings. For the toluene, ethanol and ethyl acetate mixture set, previously saved shims were loaded. The loaded shims had been optimised one week, one month and four months prior to analysis. When the toluene, octene and dibutyl ether mixture set was analysed, suitable shims were not available to load so a simulated shim was loaded instead. The simulated shim was calculated by multiplying the difference between a newly acquired shim and a shim saved seven months previously by 0.3, then adding the result to the newly acquired shim. All shimming was performed using the D_2O/H_2O standard sample, and analysis using each shim was performed on a different day due to the length of time required to analyse the samples.

The variation in lineshape within each set of spectra was measured by the mean and standard deviations of the width of the TMS peak at 50 % peak height, and these values are displayed in Table 5.3. The spectra of the calibration samples containing toluene, octene and dibutyl ether were analysed again on a different day using optimal shim

settings (this analysis will be described in section 6.2.1.3), and the TMS peak widths obtained for these spectra are also included in the table. The similarity of the values in the first two rows of the table demonstrates that the instrument is capable of achieving relatively similar linewidths on different days.

For the toluene, ethanol and ethyl acetate mixture set, the shim optimised one week before analysis produced a mean TMS peak width similar to those produced by the shims optimised just before analysis, and the shim optimised four months before analysis produced extremely large peak widths (a mean value of 3.61 Hz compared to 0.73 Hz when the shim was optimised just before analysis). Therefore the dataset acquired using the shim optimised one month before analysis was used in this work. A summary of the shim settings used to acquire each dataset analysed in this work is displayed in Table 5.4, along with the linewidth at 50 % peak height of the peak in the D_2O/H_2O standard spectrum acquired before each analysis.

Table 5.3 - Mean and standard deviation values of TMS peak width at 50 % peak height within sets of spectra acquired using different shim settings.

Mixture set	Shim	Mean width at 50 % height of TMS peak/Hz	Standard deviation of width at 50 % height of TMS peak/Hz
Toluene, octene and dibutyl ether	**Optimised before analysis**	0.96	0.26
	Optimised before analysis on different day (calibration samples only)	1.20	0.25
	Simulated	1.92	0.49
Toluene, ethanol and ethyl acetate	**Optimised before analysis**	0.73	0.38
	Optimised one week before analysis	1.08	0.27
	Optimised one month before analysis	1.89	0.20
	Optimised four months before analysis	3.61	0.24

Table 5.4 - Summary of shims used to acquire each low-field NMR dataset used in this work, and linewidths of the peak in the D_2O/H_2O standard spectrum acquired before analysis.

Dataset	Mixture set	Shim	Linewidth of D_2O/H_2O peak at 50 % peak height/Hz
1	**Toluene, octene and dibutyl ether**	**Optimised before analysis**	0.49
2	**Toluene, octene and dibutyl ether**	**Simulated**	1.56
3	**Toluene, ethanol and ethyl acetate**	**Optimised before analysis**	0.42
4	**Toluene, ethanol and ethyl acetate**	**Optimised one month before analysis**	2.06

5.2.2 Alignment

The effectiveness of each alignment method described in section 5.1.1 was assessed for the datasets detailed in Table 5.4. Datasets 1 and 2 exhibited small amounts of peak shift (< 0.2 ppm) and datasets 3 and 4 exhibited large peak shifts (up to 1.5 ppm). For each set of solvent mixtures, the objective was to optimise the parameters of each alignment method using one dataset, and apply the alignment methods with these optimised parameters to the other dataset. The results were used to compare the performance of the alignment methods. The performance of each method was assessed based on the ability of the method to align the peaks in the spectra and the effect on the RMSEP values when PLS was performed. The speed and ease of use of each method was also evaluated.

For all datatsets, global alignment of each spectrum was first performed by setting the position of the TMS peak to 0 ppm, so that only intra-spectral shifts were present. The spectral regions below 0.27 ppm and above 9.35 ppm were then removed in order to eliminate the TMS peak and reduce the size of the dataset. All alignment methods were performed on the calibration and test spectra simultaneously. One of the replicate spectra of calibration sample 7 was used as the target spectrum in all methods, as this sample contained equal amounts of each component.

5.2.2.1 Dataset 1

The parameters of each alignment method were first optimised for dataset 1 (the toluene, octene and dibutyl ether mixture spectra acquired using an optimal shim). A full factorial design of experiments (DoE) was performed for COW, PAFFT and RAFFT in order to optimise the two parameters present in each case. The values of segment length and slack displayed in Table 5.5 were initially used in the DoE for COW. The ratio of slack to segment length was used rather than the slack value, so that the relative slack would be comparable between segment lengths.

Table 5.5 - Values of segment length and slack used in initial DoE for COW.

Segment length	Slack	Ratio of slack to segment length
50	10	0.2
50	20	0.4
50	30	0.6
50	40	0.8
100	20	0.2
100	40	0.4
100	60	0.6
100	80	0.8
200	40	0.2
200	80	0.4
200	120	0.6
200	160	0.8
500	100	0.2
500	200	0.4
500	300	0.6
500	400	0.8

COW was performed using PLS Toolbox version 8.6.2 (Eigenvector, Washington, USA) in MATLAB 2016b (MathWorks, Massachusetts, USA). The units of segment length and slack are the interval between two adjacent data points in the spectrum (and each spectrum contained 5181 data points). PLS1 models were built in PLS Toolbox using the aligned calibration spectra, and used to predict the concentration (in % w/w) of each solvent present in the aligned test spectra. The RMSEP values of the PLS1 models were then calculated (Equation 2.8) in order to compare the effectiveness of each set of COW parameters. For each set of parameters, PLS1 was performed using one to ten latent variables, and the number of latent variables was included as a third factor in the DoE.

The DoE was then repeated using segment lengths of 50, 100, 150 and 200 and slack to segment length ratios of 0.1, 0.2, 0.3, 0.4, 0.5 and 0.6, in order to refine the results. Segment lengths above 200 and slack to segment length ratios above 0.6 were not included in the refined DoE, as they were found to significantly increase the computation time with no improvement to the results. (For example, the computation time increased from 25 s to 2 min 36 s upon changing the segment length from 100 to 500 with a slack to segment length ratio of 0.1, and the computation time increased from 25 s to 43 min 36 s upon changing the slack to segment length ratio from 0.1 to 0.8 with a segment length of 100. These times were measured using a MacBook Air with OS version 10.13.6, a 1.7 GHz Intel Core i7 processor and 8 GB memory.) A slack value of 1 was also included for each segment length in order to evaluate the effect of minimum slack. The minimum segment length chosen was 50, as values below 50 would not allow sufficient movement to align the toluene peak between 2 ppm and 2.3 ppm. The number of latent variables (from one to ten) to include in the PLS1 models was again included as a third factor in the DoE. The combinations of parameters used in the refined DoE were found to be more effective than those used in the initial DoE, so only the results of the refined DoE will be considered.

The PAFFT and RAFFT algorithms developed by Wong et al.[10] were obtained from the University of New South Wales website.[23] To optimise PAFFT, a DoE was performed using minimum segment length values of 1, 100, 200, 300, 400, 500, 600, 700, 800, 900 and 1000 and maximum shift to minimum segment length ratios of 0.2, 0.4, 0.6, 0.8 and 1. The units of minimum segment length and maximum shift are data

points of the spectrum. PLS1 models were built for each set of parameters, as for COW, and the number of latent variables (from one to ten) was included as a third factor in the DoE. The RMSEP values were again used to compare the effectiveness of each set of parameters. For RAFFT, maximum shift values of 10, 20, 30, 40, 50, 60, 70, 80, 90 and 100 and lookahead values of 0, 10, 20, 30, 40, 50, 60, 70, 80, 90 and 100 were used, and DoE was performed as before. The DoE was then repeated using maximum shift values of 0, 100, 200, 300, 400, 500, 600, 700, 800, 900 and 1000. Lower RMSEP values were obtained using the range of maximum shift values in the first DoE, so the results of the second DoE will not be discussed.

RSPA was performed using the algorithm in the Imperial Metabolic Profiling and Chemometrics Toolbox for Spectroscopy (IMPaCTS).[24] This algorithm utilises the function described by Veselkov et al.,[12] but does not allow alteration of any parameters other than selection of the target spectrum and normalisation. Normalisation was found to distort the spectra, so was not used. Calibration sample 7 was selected as the target spectrum and RSPA was applied using the default parameters.

The *i*coshift algorithm (version 3.0) was downloaded from the website link[25] provided by Savorani et al.[3] in the paper in which the algorithm is described. The intervals were manually defined as four regions (0.27 – 2.67 ppm, 2.67 – 4.13 ppm, 4.13 – 6.32 ppm and 6.32 – 9.35 ppm), chosen to prevent the splitting of peaks across different intervals. When a specified number of equal intervals was used instead, then either alignment was poor or artefacts were introduced, and when *i*coshift was applied to the whole spectrum without intervals then alignment was poor. The maximum shift was set to "best", as defining a maximum shift value did not improve the results. When the target spectrum was automatically chosen, poorer results were obtained due to the absence of certain peaks therefore the target spectrum was selected manually, as for the other methods. The co-shift preprocessing step did not affect the results obtained, so was not used.

The PCANS algorithm was downloaded from the link in the supplementary information of the PCANS paper by Staab et al.[22] The algorithm was operated in Python 2.7.15 (Python Software Foundation, Delaware, USA). However the output of the algorithm did not contain the aligned spectra, and instead consisted of files

containing the chemical shift positions, heights and widths of the peaks, along with the numbers of peaks present at each chemical shift position. As the aligned spectra were not in a suitable format for quantitative analysis, PCANS was not used in this work.

5.2.2.2 Dataset 2

COW, PAFFT, RAFFT and *i*coshift were then applied to dataset 2 (the toluene, octene and dibutyl ether mixture spectra acquired using a sub-optimal shim), with the optimised settings for dataset 1. PLS1 models were built as before, using the aligned calibration spectra from dataset 2 to predict the concentration of each solvent present in the aligned test spectra from dataset 2, and the RMSEP values were used to compare the effectiveness of alignment in each case. RSPA was not applied to dataset 2, as it was found to be ineffective for alignment of the peaks in dataset 1 due to the inability to change the parameters.

5.2.2.3 Dataset 3

The effectiveness of COW, PAFFT, RAFFT and *i*coshift was evaluated for the alignment of dataset 3 (the toluene, ethanol and ethyl acetate spectra acquired using an optimal shim). For COW, PAFFT and RAFFT, a full factorial DoE was performed as described in section 5.2.2.1, using the same parameters as for the toluene, octene and dibutyl ether mixtures. Again, the range of maximum shift values in the first DoE for RAFFT produced lower RMSEP values than those in the second DoE, so only the results of the first DoE for RAFFT will be considered. *I*coshift was also performed as described in section 5.2.2.1, using manually defined intervals of 0.27 – 1.64 ppm, 1.64 – 2.90 ppm , 2.90 – 6.06 ppm and 6.06 – 9.35 ppm (chosen to prevent splitting of peaks across different intervals). The co-shift preprocessing step was found to improve the results obtained for this dataset, so it was applied. PLS1 models were built as in section 5.2.2.1, and the RSMEP values obtained were used to compare the methods.

5.2.2.4 Dataset 4

PAFFT, RAFFT and *i*coshift were then applied to dataset 4 (the toluene, ethanol and ethyl acetate spectra acquired using a sub-optimal shim), with the optimum settings

determined for dataset 3. COW was not performed on dataset 4, as for dataset 3 it was extremely slow in comparison to the other alignment methods and no more effective. PLS1 models were built using each set of aligned calibration samples, as before, and used to predict the concentration of each solvent present in the corresponding aligned test samples.

5.2.3 Bucketing

5.2.3.1 Dataset 1

Bucketing was performed as a comparison to alignment, using the optimised bucketing algorithm described by Sousa et al.[4] (downloaded from the website link in the paper[26]). In order to determine the optimum bucket size and slackness values for dataset 1, a full factorial DoE was performed on the spectra, using bucket sizes of 0.01, 0.05, 0.1, 0.25, 0.5, 0.75 and 1 ppm with slackness values of 0, 0.01, 0.025, 0.05, 0.075, 0.1, 0.25, 0.5, 0.75 and 1. The slackness values are a ratio of the bucket size (with e.g. 0.01 corresponding to 1 %) and the slackness value of 0 causes the algorithm to perform conventional bucketing. The output of the algorithm consists of the bucketed spectra, the chemical shifts of each set of bucket boundaries and the size of each bucket. PLS1 models were built as described in section 5.2.2.1, and the RMSEP values obtained were calculated to assess the predictive ability of the bucketed spectra and to compare the effectiveness of bucketing and alignment.

5.2.3.2 Dataset 2

The optimum bucket size and slackness values for dataset 1 were not directly applied to dataset 2, as the optimised bucketing algorithm produces buckets of varying size, so the resulting spectra would contain a different number of data points to the spectra in dataset 1 (and the spectra in each dataset require equal numbers of data points in order to perform calibration transfer). Instead, the outputted chemical shift intervals of the buckets obtained using the optimum parameters for dataset 1 were used to manually perform bucketing on the spectra in dataset 2. For each bucket, trapezoidal numerical integration of the data points within the bucket region was performed using the “trapz” function in MATLAB 2016b (MathWorks, Massachusetts, USA) and the first data point in the bucket was subtracted (to account for the repetition of the data

points at the edges of the buckets), apart from for the first bucket. This is the same calculation used in the optimised bucketing algorithm. PLS1 models were again built with the resulting bucketed spectra, and RMSEP values were calculated.

5.2.3.3 Datasets 3 and 4

Optimised bucketing was performed on dataset 3 as for the toluene, octene and dibutyl ether mixtures, using a full factorial DoE to determine the optimum parameters. The intervals of the buckets produced using these optimum parameters were then used to manually perform bucketing on dataset 4, as described in section 5.2.3.2. The RMSEP values obtained by PLS1 were used to compare the performance of bucketing and alignment, as before.

5.2.3.4 Bucketing of Overlapping Spectra

To investigate the effectiveness of bucketing at removing the variation between spectra which exhibit a greater extent of peak overlap than the two mixture sets described above, bucketing was also applied to the low-field NMR spectra of the samples extracted from the esterification reaction mixture (described in section 4.2.3.2). Bucketing was performed using the optimised bucketing algorithm with the following parameters; a bucket size of 0.1 ppm and slackness value of 1 (the optimum parameters for dataset 1); a bucket size of 0.75 ppm and slackness value of 0.25 (the optimum parameters for dataset 3); and a bucket size of 1 ppm and slackness value of 0.25.

5.3 Results and Discussion

5.3.1 Dataset 1

The aims of this section are to optimise the parameters of each of the alignment methods for dataset 1, and to evaluate the effectiveness of each method when small amounts of peak shift (< 0.2 ppm) are present. The spectra in dataset 1 are shown in Figure 5.2, after global alignment using the TMS peak but before application of any of the alignment methods. The molecular structure of each solvent is displayed in Figure 5.3, and an assignment of the peaks present in each spectrum is displayed in Table 5.6. Although overlap was present below 2.5 ppm (of the multiplet peaks in octene and dibutyl ether and the singlet peak in toluene), no overlap was present

elsewhere and the spectrum of each analyte contained clearly resolvable peaks. Small peak shifts of up to 0.15 ppm can be observed between the spectra, particularly of the toluene peak at approximately 2 ppm. Therefore alignment of the spectra is necessary in order to perform chemometric analyses, e.g. PLS and calibration transfer.

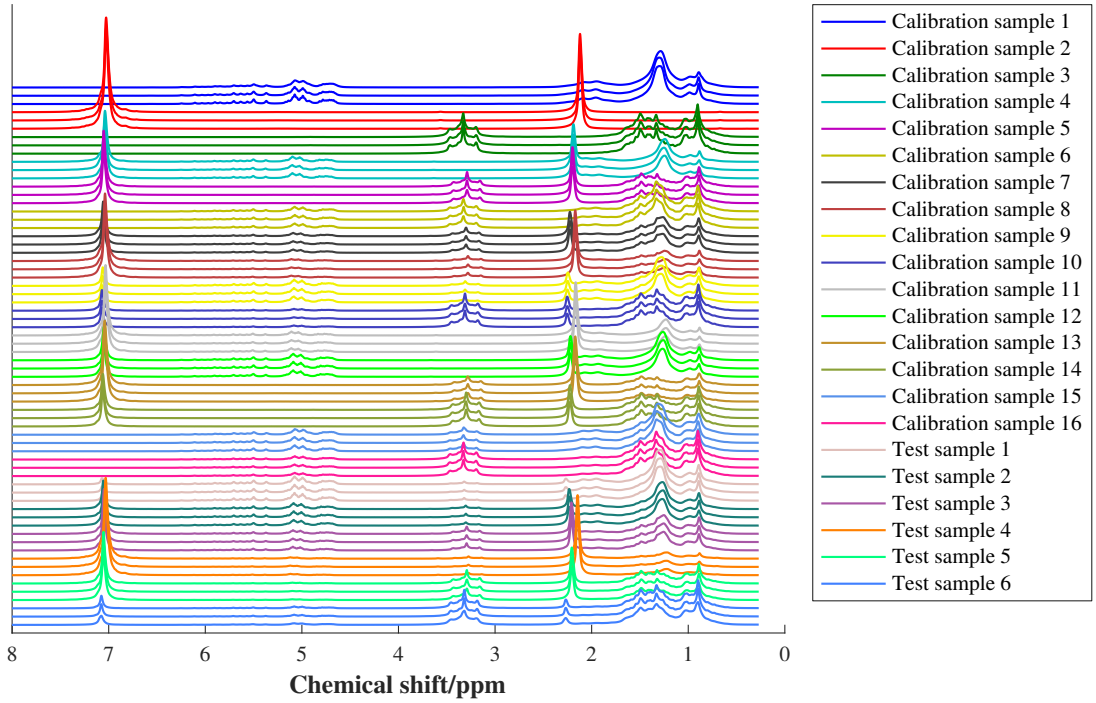

Figure 5.2 - ^{1}H low-field NMR spectra of calibration and test samples in dataset 1, without alignment (other than global alignment using the TMS peak).

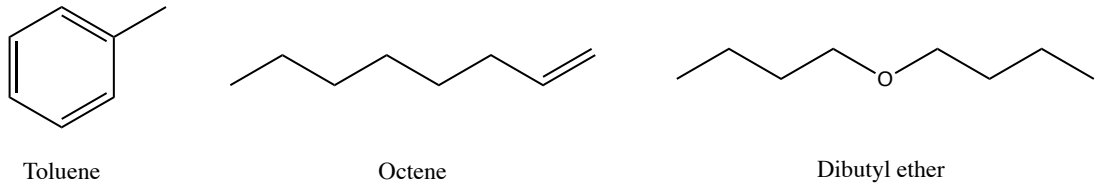

Toluene Octene Dibutyl ether

Figure 5.3 - Molecular structures of toluene, octene and dibutyl ether

Table 5.6 - Assignment of the main peaks in low-field ^{1}H NMR spectra of toluene, octene and dibutyl ether mixtures.

Peak position/ppm	Multiplicity	Peak assignment
0.5 – 2.4	Overlapping multiplets	Protons attached to unsaturated carbons in octene and dibutyl ether
2.0 – 2.3	Singlet	CH_3 group of toluene
3.1 – 3.6	Triplet	O–CH_2 groups in dibutyl ether
4.5 – 6.5	Overlapping multiplets	CH=CH_2 group in octene
6.9 – 7.2	Singlet	Aromatic protons of toluene

5.3.1.1 Optimisation of Parameters

In order to optimise the parameters for COW, PAFFT and RAFFT, the RMSEP values for dataset 1 obtained using each combination of parameters in the DoE are plotted in Figure 5.4, Figure 5.5 and Figure 5.6 respectively. Only the results obtained using two to four latent variables are shown for ease of plotting, as the inclusion of just one latent variable produced poor results and more than four latent variables are generally unnecessary for a three component mixture set, so would produce overfitting of the model. The y axis range was reduced to 0 – 4 % w/w for COW and PAFFT in order for differences in RMSEP to be more easily observed, therefore some of the poorer predictions lie outwith the range of the plots. For toluene, the spread in RMSEP value upon changing the parameters was generally smaller than for octene and dibutyl ether, and the RMSEP values were lower overall. This is because the spectrum of toluene contains only singlet peaks (Table 5.6), so alignment is more straightforward than for the octene and dibutyl ether spectra, which contain multiplet peaks.

In general for COW, higher slack values produced poorer RMSEP values (differing by over 2 % w/w in some cases) due to distortions in peak area caused by greater amounts of warping. This effect was observed to a greater extent when larger segment lengths were used, as the same ratio of slack to segment length resulted in a higher slack value for larger segment lengths. Changing the segment length had a lesser effect on the RMSEP value, and no clear trend was observed.

For PAFFT, there was no clear trend in RMSEP with minimum segment length or maximum shift value. However certain combinations of parameters produced significantly poorer predictions, e.g. high maximum shift ratios (≥ 0.6) with minimum segment lengths of 500, 800, 900 or 1000 and two latent variables produced RMSEP values outwith the range of the plots for octene and dibutyl ether. For some values of minimum segment length (e.g. 300, 400, 600 and 700), the value of maximum shift did not affect the result obtained, indicating that only small shifts were necessary to produce the best alignment. When the minimum segment length of 1 was used then the results did not differ from the unaligned spectra.

The results obtained for each of the different maximum shift values in the RAFFT DoE were relatively similar for toluene (differing by no more than 0.5 % w/w), but for octene and dibutyl ether the spread in RMSEP between latent variables became larger for higher maximum shift values (differing by over 1 % w/w). However less variation in results was observed upon altering the parameters than for COW or PAFFT, which is an advantage of RAFFT. Lower RMSEP values were generally obtained when lookahead was applied compared to when it was not applied, however each of the different lookahead values used (from 10 to 100) produced the same results, indicating that values greater than 10 were not necessary. Therefore out of these three alignment methods, RAFFT appears to be the easiest to use since optimisation of the parameters is less important.

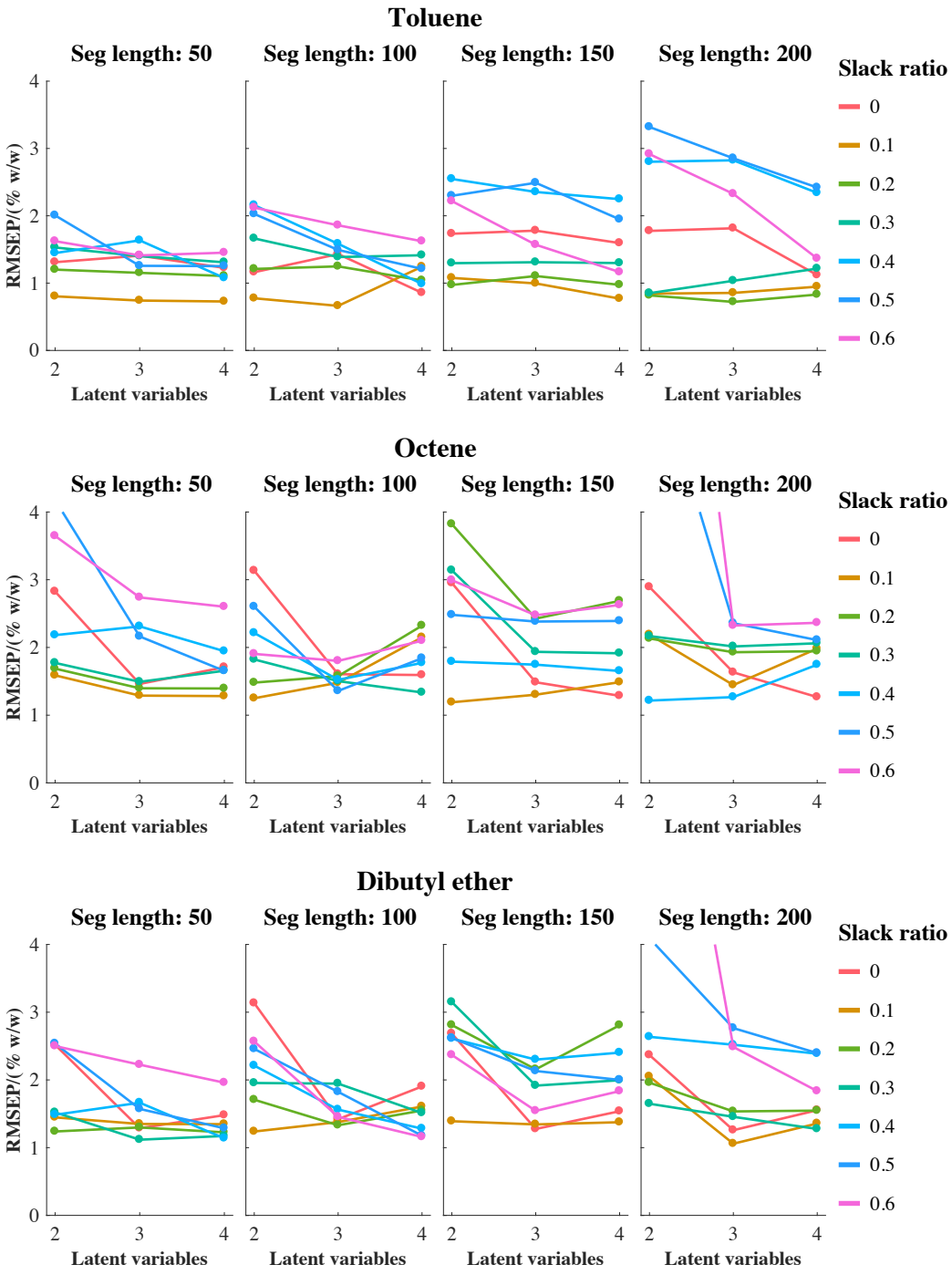

Figure 5.4 - RMSEP values obtained for PLS1 models built using dataset 1 with alignment by COW. DoE used to optimise segment length, slack and number of latent variables.

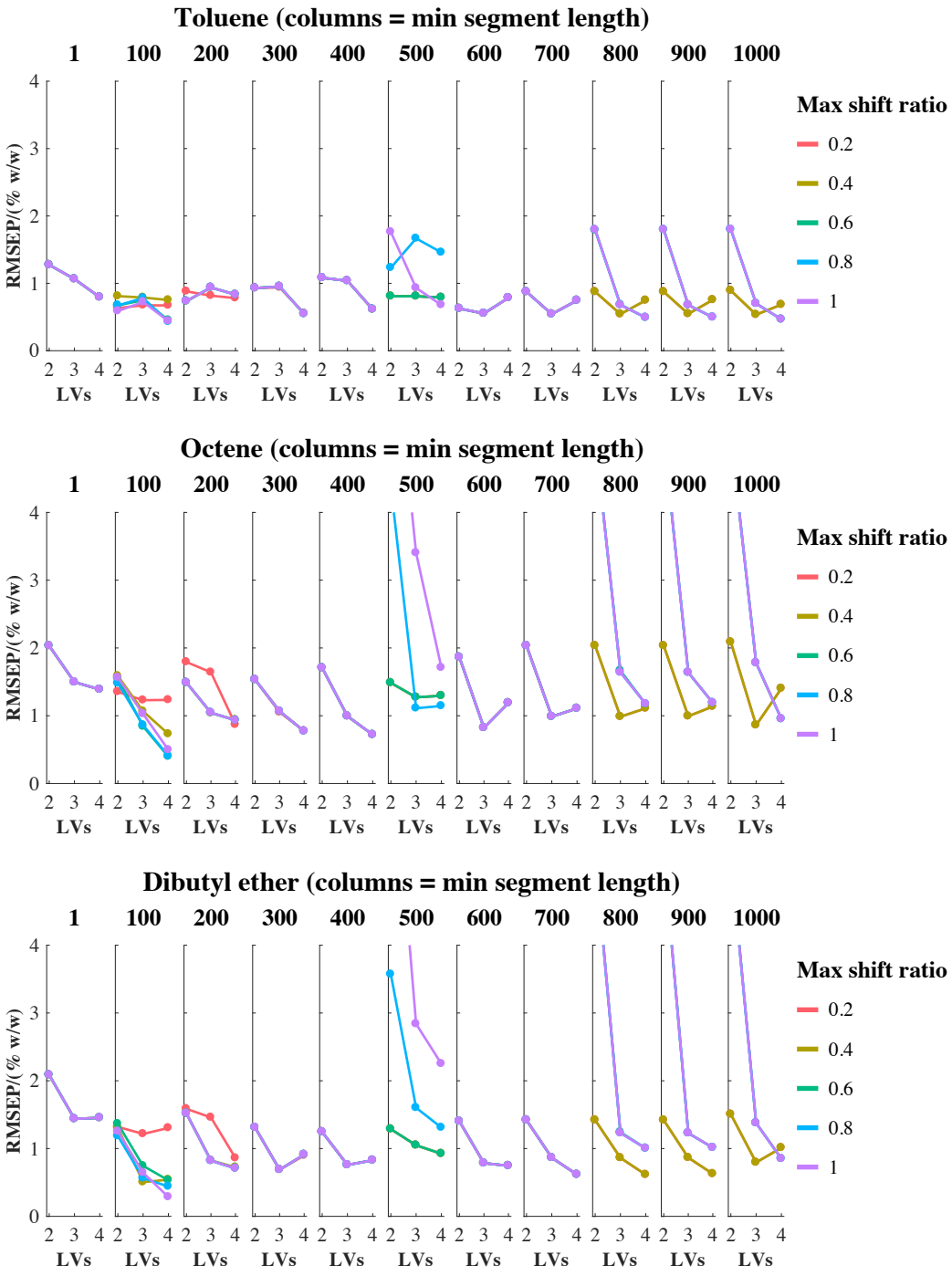

Figure 5.5 - RMSEP values obtained for PLS1 models built using dataset 1 with alignment by PAFFT. DoE used to optimise minimum segment length, maximum shift and number of latent variables.

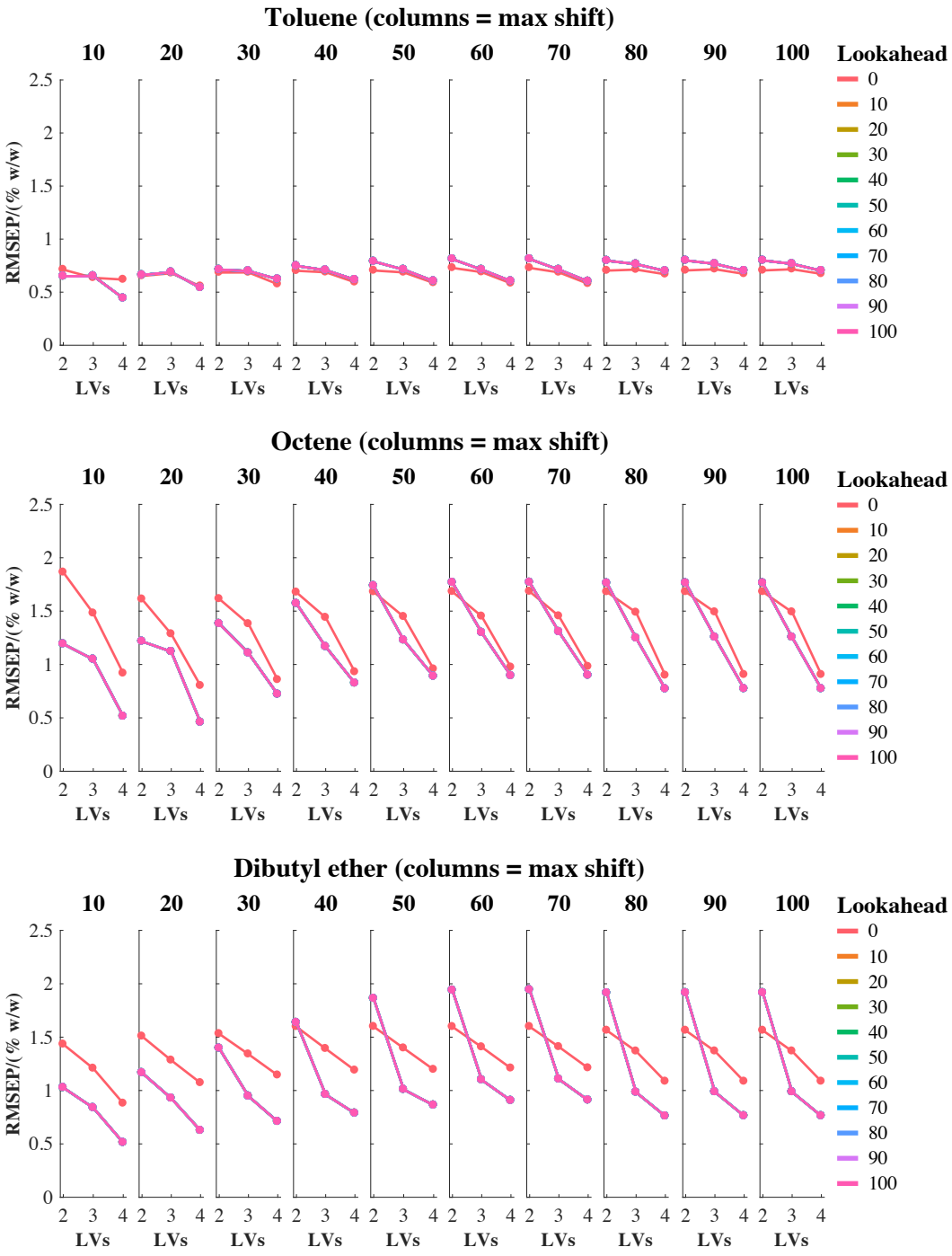

Figure 5.6 - RMSEP values obtained for PLS1 models built using dataset 1 with alignment by RAFFT. DoE used to optimise maximum shift, lookahead and number of latent variables.

When bucketing was applied using each combination of parameters in the DoE (Figure 5.7), no clear trend was observed. The predictions were generally more accurate for bucket sizes greater than 0.01 ppm, particularly for dibutyl ether (for which the RMSEP values obtained with all slackness values were above 1 % w/w when the bucket size of 0.01 ppm was used, and RMSEP values of less than 0.4 % w/w could be achieved when larger bucket sizes were used). This is unsurprising, as peak shifts of up to 0.15 ppm were present so the bucket size of 0.01 ppm was insufficient to remove the shifts. Larger slackness values (e.g. 0.5 – 1) generally produced lower RMSEP values, but for some bucket sizes, smaller slackness values (≤ 0.5) produced RMSEP values as low as 0.5 % w/w or less when four latent variables were used. Poorer predictions (of up to 3 % w/w) were obtained for octene and dibutyl ether when bucket sizes of 0.25 or 0.5 ppm and slackness values greater than 0.1 were used with two latent variables, but the results improved when more latent variables were included.

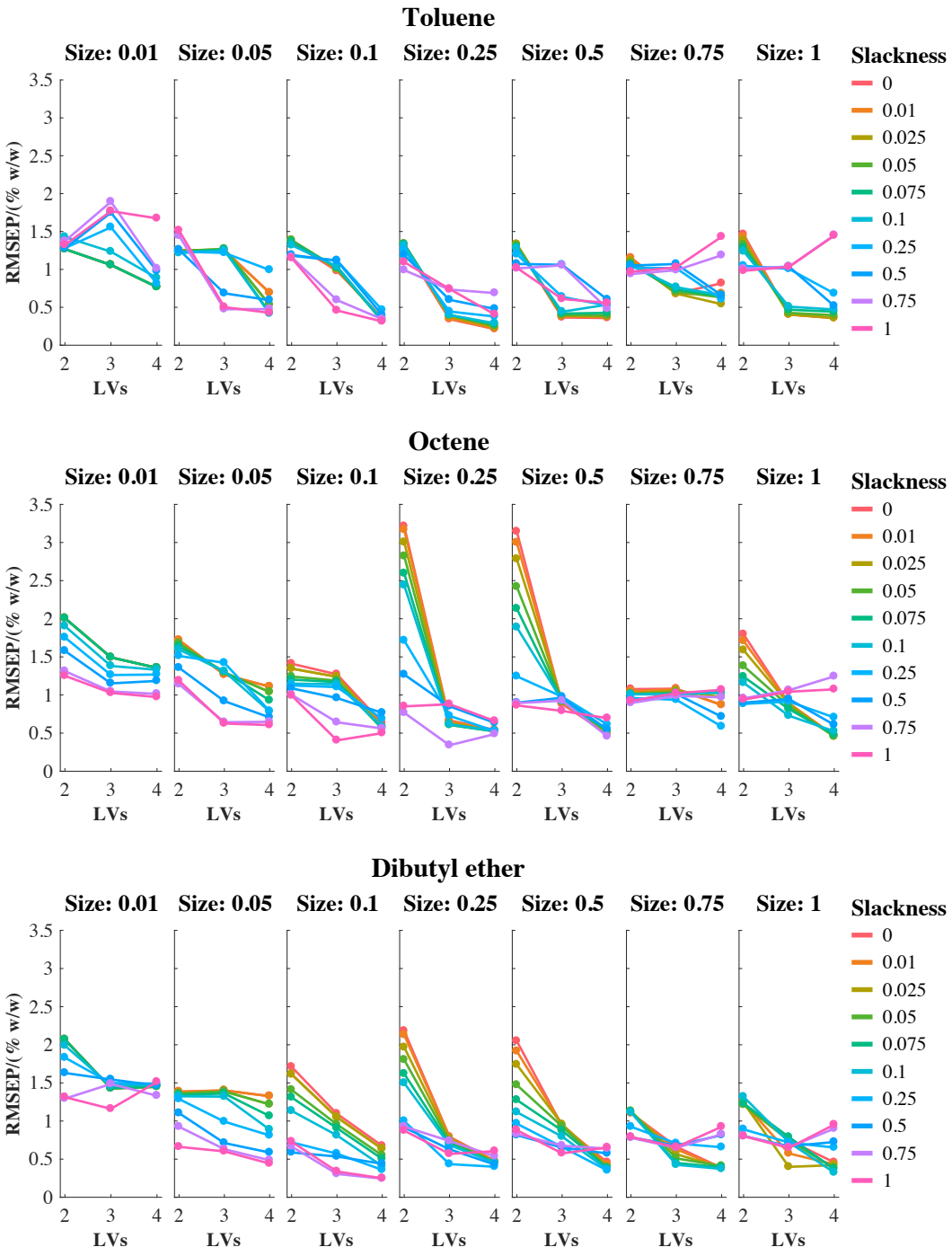

Figure 5.7 - RMSEP values obtained for PLS1 models built using dataset 1 with optimised bucketing. DoE used to optimise bucket size, slackness and number of latent variables.

The optimum parameters chosen for each method are displayed in Table 5.7. The optimum ratio of slack to segment length for COW corresponds to a slack value of 10, and the optimum ratio of maximum shift to minimum segment length for PAFFT corresponds to a maximum shift value of 60. When multiple combinations of parameters produced similar results then the lowest values were chosen for simplicity. This is particularly important for COW, as larger values of segment length and slack were found to significantly increase the computation time (as mentioned in section 5.2.2.1).

Table 5.7 - Optimum parameters determined by DoE for each method of alignment of dataset 1.

Method	Parameter 1		Parameter 2		Optimum number of LVs		
	Name	Optimum value	Name	Optimum value	Toluene	Octene	Dibutyl ether
COW	Segment length	100	Slack ratio	0.1	2	2	2
PAFFT	Minimum segment length	100	Maximum shift ratio	0.6	4	4	4
RAFFT	Maximum shift	10	Lookahead	10	4	4	4
Bucketing	Bucket size	0.1 ppm	Slackness	1	3	3	3

The computation times for each method (using the optimum parameters) are displayed in Table 5.8, along with the computation times for each DoE. RSPA was the slowest method (taking 40 seconds to align the spectra), followed by COW (which took 25 seconds using the optimum parameters). However optimisation of the parameters was not necessary for RSPA and was extremely slow for COW, taking more than 4.5 hours. This is the main disadvantage of COW compared to the other methods. PAFFT, RAFFT, *i*coshift and bucketing were significantly faster, each taking no more than 2 seconds to align/bucket the spectra using the optimum parameters. Bucketing was the fastest method, taking 39 seconds to perform the full DoE, and PAFFT was more than three times faster than RAFFT due to the absence of the recursive method.

Table 5.8 - Computation times of DoEs used to optimise parameters of alignment methods and computation times of alignment using the optimum parameters for each method (using a MacBook Air with OS version 10.13.6, a 1.7 GHz Intel Core i7 processor and 8 GB memory).

Method	Computation time of full DoE	Computation time of method using optimum parameters/s
COW	4 hours 38 min	25
PAFFT	3 min 20 s	< 1
RAFFT	10 min 52 s	~ 2
RSPA	n/a	40
***i*coshift**	n/a	< 2
Bucketing	39 s	< 1

5.3.1.2 Aligned Spectra

The spectra in dataset 1 aligned using COW, PAFFT, RSPA and *i*coshift are displayed in Figure 5.8, Figure 5.9, Figure 5.10 and Figure 5.11 respectively, to illustrate the effectiveness of each method. Similar spectra were obtained for PAFFT and RAFFT, so the spectra aligned using RAFFT can be found in Appendix 5. For COW, PAFFT and RAFFT, the optimum parameters displayed in Table 5.7 were used.

After the application of COW, the spectra were generally well aligned, although the toluene singlet peak just above 2 ppm in one of the repeat measurements of calibration sample 2 was out of alignment by 0.14 ppm. PAFFT and RAFFT were able to align all peaks, and appear to have been very effective (for example the toluene singlet peak just above 2 ppm which exhibited shifts of up to 0.15 ppm before alignment only exhibited shifts of 0.007 ppm after alignment by PAFFT). However for PAFFT, artefacts were present in the spectra due to the insertion/deletion of points, as shown in Figure 5.12. Such artefacts were also present to a smaller extent in the spectra aligned by RAFFT, and an artefact resembling part of a very small peak was present in the baseline of many of the spectra aligned by *i*coshift. This is a disadvantage of the insertion/deletion method of alignment utilised by PAFFT, RAFFT and *i*coshift over the warping method of alignment used by COW. The ability to manually define the

segments used in *i*coshift helps to reduce the occurrence of artefacts compared to PAFFT and RAFFT, and this is an advantage of *i*coshift.

*I*coshift was effective at aligning all peaks, except for the peak just below 1 ppm (which exhibited shifts of up to 0.1 ppm). This is because it lies in the same segment as the peak just above 2 ppm (because overlap was present between the peaks in this segment), and alignment of both these peaks simultaneously does not appear to have been possible. This is a disadvantage of *i*coshift compared to the other methods. RSPA does not appear to have been successful at aligning the spectra, as similar amounts of peak shift were present as to when no alignment method was applied. The ineffectiveness of RSPA is likely to be due to the inability to alter the parameters using this algorithm. The bucketed spectra using the optimum parameters are shown in Figure 5.13. Significantly fewer data points were present after the application of bucketing (81 compared to 5181 data points), and the structure of the peaks was lost. However peaks corresponding to each solvent could still be clearly resolved.

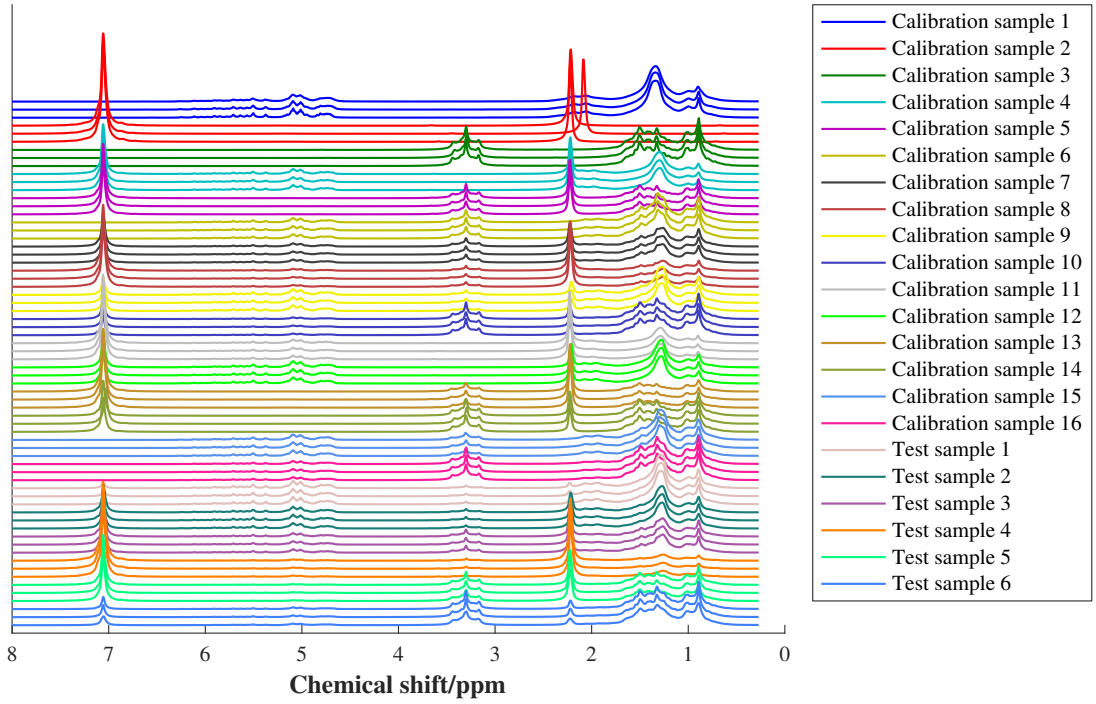

Figure 5.8 - ^{1}H low-field NMR spectra of calibration and test samples in dataset 1 with alignment by COW using optimum parameters determined by DoE (segment length = 100 and slack = 10).

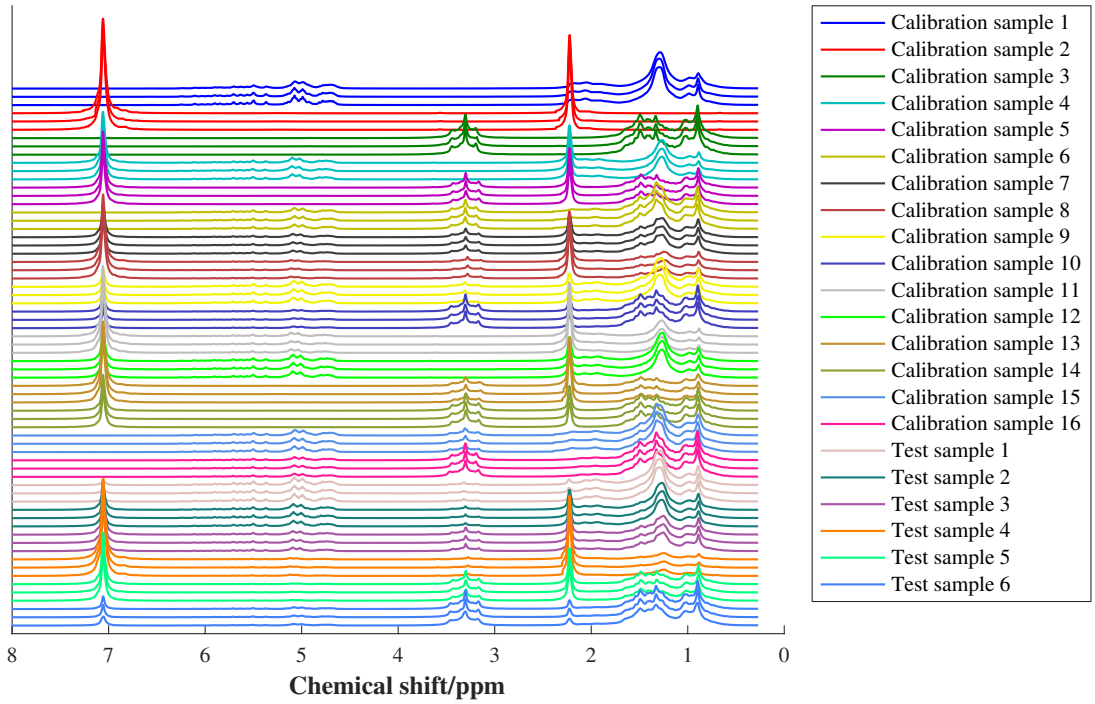

Figure 5.9 - ^{1}H low-field NMR spectra of calibration and test samples in dataset 1 with alignment by PAFFT using optimum parameters determined by DoE (minimum segment length = 100 and maximum shift = 60).

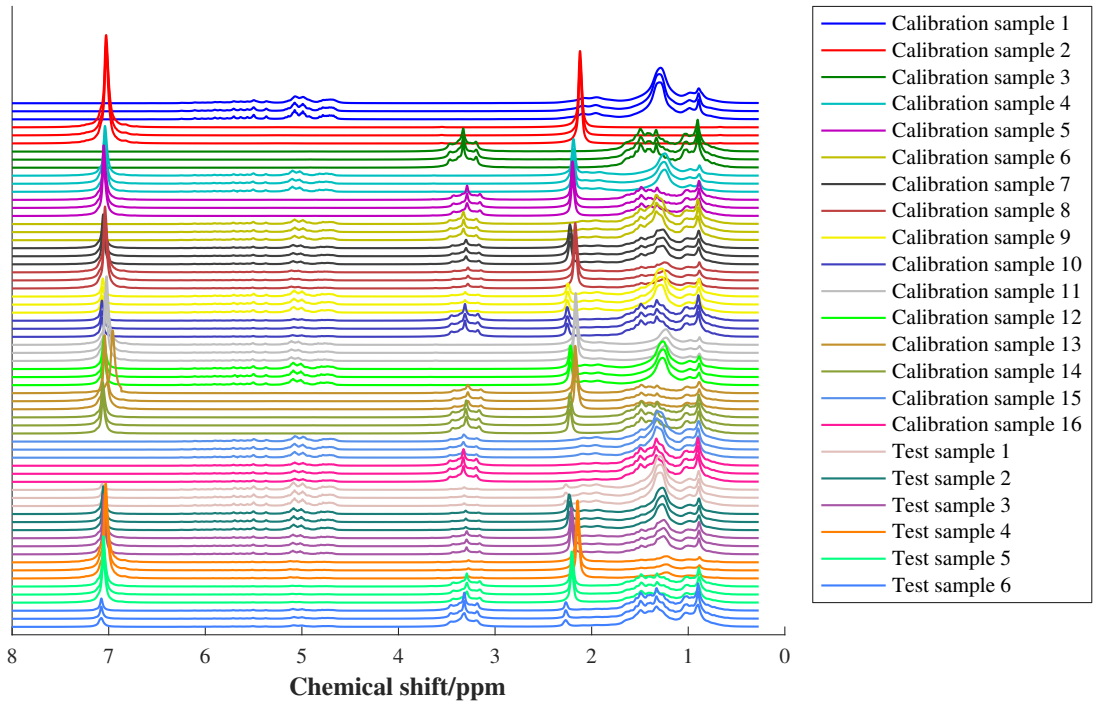

Figure 5.10 - ^{1}H low-field NMR spectra of calibration and test samples in dataset 1 with alignment by RSPA.

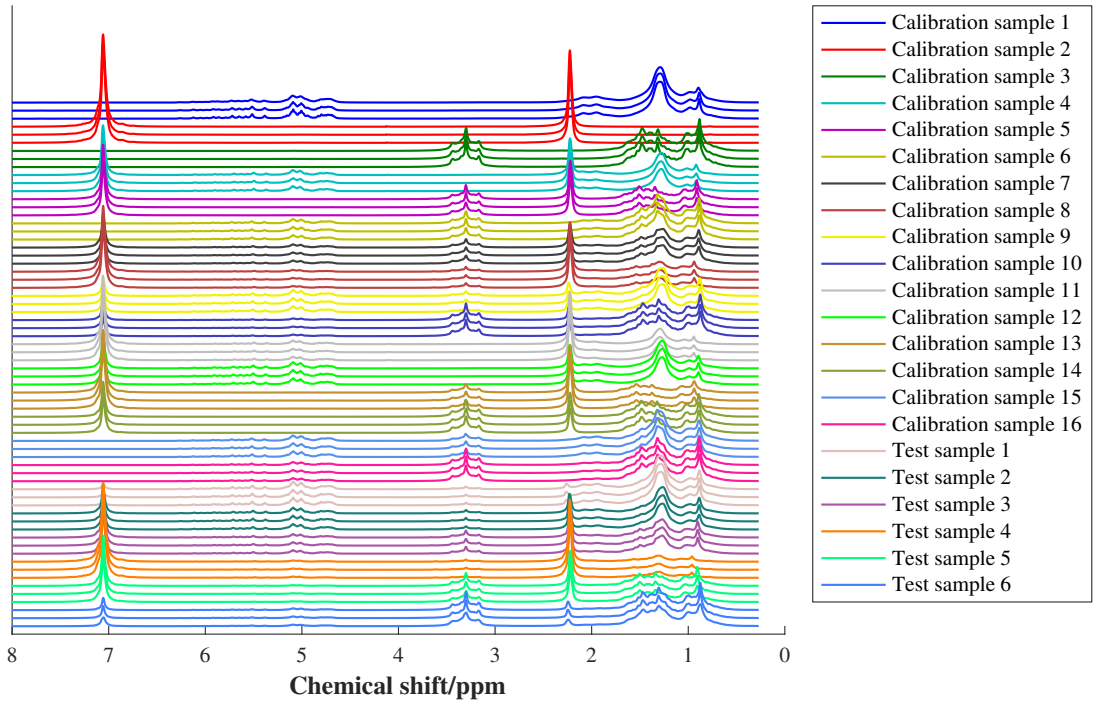

Figure 5.11 - ^{1}H low-field NMR spectra of calibration and test samples in dataset 1 with alignment by *i*coshift using manually defined intervals (0.27 – 2.67 ppm, 2.67 – 4.13 ppm, 4.13 – 6.32 ppm and 6.32 – 9.35 ppm).

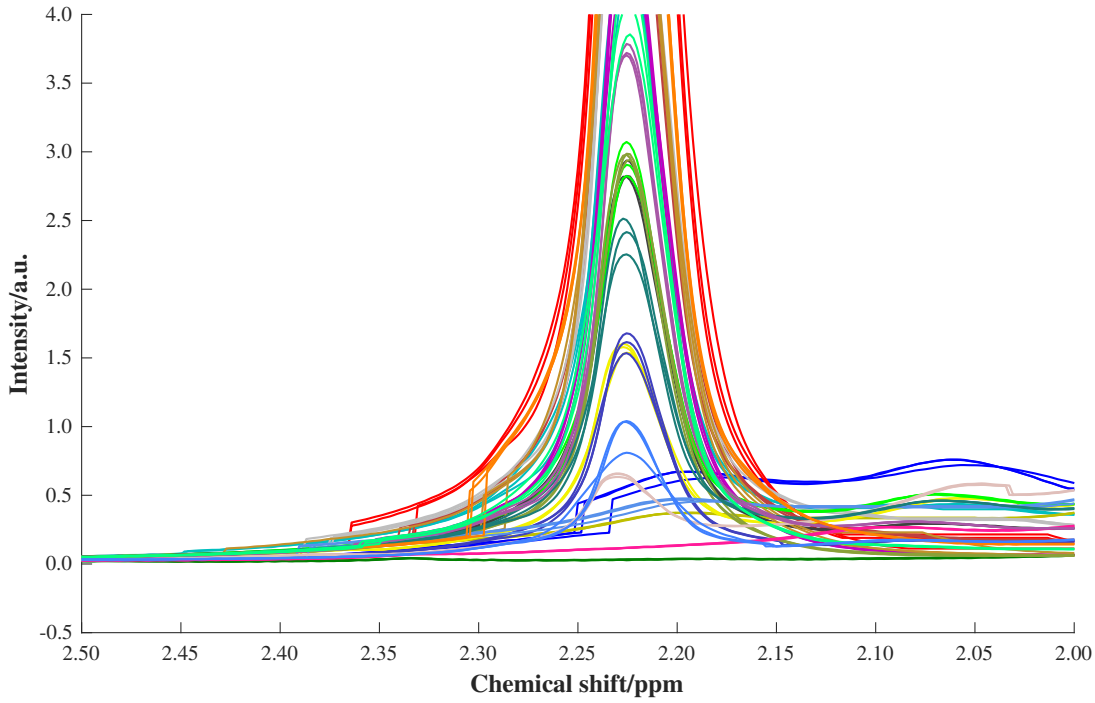

Figure 5.12 - Example of artefacts present in spectra aligned by PAFFT.

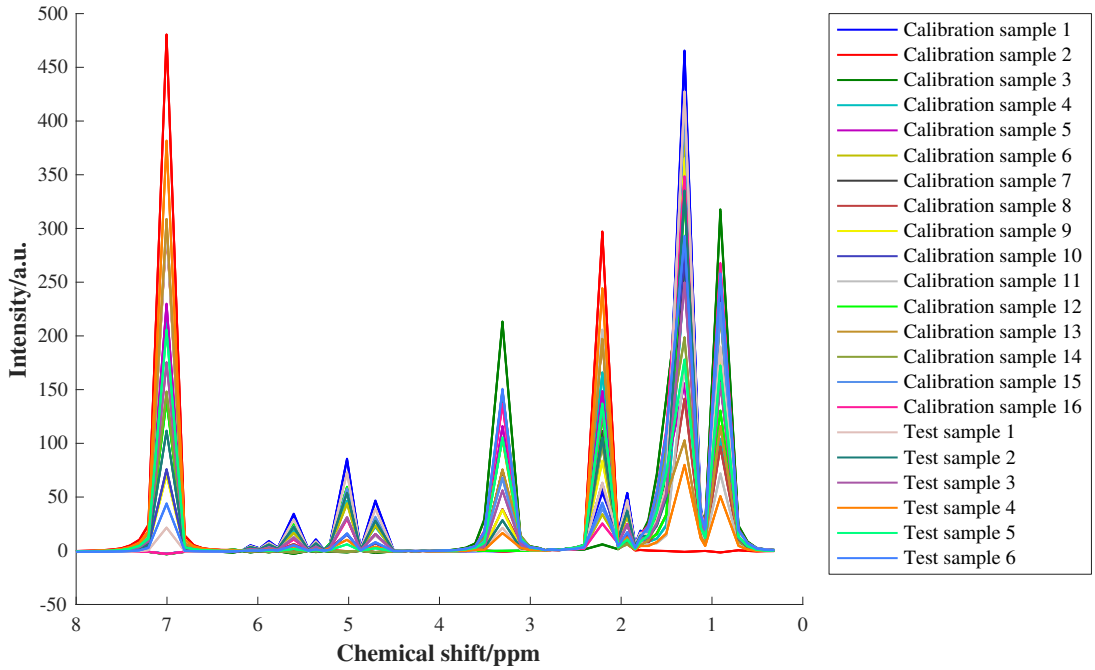

Figure 5.13 - ^{1}H low-field NMR spectra of calibration and test samples in dataset 1 with optimised bucketing using optimum parameters determined by DoE (bucket size = 0.1 ppm and slackness = 1).

5.3.1.3 RMSEP Values

To evaluate the effect of each alignment method on the predictive ability of the spectra in dataset 1, the RMSEP values obtained for PLS1 using the spectra without alignment (other than global alignment using the TMS peak), with alignment by each of the optimised methods and with optimised bucketing will be discussed. These values are displayed in Table 5.9. For the unaligned spectra and the spectra aligned by RSPA and *ic*oshift (for which DoE was not performed), the optimum number of latent variables to include in the model was chosen by examination of the RMSEP values obtained using two to four latent variables (with differences of less than 0.15 % w/w between consecutive RMSEP values taken as insignificant). Before alignment was performed, the RMSEP value for toluene was relatively low (0.79 % w/w), however four latent variables were required. The RMSEP values for octene and dibutyl ether were higher (1.50 % w/w and 1.44 % w/w), but only three latent variables were necessary.

Table 5.9 - RMSEP values for PLS1 models built using dataset 1 without alignment (other than global alignment using the TMS peak), with alignment (by COW, PAFFT, RAFFT, RSPA and *i*coshift) and with bucketing.

Alignment method	Toluene		Octene		Dibutyl ether	
	LVs	RMSEP/ (% w/w)	LVs	RMSEP/ (% w/w)	LVs	RMSEP/ (% w/w)
None	4	0.79	3	1.50	3	1.44
COW	2	0.77	2	1.25	2	1.24
PAFFT	4	0.45	4	0.40	4	0.53
RAFFT	4	0.44	4	0.51	4	0.51
RSPA	4	0.69	4	1.17	4	1.40
***i*coshift**	3	0.55	3	0.86	3	0.73
Bucketing	3	0.46	3	0.41	3	0.34

After the application of COW, only two latent variables were required for each solvent, indicating that COW has reduced the non-linearity present in the spectra. The RMSEP value of toluene was similar to that obtained before alignment, but the RMSEP values of octene and dibutyl ether were around 0.2 % w/w lower. PAFFT and RAFFT produced similar RMSEP values, both reducing the RMSEP values of octene and dibutyl ether by a factor of 3 and the RMSEP value of toluene by a factor of 2. However four latent variables were required for each solvent, suggesting that these methods may have increased the non-linearity of the variation in the octene and dibutyl ether contributions. The presence of artefacts in the spectra did not appear to worsen the RMSEP values, and the insertion/deletion process of alignment appears to be more effective than the warping process.

Four latent variables were also necessary after RSPA, and no significant difference was observed in the RMSEP values for toluene or dibutyl ether (with a reduction of 0.3 % w/w observed for octene). *I*coshift produced lower RMSEP values than COW or RSPA, but higher RMSEP values than PAFFT and RAFFT (0.55 % w/w, 0.86 % w/w and 0.73 % w/w for toluene, octene and dibutyl ether respectively). However one less RMSEP value was necessary for each solvent compared to PAFFT

and RAFFT. Overall the most effective alignment methods for this data appear to be PAFFT and RAFFT, however *i*coshift was also more effective than COW or RSPA.

After bucketing, the RMSEP values obtained for each solvent were very low (≤ 0.46 % w/w). This indicates that despite the loss of structure, bucketing was successful at improving the predictive ability of the model due to removal of the variation in peak position. However this may be because little peak overlap was present, so all components could still be clearly distinguished. For toluene and octene, bucketing produced similar RMSEP values to PAFFT and RAFFT, but for dibutyl ether, bucketing produced a lower RMSEP value than any of the alignment methods (over four times less than before alignment). Fewer latent variables were also required than for than for PAFFT or RAFFT (three rather than four). Therefore for this set of mixtures, bucketing appears to perform better than the alignment methods, particularly RSPA and COW.

5.3.2 Dataset 2

In this section, COW, PAFFT, RAFFT and *i*coshift were applied to the spectra in dataset 2, using the parameters optimised for dataset 1. Bucketing was also performed, using the intervals optimised for dataset 1. An example spectrum of calibration sample 7 (containing equal concentrations of toluene, octene and dibutyl ether) acquired with the settings of shim used in dataset 1 and dataset 2 is displayed in Figure 5.14 to illustrate the differences between the two datasets. The rest of the spectra in dataset 2 can be found in Appendix 5. In dataset 2, the peaks were broader and less defined than in dataset 1 (with the mean TMS peak linewidths given in Table 5.3), as the shim was no longer optimal.

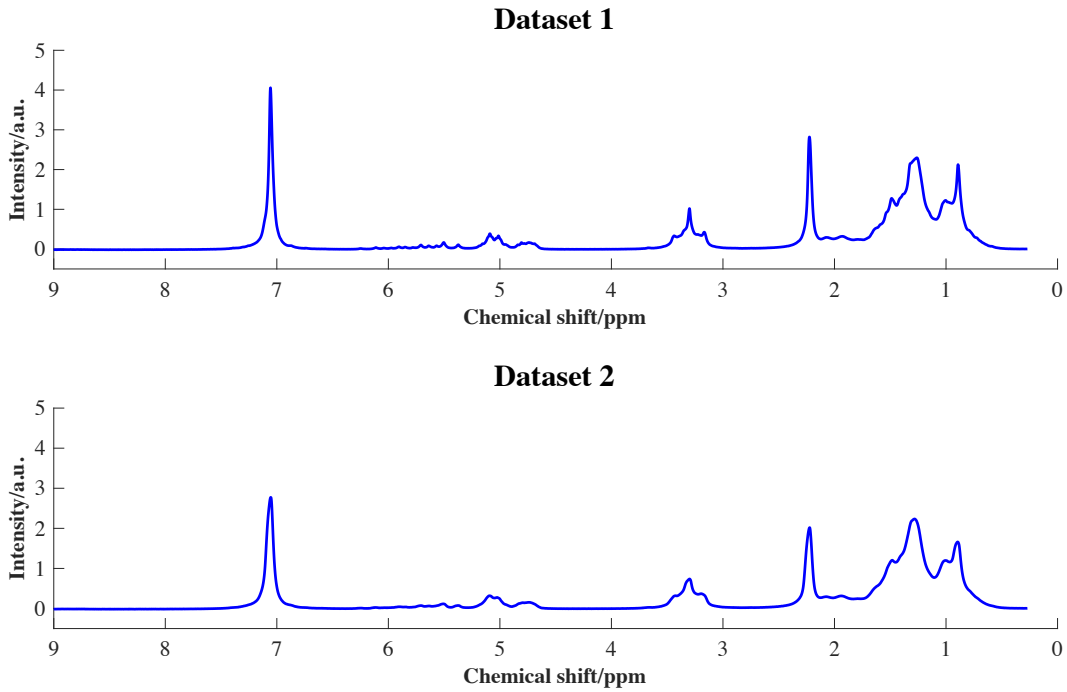

Figure 5.14 - ^{1}H low-field NMR spectrum of calibration sample 7 in datasets 1 and 2.

The RMSEP values obtained for the PLS1 models built using the spectra in dataset 2 without alignment (other than global alignment using the TMS peak), with alignment by each method and with bucketing are shown in Table 5.10. RSPA was not included due to the poor performance of the method for dataset 1. Without alignment, the RMSEP values of octene and dibutyl ether were lower than those obtained for dataset 1. This indicates that the broadening of the peaks has removed some of the variation between spectra without deteriorating the predictive ability. For toluene, the RMSEP values obtained using datasets 1 and 2 were similar.

The application of COW to the spectra in dataset 2 appears to have worsened the predictive ability, with higher RMSEP values obtained for toluene (0.1 % w/w higher) and octene (0.3 % w/w higher) compared to the results obtained without alignment, and a similar RMSEP value obtained for dibutyl ether. However for octene and dibutyl ether, fewer latent variables were necessary (two for each solvent compared to four and three before alignment). For toluene, more latent variables were required (four compared to three).

Table 5.10 - RMSEP values for PLS1 models built using dataset 2 without alignment (other than global alignment using the TMS peak), with alignment (by COW, PAFFT, RAFFT and *i*coshift) and with bucketing. Parameters optimised using dataset 1.

Alignment method	Toluene		Octene		Dibutyl ether	
	LVs	RMSEP/ (% w/w)	LVs	RMSEP/ (% w/w)	LVs	RMSEP/ (% w/w)
None	3	0.83	4	0.95	3	1.17
COW	4	0.95	2	1.25	2	1.15
PAFFT	4	0.56	4	1.00	3	1.07
RAFFT	2	0.66	3	1.01	2	1.10
***i*coshift**	4	0.44	3	0.98	3	0.75
Bucketing	3	0.75	3	0.69	3	0.38

When PAFFT was applied, the RMSEP values of toluene and dibutyl ether improved compared to those of the unaligned spectra (by 0.3 % w/w and 0.1 % w/w respectively), but the RMSEP value of octene remained similar. One extra latent variable was required for toluene, but the number of latent variables required for octene and dibutyl ether did not change. The RMSEP values obtained for RAFFT were similar to those obtained for PAFFT, but fewer latent variables were necessary (two for toluene and dibutyl ether and three for octene). Therefore although PAFFT and RAFFT were very effective at aligning relatively narrow, well-defined peaks, these methods do not appear to work as well for overlapping peaks in spectra with poorer lineshapes. However, this could be because the optimised parameters for dataset 1 were not the optimum for dataset 2. Performing separate optimisations for data collected under different conditions would be time consuming so is not ideal, particularly if a calibration model built using one set of data is then applied to a smaller number of samples from a different dataset (e.g. if alignment is performed before calibration transfer).

The absence of parameters which require optimisation is an advantage of *i*coshift. For dataset 2, *i*coshift performed best of the four alignment methods, however the RMSEP value of octene still did not improve compared to before alignment. One more latent variable was required for toluene, but one less latent variable was required for octene

compared to before alignment. Bucketing was less effective than *i*coshift, PAFFT or RAFFT for toluene (but still reduced the RMSEP by 0.1 % w/w), however for octene and dibutyl ether it performed significantly better, with RMSEP values as low as 0.38 % w/w achieved (three times lower than before bucketing). This indicates that bucketing may be more effective than any of the alignment methods at improving the predictive ability of low-field NMR spectra exhibiting little overlap or peak shift. However it is not as easy to apply as *i*coshift, as determination of the optimum bucket size and slackness value is necessary.

Therefore for the toluene, octene and dibutyl ether mixtures, bucketing was the most effective method overall and *i*coshift was the most effective of the alignment methods. PAFFT and RAFFT were effective at aligning the spectra in dataset 1, but were not as effective for dataset 2. COW produced poorer RMSEP values than the other methods due to the warping process of alignment, and RSPA was the least effective method due to the inability to alter the parameters.

5.3.3 Dataset 3

To evaluate the effectiveness of each alignment method when large peak shifts (up to 1.5 ppm) are present, the methods will be applied to the spectra in dataset 3. The spectra are displayed in Figure 5.15 (after global alignment had been performed using the TMS peak, but before the application of any alignment methods), the molecular structures of ethanol and ethyl acetate are shown in Figure 5.16, and an assignment of the peaks in the spectra is displayed in Table 5.11. Overlap of the triplets at 1 ppm and the multiplets between 3 ppm and 6 ppm was present and large amounts of peak shift occurred between spectra, particularly of the triplet around 5 ppm which shifted by up to 1.5 ppm due to hydrogen bonding and differences in the pH of the mixtures. In the other regions of the spectra (below 3 ppm and above 6 ppm), shifts of up to 0.3 ppm were present (with the ethyl acetate singlet peak just below 2 ppm the worst affected). Alignment of the peaks in these spectra is therefore more challenging than alignment of the peaks in the toluene, octene and dibutyl ether mixture spectra.

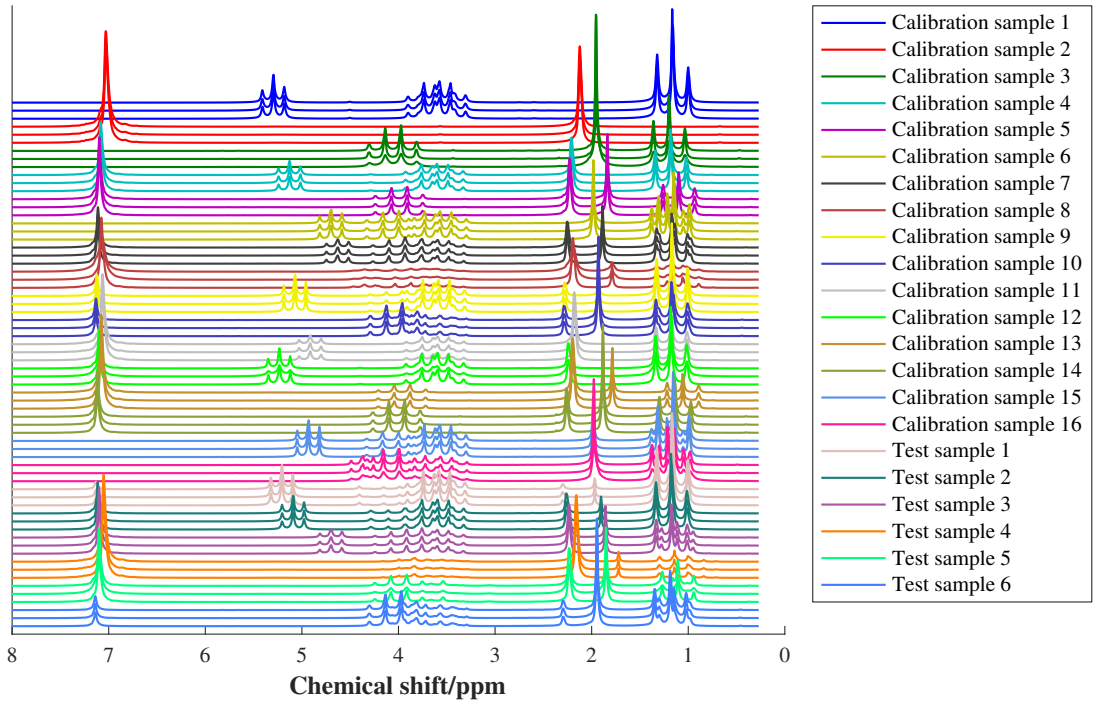

Figure 5.15 - ^{1}H low-field NMR spectra of calibration and test samples in dataset 3, without alignment (other than global alignment using the TMS peak).

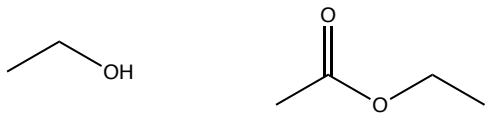

Ethanol Ethyl acetate

Figure 5.16 - Molecular structures of ethanol and ethyl acetate

Table 5.11 - Assignment of the main peaks in low-field ^{1}H NMR spectra of toluene, ethanol and ethyl acetate mixtures.

Peak position/ppm	Multiplicity	Peak assignment
0.8 – 1.5	Triplets	CH_3 group adjacent to CH_2 group in ethanol and ethyl acetate
1.7 – 2.1	Singlet	CH_3 group adjacent to C=O in ethyl acetate
2.0 – 2.4	Singlet	CH_3 group of toluene
3.0 – 5.6	Overlapping multiplets and triplet	CH_2 groups of ethanol and ethyl acetate (multiplets), OH group of ethanol (triplet)
6.9 – 7.2	Singlet	Aromatic protons of toluene

5.3.3.1 Optimisation of Parameters

To determine the optimum parameters for the alignment of dataset 3 using COW, PAFFT and RAFFT, the RMSEP values obtained using each combination of parameters in the DoE are shown in Figure 5.17, Figure 5.18 and Figure 5.19 respectively. Again, only the results for two to four latent variables are displayed and the y axis scale for each plot was limited to RMSEP values below 6 % w/w for ease of comparison of the parameters.

For COW, no clear trend was observed in the RMSEP values obtained using different parameters. For segment lengths less than 150, the slack to segment length ratio of 0.1 generally produced better RMSEP values, presumably because higher values of slack distorted the peaks, but for the segment length of 200 it generally worsened the RMSEP values, presumably because it no longer allowed enough movement to align the peaks. Ratios of slack to segment length above 0.4 generally produced worse RMSEP values than lower slack ratios, but not in every case. For example, ratios of 0.2 and 0.3 produced the poorest RMSEP values for toluene and ethanol when the segment length of 50 was used, but produced the lowest RMSEP values for the segment length of 200. This could be because for small segment lengths, the increase in RMSEP due to distortion of the peaks outweighed the improvement in RMSEP due to aligning the peaks, while at larger segment lengths the improvement in RMSEP due to alignment outweighed the increase in RMSEP due to distortion.

When the minimum PAFFT segment length of 1 was used, the results again did not differ from the unaligned spectra. For minimum segment lengths above 600, the RMSEP values were poorer than for the unaligned spectra regardless of the maximum shift value, but for minimum segment lengths less than 300, lower RMSEP values could be obtained in some cases when maximum shift values greater than or equal to 0.4 were used. For RAFFT, lower RMSEP values were again obtained when lookahead was applied compared to when it wasn't applied, but the lookahead values of 10 to 100 produced the same results. Increasing the maximum shift value improved the results for values up to 40, but beyond this value little variation was observed. The spread of results for toluene upon changing the parameters was significantly lower than for

ethanol or ethyl acetate (a range of approximately 1 % w/w for toluene and 4 % w/w for ethanol and ethyl acetate).

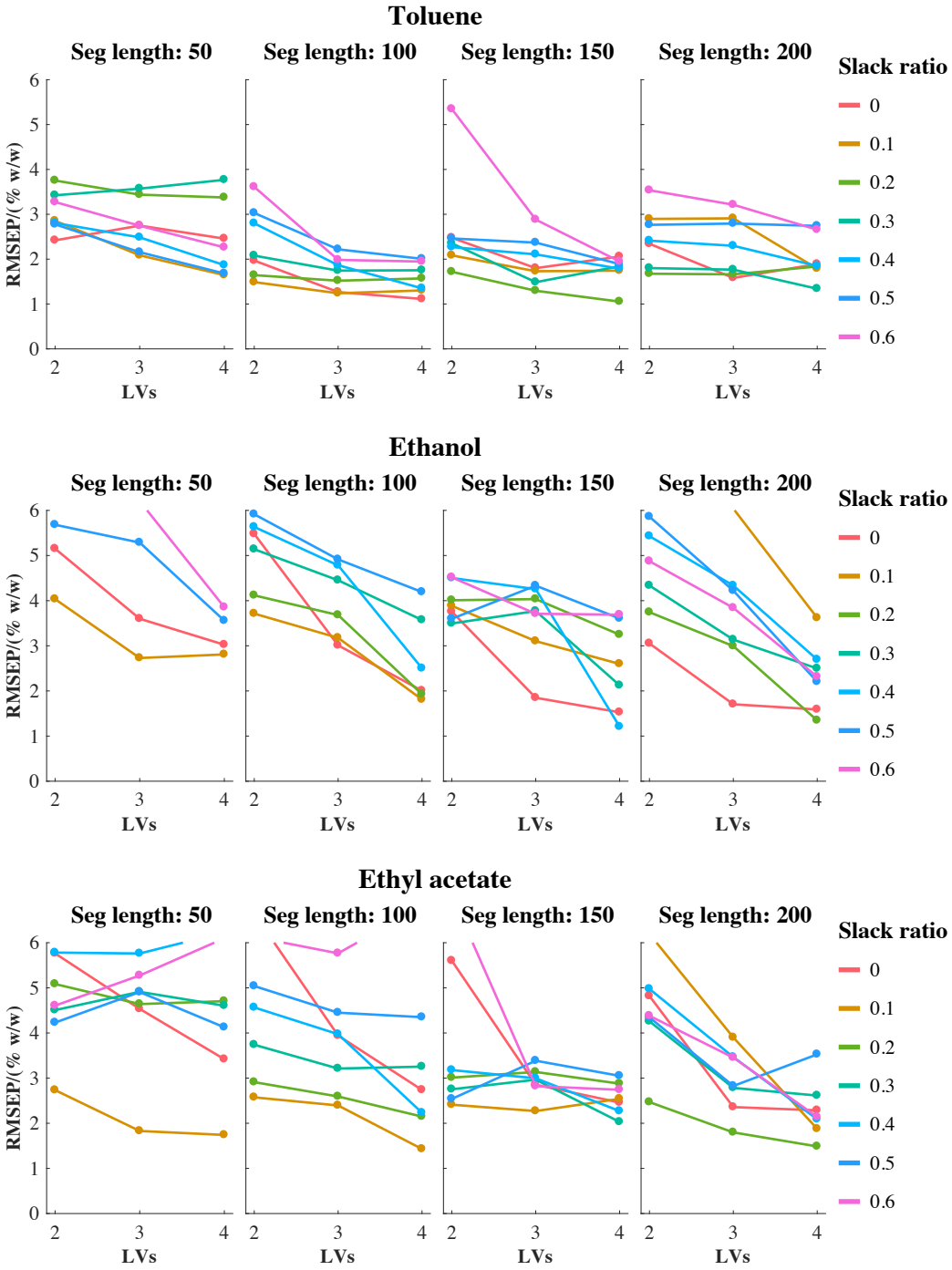

Figure 5.17 - RMSEP values obtained for PLS1 models built using dataset 3 with alignment by COW. DoE used to optimise segment length, slack and number of latent variables.

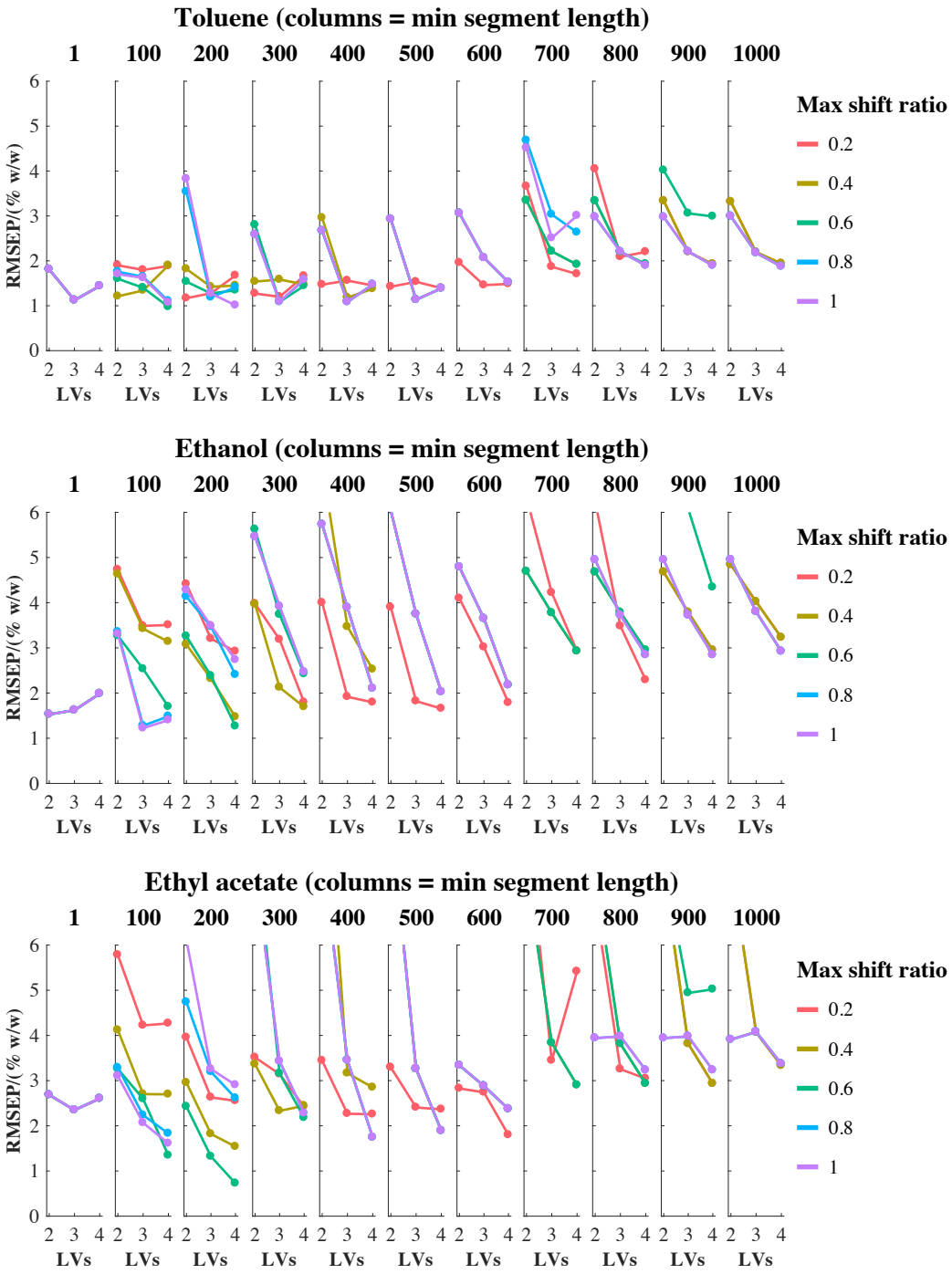

Figure 5.18 - RMSEP values obtained for PLS1 models built using dataset 3 with alignment by PAFFT. DoE used to optimise minimum segment length, maximum shift and number of latent variables.

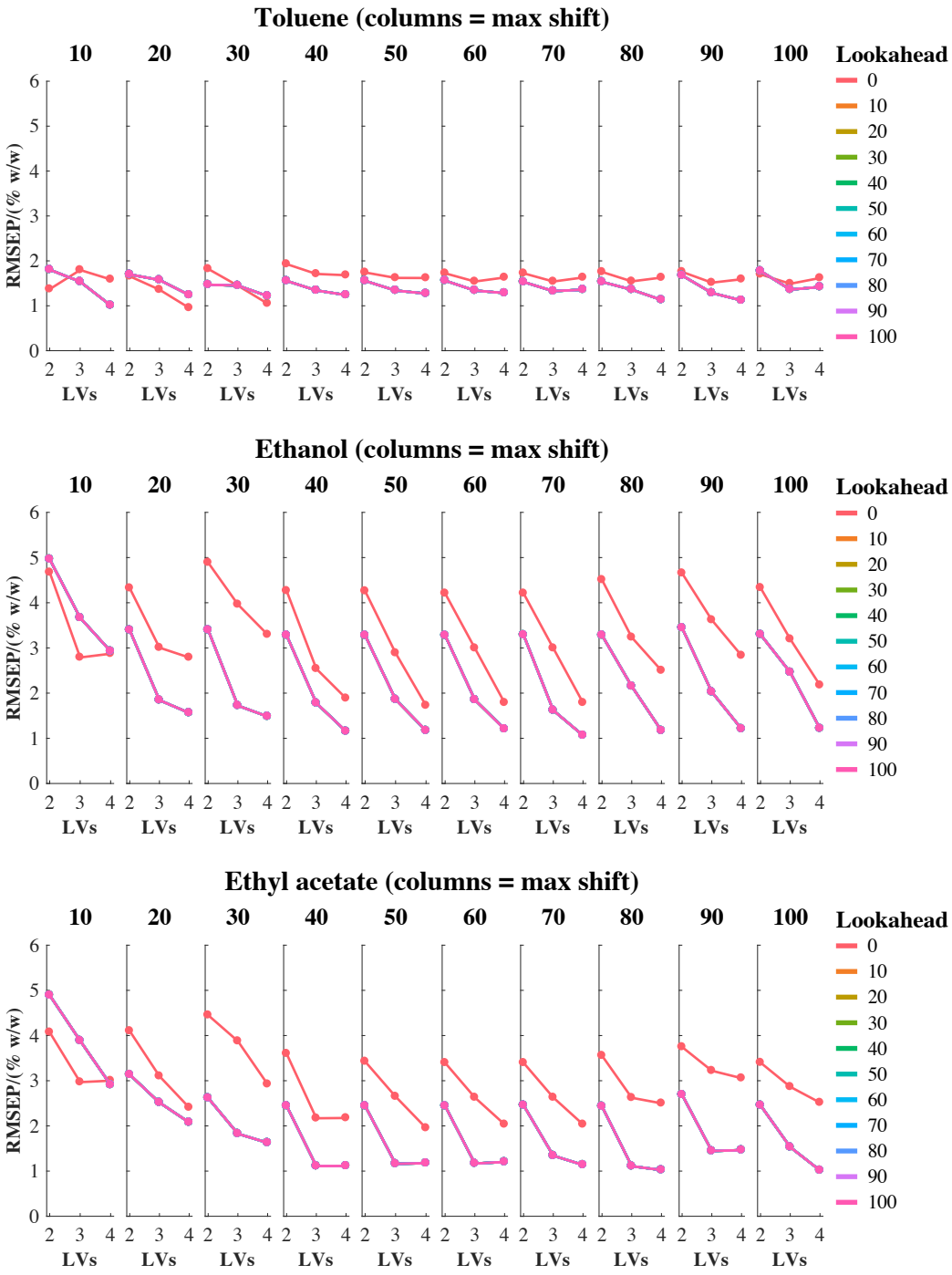

Figure 5.19 - RMSEP values obtained for PLS1 models built using dataset 3 with alignment by RAFFT. DoE used to optimise maximum shift, lookahead and number of latent variables.

When bucketing was applied (Figure 5.20), slackness values less than 0.25 generally produced poorer predictions (particularly for the bucket size of 0.75 ppm), as did bucket sizes less than 0.1 ppm. As peak shifts of up to 1.5 ppm were present, this was unsurprising. The optimum parameters chosen for each method are displayed in Table 5.12, with the optimum ratio of slack to segment length for COW corresponding to a slack value of 10, and the optimum ratio of maximum shift to minimum segment length for PAFFT corresponding to a maximum shift value of 120. The optimum values of minimum segment length (PAFFT), maximum shift (RAFFT) and bucket size were larger than for dataset 1, however the optimum parameters for COW were the same as for dataset 1. It is unsurprising that the optimum values were generally larger, as much larger peak shifts (up to 1.5 ppm compared to less than 0.2 ppm) were present in dataset 3.

Table 5.12 - Optimum parameters determined by DoE for each method of alignment of dataset 3.

Method	Parameter 1		Parameter 2		Optimum number of LVs		
	Name	Optimum value	Name	Optimum value	Toluene	Octene	Dibutyl ether
COW	Segment length	100	Slack ratio	0.1	3	4	4
PAFFT	Minimum segment length	200	Maximum shift ratio	0.6	3	4	4
RAFFT	Maximum shift	40	Lookahead	10	3	4	3
Bucketing	Bucket size	0.75 ppm	Slackness	0.25	4	4	3

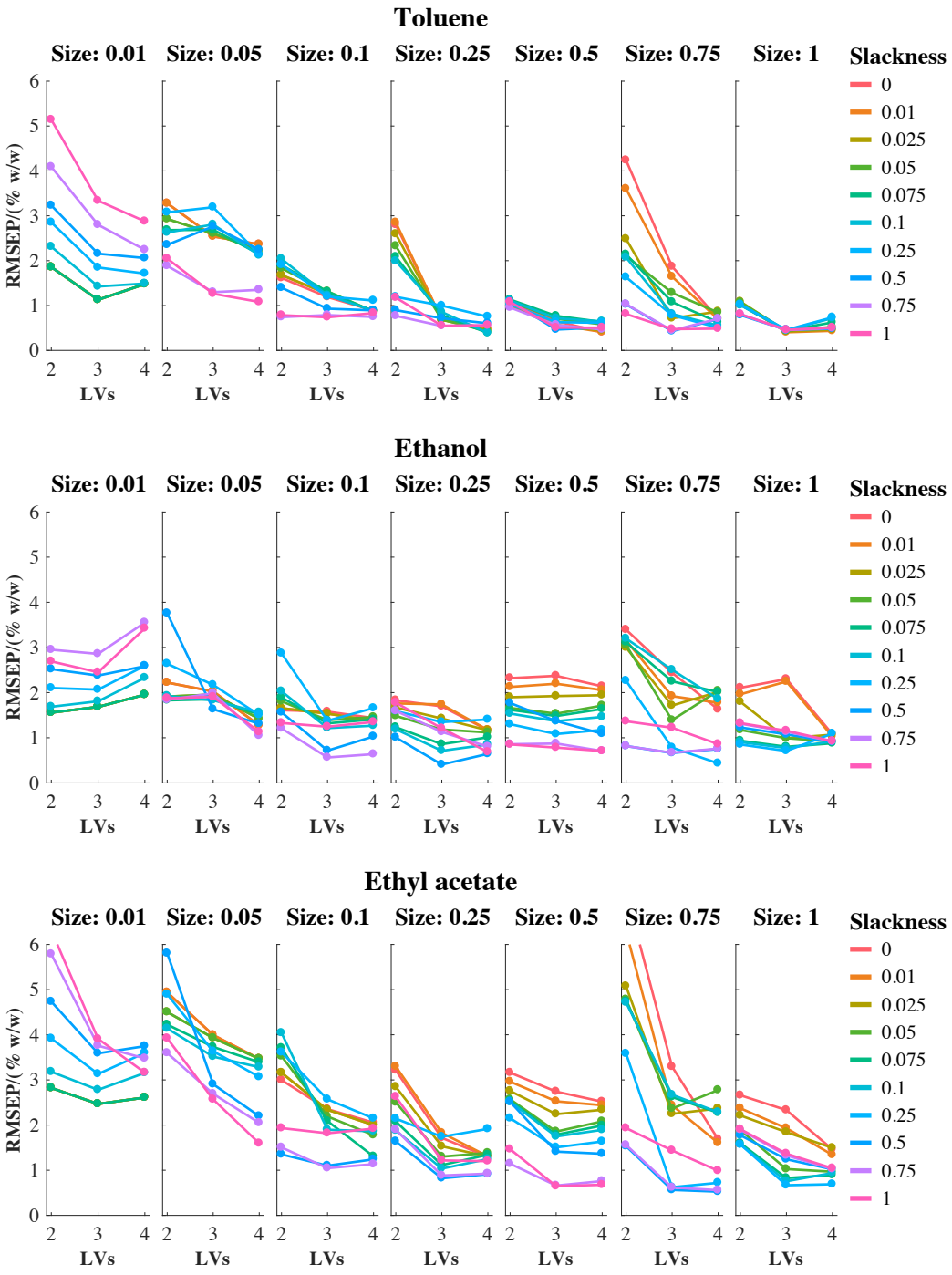

Figure 5.20 - RMSEP values obtained for PLS1 models built using dataset 3 with optimised bucketing. DoE used to optimise bucket size, slackness and number of latent variables.

5.3.3.2 Aligned Spectra

The spectra of dataset 3 are shown after alignment by COW, PAFFT, RAFFT, *i*coshift and bucketing (using the optimised parameters for COW, PAFFT, RAFFT and bucketing) in Figure 5.21, Figure 5.22, Figure 5.23 and Figure 5.24 respectively. After the application of COW, the triplet peaks just above 1 ppm and the singlet peaks just above 7 ppm appeared well aligned (shifting by less than 0.009 ppm). The two singlet peaks just above and below 2 ppm were less well aligned (shifting by up to 0.11 ppm). The multiplets around 4 ppm appear to have been aligned to some extent, however alignment of the ethanol triplet peak around 5 ppm has not been successful and shifts as large as 1 ppm were still present.

When PAFFT was applied, the three singlet peaks were well aligned in all spectra (only shifting up to 0.03 ppm) and the triplets just above 1 ppm were well aligned in most spectra (with shifts of up to 0.2 ppm present in the others). However alignment of the multiplet peaks between 3 ppm and 6 ppm was unsuccessful (with shifts as large as 1 ppm present). Similar spectra were obtained when RAFFT was applied, and the spectra aligned by RAFFT can be found in Appendix 5. With *i*coshift, the singlet peak just above 7 ppm was well aligned (shifting by no more than 0.004 ppm), the peaks below 3 ppm were relatively well aligned (shifting by no more than 0.08 ppm), and between 3 ppm and 6 ppm alignment was once again unsuccessful (with shifts of up to 1.5 ppm present). Therefore none of the alignment methods which were successful for small peak shifts (< 0.2 ppm) appear to be capable of handling peak shifts as large as 1.5 ppm.

After the application of optimised bucketing, the spectra only contained twelve data points each, with four or five maxima corresponding to the peaks. Although extreme, this combination of bucketing parameters produced the most accurate predictions of concentration overall. The optimum bucket size is significantly larger than for the toluene, octene and dibutyl ether dataset (0.75 ppm compared to 0.1 ppm), as larger buckets were required to reduce the effect of peak shift on RMSEP.

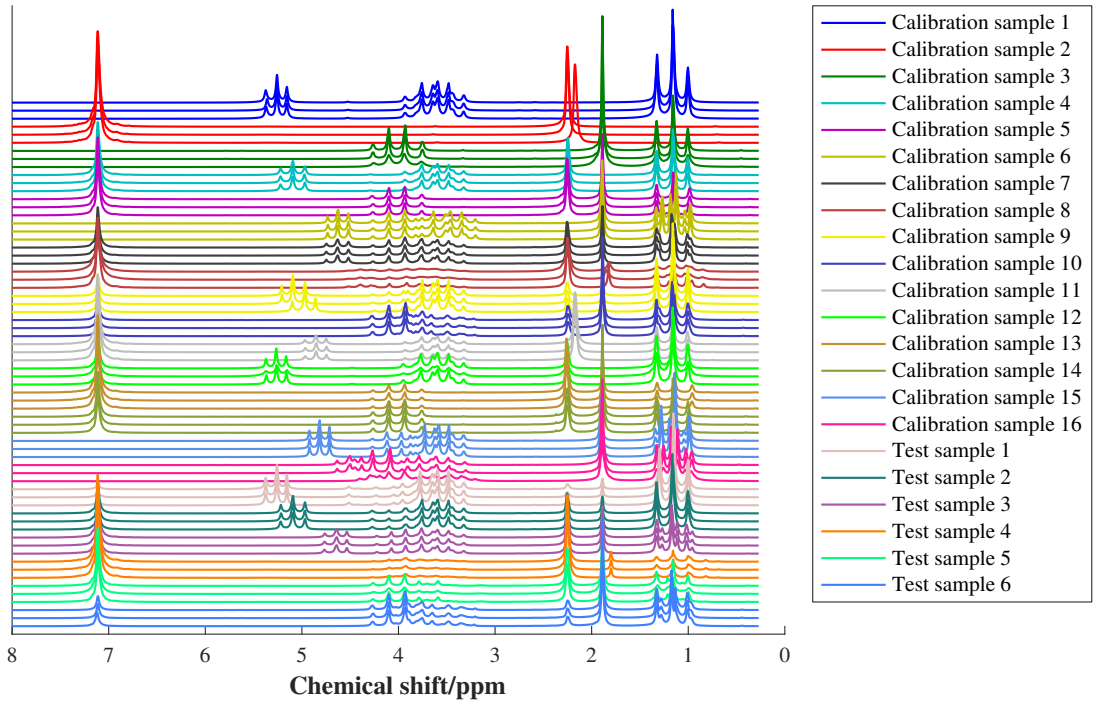

Figure 5.21 - ^{1}H low-field NMR spectra of calibration and test samples in dataset 3 with alignment by COW using optimum parameters determined by DoE (segment length = 100 and slack = 10).

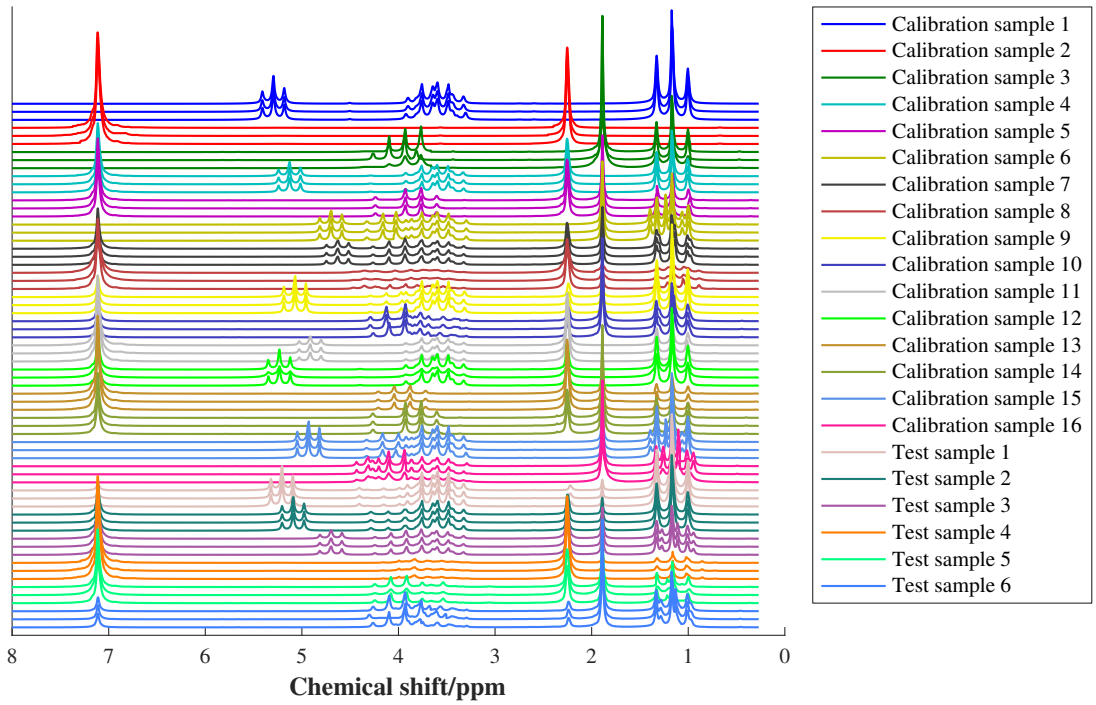

Figure 5.22 - ^{1}H low-field NMR spectra of calibration and test samples in dataset 3, with alignment by PAFFT using optimum parameters determined by DoE (minimum segment length = 200 and maximum shift = 120).

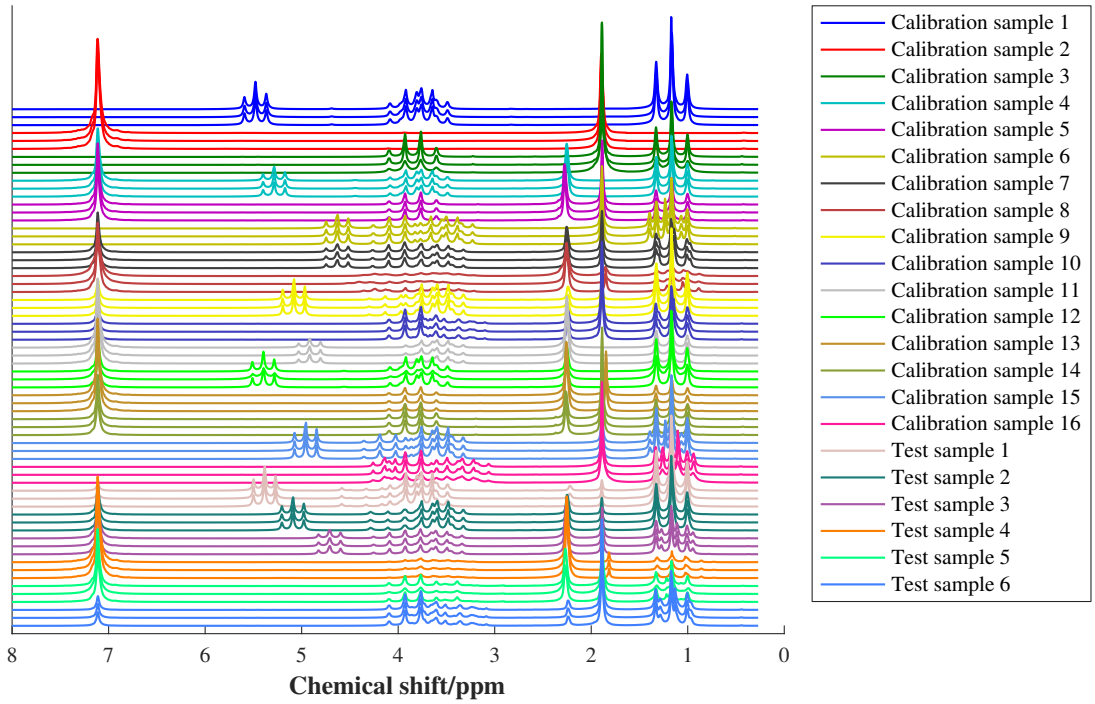

Figure 5.23 - ^{1}H low-field NMR spectra of calibration and test samples in dataset 3 with alignment by *i*coshift using manually defined intervals (0.27 – 1.64 ppm, 1.64 – 2.90 ppm , 2.90 – 6.06 ppm and 6.06 – 9.35 ppm).

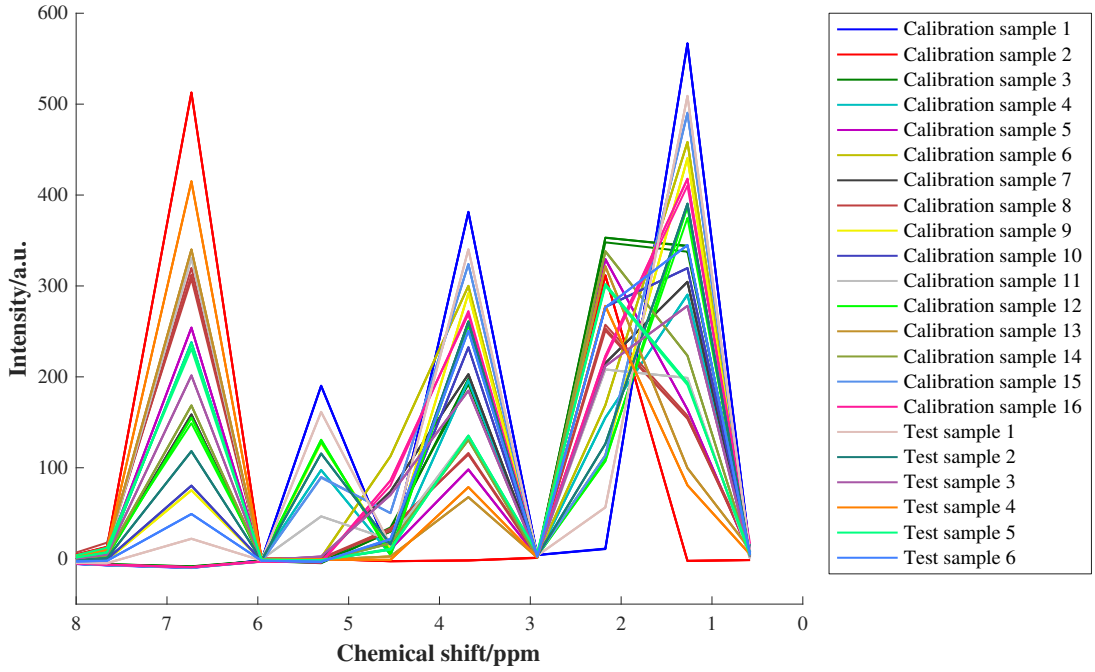

Figure 5.24 - ^{1}H low-field NMR spectra of calibration and test samples in dataset 3, with optimised bucketing using optimum parameters determined by DoE (bucket size = 0.75 ppm and slackness = 0.25).

5.3.3.3 RMSEP Values

The RMSEP values obtained for the PLS1 models built using dataset 3 without alignment, with alignment by each method and with bucketing (using the optimised parameters in each case) are displayed in Table 5.13, in order to compare the effect of each method on the predictive ability of the spectra. Without alignment, the RMSEP values for toluene and ethanol were in the same range as those obtained for the toluene, octene and dibutyl ether mixtures (0.8 – 1.5 % w/w), however the ethyl acetate RMSEP value was almost 1 % w/w higher due to the peak shifts present.

After the application of COW, the RMSEP values for toluene and ethanol increased by 0.1 % w/w and 0.3 % w/w respectively, but the RMSEP value for ethyl acetate decreased by almost 1 % w/w. For PAFFT the value for toluene was similar to that obtained using COW, but the values for ethanol and ethyl acetate were both less than without alignment (with the value for ethyl acetate decreasing by more than a factor of 3). However for COW and PAFFT, four latent variables were necessary for ethanol and ethyl acetate (compared to two and three latent variables without alignment). Similar results to PAFFT were obtained for RAFFT, but the RMSEP value for ethyl acetate was 0.4 % w/w higher and required one less latent variable. Therefore both these methods were more effective at increasing the predictive ability of the spectra than COW, even though the spectra could not be fully aligned.

Table 5.13 - RMSEP values for PLS1 models built using dataset 3 without alignment (other than global alignment using the TMS peak), with alignment (by COW, PAFFT, RAFFT and *i*coshift) and with bucketing.

Alignment method	Toluene		Ethanol		Ethyl acetate	
	LVs	RMSEP/ (% w/w)	LVs	RMSEP/ (% w/w)	LVs	RMSEP/ (% w/w)
None	3	1.12	2	1.53	3	2.35
COW	3	1.24	4	1.81	4	1.43
PAFFT	3	1.27	4	1.27	4	0.73
RAFFT	3	1.34	4	1.15	3	1.11
***i*coshift**	3	0.90	4	2.47	4	2.92
Bucketing	4	0.51	4	0.43	3	0.62

Of the four alignment methods, only *i*coshift reduced the RMSEP value of toluene (by 0.1 % w/w). However *i*coshift exhibited the poorest performance for ethanol and ethyl acetate, increasing the RMSEP value of ethyl acetate by 0.6 % w/w and increasing the RMSEP value of ethanol by almost 1 % w/w. In addition, four latent variables were required for both these solvents. This may be because the segment lengths used in *i*coshift were larger than for the other methods (since they were manually defined in order to treat each spectral region separately), meaning that more peaks were present within each segment. If peaks within the segment shift to different extents, then alignment of all peaks will not be possible. Ethanol and ethyl acetate experienced greater peak overlap than toluene, therefore the *i*coshift algorithm experienced greater difficulty in aligning these components. PAFFT and RAFFT exhibited the overall best performance of the alignment methods for dataset 3, with PAFFT producing the lowest RMSEP value for ethyl acetate and RAFFT producing the lowest RMSEP value for ethanol.

The RMSEP values obtained for the bucketed spectra would be expected to be poor in this case, as all peak structure was lost. However the RMSEP values for all three solvents were low (≤ 0.62 % w/w), and the results were better than for any of the alignment methods (for which the lowest RMSEP values achieved were 0.90 % w/w for toluene, 1.15 % w/w for ethanol and 0.73 % w/w for ethyl acetate). This suggests that accurate predictions of concentration can still be obtained with only a few data points, as long as maxima corresponding to each component are present. Therefore it may be possible to perform accurate quantitative analysis with low resolution instruments. The ability to achieve low RMSEP values when large peak shifts were present further demonstrates the suitability of low-field NMR spectroscopy for quantitative analysis.

5.3.4 Dataset 4

PAFFT, RAFFT, *i*coshift and bucketing were then applied to the spectra in dataset 4, using the parameters optimised for dataset 3. COW was not included, as the computation time for COW was significantly longer than for the other methods (Table 5.8) and it was less effective at aligning the spectra in dataset 3. Example spectra of calibration sample 7 (containing equal concentrations of toluene, ethanol and ethyl

acetate) from datasets 3 and 4 are shown in Figure 5.25 to illustrate the differences between the datasets. The spectra of the rest of the samples in dataset 4 are displayed in Appendix 5. As for the toluene, octene and dibutyl ether datasets, the use of a sub-optimal shim to acquire the spectra has caused broadening of the peaks, a decrease in intensity and loss of fine structure.

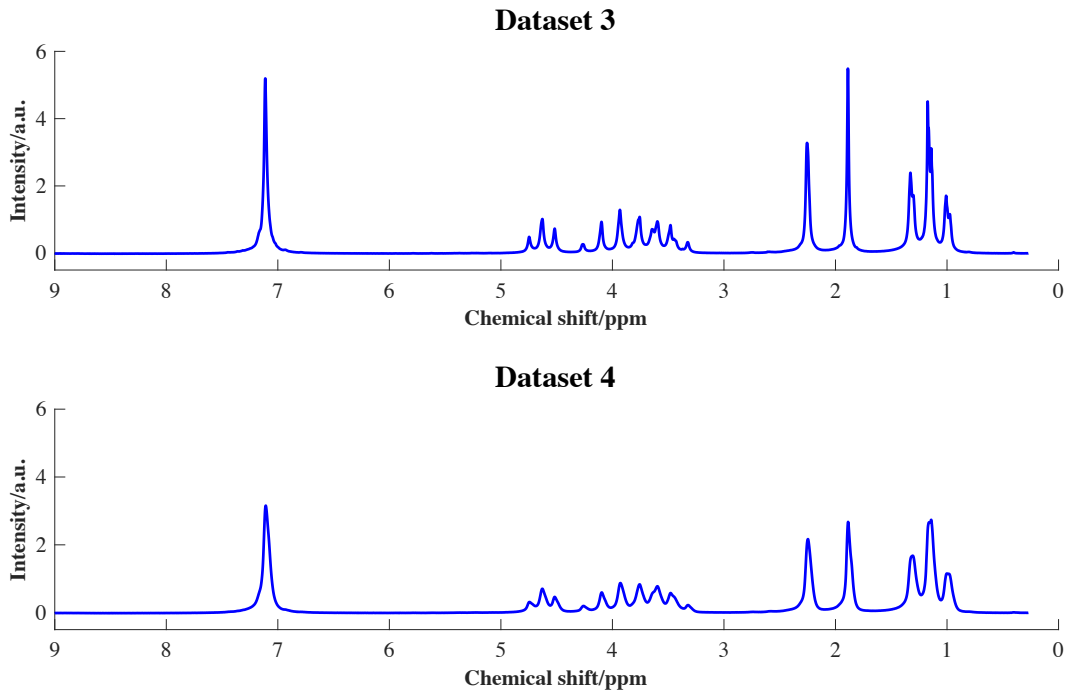

Figure 5.25 - ^{1}H low-field NMR spectrum of calibration sample 7 in datasets 3 and 4.

The RMSEP values obtained for the PLS1 models built using the spectra in dataset 4 without alignment (other than global alignment using the TMS peak), with alignment by PAFFT, RAFFT and *i*coshift, and with bucketing are displayed in Table 5.14. Without alignment, the RMSEP value for toluene was similar to that obtained for dataset 3, and the ethanol and ethyl acetate values were 0.14 % w/w and 0.31 % w/w lower respectively. This again suggests broadening of the peaks has removed some of the variation between the spectra, improving their predictive ability. However four rather than three latent variables were required for ethyl acetate.

PAFFT and RAFFT both decreased the RMSEP values for all solvents by 0.14 – 0.98 % w/w, with RAFFT performing slightly better for toluene and ethanol (by around 0.1 % w/w) and PAFFT performing slightly better for ethyl acetate (by

0.07 % w/w). Four latent variables were required for all solvents, an increase from the numbers required for toluene and ethanol before alignment. This indicates that the ineffectiveness of PAFFT and RAFFT at reducing the RMSEP values for dataset 2 was a result of the parameters used, rather than an inability of the method to align spectra of poorer lineshape. *i*coshift worsened the RMSEP values for all three solvents by 0.09 – 0.68 % w/w, and for ethanol a greater number of latent variables was required after *i*coshift (four compared to two). This corresponds to the results observed for dataset 3, confirming that *i*coshift is less effective than PAFFT or RAFFT when large peak shifts (of up to 1.5 ppm) are present, despite being effective for small amounts of peak shift (< 0.2 ppm).

Table 5.14 - RMSEP values for PLS1 models built using dataset 4 without alignment (other than global alignment using the TMS peak), with alignment (by PAFFT, RAFFT and *i*coshift) and with bucketing. Parameters optimised using dataset 3.

Alignment method	Toluene		Ethanol		Ethyl acetate	
	LVs	RMSEP/ (% w/w)	LVs	RMSEP/ (% w/w)	LVs	RMSEP/ (% w/w)
None	3	1.11	2	1.39	4	2.04
PAFFT	4	0.97	4	1.18	4	1.06
RAFFT	4	0.89	4	1.08	4	1.13
***i*coshift**	3	1.20	4	1.97	4	2.72
Bucketing	4	0.54	4	0.40	3	0.58

Bucketing again produced lower RMSEP values than any of the alignment methods (0.40 – 0.58 % w/w), as the variation in peak position between the spectra was eliminated. Therefore, although alignment was able to improve the predictive ability of the spectra when large peak shifts were present, bucketing was more effective despite the fact the bucketed spectra contained only twelve data points. However, in this work the analytes were chosen so that each had a clearly distinguishable peak, and bucketing may not produce such accurate predictions of concentration when greater amounts of peak overlap are present.

5.3.5 Bucketing of Overlapping Spectra

To determine whether bucketing is as effective at removing variations in peak position between spectra which exhibit greater amounts of overlap than the ternary mixtures used in this work, optimised bucketing was also applied to the esterification reaction mixture spectra presented in section 4.3.4.2. The resulting spectra are displayed in Figure 5.26. When the optimum bucketing parameters for dataset 1 (a bucket size of 0.1 ppm with a slackness value of 1) were applied to these spectra, the bucket size was clearly too small to remove the shifts of the acetic acid OH peak (present just below 6 ppm, just above 8 ppm and just below 9 ppm). At this bucket size, acetic acid, butanol and butyl acetate could still be resolved but the acetic anhydride singlet peak at 2.2 ppm was combined with the butyl acetate and acetic acid singlet peaks just above 2 ppm. Therefore acetic anhydride could no longer be resolved from the other components.

The optimum bucketing parameters for dataset 3 (a bucket size of 0.75 ppm with a slackness value of 0.25) were also insufficient to remove the shifts of the OH peak. When these parameters were applied, the butanol and butyl acetate multiplets around 4 ppm were combined, so none of the components other than acetic acid could be resolved. Increasing the bucket size to 1 ppm still did not remove the OH peak shifts (with the peak present at around 6.6 ppm after 5 minutes and around 8.5 ppm after 30 minutes and one hour). At this bucket size, almost all other spectral information has been lost and it was again not possible to distinguish any of the components other than acetic acid. Therefore quantitative analysis using such spectra would not be possible. These results confirm that for spectra exhibiting greater overlap than the ternary mixtures used in this work, bucketing is not suitable for removing peak shifts and the use of alignment methods is necessary.

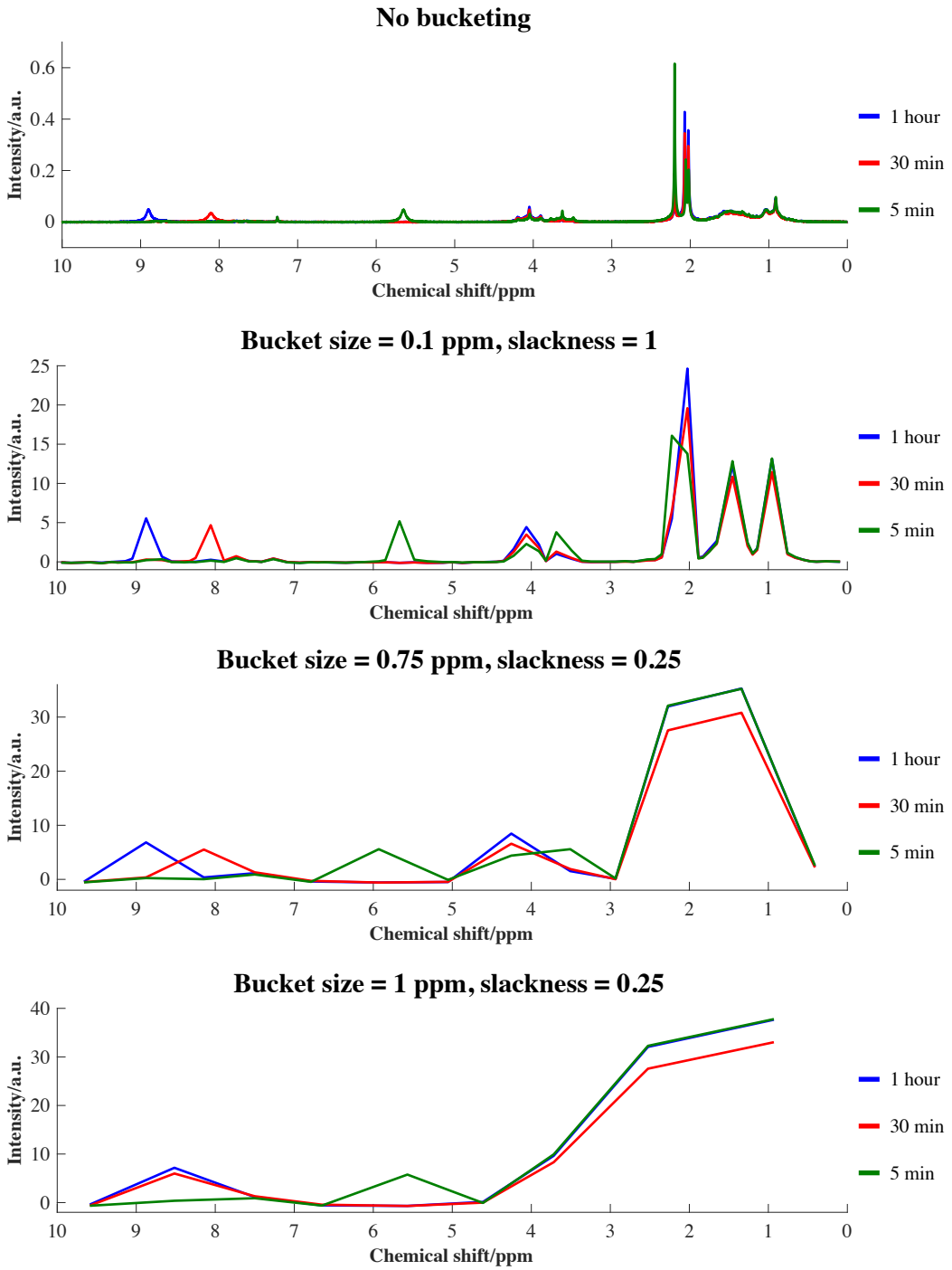

Figure 5.26 - Low-field ^{1}H NMR spectra of esterification reaction mixture samples in chloroform, extracted at 5 minutes, 30 minutes and 1 hour after the addition of butanol; without bucketing and with bucketing using three different sets of parameters.

5.4 Conclusions

Although none of the alignment methods were able to fully align the low-field NMR spectra when peak shifts of up to 1.5 ppm were present, it was still possible to improve the performance of PLS using alignment. This demonstrates the suitability of the spectrometer for quantitative analysis, as it was possible to achieve low RMSEP values for spectra exhibiting both little (< 0.2 ppm) and large (up to 1.5 ppm) amounts of peak shift. Of the alignment methods examined, RAFFT and PAFFT performed best overall. However, RAFFT and PAFFT did not perform particularly well for dataset 2. This is likely to be due to the parameters chosen, which were optimised for dataset 1. The requirement for optimisation of the parameters is a disadvantage of PAFFT, RAFFT and COW, as optimisation can be time consuming and the optimum parameters for spectra collected under different conditions may vary.

A major advantage of *i*coshift is that it is not necessary to optimise parameters such as segment length or shift. *I*coshift performed best of the alignment methods when peak shifts of less than 0.2 ppm were present (especially for dataset 2), but was not effective when large amounts of peak shift and overlap were present. This is likely to be because the spectra were split into four manually defined segments (to avoid the introduction of artefacts, which can occur when peaks are split across different segments), meaning that the segments used in *i*coshift were larger than for the other methods.

Although COW was relatively effective at aligning peaks (except when large shifts of up to 1.5 ppm were present), the distortion of peaks tended to decrease the predictive ability of the spectra. In addition COW was significantly slower than PAFFT, RAFFT, *i*coshift and bucketing, sometimes taking several hours rather than seconds or minutes to perform the computation. RSPA was not effective due to the inability to alter parameters within the algorithm which was used, but if the parameters could be altered as described by Veselkov et al.[12] then the method may be more effective. However it is unlikely that RSPA would be able to align the large amounts of peak shift present in the toluene, ethanol and ethyl acetate mixture spectra due to its similarity to RAFFT. In addition, RSPA was also significantly slower than PAFFT, RAFFT, *i*coshift and bucketing (taking 40 seconds to perform, compared to 2 seconds or less).

Optimised bucketing was able to significantly improve the predictive ability of the spectra for both datasets (producing RMSEP values ≤ 0.75 % w/w for all models), as it eliminated the peak shifts between the spectra. However bucket sizes of 0.75 ppm were necessary when large peak shifts were present, so the majority of the spectral information was lost. Despite this, bucketing of the spectra produced more accurate predictions than alignment. The application of bucketing to the esterification reaction mixture spectra suggested that bucketing would not be as effective at removing peak shifts between spectra exhibiting greater overlap. Therefore the alignment methods evaluated in this work would be more suitable. Analysis of the variance between the results obtained using each alignment method could be carried out next, in order to determine how significant the observed differences were. In addition, the combination of bucketing and alignment could be investigated.

5.5 References

1. T. N. Vu and K. Laukens, *Metabolites*, 2013, **3**, 259–276.
2. L. R. Euceda, G. F. Giskeodegard and T. F. Bathen, *Scand. J. Clin. Lab. Invest.*, 2015, **75**, 193–203.
3. F. Savorani, G. Tomasi and S. B. Engelsen, *J. Magn. Reson.*, 2010, **202**, 190–202.
4. S. A. A. Sousa, A. Magalhães and M. M. C. Ferreira, *Chemom. Intell. Lab. Syst.*, 2013, **122**, 93–102.
5. K. H. Liland, *Trends Anal. Chem.*, 2011, **30**, 827–841.
6. N. P. V. Nielsen, J. M. Carstensen and J. Smedsgaard, *J. Chromatogr. A*, 1998, **805**, 17–35.
7. D. P. Killeen, O. C. Watkins, C. E. Sansom, D. H. Andersen, K. C. Gordon and N. B. Perry, *Phytochem. Anal.*, 2017, **28**, 50–57.
8. M. Kompany-Zareh, S. Gholami and B. Kaboudin, *J. Chromatogr. A*, 2012, **4**, 162–170.
9. S. Masoum, C. Malabat, M. Jalali-Heravi, C. Guillou, S. Rezzi and D. N. Rutledge, *Anal. Bioanal. Chem.*, 2007, **387**, 1499–1510.
10. J. W. H. Wong, C. Durante and H. M. Cartwright, *Anal. Chem.*, 2005, **77**, 5655–5661.

11. T. G. Bloemberg, J. Gerretzen, A. Lunshof, R. Wehrens and L. M. C. Buydens, *Anal. Chim. Acta*, 2013, **781**, 14–32.
12. K. A. Veselkov, J. C. Lindon, T. M. D. Ebbels, D. Crockford, V. V. Volynkin, E. Holmes, D. B. Davies and J. K. Nicholson, *Anal. Chem.*, 2009, **81**, 56–66.
13. R. B. Gil, R. Lehmann, P. Schmitt-Kopplin and S. S. Heinzmann, *Anal. Bioanal. Chem.*, 2016, **408**, 4683–4691.
14. N. MacKinnon, W. Ge, A. P. Khan, B. S. Somashekar, P. Tripathi, J. Siddiqui, J. T. Wei, A. M. Chinnaiyan, T. M. Rajendiran and A. Ramamoorthy, *Anal. Chem.*, 2012, **84**, 5372–5379.
15. Y. B. Monakhova and B. W. K. Diehl, *J. Am. Oil Chem. Soc.*, 2016, **93**, 27–36.
16. M. O. Salazar, P. L. Pisano, M. G. Sierra and R. L. E. Furlan, *Microchem. J.*, 2018, **141**, 264–270.
17. J. Y. Jeong, *Korean J. Agric. Sci.*, 2018, **45**, 455–461.
18. L. Le Moyec, L. Mille-Hamard, M. N. Triba, C. Breuneval, H. Petot and V. L. Billat, *Anal. Bioanal. Chem.*, 2012, **404**, 593–602.
19. M. Boiani, U. Sundekilde, L. M. Bateman, D. G. McCarthy, A. R. Maguire, A. Gulati, T. P. Guinee, M. Fenelon, D. Hennessy, R. J. FitzGerald and P. M. Kelly, *Int. Dairy J.*, 2019, **91**, 155–164.
20. S. Kern, K. Meyer, S. Guhl, P. Grasser, A. Paul, R. King and M. Maiwald, *Anal. Bioanal. Chem.*, 2018, **410**, 3349–3360.
21. E. R. McCarney, R. Dykstra and P. Galvosas, *Magn. Reson. Imaging*, 2019, **56**, 103–109.
22. J. M. Staab, T. M. O'Connell and S. M. Gomez, *BMC Bioinf.*, 2010, **11**, 123.
23. The University of New South Wales, SpecAlign - processing and alignment of spectral datasets, https://powcs.med.unsw.edu.au/research/adult-cancer-program/services-resources/specalign, (accessed 20th July, 2018).
24. Imperial College London, IMPaCTS - Imperial Metabolic Profiling and Chemometrics Toolbox for Spectroscopy: CSM RSPA, https://csmsoftware.github.io/docs/impacts/csm_rspa.html, (accessed 23rd July, 2018).

25. University of Copenhagen, Quality and Technology - The home page of chemometrics and spectroscopy, http://www.models.life.ku.dk, (accessed 14th March, 2018).
26. Instituto de química - Universidade Estadual de Campinas, Laboratório de Quimiometria Teórica e Aplicada, http://lqta.iqm.unicamp.br, (accessed 29th May, 2018).

6 Evaluation of Calibration Transfer and Reference Deconvolution as a Solution to Lineshape Deterioration in Low-Field NMR Spectroscopy

6.1 Introduction

The reduced size and cost of low-field NMR spectrometers make them far more suitable for use in process monitoring than high-field instruments, however there are a number of instrumental issues which may arise, and these can have a detrimental effect on the spectra. Variations in the magnetic field can occur over time, and shimming is performed in order to correct for these variations. However if the magnetic field varies between shimming then the saved shim settings will no longer correct the inhomogeneities present.[1, 2] The magnets used in low-field NMR spectrometers are sensitive to temperature and the temperature of the magnet is controlled to the order of thousandths of a degree Celsius. Any deviations caused by variation in room temperature or sample temperature can therefore cause the performance of the instrument to deteriorate.[1, 3]

Deviations from the optimum operating conditions of the instrument can have a number of effects on the spectra, such as broadening and reduction in the intensity of peaks, deterioration in lineshape and loss of fine structure, and shifts in peak position. In extreme cases, the lock signal may be lost or inhomogeneities in the magnetic field may become so severe that shimming must be performed again. Therefore the instrumental stability of the low-field NMR spectrometer used in Chapter 5 was investigated in this chapter, to examine the deterioration of its performance over time.

Spectra acquired under different conditions may vary in lineshape, for example if a different instrument is used, if the magnetic field drifts over the course of analysis (e.g. during the monitoring of a long process when shimming might be challenging) or if an instrument is unable to obtain the same lineshape on different days. The instrument used in this work is capable of obtaining similar lineshapes on different days (as shown in Table 5.3), therefore previously saved shims which are no longer optimal were loaded in order to produce spectra of different lineshapes, as described in Chapter 5. This simulates the effect of acquiring spectra on different instruments. The ability to

apply a model built under one set of conditions (e.g. one instrument) to spectra collected under a different set of conditions (e.g. a different instrument) would save time and resources, as it would prevent the need to re-analyse every calibration sample under the new set of conditions. Thus in this chapter two different methods, reference deconvolution and calibration transfer, will be compared for the elimination of differences between low-field NMR spectra of different lineshapes.

6.1.1 Reference Deconvolution

Reference deconvolution (described in section 2.3.4) is commonly used to improve the lineshape of peaks in NMR spectra. It has been utilised in both high-field[4-7] and low-field NMR spectroscopy.[1, 8] In order to perform reference deconvolution, it is necessary for a reference peak to be present in every sample. Usually a singlet peak is chosen, as reference deconvolution is unable to supply information when the reference signal falls to zero in the time domain (i.e. within multiplets), but it is also possible to perform interpolation to allow the use of multiplet reference signals.[9] However the reference signal must be well-resolved, and artefacts can be introduced if the reference peak is contaminated by other signals in the spectrum.[4] Therefore unless a suitable reference peak is present in every spectrum, the addition of a standard is required, which inhibits the use of reference deconvolution in on-line reaction monitoring. Artefacts can also be introduced due to truncation of the reference signal, baseline errors, random noise or temperature gradients within the sample. In addition, reference deconvolution is only able to correct for errors in linewidth which are the same for all signals in the spectrum.[4, 9]

The ideal reference signal is usually based on either a Lorenzian lineshape, a Gaussian lineshape or a combination of the two. A line broadening factor can also be applied to the ideal lineshape in order to increase or decrease the widths of the peaks in the spectrum. Increasing the linewidth can improve the signal to noise ratio of the spectrum at the cost of resolution, and decreasing the linewidth has the opposite effect.[4, 6] Ebrahimi et al.[6] have demonstrated that for high-field ^{1}H NMR spectra of metabolites, reference deconvolution produces more accurate predictions of concentration than the application of line broadening alone.

6.1.2 Calibration Transfer

An alternative to reference deconvolution is calibration transfer, described in section 2.3.3, which has been used extensively in optical spectroscopy.[10, 11] Calibration transfer by methods such as SST, DS and PDS (detailed in section 2.3.3) involve analysing a small number of calibration samples under each set of conditions in order to calculate a transfer function, which can then be used to correct the lineshape of the peaks. This allows a calibration model built under one set of conditions to be applied to spectra collected under a different set of conditions. The main advantage of calibration transfer over reference deconvolution is that the presence of a well resolved reference peak is not necessary. In addition, it is able to correct for differences other than linewidth, e.g. intensity changes.[12] However a limitation is that the effectiveness of the method depends on the choice of samples used to calculate the transfer function, and these samples must be representative of the dataset as a whole. In complex mixtures, some components may be underrepresented or absent from the transfer samples, so calibration transfer will not be effective for these components.[12, 13] The shifting of peaks of the same component between samples may also mean that the component is no longer accurately represented by the model, as shifted peaks may no longer be recognised as the same component.

Calibration transfer is not widely used in NMR spectroscopy, but some examples have been demonstrated. At high field, DS and PDS have been demonstrated for the transfer of calibration models between different NMR spectrometers and instrumental configurations,[12, 14] and these methods have also been compared to double-window PDS (an extension of the PDS method involving two windows)[13] and hybrid calibration (in which the FIDs from each instrument are added together and the regression vector recalculated).[11] DS, PDS and double-window PDS were all found to be effective. PDS produced the lowest RMSEP values for the transfer of PLS models built for authenticity control of sunflower lecithin between different instruments, with DS producing comparably low RMSEP values but introducing noise into the spectra. Hybrid calibration was the least effective of the methods.[11] For the transfer of PLS models built with metabolic data acquired using different instrumental configurations, DS was found to be more effective than PDS, but required a greater number of transfer samples.[13]

At low field, DS, PDS and hybrid calibration have been compared for the transfer of calibration models between a measured set of FIDs and the same set of FIDs with alterations made to simulate a different instrument.[15] PDS was found to be the most effective method. However, the instrument only provided information in the time domain. In the study carried out by Alam et al.,[13] reference deconvolution was applied as a preprocessing technique before calibration transfer (by DS, PDS and double-window PDS) at high field, and this was found to be more effective for the prediction of metabolite concentrations than the application of reference deconvolution alone. However calibration transfer alone has not been compared to reference deconvolution at high field, and no comparisons have been performed at low field.

The aims of this chapter are to investigate the instrumental stability of the low-field NMR spectrometer and to compare the effectiveness of calibration transfer and reference deconvolution to correct for differences between low-field NMR spectra collected under different conditions. The combination of reference deconvolution and calibration transfer was also evaluated. In addition, the ability of reference deconvolution to eliminate short-term variation between spectra collected under the same conditions was investigated.

6.2 Experimental

6.2.1 Instrumental Stability

6.2.1.1 Stability Over Time

In order to examine the extent of peak shift and linewidth deterioration over time and to determine the cause of these issues, an investigation into the instrumental stability of the Magritek Spinsolve Carbon NMR spectrometer (with a proton channel operating at 43 MHz) used in Chapter 5 was performed. The stability of the instrument over time was first monitored, using a single sample which was not removed from the spectrometer between spectral acquisitions. This will determine whether any changes observed upon the consecutive analysis of samples can be attributed to the insertion and removal of the samples from the instrument.

A sample of methanol (ISOTEC NMR reference standard for low temperature calibration, supplied by Sigma Aldrich, Steinheim, Germany) was inserted into the

instrument and a ^{1}H NMR spectrum was measured every hour over a period of 63 hours. The parameters used were the same as for the solvent mixture analysis described in section 5.2.1, however in this case each measurement was a single scan consisting of 32,768 data points, and was zero filled to 524,288 data points so that the positions of the maxima of the peaks could be determined as accurately as possible. The instrument was operated via Spinsolve Expert software, as before.

The experiment was carried out after the instrument had been switched off for a couple of weeks over the Christmas break (after shimming to obtain a sufficiently narrow linewidth of < 0.5 Hz) in order to measure the deterioration of the linewidth over time, and was repeated a week later using the same parameters. The linewidth of each peak in the methanol spectrum at 50 % of the peak height was calculated, and used to compare the stability of the instrument during each experiment.

6.2.1.2 Sample Temperature

As sample temperature can affect the spectrum obtained,[16] the length of time taken for the temperature of a sample to reach the temperature of the magnet was measured. The methanol sample was used, as it is possible to calculate the temperature of methanol from the chemical shift separation of the peaks in its ^{1}H NMR spectrum.[17] The sample was inserted into the instrument at room temperature and its ^{1}H NMR spectrum was measured every 30 seconds for 20 minutes. The experiment was carried out using the standard Spinsolve software rather than Spinsolve Expert in order for the magnet temperature to be observed. The standard software allows less flexibility in altering the instrumental parameters, but the magnet temperature cannot be recorded using Spinsolve Expert. A receiver gain value of 28 dB, dwell time of 200 µs, acquisition delay of 39.47958 µs, bandwidth of 5 kHz and 90° pulse duration of 11.1 µs were used. For each measurement, a single scan consisting of 32,768 data points was collected and zero filled to 524,288 data points (in order to determine the positions of the maxima of the peaks as accurately as possible). Zero order phase correction was automatically applied by the software, optimised for each spectrum.

The experiment was then repeated using the same procedure as for the solvent mixture analysis described in Chapter 5. The tube containing the methanol sample was cooled in the freezer at approximately –20 °C for an hour, then removed from freezer and

heated in a water bath at approximately 30 °C for two minutes before insertion into the spectrometer. This should confirm whether the solvent mixture samples had been left in the instrument for a sufficient length of time before analysis.

The ^{1}H NMR spectrum of methanol consists of two singlet peaks (corresponding to the CH_3 and OH groups), and for each measured spectrum, the chemical shift difference between the maxima of the two peaks was measured. The sample temperature was then calculated using Equation 6.1, as described by Ammann et al.[17] (where $\Delta\delta$ is the chemical shift difference between the two peaks in the spectrum of methanol).

$$T\,(K)\,(\text{methanol}) = 409.0 - 36.54\,\Delta\delta - 21.85\,(\Delta\delta)^2 \qquad \textbf{Equation 6.1}$$

6.2.1.3 Magnet Temperature

It was hypothesised that the insertion/removal of samples may affect the temperature of the magnet, which can produce deterioration in peak shape and linewidth. To examine the effect of insertion/removal of samples on the magnet temperature, the calibration samples from the toluene, octene and dibutyl ether dataset (Table 5.1) were analysed as described in section 5.2.1, while recording the temperature of the magnet.

The standard Spinsolve software was used, with the settings described in section 6.2.1.2. For each measurement, a single scan consisting of 32,768 data points was collected and zero filled to 65,536 data points in order to improve the digital resolution of the spectra. Zero order phase correction was again automatically applied by the software, optimised for each spectrum. Measurements of magnet temperature were acquired every minute and smoothing was performed using the "smooth" function in the MATLAB 2016b (MathWorks, Massachusetts, USA) Curve Fitting Toolbox 3.5.4. The Savitzky-Golay method was used, with 21 data points included in the calculation.

The temperature of the magnet was also recorded over a 24 hour period when the instrument was not in use, for reference. In this case, measurements of magnet temperature were acquired every 15 seconds. Smoothing was performed as before, with 81 data points included in the calculation (since the measurements were acquired four times more frequently than in the previous experiment).

6.2.2 Short-Term Variation

6.2.2.1 Toluene, Octene and Dibutyl Ether Mixtures

To correct for the short-term variation of low-field NMR spectra (i.e. changes which occur between spectra of the same dataset during the course of analysis), reference deconvolution can be applied. The low-field ^{1}H NMR datasets detailed in Chapter 5 were used, and the toluene, octene and dibutyl ether mixtures (which exhibited < 0.2 ppm of peak shift) will be discussed first. The compositions of the mixtures, which were split into calibration and test samples, were given in Table 5.1 and Table 5.2. The samples were analysed under two different sets of conditions; a shim optimised before analysis (dataset 1) and a loaded shim which was not optimal (dataset 2). Details of the acquisition of these datasets and the differences in lineshape present were given in section 5.2.1. For both datasets, the same method of analysis was applied to all spectra.

Reference deconvolution was performed on each spectrum in MATLAB 2016b, using code from the GNAT software package.[18] The region from –0.2 ppm to 0.2 ppm (in which the TMS peak was present), consisting of 230 data points, was used as the reference peak in each spectrum. The ideal lineshape was based on a Lorentzian curve with a line broadening factor of 1 Hz. Ebrahimi et al.[6] state that the use of a Lorentzian target lineshape with a width close to that of the experimental reference peak should allow errors to be corrected without significantly altering the appearance of the spectrum. Therefore a line broadening factor of 1 Hz was used, since this linewidth (at 50 % peak height) is the threshold below which the performance of the instrument is considered acceptable when shimming is performed in Spinsolve.

For each dataset, PLS1 models were built in PLS Toolbox version 8.6.2 (Eigenvector, Washington, USA) with the deconvoluted calibration spectra and used to predict the concentration (in % w/w) of each solvent present in the corresponding deconvoluted test spectra. RMSEP values (Equation 2.8) were then calculated to assess the predictive abilities of the models. The number of latent variables to include in each PLS1 model was determined by examination of the RMSEP values obtained using one to ten latent variables. Before PLS was performed, the spectra were globally aligned to the TMS peak and the spectral regions below 0.27 ppm and above 9.35 ppm were

removed to eliminate the TMS peak and reduce the size of the dataset. The linewidth at 50 % peak height of the toluene singlet peak at 7 ppm was measured for the test samples, and the mean and standard deviation values obtained for each dataset with and without reference deconvolution were compared. This peak was chosen as it is a well-resolved singlet.

Alignment of the deconvoluted spectra was performed using *i*coshift, as described in section 5.2.2. *I*coshift was chosen over the other alignment methods as it produced the overall lowest RMSEP values for the toluene, octene and dibutyl ether mixtures. Although other alignment methods such as RAFFT could equally have been used, the method which gave the overall lowest RMSEP values for each dataset was chosen, as this information was already available based on the comparison carried out in Chapter 5. Optimised bucketing was also performed after reference deconvolution, using the optimised bucket widths obtained for dataset 1 without reference deconvolution, as described in section 5.2.3. PLS1 models were built and the RMSEP values were used to compare the models.

The same analysis method was then repeated for dataset 2. When bucketing was performed, the optimised bucket widths obtained for dataset 1 without reference deconvolution were applied to the deconvoluted spectra of dataset 2.

6.2.2.2 Toluene, Ethanol and Ethyl Acetate Mixtures

Reference deconvolution was then applied to the toluene, ethanol and ethyl acetate spectra (which exhibited up to 1.5 ppm of peak shift) in datasets 3 and 4 using the same procedure as for datasets 1 and 2, in order to correct for variation within each dataset. Dataset 3 was acquired using an optimal shim and dataset 4 was acquired using a loaded sub-optimal shim. Further details are given in section 5.2.1.

After the application of reference deconvolution, alignment was performed using RAFFT. RAFFT was chosen based on the results of Chapter 5, as RAFFT and PAFFT were found to produce the lowest RMSEP values for this mixture set and RAFFT required fewer latent variables than PAFFT in several cases. The RAFFT parameters optimised for dataset 3 without reference deconvolution, as described in section 5.2.2, were applied to the deconvoluted spectra from datasets 3 and 4. Bucketing was also

performed after reference deconvolution using the optimised bucket widths obtained for dataset 3 without reference deconvolution, as described in section 5.2.3.

6.2.3 Long-Term Variation

6.2.3.1 Toluene, Octene and Dibutyl Ether Mixtures

Both calibration transfer and reference deconvolution can be used to correct for long-term variation of spectra (i.e. variation between different datasets). Calibration transfer was performed in order to make the toluene, octene and dibutyl ether spectra in dataset 2 resemble those in dataset 1. The spectra of calibration samples 1 – 3 and 8 – 10 in each dataset were used to calculate a transfer function by SST. This subset of samples was chosen to symmetrically span the range of the ternary diagram displayed in Figure 5.1, in order for each solvent to be represented equally, and included the three pure component samples and three ternary mixtures. SST was chosen as the method of calibration transfer to use, since it had been found to be more effective than DS for the transfer of MIR spectra between different instruments in Chapter 3 and was easier to implement than PDS.

SST was performed in MATLAB 2016b (MathWorks, Massachusetts, USA) with the algorithm described by Du et al. (without scaling),[19] using each possible number of singular values from one to ten. The spectral regions below 0.27 ppm and above 9.35 ppm were removed prior to calibration transfer. The transfer function was then applied to the test spectra in dataset 2. PLS1 models were built in PLS Toolbox using the calibration spectra in dataset 1, and used to predict the concentration (in % w/w) of each component present in the transferred test spectra of dataset 2. RMSEP values were calculated as before, and these values were used to assess the effectiveness of calibration transfer. The PLS1 models were also used to predict the concentration of each component present in the test spectra of dataset 2 without SST, and the predictions obtained without and with SST were compared. The optimum number of singular values to include in the SST calculation was determined by comparison of the RMSEP values obtained for the PLS1 models when each number of singular values from one to ten were used. The plots of RMSEP versus number of singular values can be found in Appendix 6.

Calibration transfer was initially performed on the spectra without alignment (which had been aligned globally using the TMS peak as described in section 5.2.2 but to which no alignment method had been applied), and was then repeated after alignment by *i*coshift and after optimised bucketing (as described in section 6.2.2.1). PLS1 models were built using the aligned/bucketed spectra from dataset 1, and applied to the aligned/bucketed test spectra from dataset 2 (with and without SST). The width at 50 % peak height of the toluene singlet peak at 7 ppm was measured for the test spectra in dataset 1, dataset 2 without SST, dataset 2 with SST, and dataset 2 with alignment and SST. For each set of test spectra, the mean and standard deviation of these widths were calculated.

As a comparison to SST, reference deconvolution was also used to correct for variation between the datasets. Reference deconvolution was performed as described in section 6.2.2.1, but in this case, the PLS1 models were built with the deconvoluted calibration spectra from dataset 1 and used to predict the concentration of each solvent present in the deconvoluted test spectra from dataset 2. This procedure was repeated with *i*coshift performed after reference deconvolution, then with optimised bucketing performed after reference deconvolution. The RMSEP values obtained for bucketing alone were also compared to those obtained for SST and for reference deconvolution, in order to assess the effectiveness of bucketing at removing the variation between the datasets.

The combination of reference deconvolution and calibration transfer was then examined, in order to assess the effect of applying both methods. SST was repeated with the spectra obtained by reference deconvolution, using the same procedure as for the spectra without reference deconvolution. The analysis was again performed without alignment, with alignment by *i*coshift and with optimised bucketing. *I*coshift and bucketing were applied after reference deconvolution, but before SST. A summary diagram of the analysis methods applied to the toluene, octene and dibutyl ether mixture spectra is displayed in Figure 6.1.

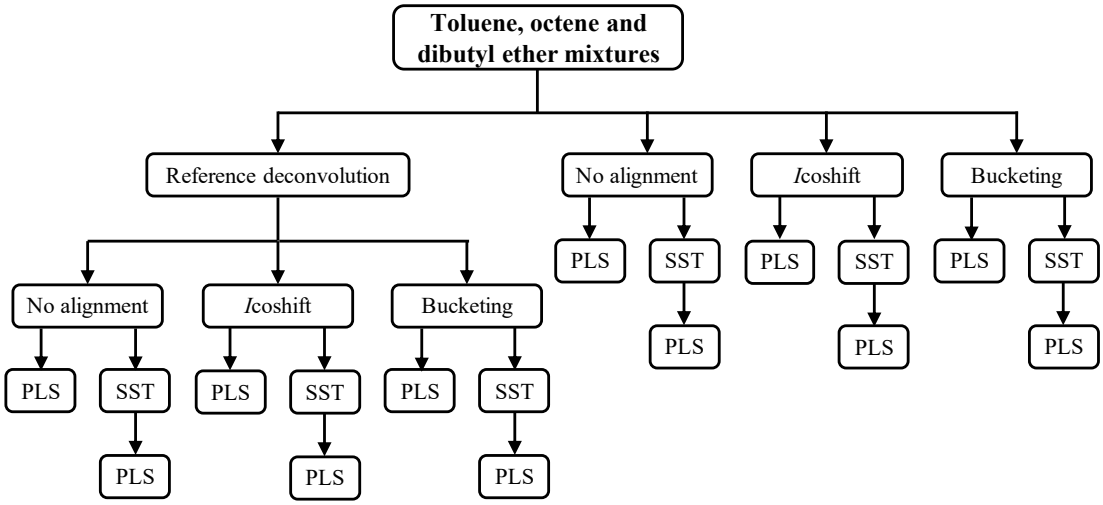

Figure 6.1 - Summary of analysis methods applied to ^{1}H low-field NMR spectra of toluene, octene and dibutyl ether mixtures

6.2.3.2 Toluene, Ethanol and Ethyl Acetate Mixtures

Calibration transfer between the toluene, ethanol and ethyl acetate spectra in datasets 3 and 4 was then performed using the procedure described in section 6.2.3.1 (with dataset 3 in place of dataset 1 and dataset 4 in place of dataset 2). PLS1 models were built as before, with the calibration spectra from dataset 3, and used to predict the concentrations of each solvent present in the test spectra from dataset 4. For these datasets, RAFFT was used to align the spectra as described in section 6.2.2.2. Reference deconvolution was performed as for the toluene, octene and dibutyl ether mixtures (section 6.2.3.1), and the analysis was repeated with RAFFT performed prior to PLS and optimised bucketing performed prior to PLS, as before.

Bucketing was not performed prior to SST for these mixtures, as the optimum bucket size determined in Chapter 5 was large enough to remove the differences between datasets 3 and 4, therefore calibration transfer would no longer be necessary. The effect of bucketing after reference deconvolution will still be examined for this dataset, however, as reference deconvolution changes the shape of the peaks so the results of bucketing may be different. The effectiveness of bucketing at removing the variation between the datasets was also compared to that of calibration transfer and reference deconvolution.

SST was then repeated with the spectra obtained by reference deconvolution, using the same procedure as before. The analysis was performed using the spectra without alignment, and repeated using the spectra aligned by RAFFT (with RAFFT performed after reference deconvolution but before SST). A summary of the analysis methods applied to the toluene, ethanol and ethyl acetate mixture spectra is given in Figure 6.2.

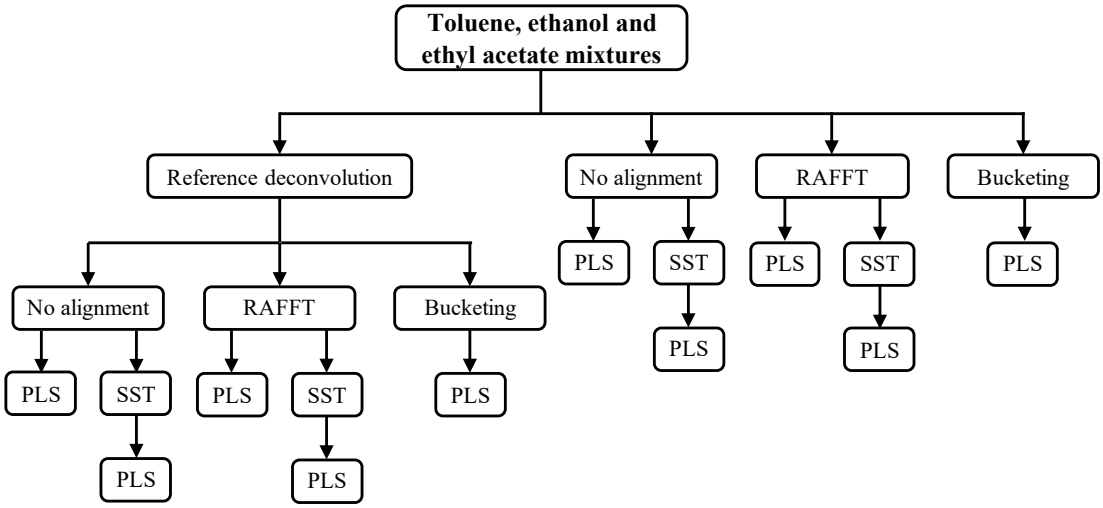

Figure 6.2 - Summary of analysis methods applied to ^{1}H low-field NMR spectra of toluene, ethanol and ethyl acetate mixtures

6.3 Results and Discussion

6.3.1 Instrumental Stability

6.3.1.1 Stability Over Time

To investigate the stability of the low-field NMR spectrometer, the spectra of methanol collected over time were evaluated. The methanol spectra collected every hour over a period of 63 hours after the instrument had recently been switched off are shown in Figure 6.3. A shift in peak position (of around 0.1 ppm) and a decrease in peak height (of up to 5 a.u.) can be observed over the course of analysis. When the experiment was repeated a week later (Figure 6.4), the spectra did not appear to change over time. Figure 6.5 displays the linewidths at 50 % height for each of the two peaks. In the first experiment, the linewidth increased by up to 0.06 ppm over the course of the experiment, indicating rapid deterioration of performance as the homogeneity of the magnetic field decreased. After the instrument had been on for a week, however, the

linewidth remained relatively stable over the course of the experiment and an improvement of up to 0.005 ppm could even be observed with time.

These results demonstrate that the stability of the instrument greatly deteriorates after it has been switched off, and despite being able to achieve desirable linewidths by shimming after it has been turned back on, the performance will not last. It is therefore necessary for the spectrometer to remain on for a period of several days before use. The stability of the linewidths observed in the second experiment demonstrate that the instrument is capable of achieving reproducible results over time, indicating that any deterioration observed during consecutive analysis of different samples can be attributed to the insertion/removal of the samples from the instrument.

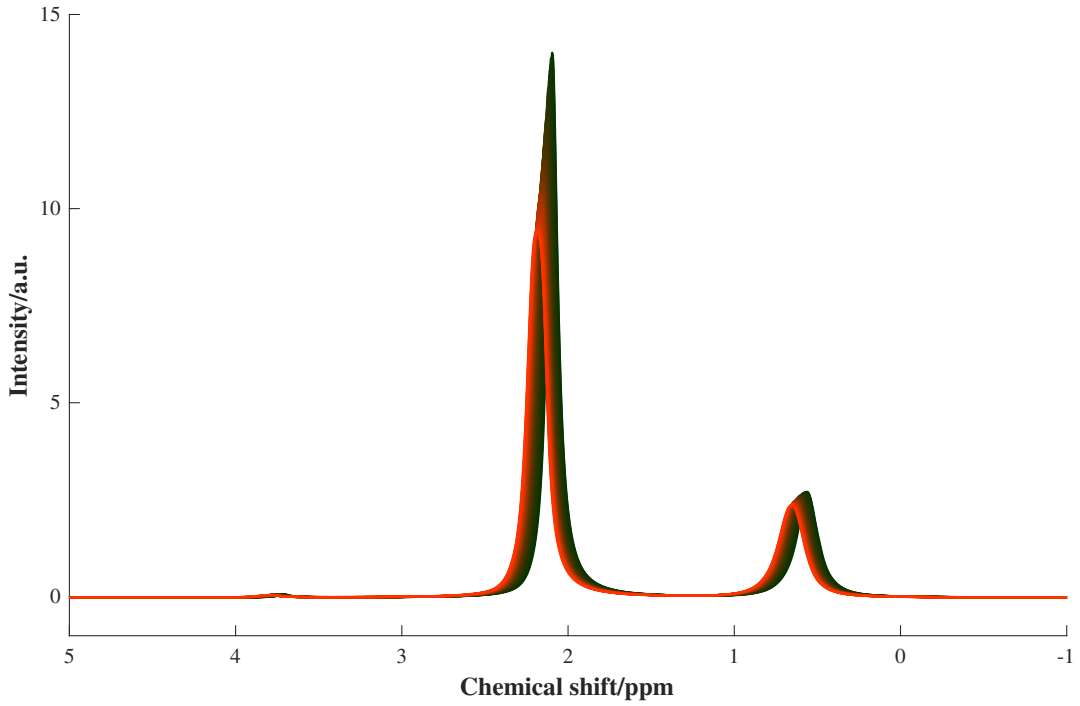

Figure 6.3 - Low-field ^{1}H NMR spectra of methanol collected every hour for 63 hours when the instrument had just been switched on (black represents the start of the experiment and red represents the end of the experiment).

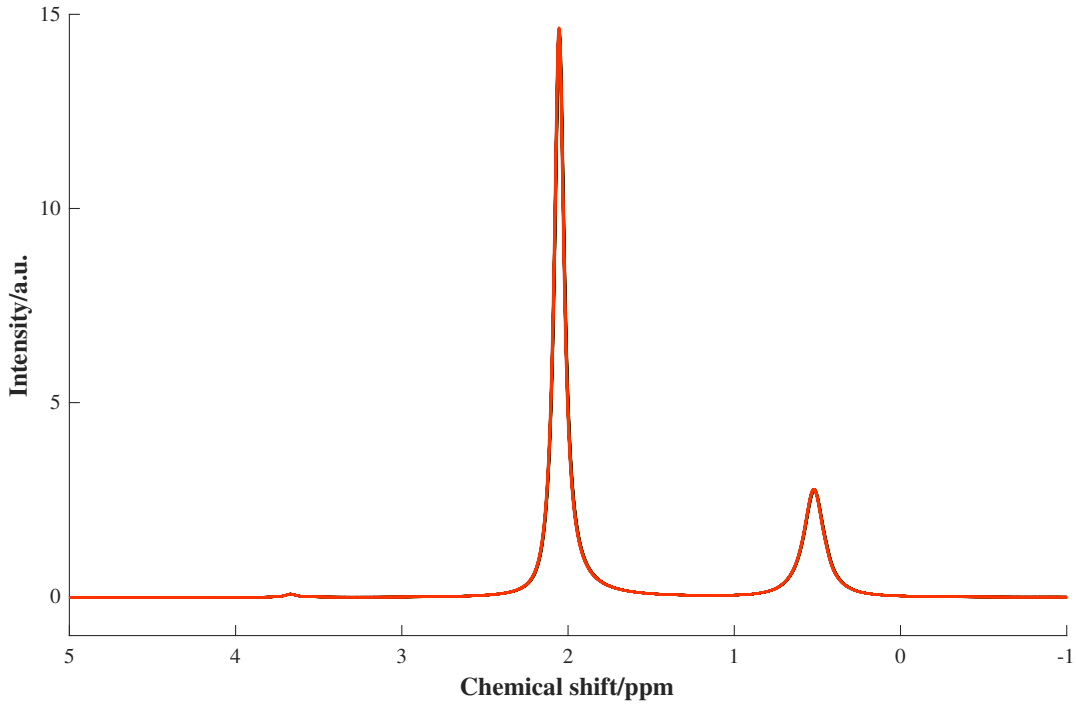

Figure 6.4 - Low-field ^{1}H NMR spectra of methanol collected every hour for 63 hours one week after the instrument had been switched on (black represents the start of the experiment and red represents the end of the experiment).

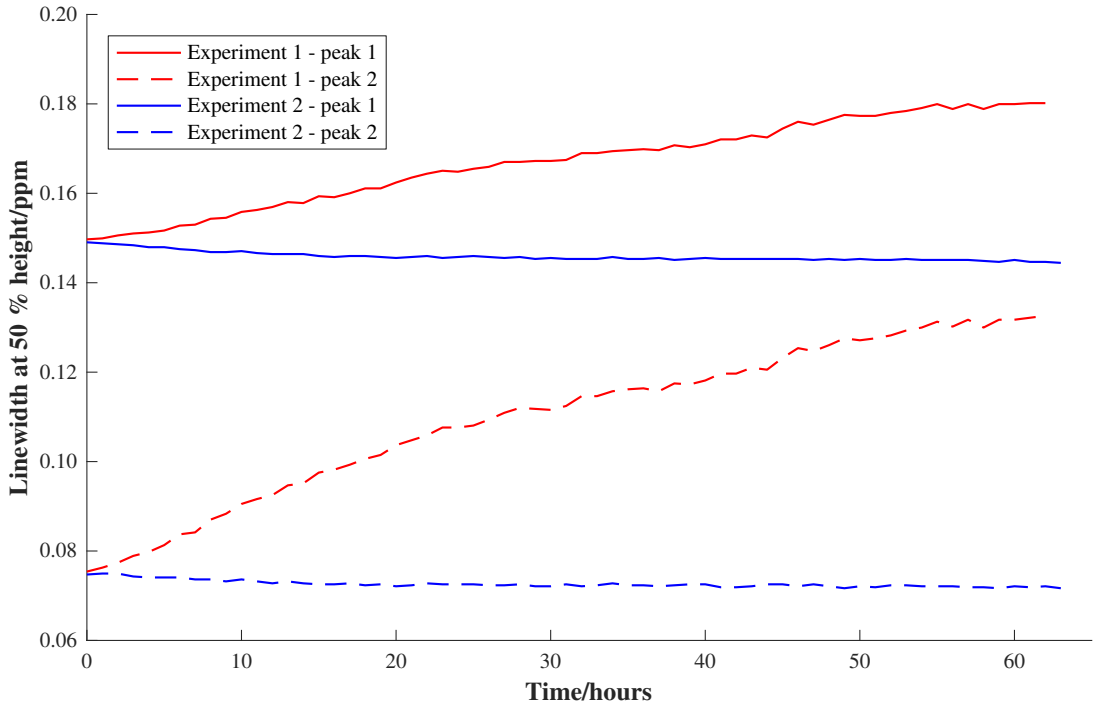

Figure 6.5 - Linewidth at 50 % peak height for the peaks in low-field ^{1}H NMR spectra of methanol collected every hour after the instrument had just been switched on (red) and one week later (blue). Solid line represents the peak at approximately 0.5 ppm (peak 1) and dashed line represents the peak at approximately 2 ppm (peak 2).

6.3.1.2 Sample Temperature

In order to determine the length of time required for a sample to reach the temperature of the instrument, the time taken for a sample of methanol to reach the magnet temperature was investigated. Plots of methanol sample temperature (calculated from the ^{1}H NMR spectra using Equation 6.1) versus time, upon insertion of the sample into the spectrometer at room temperature and upon insertion of the sample after heating to approximately the temperature of the magnet are shown in Figure 6.6. The corresponding ^{1}H NMR spectra can be found in Appendix 6.

When the methanol sample was heated prior to analysis, the sample temperature appeared to be relatively stable from the beginning of the analysis. The fluctuations observed (of up to 0.6 °C) can be attributed to slight differences in the point at which the peak maximum occurred for each spectrum. When the sample was inserted into the instrument at room temperature (approximately 22 °C), it took around 8 minutes to reach the temperature of the magnet (28.5 °C). In order to obtain reproducible

results, it is therefore necessary either to heat the sample before insertion or to wait at least 8 minutes (possibly longer if the temperature of the room varies) before analysis is performed.

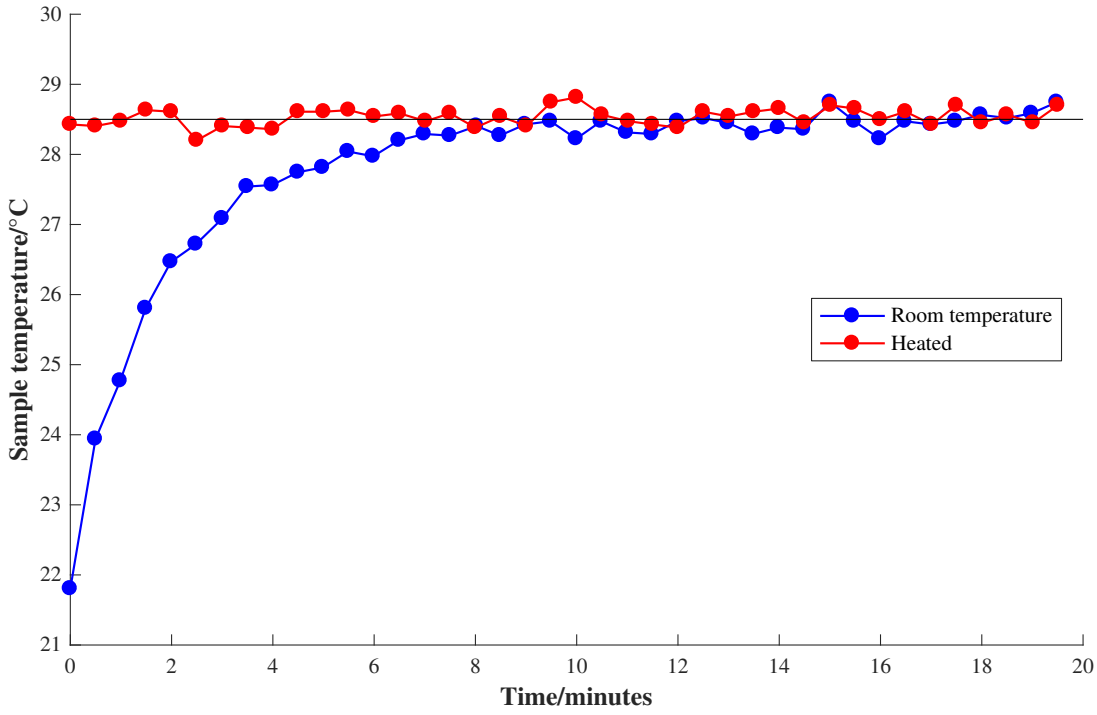

Figure 6.6 - Sample temperature versus time for a sample of methanol starting from room temperature (blue) and approximately 28.5 °C (red) after insertion into low-field NMR spectrometer.

It is difficult to heat the sample tube to exactly the same temperature as the magnet, as heat is lost upon removal of the sample from the water bath/heating apparatus. In addition the magnet temperature is controlled to the order of thousandths of a degree Celsius, so it is impossible for samples to be exactly the same temperature as the magnet upon insertion. This is the reason that the tubes containing the solvent mixtures analysed in Chapter 5 were heated to approximately 30 °C (allowing for a small decrease in temperature after removal from the water bath) and left in the NMR spectrometer for five minutes prior to analysis. The plot of sample temperature against time for the methanol sample which was heated in the same manner as the solvent mixtures (shown in red) confirms that the solvent mixtures should have reached the temperature of the magnet by the time the spectra were acquired.

6.3.1.3 Magnet Temperature

To investigate the stability of the magnet temperature, the temperature of the magnet while analysing the calibration samples (of the mixture set containing toluene, octene and dibutyl ether), and for several hours before/after the analysis, was plotted against time (Figure 6.7). During the period in which the samples were analysed (illustrated by the arrows), a small decrease in magnet temperature was observed, with the average value (as estimated by smoothing) falling to approximately 28.498 – 28.499 °C. This is presumably due to cooling of the magnet upon the consecutive insertion of a large number of sample tubes, and a time lag in the response of the magnet heater. The magnet temperature then began to rise again as the heater became more effective. After the experiment was finished, the magnet temperature continued to rise (as the heater overcompensated) and reached an average of approximately 28.501 – 28.502 °C before the magnet began to cool.

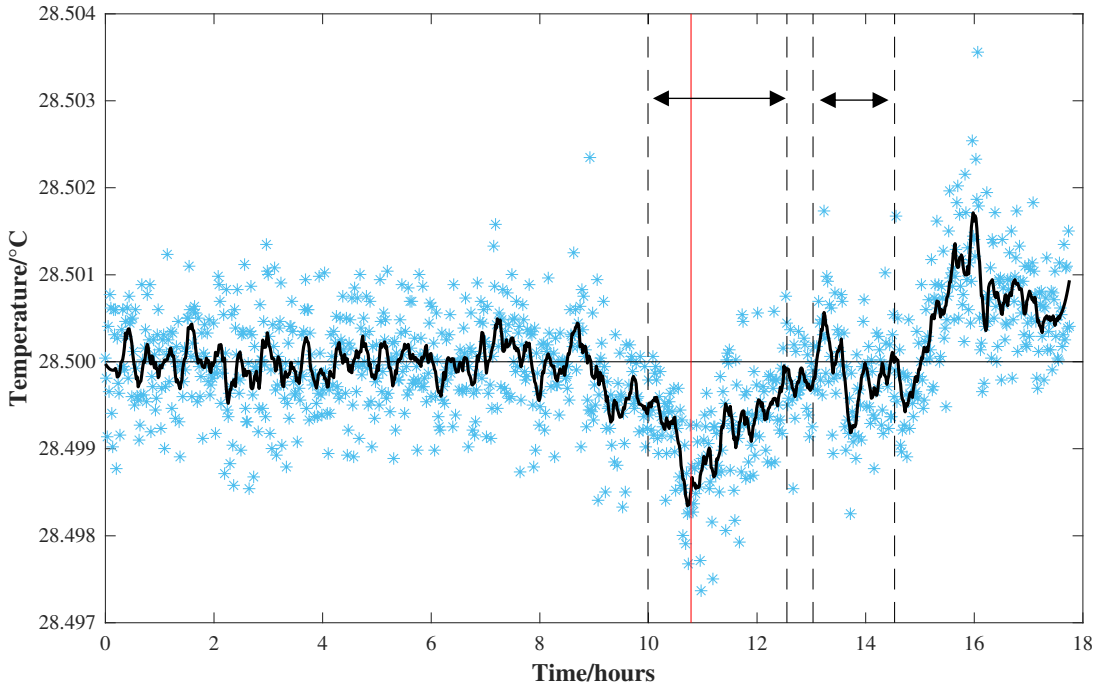

Figure 6.7 - Magnet temperature (black represents smoothed data and blue represents raw data) of low-field NMR spectrometer while analysing calibration samples (regions represented by arrows). Red line represents point at which sample with poorest spectrum was inserted into the instrument.

The spectra of the calibration samples acquired while the magnet temperature was monitored are shown in Figure 6.8, with the spectral region containing the TMS peak displayed in Figure 6.9 to allow closer observation of the lineshape. The intensity scale differed by several orders of magnitude compared to that of the spectra acquired using Spinsolve Expert because Spinsolve Expert applies scaling to account for changes in receiver gain (so that spectra acquired using different values of receiver gain will have the same area) and the standard Spinsolve software does not. In some spectra, the lineshape deteriorated so that the TMS peak became broader and was no longer a singlet. No clear trend was observed with time, as spectra with poor lineshape were acquired at various different points in time throughout the experiment, however overall fewer spectra with poor lineshape were observed at the start of the experiment.

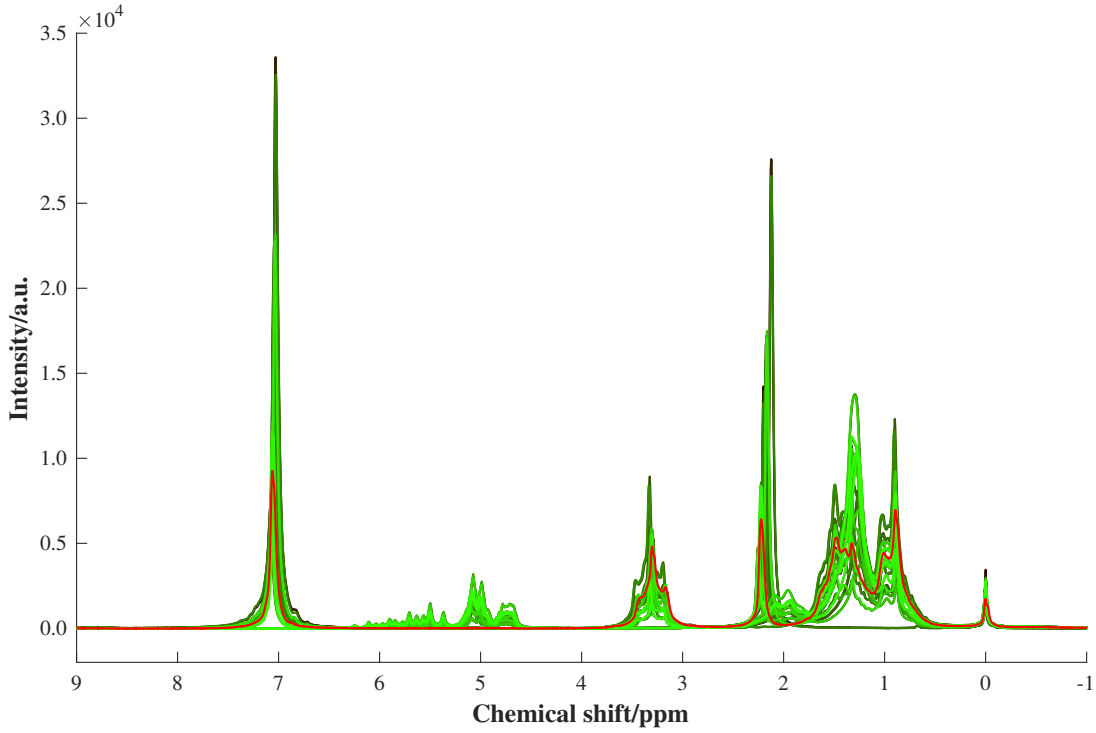

Figure 6.8 - Low-field ^{1}H NMR spectra of calibration samples (toluene, octene and dibutyl ether mixtures) collected while magnet temperature was monitored. Black represents the start of the experiment, green represents the end of the experiment and red represents the spectrum with poorest lineshape.

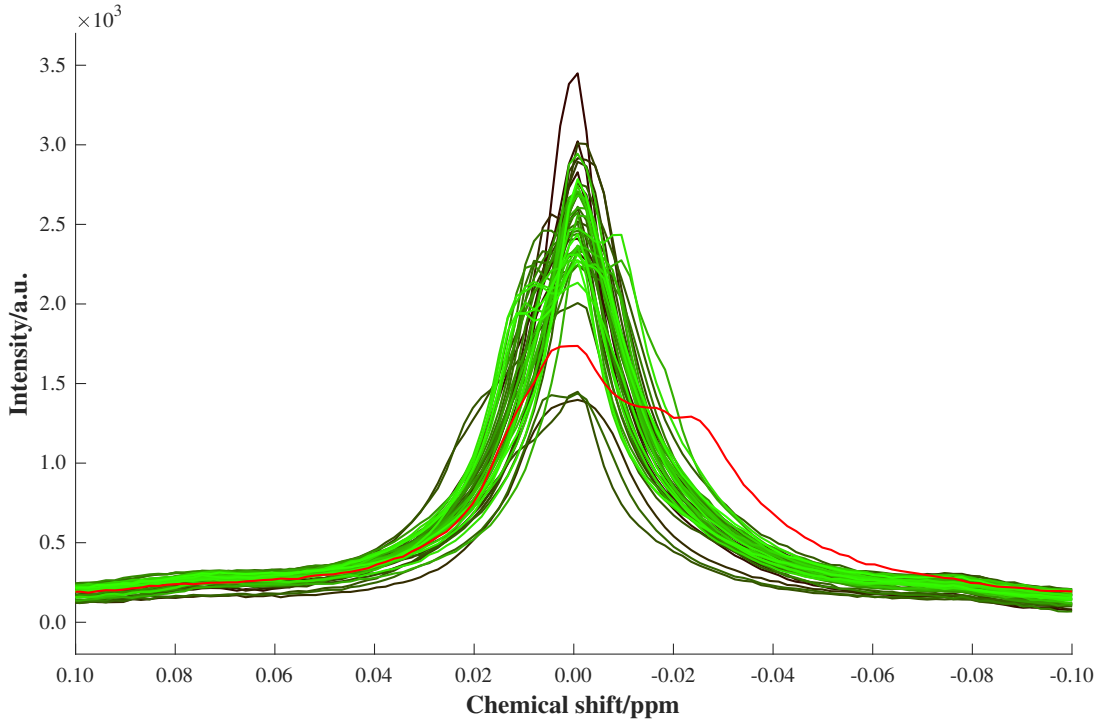

Figure 6.9 - TMS peak in low-field ^{1}H NMR spectra of calibration samples (toluene, octene and dibutyl ether mixtures) collected while magnet temperature was monitored. Black represents the start of the experiment, green represents the end of the experiment and red represents the spectrum with poorest lineshape.

A spectrum with a particularly poor lineshape is highlighted in red. The TMS peak was broad and severely misshapen, and loss of fine structure of the multiplet peaks can be observed in the full spectrum. The time point at which this sample was inserted into the spectrometer before the poorest spectrum was acquired is illustrated as a red line in Figure 6.7 (with the spectrum acquired five minutes later). This time point corresponds to the point at which the magnet temperature had dropped the lowest, indicating that the deterioration in lineshape observed is a result of the deviation of the magnet temperature from its optimum value. The lack of clear trend with time may be due to the continual fluctuations in the measurements of magnet temperature (as observed in the raw magnet temperature measurements represented by the blue markers), or it may be due to the contribution of other instrumental factors which cannot easily be measured. These results illustrate the importance of stable magnet temperature, as changes as small as one or two thousandths of a degree can produce significant deterioration in performance.

The temperature of the magnet over a 24 hour period when the instrument was not in use is plotted against time in Figure 6.10. Although the magnet temperature readings continually fluctuated, the smoothed data demonstrates that the average temperature remained stable over time and the deviations observed in Figure 6.7 lay outwith the magnet temperature range observed when the instrument was not in use. Therefore the deviations in magnet temperature can be attributed to the insertion/removal of samples from the instrument, despite the attempt to heat the samples to the same temperature as the magnet before insertion. This is a major issue, as it is likely that users of the spectrometer will want to analyse a number of samples consecutively, and an autosampler is available from Magritek for this purpose.[20]

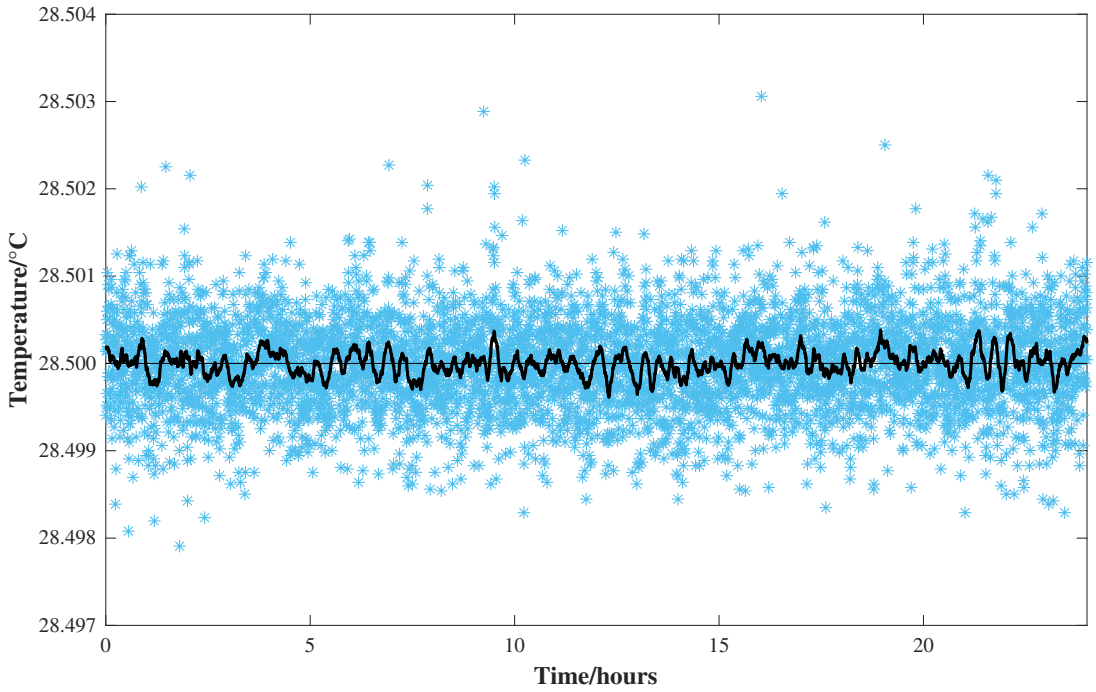

Figure 6.10 - Magnet temperature (black represents smoothed data and blue represents raw data) of low-field NMR spectrometer when instrument was not in use.

A solution may be to leave each sample in the instrument for longer before analysis in order to minimise the disturbance to the magnet temperature, however experiments involving large numbers of samples will then become significantly more time consuming. As well as the implications for building calibration models, this issue may cause problems in reaction monitoring by low-field NMR spectroscopy. At-line analysis is likely to involve the continual insertion/removal of samples, and flowing a

reaction mixture through the instrument during on-line analysis may also affect the magnet temperature. Heating/cooling of the reaction mixture to the magnet temperature before it is flowed through the instrument may be a solution, however this would alter the reaction rate so the sample may no longer be representative of the reaction mixture. Investigation of the extent to which the magnet temperature is affected by flowing the reaction mixture through the instrument would therefore be recommended before flow NMR spectroscopy at low field is used to monitor a reaction.

6.3.2 Short-Term Variation

6.3.2.1 Toluene, Octene and Dibutyl Ether Mixtures

In this section, the effectiveness of reference deconvolution at reducing the variation within datasets 1 and 2 (the toluene, octene and dibutyl ether mixture spectra analysed using different shim settings) was assessed. The low-field ^{1}H NMR spectra of the calibration and test samples in these datasets (without reference deconvolution) can be found in Appendix 5, and an example spectrum from each dataset is displayed in Figure 5.14. A spectrum of calibration sample 7 (which contained equal concentrations of toluene, octene and dibutyl ether) from dataset 1 is shown in Figure 6.11, with and without reference deconvolution. With reference deconvolution, the peaks in the spectra were of lower intensity (less than 2.5 a.u. compared to up to 4 a.u.) and the multiplet structures were more defined. The bottom edges of the peaks also changed shape to increase sharply rather than gradually. A spectrum of the same sample from dataset 2 is displayed with and without reference deconvolution in Figure 6.12. Reference deconvolution enhanced the fine structure of the peaks and decreased their intensity (by up to 1 a.u.), but to a lesser extent than in dataset 1, as the peaks were of lower intensity to begin with (less than 3 a.u.).

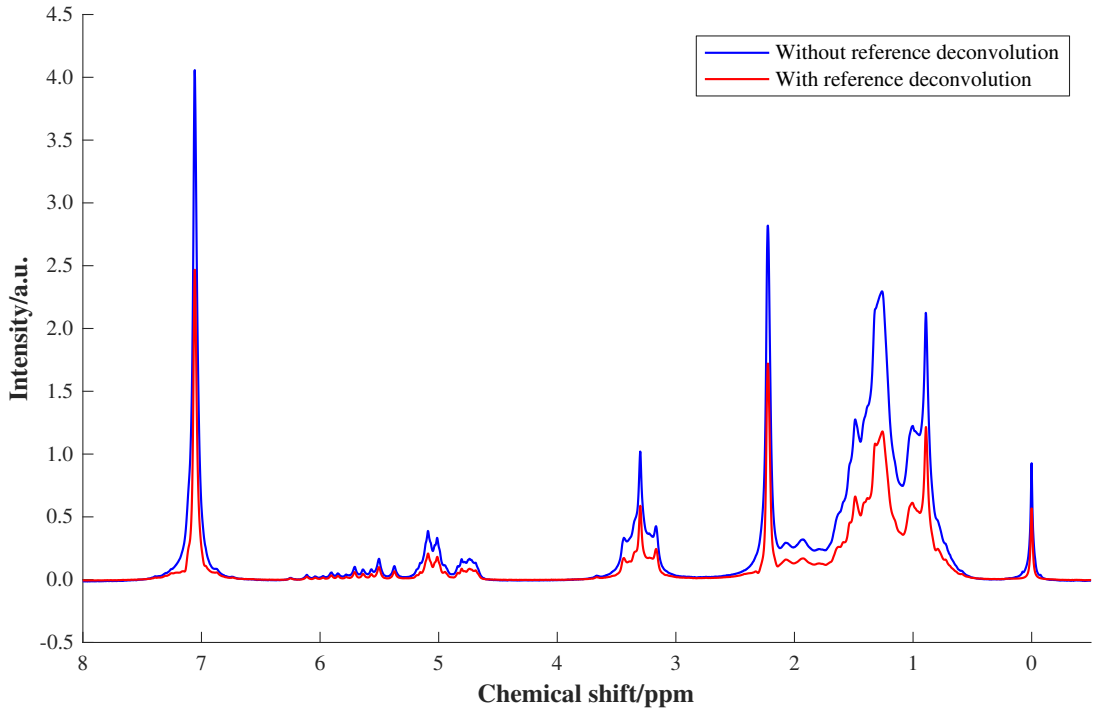

Figure 6.11 - ^{1}H low-field NMR spectrum of calibration sample 7 from dataset 1, without (blue) and with (red) reference deconvolution.

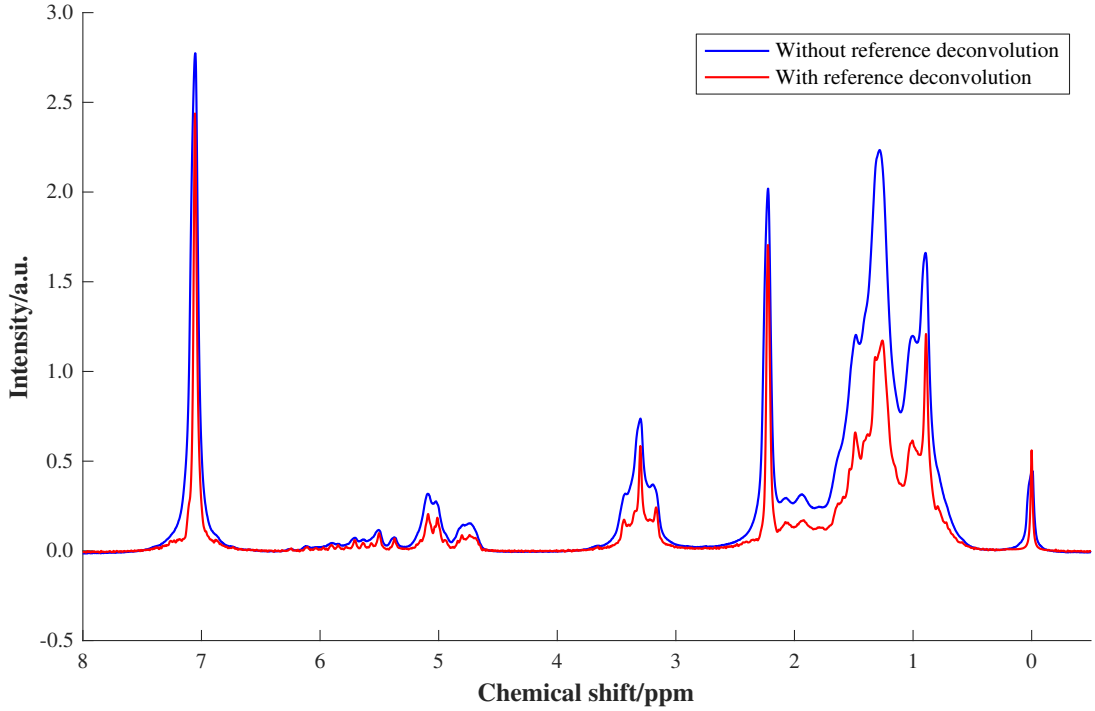

Figure 6.12 - ^{1}H low-field NMR spectrum of calibration sample 7 from dataset 2, without (blue) and with (red) reference deconvolution.

The mean and standard deviations of the linewidths at 50 % height for the aromatic toluene peak in the test spectra of datasets 1 and 2, without and with reference deconvolution, are displayed in Table 6.1. For dataset 1, the mean values obtained when reference deconvolution was applied were similar to those obtained without reference deconvolution (decreasing by only 4.6 x 10^{-3} ppm). However the application of reference deconvolution to dataset 2 decreased the mean linewidth by a factor of 1.7, since the line broadening factor used was less than the width of the peaks in the original spectra. The standard deviation of the linewidths decreased for both datasets when reference deconvolution was applied, by a factor of 1.8 for dataset 1 and a factor of 4 for dataset 2. This demonstrates the effectiveness of reference deconvolution at reducing the variation within datasets, particularly for spectra of poor lineshape. The effectiveness of reference deconvolution at reducing the variation between the datasets will be discussed in section 6.2.3.

Table 6.1 - Mean and standard deviation values of the width at 50 % peak height of the toluene peak at 7 ppm within the test spectra of datasets 1 and 2, without and with reference deconvolution.

Dataset	Reference deconvolution	Mean width at 50 % height of toluene peak at 7 ppm/ppm	Standard deviation of width at 50 % height of toluene peak at 7 ppm/ppm
1	**Without**	0.0387	0.0055
	With	0.0341	0.0031
2	**Without**	0.0569	0.0105
	With	0.0336	0.0026

In the first repeat measurement of calibration sample 2 in dataset 2, the application of reference deconvolution introduced a large amount of noise (up to 0.4 a.u. in intensity) into the baseline (shown in Figure 6.13), as a result of particularly poor TMS peak shape. This measurement was therefore excluded from the PLS1 models built using the deconvoluted calibration spectra in dataset 2. This is a disadvantage of reference deconvolution, as changes in the homogeneity of the magnetic field (which cause the shim settings to no longer be optimal) often produce distortion in the shape of the TMS peak, as discussed in Chapter 5, which can lead to this effect. The presence of

temperature gradients within the sample (e.g. as a result of the magnet temperature deviations discussed in Chapter 5) can also introduce noise when reference deconvolution is applied, as they will affect the lineshape of each signal differently.[4] In addition, the peaks in this spectrum may have become so broad due to deterioration of the shim that the penalty in the signal to noise ratio outweighed the benefits of resolution enhancement (as described by Morris et al.[4, 6]) when the line broadening factor of 1 Hz was used. The spectra of the rest of the samples in datasets 1 and 2 with reference deconvolution can be found in Appendix 6.

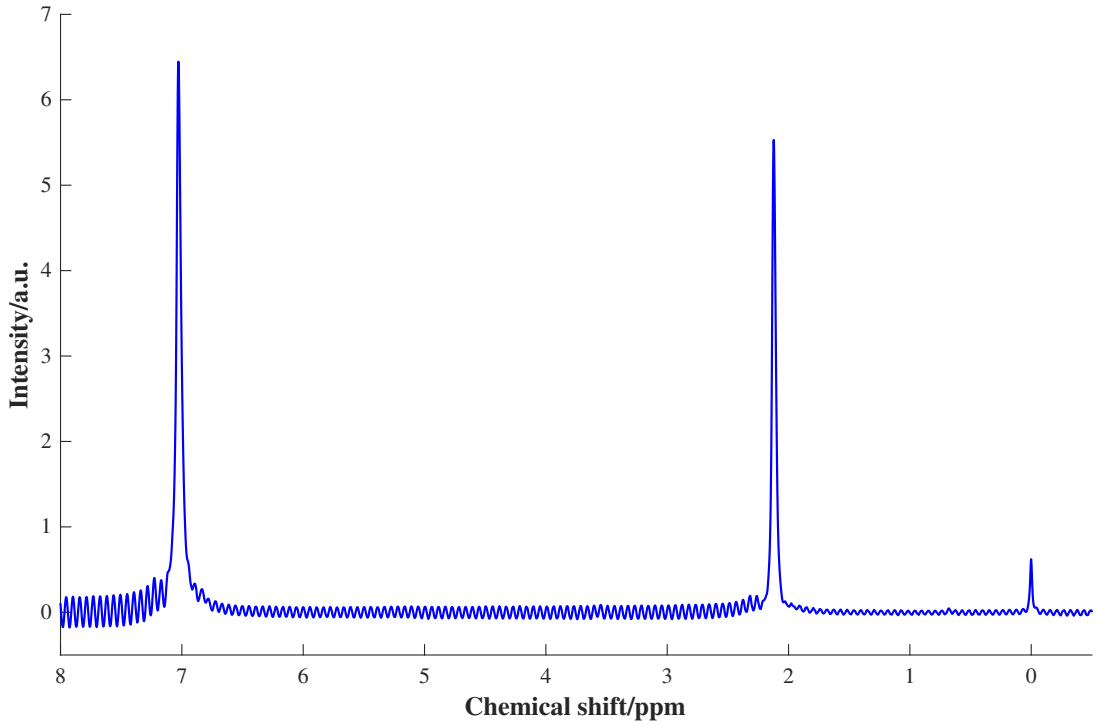

Figure 6.13 - ^{1}H low-field NMR spectrum of calibration sample 2 (first repeat measurement) from dataset 2, with reference deconvolution.

The RMSEP values obtained when PLS1 was performed (using the calibration spectra from the same dataset as the test spectra) without and with reference deconvolution are shown in Table 6.2 and Table 6.3, for datasets 1 and 2 respectively. For dataset 2, the spectrum containing the noise was excluded from the calibration models built with the deconvoluted spectra. The results obtained without reference deconvolution were discussed in more detail in Chapter 5. Lower RMSEP values were generally obtained for toluene than for the other two solvents, as the spectrum of toluene contains only singlet peaks which are easier to model.

Table 6.2 - RMSEP values for PLS1 models built using dataset 1 without and with reference deconvolution; without alignment, with alignment and with bucketing.

Alignment	Reference deconvolution	Toluene		Octene		Dibutyl ether	
		LVs	RMSEP/ (% w/w)	LVs	RMSEP/ (% w/w)	LVs	RMSEP/ (% w/w)
None	Without	4	0.79	3	1.50	3	1.44
	With	3	1.13	3	1.35	3	1.42
*i*coshift	Without	3	0.55	3	0.86	3	0.73
	With	3	0.46	3	0.74	3	0.58
Bucketing	Without	3	0.46	3	0.41	3	0.34
	With	3	0.29	3	0.36	3	0.27

Table 6.3 - RMSEP values for PLS1 models built using dataset 2 without and with reference deconvolution; without alignment, with alignment and with bucketing.

Alignment	Reference deconvolution	Toluene		Octene		Dibutyl ether	
		LVs	RMSEP/ (% w/w)	LVs	RMSEP/ (% w/w)	LVs	RMSEP/ (% w/w)
None	Without	3	0.83	4	0.95	3	1.17
	With	4	0.83	3	1.38	4	1.30
*i*coshift	Without	4	0.44	3	0.98	3	0.75
	With	3	0.57	3	0.72	3	0.61
Bucketing	Without	3	0.75	3	0.69	3	0.38
	With	3	0.41	3	0.39	3	0.20

For dataset 1 without alignment, the application of reference deconvolution decreased the RMSEP value for octene by 0.15 % w/w but increased the RMSEP value for toluene by around 0.2 % w/w. However one less latent variable was required for toluene after reference deconvolution. The RMSEP value obtained for dibutyl ether was similar to that obtained without reference deconvolution. For dataset 2, the toluene RMSEP value remained similar, but the octene and dibutyl ether RMSEP values increased by around 0.4 % w/w and 0.1 % w/w respectively when reference

deconvolution was applied (with one more latent variable required for toluene and dibutyl ether compared to without reference deconvolution, but one less latent variable required for ethanol).

This suggests that reference deconvolution may have decreased rather than increased the predictive ability of the spectra, particularly for dataset 2. As the shim was not optimal for this dataset, the peaks were broader than in dataset 1 (with a mean TMS peak width of 1.92 Hz at 50 % peak height compared to 0.96 Hz) and less variation was present between the spectra without reference deconvolution (with RMSEP values ≤ 1.17 % w/w obtained compared to ≤ 1.50 % w/w). The application of reference deconvolution caused the peaks to become narrower and more similar to those of dataset 1 (as will be discussed in section 6.2.3), explaining the increase in RMSEP observed.

When alignment was performed after reference deconvolution, the RMSEP values for dataset 1 decreased by around 0.1 % w/w compared to the RMSEP values obtained after alignment alone. For dataset 2 with alignment, the application of reference deconvolution appears to have been more effective at reducing the variation between the spectra than it was when alignment was not applied. The RMSEP values of octene and dibutyl ether decreased by around 0.3 % w/w and 0.1 % w/w respectively (compared to the values obtained for alignment without reference deconvolution) and one less latent variable was required for toluene. However the RMSEP value obtained for toluene increased by around 0.1 % w/w.

The application of reference deconvolution and bucketing produced the overall lowest RMSEP values for both datasets, ranging from 0.2 % w/w to 0.4 % w/w. For dataset 1, a reduction in RMSEP of 0.05 – 0.2 % w/w was observed compared to bucketing alone, and for dataset 2, a reduction in RMSEP of 0.2 – 0.3 % w/w was obtained. These results again suggest that the use of reference deconvolution to reduce the variation within the datasets was successful.

6.3.2.2 Toluene, Ethanol and Ethyl Acetate Mixtures

The effectiveness of reference deconvolution at reducing the variation within datasets 3 and 4 (the toluene, ethanol and ethyl acetate mixture spectra acquired using different shim settings) was then assessed. Example spectra from each dataset are displayed in

Figure 5.25, and the full sets of spectra (without reference deconvolution) can be found in Appendix 5. Figure 6.14 displays a spectrum of calibration sample 7 (which contained equal concentrations of toluene, ethanol and ethyl acetate) from dataset 3, with and without reference deconvolution. When reference deconvolution was applied, the shape of the peaks again changed so that the points where the edges met the baseline (particularly between the peaks of multiplets) were more defined with greater separation. The peaks in the spectrum with reference deconvolution were also of lower intensity (less than 3 a.u. compared to more than 5 a.u. without reference deconvolution).

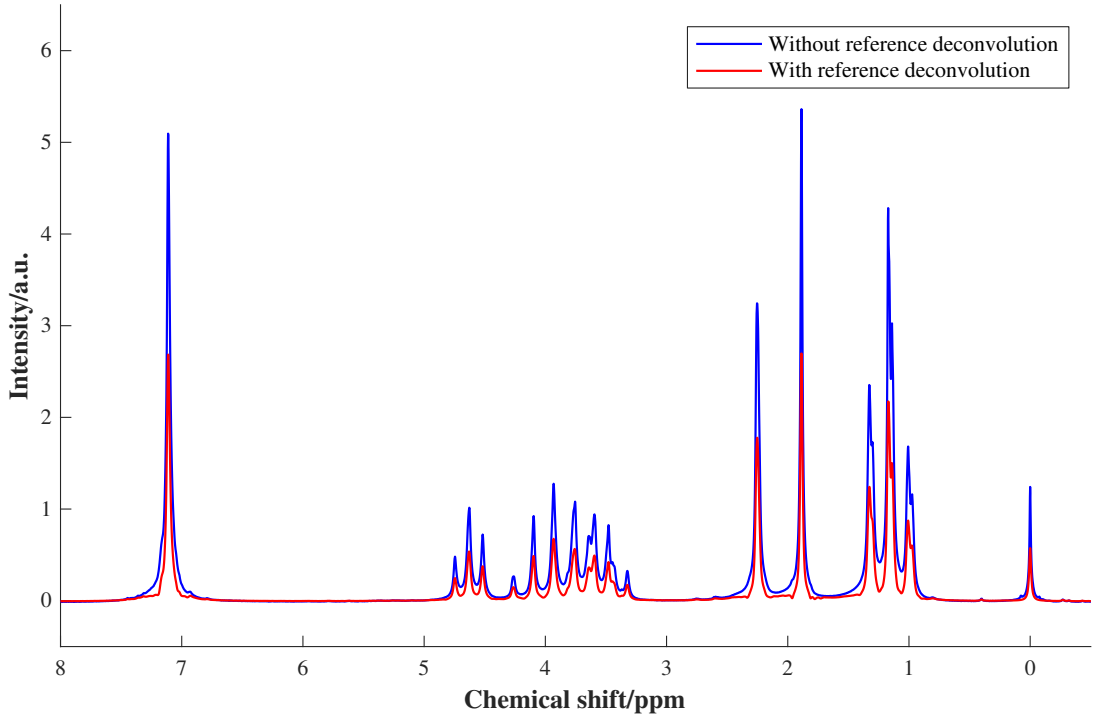

Figure 6.14 - ^{1}H low-field NMR spectrum of calibration sample 7 from dataset 3, without (blue) and with (red) reference deconvolution.

A spectrum of calibration sample 7 from dataset 4 is shown with and without reference deconvolution in Figure 6.15. The peaks in the spectrum again became more defined after reference deconvolution and the intensity of the peaks decreased from just under 3.5 a.u. to just above 2 a.u. When reference deconvolution was applied to the spectra in dataset 4, two of the spectra (the first repeat measurement of calibration sample 3 and the second repeat measurement of calibration sample 7) had a large amount of noise present in the baseline (up to 0.45 a.u.) due to distortion of the TMS peak shape,

as shown in Figure 6.16. These spectra were therefore not included in the calibration models built using dataset 4. The rest of the spectra from datasets 3 and 4 with reference deconvolution are displayed in Appendix 6.

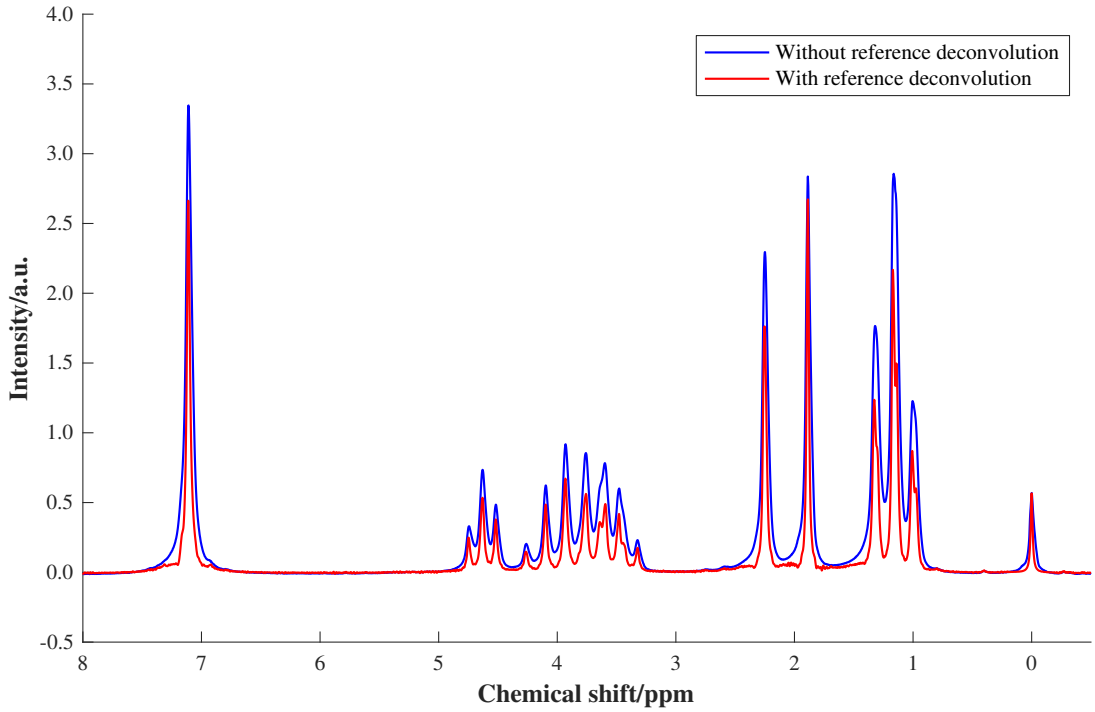

Figure 6.15 - ^{1}H low-field NMR spectrum of calibration sample 7 from dataset 4, without (blue) and with (red) reference deconvolution.

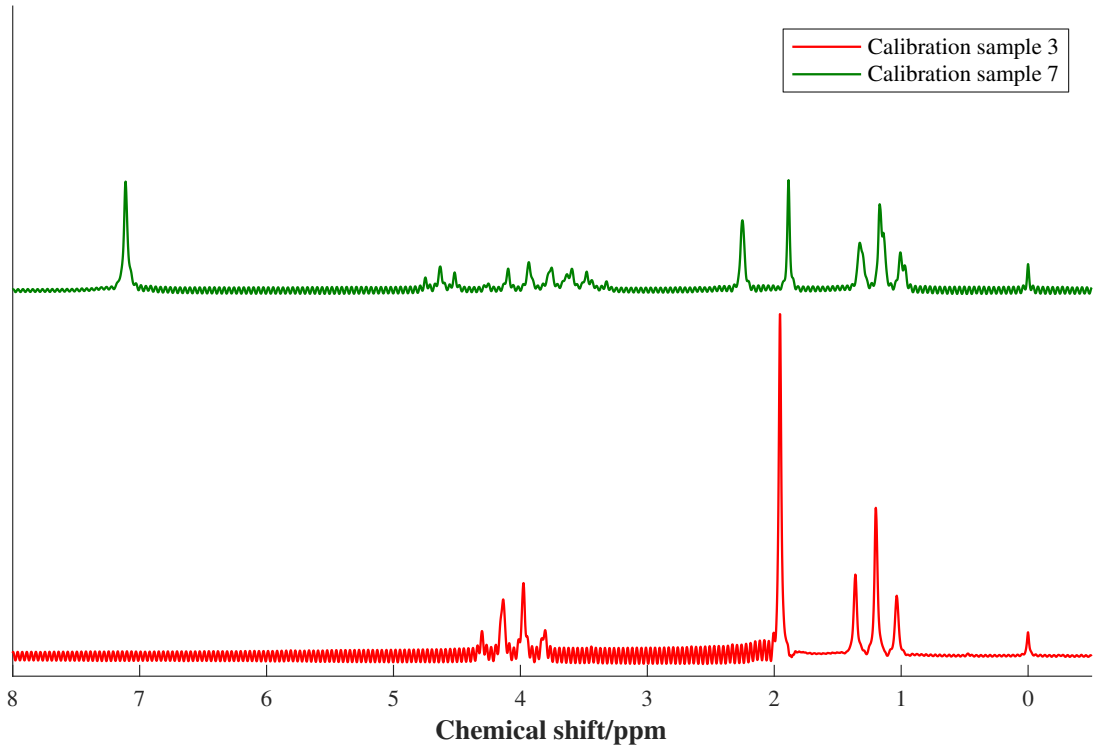

Figure 6.16 - ^{1}H low-field NMR spectra of calibration samples 3 (first repeat measurement) and 7 (second repeat measurement) from dataset 4, with reference deconvolution.

With reference deconvolution, the mean linewidth of the aromatic toluene peak at 50 % height for the test spectra in dataset 3 (Table 6.4) was similar to the value obtained without reference deconvolution (decreasing by only 2.2 x 10^{-3} ppm). A greater difference was observed for dataset 4 (as the peaks of the original spectra were broader since the shim was not optimal), with reference deconvolution causing the mean linewidth to decrease by a factor of 1.6. The standard deviation of the linewidths decreased by a factor of 3 upon the application of reference deconvolution to dataset 3, and by a factor of 2 for dataset 4. This corresponds to the results observed for datasets 1 and 2, further demonstrating that reference deconvolution is able to reduce the short-term variation of spectra within the same dataset.

Table 6.4 - Mean and standard deviation values of the width at 50 % peak height of the toluene peak at 7 ppm within the test spectra of datasets 3 and 4, without and with reference deconvolution.

Dataset	Reference deconvolution	Mean width at 50 % height of toluene peak at 7 ppm/ppm	Standard deviation of width at 50 % height of toluene peak at 7 ppm/ppm
3	**Without**	0.0356	0.0079
	With	0.0334	0.0025
4	**Without**	0.0546	0.0056
	With	0.0336	0.0024

The RMSEP values for PLS1 (using the calibration spectra from the same dataset as the test spectra in each case), without and with reference deconvolution, are shown in Table 6.5 and Table 6.6 for datasets 3 and 4 respectively. For datasets 3 and 4 without alignment, the application of reference deconvolution decreased the RMSEP value of ethanol by 0.2 % w/w, but increased the RMSEP values of toluene and ethyl acetate by 0.6 – 0.7 % w/w and 0.2 – 0.3 % w/w respectively. For dataset 4, one more latent variable was required for toluene with reference deconvolution but one less latent variable was required for ethyl acetate. Reference deconvolution therefore appears to have worsened the predictive abilities of the spectra. As reference deconvolution was able to decrease the variation in linewidth of the spectra, it may be that the relative areas of the peaks were altered in the process (particularly the singlet peaks), explaining the decrease in the predictive ability of the spectra.

When RAFFT was applied, the RMSEP values of toluene decreased by 0.2 – 0.4 % w/w compared to without reference deconvolution, but the RMSEP values of ethanol and ethyl acetate each increased by a factor of 2 or 3. For dataset 3, two less latent variables were necessary for ethanol but one more latent variable was necessary for ethyl acetate compared to without reference deconvolution. For dataset 4, two less latent variables were required for toluene compared to without reference deconvolution. As RAFFT (or any of the other alignment methods evaluated in Chapter 5) was unable to remove the peak shifts of ethanol and ethyl acetate between 3 and 6 ppm, this suggests that reference deconvolution has increased the differences

caused by peak shift. Therefore although reference deconvolution is able to reduce the variation between spectra when only small peak shifts (< 0.2 ppm) are present, it is not particularly effective when large peak shifts (up to 1.5 ppm) are present. The application of bucketing to the deconvoluted spectra made no significant difference to the RMSEP values for either dataset, as they differed by no more than 0.03 % w/w.

Table 6.5 - RMSEP values for PLS1 models built using dataset 3 without and with reference deconvolution; without alignment, with alignment and with bucketing.

Alignment	Reference deconvolution	Toluene		Ethanol		Ethyl acetate	
		LVs	RMSEP/ (% w/w)	LVs	RMSEP/ (% w/w)	LVs	RMSEP/ (% w/w)
None	Without	3	1.12	2	1.53	3	2.35
	With	3	1.82	2	1.30	3	2.59
RAFFT	Without	3	1.34	4	1.15	3	1.11
	With	3	0.94	2	3.44	4	3.00
Bucketing	Without	4	0.51	4	0.43	3	0.62
	With	4	0.53	4	0.44	3	0.64

Table 6.6 - RMSEP values for PLS1 models built using dataset 4 without and with reference deconvolution; without alignment, with alignment and with bucketing.

Alignment	Reference deconvolution	Toluene		Ethanol		Ethyl acetate	
		LVs	RMSEP/ (% w/w)	LVs	RMSEP/ (% w/w)	LVs	RMSEP/ (% w/w)
None	Without	3	1.11	2	1.39	4	2.04
	With	4	1.70	2	1.18	3	2.47
RAFFT	Without	4	0.89	4	1.08	4	1.13
	With	2	0.70	4	2.99	4	2.86
Bucketing	Without	4	0.54	4	0.40	3	0.58
	With	4	0.53	4	0.41	3	0.55

6.3.3 Long-Term Variation

The aim of this section is to compare the effectiveness of calibration transfer and reference deconvolution for elimination of the differences between spectra acquired under different conditions. The comparison will first be carried out for the toluene, octene and dibutyl ether spectra (datasets 1 and 2), which exhibited peak shifts < 0.2 ppm, and repeated using the toluene, ethanol and ethyl acetate spectra (datasets 3 and 4), which exhibited peak shifts up to 1.5 ppm.

6.3.3.1 Toluene, Octene and Dibutyl Ether Mixtures

6.3.3.1.1 Calibration Transfer

SST was applied to the test spectra in dataset 2, in order to make them resemble the test spectra in dataset 1. The spectra of the test samples in dataset 2 are shown with SST in Figure 6.17. One singular value was included in the SST calculation, as this number produced the overall lowest RMSEP value (illustrated by the plots of RMSEP versus number of singular values in Appendix 6). This is likely to be because one singular value dominated the spectral space due to shifting of peaks between the spectra. Distortions consisting of small negative regions and noise were observed at the edges of some peaks, e.g. the toluene singlet peaks at 7 ppm and just above 2 ppm. This is a result of peak shifts between the transfer spectra and/or the test spectra, which caused the transfer spectra to no longer be representative of the test spectra in the regions where peak shifts occurred.

When alignment of the spectra was performed before the application of SST (Figure 6.18), the peaks no longer appeared distorted. However a sharp negative peak was present just below 1 ppm in the spectra of test sample 4 due to misalignments of the peaks in this region. In this case, the inclusion of six singular values produced the lowest RMSEP value (illustrated in the plots in Appendix 6). The application of alignment meant that the first singular value no longer described the majority of the variation between the datasets, so a larger number of singular values was required. When bucketing was applied before SST (Figure 6.19), no noise was produced in the baseline when calibration transfer was performed due to elimination of the effect of peak shift, and three singular values were found to be the optimum.

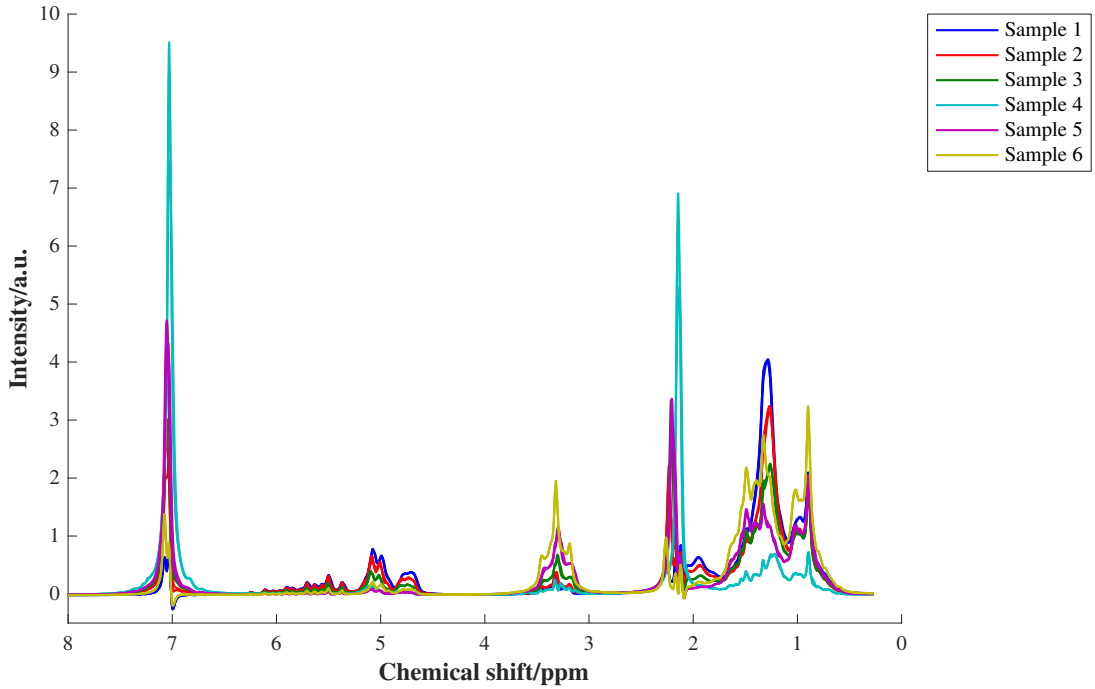

Figure 6.17 - ^{1}H low-field NMR spectra of test samples in dataset 2 (no alignment), with calibration transfer by SST (using 1 singular value).

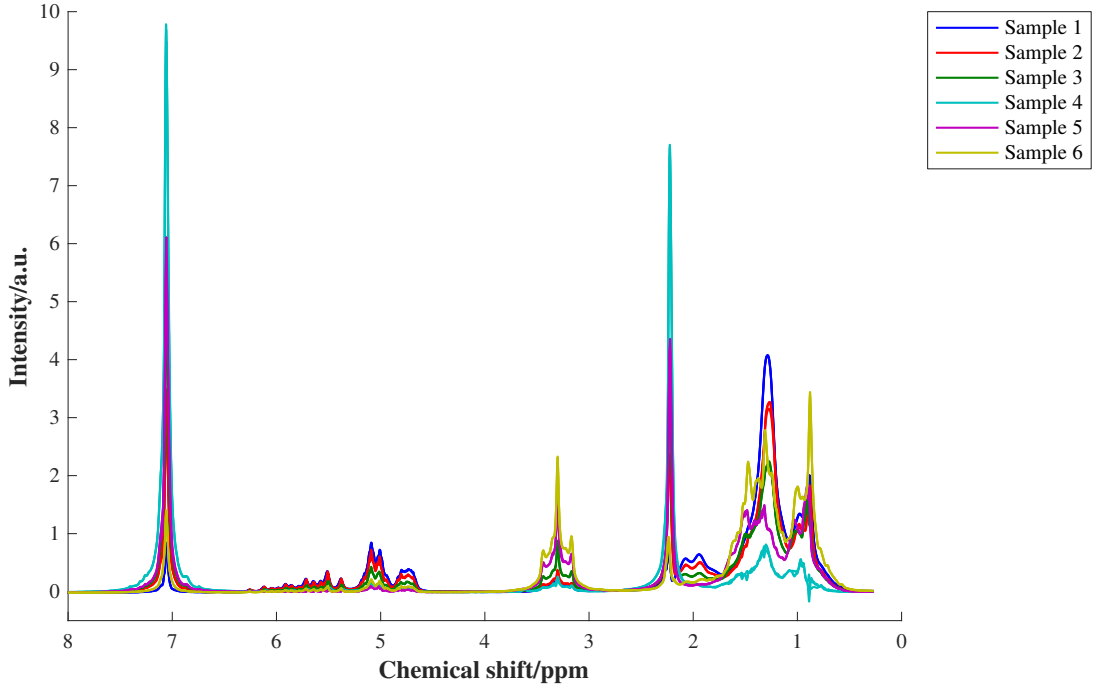

Figure 6.18 - ^{1}H low-field NMR spectra of test samples in dataset 2, with alignment by *i*coshift and calibration transfer by SST (using 6 singular values).

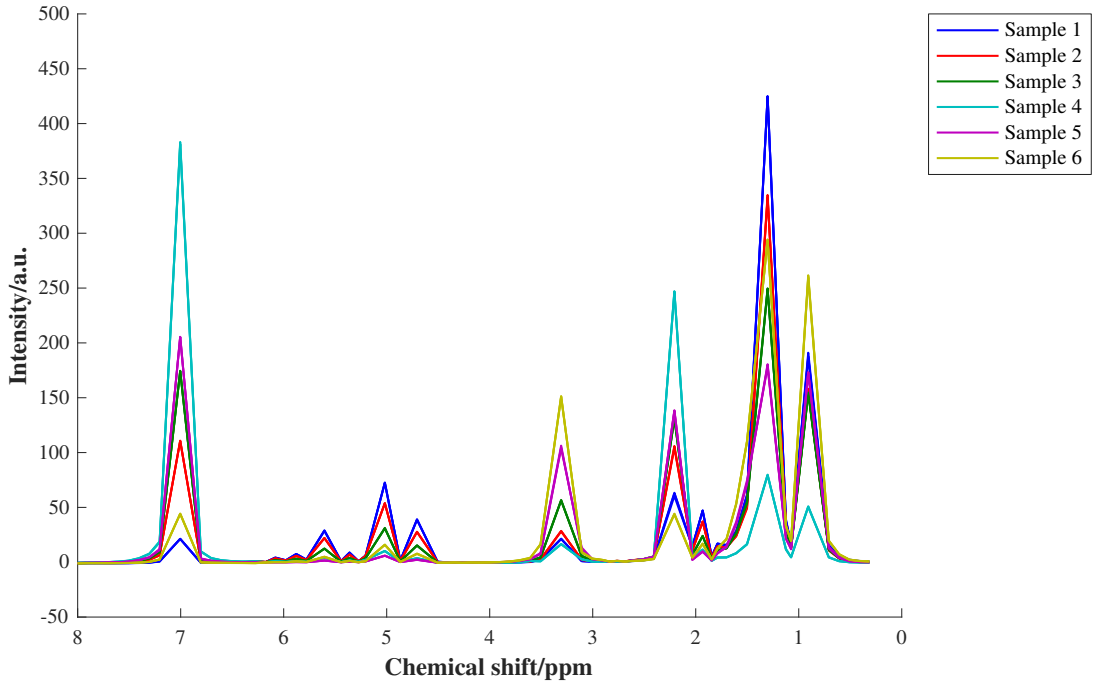

Figure 6.19 - ^{1}H low-field NMR spectra of test samples in dataset 2, with optimised bucketing and calibration transfer by SST (using 3 singular values).

An example spectrum of test sample 2 from dataset 2 is shown without and with SST in Figure 6.20, overlaid with a spectrum of the same sample from dataset 1. Without SST, the peaks in the spectrum from dataset 2 appeared broader than the peaks in the spectrum from dataset 1 and the singlet peaks were of lower intensity (up to 1.5 a.u. less). The shape of the peaks was also less defined. With SST applied to dataset 2, the shape of the peaks became more defined. However the toluene singlet peaks were still of much lower intensity (around 1 a.u. less) than in dataset 1, and noise was introduced into the edge of the peak just above 2 ppm. This may be due to inability of SST to handle peak shifts, as the toluene singlet peaks exhibited the greatest shifts and covered a smaller region of the x axis (as they were narrower), so the transformation of these peaks will have been more challenging.

The mean and standard deviations of the linewidths at 50 % height of the aromatic toluene peak in the test spectra (from dataset 1, dataset 2 without SST, dataset 2 with SST, and dataset 2 with alignment and SST) are displayed in Table 6.7. Without SST, the mean linewidths for dataset 2 were higher than those of dataset 1 by a factor of 1.5, and the standard deviation was higher by a factor of 2. The application of SST with no alignment made little difference to the linewidths (with the mean value decreasing by

1.3 x 10^{-3} ppm and the standard deviation increasing by 2.9 x 10^{-3} ppm). This indicates that SST is not particularly effective at removing the variation between datasets when peak shifts are present.

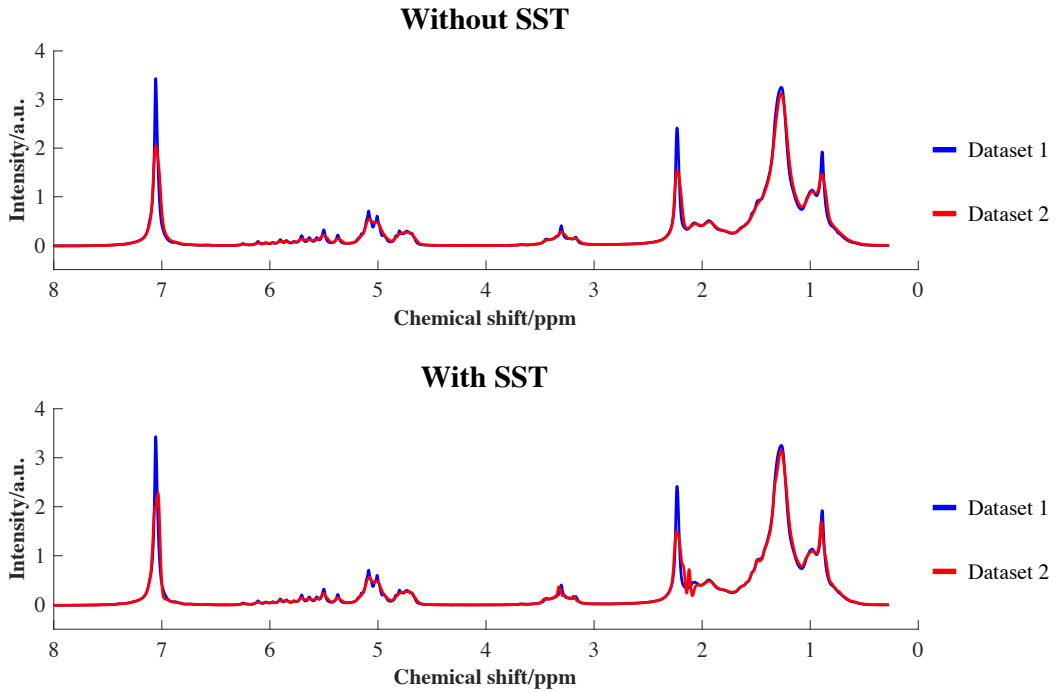

Figure 6.20 - ^{1}H low-field NMR spectrum of test sample 2 in dataset 1 (blue) and dataset 2 without and with calibration transfer by SST (red), no alignment (1 singular value included).

Table 6.7 - Mean and standard deviation values of the width at 50 % peak height of the toluene peak at 7 ppm within the test spectra of dataset 1 and of dataset 2 without SST, with SST and with *i*coshift followed by SST.

Data	Mean width at 50 % height of toluene peak at 7 ppm/ppm	Standard deviation of width at 50 % height of toluene peak at 7 ppm/ppm
Dataset 1	0.0387	0.0055
Dataset 2	0.0569	0.0105
Dataset 2 with SST	0.0556	0.0134
Dataset 2 with *i*coshift and SST	0.0379	0.0054

When alignment was performed prior to calibration transfer (Figure 6.21), the spectrum from dataset 2 became more similar to the spectrum from dataset 1, with peaks of higher intensity (around 3 a.u.) and more defined shape so that the multiplets were more apparent. The mean linewidth of the aromatic toluene peak in the test spectra decreased by a factor of 1.5 and the standard deviation decreased by a factor of 2, compared to the values obtained without SST. These values were more similar to those obtained for dataset 1 (3.79×10^{-2} ppm compared to 3.87×10^{-2} ppm for the mean, and 5.4×10^{-3} ppm compared to 5.5×10^{-3} ppm for the standard deviation). The application of *i*coshift alone does not alter the linewidths of the peaks, therefore the values displayed for datasets 1 and 2 without alignment or SST were the same as those obtained for datasets 1 and 2 with alignment. These results demonstrate the effectiveness of SST at reducing the differences between well-aligned spectra acquired under different conditions. However the spectra were not identical, due to variations in the repeat measurements of the transfer and test samples within the same dataset. When bucketing was performed (Figure 6.22), the spectra of test sample 2 from each dataset were almost identical without SST, and the application of SST produced no noticeable difference in the spectra.

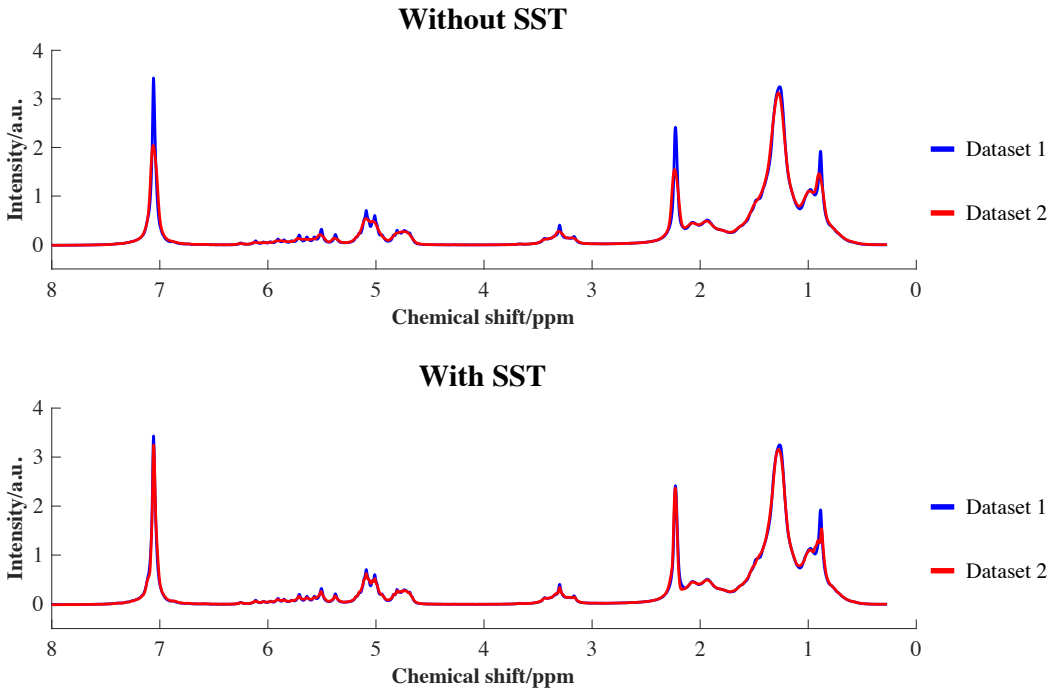

Figure 6.21 - ^{1}H low-field NMR spectrum of test sample 2 in dataset 1 (blue) and dataset 2 without and with calibration transfer by SST (red), aligned by *i*coshift (6 singular values included).

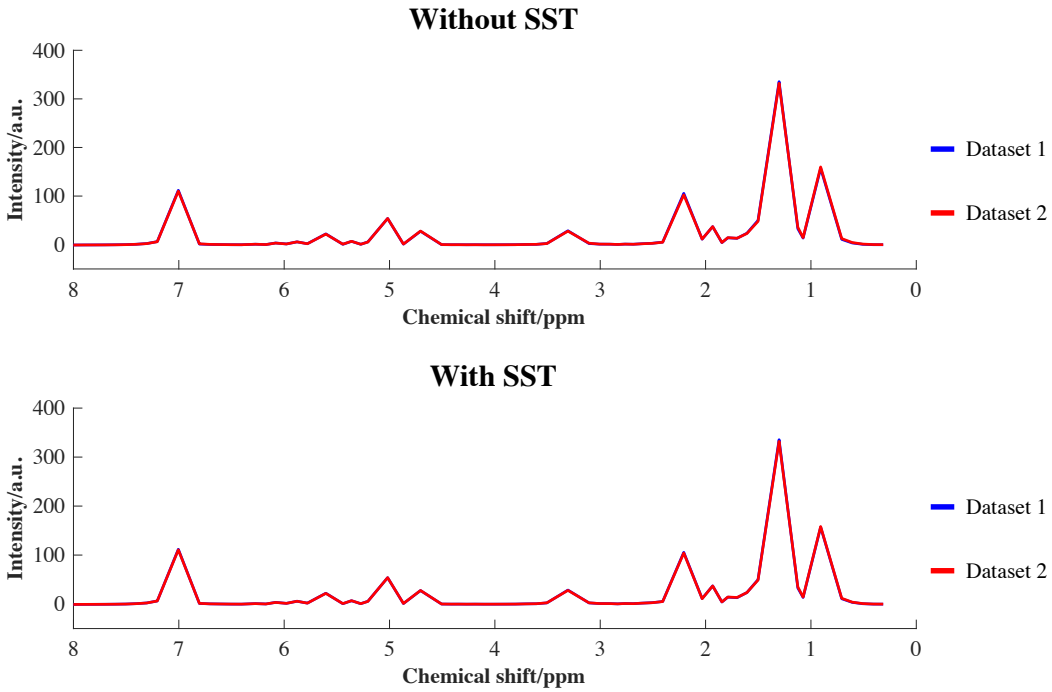

Figure 6.22 - ^{1}H low-field NMR spectrum of test sample 2 in dataset 1 (blue) and dataset 2 without and with calibration transfer by SST (red), with optimised bucketing (3 singular values included).

6.3.3.1.2 Reference Deconvolution

The effectiveness of reference deconvolution at removing the differences between the spectra in datasets 1 and 2 was then evaluated. Spectra of calibration sample 7 from datasets 1 and 2 with reference deconvolution are shown overlaid in Figure 6.23. The same spectra without reference deconvolution were displayed in Figure 5.14, and the differences were discussed in section 5.3.2. With reference deconvolution, these differences were no longer observed and the two spectra appeared almost identical.

When the mean linewidth of the aromatic toluene peak in the test spectra of dataset 2 (given in Table 6.1) was compared to that of dataset 1, the values differed by a factor of 1.5 when reference deconvolution was not applied but became similar with reference deconvolution (differing by only 5 x 10^{-4} ppm). The standard deviation in the linewidths also became similar, decreasing by a factor of 4 to become only 5 x 10^{-4} ppm lower than for dataset 1. This illustrates that reference deconvolution was successful in eliminating the differences between the spectra from datasets 1 and 2. The RMSEP values obtained with SST and with reference deconvolution will be

discussed in section 6.3.3.1.4, in order to assess the effectiveness of these methods when PLS1 models built using one dataset were applied to another dataset.

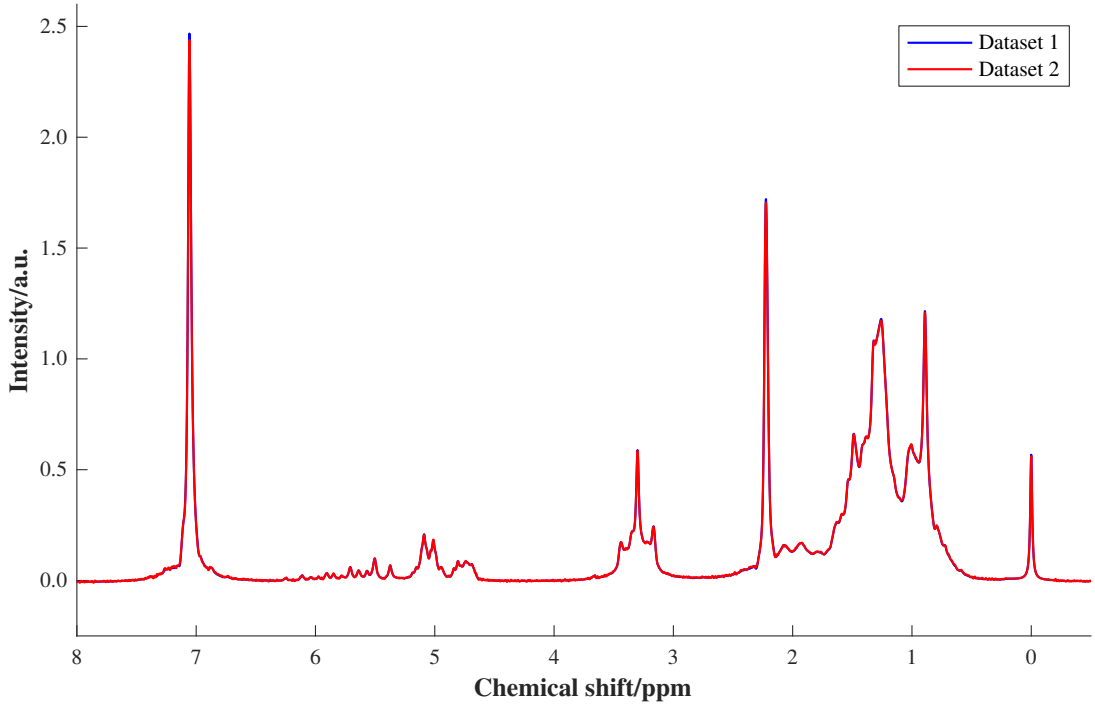

Figure 6.23 - ^{1}H low-field NMR spectrum of calibration sample 7 from datasets 1 (blue) and 2 (red), with reference deconvolution.

6.3.3.1.3 Reference Deconvolution and Calibration Transfer

To evaluate the combination of reference deconvolution and calibration transfer, a spectrum of test sample 2 from dataset 2 with reference deconvolution applied is shown without/with SST in Figure 6.24, overlaid with the same spectrum from dataset 1 with reference deconvolution applied. Little difference was observed between datasets 1 and 2, with or without SST. When *i*coshift was performed before SST, similar results were observed, and the plot can be found in Appendix 6. The mean and standard deviation values of the linewidths at 50 % peak height of the aromatic toluene peak are displayed in Table 6.8, and were also similar in all cases (differing by no more than 5 x 10^{-4} ppm). This indicates that reference deconvolution alone was sufficient to remove the variation between the datasets, and that the application of SST made little difference to the spectra.

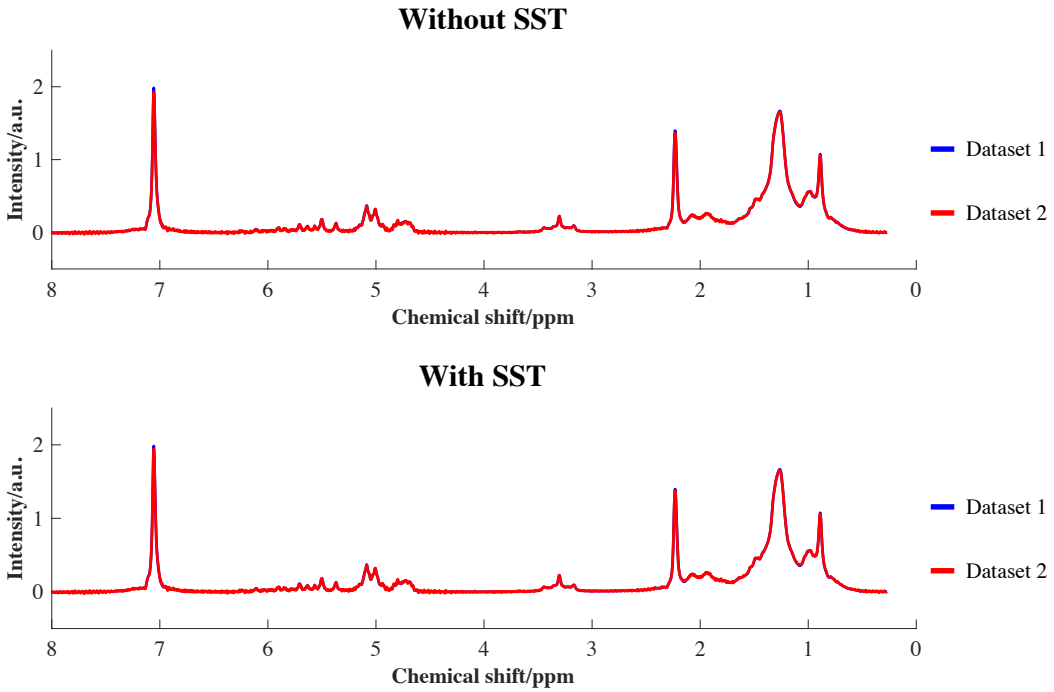

Figure 6.24 - ^{1}H low-field NMR spectrum of test sample 2 in dataset 1 (blue) and dataset 2 without and with calibration transfer by SST (red), no alignment (1 singular value included). With reference deconvolution applied to datasets 1 and 2 before SST.

Table 6.8 - Mean and standard deviation values of the width at 50 % peak height of the toluene peak at 7 ppm within the test spectra of dataset 1 and of dataset 2 without SST, with SST and with *i*coshift followed by SST. With reference deconvolution applied to datasets 1 and 2 before SST.

Data (all with reference deconvolution)	Mean width at 50 % height of toluene peak at 7 ppm/ppm	Standard deviation of width at 50 % height of toluene peak at 7 ppm/ppm
Dataset 1	0.0341	0.0031
Dataset 2	0.0336	0.0026
Dataset 2 with SST	0.0337	0.0026
Dataset 2 with *i*coshift and SST	0.0336	0.0026

When bucketing was applied prior to SST (after reference deconvolution), a difference of up to 11 a.u. was introduced between the spectra of test sample 2 from datasets 1 and 2 (Figure 6.25). Without SST, the spectra appeared similar. This suggests that the

application of SST increased the variation between the two datasets, compared to the application of reference deconvolution and bucketing without SST.

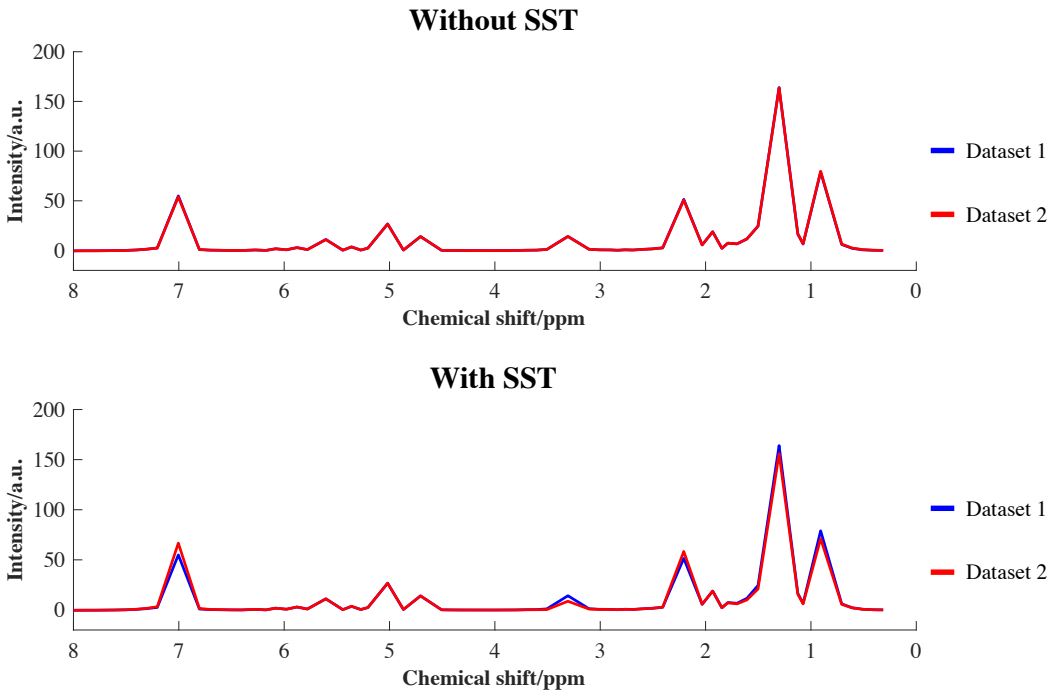

Figure 6.25 - ^{1}H low-field NMR spectrum of test sample 2 in dataset 1 (blue) and dataset 2 without and with calibration transfer by SST (red), with optimised bucketing (1 singular value included). With reference deconvolution applied to datasets 1 and 2 before SST.

Only one singular value was necessary in all cases, indicating that only one major source of variation between the two datasets was present after the application of reference deconvolution and SST. The rest of the test spectra with reference deconvolution and SST applied (without alignment, with alignment and with bucketing) are displayed in Appendix 6.

6.3.3.1.4 Comparison of RMSEP Values

The RMSEP values for the PLS1 models built using the calibration spectra from dataset 1, applied to the test spectra from dataset 2 (without SST or reference deconvolution, with SST, with reference deconvolution and with both reference deconvolution and SST), are displayed in Table 6.9. Without SST or reference deconvolution, higher RMSEP values were obtained with alignment compared to without alignment ($\leq$ 2.71 % w/w compared to $\leq$ 1.53 % w/w) and one less latent

variable was required for toluene and octene. This is likely to be due to the difference between the two sets of spectra increasing as a result of alignment, causing the RMSEP values to worsen when the PLS models built using dataset 1 were applied to spectra from dataset 2.

Table 6.9 - RMSEP values for PLS1 models built using calibration spectra from dataset 1 and applied to test spectra from dataset 2 (without alignment, with alignment and with bucketing); without calibration transfer or reference deconvolution, with calibration transfer, with reference deconvolution, and with both reference deconvolution and calibration transfer.

Alignment	Transformation	Toluene		Octene		Dibutyl ether	
		LVs	RMSEP/ (% w/w)	LVs	RMSEP/ (% w/w)	LVs	RMSEP/ (% w/w)
None	None	4	1.15	4	1.44	3	1.53
	SST (1 SV)	3	0.95	4	1.15	4	1.41
	Reference deconvolution	4	1.00	3	1.40	3	1.42
	Reference deconvolution and SST (1 SV)	3	1.09	3	1.37	3	1.42
*i*coshift	None	1	2.71	3	2.06	3	1.24
	SST (6 SVs)	3	0.40	3	1.11	3	0.96
	Reference deconvolution	3	0.59	3	0.74	3	0.68
	Reference deconvolution and SST (1 SV)	3	0.50	3	0.72	3	0.67
Bucketing	None	3	0.46	3	0.41	3	0.34
	SST (3 SVs)	3	0.59	3	0.57	3	0.39
	Reference deconvolution	3	0.36	3	0.32	3	0.28
	Reference deconvolution and SST (1 SV)	1	4.71	2	0.34	2	4.70

With no alignment, SST reduced the RMSEP values of all three solvents by 0.1 – 0.3 % w/w. One less latent variable was required for toluene but one more latent variable was required for ethyl acetate after SST. With alignment, the RMSEP value for toluene decreased by 2.3 % w/w (although two more latent variables were required), the value for octene decreased by 1 % w/w and the value for dibutyl ether decreased by 0.3 % w/w. This clearly demonstrates the effectiveness of SST at reducing the variation between the datasets.

Reference deconvolution was less effective than SST when alignment was not performed, producing similar RMSEP values (when the PLS models built with the calibration spectra from dataset 1 were applied to the test spectra from dataset 2) to SST for toluene and dibutyl ether, and an RMSEP value 0.3 % w/w higher than SST for octene. One less latent variable was required for octene and dibutyl ether compared to SST, and one more latent variable was required for toluene. With alignment, however, reference deconvolution produced lower RMSEP values (by 0.3 – 0.4 % w/w) than SST for octene and dibutyl ether. For toluene, the RMSEP value was 0.2 % w/w higher for reference deconvolution than SST (but still 4.5 times lower than for alignment without reference deconvolution or SST). Therefore reference deconvolution also appeared to be effective, particularly when alignment of the spectra was performed afterwards. The application of SST after reference deconvolution had little effect on the results (although one less latent variable was required for toluene when no alignment was performed). This again indicates that SST is unnecessary if reference deconvolution has been performed.

When bucketing was performed without SST or reference deconvolution, the RMSEP values (obtained when PLS1 models built with the calibration samples from dataset 1 were applied to the test spectra from dataset 2) decreased to 0.34 – 0.46 % w/w, compared to 1.15 – 1.53 % w/w without bucketing. This indicates that bucketing was able to reduce the variation between the datasets to a greater extent than SST or reference deconvolution. However as discussed in Chapter 5, the spectrum of each component used in this work contained clearly distinguishable peaks and bucketing is not likely to produce such accurate predictions when this is not the case.

The application of SST after bucketing produced an increase in the RMSEP values of all three solvents of 0.39 – 0.59 % w/w. As no noticeable difference could be observed in the bucketed spectra with and without SST (shown in Figure 6.22), and lower RMSEP values were obtained without SST, calibration transfer appears to be unnecessary after bucketing using these parameters. The application of bucketing after reference deconvolution produced the lowest RMSEP values of all (0.28 – 0.36 % w/w). However these values were no more than 0.1 % w/w different than from when bucketing was applied to the spectra without reference deconvolution (and the same number of latent variables were necessary for all components).

When SST was performed after reference deconvolution and bucketing, the toluene and dibutyl ether RMSEP values significantly worsened (increasing as high as 4.71 % w/w). This may have been because the combination of reference deconvolution and bucketing introduced differences to the toluene and dibutyl ether spectra between the datasets, and these differences were not fully reflected in the transfer samples. Fewer latent variables were required compared to without SST, indicating that SST has reduced the number of sources of variation in the spectra. For octene, the RMSEP value was similar to that obtained for reference deconvolution and bucketing without SST, but one less latent variable was required. Therefore the use of bucketing alone appears to be sufficient for removing long-term variation between spectra exhibiting little peak shift or overlap.

6.3.3.2 Toluene, Ethanol and Ethyl Acetate Mixtures

6.3.3.2.1 Calibration Transfer

The effectiveness of SST at removing the differences between the test spectra in datasets 3 and 4 was then examined. The spectra of the test samples from dataset 4 (toluene, ethanol and ethyl acetate mixtures) are shown with SST in Figure 6.26. Noise consisting of small negative distortions was again present at 2 ppm and 7 ppm, as a result of shifts between the transfer spectra and/or test spectra. Just above 5 ppm, noise resembling a multiplet peak was present in the baseline of test sample 6. This is a result of the large shifts (up to 1.5 ppm) of the multiplet peaks between 3 ppm and 6 ppm, and is an issue with using calibration transfer when peak shifts are present. The application of RAFFT (Figure 6.27) removed the noise at 2 and 7 ppm, but worsened

the noise just above 5 ppm (with negative peaks up to 0.6 a.u. in intensity present). This is due to the inability of RAFFT to align the peaks in this region. The number of singular values required to produce the lowest RMSEP values increased from two to three upon the application of RAFFT, presumably due to domination of the spectral space by low numbers of singular values when the spectra exhibited greater amounts of peak shift.

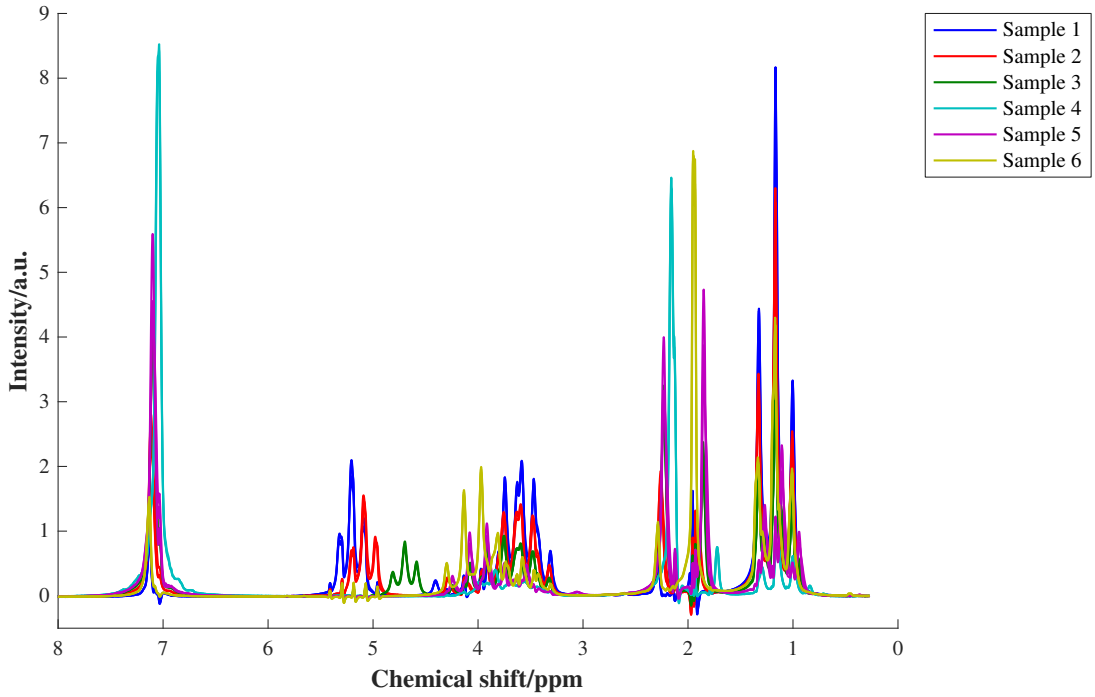

Figure 6.26 - ^{1}H low-field NMR spectra of test samples in dataset 4 (no alignment), with calibration transfer by SST (using 2 singular values).

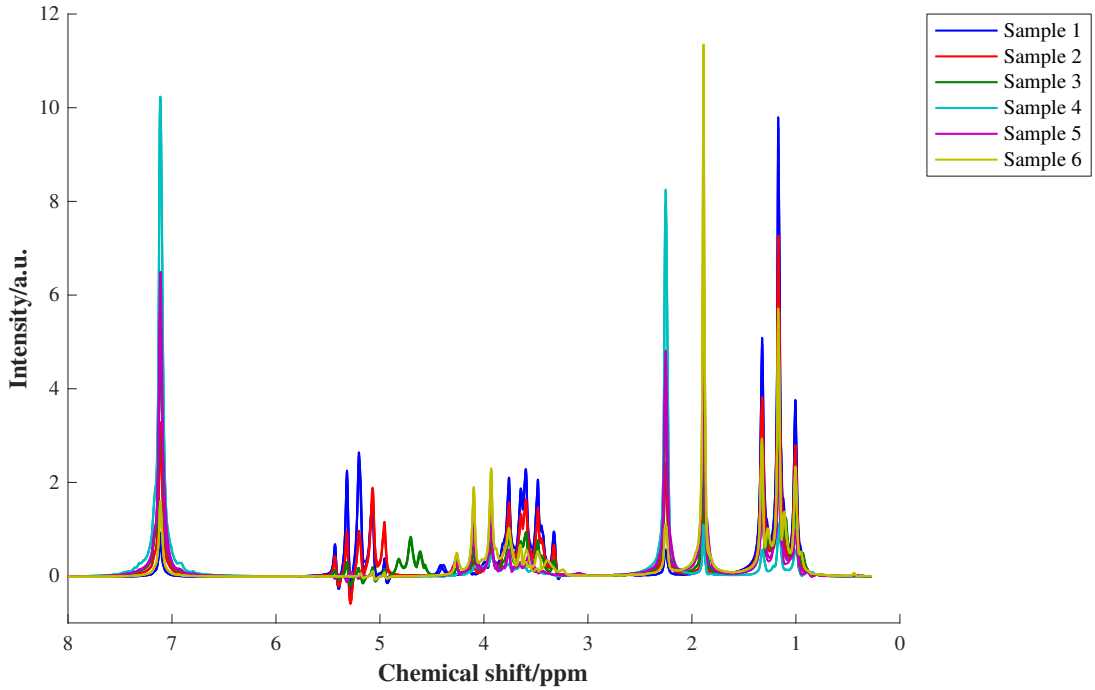

Figure 6.27 - ^{1}H low-field NMR spectra of test samples from dataset 4, with alignment by RAFFT and calibration transfer by SST (using 3 singular values).

A spectrum of test sample 2 from dataset 4 is shown without and with SST in Figure 6.28, overlaid with the same spectrum from dataset 3. The application of SST introduced noise into the singlet peak just below 2 ppm and into the baseline at the edge of the triplet peak just above 5 ppm. The intensity of the peaks increased by up to 1.5 a.u. with SST, but the spectrum still differed from dataset 3. The mean and standard deviations of the linewidths of the aromatic toluene peak present in the test samples (for dataset 3, dataset 4 without SST, dataset 4 with SST and dataset 4 with alignment) are displayed in Table 6.10. The mean linewidth for dataset 4 was similar with and without SST (differing by only 3.5 x 10^{-3} ppm), and was still higher than that of dataset 3 by a factor of 1.4. The standard deviation of the linewidths increased by a factor of 2 with SST (compared to without SST), indicating that the variation of the toluene peak increased as a result of calibration transfer.

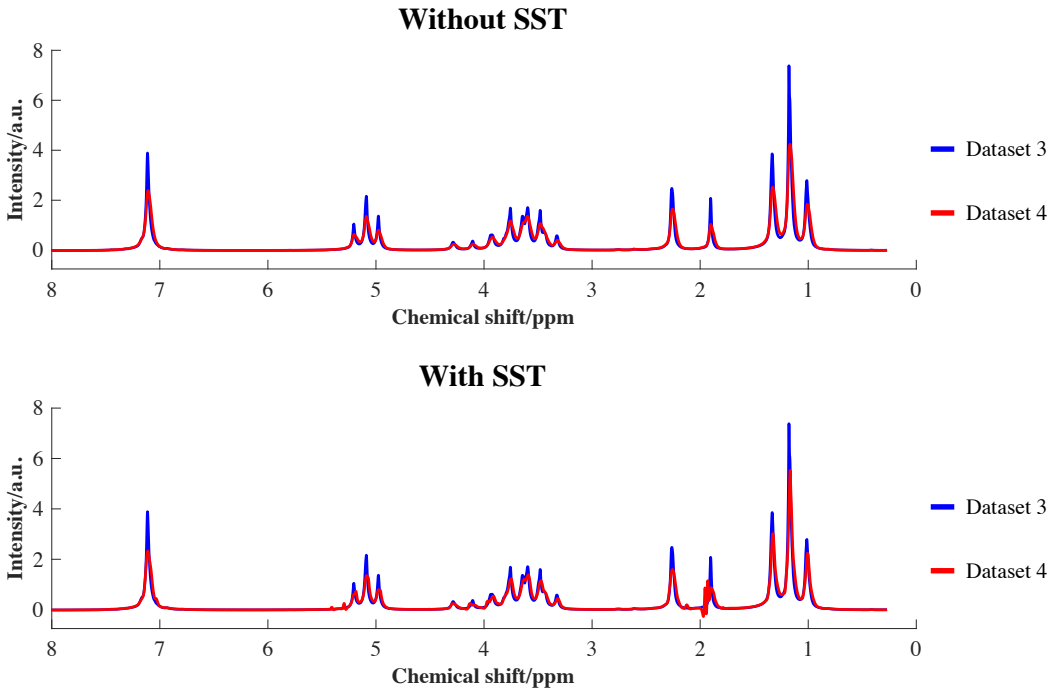

Figure 6.28 - ^{1}H low-field NMR spectrum of test sample 2 in dataset 3 (blue) and dataset 4 without and with calibration transfer by SST (red), no alignment (2 singular values included).

Table 6.10 - Mean and standard deviation values of the width at 50 % peak height of the toluene peak at 7 ppm within the test spectra of dataset 3 and of dataset 4 without SST, with SST and with RAFFT followed by SST.

Data	Mean width at 50 % height of toluene peak at 7 ppm/ppm	Standard deviation of width at 50 % height of toluene peak at 7 ppm/ppm
Dataset 3	0.0356	0.0079
Dataset 4	0.0546	0.0056
Dataset 4 with SST	0.0511	0.0101
Dataset 4 with RAFFT and SST	0.0384	0.0046

When RAFFT was performed prior to calibration transfer (Figure 6.29), the spectrum became more similar to that of dataset 3, with peaks of higher intensity (within 1 a.u. of the spectrum from dataset 3) and greater definition. The noise just below 2 ppm was

no longer present, but the noise just above 5 ppm worsened, resembling extra peaks in the multiplet ranging from 0.8 a.u. to –0.6 a.u. in intensity. The mean linewidth of the aromatic toluene peak in the test spectra was more similar to that of dataset 3 (differing by only 2.8 x 10^{-3} ppm), and the standard deviation of the linewidth was 1 x 10^{-3} ppm less. As for *i*coshift, the application of RAFFT does not alter the linewidths of the peaks, so the values displayed for datasets 3 and 4 without alignment or SST were the same as those obtained for datasets 3 and 4 with RAFFT. These results again demonstrate that SST is effective at removing the long-term variation between spectra when peak shifts are not present, but that the movement of peaks can cause problems.

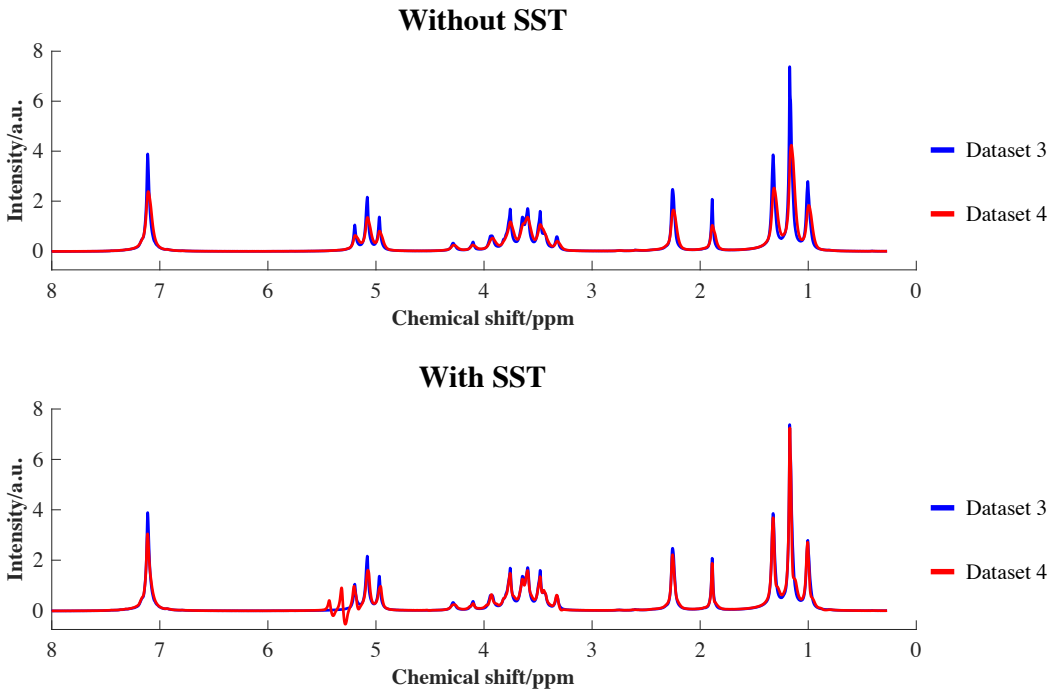

Figure 6.29 - ^{1}H low-field NMR spectrum of test sample 2 in dataset 3 (blue) and dataset 4 without and with calibration transfer by SST (red), aligned by RAFFT (3 singular values included).

6.3.3.2.2 Reference Deconvolution

To evaluate the effectiveness of reference deconvolution at removing the differences between the test spectra in datasets 3 and 4, a spectrum of calibration sample 7 from each dataset with reference deconvolution is overlaid in Figure 6.30. The spectra without reference deconvolution were discussed in section 5.3.4. When reference deconvolution was applied the spectra appeared almost identical, with an intensity

difference of less than 0.03 a.u. present. The mean and standard deviations of the linewidths of the aromatic toluene peak in the test spectra of datasets 3 and 4 were given in Table 6.4. Without reference deconvolution, the mean linewidth for dataset 4 was greater than that of dataset 3 by a factor of 1.5, but with reference deconvolution the values were similar (differing by only 2 x 10^{-4} ppm). The standard deviations of the linewidths also differed by a factor of 1.4 without reference deconvolution, but only by 1 x 10^{-4} ppm with reference deconvolution. Reference deconvolution therefore appears to have been effective at removing the differences between the two sets of spectra.

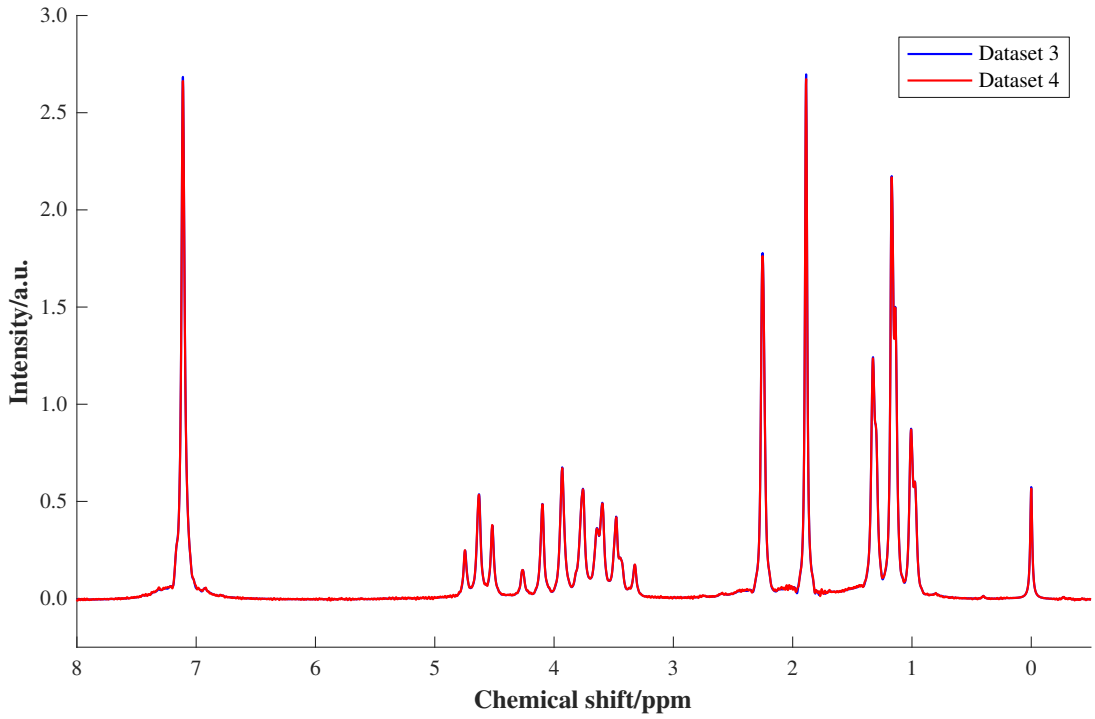

Figure 6.30 - ^{1}H low-field NMR spectrum of calibration sample 7 from dataset 3 (blue) and dataset 4 (red), with reference deconvolution.

6.3.3.2.3 Reference Deconvolution and Calibration Transfer

An example spectrum of test sample 2 from dataset 4 with reference deconvolution is shown without/with SST in Figure 6.31, overlaid with the same sample from dataset 3 with reference deconvolution. Without SST the spectra were similar, and the application of SST appeared to have little effect. The same plots are shown with RAFFT applied prior to SST in Figure 6.32. Again the spectra were similar, however

SST introduced noise in the form of a small negative peak (around 0.2 a.u. in intensity) into the spectrum. This was due to the presence of noise in this region of the baseline of several of the spectra (introduced as a result of deterioration of the TMS peak lineshape).

The mean and standard deviations of the linewidths at 50 % peak height of the aromatic toluene peak in the test samples are displayed in Table 6.11. Again, the application of SST does not appear to have affected the results (with the mean value differing by no more than 3 x 10^{-4} ppm and the standard deviations differing by no more than 2 x 10^{-4} ppm). This corresponds to the results obtained for the toluene, octene and dibutyl ethyl mixtures, and indicates that the application of SST after reference deconvolution is unnecessary.

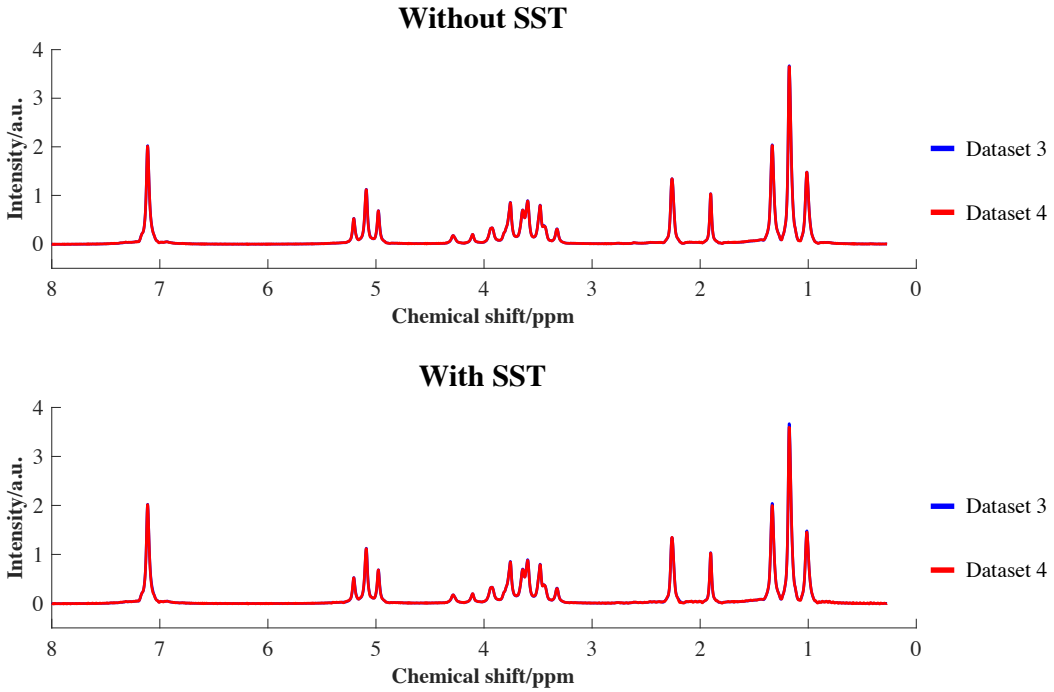

Figure 6.31 - ^{1}H low-field NMR spectrum of test sample 2 in dataset 3 (blue) and dataset 4 without and with calibration transfer by SST (red), no alignment (3 singular values included). With reference deconvolution applied to datasets 3 and 4 before SST.

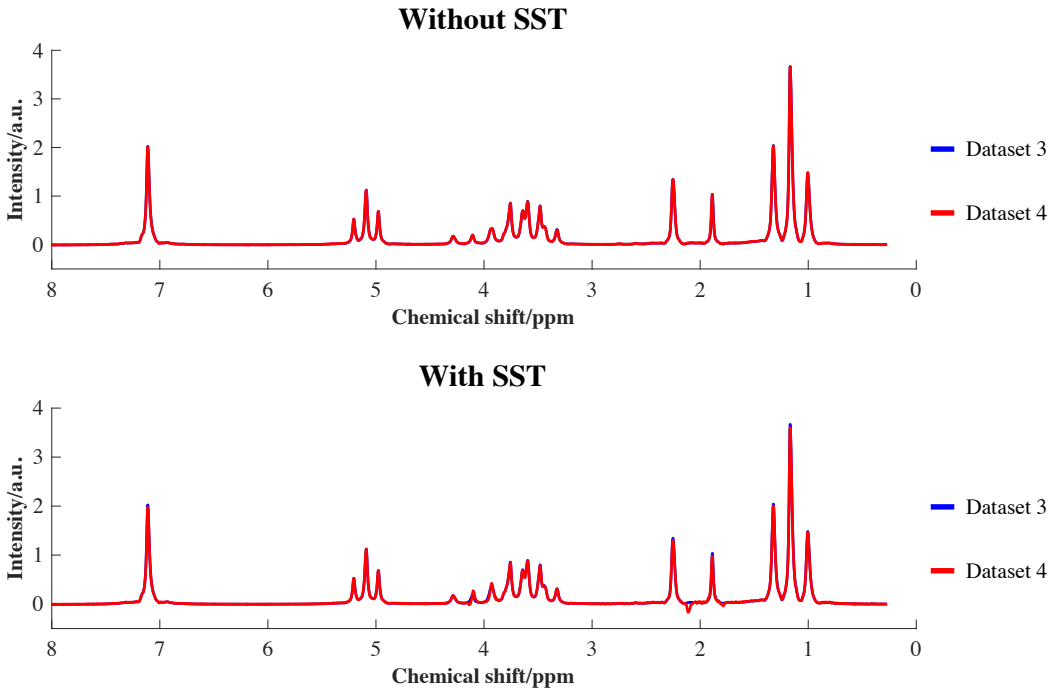

Figure 6.32 - ^{1}H low-field NMR spectrum of test sample 2 in dataset 3 (blue) and dataset 4 without and with calibration transfer by SST (red), aligned by RAFFT (1 singular value included). With reference deconvolution applied to datasets 3 and 4 before SST.

Table 6.11 - Mean and standard deviation values of the width at 50 % peak height of the toluene peak at 7 ppm within the test spectra of dataset 3 and of dataset 4 without SST, with SST and with RAFFT followed by SST. With reference deconvolution applied to datasets 3 and 4 before SST.

Data	Mean width at 50 % height of toluene peak at 7 ppm/ppm	Standard deviation of width at 50 % height of toluene peak at 7 ppm/ppm
Dataset 3	0.0334	0.0025
Dataset 4	0.0336	0.0024
Dataset 4 with SST	0.0337	0.0025
Dataset 4 with RAFFT and SST	0.0335	0.0026

6.3.3.2.4 Comparison of RMSEP Values

When the PLS1 models built using the calibration spectra from dataset 3 were applied to the test spectra in dataset 4 (without SST or reference deconvolution, with SST, with reference deconvolution and with both reference deconvolution and SST), the RMSEP values displayed in Table 6.12 were obtained. Before SST, the RMSEP value for toluene was fairly low (1.46 % w/w) and the RMSEP values for ethanol and ethyl acetate were higher (2.84 % w/w and 2.52 % w/w respectively). The application of RAFFT had no significant effect on the RMSEP value for toluene, but increased the RMSEP values for ethanol and ethyl acetate by 0.5 % w/w and 0.8 % w/w respectively. This indicates that alignment caused the differences between the spectra in datasets 3 and 4 to become more pronounced, perhaps because the peaks in each dataset were shifted to a different extent. However one less latent variable was required after RAFFT.

When SST was applied to the test spectra of dataset 4, the RMSEP values for all solvents decreased by up to 1.1 % w/w without RAFFT and up to 2.3 % w/w with RAFFT. The number of latent variables required remained the same in most cases, but one extra latent variable was necessary after SST for ethanol in dataset 4. Lower RMSEP values could be obtained when RAFFT was applied before SST, compared to SST alone ($\leq$ 1.01 % w/w compared to $\leq$ 1.75 % w/w). This again indicates that alignment has improved the performance of SST, and that SST has been successful despite the noise caused by peak movement.

Without alignment, the application of reference deconvolution decreased the RMSEP value of ethanol by a factor of 2 (when the PLS models were built using the calibration spectra from dataset 3 and applied to the test spectra from dataset 4), but increased the RMSEP values of toluene and ethyl acetate by up to 0.4 % w/w. This may be because the large peak shifts exhibited by ethanol were caused by the interaction of components and so were similar for the two datasets, therefore reference deconvolution reduced the differences between the ethanol peaks by removing the variation in lineshape. For the other components, reference deconvolution appears to have increased the difference in predictive ability between the two sets of spectra. However two less latent variables were required for ethanol and one less latent variable was required for ethyl

acetate compared to without reference deconvolution. As the variation in the linewidth of the aromatic toluene peak between the two datasets decreased upon reference deconvolution, it would be expected that the RMSEP values would decrease. Therefore it is possible that the application of reference deconvolution may have altered the areas of the peaks to different extents, reducing the predictive abilities of the toluene and ethyl acetate spectra.

Table 6.12 - RMSEP values for PLS1 models built using calibration spectra from dataset 3 and applied to test spectra from dataset 4 (without alignment, with alignment and with bucketing); without calibration transfer or reference deconvolution, with calibration transfer, with reference deconvolution, and with both reference deconvolution and calibration transfer.

Alignment	Transformation	Toluene		Ethanol		Ethyl acetate	
		LVs	RMSEP/ (% w/w)	LVs	RMSEP/ (% w/w)	LVs	RMSEP/ (% w/w)
None	None	3	1.46	4	2.84	4	2.52
	SST (2 SVs)	3	1.33	4	1.74	4	1.75
	Reference deconvolution	3	1.85	2	1.41	3	2.68
	Reference deconvolution and SST (3 SVs)	4	1.68	2	1.17	3	2.50
RAFFT	None	3	1.42	3	3.23	3	3.36
	SST (3 SVs)	3	0.83	4	1.01	3	1.01
	Reference deconvolution	3	0.87	2	3.36	4	2.97
	Reference deconvolution and SST (1 SV)	3	0.59	2	3.24	4	3.12
Bucketing	None	4	0.50	4	0.42	3	0.54
	Reference deconvolution	4	0.51	4	0.42	3	0.56

When RAFFT was applied after reference deconvolution, the RMSEP values of toluene and ethyl acetate decreased by 0.5 % w/w and 0.4 % w/w respectively

(compared to the values obtained for RAFFT alone), and the RMSEP value of ethanol increased by 0.1 % w/w. One less latent variable was required for ethanol and one more latent variable was required for ethyl acetate compared to when RAFFT was applied without reference deconvolution. This indicates that reference deconvolution decreased the differences between the two sets of spectra to an extent. However the RMSEP values were significantly higher than those obtained using SST (≤ 3.36 % w/w compared to ≤ 1.01 % w/w with RAFFT, and ≤ 2.68 % w/w compared to ≤ 1.75 % w/w without RAFFT). This suggests that when large amounts of peak shift are present, calibration transfer is more effective than reference deconvolution at removing the differences between spectra acquired under different conditions, despite the presence of noise in the transferred test spectra. It is unsurprising that calibration transfer was more effective than reference deconvolution at removing the differences between the datasets, as the transfer function in reference deconvolution was calculated from a reference peak within the same spectrum, therefore differences between the datasets were not taken into account. In SST, on the other hand, spectral information obtained using both datasets was used to calculate the transfer function.

When both reference deconvolution and SST were applied, the RMSEP values decreased by a small amount (up to 0.2 % w/w) compared to the values obtained for reference deconvolution alone. However, one more latent variable was required for toluene and the RMSEP value was higher than before reference deconvolution. When RAFFT was also applied, the RMSEP values of toluene and ethanol decreased by 0.3 % w/w and 0.1 % w/w respectively when SST was performed after reference deconvolution (compared to the results obtained with reference deconvolution and no SST), but the RMSEP value for ethyl acetate increased by 0.15 % w/w. Therefore the application of SST after reference deconvolution made little difference to the results, and more accurate predictions could be obtained using SST without reference deconvolution. This again suggests that reference deconvolution has been successful at removing the variation between the spectra, but that small differences in relative area were introduced into the peaks, worsening the RMSEP values. The application of SST to the deconvoluted spectra therefore made little difference, as the variation between the datasets had already been removed.

The application of bucketing significantly reduced the RMSEP values obtained for all solvents (from ≤ 1.46 % w/w to ≤ 0.54 % w/w) when the PLS1 model built with dataset 3 was applied to the test spectra of dataset 4. These values were lower than those obtained for SST or reference deconvolution, again indicating that bucketing was more effective at removing long-term variation than calibration transfer or reference deconvolution for this data. The application of bucketing after reference deconvolution produced similar RMSEP values to those obtained for bucketing alone (differing by ≤ 0.02 % w/w), again indicating that the application of reference deconvolution in addition to bucketing was unnecessary. However as discussed in Chapter 5, very large bucket sizes (0.75 ppm with a slackness of 0.25) were required in order to eliminate the peak shift in this dataset, with the resulting spectra consisting of only 12 data points. These bucket sizes are so large that the shape of the peaks is no longer important, so the success of bucketing at removing the variation between the datasets is unsurprising. The components present in these mixtures can still be distinguished from the bucketed spectra (as they were chosen so that each component had at least one clearly resolvable peak) but for other datasets exhibiting greater overlap, the RMSEP values are likely to become poorer when such large bucket sizes are used. In these cases, the use of calibration transfer or reference deconvolution may be more effective than bucketing in allowing the transfer of calibration models between spectra acquired under different conditions.

6.4 Conclusions

The performance of the low-field NMR spectrometer appeared to be stable over time (provided the instrument had been switched on for several days prior to analysis), however performance began to deteriorate when samples were continually inserted and removed from the instrument. This is believed to be due to deviations in the magnet temperature from its optimum value, although the lack of a clear correlation between magnet temperature and lineshape deterioration suggests that other factors may also have contributed. These could include temperature gradients within the sample or instrument and the temperature at other points within the instrument which cannot easily be measured. Despite attempting to control the temperature of the samples upon insertion into the instrument and to ensure that the samples had reached

the temperature of the magnet before spectra were acquired, deviations in magnet temperature of one or two thousandths of a degree Celsius were observed and produced a noticeable deterioration in lineshape. These findings suggest that flowing a reaction mixture through the instrument during on-line reaction monitoring may have a similar effect on the magnet temperature. Therefore investigation of the extent of this effect during flow analysis would be recommended before performing on-line NMR spectroscopy with the instrument.

The effectiveness of reference deconvolution for removing the short-term variation of spectra within the same dataset has been evaluated. The variation in linewidth (measured using the aromatic toluene peak in the test samples) was found to decrease upon the application of reference deconvolution and when the spectra were well-aligned, the RMSEP values of the PLS1 models also decreased. However reference deconvolution was not effective at reducing the RMSEP values when peak shifts were present. This further demonstrates the importance of alignment, as discussed in Chapter 5. As a decrease in the linewidth variation was observed when peak shifts were present but an improvement in RMSEP was not, it may be that reference deconvolution altered the areas of the peaks to different extents, reducing the predictive ability of the spectra.

For elimination of the long-term variation between spectra acquired under different conditions, calibration transfer and reference deconvolution were compared. There are both advantages and disadvantages associated with each method. The main advantage of calibration transfer is that no reference peak is required, so it is not necessary to add a standard. The necessity for a well resolved reference peak in reference deconvolution means that unless a suitable peak is present in every sample, a standard (e.g. TMS) must be added. This inhibits the use of reference deconvolution in on-line reaction monitoring. However, a disadvantage of calibration transfer is that shifting of peaks within the transfer or test sample sets can produce noise and distortions in the transformed spectra, as the transfer sample set is no longer representative of the test spectra in the regions where peak shifts occur. An advantage of using reference deconvolution instead of calibration transfer is that no measurement of calibration samples is required under the new set of conditions. However, distortion of the lineshape of the reference peak can introduce large amounts of noise when reference

deconvolution is carried out, as the distorted reference peak may no longer resemble a singlet and the extent of distortion may differ for each signal. This is a major problem when the stability of the instrument decreases over the course of analysis, as it prevents the application of reference deconvolution when the lineshape of the spectra has deteriorated.

When little peak shift was present in the spectra (< 0.2 ppm), calibration transfer and reference deconvolution both reduced the RMSEP values obtained when a model built with dataset 1 was applied to dataset 2, particularly when alignment was also performed. The linewidths of the peaks in the spectra (measured using the aromatic toluene peak in the test samples) also became more similar. For the spectra exhibiting large amounts of peak shift (up to 1.5 ppm), calibration transfer was more effective than reference deconvolution at allowing PLS1 models built with dataset 3 to be applied to dataset 4 (particularly for ethanol and ethyl acetate after alignment), despite the presence of noise and distortions in the transformed spectra. However, reference deconvolution was able to reduce the difference in linewidth between the two sets of spectra. The application of calibration transfer after reference deconvolution produced similar results to reference deconvolution alone.

Bucketing of the spectra was more effective than calibration transfer or reference deconvolution, as the spectrum of each component contained clearly distinguishable peaks. However bucketing is not likely to be as successful when greater overlap of peaks is present. Calibration transfer would be recommended for use in these cases, with alignment of the spectra performed prior to transfer. The next step in assessing the suitability of the low-field NMR spectrometer for process monitoring would be to monitor a reaction using the instrument and to apply these findings to the spectra collected.

6.5 References

1. E. Danieli, J. Perlo, A. L. L. Duchateau, G. K. M. Verzijl, V. M. Litvinov, B. Blumich and F. Casanova, *ChemPhysChem*, 2014, **15**, 3060–3066.
2. K. Singh and B. Blumich, *Trends Anal. Chem.*, 2016, **83**, 12–26.

3. Magritek, The Lock and the importance of field stability, http://www.magritek.com/2014/08/12/the-lock-and-the-importance-of-field-stability/, (accessed 29th April, 2019).
4. G. A. Morris, H. Barjat and T. J. Horne, *J. Prog. Nucl. Magn. Reson. Spectrosc.*, 1997, **31**, 197–257.
5. K. R. Metz, M. M. Lam and A. G. Webb, *Concepts Magn. Reson.*, 2000, **12**, 21–42.
6. P. Ebrahimi, M. Nilsson, G. A. Morris, H. M. Jensen and S. B. Engelsen, *J. Chemom.*, 2014, **28**, 656–662.
7. E. J. Kibrik, O. Steinhof, G. Scherr, W. R. Thiel and H. Hasse, *Ind. Eng. Chem. Res.*, 2014, **53**, 12602–12613.
8. M. H. M. Killner, Y. G. Linck, E. Danieli, J. J. R. Rohwedder and B. Blumich, *Fuel*, 2015, **139**, 240–247.
9. H. Barjat, G. A. Morris, A. G. Swanson, S. Smart and S. C. R. Williams, *J. Magn. Reson., Ser. A*, 1995, **116**, 206–214.
10. J. J. Workman, Jr., *Appl Spectrosc*, 2018, **72**, 340–365.
11. Y. B. Monakhova and B. W. K. Diehl, *Magn. Reson. Chem.*, 2016, **54**, 712–717.
12. T. M. Alam and M. K. Alam, *J. Chemom.*, 2010, **24**, 261–272.
13. T. M. Alam, M. K. Alam, S. K. McIntyre, D. E. Volk, M. Neerathilingam and B. A. Luxon, *Anal. Chem.*, 2009, **81**, 4433–4443.
14. Y. B. Monakhova and S. P. Mushtakova, *J. Anal. Chem.*, 2017, **72**, 147–155.
15. J. Gislason, H. Chan and M. Sardashti, *Appl. Spectrosc.*, 2001, **55**, 1553–1560.
16. A. C. Wang and A. Bax, *J. Biomol. NMR*, 1993, **3**, 715–720.
17. C. Ammann, P. Meier and A. E. Merbach, *J. Magn. Reson.*, 1982, **46**, 319–321.
18. L. Castanar, G. D. Poggetto, A. A. Colbourne, G. A. Morris and M. Nilsson, *Magn. Reson. Chem.*, 2018, **56**, 546–558.
19. W. Du, Z. P. Chen, L. J. Zhong, S. X. Wang, R. Q. Yu, A. Nordon, D. Littlejohn and M. Holden, *Anal. Chim. Acta*, 2011, **690**, 64–70.

20. Magritek, Introducing the new Spinsolve Autosampler, http://www.magritek.com/2019/02/18/introducing-the-new-spinsolve-autosampler/, (accessed 12th April, 2019).

7 Conclusions and Further Work

7.1 Mid-Infrared Spectroscopy

The performance of a novel, robust MIR spectrometer designed for use in process environments has been assessed. The spectrometer contains no fibre optics and its robustness is due to the use of the Sagnac interferometer, which contains no moving parts. This provides a solution to some of the issues which have prevented the widespread use of MIR spectroscopy in process analysis. Accurate predictions of concentration could be obtained using the instrument and its performance was comparable to that of a laboratory based MIR spectrometer. The novel spectrometer is therefore suitable for the quantitative *in situ* analysis of liquids and opens up new opportunities for process monitoring in the MIR region, for example the ability to utilise MIR spectroscopy in particularly harsh environments.

Calibration transfer between the laboratory and process MIR spectrometers was effective, demonstrating the ability to build a model in the laboratory for application to a process. This can save time and resources, as it eliminates the need to acquire a full set of calibration spectra within the process environment. PDS and SST were found to be more effective at transferring the models than DS. SST would be recommended for future use, as it is easier to determine an optimum number of singular values than an optimum PDS window size since there is a smaller number of possible values. Altering the transfer sample set did not significantly affect the predictions obtained, as long as the subset of samples used for transfer was representative of the test samples. Six transfer samples appeared to be the optimum number to include, however the number of transfer samples was less important than the choice of transfer samples.

A suggestion for future work would be to repeat the comparison of different calibration transfer methods and transfer sample subsets using more complex mixtures, to determine whether the same trends are observed. In addition, calibration transfer between different Keit spectrometers could be performed by building a model using one instrument and transferring it to the others. This would eliminate the need to build separate calibration models with each instrument, and the effectiveness of the models should not change over time due to the robustness of the instruments.

The ability of the novel MIR spectrometer to monitor an esterification reaction has also been demonstrated to further evaluate its performance. Accurate profiles of relative concentration could be obtained from the spectra using multivariate curve resolution, therefore the spectrometer appears to be suitable for *in situ* reaction monitoring. Differences in reaction rate upon changing the temperature of the reaction vessel could also be detected. The next step could be to monitor a range of different reactions, in order to further verify the suitability of the spectrometer for *in situ* monitoring of liquid processes.

Of the three MCR toolboxes evaluated for decomposition of the esterification reaction mixture spectra into their pure component contributions, GUIPRO was the most effective due to the ability to apply penalty functions to the constraints. The MCR-ALS toolbox was less effective as only hard constraints could be applied, and in PLS Toolbox the application of penalty functions produced poorer predictions than the application of hard constraints. GUIPRO would therefore be recommended for the analysis of MIR reaction mixture spectra, with reference spectra applied as soft equality constraints and non-negativity applied to both the concentration and spectral data. The choice of sensitivity value is important to consider, and the convergence tolerance can also affect the results obtained. These findings could facilitate the application of MCR to MIR reaction mixture spectra acquired during process monitoring. The use of MCR rather than calibration based methods such as PLS saves resources and time, as it is no longer necessary to build a calibration model.

In addition to robustness, the increased sensitivity and resolution of MIR spectrometers would be desirable for process analysis. Miniaturisation would also facilitate the installation of MIR spectrometers in process environments. At present the majority of miniature MIR spectrometers have limited resolution or lack robustness due to the presence of moving parts. However advances in technology such as QCLs, MEMS filters and uncooled detector arrays provide a potential solution. QCLs are compact, robust and capable of achieving high sensitivity and specificity. The use of MEMS filters facilitates the miniaturisation of spectrometers and uncooled detector arrays can increase the achievable performance. These advances will aid the development of miniature MIR spectrometers capable of achieving high sensitivity

and resolution, and it is likely that this will lead to MIR spectroscopy becoming more widely used in process analysis in the future.

7.2 NMR Spectroscopy

The instrumental stability of a low-field NMR spectrometer was evaluated, and the performance was found to be stable over time (as long as the instrument had been left on for several days prior to analysis). However the continual insertion and removal of samples caused the performance to deteriorate, producing spectra of poor lineshape. This effect is believed to have been caused by small changes in magnet temperature (of one or two thousandths of a degree Celsius). Despite best efforts to keep the magnet temperature under control (by heating each sample to the temperature of the magnet before insertion and ensuring that the sample temperature had stabilised before spectra were acquired), drifts in magnet temperature occurred over time due to a lag in the effect of the heater/cooler system within the instrument. No obvious correlation between magnet temperature and lineshape deterioration was observed, although the poorest lineshape corresponded to the time region in which the magnet temperature was lowest. Therefore it is possible that the lineshape deterioration was due to a combination of factors (e.g. changes in temperature at different points inside the instrument or temperature gradients within the sample/instrument) rather than purely the magnet temperature.

As well as the ability to analyse a number of samples consecutively (e.g. when building a calibration model or using an autosampler), these findings have implications on the ability to monitor reactions using the instrument. At-line analysis also normally requires the consecutive analysis of different samples, and flowing a reaction mixture through the instrument during on-line analysis is likely to have a similar effect on the magnet temperature. Investigation of this effect would therefore be recommended before flow NMR spectroscopy is performed using the spectrometer.

As a solution to the issues of peak shift and lineshape deterioration in low-field NMR spectra, chemometrics was utilised. A range of alignment methods which had been shown to be successful at high field were evaluated to solve the problem of peak shift. Of these methods, RAFFT, PAFFT and *i*coshift were the most effective. The advantage of *i*coshift over the other methods is that optimisation of parameters (such

as segment length and slackness) is not necessary. *I*coshift was found to perform well when little peak shift was present within the spectra (< 0.2 ppm), but was not particularly effective when large amounts of peak shift were present (up to 1.5 ppm). RAFFT and PAFFT were more effective in this case (with RAFFT performing best overall), however it was still not possible to fully align the peaks with these methods. Despite this, significant improvements in RMSEP could be obtained.

Optimised bucketing of the spectra was found to produce the greatest improvement in RMSEP, however when peak shifts of up to 1.5 ppm were present then very large bucket sizes were necessary and almost all spectral information was lost. The effectiveness of bucketing in this case was believed to be due to each component containing at least one clearly resolved peak, which produced a maximum in the bucketed spectra. When bucketing was performed on the low-field NMR spectra collected during the esterification reaction (which exhibited greater overlap), the components could no longer be resolved at the bucket sizes required to remove the peak shifts. Therefore bucketing is not likely to produce such accurate predictions of concentration in cases where the components exhibit greater peak overlap. The application of both bucketing (using smaller bucket sizes) and alignment to the spectra may further improve the results, and is a suggestion for future work.

To solve the problem of lineshape deterioration, calibration transfer and reference deconvolution were evaluated. The effectiveness of reference deconvolution for removing the short-term variation between samples acquired under the same conditions was first assessed. Reference deconvolution was found to reduce the variation in linewidth within each dataset, and improved the results of PLS when the spectra were well-aligned. However when peak shifts were present, the RMSEP values did not improve. These results suggest that reference deconvolution was successful at reducing the variation between spectra, but altered the relative areas of the peaks, which affected the predictive abilities of the spectra.

The performance of calibration transfer and reference deconvolution was then compared for the removal of long-term variation between spectra collected under different conditions. Reference deconvolution is more commonly used in NMR spectroscopy, however it requires the presence of a well resolved reference peak in

every sample, so an internal standard may have to be added. This is undesirable, as it inhibits the use of reference deconvolution in reaction monitoring (e.g. by flow NMR spectroscopy). In addition, deterioration in the lineshape of the reference peak can introduce large amounts of noise into the spectra. The main advantage of calibration transfer is that the presence of a reference peak is not required. However it is necessary to analyse a subset of calibration samples to use as transfer samples, and the shifting of peaks can introduce noise into the spectra.

When little peak shift (< 0.2 ppm) was present, both calibration transfer and reference deconvolution were found to be effective at allowing a calibration model built under one set of conditions (an optimal shim) to be applied to spectra collected under a different set of conditions (a sub-optimal shim, loaded to simulate the effect of changing instrument/conditions). For the dataset exhibiting large peak shifts (up to 1.5 ppm), calibration transfer was more effective than reference deconvolution despite the presence of noise in some of the spectra. The application of calibration transfer after reference deconvolution made little difference to the spectra (compared to reference deconvolution alone). Bucketing again produced the most accurate predictions, as it eliminated the differences between spectra acquired with different shims. However, as mentioned before, it is not likely to be so effective for spectra with greater peak overlap. Calibration transfer would therefore be recommended as a solution to lineshape deterioration.

Therefore it is suggested that if variation is present within a low-field NMR dataset then reference deconvolution should be applied, and if variation between datasets is present then calibration transfer would be more suitable. When small peak shifts (< 0.2 ppm) are present then *i*coshift should be applied after reference deconvolution/before calibration transfer, and when larger peak shifts are present then RAFFT should be used instead.

The effectiveness of different methods of calibration transfer could be evaluated in the future (as only SST was used in this work), and investigation into changing the transfer sample set used in SST could be carried out to determine whether the trend is the same as for the mid-infrared spectra. Singh et al.[1, 2] have utilised high-field NMR spectroscopy to supply reference values of concentration for PLS models built at low

field, but the suitability of calibration transfer between high and low-field NMR spectrometers could also be investigated. This would allow calibration models built using a high-field instrument to be applied to spectra collected in a process environment. However the resolution of peaks is likely to be different at high and low field, and resolving the peaks would be a challenge. The effectiveness of reference deconvolution using different ideal reference peaks (i.e. a Gaussian lineshape and/or different line broadening factors) could also be evaluated.

The ability to obtain accurate predictions of concentration despite the issues encountered demonstrates the effectiveness of low-field NMR spectroscopy for quantitative analysis. The reduced size and cost of low-field NMR spectrometers compared to high-field instruments facilitates their installation in process environments, providing a solution to some of the issues which have prevented the widespread use of NMR spectroscopy in process analysis. However there are still drawbacks, for example the low sensitivity compared to other techniques (e.g. optical spectroscopy) and the temperature sensitivity of the magnet. In order to analyse complex mixtures by low-field NMR spectroscopy, an improvement in resolution would also be necessary. Further advances in magnet technology may help to solve these problems in the future.

A number of applications of low-field NMR spectroscopy in process monitoring have already been demonstrated, and the results of this work suggest that NMR spectroscopy has the potential to become far more widely used in process analysis in the future. The next step would be to investigate the extent of the lineshape deterioration and peak movement present during on-line reaction monitoring. The effectiveness of the solutions demonstrated in this work could then be assessed for application to low-field NMR spectra collected during reactions.

7.3 References

1. K. Singh, S. P. Kumar and B. Blumich, *Fuel*, 2019, **243**, 192–201.
2. K. Singh and B. Blumich, *Polymer*, 2018, **141**, 154–165.

Appendices

Appendix 3: Additional Figures Corresponding to Chapter 3

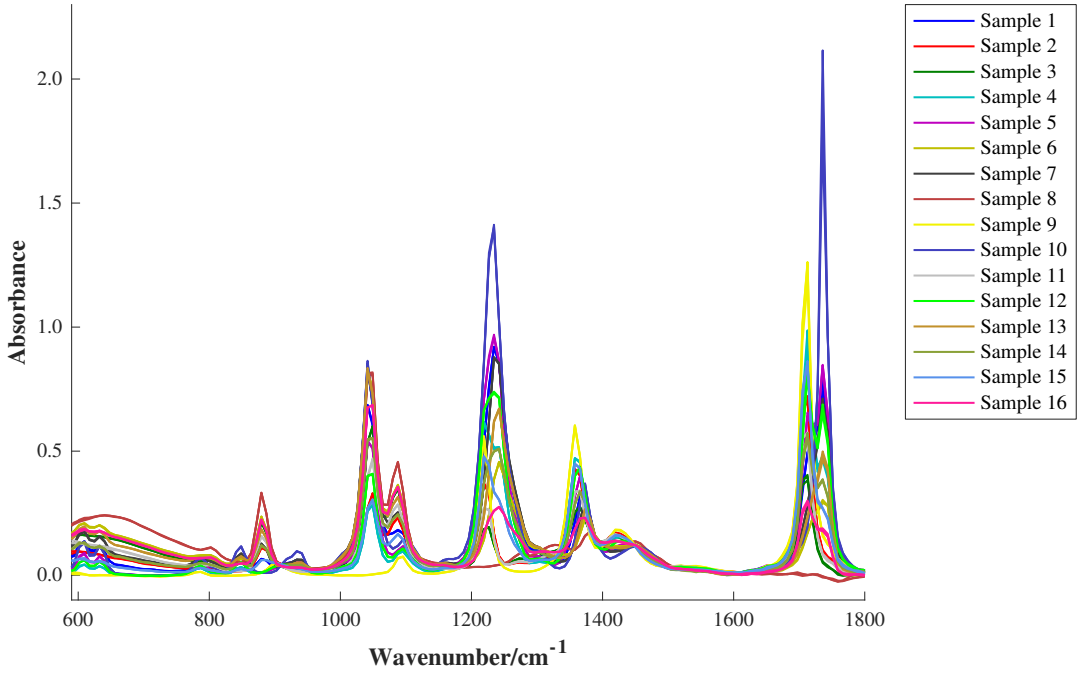

Figure 3.16 - Spectra of calibration samples containing acetone, ethanol and ethyl acetate obtained using the MB3000 spectrometer at 16 cm^{-1} resolution, average of 19 scans.

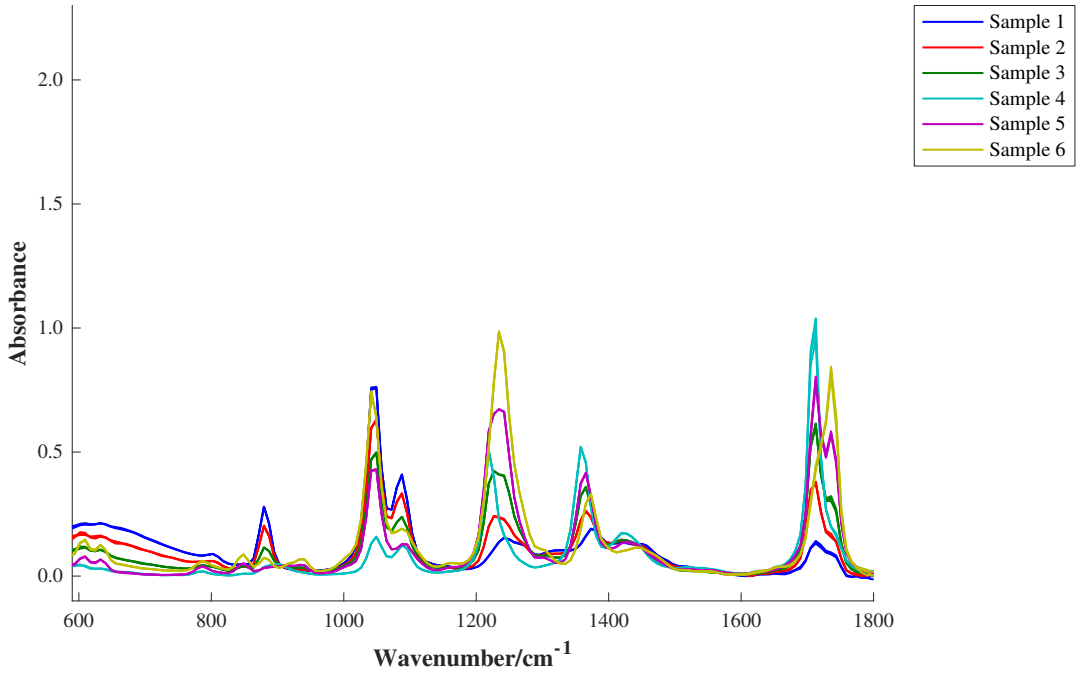

Figure 3.17 - Spectra of test samples containing acetone, ethanol and ethyl acetate obtained using the MB3000 spectrometer at 16 cm^{-1} resolution, average of 19 scans.

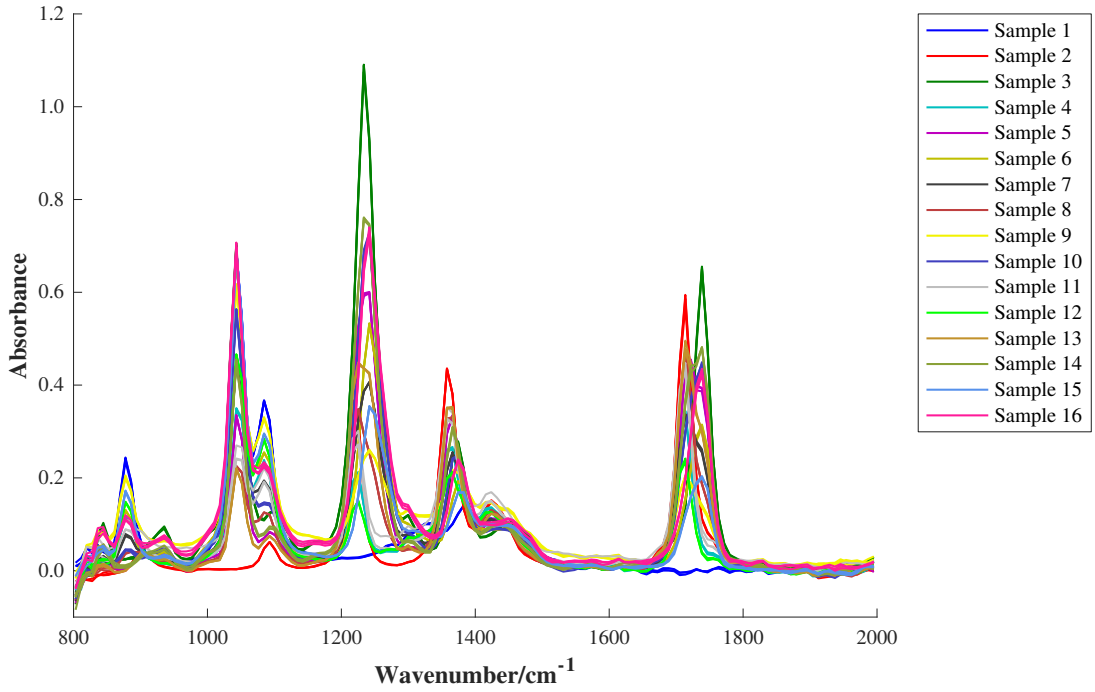

Figure 3.18 - Spectra of calibration samples containing acetone, ethanol and ethyl acetate obtained using the Keit spectrometer at 16 cm^{-1} resolution, average of 19 scans.

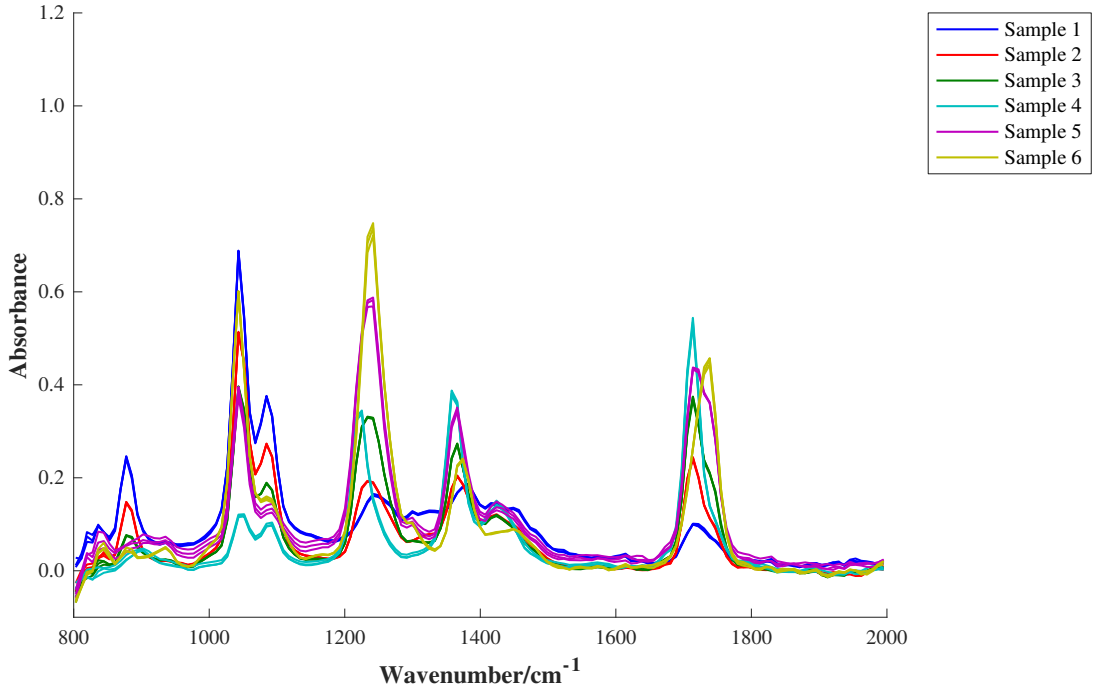

Figure 3.19 - Spectra of test samples containing acetone, ethanol and ethyl acetate obtained using the Keit spectrometer at 16 cm^{-1} resolution, average of 19 scans.

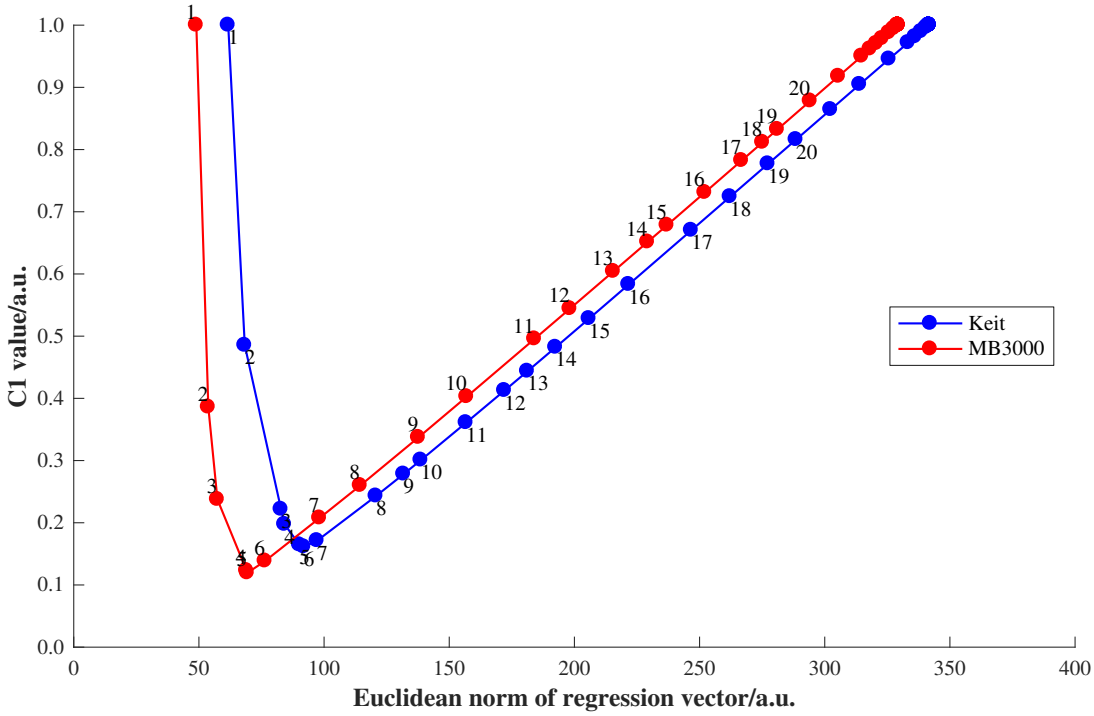

Figure 3.20 - C1 value versus Euclidean norm of regression vector for acetone PLS1 models built using Keit and MB3000 data (> 20 LVs not labelled due to overlap).

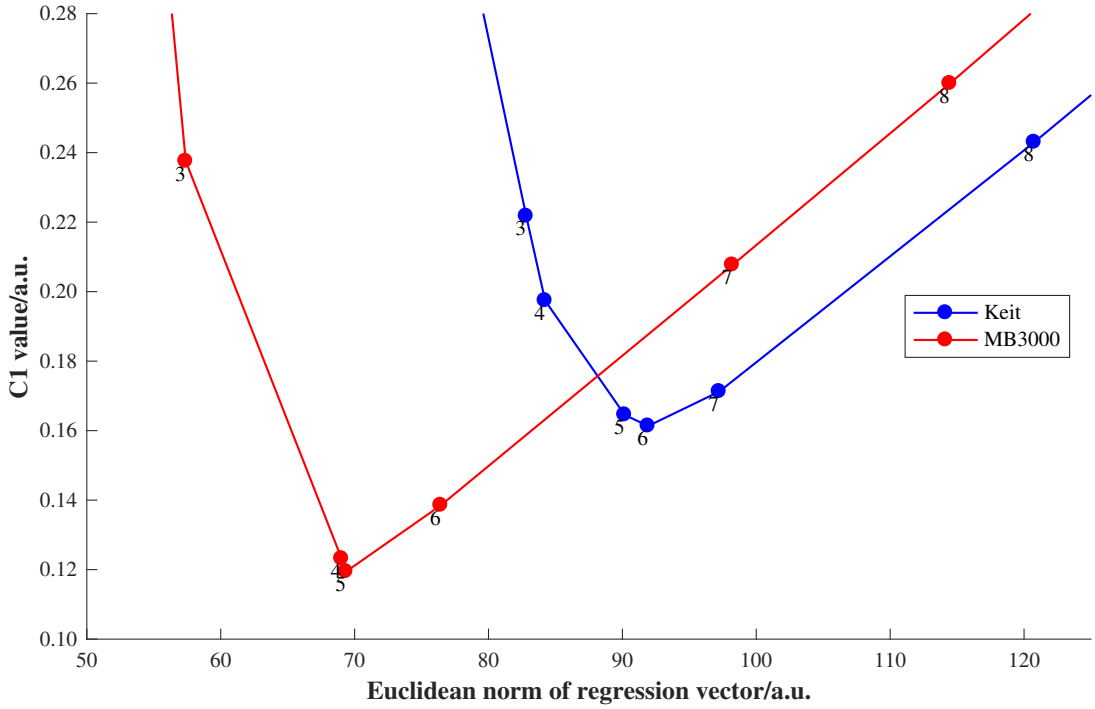

Figure 3.21 - C1 value versus Euclidean norm of regression vector for acetone PLS1 models built using Keit and MB3000 data, zoomed in on minimum so labels can be read.

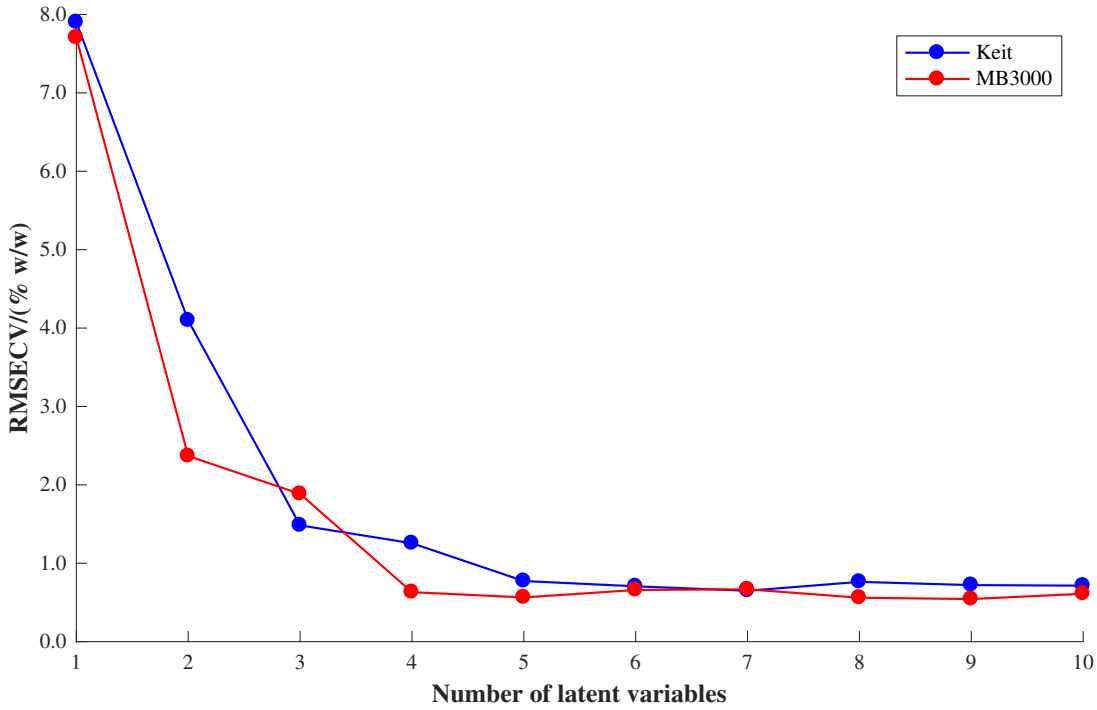

Figure 3.22 - RMSECV versus number of latent variables for acetone PLS1 models built using Keit and MB3000 data.

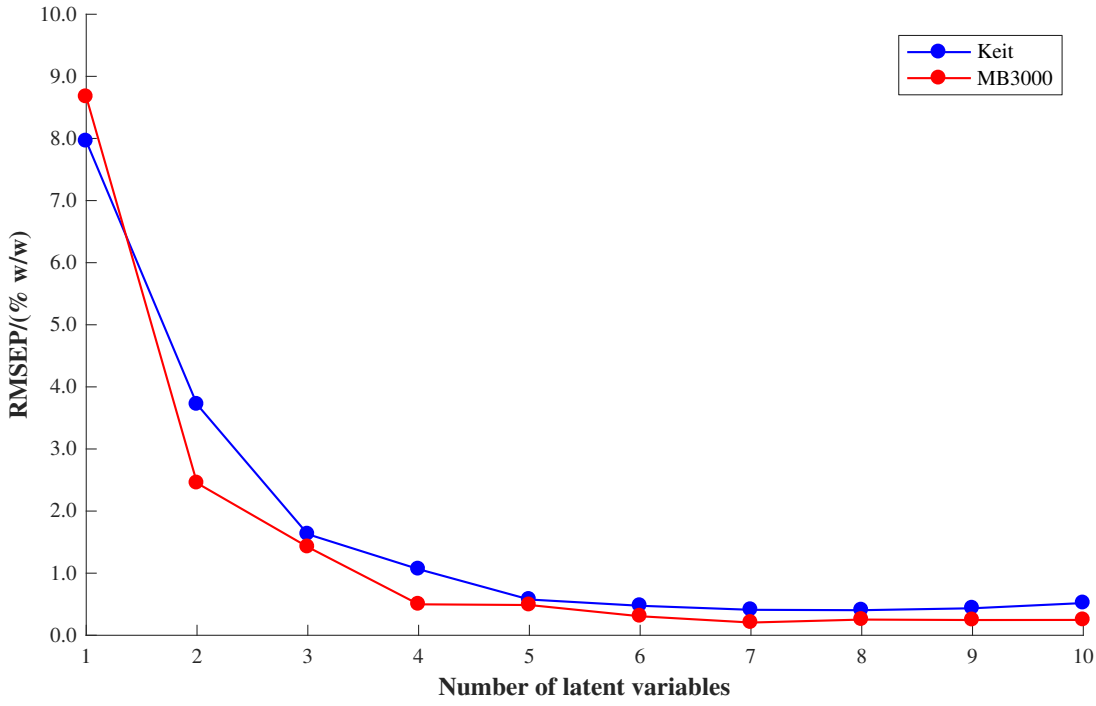

Figure 3.23 - RMSEP value versus number of latent variables for acetone PLS1 models built using Keit and MB3000 data.

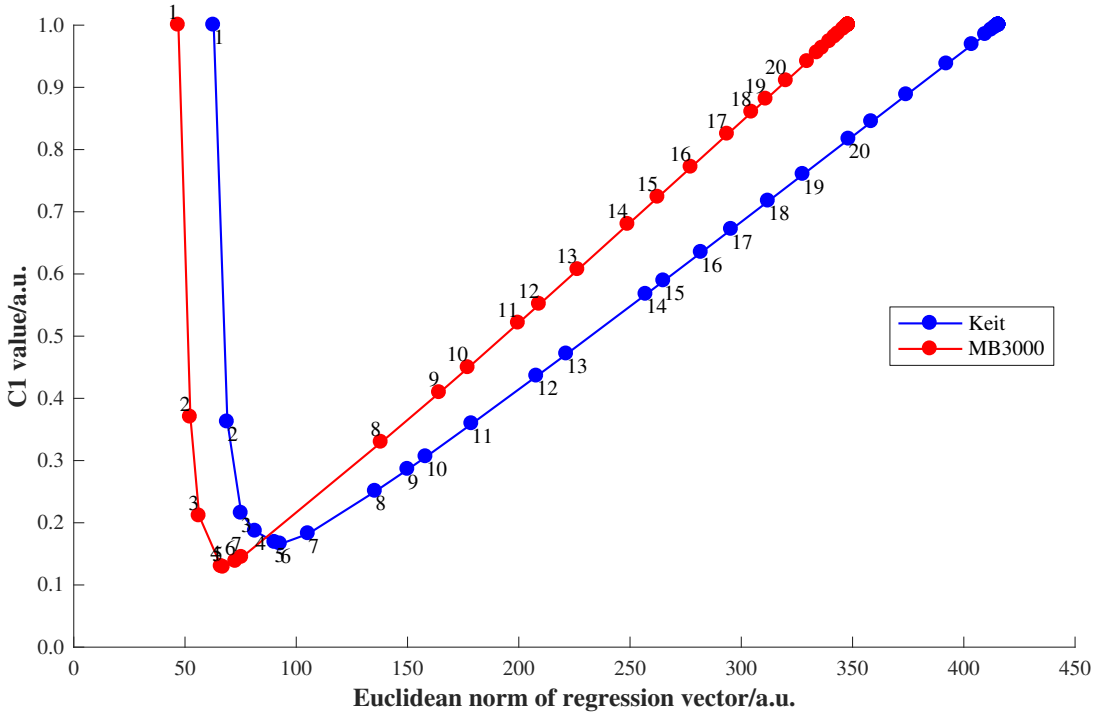

Figure 3.24 - C1 value versus Euclidean norm of regression vector for ethanol PLS1 models built using Keit and MB3000 data (> 20 LVs not labelled due to overlap).

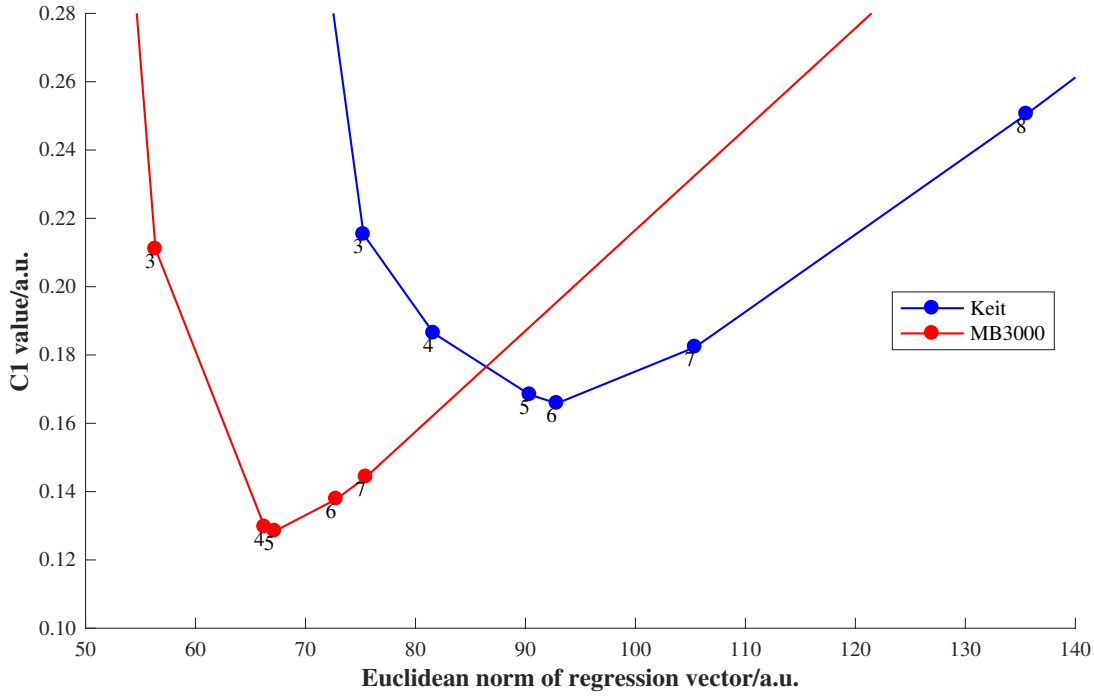

Figure 3.25 - C1 value versus Euclidean norm of regression vector for ethanol PLS1 models built using Keit and MB3000 data, zoomed in on minimum so labels can be read.

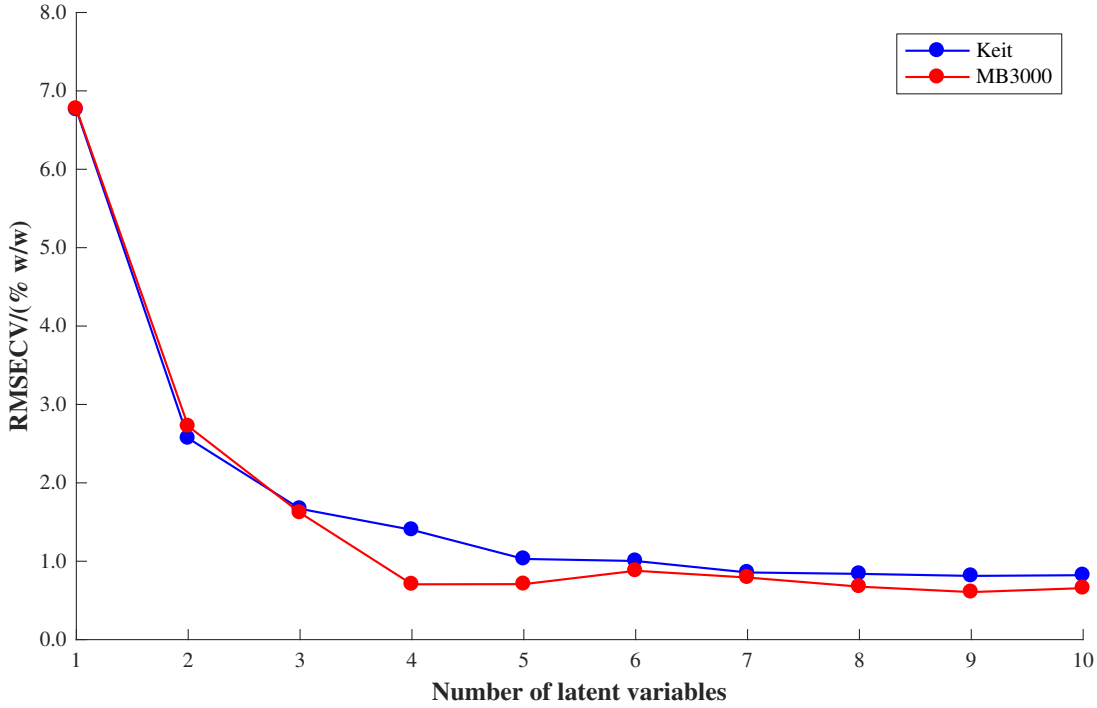

Figure 3.26 - RMSECV versus number of latent variables for ethanol PLS1 models built using Keit and MB3000 data.

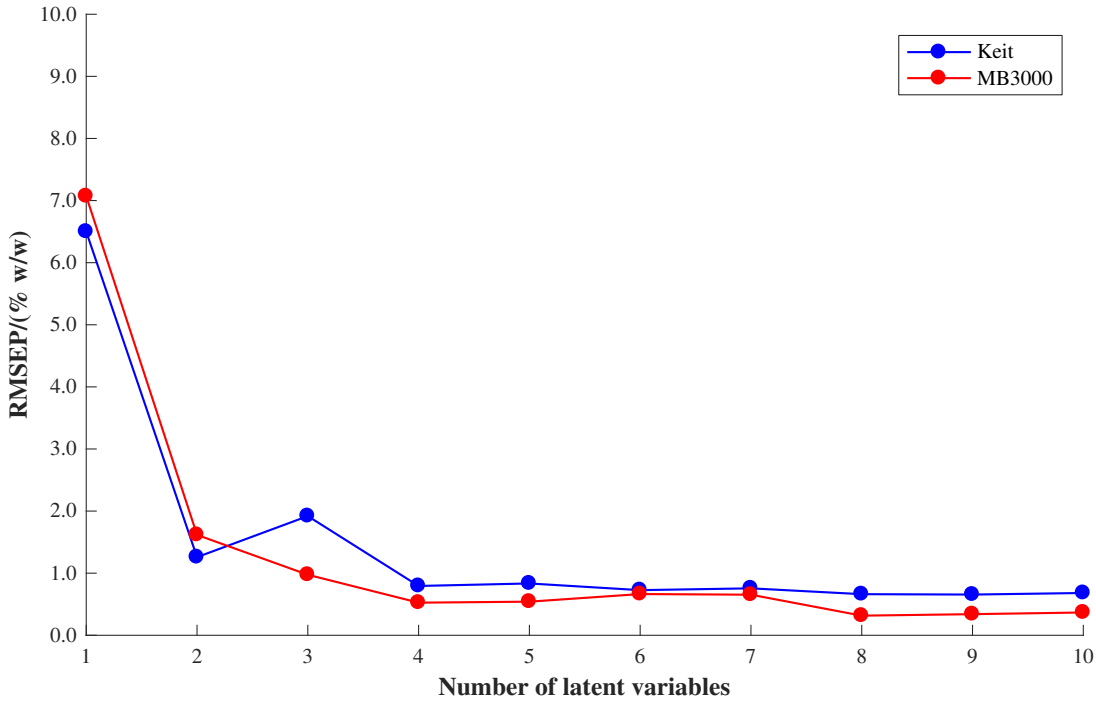

Figure 3.27 - RMSEP versus number of latent variables for ethanol PLS1 models built using Keit and MB3000 data.

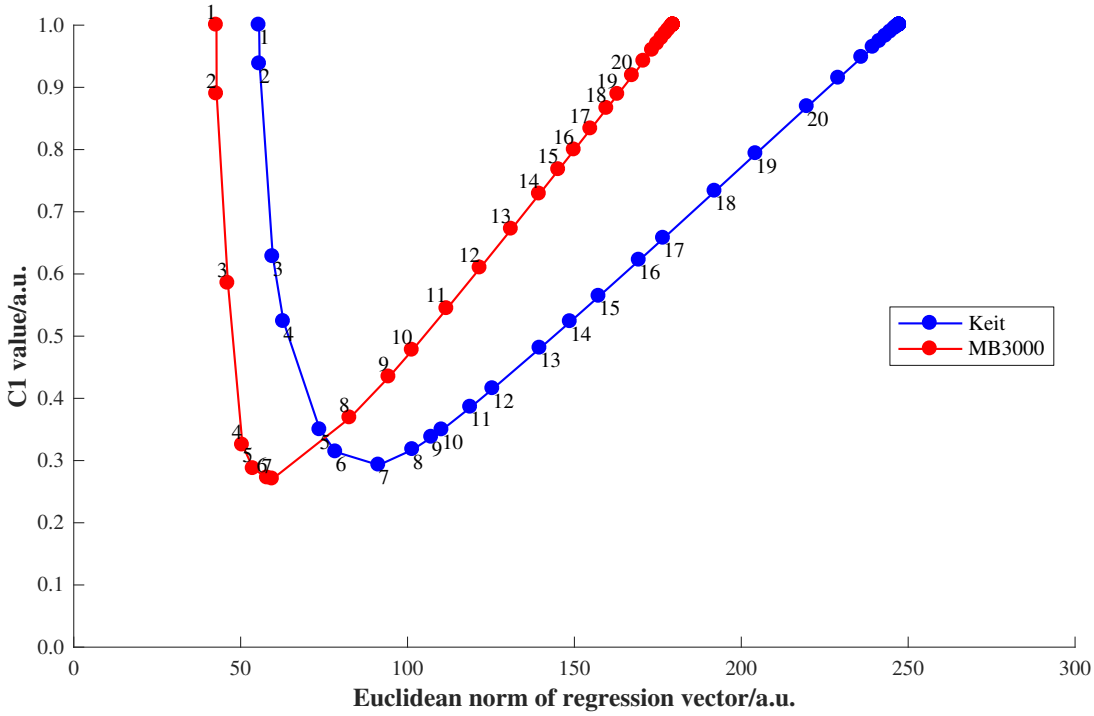

Figure 3.28 - C1 value versus Euclidean norm of regression vector for ethyl acetate PLS1 models built using Keit and MB3000 data (> 20 LVs not labelled due to overlap).

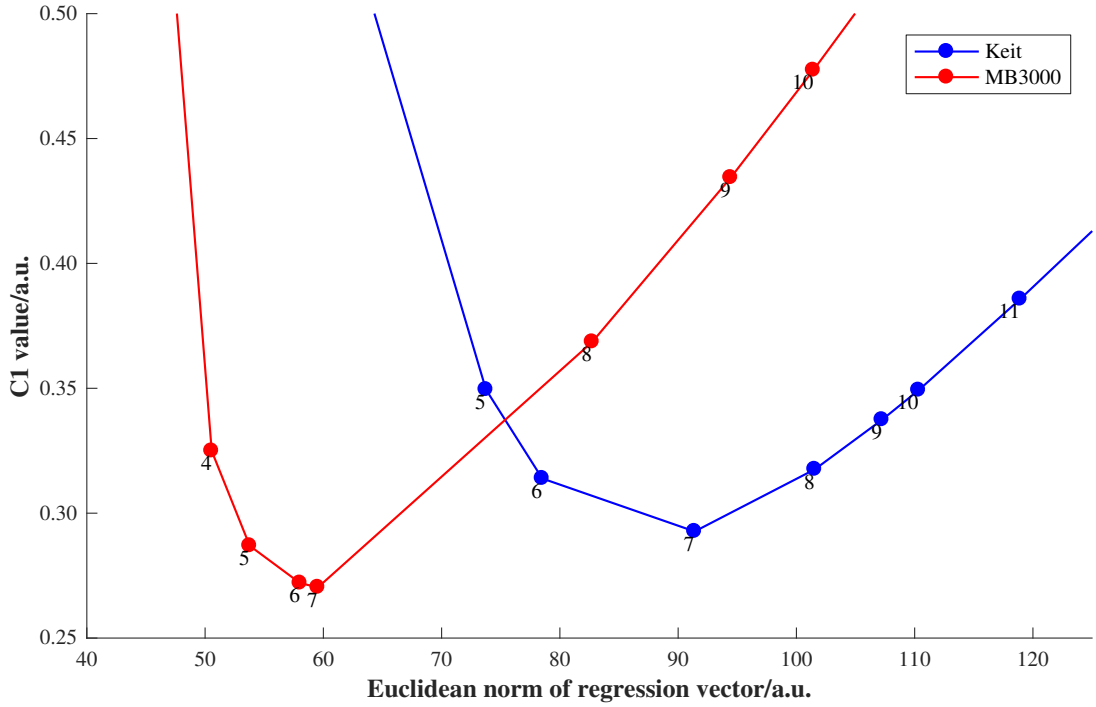

Figure 3.29 - C1 value versus Euclidean norm of regression vector for ethyl acetate PLS1 models built using Keit and MB3000 data, zoomed in on minimum so labels can be read.

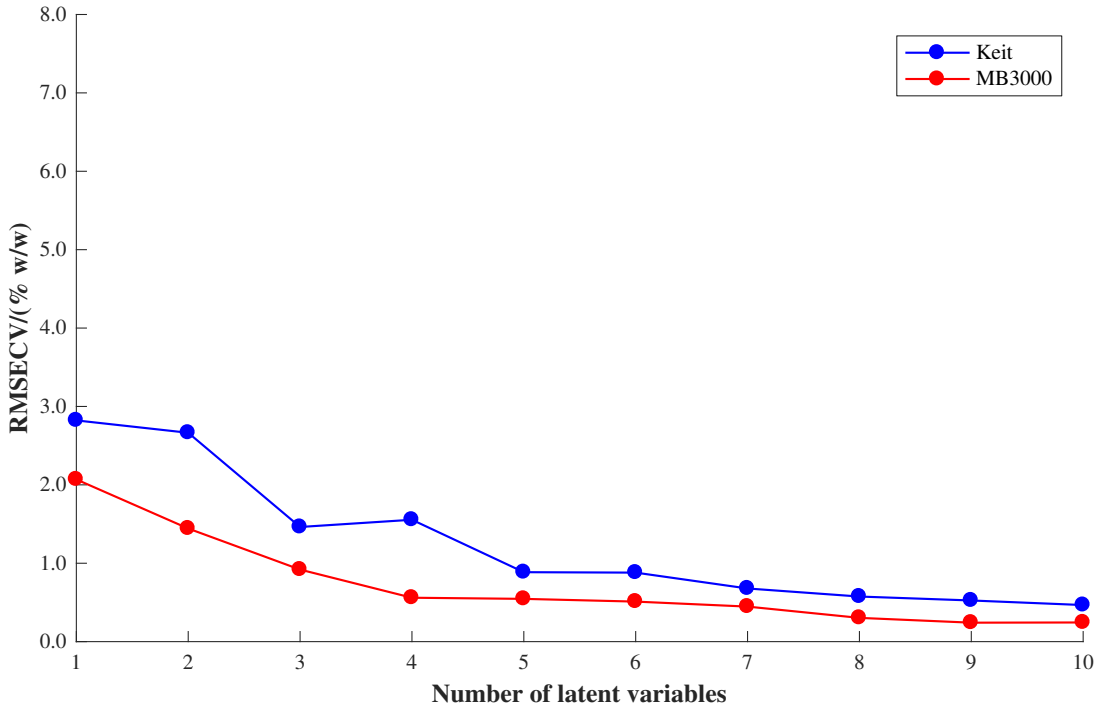

Figure 3.30 - RMSECV value versus number of latent variables for ethyl acetate PLS1 models built using Keit and MB3000 data.

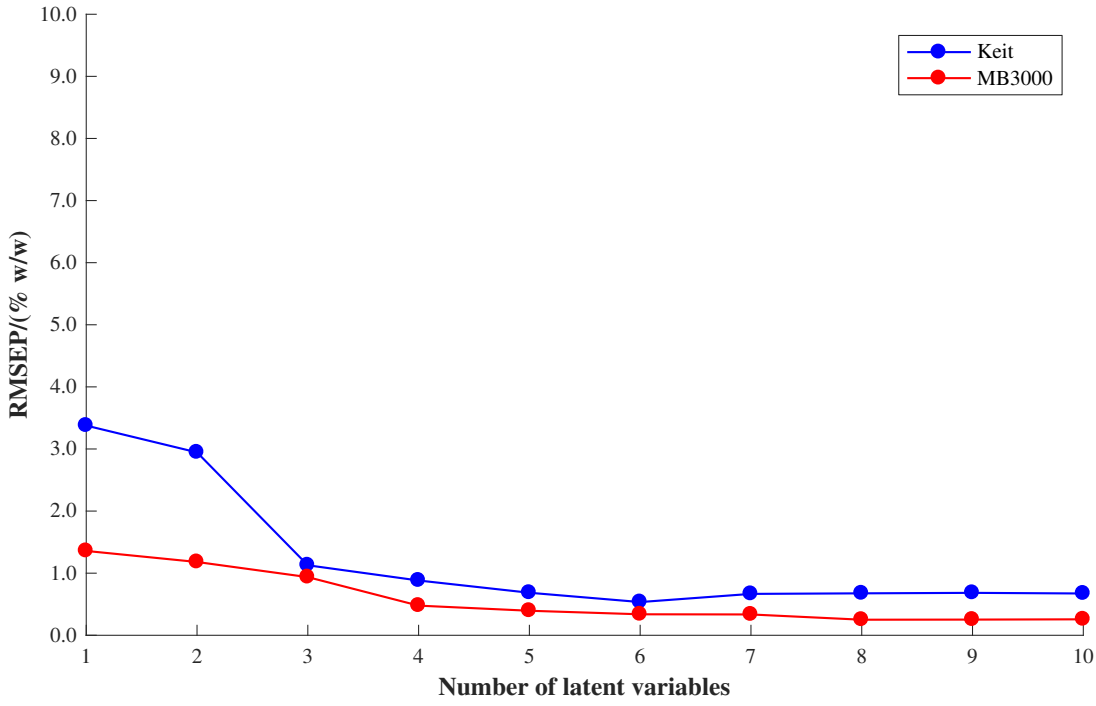

Figure 3.31 - RMSEP value versus number of latent variables for ethyl acetate PLS1 models built using Keit and MB3000 data.

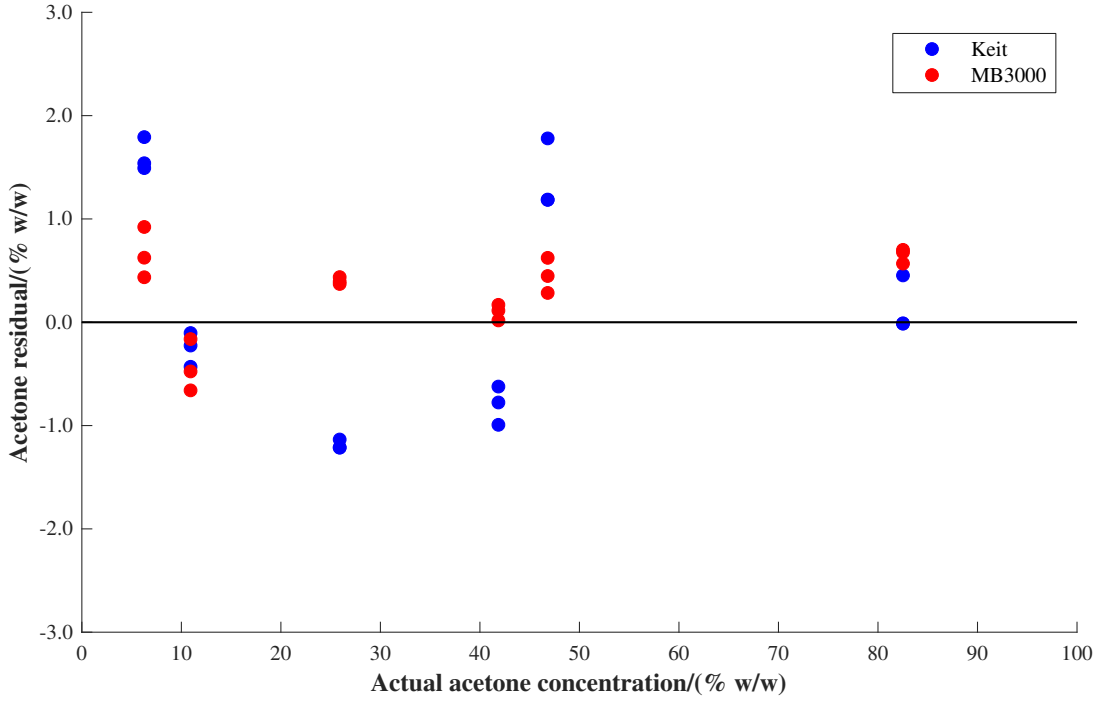

Figure 3.32 - Residual error in predictions of acetone concentration versus actual acetone concentration for the PLS1 models built using spectra obtained by the Keit and MB3000 spectrometers.

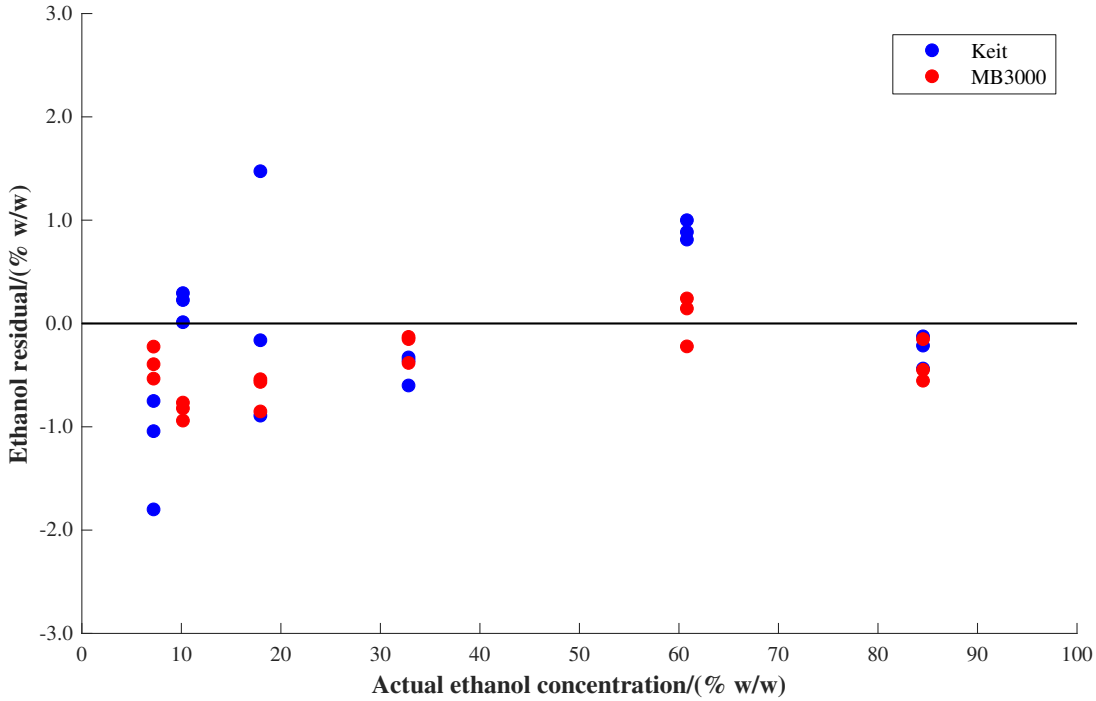

Figure 3.33 - Residual error in predictions of ethanol concentration versus actual ethanol concentration for the PLS1 models built using spectra obtained by the Keit and MB3000 spectrometers.

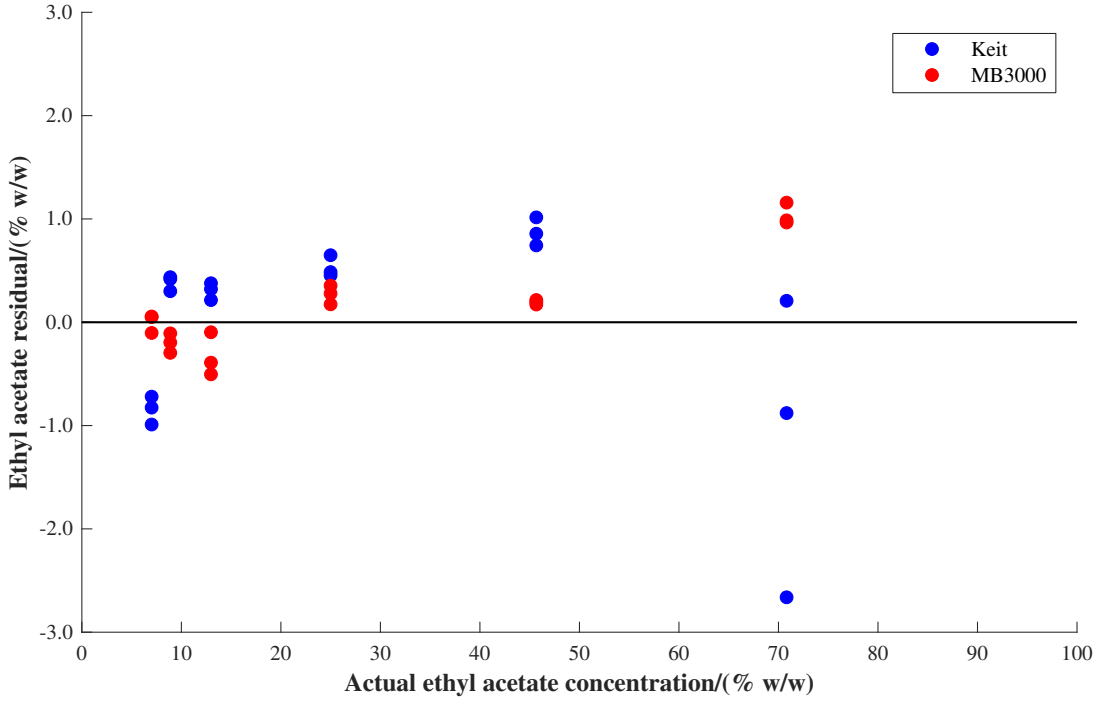

Figure 3.34 - Residual error in predictions of ethyl acetate concentration versus actual ethyl acetate concentration for the PLS1 models built using spectra obtained by the Keit and MB3000 spectrometers.

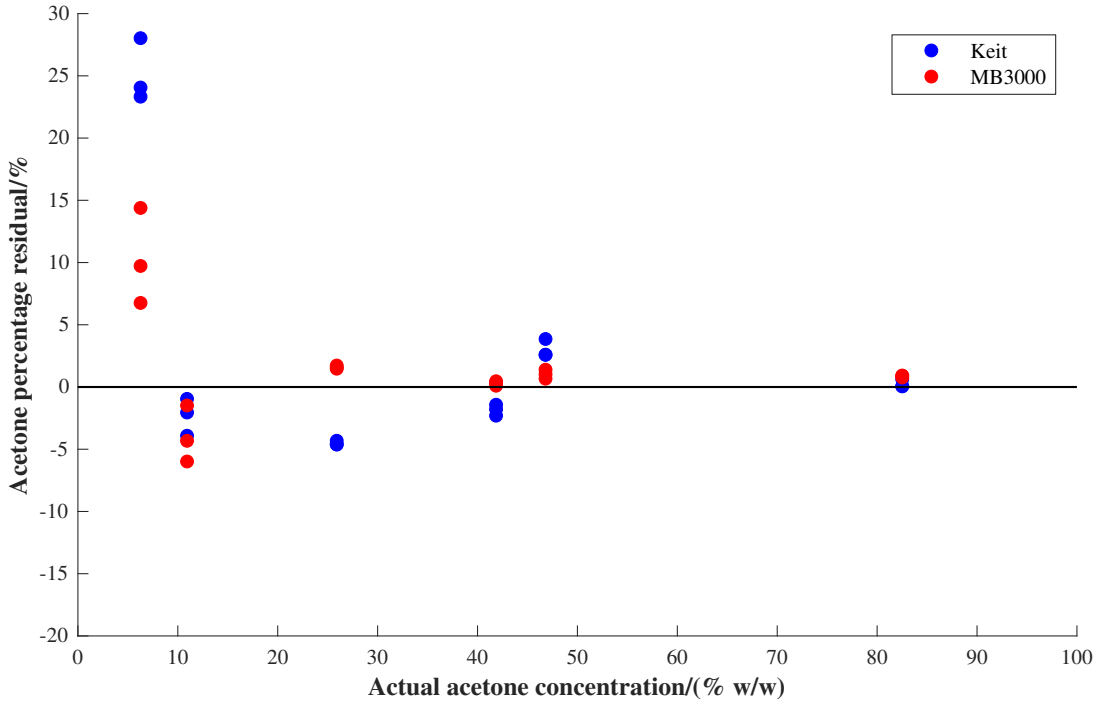

Figure 3.35 - Percentage residual error in predictions of acetone concentration versus actual acetone concentration for the PLS1 models built using spectra obtained by the Keit and MB3000 spectrometers.

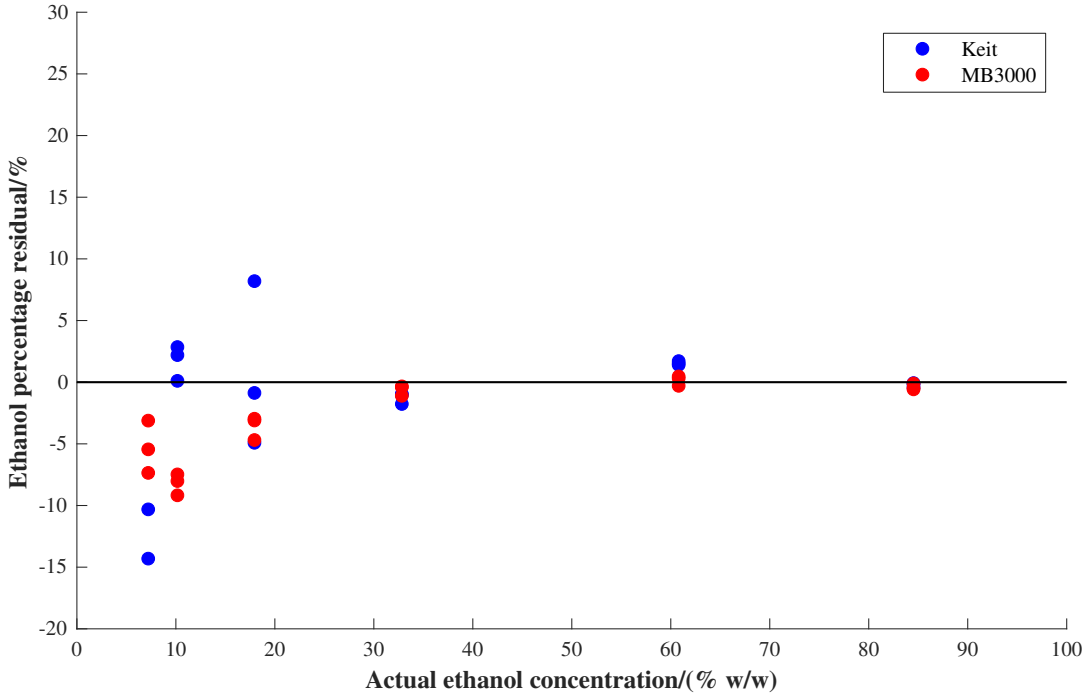

Figure 3.36 - Percentage residual error in predictions of ethanol concentration versus actual ethanol concentration for the PLS1 models built using spectra obtained by the Keit and MB3000 spectrometers.

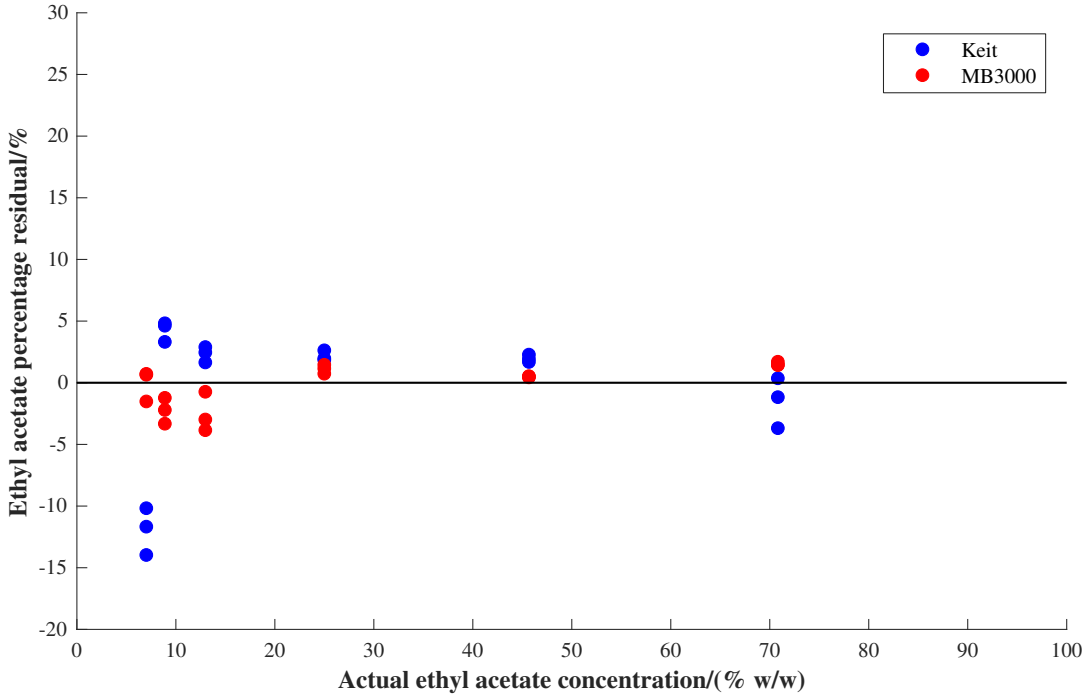

Figure 3.37 - Percentage residual error in predictions of ethyl acetate concentration versus actual ethyl acetate concentration for the PLS1 models built using spectra obtained by the Keit and MB3000 spectrometers.

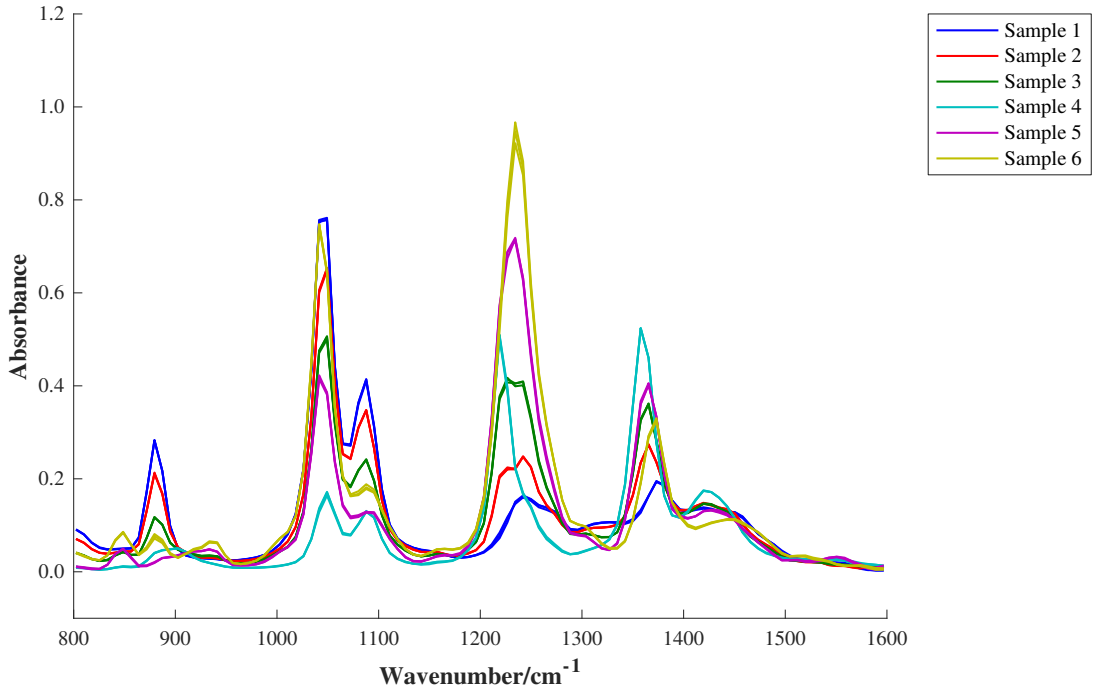

Figure 3.38 - Spectra of test samples acquired using the Keit spectrometer after calibration transfer by DS, average of 19 scans.

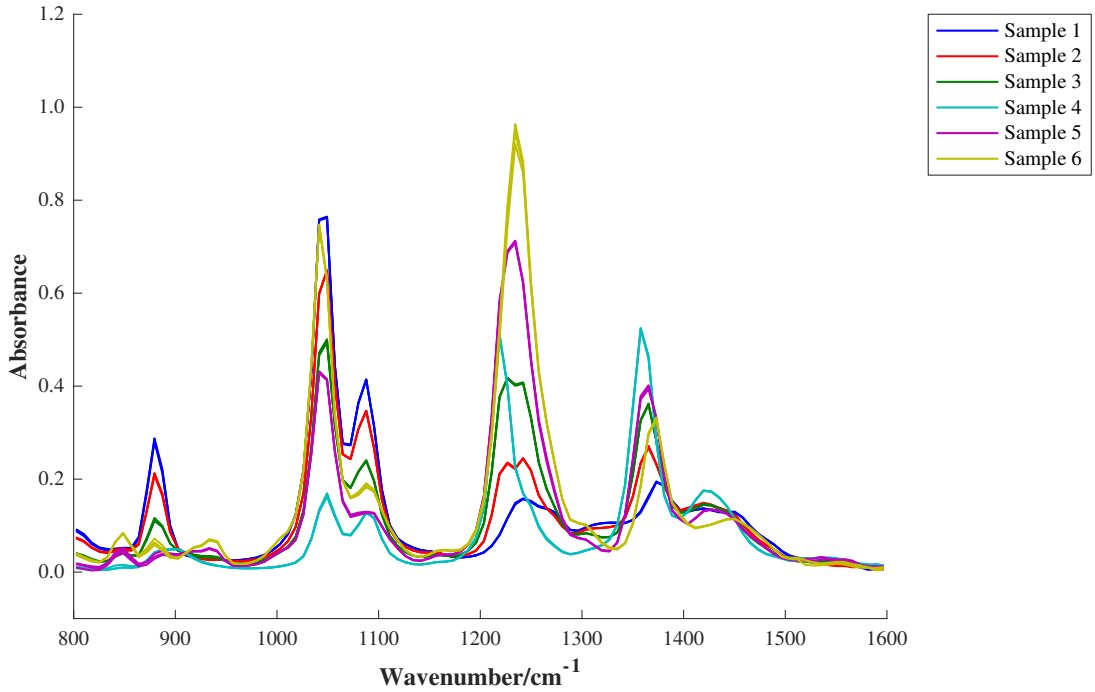

Figure 3.39 - Spectra of test samples acquired using the Keit spectrometer after calibration transfer by PDS (window size = 41), average of 19 scans.

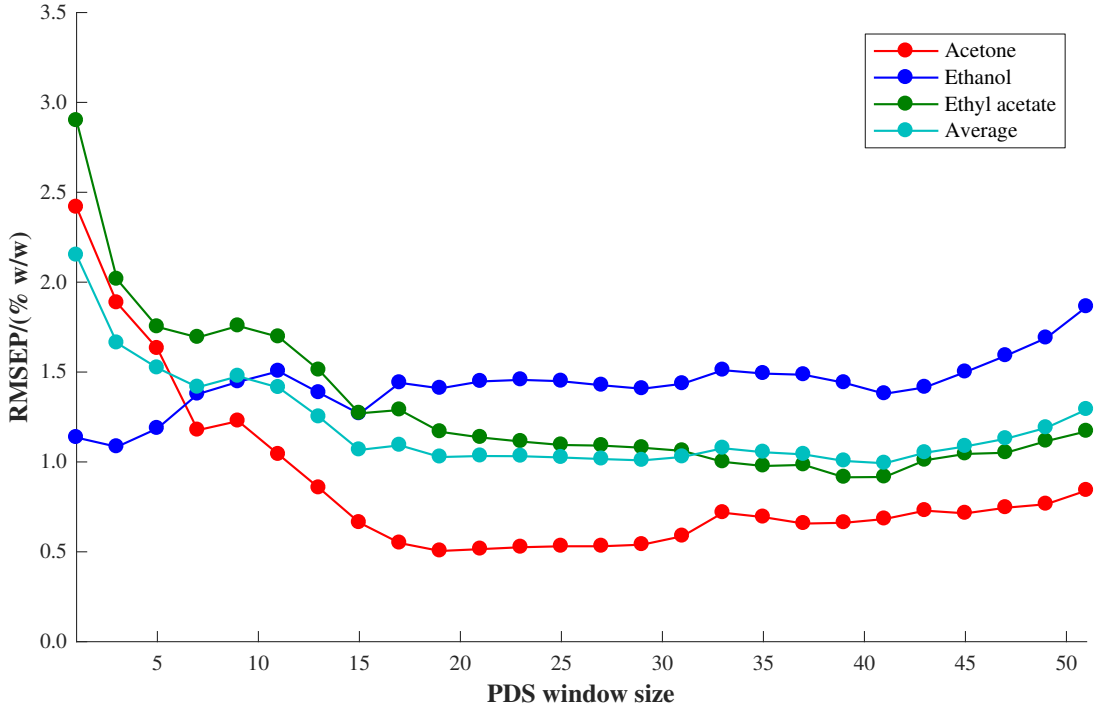

Figure 3.40 - RMSEP versus PDS window size for PLS1 models built using MB3000 calibration data and applied to Keit test data after PDS.

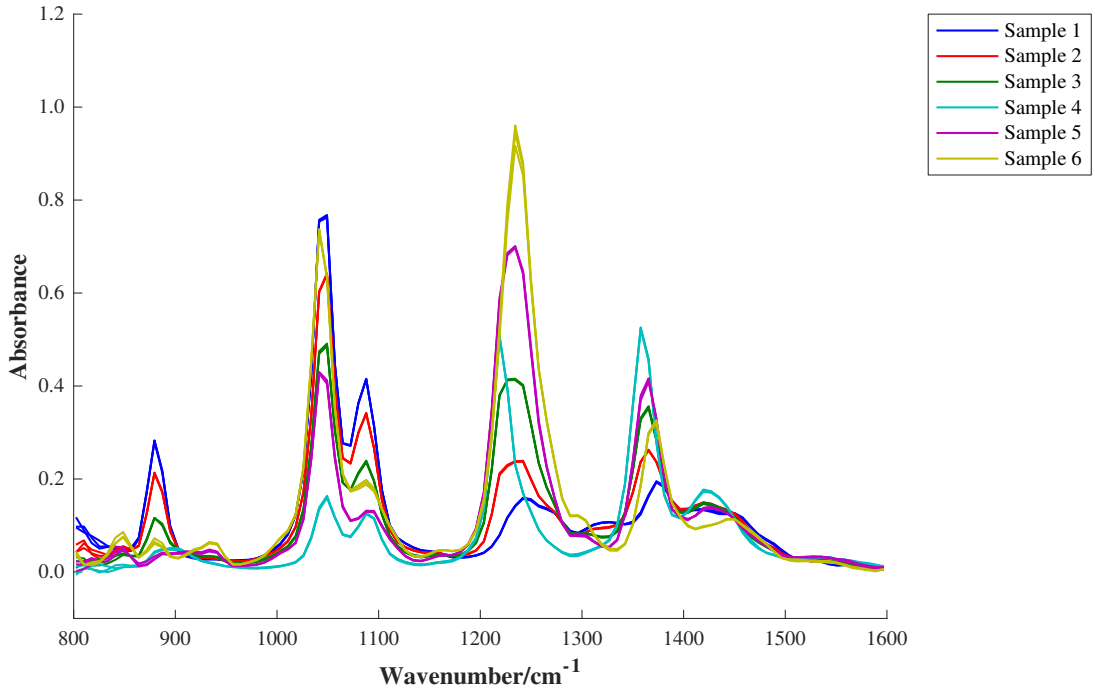

Figure 3.41 - Spectra of test samples acquired using the Keit spectrometer after calibration transfer by SST using 5 singular values, average of 19 scans.

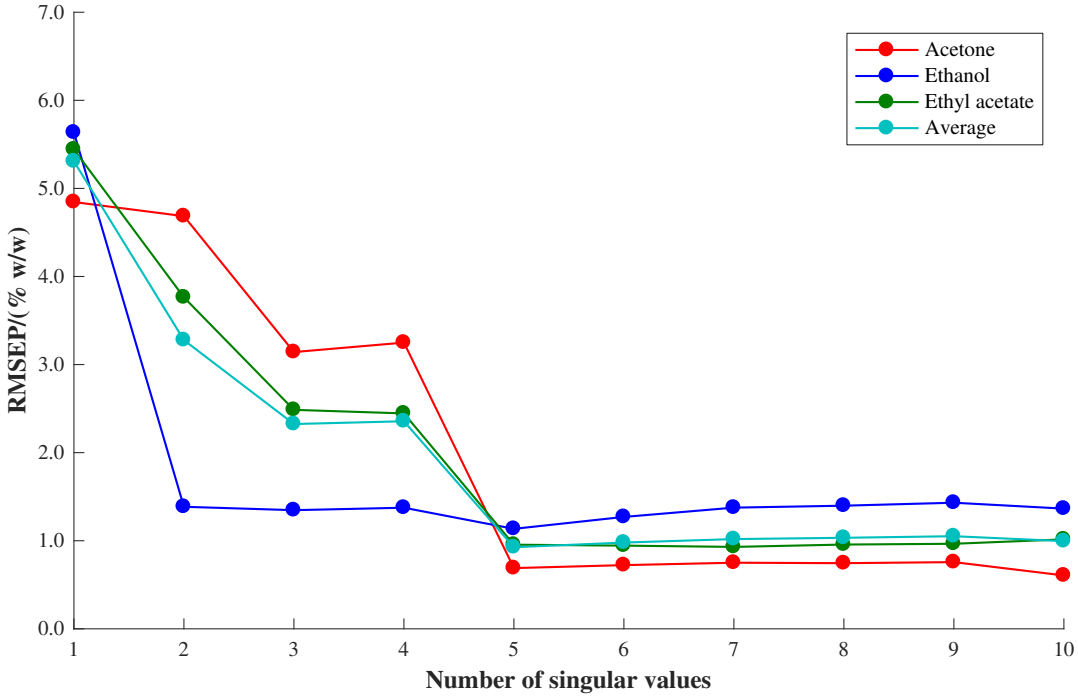

Figure 3.42 - RMSEP versus number of singular values for PLS1 models built using MB3000 calibration data and applied to Keit test data after SST when calibration samples 1 – 3 and 8 – 10 were used as transfer samples.

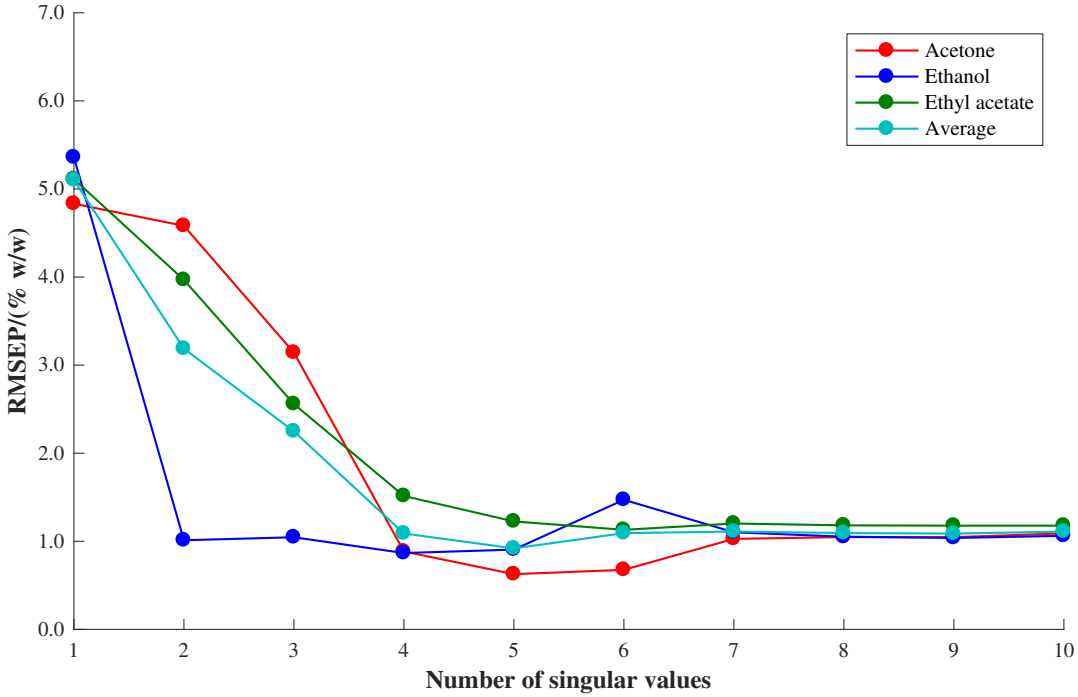

Figure 3.43 - RMSEP versus number of singular values for PLS1 models built using MB3000 calibration data and applied to Keit test data after SST when calibration samples 11 – 16 were used as transfer samples.

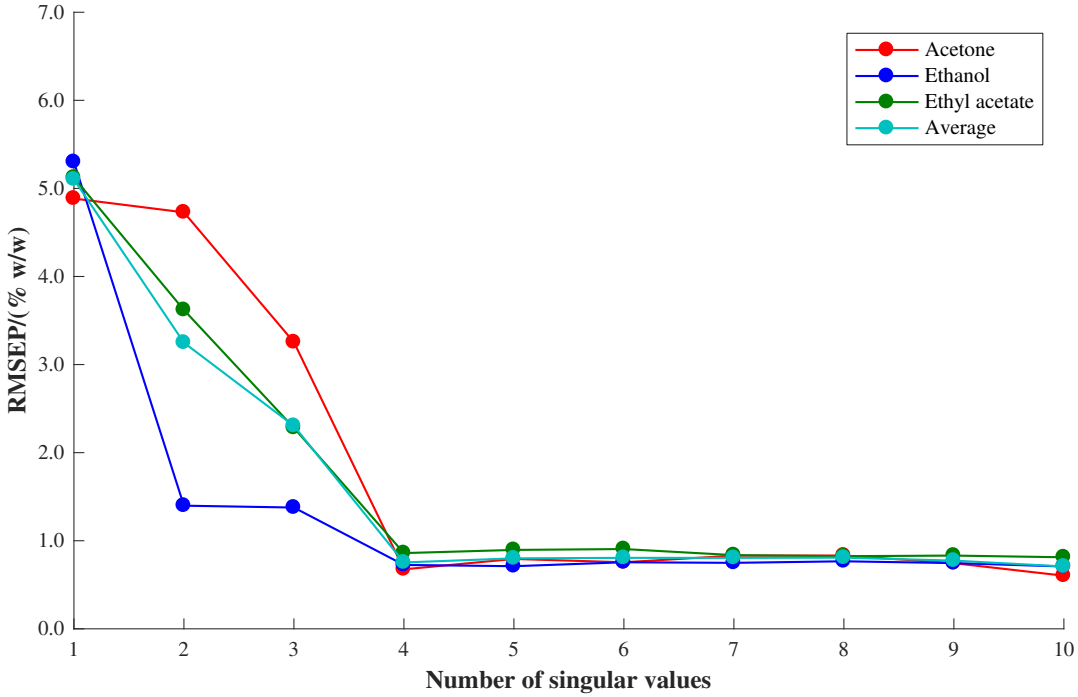

Figure 3.44 - RMSEP versus number of singular values for PLS1 models built using MB3000 calibration data and applied to Keit test data after SST when calibration samples 4 – 6 and 8 – 10 were used as transfer samples.

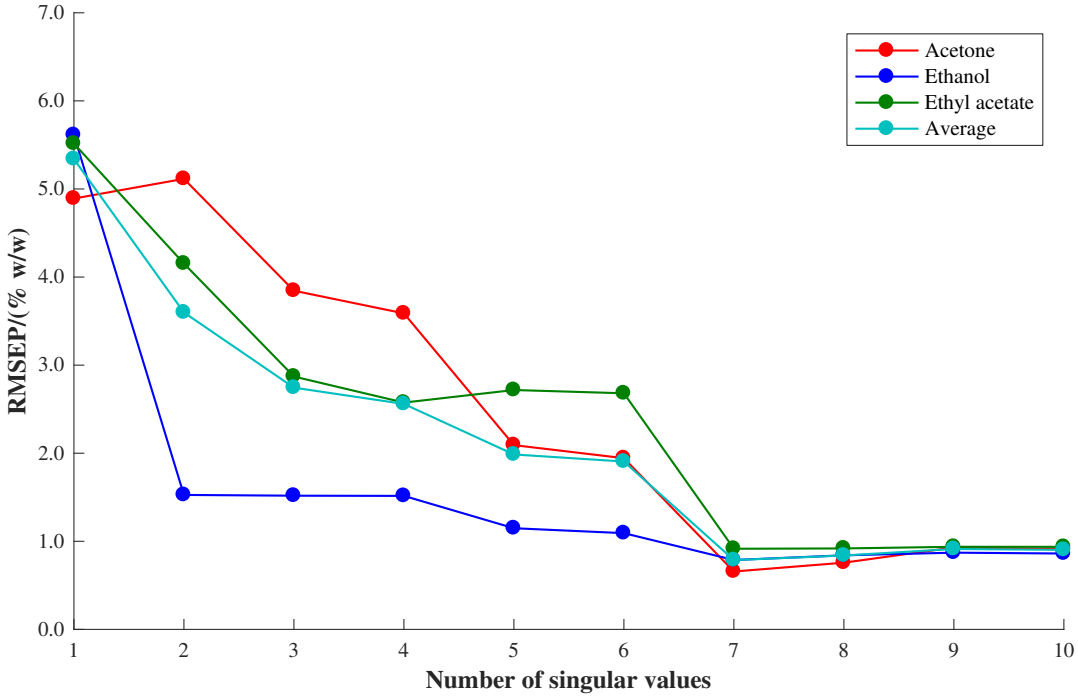

Figure 3.45 - RMSEP versus number of singular values for PLS1 models built using MB3000 calibration data and applied to Keit test data after SST when calibration samples 1 – 3, 12, 13 and 16 were used as transfer samples.

Appendix 4: Additional Figures Corresponding to Chapter 4

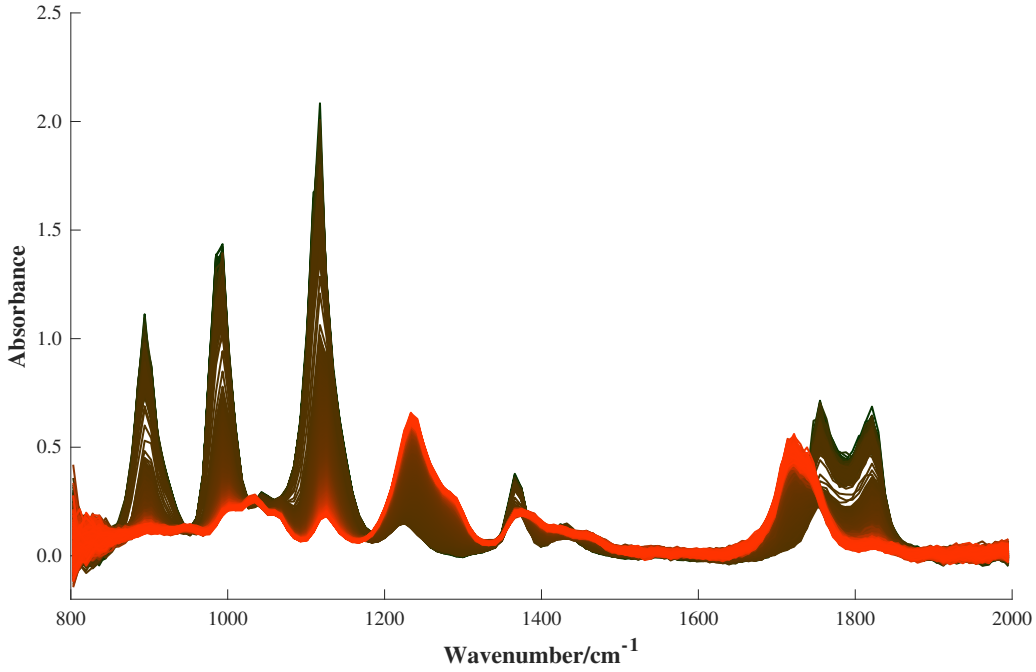

Figure 4.27 - Spectra collected during esterification reaction at 40 °C (first repeat) using the Keit spectrometer (single spectrum measured every 1.6 seconds). Black represents the start of the reaction and red represents the end of the reaction.

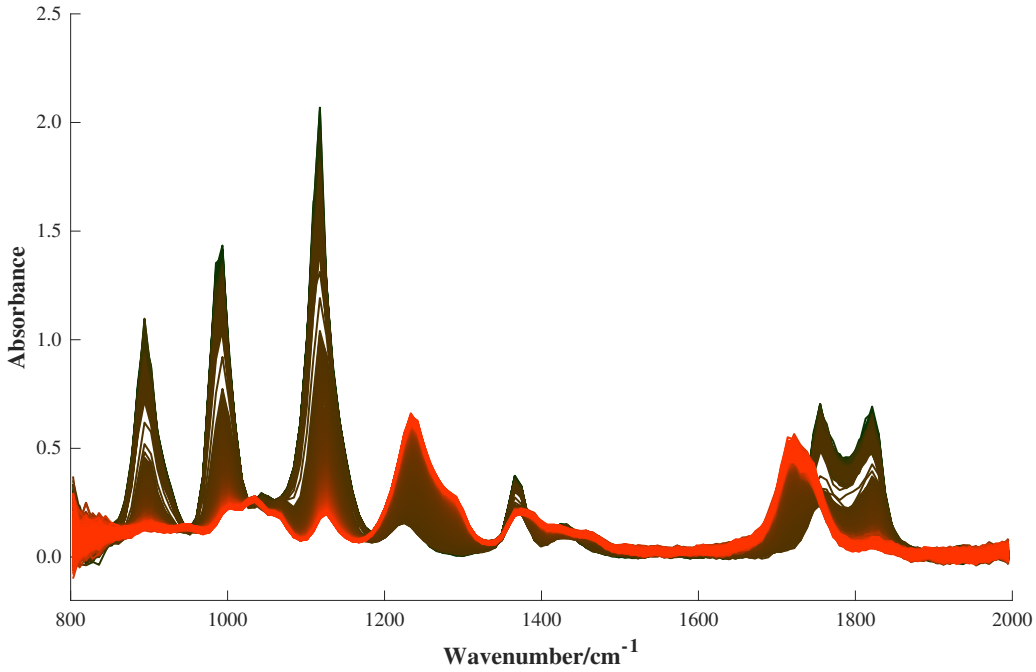

Figure 4.28 - Spectra collected during esterification reaction at 40 °C (second repeat) using the Keit spectrometer (single spectrum measured every 1.6 seconds). Black represents the start of the reaction and red represents the end of the reaction.

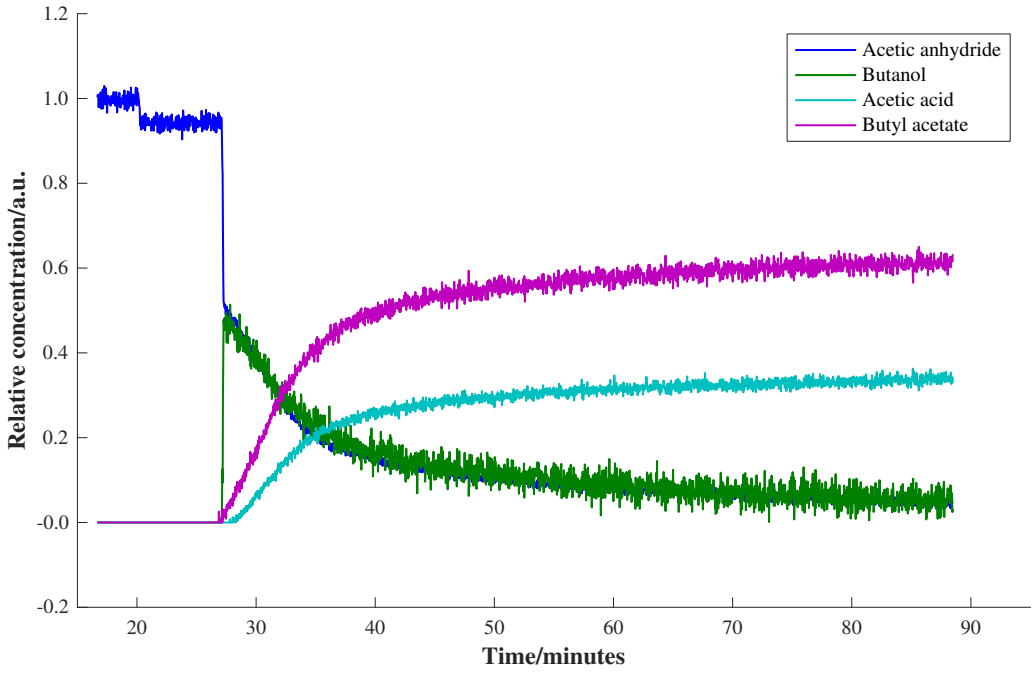

Figure 4.29 - Estimated concentration profiles (by GUIPRO) of components present in the reaction mixture spectra collected during esterification reaction at 40 °C (second repeat) using the Keit spectrometer.

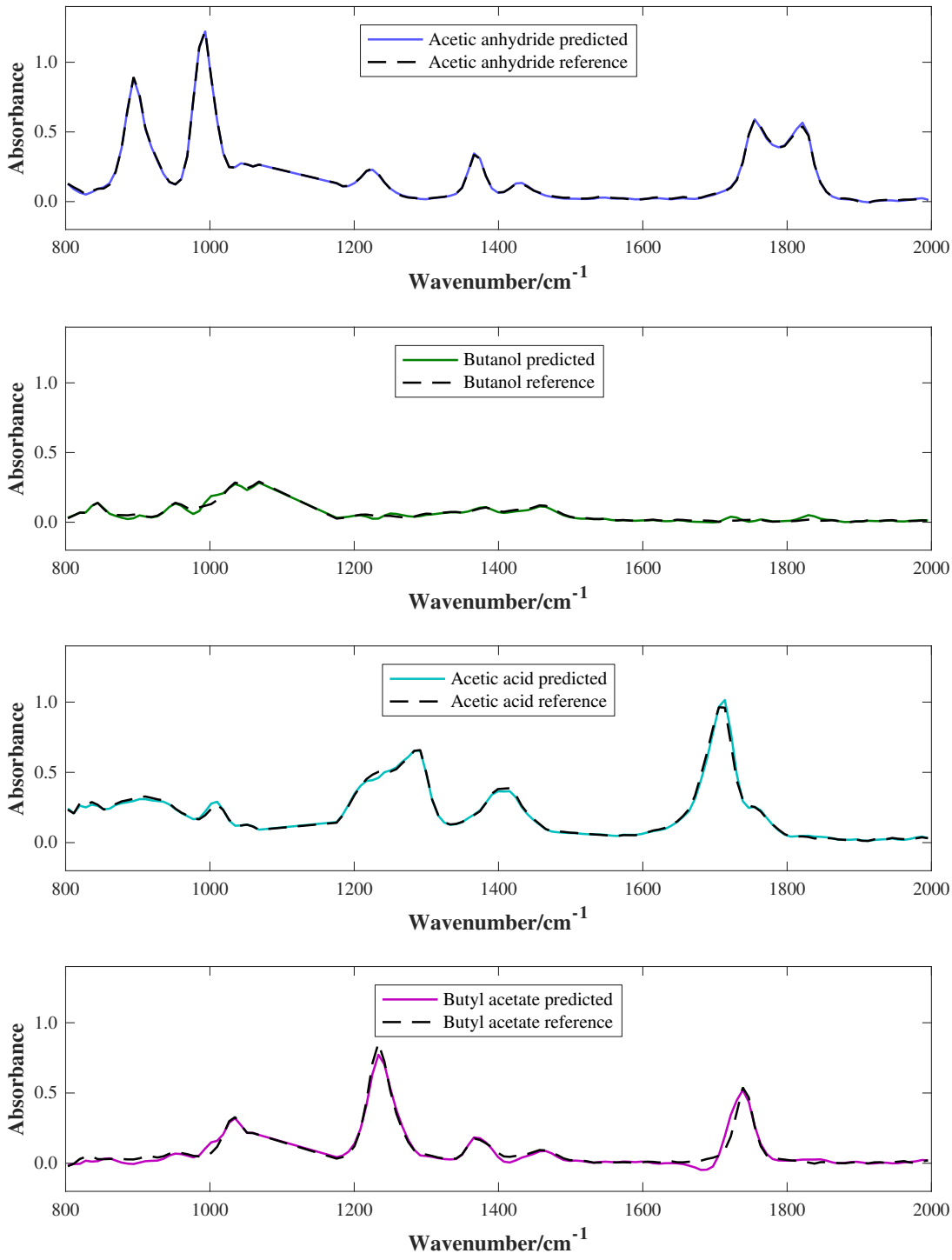

Figure 4.30 - Estimated pure spectra (by GUIPRO) of components present in the reaction mixture spectra collected during esterification reaction at 40 °C (second repeat) using the Keit spectrometer (solid lines), and reference pure component spectra collected using the Keit spectrometer (dashed lines).

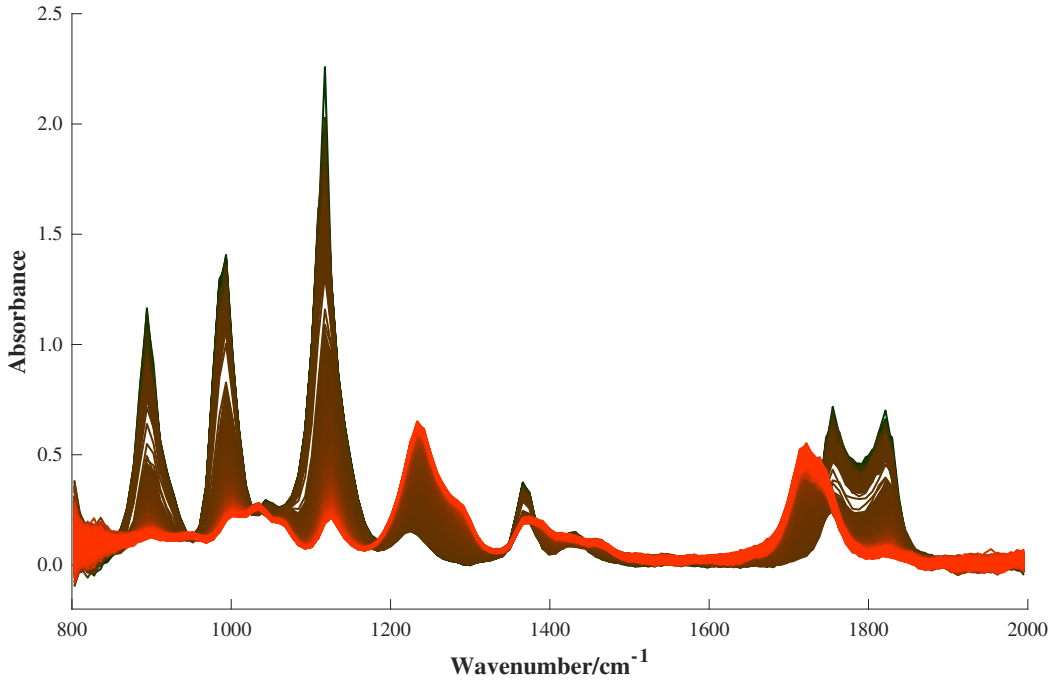

Figure 4.31 - Spectra collected during esterification reaction at 40 °C (third repeat) using the Keit spectrometer (single spectrum measured every 1.6 seconds). Black represents the start of the reaction and red represents the end of the reaction.

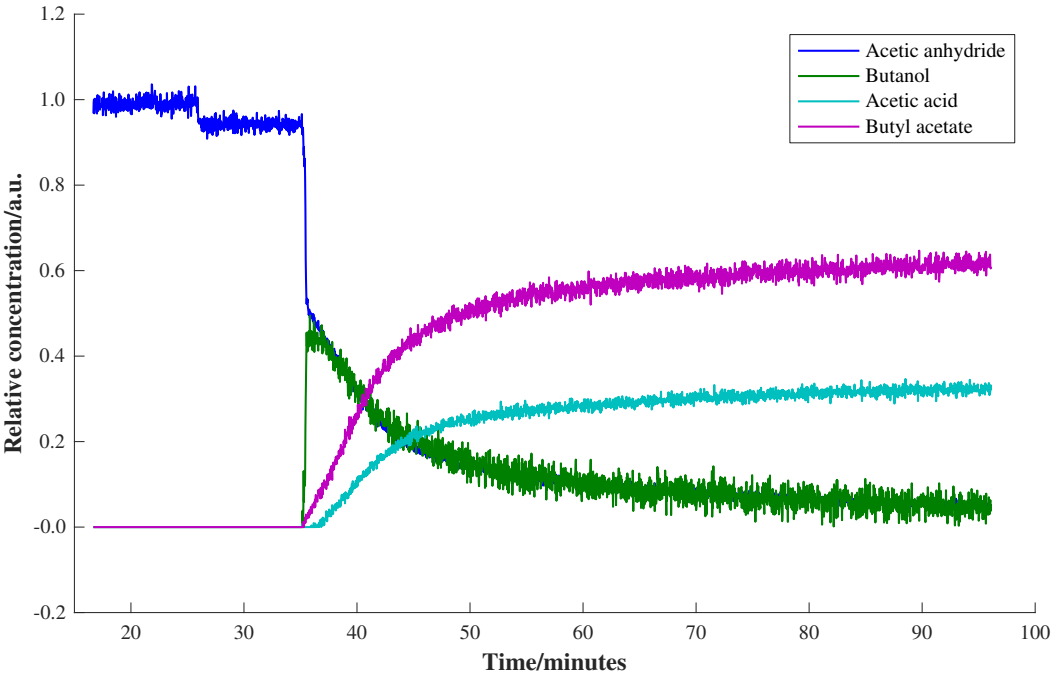

Figure 4.32 - Estimated concentration profiles (by GUIPRO) of components present in the reaction mixture spectra collected during esterification reaction at 40 °C (third repeat) using the Keit spectrometer.

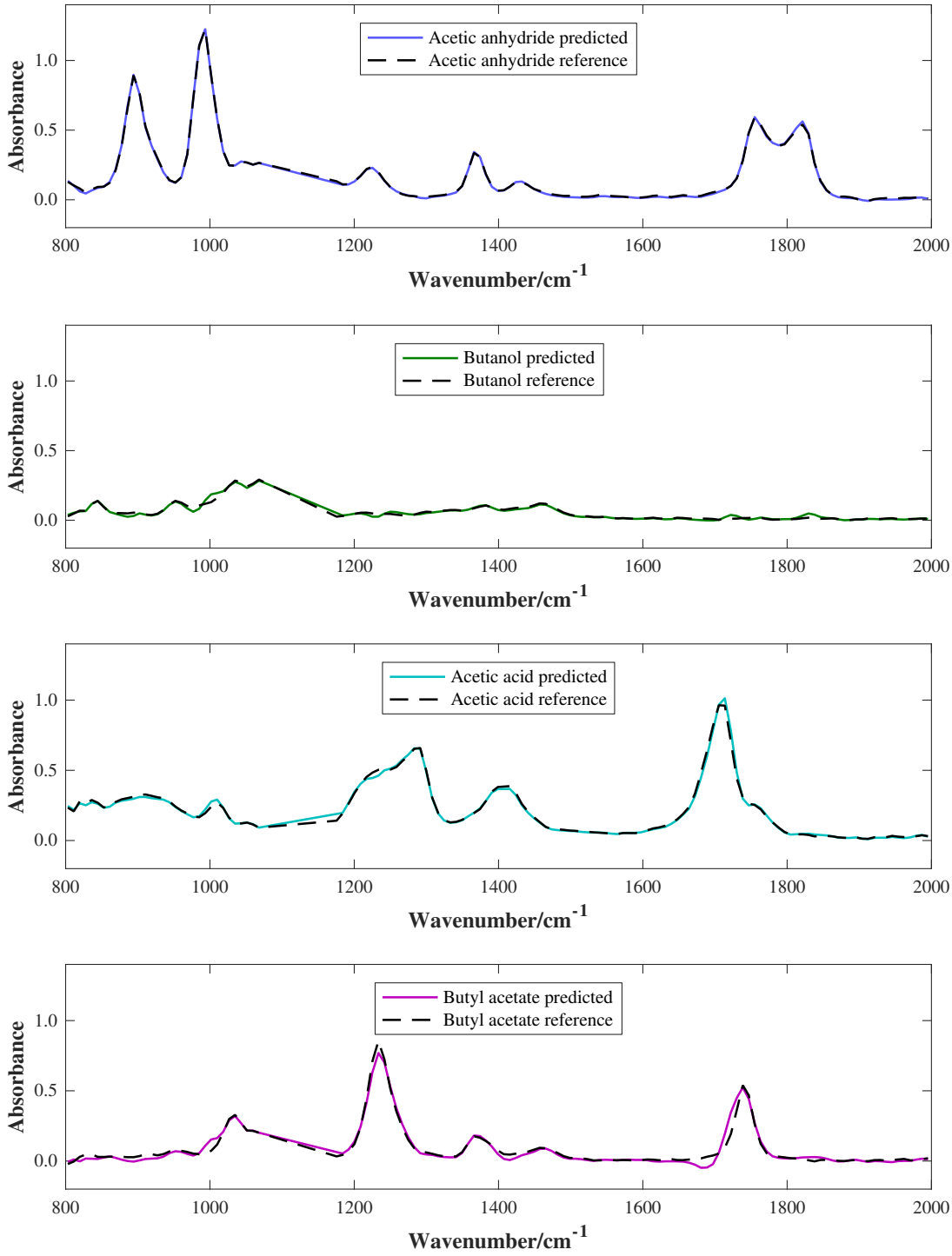

Figure 4.33 - Estimated pure spectra (by GUIPRO) of components present in the reaction mixture spectra collected during esterification reaction at 40 °C (third repeat) using the Keit spectrometer (solid lines), and reference pure component spectra collected using the Keit spectrometer (dashed lines).

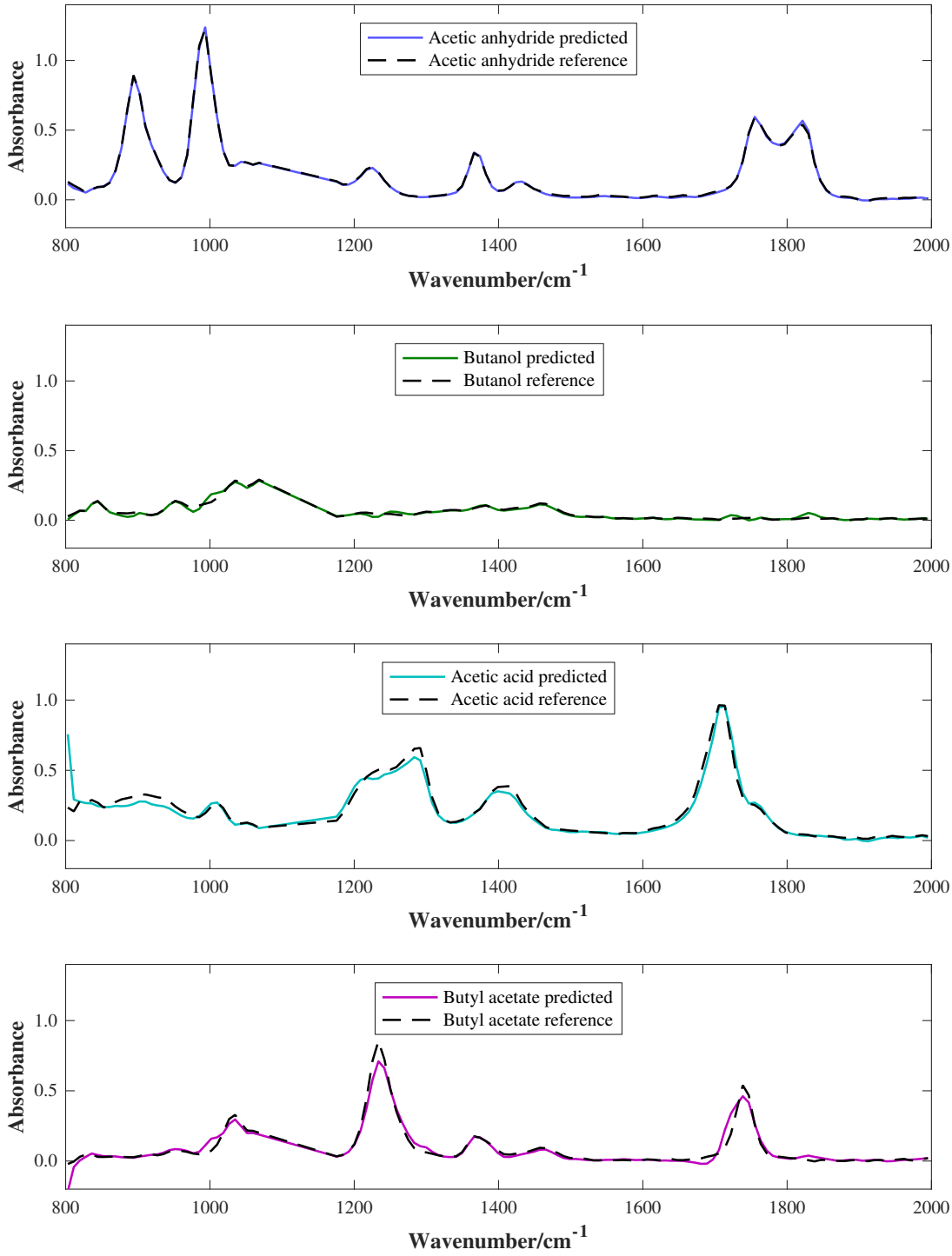

Figure 4.34 - Estimated pure spectra (by GUIPRO) of components present in the reaction mixture spectra collected during esterification reaction at 40 °C with acetic acid dosed in approximately one hour after the addition of butanol (solid lines) and reference pure component spectra (dashed lines), all acquired using the Keit spectrometer. Product reference spectra collected at 70 °C.

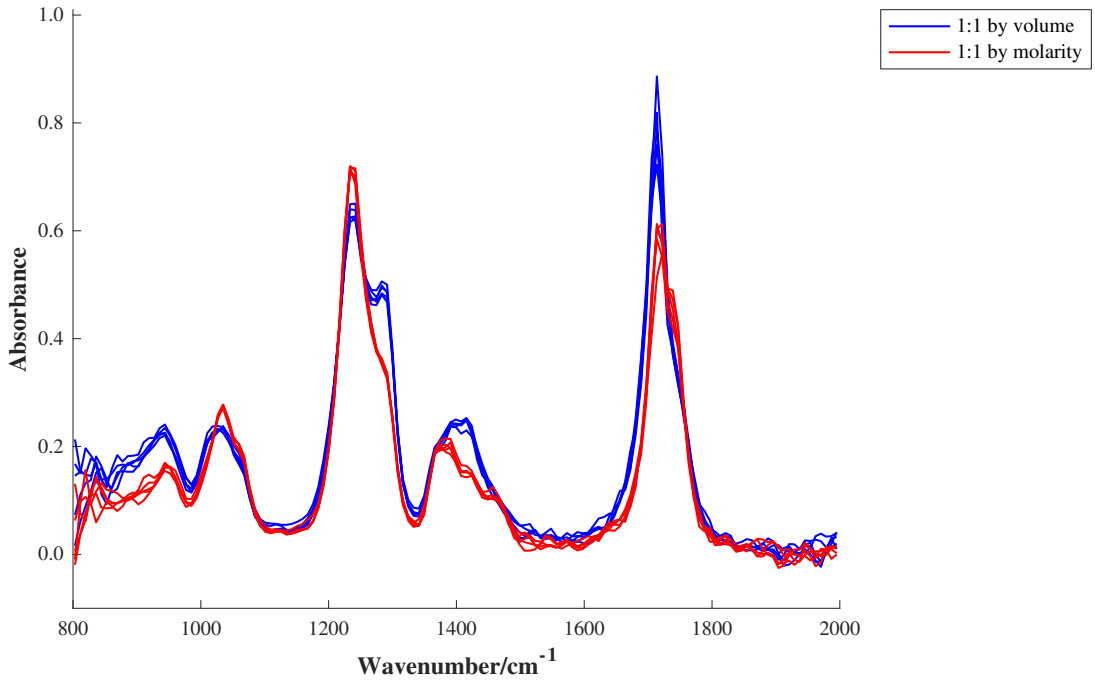

Figure 4.35 - Spectra of 1:1 mixtures of acetic acid and butyl acetate by molarity (red) and by volume (blue), measured using the Keit spectrometer.

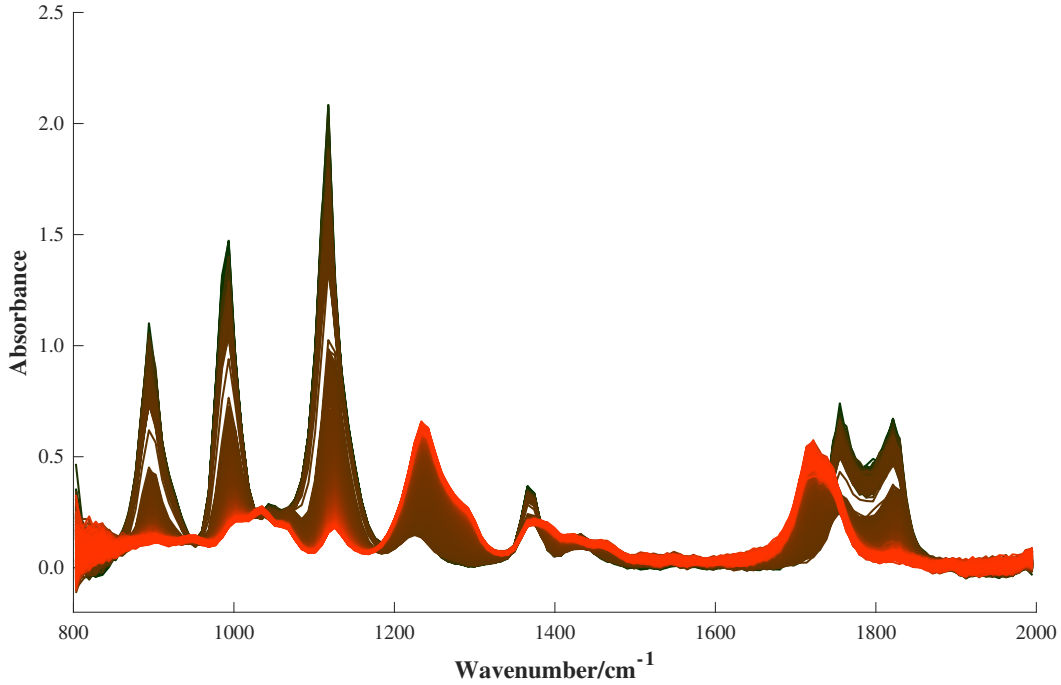

Figure 4.36 - Spectra collected during esterification reaction at 40 °C using the Keit spectrometer (single spectrum measured every 1.6 seconds), with samples removed for NMR analysis at 5, 30 and 60 minutes after the addition of butanol. Black represents the start of the reaction and red represents the end of the reaction.

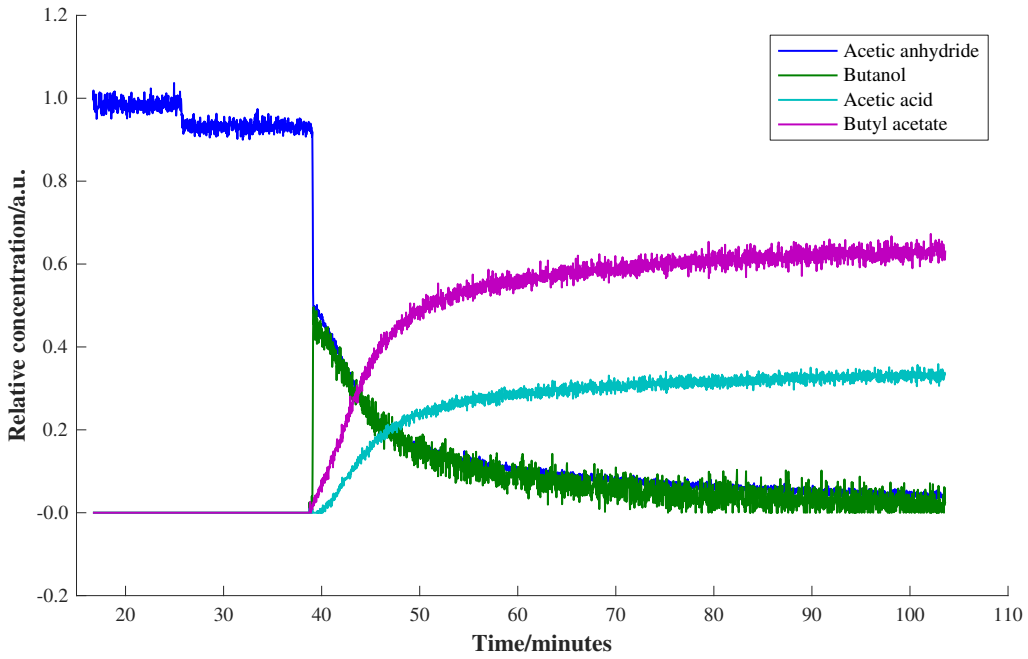

Figure 4.37 - Estimated concentration profiles (by GUIPRO) of components present in the reaction mixture spectra collected during esterification reaction at 40 °C using the Keit spectrometer, with samples removed for NMR analysis at 5, 30 and 60 minutes after the addition of butanol.

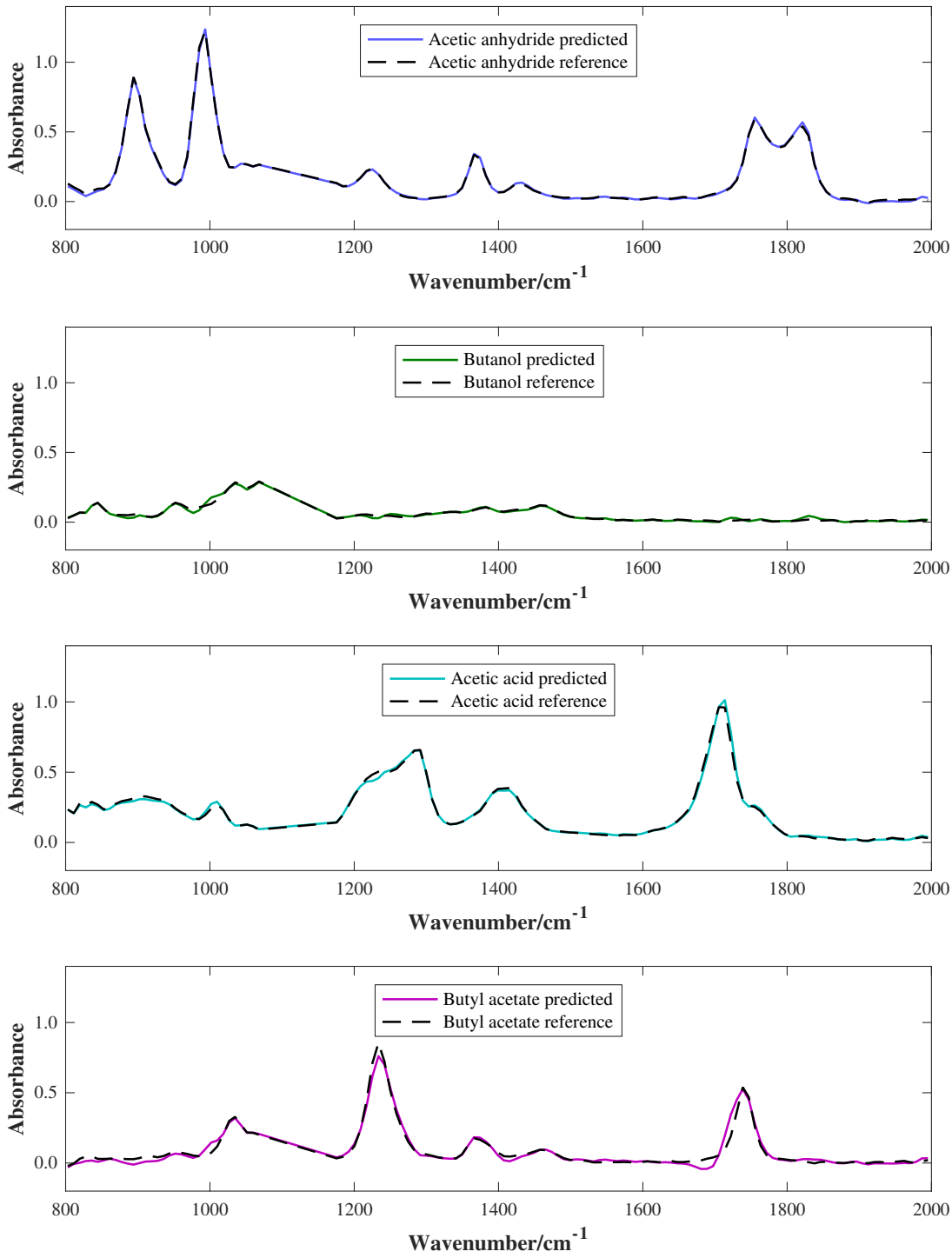

Figure 4.38 - Estimated pure spectra (by GUIPRO) of components present in the reaction mixture spectra collected during esterification reaction at 40 °C with samples removed for NMR analysis at 5, 30 and 60 minutes after the addition of butanol (solid lines) and reference pure component spectra (dashed lines), all acquired using the Keit spectrometer.

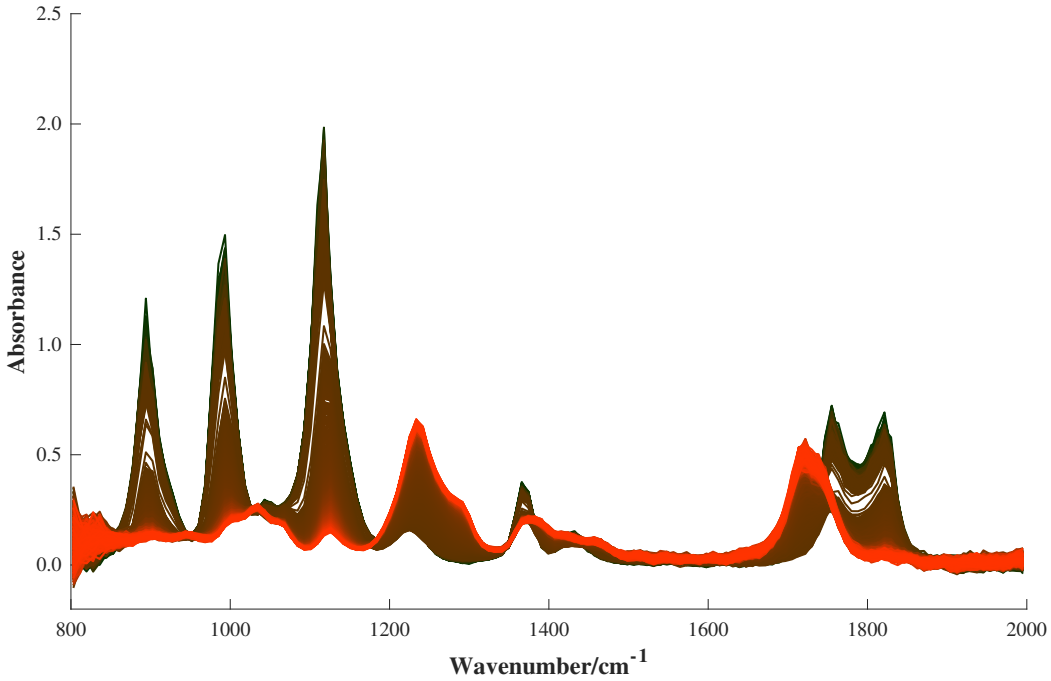

Figure 4.39 - Spectra collected during esterification reaction at 50 °C using the Keit spectrometer (single spectrum measured every 1.6 seconds). Black represents the start of the reaction and red represents the end of the reaction.

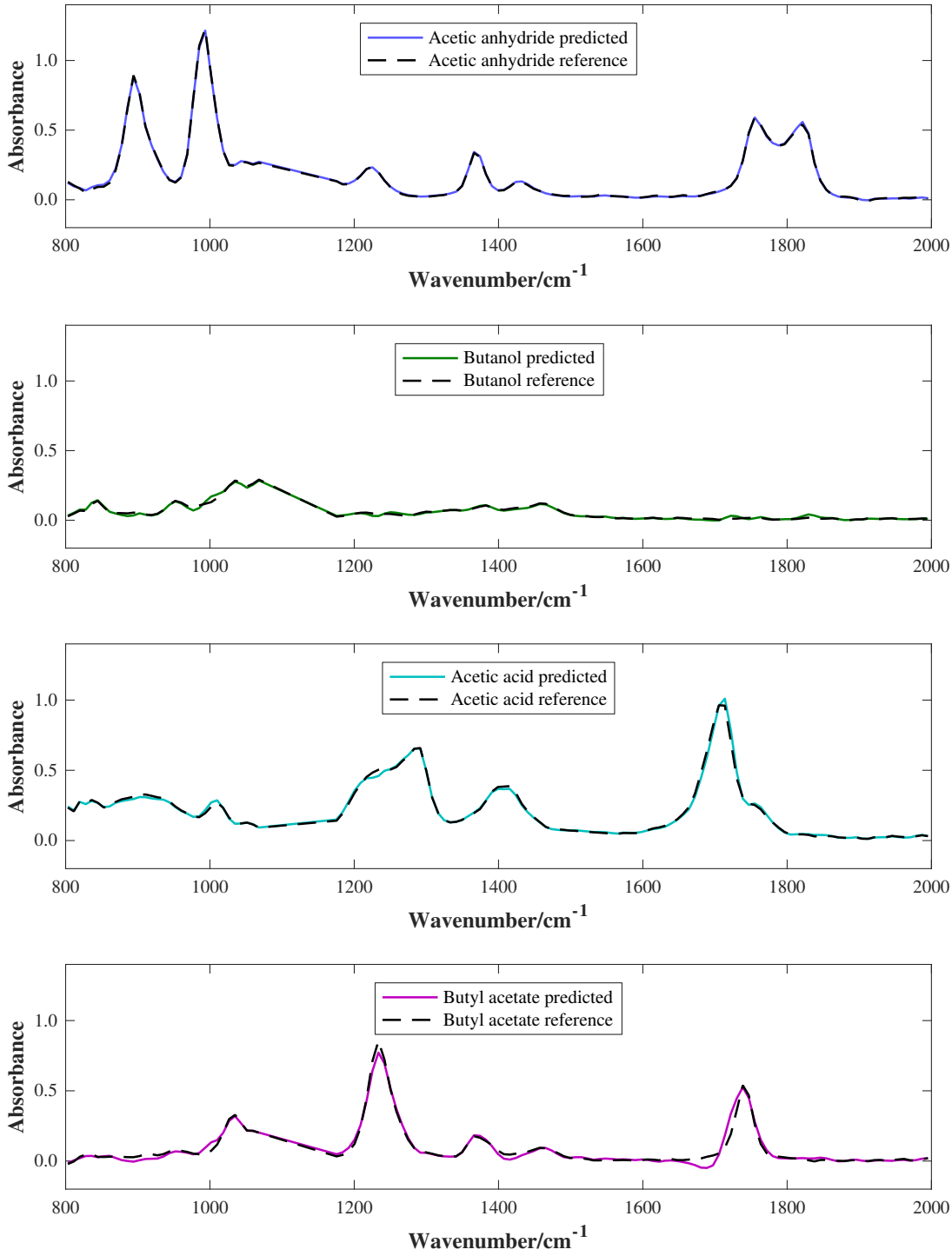

Figure 4.40 - Estimated pure spectra (by GUIPRO) of components present in the reaction mixture spectra collected during esterification reaction at 50 °C using the Keit spectrometer (solid lines), and reference pure component spectra collected using the Keit spectrometer (dashed lines).

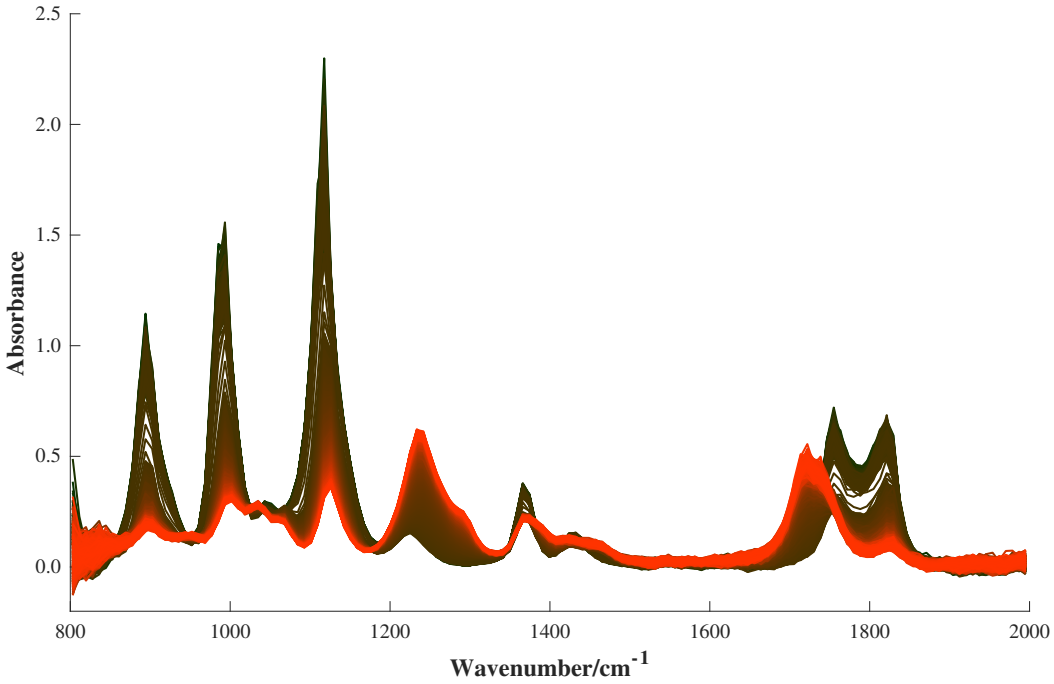

Figure 4.41 - Spectra collected during esterification reaction at 20 °C using the Keit spectrometer (single spectrum measured every 1.6 seconds). Black represents the start of the reaction and red represents the end of the reaction.

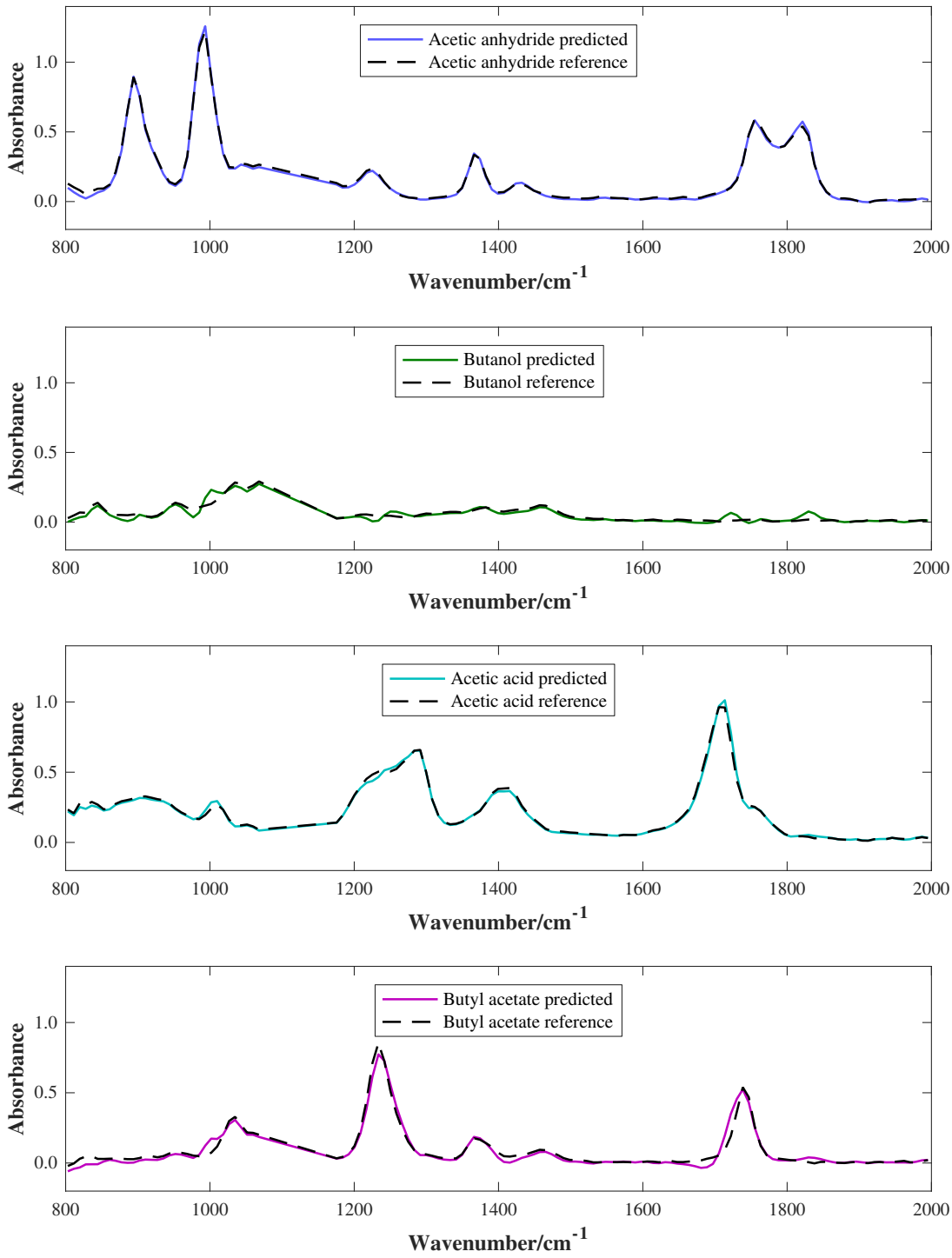

Figure 4.42 - Estimated pure spectra (by GUIPRO) of components present in the reaction mixture spectra collected during esterification reaction at 20 °C using the Keit spectrometer (solid lines), and reference pure component spectra collected using the Keit spectrometer (dashed lines)

Appendix 5: Additional Figures Corresponding to Chapter 5

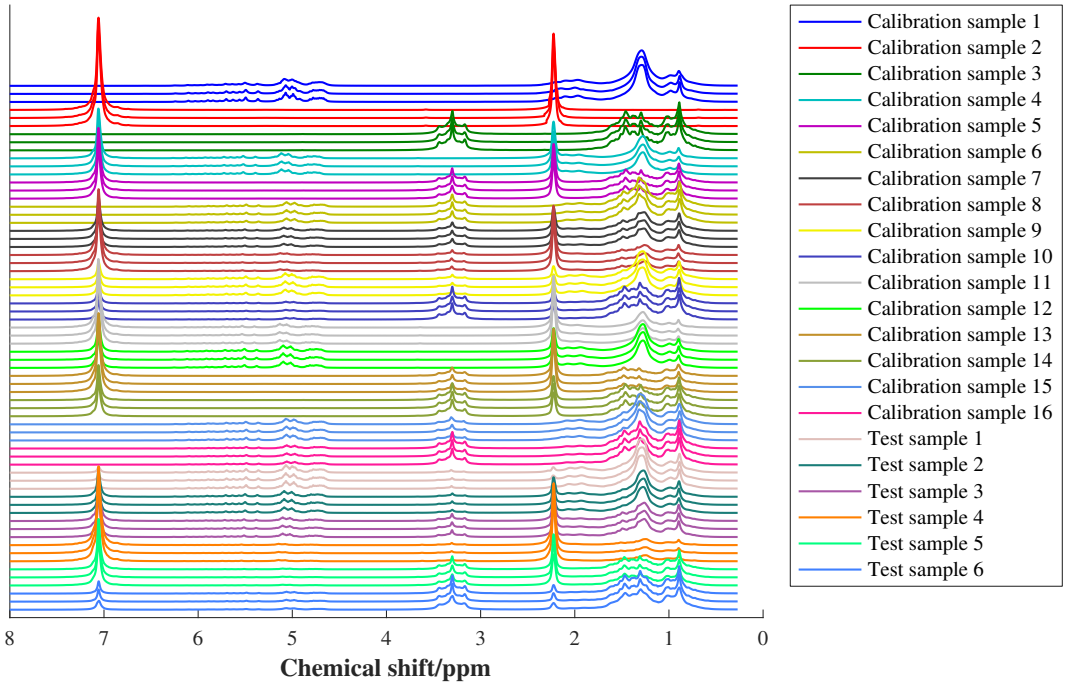

Figure 5.27 - ^{1}H low-field NMR spectra of calibration and test samples in dataset 1 with alignment by RAFFT using optimum parameters determined by DoE (maximum shift = 10 and lookahead = 10).

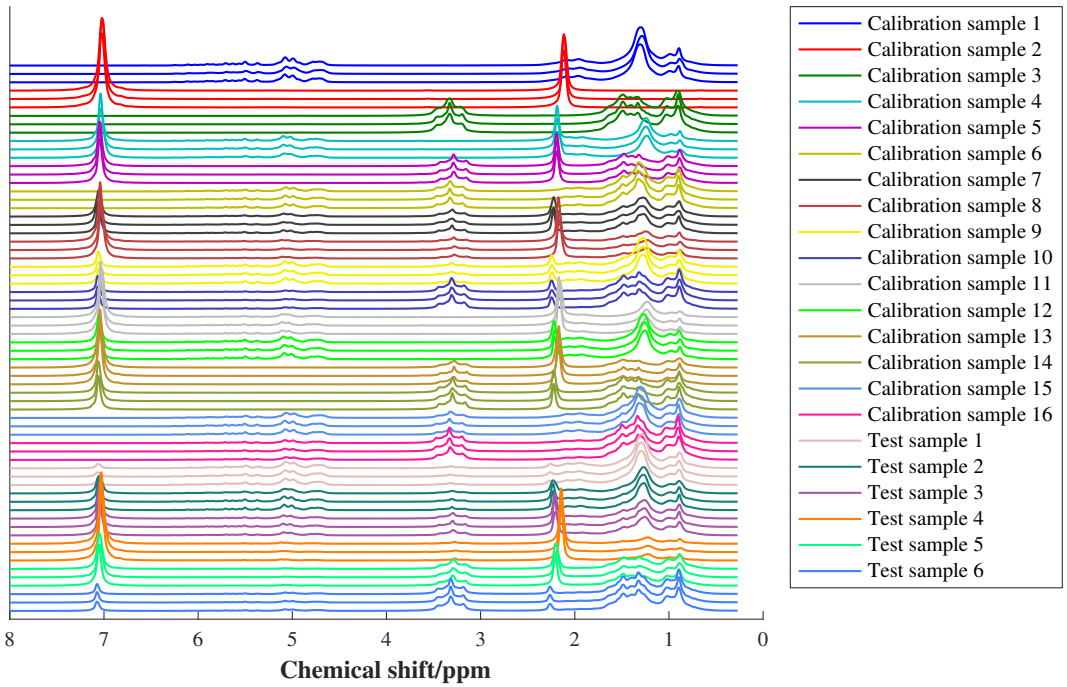

Figure 5.28 - ^{1}H low-field NMR spectra of calibration and test samples in dataset 2, without alignment.

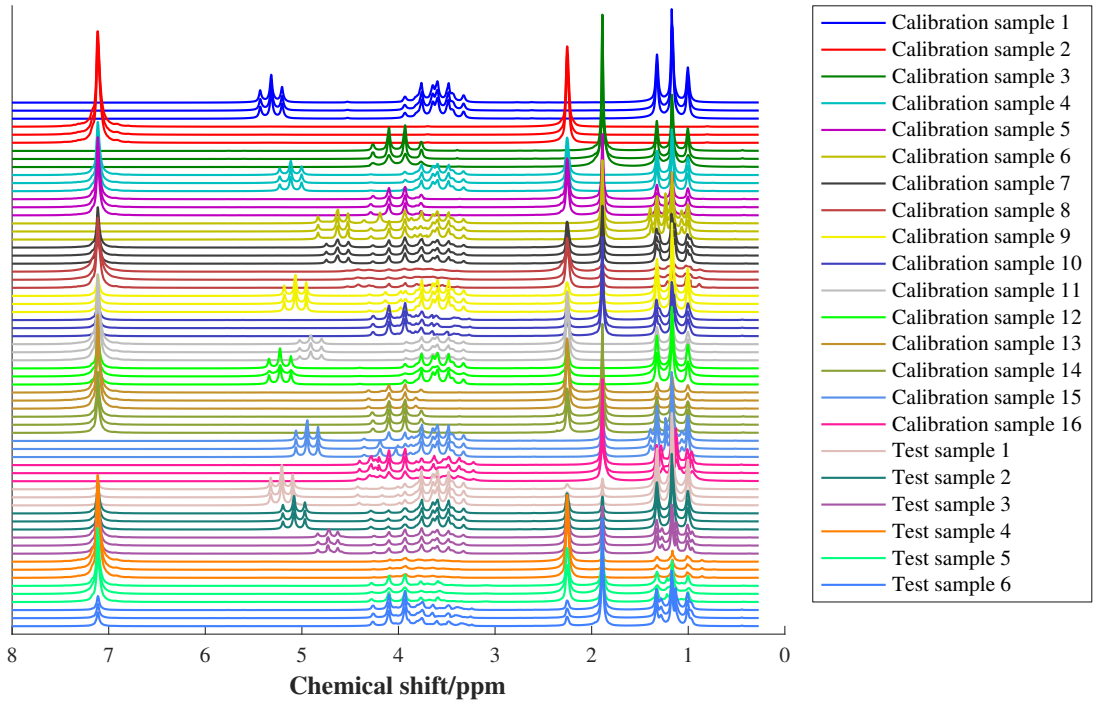

Figure 5.29 - ^{1}H low-field NMR spectra of calibration and test samples in dataset 3 with alignment by RAFFT using optimum parameters determined by DoE (maximum shift = 40 and lookahead = 10).

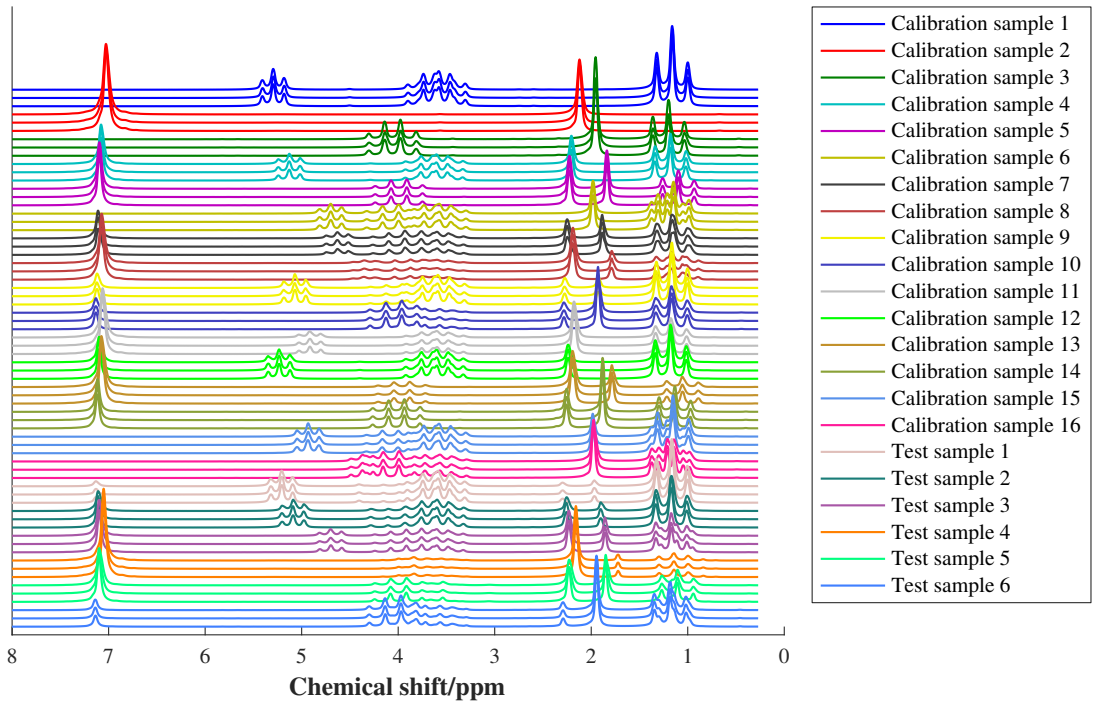

Figure 5.30 - ^{1}H low-field NMR spectra of calibration and test samples in dataset 4, without alignment.

Appendix 6: Additional Figures Corresponding to Chapter 6

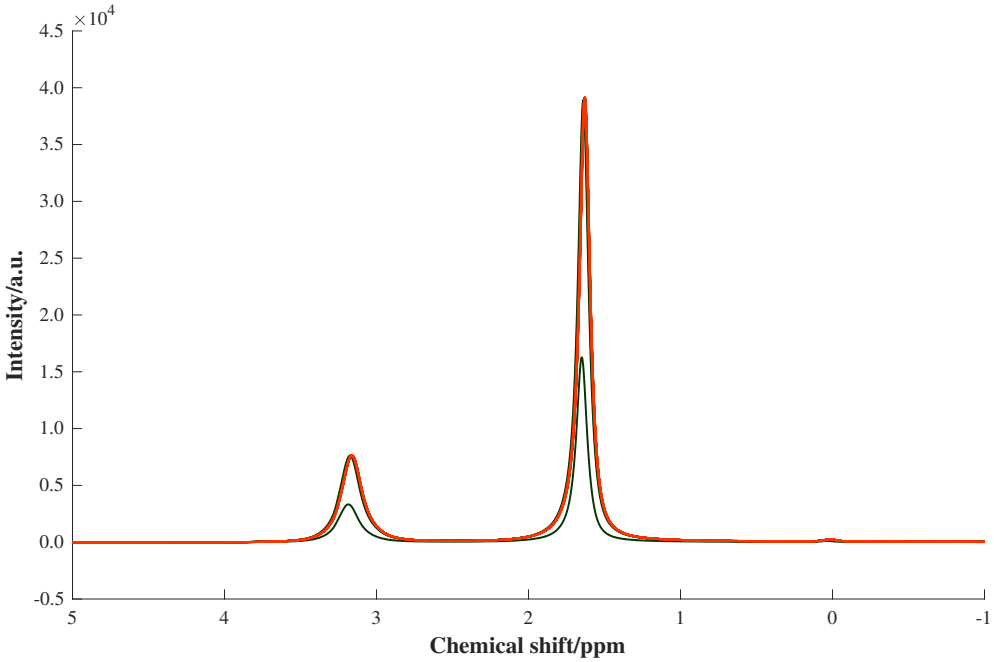

Figure 6.33 - Low-field ^{1}H NMR spectra of methanol collected every 30 seconds for 20 minutes starting from approximately 28.5 °C. Black represents the start of the experiment and red represents the end of the experiment.

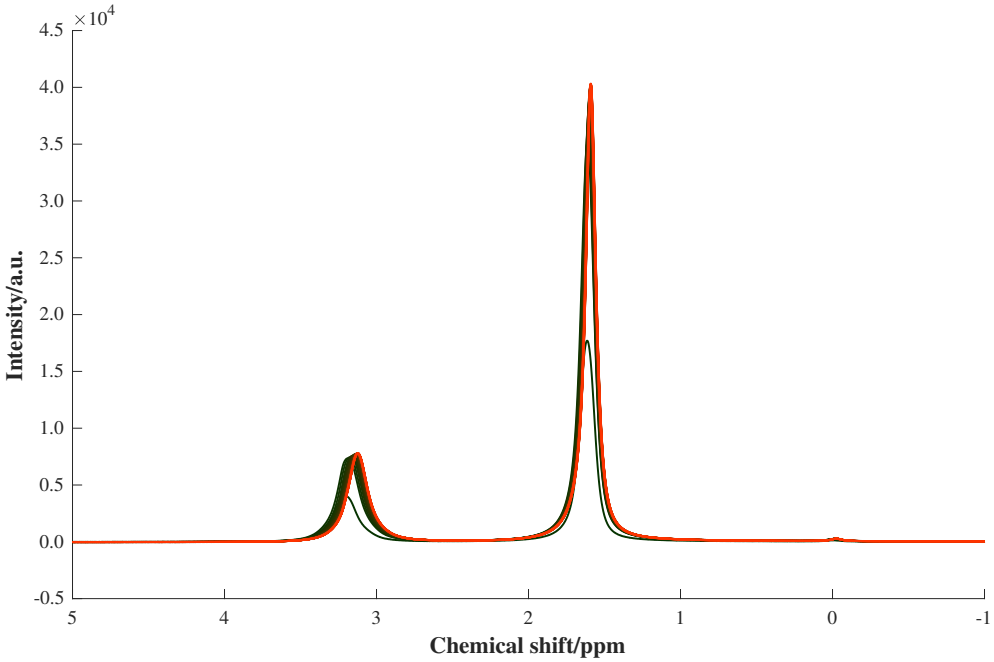

Figure 6.34 - Low-field ^{1}H NMR spectra of methanol collected every 30 seconds for 20 minutes starting from room temperature. Black represents the start of the experiment and red represents the end of the experiment.

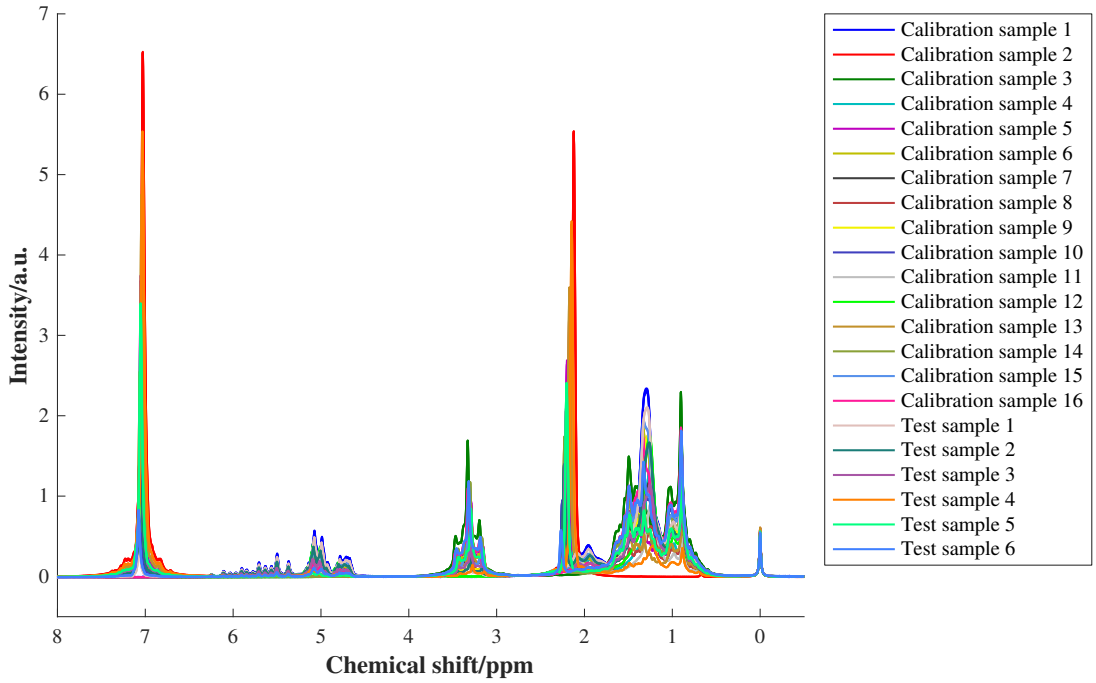

Figure 6.35 - ^{1}H low-field NMR spectra of calibration and test samples in dataset 1, after reference deconvolution.

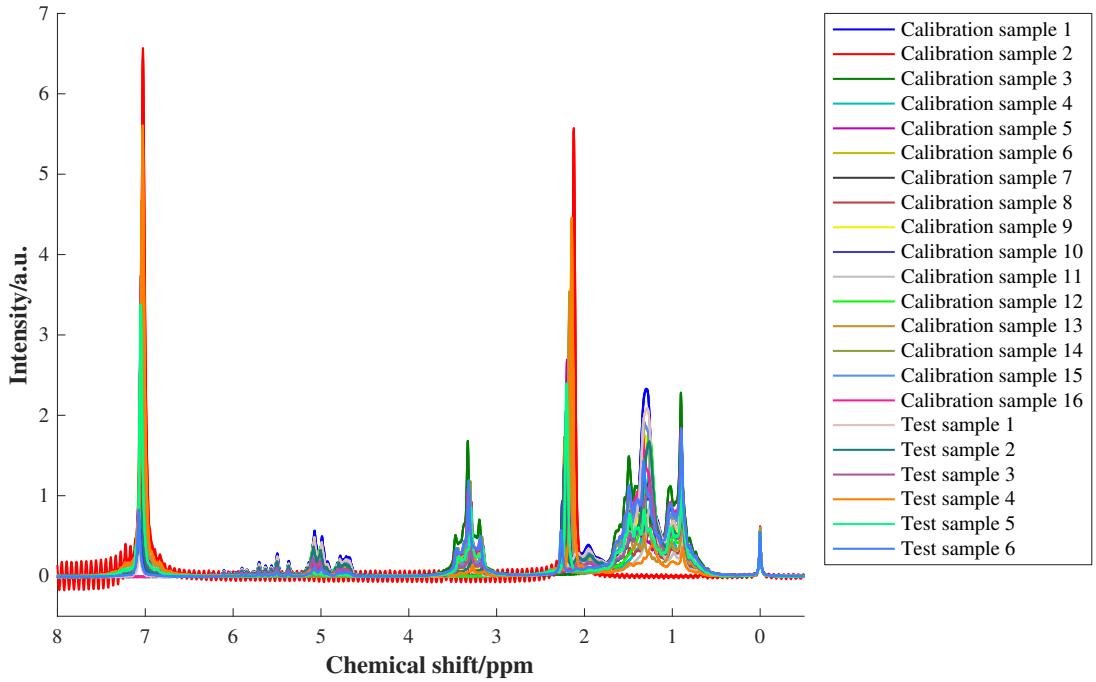

Figure 6.36 - ^{1}H low-field NMR spectra of calibration and test samples in dataset 2, after reference deconvolution.

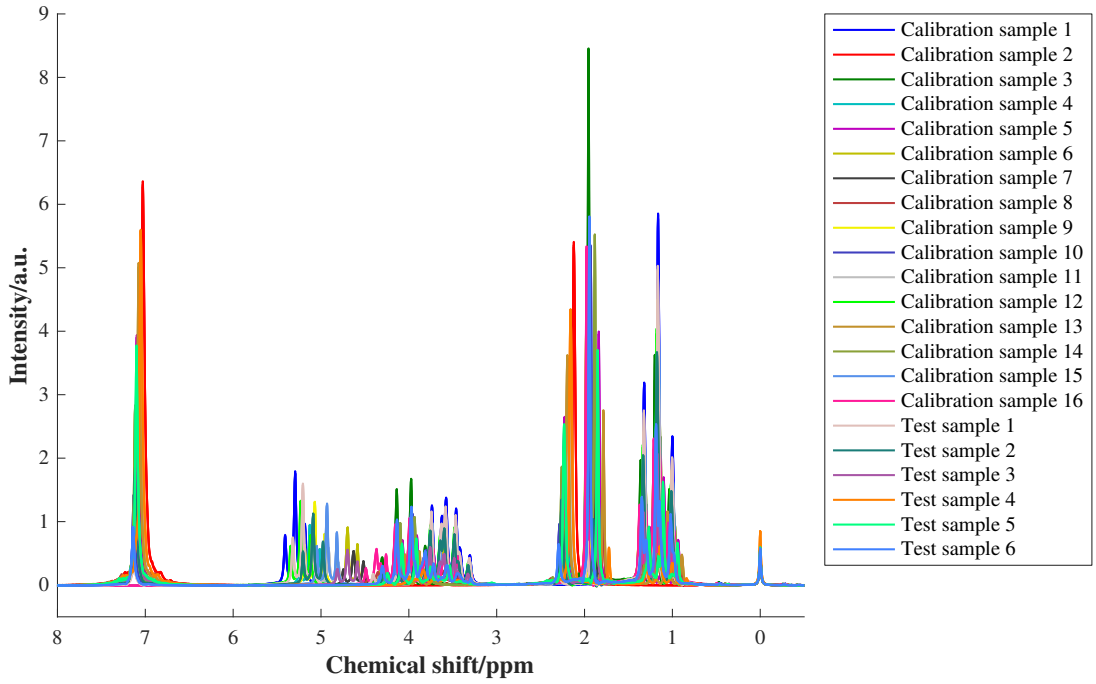

Figure 6.37 - ^{1}H low-field NMR spectra of calibration and test samples in dataset 3, after reference deconvolution.

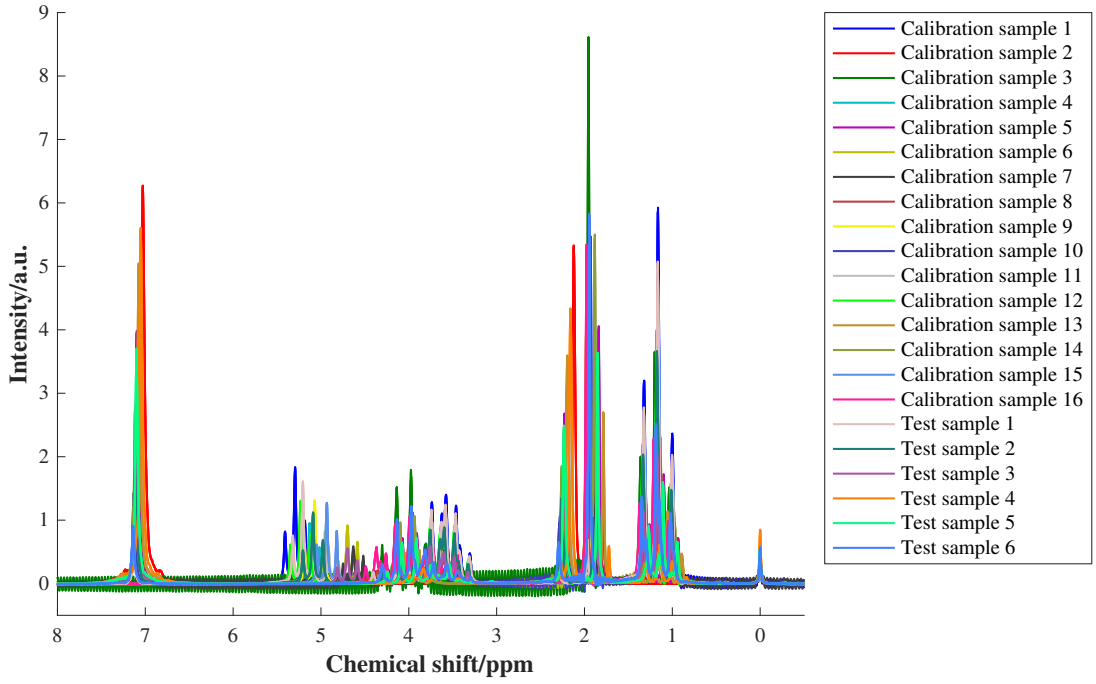

Figure 6.38 - ^{1}H low-field NMR spectra of calibration and test samples in dataset 4, after reference deconvolution.

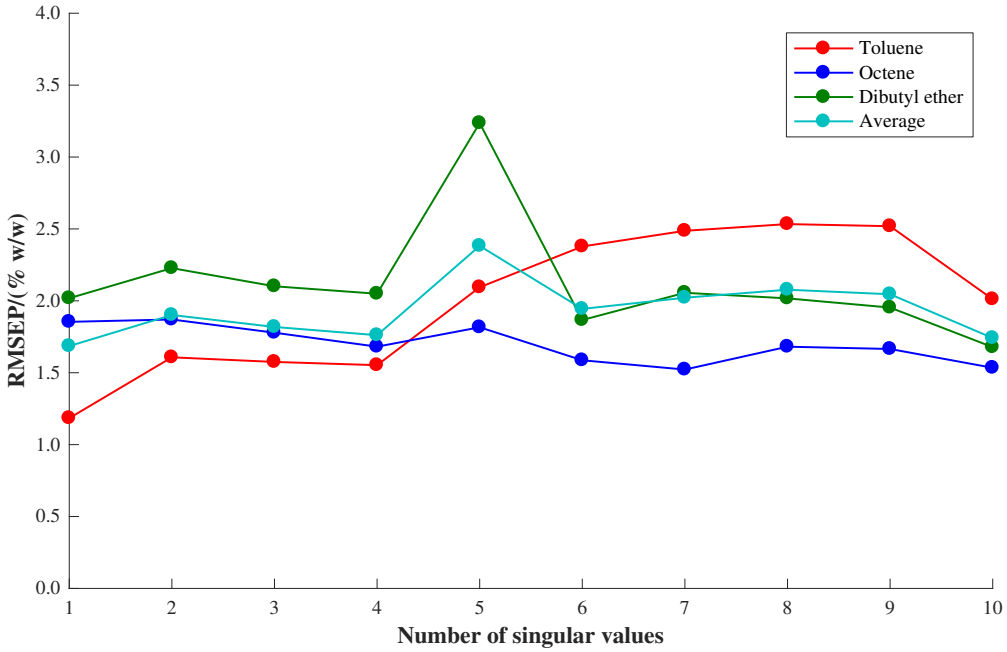

Figure 6.39 - RMSEP versus number of singular values for PLS1 models built using ^{1}H low-field NMR spectra of calibration samples in dataset 1, applied to the test samples in dataset 2 after SST (no alignment, 2 LVs included).

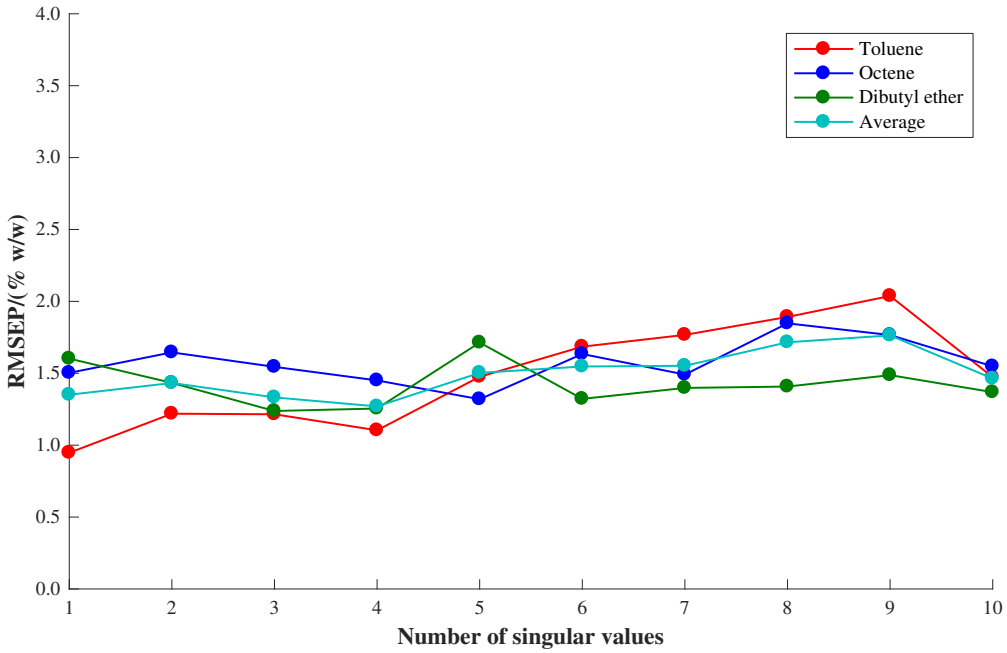

Figure 6.40 - RMSEP versus number of singular values for PLS1 models built using ^{1}H low-field NMR spectra of calibration samples in dataset 1, applied to the test samples in dataset 2 after SST (no alignment, 3 LVs included).

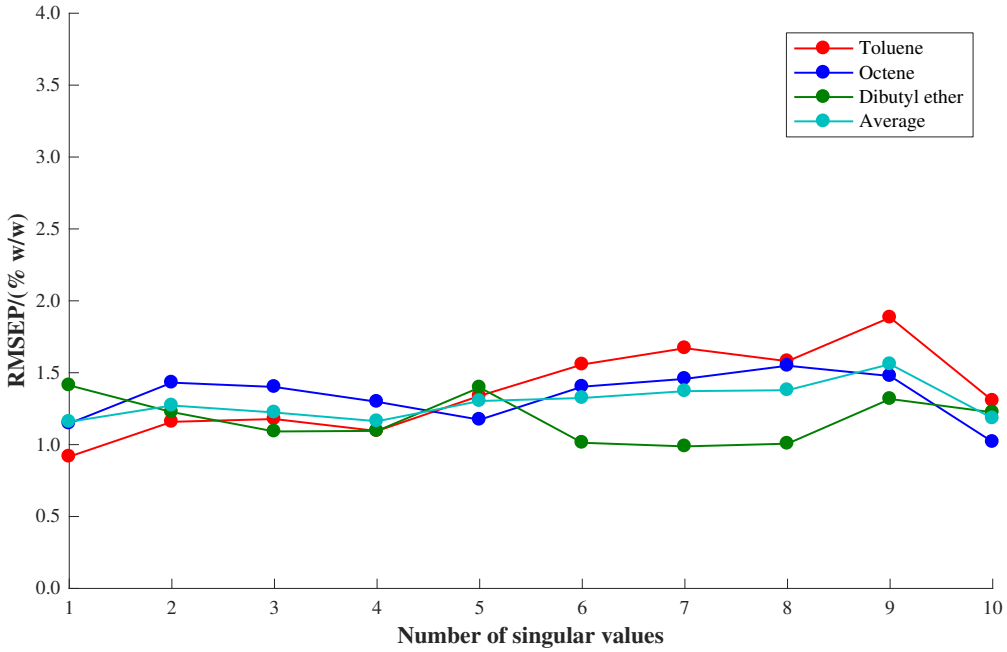

Figure 6.41 - RMSEP versus number of singular values for PLS1 models built using ^{1}H low-field NMR spectra of calibration samples in dataset 1, applied to the test samples in dataset 2 after SST (no alignment, 4 LVs included).

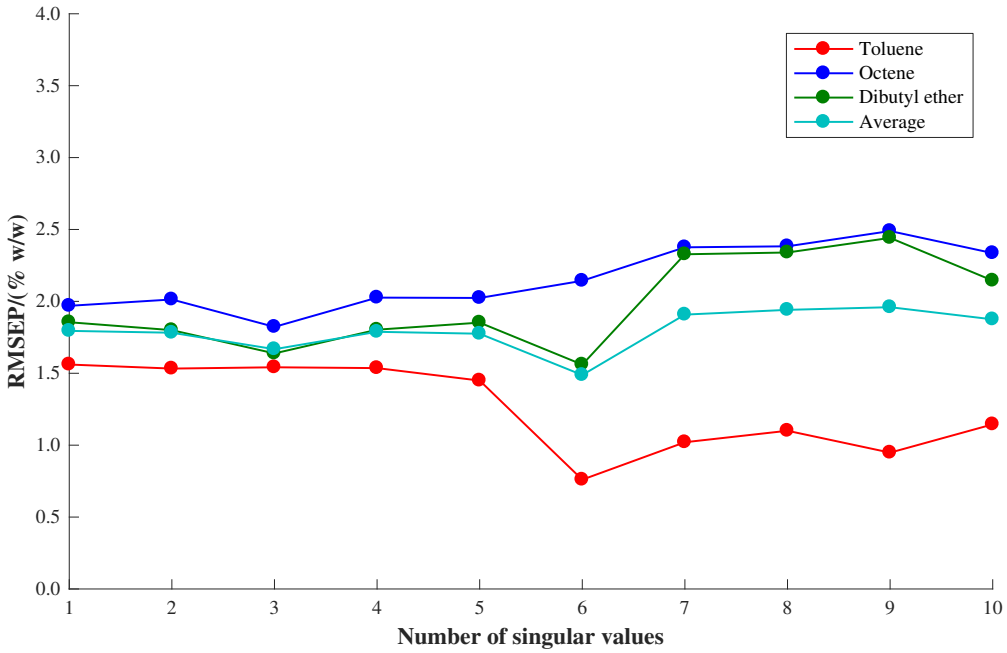

Figure 6.42 - RMSEP versus number of singular values for PLS1 models built using ^{1}H low-field NMR spectra of calibration samples in dataset 1, applied to the test samples in dataset 2 after SST (aligned with *ic*oshift, 2 LVs included).

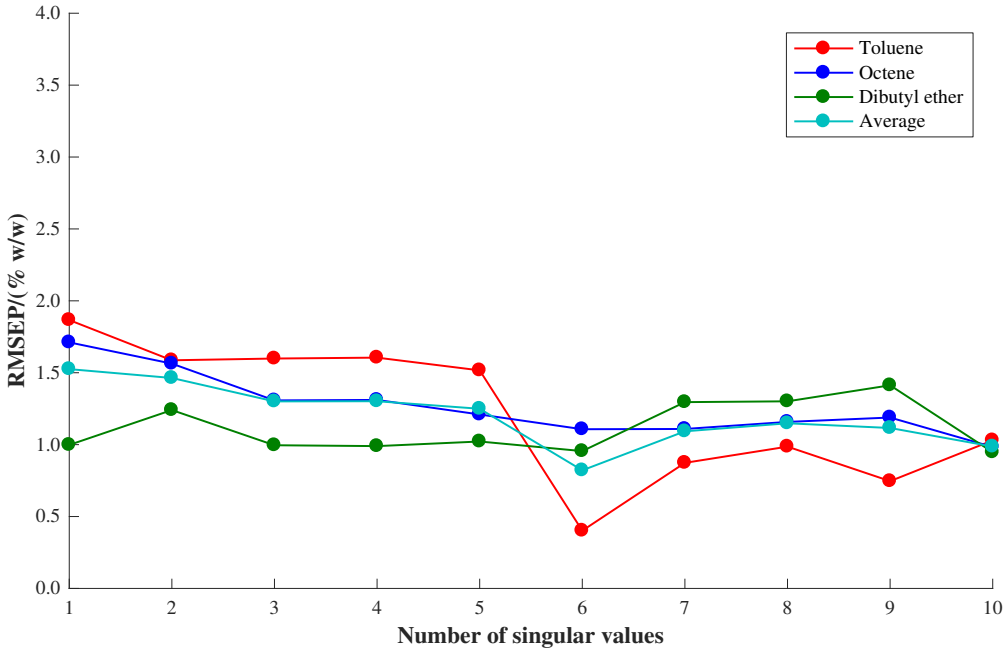

Figure 6.43 - RMSEP versus number of singular values for PLS1 models built using ^{1}H low-field NMR spectra of calibration samples in dataset 1, applied to the test samples in dataset 2 after SST (aligned with *ic*oshift, 3 LVs included).

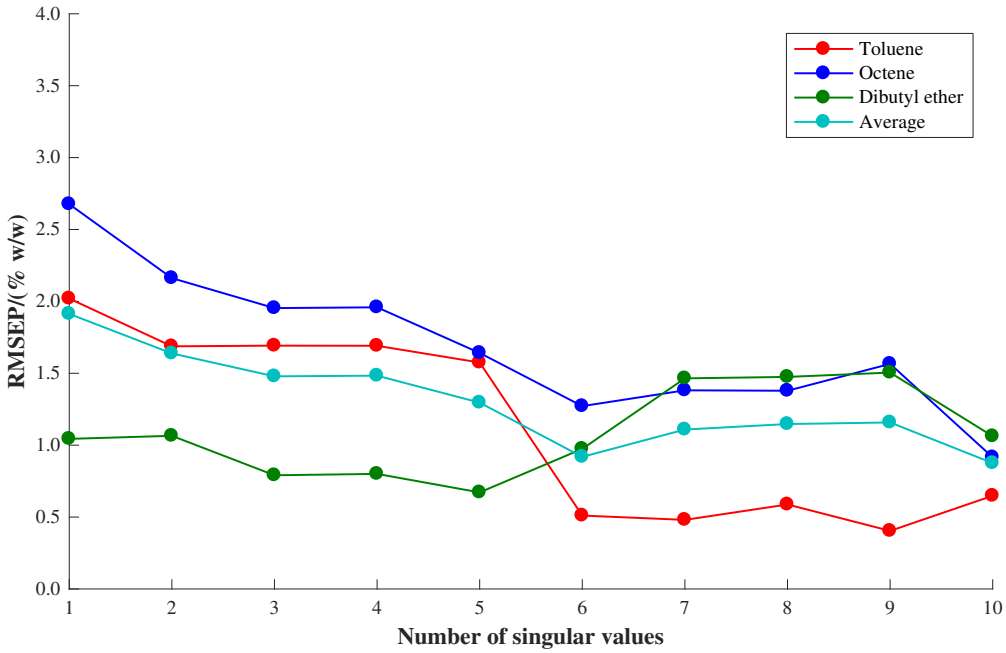

Figure 6.44 - RMSEP versus number of singular values for PLS1 models built using ^{1}H low-field NMR spectra of calibration samples in dataset 1, applied to the test samples in dataset 2 after SST (aligned with *ic*oshift, 4 LVs included).

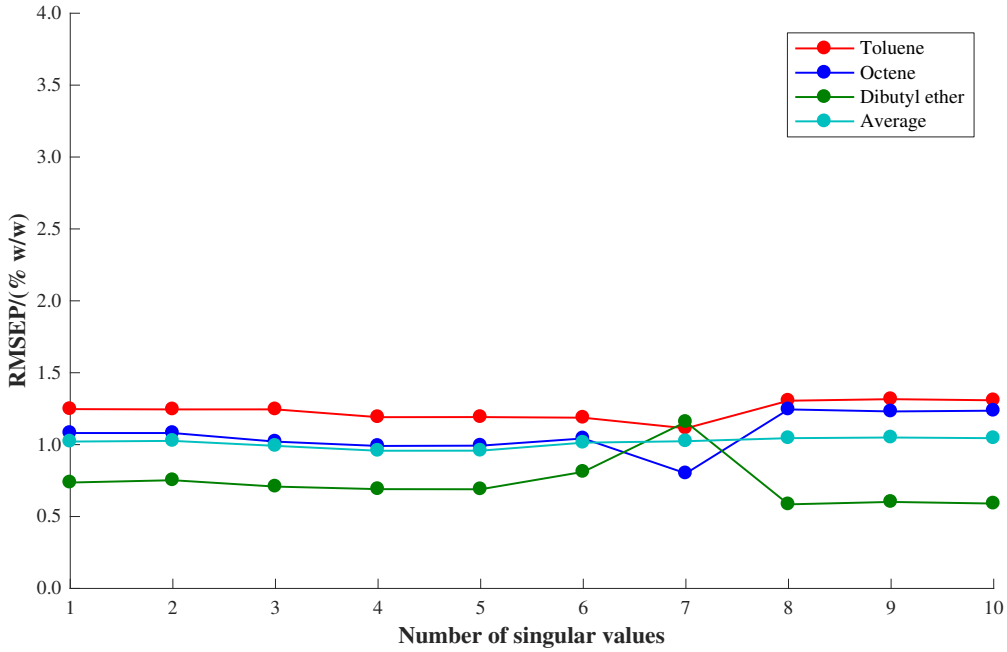

Figure 6.45 - RMSEP versus number of singular values for PLS1 models built using ^{1}H low-field NMR spectra of calibration samples in dataset 1, applied to the test samples in dataset 2 after SST (with bucketing, 2 LVs included).

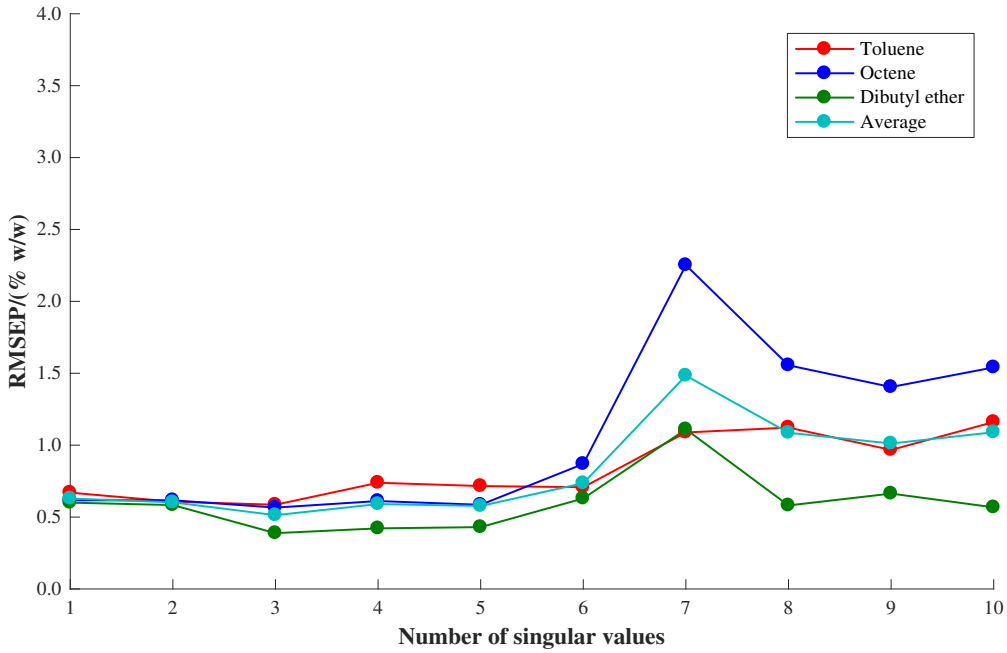

Figure 6.46 - RMSEP versus number of singular values for PLS1 models built using ^{1}H low-field NMR spectra of calibration samples in dataset 1, applied to the test samples in dataset 2 after SST (with bucketing, 3 LVs included).

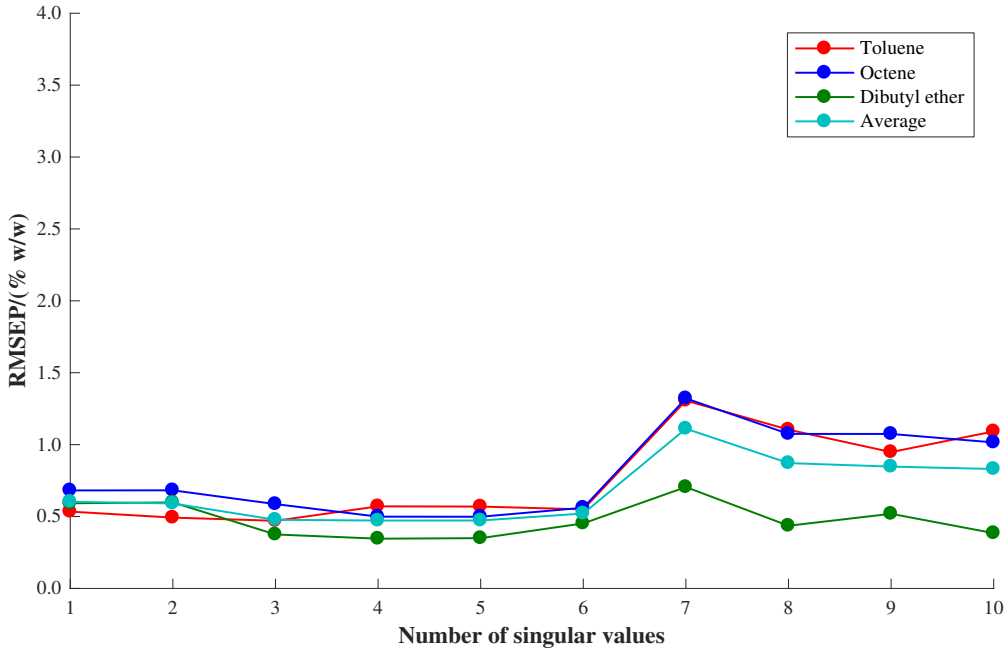

Figure 6.47 - RMSEP versus number of singular values for PLS1 models built using ^{1}H low-field NMR spectra of calibration samples in dataset 1, applied to the test samples in dataset 2 after SST (with bucketing, 4 LVs included).

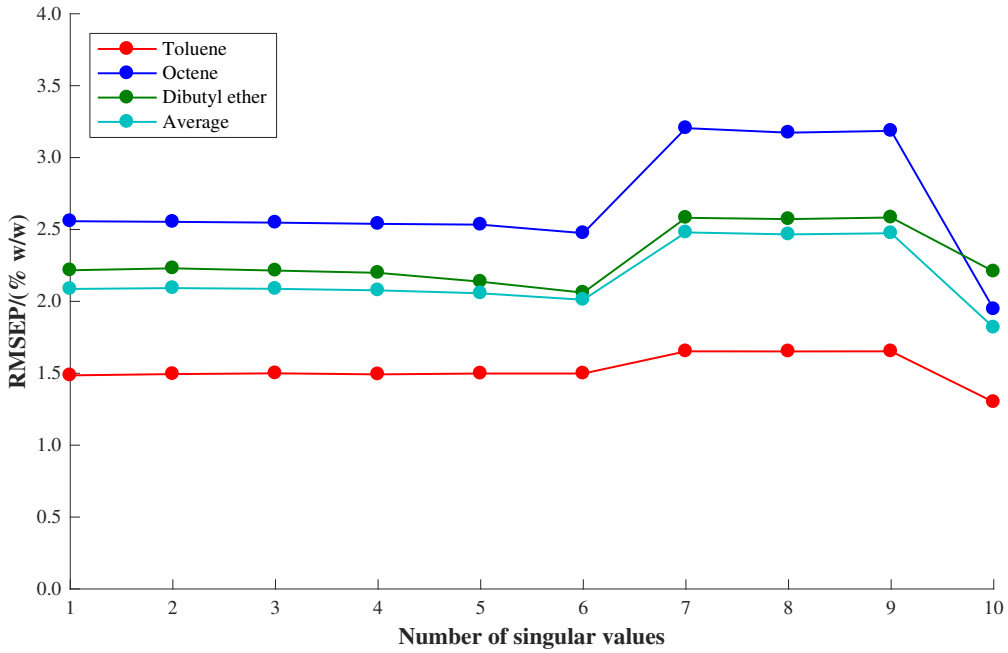

Figure 6.48 - RMSEP versus number of singular values for PLS1 models built using ^{1}H low-field NMR spectra of calibration samples in dataset 1 with reference deconvolution, applied to the test samples in dataset 2 with reference deconvolution and SST (no alignment, 2 LVs included).

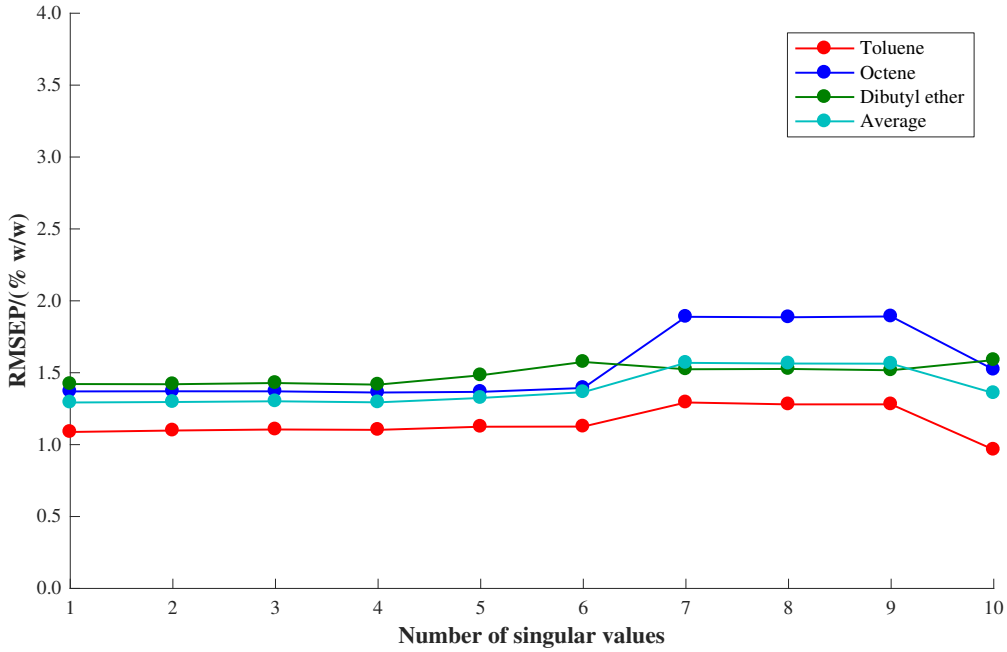

Figure 6.49 - RMSEP versus number of singular values for PLS1 models built using ^{1}H low-field NMR spectra of calibration samples in dataset 1 with reference deconvolution, applied to the test samples in dataset 2 with reference deconvolution and SST (no alignment, 3 LVs included).

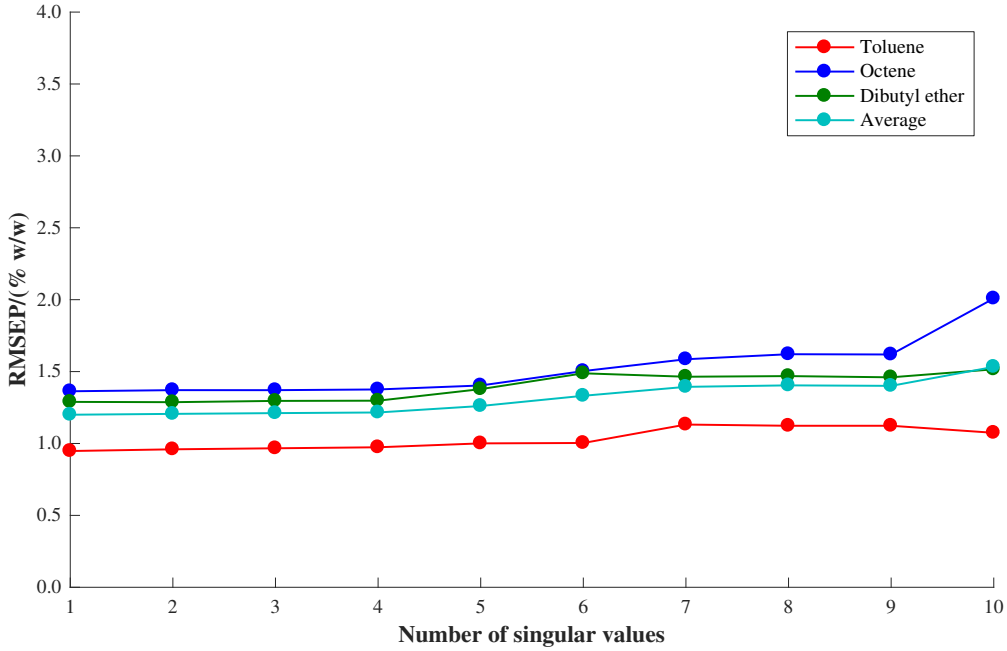

Figure 6.50 - RMSEP versus number of singular values for PLS1 models built using ^{1}H low-field NMR spectra of calibration samples in dataset 1 with reference deconvolution, applied to the test samples in dataset 2 with reference deconvolution and SST (no alignment, 4 LVs included).

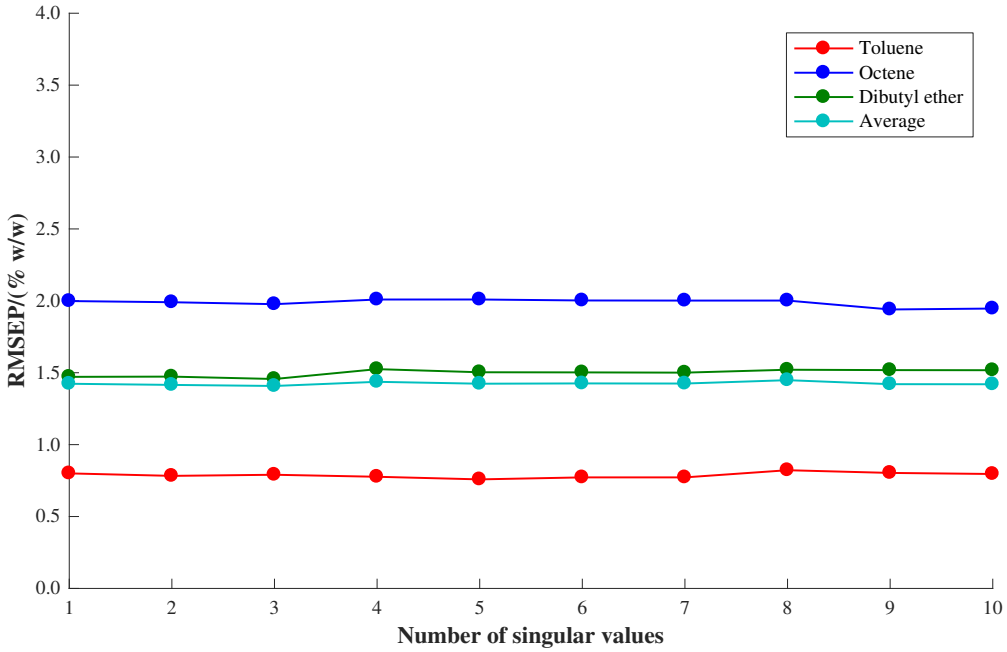

Figure 6.51 - RMSEP versus number of singular values for PLS1 models built using ^{1}H low-field NMR spectra of calibration samples in dataset 1 with reference deconvolution, applied to the test samples in dataset 2 with reference deconvolution and SST (aligned with *i*coshift, 2 LVs included).

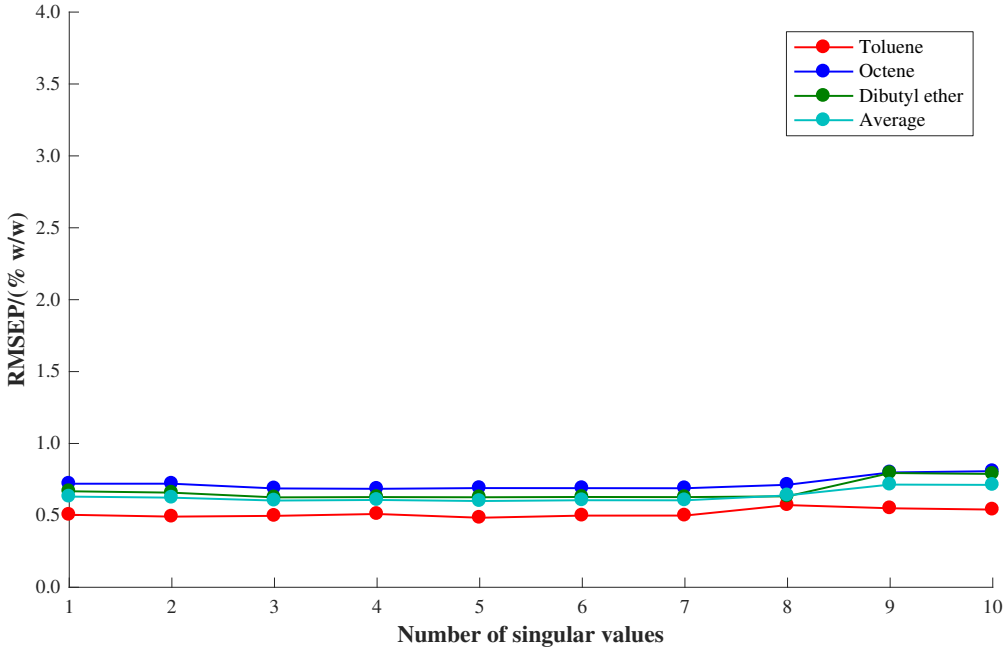

Figure 6.52 - RMSEP versus number of singular values for PLS1 models built using ^{1}H low-field NMR spectra of calibration samples in dataset 1 with reference deconvolution, applied to the test samples in dataset 2 with reference deconvolution and SST (aligned with *i*coshift, 3 LVs included).

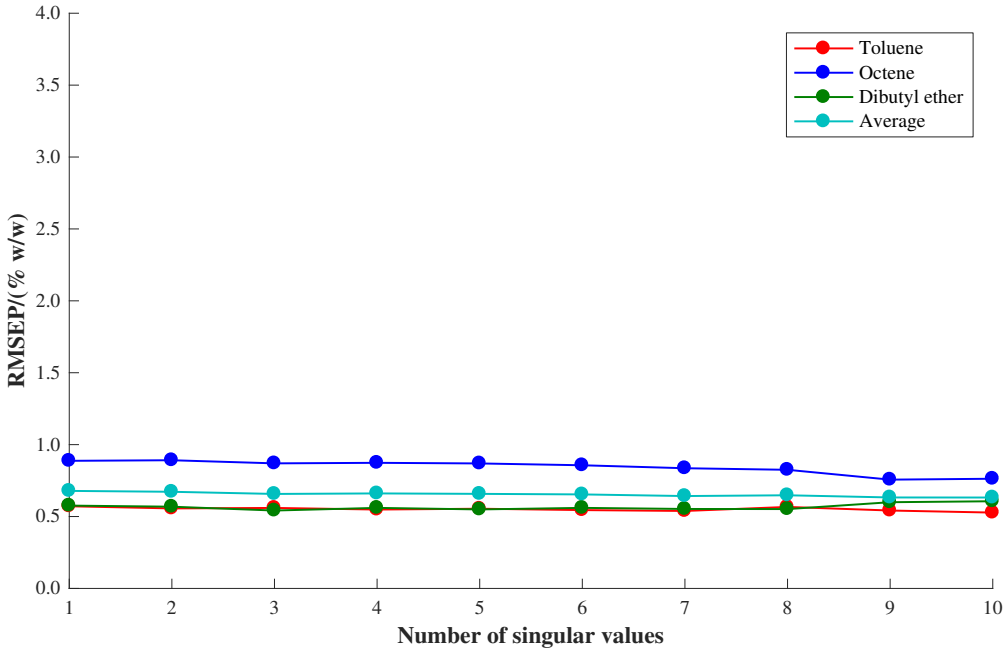

Figure 6.53 - RMSEP versus number of singular values for PLS1 models built using ^{1}H low-field NMR spectra of calibration samples in dataset 1 with reference deconvolution, applied to the test samples in dataset 2 with reference deconvolution and SST (aligned with *i*coshift, 4 LVs included).

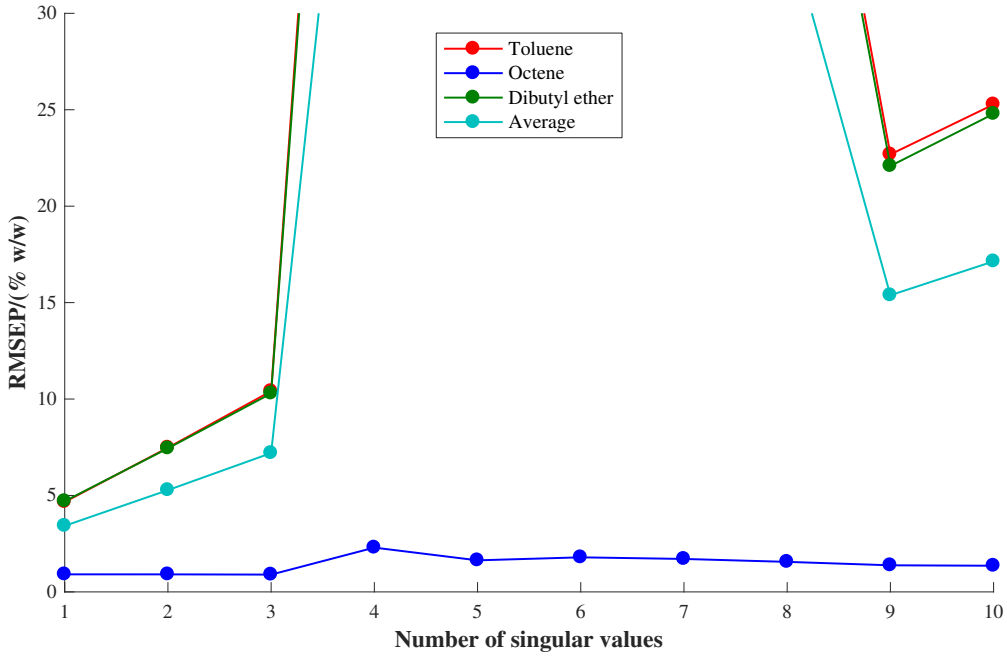

Figure 6.54 - RMSEP versus number of singular values for PLS1 models built using ^{1}H low-field NMR spectra of calibration samples in dataset 1 with reference deconvolution, applied to the test samples in dataset 2 with reference deconvolution and SST (with bucketing, 2 LVs included, only RMSEP values < 30 % w/w shown so worst values lie outwith range of plot).

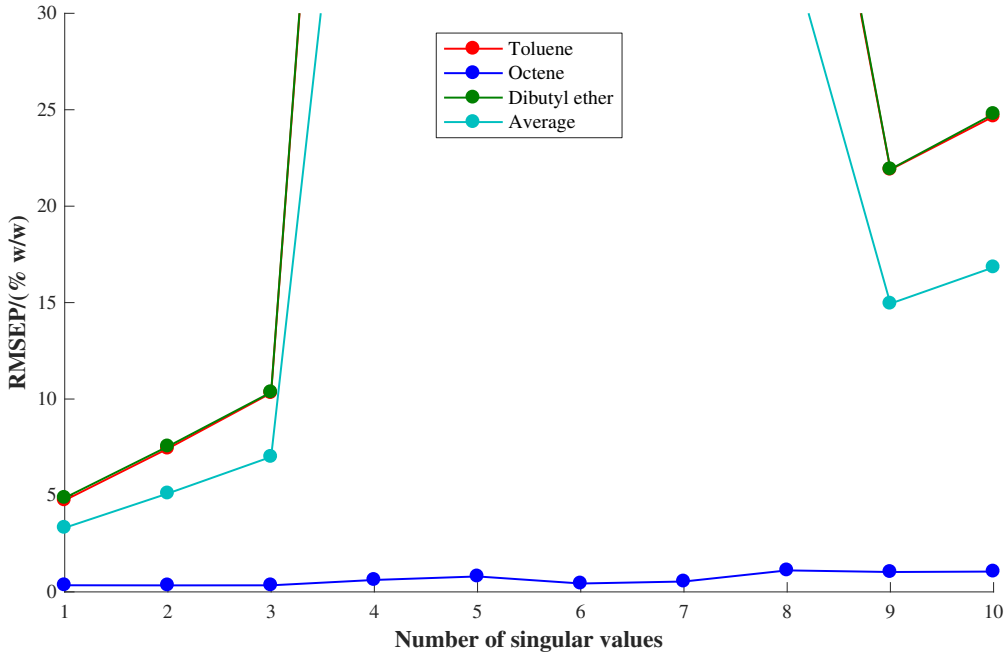

Figure 6.55 - RMSEP versus number of singular values for PLS1 models built using ^{1}H low-field NMR spectra of calibration samples in dataset 1 with reference deconvolution, applied to the test samples in dataset 2 with reference deconvolution and SST (with bucketing, 3 LVs included, only RMSEP values < 30 % w/w shown so worst values lie outwith range of plot).

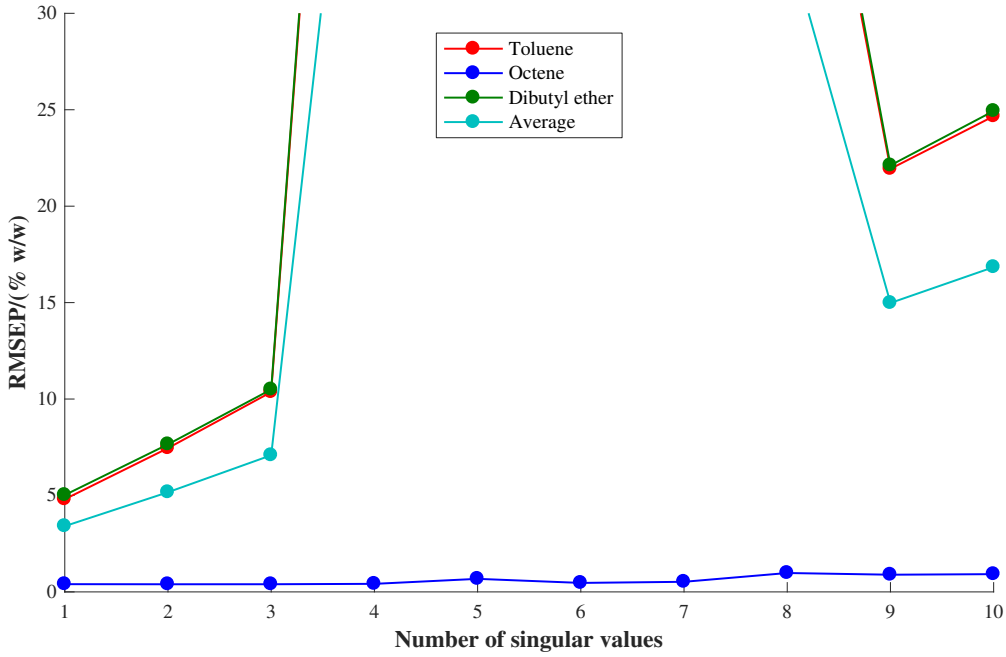

Figure 6.56 - RMSEP versus number of singular values for PLS1 models built using ^{1}H low-field NMR spectra of calibration samples in dataset 1 with reference deconvolution, applied to the test samples in dataset 2 with reference deconvolution and SST (with bucketing, 4 LVs included, only RMSEP values < 30 % w/w shown so worst values lie outwith range of plot).

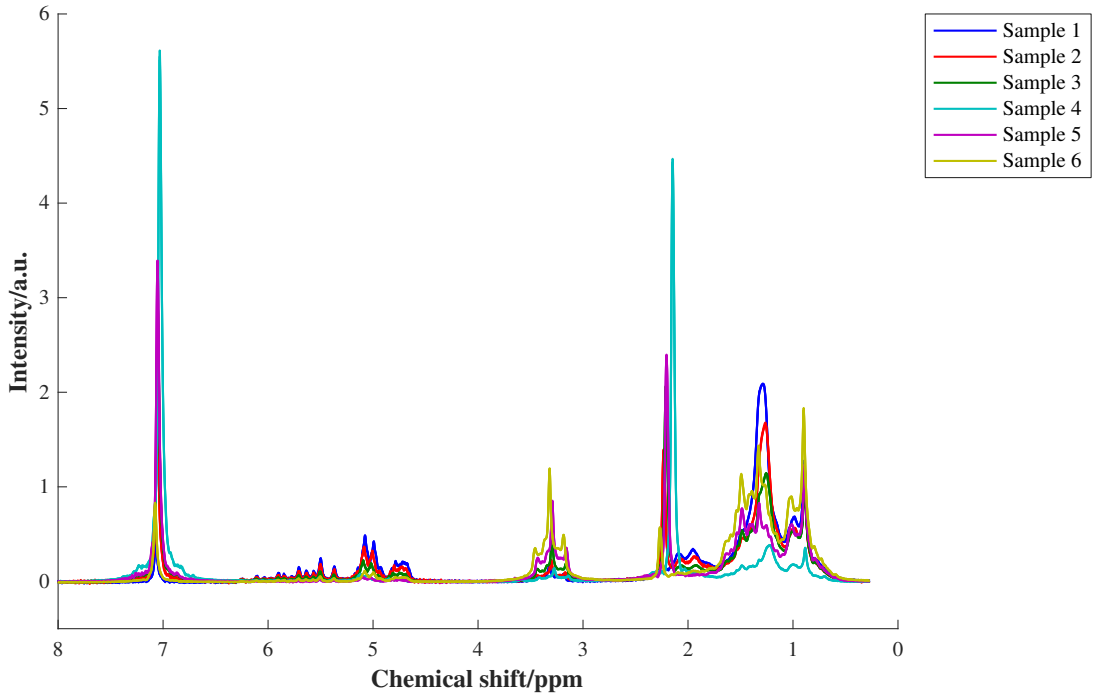

Figure 6.57 - ^{1}H low-field NMR spectra of test samples in dataset 2 (no alignment), with reference deconvolution and calibration transfer by SST (using 1 singular value).

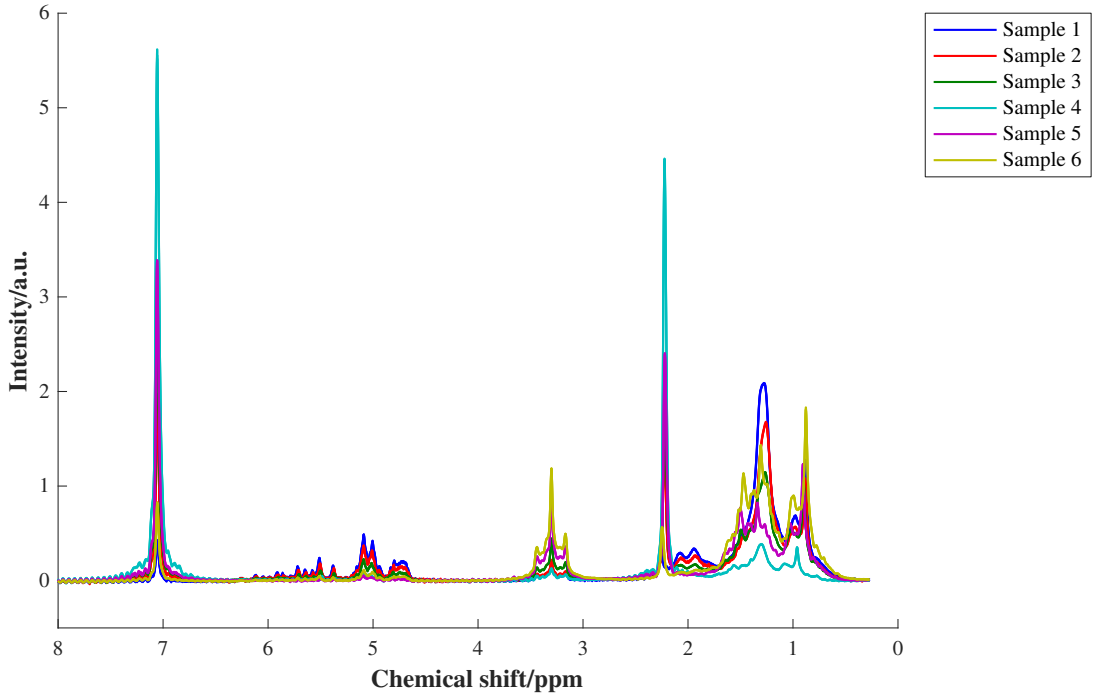

Figure 6.58 - ^{1}H low-field NMR spectra of test samples in dataset 2, with reference deconvolution, alignment by *i*coshift and calibration transfer by SST (using 1 singular value).

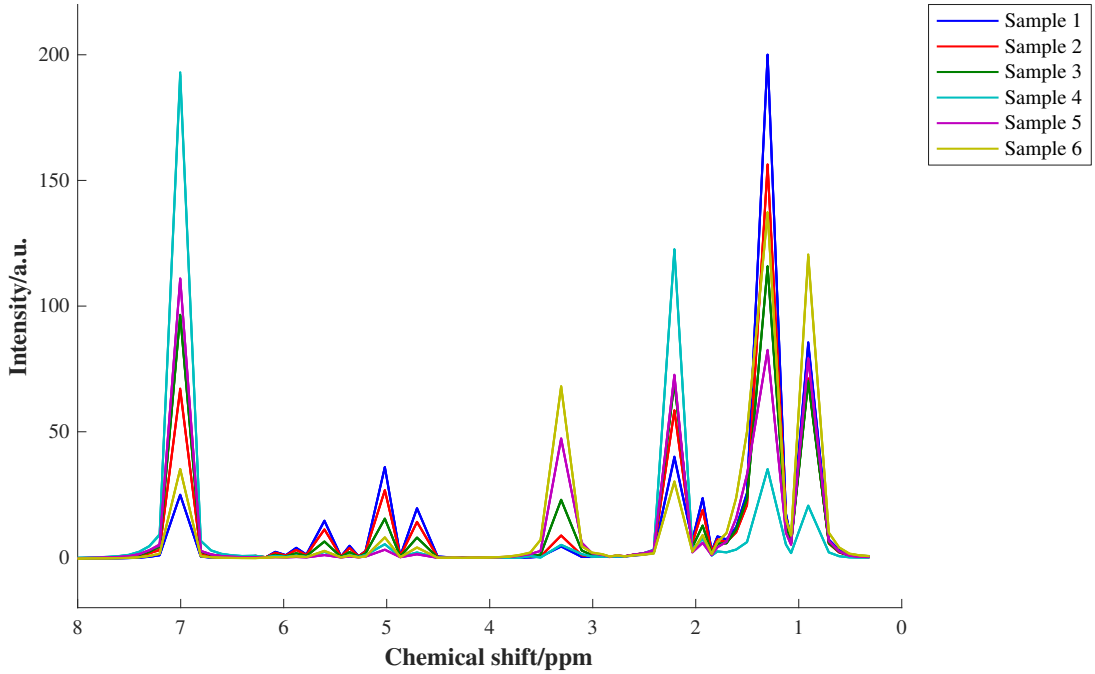

Figure 6.59 - ^{1}H low-field NMR spectra of test samples in dataset 2, with reference deconvolution, optimised bucketing and calibration transfer by SST (using 1 singular value).

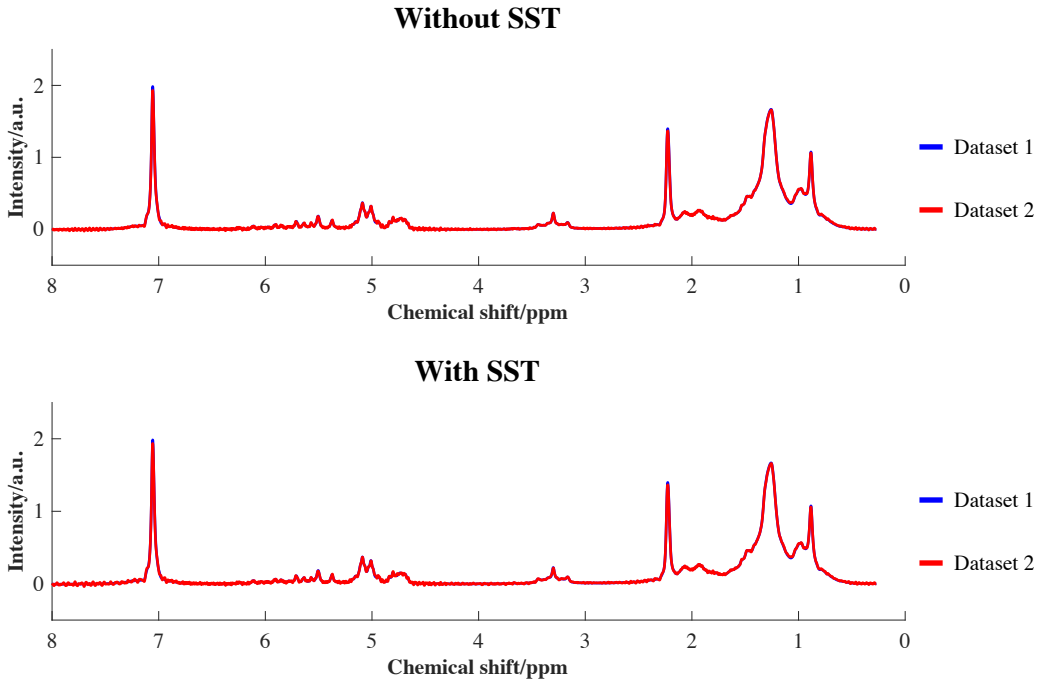

Figure 6.60 - ^{1}H low-field NMR spectrum of test sample 2 in dataset 1 (blue) and dataset 2 without and with calibration transfer by SST (red), aligned by *ic*oshift (1 singular value included). With reference deconvolution applied to datasets 1 and 2 before SST.

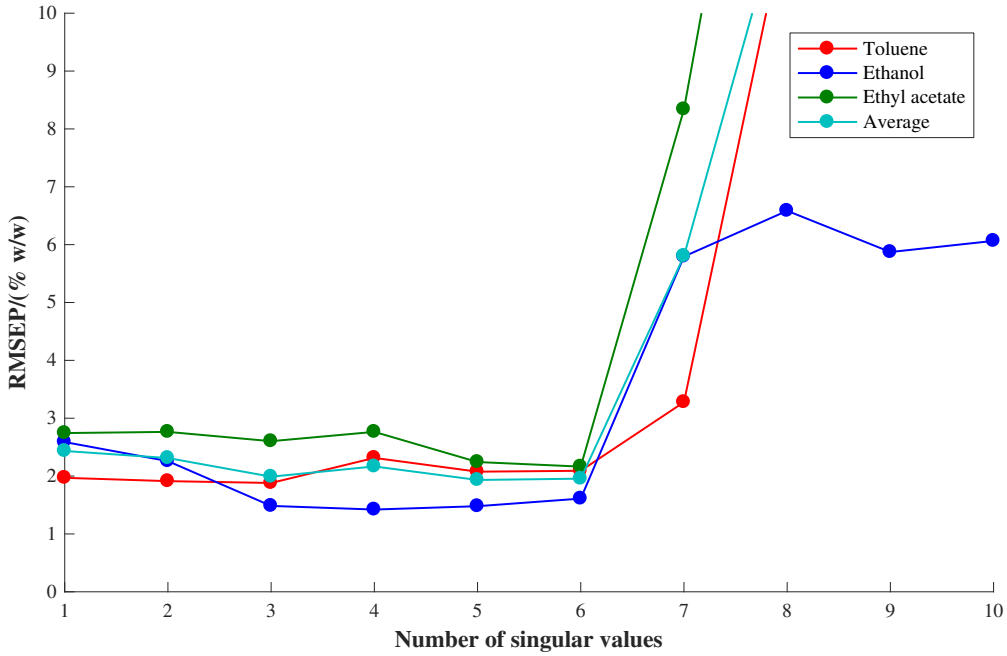

Figure 6.61 - RMSEP versus number of singular values for PLS1 models built using ^{1}H low-field NMR spectra of calibration samples in dataset 3, applied to the test samples in dataset 4 after SST (no alignment, 2 LVs included, only RMSEP values < 10 % w/w shown so worst values lie outwith range of plot).

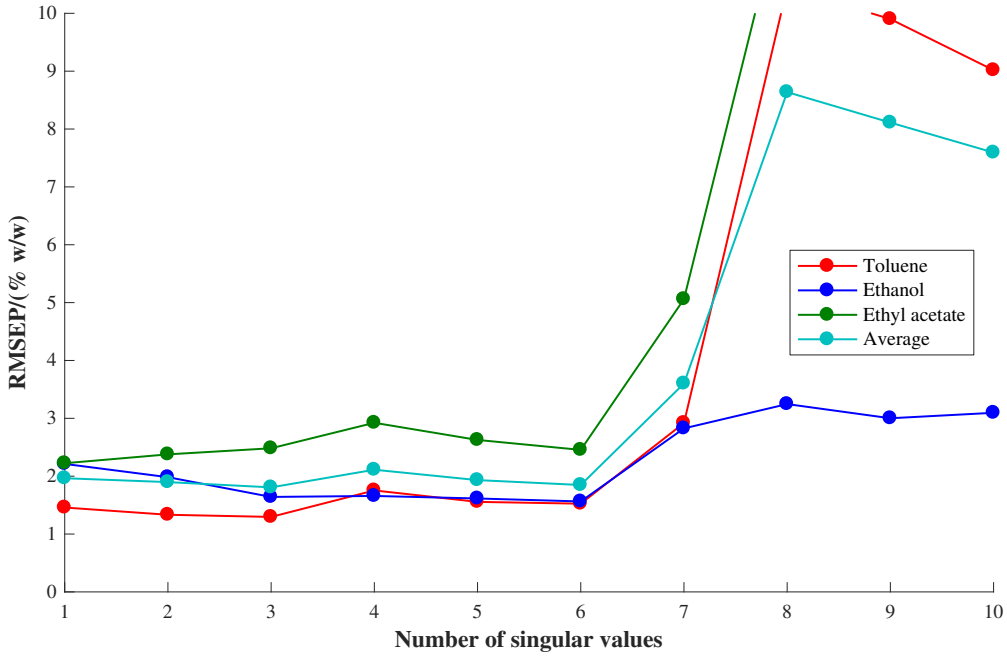

Figure 6.62 - RMSEP versus number of singular values for PLS1 models built using ^{1}H low-field NMR spectra of calibration samples in dataset 3, applied to the test samples in dataset 4 after SST (no alignment, 3 LVs included, only RMSEP values < 10 % w/w shown so worst values lie outwith range of plot).

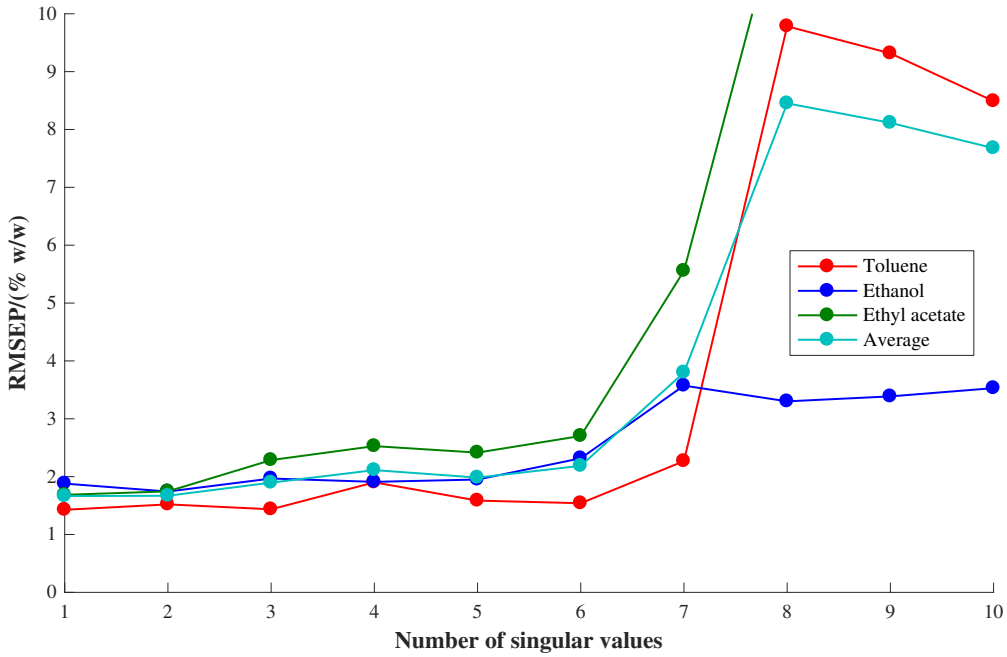

Figure 6.63 - RMSEP versus number of singular values for PLS1 models built using ^{1}H low-field NMR spectra of calibration samples in dataset 3, applied to the test samples in dataset 4 after SST (no alignment, 4 LVs included, only RMSEP values < 10 % w/w shown so worst values lie outwith range of plot).

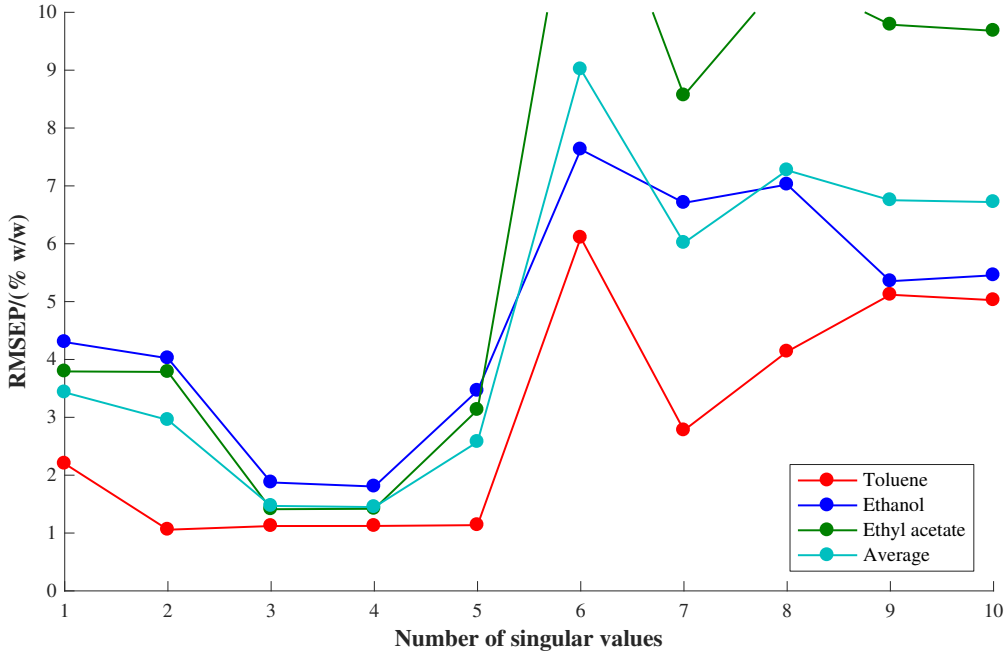

Figure 6.64 - RMSEP versus number of singular values for PLS1 models built using ^{1}H low-field NMR spectra of calibration samples in dataset 3, applied to the test samples in dataset 4 after SST (aligned with RAFFT, 2 LVs included, only RMSEP values < 10 % w/w shown so worst values lie outwith range of plot).

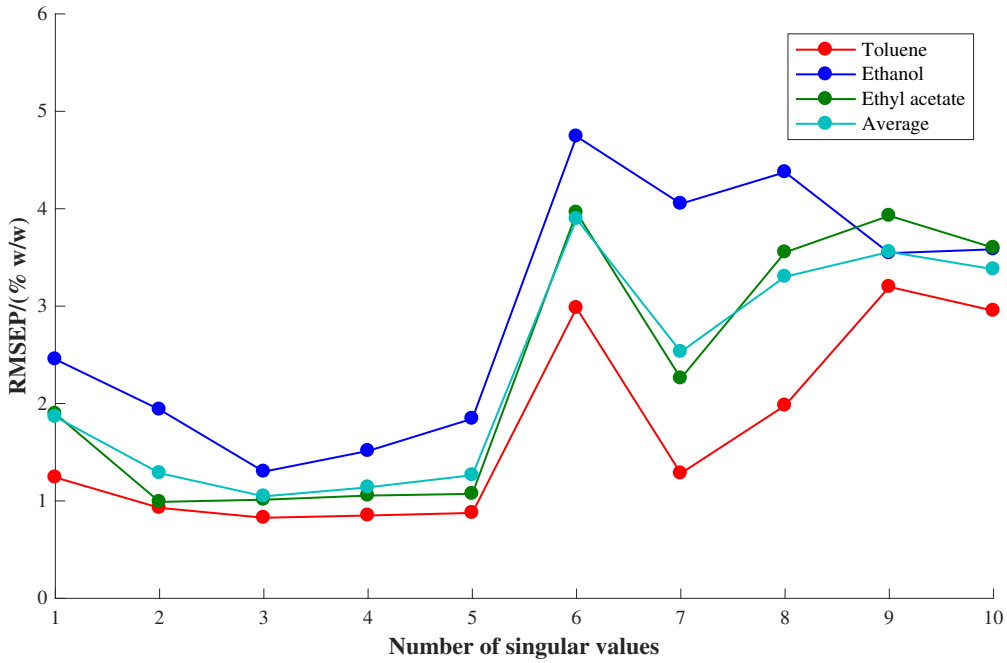

Figure 6.65 - RMSEP versus number of singular values for PLS1 models built using ^{1}H low-field NMR spectra of calibration samples in dataset 3, applied to the test samples in dataset 4 after SST (aligned with RAFFT, 3 LVs included).

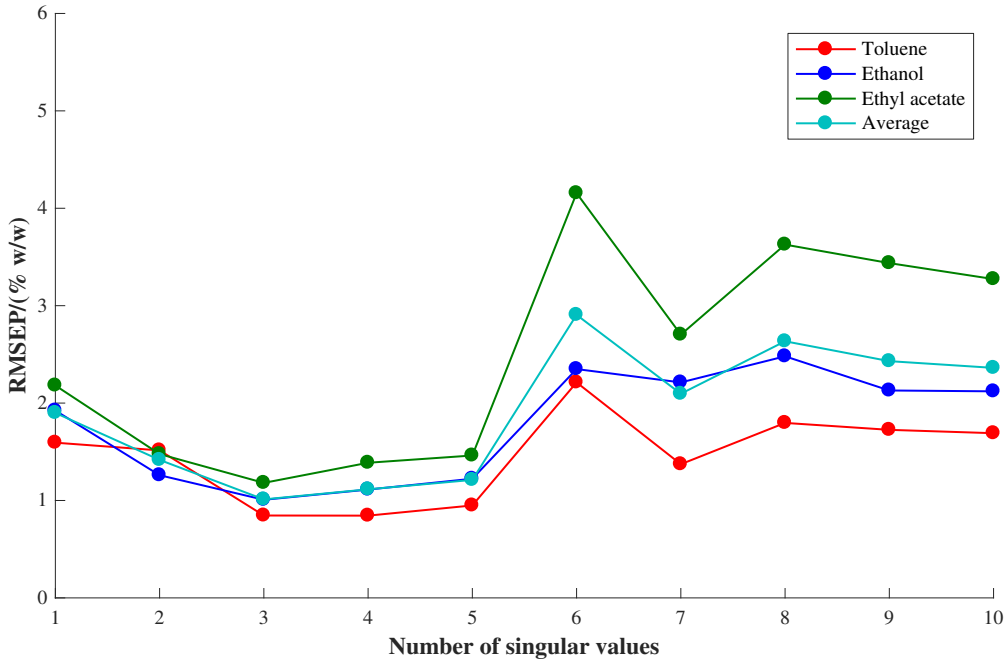

Figure 6.66 - RMSEP versus number of singular values for PLS1 models built using ^{1}H low-field NMR spectra of calibration samples in dataset 3, applied to the test samples in dataset 4 after SST (aligned with RAFFT, 4 LVs included).

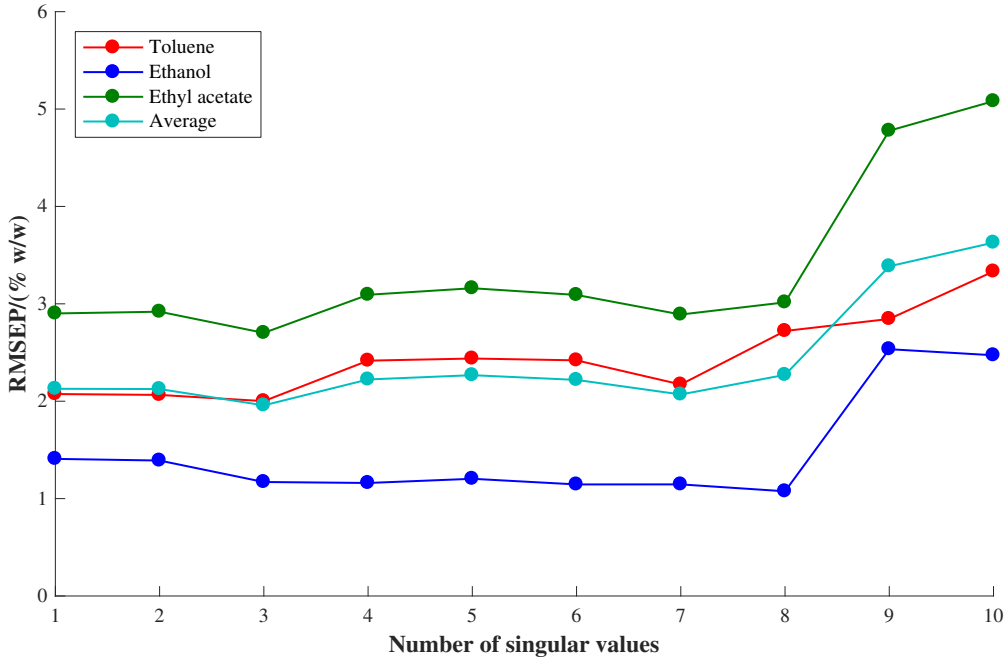

Figure 6.67 - RMSEP versus number of singular values for PLS1 models built using ^{1}H low-field NMR spectra of calibration samples in dataset 3 with reference deconvolution, applied to the test samples in dataset 4 with reference deconvolution and SST (no alignment, 2 LVs included).

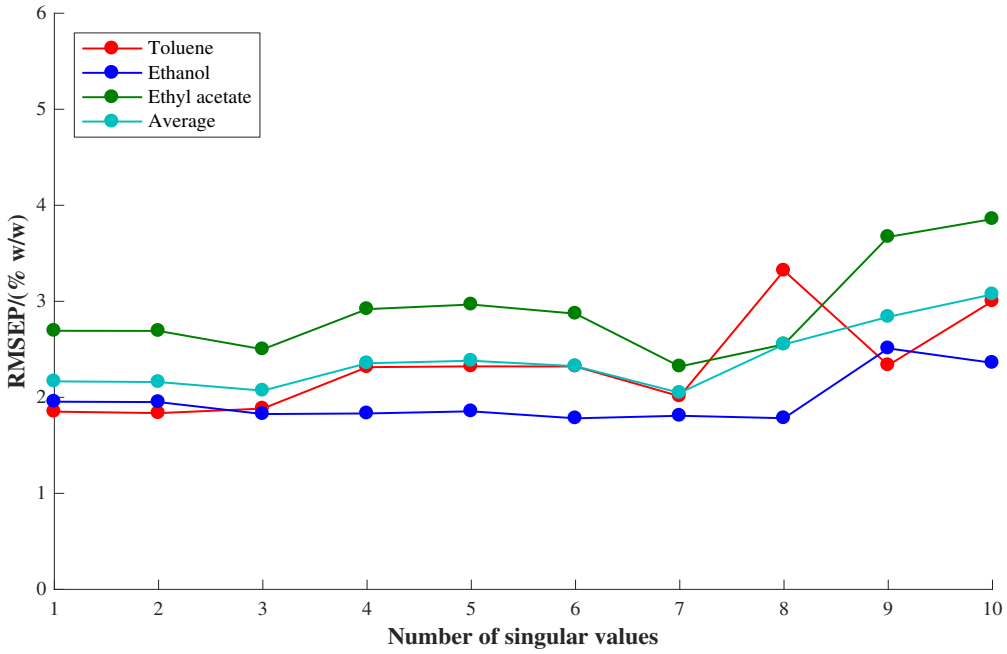

Figure 6.68 - RMSEP versus number of singular values for PLS1 models built using ^{1}H low-field NMR spectra of calibration samples in dataset 3 with reference deconvolution, applied to the test samples in dataset 4 with reference deconvolution and SST (no alignment, 3 LVs included).

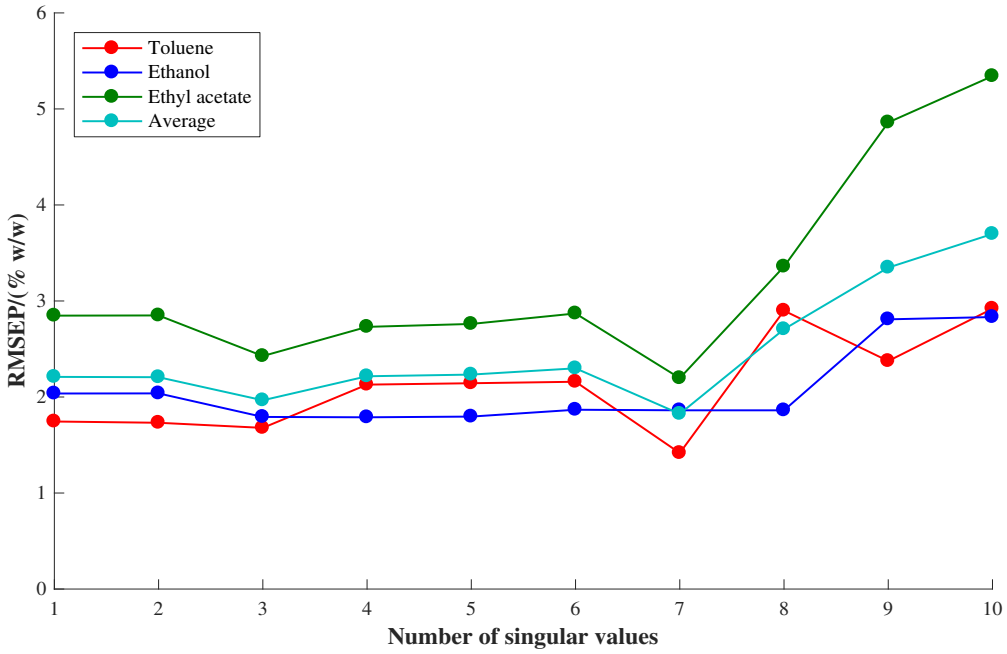

Figure 6.69 - RMSEP versus number of singular values for PLS1 models built using ^{1}H low-field NMR spectra of calibration samples in dataset 3 with reference deconvolution, applied to the test samples in dataset 4 with reference deconvolution and SST (no alignment, 4 LVs included).

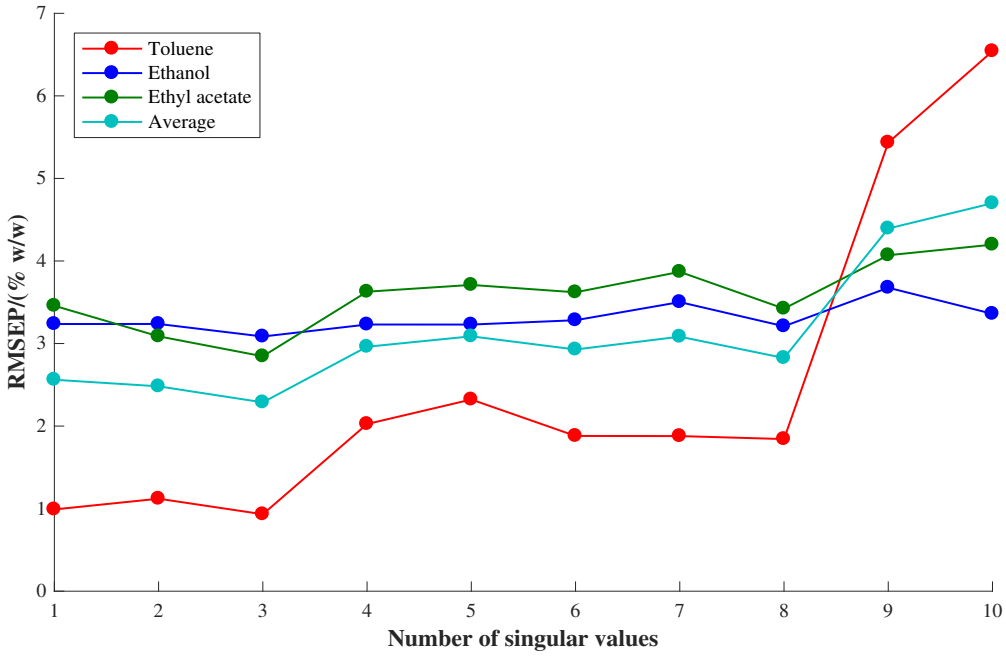

Figure 6.70 - RMSEP versus number of singular values for PLS1 models built using ^{1}H low-field NMR spectra of calibration samples in dataset 3 with reference deconvolution, applied to the test samples in dataset 4 with reference deconvolution and SST (aligned with RAFFT, 2 LVs included).

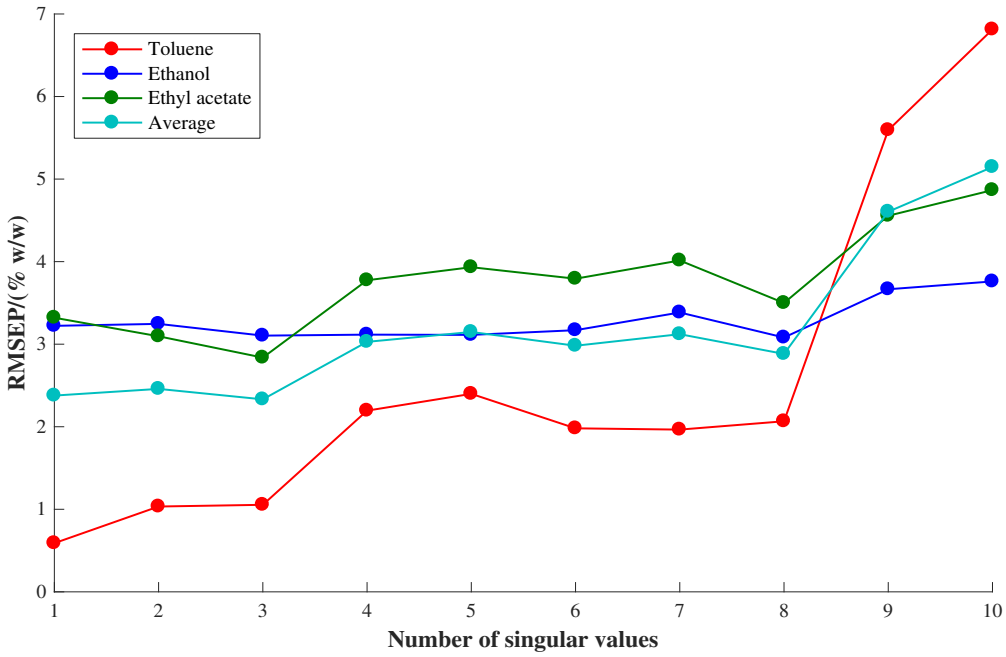

Figure 6.71 - RMSEP versus number of singular values for PLS1 models built using ^{1}H low-field NMR spectra of calibration samples in dataset 3 with reference deconvolution, applied to the test samples in dataset 4 with reference deconvolution and SST (aligned with RAFFT, 3 LVs included).

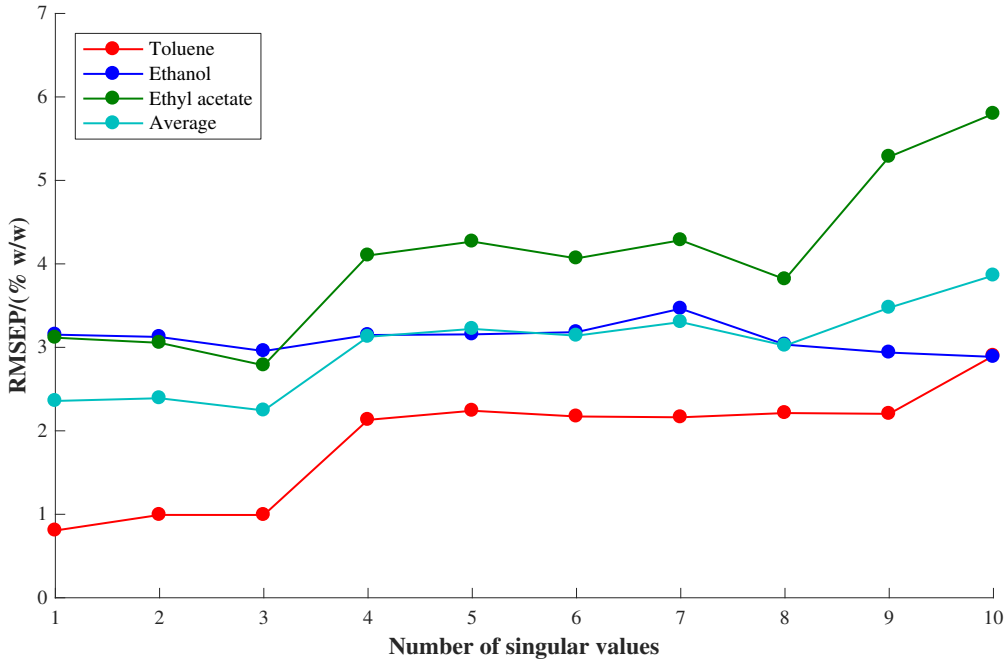

Figure 6.72 - RMSEP versus number of singular values for PLS1 models built using ^{1}H low-field NMR spectra of calibration samples in dataset 3 with reference deconvolution, applied to the test samples in dataset 4 with reference deconvolution and SST (aligned with RAFFT, 4 LVs included).

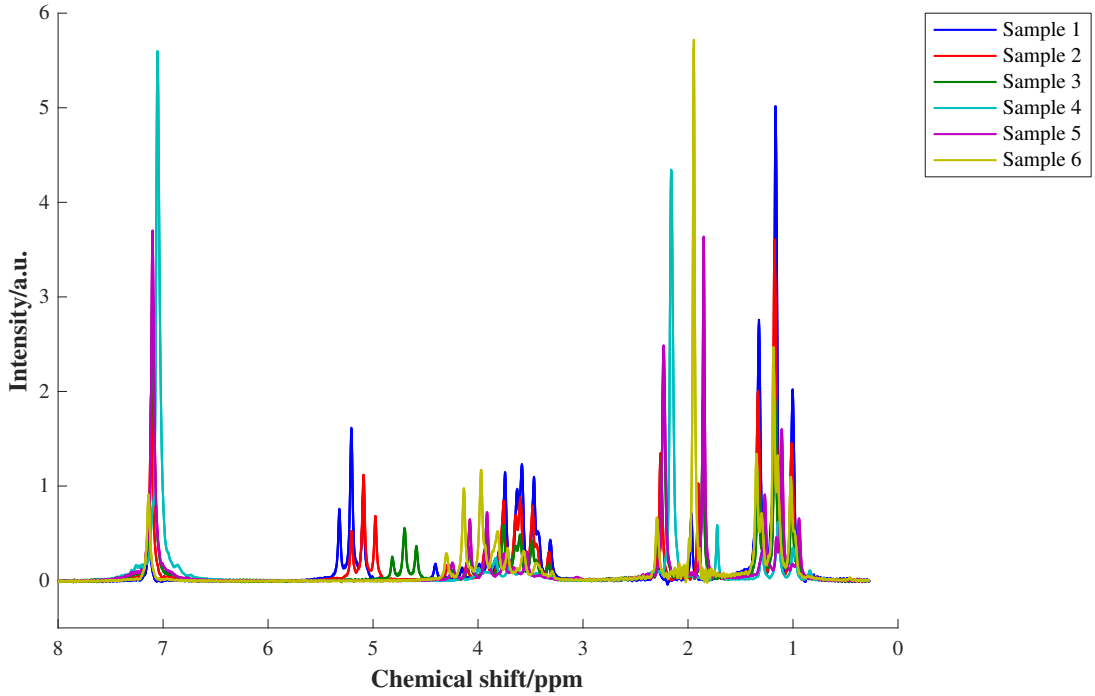

Figure 6.73 - ^{1}H low-field NMR spectra of test samples in dataset 4 (no alignment), with reference deconvolution and calibration transfer by SST (using 3 singular values).

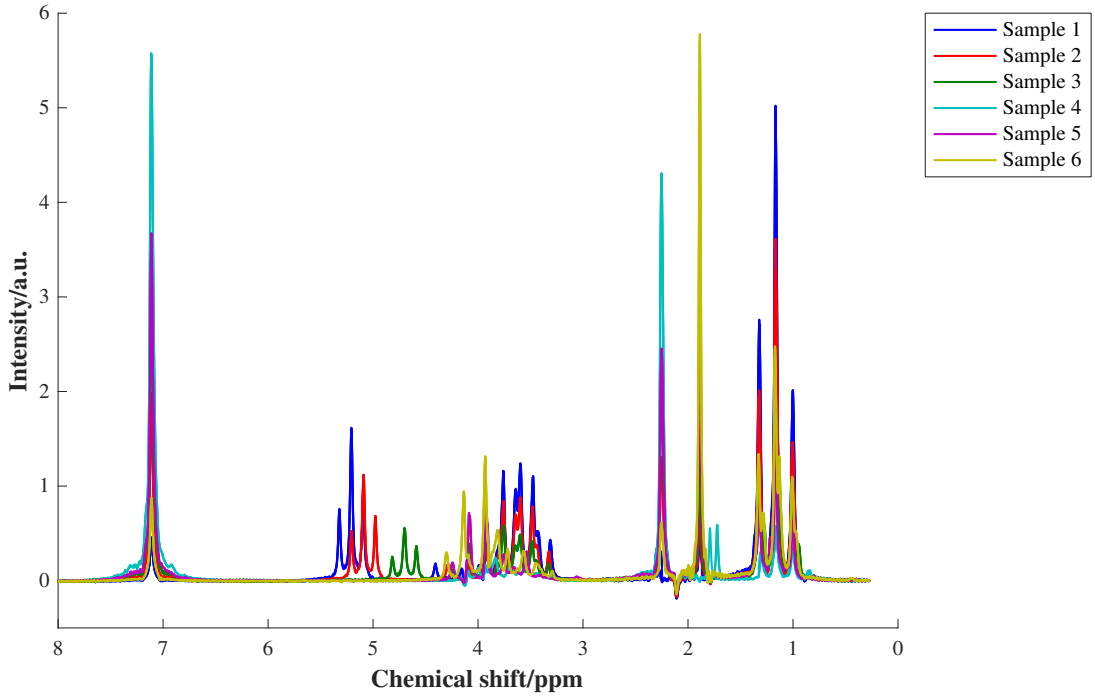

Figure 6.74 - ^{1}H low-field NMR spectra of test samples in dataset 4, with reference deconvolution, alignment by RAFFT and calibration transfer by SST (using 1 singular value).